UNIFIED MODEL FOR CONCRETE COLUMNS CONFINED BY FIBER-REINFORCED POLYMER JACKETS WITH PRACTICAL APPLICATIONS

by

Domingo A. Moran

A dissertation submitted to the faculty of
The University of Utah
in partial fulfillment of the requirements for the degree of

Doctor of Philosophy

Department of Civil and Environmental Engineering

The University of Utah

May 2011

Copyright © Domingo A. Moran 2011

All Rights Reserved

The University of Utah Graduate School

STATEMENT OF DISSERTATION APPROVAL

The dissertation of **Domingo A. Moran**

has been approved by the following supervisory committee members:

Chris Pantelides	, Chair	**04/30/2009** Date Approved
Larry Reaveley	, Member	**04/30/2009** Date Approved
Janice Chambers	, Member	**04/30/2009** Date Approved
Evert Lawton	, Member	**04/30/2009** Date Approved
Daniel Adams	, Member	**04/30/2009** Date Approved

and by **Paul J. Tikalsky**, Chair of the Department of **Civil and Environmental Engineering**

and by Charles A. Wight, Dean of The Graduate School.

ABSTRACT

Despite numerous experimental and analytical investigations on the compressive behavior of fiber-reinforced polymer (FRP) confined concrete sections, researchers have been unable to develop a unified theoretical stress-strain model that can accurately capture and describe the axial compressive and resultant transverse dilation behavior of various FRP-jacketed concrete column shapes.

In this dissertation, a mechanics-based unified stress-strain model is introduced; this model is applicable to FRP-confined concrete sections of various shapes that can accurately capture both the compressive and dilation behavior of rectangular, square, oval, circular, and elliptical FRP-confined concrete members using the concept of diagonal dilation and diagonal equilibrium of the FRP-confined concrete section with a minimum number of curve-fitting parameters based on experiments.

This is accomplished by including the general concepts of elasticity, damage mechanics, soils mechanics, and plasticity theory in the development of a theoretically sound mechanics-based stress-strain model for FRP-confined concrete that takes into consideration the macrostructural effects of the increase in internal damage (i.e., increase in dilation) and the beneficial effects contributed by the kinematic restraint provided by the confining elastic FRP jacket.

The proposed stress-strain model's ability to accurately describe the compressive behavior of FRP-confined concrete of various geometrical shapes will depend on its

ability to capture the restraint sensitivity of the confined concrete core and the effects that the shape of the confining FRP jacket has on the jacket's ability to restrain the transverse dilation of the confined concrete core.

To my dad, may he rest in peace.

To my one and true friend, the love of my life, my wife Judy,

and to my life, my kids David and Ana.

TABLE OF CONTENTS

LIST OF TABLES

ACKNOWLEDGEMENTS

I would like to thank each of the five members of my committee, Janice J. Chambers, Evert C. Lawton, Lawrence D. Reaveley, Daniel O. Adams, and Chris P. Pantelides, for their support and guidance in making this dissertation possible. The advice, patience, and assistance received from my advisor Chris P. Pantelides were instrumental in completing the work presented in this dissertation.

Finally I would like to thank my wife, Judith A. Moran, and kids, David A. Moran and Ana Y. Moran, for their loving support, patience, and encouragements throughout this period of our lives.

CHAPTER 1

INTRODUCTION

In recent years, fiber-reinforced polymer (FRP) reinforcement has been introduced for shear and flexural strengthening of reinforced concrete beams, columns, beam-column members, and beam-column joints. These advanced composite materials are used widely in the aerospace and sports industries. Recently, their use has been extended to the development of new rehabilitation, strengthening, and repair technologies for improving existing reinforced concrete.

Rehabilitation and strengthening techniques of applying surface-bonded FRP reinforcement to reinforced concrete columns and beams are a relatively new field of research that has received much attention in the last 30 years. Researchers have used externally applied FRP reinforcement for the seismic retrofit of reinforced concrete columns and bridge systems (Saadatmanesh et al. 1994, Seible et al. 1997, Xiao and Ma 1997, Pantelides et al. 1999, 2001, Ozbakkaloglu and Saatcioglu 2006, 2007); for improving the flexural (Haragli 2005, Mosalam et al. 2007, Binici and Mosalam 2007,) and compressive (Demers and Neale 1999, Pessiki et al. 2001, Mathys et al. 2005, Tastani et al. 2006, Eid et al. 2008, 2009) behavior of reinforced concrete columns; for improving the shear and flexural behavior of reinforced concrete beams (Saadatmanesh and Ehsani 1991, Ritchie et al. 1991, Triantafillou et al. 1992, Al-Sulaimani et al. 1994, Kaliakin et

al. 1996, Chajes et al. 1995 Varastehpour and Hamelin 1997, Triantafillou 1998, Rahimi and Hutchison 2001), among others; and improving the shear capacity of reinforced concrete beam-column connections (Gergely et al. 1998, Pantelides et al. 1999, 2001, Antonopoulus and Triantofillou 2002).

One major impediment encountered by many researchers is the development of a theoretical stress-strain model that can accurately describe the axial compressive behavior and axial strain-induced dilation behavior of rectangular, square, oval, circular, and elliptical FRP-jacketed concrete columns. Until recently, the development of stress-strain models for FRP-confined concrete sections has been limited to specific cross-sectional jacket shapes, such as circular or square sections which are subjected to essentially uniform equibiaxial confinement. The goal of this investigation is to develop a unified theoretical mechanics-based stress-strain model that can accurately describe the compressive and dilation behavior of several common types of FRP-jacketed concrete column sections, using the concepts of diagonal dilation and equilibrium of FRP-confined concrete and a Mohr-Coulomb-type failure criterion for confined concrete. To the knowledge of the writer, a unified stress-strain model based on theoretical mechanics that can accurately represent the uniaxial compressive behavior of FRP-confined concrete sections of various cross-sectional shapes has not been achieved to date by other researchers.

CHAPTER 2

LITERATURE REVIEW

Compressive Stress-Strain Models for Plain Concrete

Since the mid-1930s, research into the compressive stress-strain behavior of plain concrete columns has yielded the development of several analytical stress-strain models for confined and unconfined concrete. Among these models, the most recognized and widely used is the Popovics (1973) fractional model for plain concrete in compression. Several researchers (Carreira and Chu 1985, Collins et al. 1993, Wee et al. 1996, Mansur et al. 1997, Chin et al. 1997) have incorporated and improved the accuracy of the Popovics (1973) fractional model in modeling the compressive stress-strain behavior of low, medium, and high-strength concrete. Pantazopoulou (1995) and Pantazopoulou and Mills (1995) have recognized that the nonlinearity of the compressive behavior of plain unconfined concrete is due to the reduction in the load-carrying area of the concrete cross section in compression that results from the expansion (i.e., dilation) induced by micro cracking suffered by the area supporting the axial load.

There has been a significant amount of research in the compressive behavior of concrete in biaxial (Kupfer et al. 1969, Mills and Zimmerman 1970, Kupfer and Gerstle 1973, Darwin and Pecknold 1977, Gerstle 1981a) and triaxial compression state of stress (Richart et al. 1928, Mills and Zimmerman 1970, Palaniswany and Shah 1974, Newman and Newman 1971, Kotsovos and Newman 1978, Gerstle 1981b, Imran 1994, Xie et al.

1995, Attard ands Setunge 1996, Ansari and Li 1998, Sfer et al. 2002). These experimental investigations have shown that the behavior of concrete under either biaxial or triaxial compressive stresses improves significantly in terms of an increase in the ultimate major principal compressive strength and strain and an increase in strain ductility. For the majority of biaxial and triaxial plain concrete tests, the out-of-plane confinement was provided by mechanical means (i.e., platens, brushes, etc.). In the case of concrete cylinders in a triaxial compression state of stress, the out-of-plane lateral confinement was provided by means of fluid pressure, which was maintained constant (Richart et al. 1928, Palaniswany and Shah 1974, Kotsovos and Newman 1978, Gerstle 1981b, Imran 1994, Xie et al. 1995, Ansari and Li 1998, Sfer et al. 2002), or it was increased in a stepwise manner (Imran 1994) as the principal compressive axial load was monotonically increased. Pantazopoulou (1995) recognized that the enhancement in compressive strength and ductility of concrete in the biaxial and triaxial compression state of stress is associated with the kinematic restraint imposed at the surface of the concrete member by the confining device.

Confinement Models for Concrete Confined by Transverse Steel Reinforcement

Several analytical stress-strain models for reinforced concrete members passively confined by transverse steel reinforcement have been introduced in the past. A majority of these models were derived based on the compressive behavior of rectangular, circular, and square reinforced concrete members restrained by closely spaced transverse steel reinforcement. Sheikh (1982) and Sakai and Sheikh (1989) produced a series of excellent reviews on the majority of the analytical confinement models developed prior to 1989.

The most notable stress-strain models for normal weight, medium-strength (20-40 MPa) concrete developed prior to 1989 are the Mander et al. (1988) analytical model for steel-confined concrete, which utilized the Popovics (1973) fractional model, and the Ahmad and Shah (1982a,b) stress-strain model. For the case of steel confined, high-strength concrete (40-80 MPa) members, the most notable stress-strain models are those introduced by Saatcioglu and Razvi (1992), Saatcioglu et al. (1995), Cusson and Paultre (1995), Ibrahim and McGregor (1996), and Attard and Setunge (1996).

Confinement Models for Concrete Confined by FRP Jackets

Since the early attempts by Kurt (1978) on the stress-strain behavior of concrete-filled structural PVC columns and by Fardis and Khalili (1981, 1982) on the stress-strain behavior of FRP-confined concrete cylinders, numerous experiments have been performed to investigate the compressive stress-strain behavior of concrete confined by FRP spirals (Ahmad et al. 1991, Nanni and Bradford 1995), bonded FRP wraps (Harmon and Slattery 1992, Demers et al. 1996, Picher et al. 1996, Kharbari and Gao 1997, Miyauchi et al. 1997, Watanabe et al. 1997, Harmon et al. 1998b, Kono et al. 1998, Saaman et al. 1998, Toutanji 1999, Rochette and Labossièrre 2000, Wu and Xiao 2000, Xiao and Wu 2000, 2003, Carey 2002, Teng and Lam 2002, 2004, Lam and Teng 2003a,b, Carey and Harries 2003, Chaallal et al. 2003a,b, Tamusz et al. 2006, 2007, Saenz and Pantelides 2007, Toutanji et al. 2007, Shehata et al. 2007), among others, and nonbonded FRP tubes (Mirmiran 1997, Mirmiran and Shahawy 1996, 1997a,b, Saafi et al. 1999, Fam and Rizkalla 2001a,b, Carey 2003, Carey and Harries 2003, Yan and Pantelides 2006, Yan et al. 2006), among others.

Since the 1990s, the development of stress-strain models for FRP-confined concrete was limited to modification of the Mander et al. (1988) confinement model originally developed for reinforced concrete members confined by transverse steel reinforcement or steel jackets (Saadatmanesh et al. 1994, Mirmiran and Shahawy 1996, Spoelstra and Monti 1999, Fam and Rizkalla 2001a,b).

Beginning in the late 1990s and early 2000s, several models specifically suited for FRP-confined concrete columns have been proposed, in particular the models introduced by Miyauchi et al. (1997), Kono et al. (1998), Saaman et al. (1998), Toutanji (1999), Saafi et al. (1999), and Xiao and Wu (2000).

De Lorenzis and Tepfers (2003), Lam and Teng (2003a), and Teng and Lam (2004) produced a series of excellent reviews on the majority of the analytical and empirical stress-strain models for FRP-confined developed prior to 2003.

In recent years, researchers have successfully developed stress-strain models for rectangular (Restrepo and DeVino 1996, Lam and Teng 2003a, Chaalal et al. 2003a, Monti and Nistico 2007), square (Campione and Miraglia 2003, Lam and Teng 2003b, Masia et al. 2004, Marques et al. 2004, Monti and Nistico 2007), circular (Kharbari and Gao 1997, Harmon et al. 1998b, Saaman et al. 1998, Spoelstra and Monti 1999, Toutanji 1999, Saafi et al. 1999, Wu and Xiao 2000a,b, Lam and Teng 2002, Xiao and Wu 2002, 2003, Fujikake et al. 2004, Marques et al. 2004, Mandal et al. 2005, Saenz and Pantelides 2007, Teng et al. 2007) and elliptical (Teng and Lam 2002, Yan 2005, Yan and Pantelides 2006) FRP-confined concrete sections.

Damage-Based Constitutive Models for Concrete Confined by FRP Jackets

Despite the successful application of the aforementioned models, few models can accurately capture the dilation and compressive behavior of passively and actively confined concrete as the damage-based model introduced by Imran (1994), Pantazopoulou and Mills (1995), Pantazopoulou (1995), and Imran and Pantazopoulou (1996). These constitutive models are the first to recognize that concrete is a restraint sensitive material, rather than a pressure sensitive material, as is typically assumed in the analysis of reinforced concrete sections. This implies that if lateral kinematic restraint is provided during loading, the confining element will induce some confining pressure whose magnitude will depend on the lateral stiffness of the confining device. In addition, during loading, the stiffness of the confining device can also determine the degree of volumetric expansion (if any) by controlling the degree of micro-crack and macro-crack growth and the contraction, compaction, collapse, or nucleation of internal voids and capillary pores present within the microstructure of the concrete core.

Recently, several investigators including Spoelstra and Monti (1999), Marques et al. (2004), and Saenz (2004) have attempted to incorporate the damaged-based model introduced by Pantazopoulou (1995) into biaxial confinement models that describe the compressive behavior of circular (Spoelstra and Monti 1999, Saenz 2004) and square (Marques et al. 2004) FRP-confined concrete sections. Unfortunately, Pantazopoulou's (1995) damage-based model can only capture the compressive and dilation behavior of unconfined and passively and actively confined circular concrete sections.

The Spoelstra and Monti (1999) model is an iterative stress-train model for circular FRP-confined concrete sections that combines the Pantazopoulou (1995) damage-based model's ability to capture the compressive and dilation behavior of unconfined and confined circular concrete sections, with the Mander et al. (1988) confinement model's ability to capture the increase in the ultimate compressive strength and strain that result from the passive confining pressure provided by the restraining circular FRP jacket.

Recently, Marques et al. (2004) introduced an iterative model that can be considered to be an updated version of the Spoelstra and Monti (1999) model for predicting the compressive behavior of both circular and square FRP-confined concrete sections.

The Saenz (2004) model is a constitutive model that combines the Pantazopoulou (1995) model with unique volumetric and dilation formulations that can accurately capture the dilation and compressive behavior of circular FRP-confined concrete sections.

The Yan (2005) stress-strain model is a constitutive model that combines the Willam and Warnke (1975) parabolic ultimate surface for concrete in a triaxial compression state of stress and the Pantazopoulou (1995) dilation model to capture the compressive behavior and resultant average transverse dilation of elliptical and circular FRP-confined concrete sections.

In this investigation, the proposed stress-strain model takes into consideration the shortcomings of other stress-strain models for FRP-confined concrete sections developed in the past and expands upon the knowledge obtained by these researchers. This is accomplished herein by developing a theoretically sound, mechanics-based stress-strain model for FRP-confined concrete sections of various geometric shapes that can

accurately capture both the strain-softening compressive behavior of concrete members confined by low transverse stiffness FRP jackets and the quasi-bilinear strain-hardening compressive behavior of members confined by moderate to high transverse stiffness FRP jackets.

A generalized and theoretically sound stress-strain model based on fundamental principles allows for accurate estimates of the displacement and curvature ductility of reinforced concrete beam-columns and the FRP jacket thickness that is required to achieve a certain performance level during a seismic event.

CHAPTER 3

RESEARCH GOALS

Thus far, investigators have not developed a unified theoretical stress-strain model that can accurately capture and describe the axial compressive and transverse dilation behavior of various FRP-jacketed concrete column shapes.

Despite numerous experimental and analytical investigations, there is a lack of a unified stress-strain model that can accurately capture at a fundamental level and in a unified manner the compressive behavior of rectangular, square, oval, circular, and elliptical FRP-confined concrete members.

The principal goals of this dissertation are as follows:

1. To develop a theoretically sound unified damage-based model for rectangular, square, oval, circular and elliptical FRP-confined concrete sections in compression.
2. To develop a theoretically sound design procedure for estimating the required FRP jacket thickness for concrete column sections of various shapes confined by FRP jackets, that are subjected to combined axial compression and flexure, to achieve a certain performance level during a seismic event.

Unified Damage-Based Model for FRP-Confined Concrete

The first goal of this dissertation is to develop a unified damage-based model for rectangular, square, circular, and elliptical FRP-confined concrete compression members

that can accurately capture both the axial strain-induced dilation and compressive behavior.

In this dissertation, a general mechanics-based and theoretically sound damage model for FRP-confined concrete is developed, applicable to bonded and unbonded FRP jackets of various geometrical shapes, with a limited number of curve-fitting parameters. The model predicts the dilation and axial compressive behavior of FRP-confined concrete sections exhibiting either a strain-softening or strain-hardening compressive behavior, as shown in **Figure 3.1**.

The stress-strain models for FRP-confined concrete sections introduced thus far by others researchers are of limited applicability. This may include limitations on the FRP jacket shape (i.e., circular or square sections); limitations on the FRP jacket construction type (i.e., bonded, or unbonded); limitations on the type of compressive behavior (i.e., strain softening or strain hardening); and limitations imposed by the use of curve fitting techniques of experimental data, among others. In this dissertation, a new theoretical stress-strain model for FRP-confined concrete sections is introduced which considers the shortcomings of models introduced in the past and expands upon the knowledge obtained thus far by other researchers.

A model's ability to accurately describe the compressive behavior of FRP-confined concrete of various geometrical cross-sectional shapes depends on its ability to capture the restraint sensitivity of the confined concrete core. A constitutive model for FRP-confined concrete needs to recognize that restraint sensitivity of the concrete core not only affects its compressive strength and ductility but also its axial strain-induced transverse dilation behavior.

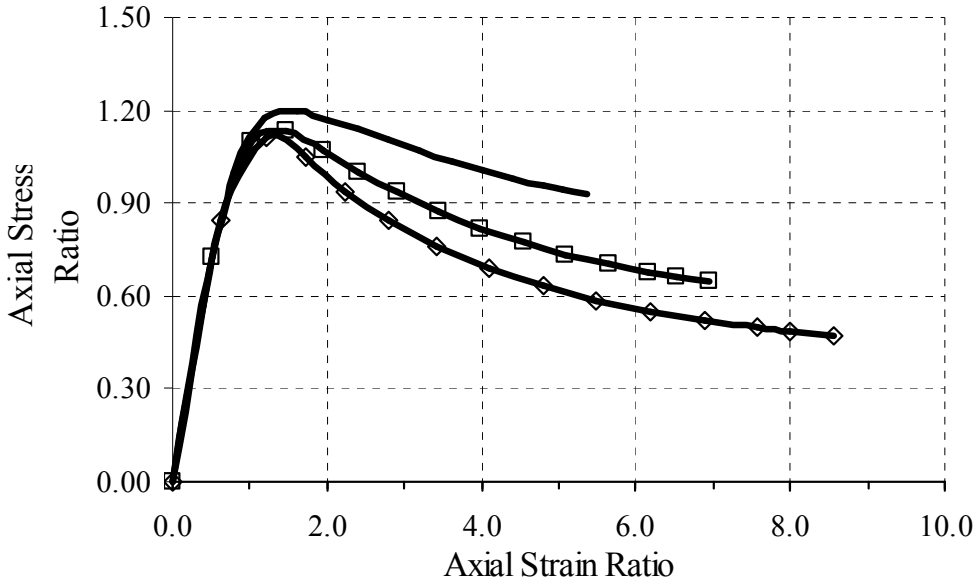

(a)

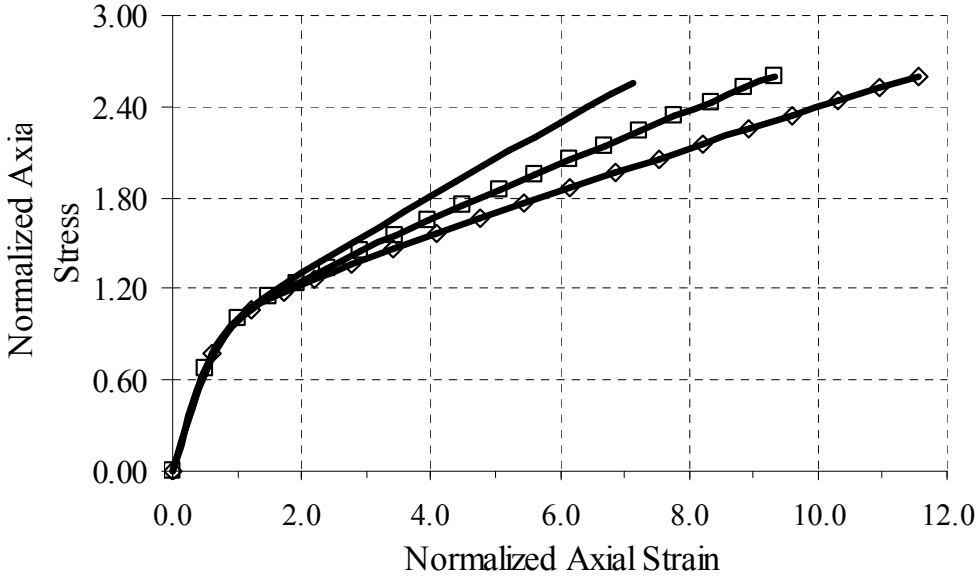

(b)

Figure 3.1 Typical axial stress-strain ratio curves of concrete sections exhibiting (a) strain-softening and (b) strain-hardening compressive behavior.

The unconfined and confined concrete core is considered to be a restraint sensitive material rather than a pressure sensitive material (Pantazopoulou 1995). This indicates that the dilation behavior of the FRP-confined concrete depends on the lateral kinematic restraint provided by the thin elastic FRP jacket at the surface of the confined concrete core, rather than on the passive confining pressure provided by the restraining FRP jacket that results from transverse dilation of the FRP-confined concrete core.

FRP Jacket Design Procedure

The second goal of this research is the development of a moment versus curvature based design procedure for estimating the required FRP jacket thickness and size for rectangular, square, and circular reinforced concrete columns confined by FRP jackets to attain an increase in axial strength or ductility in order to achieve a given performance level during a seismic event.

Typically, existing circular concrete sections are confined by circular FRP jackets. However, existing square concrete sections can be confined by either square FRP jackets or they can be shape modified using circular FRP jackets (Yan 2005). Furthermore, existing rectangular concrete sections can be confined by rectangular FRP jackets or they can be shape-modified using either oval or elliptical FRP jackets (Yan 2005).

The applicability of the damage-based model for FRP-confined concrete proposed herein is expanded and included in the development of a design procedure for estimating the required FRP jacket thickness based on the expected displacement and curvature ductility demand imposed on reinforced concrete columns during a seismic event.

CHAPTER 4

GEOMETRIC AND MECHANICAL PROPERTIES OF CONCRETE SECTIONS CONFINED BY FIBER-REINFORCED POLYMER JACKETS

In this chapter, a unique set of analytical relationships are introduced in modeling the compressive stress-strain and transverse dilation behavior of rectangular, square, oval, circular, and elliptical concrete sections confined by thin elastic FRP jackets. The proposed model requires the introduction of a series of unique mathematical relationships for the geometric and mechanical properties of the confining FRP jacket, which are then used in modeling both the dilatancy and compressive behavior of FRP-confined concrete sections of various geometrical shapes (rectangular, square, oval, circular, and elliptical concrete sections in particular), as demonstrated in Chapters 6, 7, 8 and 10, subjected to either a uniform (circular) or a nonuniform (rectangular, square, oval and elliptical) triaxial compression state of stress, as demonstrated in Chapter 9.

In this chapter a series of mathematical relationships are developed to describe the geometric and mechanical properties of FRP-confined concrete (FCC) sections of various shapes, which includes circular, elliptical, rectangular, square, and oval sections. These relationship are then incorporated into Chapters 5-10 to describe the uniaxial compressive

behavior and the transverse and diagonal dilation behavior of FRP-confined concrete sections.

Geometric and Mechanical Properties of FRP-Confined Concrete Sections

In this investigation, several geometric **Figure 4.1** and mechanical properties of FCC sections were found to affect the dilation and axial compressive behavior of the FCC sections shown in **Figure 4.2**, as a result of the elastic properties of the confining FRP jacket.

FRP-Confined Concrete Section Geometry

In this investigation it was found that in addition to the FRP jacket stiffness, the shape of the FRP-confined concrete cross-section, as shown in **Figures 4.1** and **4.2**, constitutes the greatest contribution to both the dilatancy and axial compressive stress-strain behavior of the FCC section. The geometric parameters of the FRP-jacketed sections, shown in **Figures 4.1** and **4.2**, which significantly affect the compressive and dilation behavior of the FCC are as follows

1. The aspect ratio of the section α_{sh}
2. The angle of inclination of the main diagonal D_c of the FCC section θ_d
3. The jacket corner aspect ratio of rectangular, square, and oval FCC sections α_j
4. The shape of the effectively confined concrete core, as defined by the confining efficiency k_e of the FRP jacket and

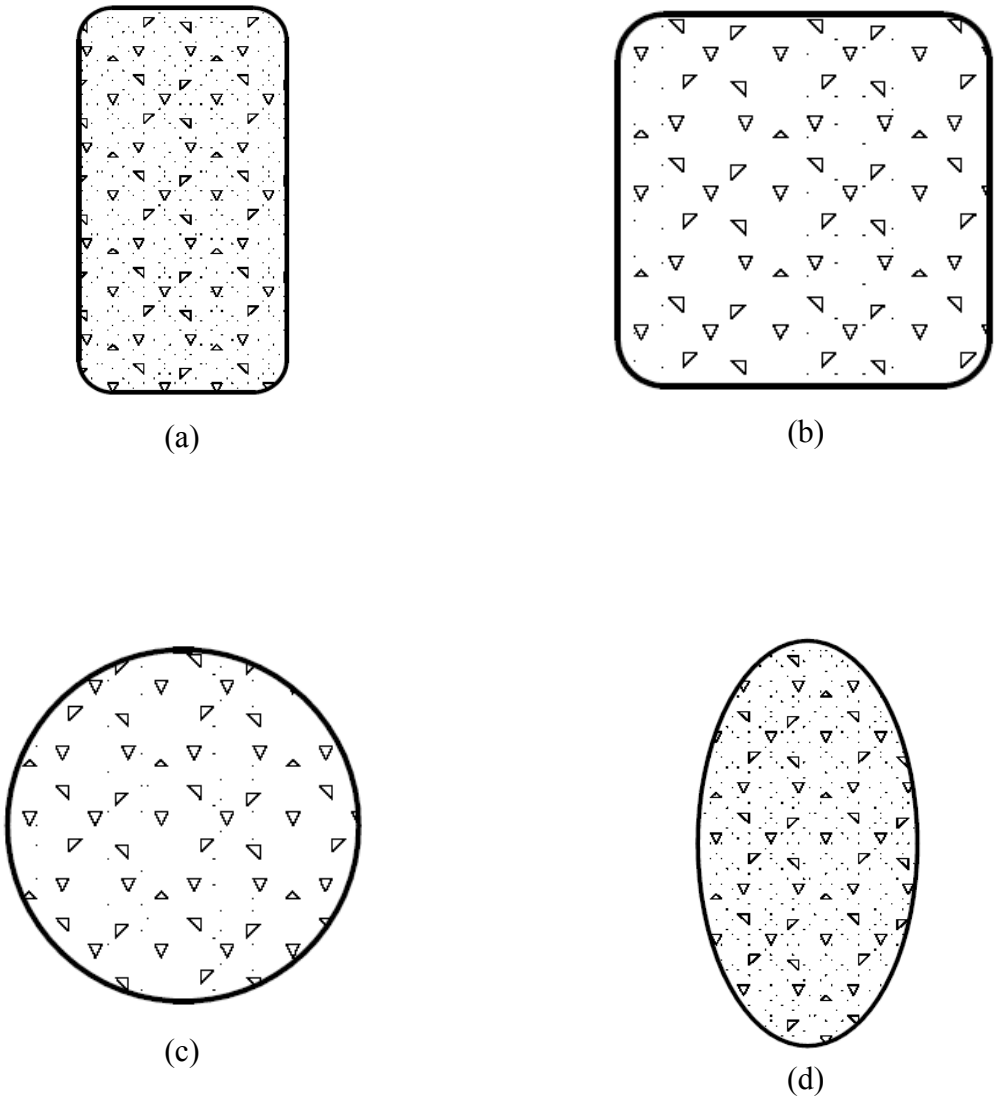

Figure 4.1 FRP-confined concrete sections of various shapes: (a) rectangular, (b) square, (c) circular, and (d) elliptical.

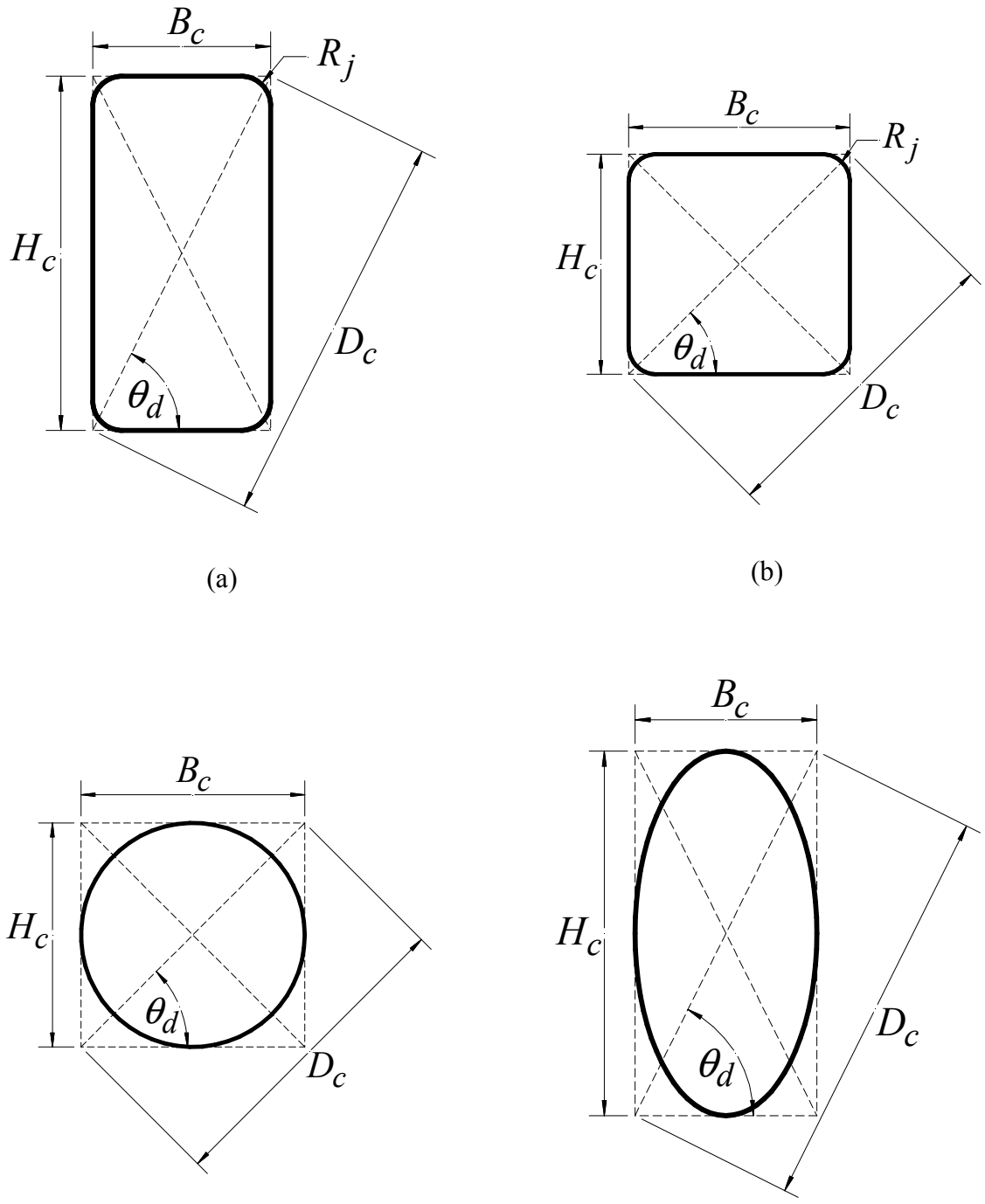

Figure 4.2 Geometry of FRP-confined concrete sections of various shapes: (a) rectangular, (b) square, (c) circular, and (d) elliptical.

5. The effective transverse stiffness $\left(C_{je}\right)_{sh}$ and normalized transverse stiffness $\left(K_{je}\right)_{sh}$ of the confining elastic FRP jacket.

These geometric parameters and mechanical properties of the FCC section are introduced in what follows.

The angle of inclination θ_d of the main diagonal D_c and the section aspect ratio α_{sh} of the FCC sections shown in **Figure 4.2** are given by:

$$\theta_d = \tan^{-1}\left(\alpha_{sh}\right) \tag{4.1}$$

$$\alpha_{sh} = \frac{H_c}{B_c} \tag{4.2}$$

$$D_c = \sqrt{\left(H_c\right)^2 + \left(B_c\right)^2} = H_c\sqrt{1+\left(\frac{1}{\alpha_{sh}}\right)^2} = B_c\sqrt{1+\left(\alpha_{sh}\right)^2} \tag{4.3}$$

where B_c and H_c are the overall minor and major dimensions of the FCC cross-section, respectively, as shown in **Figure 4.2** and the oval section shown in **Figure 4.3**.

The jacket corner aspect ratio α_j of the rectangular, square, and circular FCC sections shown in **Figure 4.2** and the oval section of **Figure 4.3** are defined as:

$$\alpha_j = \frac{R_j}{H_c} = \frac{R_j}{\alpha_{sh}B_c} \tag{4.4}$$

where $0 \le \alpha_j \le 0.50$. The upper bound value of $\alpha_j = 0.50$ represents the special case of a circular FRP-confined concrete section for which $D_j = H_c = B_c = 2R_j$ (i.e., $\alpha_{sh} = 1.0$ and $\alpha_j = 0.50$).

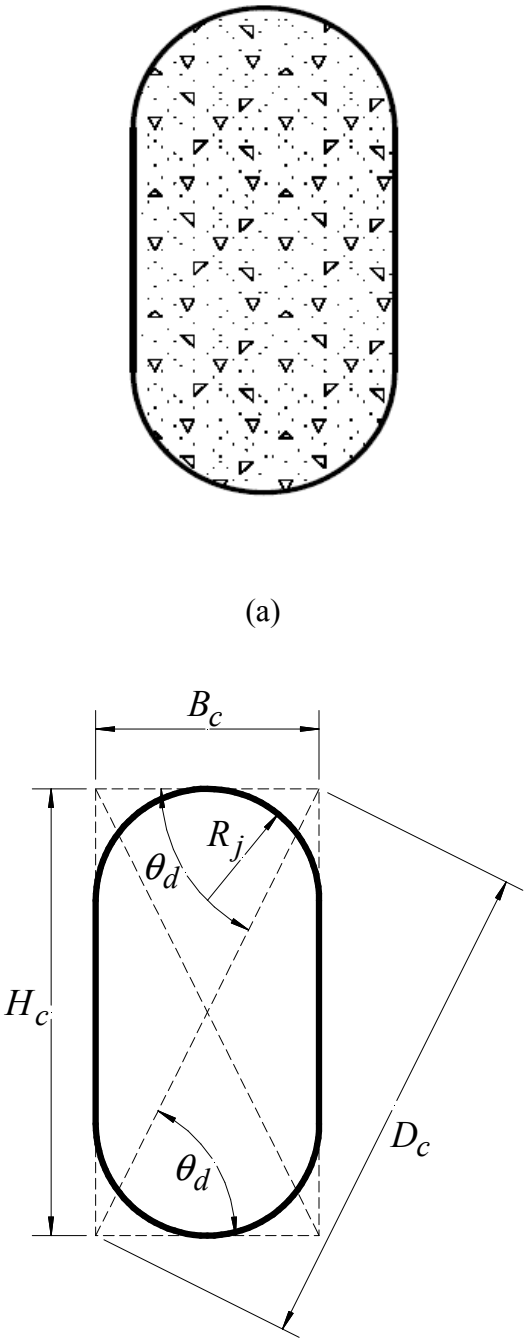

Figure 4.3 Oval FRP-confined concrete sections: (a) typical section and (b) typical geometry.

The lower bound value of $\alpha_j = 0$ indicates that no rounding of the corners is provided. Also, D_j is the overall diameter of the circular FCC section.

For rectilinear sections, such as rectangular, square, and oval FCC sections, the upper bound value of α_j is given by $(\alpha_j)_{\max} = 1/(2\alpha_{sh})$, or when $R_j = B_c/2$. When $\alpha_{sh} = 1.0$ and $(\alpha_j)_{\max} = 0.50$ it indicates a circular FCC section, whereas when $\alpha_{sh} > 1.0$, an oval FRP-confined section occurs when $R_j = B_c/2$ or when $\alpha_j = (\alpha_j)_{\max} = 1/(2\alpha_{sh})$, as shown in **Figure 4.3.**

Another geometric parameter that significantly influences the dilation and compressive behavior of FCC sections is the shape of the effectively confined concrete core, as shown in **Figure 4.4**. In this figure, the ineffectively confined concrete core along the faces of the square and rectangular FCC section is shown as cross-hatched areas.

These areas are approximated by parabolas with an initial tangent equal to the aspect ratio α_{sh} at the minor B_c sides and an initial tangent equal to the inverse of the aspect ratio $1/\alpha_{sh}$ at the major H_c sides as shown in **Figure 4.4**. From these figures, it can be observed that the effectively confined section has a major H_{eff} and minor B_{eff} dimension and an effective aspect ratio α_{eff}, that are given by:

$$\alpha_{eff} = \frac{H_{eff}}{B_{eff}} = \frac{h_{eff}}{b_{eff}} = \alpha_{sh} \tag{4.5}$$

$$H_{eff} = \frac{H_c}{2}(1 + 2\alpha_{sh}\alpha_j) \;;\; B_{eff} = \frac{B_c}{2}(1 + 2\alpha_{sh}\alpha_j) \tag{4.6}$$

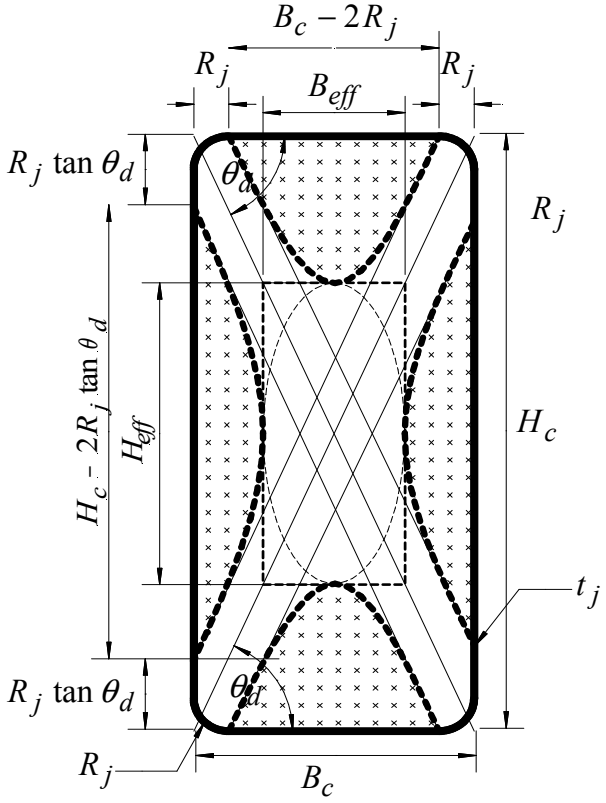

(a)

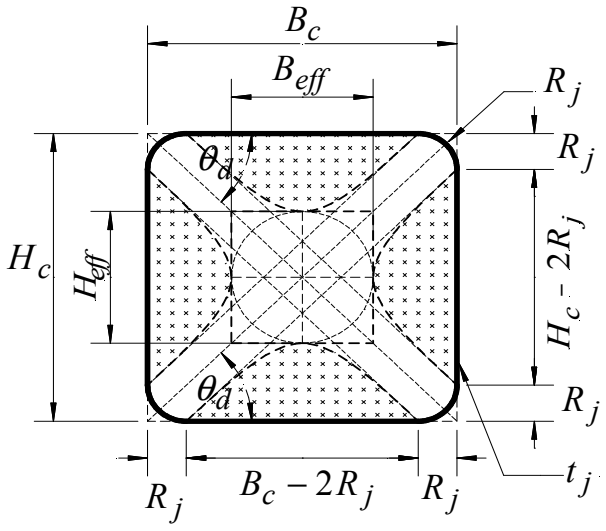

(b)

Figure 4.4 Geometry of effectively FRP-confined concrete in (a) rectangular and (b) square sections.

$$h_{eff} = \frac{H_{eff}}{2} \;\; ; \;\; b_{eff} = \frac{B_{eff}}{2} \tag{4.7}$$

where h_{eff} and b_{eff} are the major and minor axes of the effectively confined elliptical or circular concrete core shown in **Figure 4.4**. The analysis of the rectangular FCC sections shown in **Fig. 4.4** is similar to the analysis of rectangular reinforced FCC sections introduced by Lam and Teng (2003b)

It is demonstrated herein that the shape of the FCC core and the geometric parameters introduced in Eqs. (4.1) through (4.7) contribute to the overall decrease or increase in both the compressive strength and strain ductility of the FRP-confined concrete sections considered in **Figures 4.1-4.4,** as established in Chapters 9 and 10. In addition, these geometric parameters also significantly influence the transverse dilation behavior of the FRP-confined concrete core, as demonstrated in Chapters 7 and 8.

FRP Jacket Confining Efficiency

The confining efficiency of the confining element, be it closely spaced transverse steel reinforcement, steel jackets, or FRP jackets, is a geometric and mechanical property of the FRP-confined concrete section that determines the effectiveness of the confining FRP jacket layout in curtailing the axial strain-induced transverse dilation of the confined concrete core.

The confinement efficiency k_e (Mander et al. 1988) of the transverse reinforcement, which is defined as the ratio of the least effectively confined concrete core area A_{ec} to the net concrete core area A_{nj} is given by:

$$k_e = \frac{A_{ec}}{A_{nj}} = 1 - \frac{A_{ic}}{A_{nj}} \tag{4.8}$$

$$A_{ec} = A_{nj} - A_{ic} \tag{4.9}$$

where A_{ic} is the ineffectively confined concrete core area.

In this chapter, a series of analytical relationships are developed using the concept of an effectively FRP-confined concrete core introduced by Mander et al. (1998), Restrepo and De Vino (1996), and Lam and Teng (2003b). The rate of dilatancy of the FRP-jacketed concrete was found to be significantly affected by the confining efficiency of the FRP jacket k_e, since the dilatancy of the FRP-confined concrete depends on the lateral stiffness of the FRP jacket. In addition, the lateral stiffness of the FRP jacket C_{je}, shown in the following sections, depends on the geometry of the concrete section, the mechanical properties of the FRP jacket, and the confining efficiency of the FRP jacket. A low jacket confining efficiency k_e results in a reduction in the transverse stiffness of the confining elastic rectangular and square FRP jackets in comparison to that of oval, circular, and elliptical FRP jackets.

FRP Jacket Reinforcement Ratio

The reinforcement ratio of the confining transverse reinforcement ρ_{tr} be it closely spaced steel reinforcement, steel jackets, or FRP jackets, is a geometric property of the confining element that is defined as the ratio of the volume of transverse reinforcement V_{tr} to the volume of the confined concrete core V_c, as:

$$\rho_{tr} = \frac{V_{tr}}{V_c} \tag{4.10}$$

For the case of FRP-confined concrete sections, the transverse reinforcement ratio ρ_j of the confining FRP jacket is given by:

$$\rho_j = \frac{V_j}{V_c} \tag{4.11}$$

where V_j is the unit volume of the thin confining elastic FRP jacket, for a unit length FCC section; V_j is essentially equal to the perimeter of the confined concrete core p_{core}, times the thickness of the FRP jacket t_j. For a unit length FCC section, the concrete volume V_c is equal to the net area of the FCC core.

The reinforcement ratio of the FRP jacket, as shown in **Figures 4.2** and **4.3**, depends on the shape of FRP-confined concrete core and the thickness t_j of the confining FRP jacket. As a result, the reinforcement ratio of the confining FRP jacket of any given shape $(\rho_j)_{sh}$ can be expressed as:

$$(\rho_j)_{sh} = \left(\frac{V_j}{V_c}\right)_{sh} = \left(\frac{2t_j}{H_c}\right) C_{sh} \tag{4.12}$$

where C_{sh} is the FRP jacket reinforcement ratio coefficient. A series of mathematical relationships for the jacket reinforcement ratio coefficient C_{sh} of the FRP jacket shapes considered in **Figures 4.2** and **4.3** are introduced in this chapter.

FRP Jacket Confining Stiffness

The lateral confining stiffness of the transverse reinforcement, be it closely spaced transverse steel, steel jackets, or FRP jackets, is a mechanical property of the confining element that depends on the geometric reinforcement ratio of the confining element. For the case of thin elastic FRP jackets having an average transverse modulus E_j and thickness t_j, the transverse stiffness of the FRP jackets C_j, shown in **Figures 4.2** and **4.3**, is defined in what follows.

The effective confining stiffness of the elastic FRP jacket C_{je} is given by:

$$C_{je} = k_e C_j \;\; ; \;\; C_j = \frac{1}{2}\rho_j E_j \tag{4.13}$$

where k_e is the confining efficiency of the FRP jacket as defined in Eq. (4.8). The effective confining stiffness $\left(C_{je}\right)_{sh}$ of an FRP jacket of a given shape, as shown in **Figure 4.2** and **4.3**, is expressed as:

$$\left(C_{je}\right)_{sh} = \left(\frac{t_j}{H_c}\right)\left(k_e\right)_{sh} C_{sh} E_j \tag{4.14}$$

The effective transverse modulus of the FRP jacket along the minor $\left(E_{je}\right)_B$ and major $\left(E_{je}\right)_H$ axes of the FRP-confined concrete section is:

$$\left(E_{je}\right)_B = \left(\frac{2t_j}{H_c}\right)\left(k_e\right)_{sh} E_j \tag{4.15}$$

$$\left(E_{je}\right)_H = \left(\frac{2t_j}{B_c}\right)\left(k_e\right)_{sh} E_j \tag{4.16}$$

The effective confining stiffness $\left(C_{je}\right)_{sh}$ of Eq. (4.14) can be rewritten in terms of $\left(E_{je}\right)_B$ and $\left(E_{je}\right)_H$ as follows:

$$\left(C_{je}\right)_{sh} = \frac{C_{sh}}{2}\left(E_{je}\right)_B = \frac{C_{sh}}{2\alpha_{sh}}\left(E_{je}\right)_H \tag{4.17}$$

The normalized effective stiffness K_{je} of the confining elastic FRP jacket is defined as the ratio of the effective confining stiffness of the FRP jacket C_{je} to the unconfined peak compressive strength of the concrete core f_{co}, as follows:

$$K_{je} = \frac{C_{je}}{f_{co}} \tag{4.18}$$

For an FRP jacket of a given shape, the normalized effective confining stiffness of the FRP jacket $\left(K_{je}\right)_{sh}$, as shown in **Figures 4.2** and **4.3**, is expressed as:

$$\left(K_{je}\right)_{sh} = \frac{\left(C_{je}\right)_{sh}}{f_{co}} \tag{4.19}$$

The effective confining stiffness $\left(C_{je}\right)_{sh}$ and the normalized effective stiffness $\left(K_{je}\right)_{sh}$ of the FRP jacket affect the axial strain-induced dilatancy (i.e., Poisson's effects) and the axial compressive behavior of the FRP concrete sections shown in **Figures 4.2** and **4.3**.

In what follows, a series of numerical relationships are introduced to define the geometric and mechanical properties of rectangular, square, oval, circular and elliptical FRP-confined concrete sections, including elliptical, oval and circular shape modifying FRP jackets.

Rectangular Sections

Confining Efficiency

The concept of effectively confined concrete introduced by Restrepo and deVino (1996) and Lam and Teng (2003) is incorporated into the definition of the FRP jacket confining efficiency k_e. This concept is used in the analysis of rectangular, circular and elliptical reinforced columns confined by continuous oval, circular, or elliptical FRP jackets.

The confining efficiency k_e of oval, circular and elliptical FRP jackets are derived from the general analysis of the effectively confined concrete core area of a rectangular column with rounded corners confined by a continuous rectangular FRP jacket.

The gross cross-sectional area of a rectangular FRP-confined concrete (RFCC) section, as shown in **Figures 4.2(a)** and **4.4(a)**, is defined as:

$$A_g = B_c H_c = \alpha_{sh} (B_c)^2 = \frac{(H_c)^2}{\alpha_{sh}} \tag{4.20}$$

For the case of rectangular, as shown in **Figures 4.2(a)** and **4.4(a)**, and square, as shown in **Figures 4.2(b)** and **4.4(b)**, FRP-jacketed concrete sections, the corners are typically rounded in order to minimize the effects of stress-concentrations at the sharp

corners and to mitigate the premature failure of the FRP jacket due to the presence of sharp edges.

Corner rounding also increases the confining efficiency k_e of the FRP jacket by increasing the effectively confined concrete core area A_{ec}. Accounting for the rounding of the corners to an average radius R_j the net cross-sectional area A_{nj} of a RFCC section, as shown in **Figure 4.5**, is defined as:

$$A_{nj} = A_g - A_r = \frac{(H_c)^2}{\alpha_{sh}}\left[1 - \alpha_{sh}(4-\pi)(\alpha_j)^2\right] = \alpha_{sh}(B_c)^2\left[1 - \alpha_{sh}(4-\pi)(\alpha_j)^2\right] \quad (4.21)$$

$$A_r = (4-\pi)(R_j)^2 = (H_c)^2(4-\pi)(\alpha_j)^2 = (B_c)^2(4-\pi)(\alpha_{sh}\alpha_j)^2 \quad (4.22)$$

where A_r is a reduction in area due to rounding of corners to an average radius, R_j. Rounding of the corners is typically limited to small values due to the presence of transverse and longitudinal steel reinforcing bars just inside the corner, which is typically in the range of 38-75 mm.

The ineffectively confined concrete core area A_{ic}, as shown in **Figure 4.5**, is given by:

$$A_{ic} = (A_{ic})_B + (A_{ic})_H \quad (4.23)$$

where $(A_{ic})_B$ and $(A_{ic})_H$ are the ineffectively confined concrete area along the minor B_c, and major H_c, faces of the RFCC section, respectively. The ineffectively confined core area A_{ic} in a RCC section is shown as a hatched area in **Figure 4.5**.

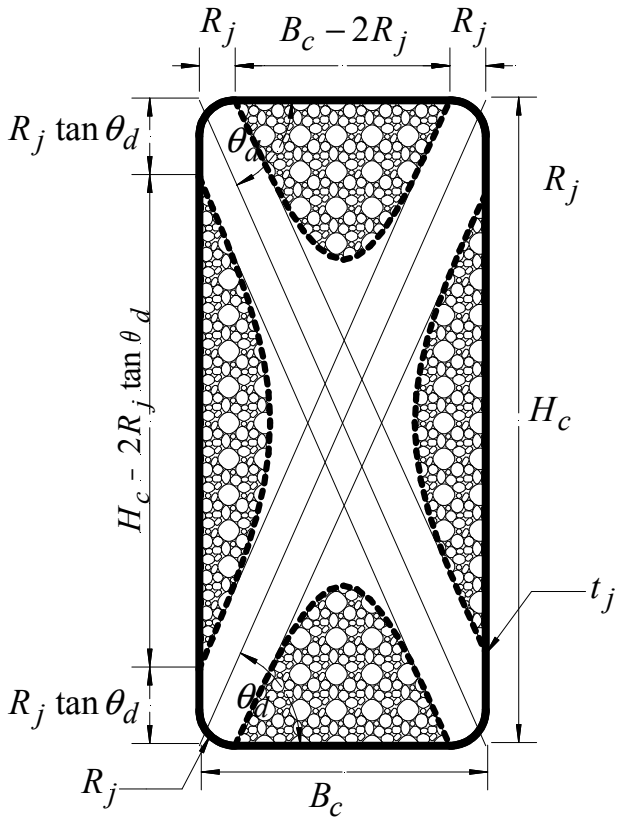

Figure 4.5 Geometry of effectively confined concrete in rectangular FRP-confined sections.

This hatched area is assumed governed by a second degree parabola with an initial diagonal angle of inclination θ_d that initiates at a distance R_j from the member's edge at the minor B_c dimension and at a distance $\alpha_{sh} R_j$ at the major H_c dimension.

Lam and Teng (2003b) recognized that the ineffectively confined concrete area along the minor B_c and major H_c faces of the RFCC section, $(A_{ic})_B$ and $(A_{ic})_H$, respectively, are given by:

$$(A_{ic})_B = \frac{H_c (B_c^{'})^2}{3B_c} = \frac{1}{3\alpha_{sh}} \left[H_c \left(1 - 2\alpha_{sh}\alpha_j\right)\right]^2 \tag{4.24}$$

$$(A_{ic})_H = \frac{B_c (H_c^{'})^2}{3H_c} = \frac{\alpha_{sh}}{3} \left[B_c \left(1 - 2\alpha_{sh}\alpha_j\right)\right]^2 \tag{4.25}$$

$$H_c^{'} = H_c - 2R_j \tan\theta_d = H_c\left(1 - 2\alpha_{sh}\alpha_j\right) \; ; \quad B_c^{'} = B_c - 2R_j = B_c\left(1 - 2\alpha_{sh}\alpha_j\right) \tag{4.26}$$

Substituting Eqs. (4.24) and (4.25) into Eq. (4.23) yields the total ineffectively confined concrete core area A_{ic}:

$$A_{ic} = \frac{2}{3\alpha_{sh}} \left[H_c \left(1 - 2\alpha_{sh}\alpha_j\right)\right]^2 \tag{4.27}$$

Substituting A_{nj} of Eq. (4.21), A_{ic} of eq. (4.27), into A_{ec} of Eq. (4.9) yields:

$$A_{ec} = \frac{(H_c)^2}{3\alpha_{sh}} \left\{ 3\left[1 - \alpha_{sh}(4-\pi)(\alpha_j)^2\right] - 2\left(1 - 2\alpha_{sh}\alpha_j\right)^2 \right\} \tag{4.28}$$

Substituting A_{nj} of Eq. (4.21) and A_{ic} of Eq. (4.27) into k_e of Eq. (4.8) yields:

$$(k_e)_{re} = 1 - \frac{2}{3}\left[\frac{(1-2\alpha_{sh}\alpha_j)^2}{1-\alpha_{sh}(4-\pi)(\alpha_j)^2}\right] \tag{4.29}$$

This relationship indicates that the confining efficiency of the confining rectangular FRP jacket $(k_e)_{re}$, depends on the geometry of the FRP-confined concrete as measured by the jacket corner aspect ratio α_j and the aspect ratio α_{sh}.

The minimum confining efficiency of $(k_e)_{re} = 1/3$ occurs when no rounding of the corners is provided (i.e., $\alpha_j = 0$). The maximum confining efficiency of $(k_e)_{re} = 1.0$ occurs when the corners of the rectangular section are rounded to a radius R_j equal to one half of the minor dimension B_c (i.e., $R_j = B_c/2$ or $\alpha_j = 1/(2\alpha_{sh})$) which is the case of a circular FRP-confined concrete (CFCC) section, as shown in **Figure 4.2(c),** when $\alpha_{sh} = 1.0$ or an oval FRP-confined concrete (OFCC) section, as shown in **Figure 4.3(b)**, when $\alpha_{sh} > 1.0$.

Reinforcement Ratio

Using Eq. (4.12), the reinforcement ratio of the confining rectangular FRP jacket $(\rho_j)_{re}$, of **Figure 4.5** is given by:

$$(\rho_j)_{re} = \left(\frac{V_j}{V_c}\right)_{re} = \left(\frac{2t_j}{H_c}\right)C_{re} \tag{4.30}$$

$$C_{re} = \frac{(1+\alpha_{sh}) - (4-\pi)\alpha_j\alpha_{sh}}{1-\alpha_{sh}(4-\pi)(\alpha_j)^2} \tag{4.31}$$

where C_{re} is the reinforcement ratio coefficient of the confining rectangular FRP jacket.

Effective and Normalized Effective Confining Stiffness

The effective stiffness of a RFCC section $\left(C_{je}\right)_{re}$, can be found by setting $\left(C_{je}\right)_{sh} = \left(C_{je}\right)_{re}$ in Eq. (4.17) and substituting the confining efficiency $\left(k_e\right)_{rec}$ of Eq. (4.29) and the reinforcement ratio coefficient C_{re} of Eq. (4.31) into Eq. (4.17). The normalized effective confining stiffness $\left(K_{je}\right)_{re}$ of a rectangular FRP jacket can be found by setting $\left(K_{je}\right)_{sh} = \left(K_{je}\right)_{re}$ in Eq. (4.17).

Square Sections

Confining Efficiency

A square FRP-confined concrete (SFCC) section with rounded corners is the special case of a rectangular FRP-confined concrete (RFCC) section with rounded corners with a unity aspect ratio (i.e., $\alpha_{sh} = 1.0$). As a result, the confining efficiency $\left(k_e\right)_{sq}$ of the square FRP-confined concrete section shown in **Figure 4.6** can be found by substituting $\alpha_{sh} = 1.0$ into the confining efficiency k_e of Eq. (4.29), which yields:

$$\left(k_e\right)_{sq} = 1 - \frac{2}{3}\left[\frac{\left(1-2\alpha_j\right)^2}{1-\left(4-\pi\right)\left(\alpha_j\right)^2}\right] \tag{4.32}$$

The above relationship indicates that confining efficiency of the confining square FRP jacket $\left(k_e\right)_{sq}$ is solely dependent on the rounding of the corners of the FRP-confined concrete as measured by the jacket corner aspect ratio α_j.

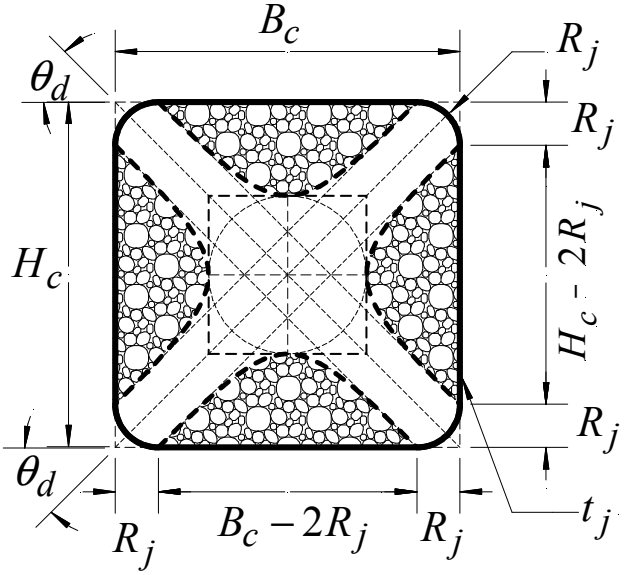

Figure 4.6 Geometry of effectively confined concrete in square FRP-confined sections.

As for rectangular sections, the minimum confining efficiency of $(k_e)_{sq} = 1/3$ occurs when no rounding of the corners is provided in a SFCC section (i.e., $\alpha_j = 0$). The maximum confining efficiency of $(k_e)_{sq} = 1.0$ occurs when the corners of the square section are rounded to a radius R_j equal to one half of the minor dimension B_c (i.e., $R_j = B_c/2$ or $\alpha_j = 1/2$) which is the case of a CFCC section, as shown in **Figure 4.2(c)**.

Reinforcement Ratio

Setting $(\rho_j)_{sh} = (\rho_j)_{sq}$ in Eq. (4.12), and setting $\alpha_{sh} = 1.0$ in Eq. (4.31), yields the reinforcement ratio $(\rho_j)_{sq}$ of the confining square FRP jacket of **Figure 4.6**:

$$(\rho_j)_{sq} = \left(\frac{V_j}{V_c}\right)_{sq} = \left(\frac{2t_j}{H_c}\right) C_{sq} \tag{4.33}$$

$$C_{sq} = \left(\frac{H_c}{2t_j}\right)(\rho_j)_{sq} = \frac{2-(4-\pi)\alpha_j}{1-(4-\pi)(\alpha_j)^2} \tag{4.34}$$

where C_{sq} is the reinforcement ratio coefficient of the confining square FRP jacket.

Effective and Normalized Effective Confining Stiffness

The effective stiffness of a square FRP jacket $(C_{je})_{sq}$ can be found by setting $(C_{je})_{sh} = (C_{je})_{sq}$ in Eq. (4.17) and substituting $(k_e)_{sq}$ of Eq. (4.32) and C_{sq} of Eq. (4.34) into Eq. (4.17). The normalized effective confining stiffness of a square FRP

jacket $(K_{je})_{sq}$ can be found by setting $(K_{je})_{sh} = (K_{je})_{sq}$ and substituting $(C_{je})_{sq}$ into Eq. (4.19).

Oval Sections

Confining Efficiency

An oval FRP-confined concrete (OFCC) section with a radius equal to one half the minor dimension B_c, is a special case of a RFCC section with rounded corners with a corner aspect ratio α_j equal to one half the inverse aspect ratio α_{sh} (i.e., $\alpha_j = 1/(2 \cdot \alpha_{sh})$). As a result, the confining efficiency $(k_e)_{ov}$ of the OFCC section shown in **Figure 4.7** can be found by substituting $\alpha_j = 1/(2 \cdot \alpha_{sh})$ into the k_e of Eq. (4.29), which yields $(k_e)_{ov} = 1.0$.

This indicates that the maximum confining efficiency of $(k_e)_{ov} = 1.0$ occurs when the section is an OFCC section. This indicates that the confining efficiency $(k_e)_{ov}$ of the confining oval FRP jacket is a constant and is independent of the aspect ratio α_{sh} of the OFCC section.

Reinforcement Ratio

Setting $(\rho_j)_{sh} = (\rho_j)_{ov}$ in Eq. (4.12), and setting $\alpha_{sh} = 1/2\alpha_j$ in Eq. (4.31), yields the reinforcement ratio $(\rho_j)_{ov}$ of the confining oval FRP jacket of **Figure 4.7**:

$$(\rho_j)_{ov} = \left(\frac{V_j}{V_c}\right)_{ov} = \left(\frac{2t_j}{H_c}\right) C_{ov} \tag{4.35}$$

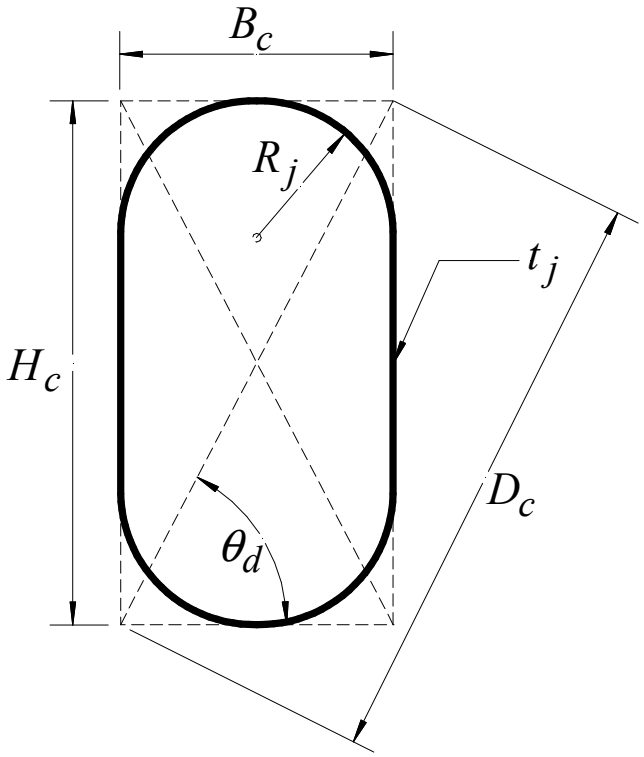

Figure 4.7 Typical geometry of an oval FRP-confined concrete section.

$$C_{ov} = \frac{4\alpha_{sh}(\alpha_{sh} - 1) + 2\pi\alpha_{sh}}{4(\alpha_{sh} - 1) + \pi} \tag{4.36}$$

where C_{ov} is the reinforcement ratio coefficient of the confining oval FRP jacket.

Effective and Normalized Effective Confining Stiffness

The effective stiffness of an oval FRP jacket $(C_{je})_{ov}$ can be found by setting $(C_{je})_{sh} = (C_{je})_{ov}$ in Eq. (4.17) and substituting $(k_e)_{ov} = 1.0$ and C_{ov} of Eq. (4.36) into Eq. (4.17).

The normalized effective confining stiffness of an oval FRP jacket $(K_{je})_{ov}$ can be found by setting $(K_{je})_{sh} = (K_{je})_{ov}$ and substituting $(C_{je})_{sh} = (C_{je})_{ov}$ into Eq. (4.19).

Circular Sections

Confining Efficiency

A circular FRP-confined concrete (CFCC) section is the special case of a RFCC section with rounded corners with a unity aspect ratio (i.e., $\alpha_{sh} = 1.0$) and a jacket corner ratio of $\alpha_j = 1/2$.

The confining efficiency $(k_e)_{ci}$ of the CFCC section shown in **Figure 4.8** can be found by substituting $\alpha_{sh} = 1.0$ and $\alpha_j = 1/2$ into $(k_e)_{re}$ of Eq. (4.29) or substituting $\alpha_j = 1/2$ into $(k_e)_{sq}$ of Eq. (4.32) which yields $(k_e)_{ci} = 1.0$.

This indicates that the confining efficiency $(k_e)_{ci}$ of the confining circular FRP jacket is a constant and is independent of the size (i.e., diameter D_j) of the CFCC section.

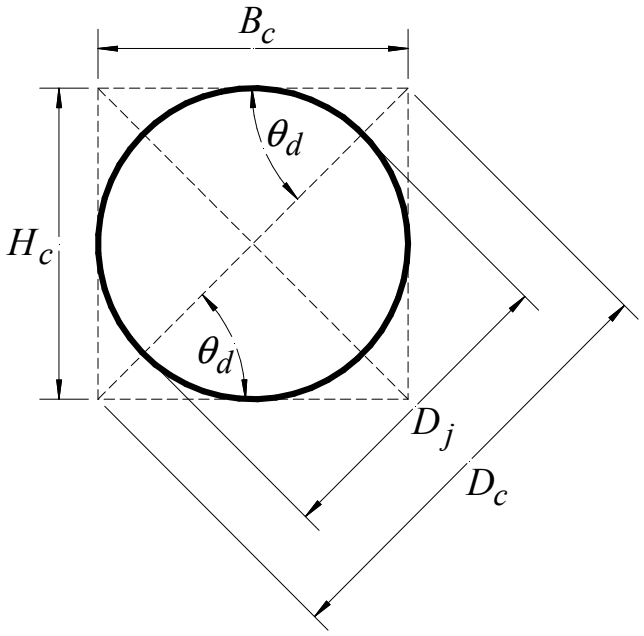

Figure 4.8 Typical geometry of a circular FRP-confined concrete section.

Reinforcement Ratio

Setting $(\rho_j)_{sh} = (\rho_j)_{ci}$ in Eq. (4.12), and $H_c = B_c = D_j$, $\alpha_{sh} = 1.0$ and $\alpha_j = 1/2$ in Eq. (4.31), yields the reinforcement ratio $(\rho_j)_{ci}$ of the confining circular FRP jacket of **Figure 4.8** is given by:

$$(\rho_j)_{ci} = \left(\frac{V_j}{V_c}\right)_{ci} = \left(\frac{2t_j}{D_j}\right) C_{ci} \;\; ; \;\; C_{ci} = 2.0 \tag{4.37}$$

where C_{ci} is the reinforcement ratio coefficient of the confining circular FRP jacket.

Effective and Normalized Effective Confining Stiffness

The effective stiffness of a circular FRP jacket $(C_{je})_{ci}$, can be found by setting $(C_{je})_{sh} = (C_{je})_{ci}$ in Eq. (4.17) and substituting the confining efficiency $(k_e)_{cir} = 1.0$ and the reinforcement ratio coefficient C_{ci} of Eq. (4.37) into Eq. (4.17).

The normalized effective confining stiffness of a circular FRP jacket $(K_{je})_{ci}$, can be found by setting $(K_{je})_{sh} = (K_{je})_{ci}$ and substituting $(C_{je})_{sh} = (C_{je})_{ci}$ into Eq. (4.19).

Elliptical Sections

The geometric properties of an elliptical FRP jacket, as shown in **Figure 4.9**, are the distance of the foci c_{el}, the elliptical eccentricity e_{el}, and the elliptical perimeter coefficient λ_{el}, which are defined in terms of the major h_c and minor b_c axis dimension of the elliptical FRP-confined concrete section as follows:

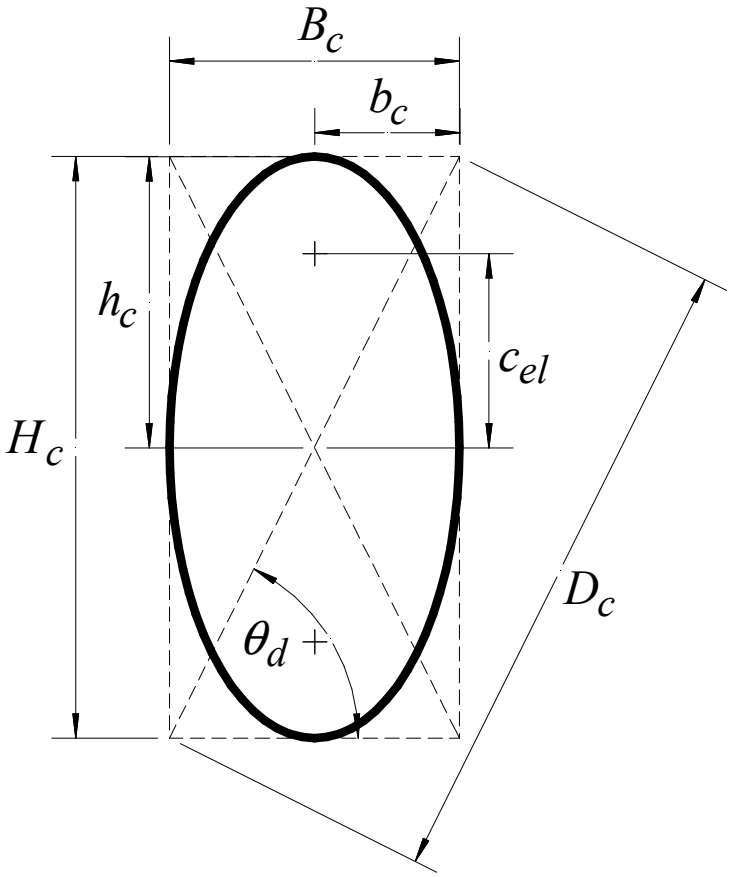

Figure 4.9 Typical geometry of an elliptical FRP-confined concrete section.

$$c_{el} = \sqrt{(h_c)^2 - (b_c)^2} = h_c \sqrt{1 - \frac{1}{(\alpha_{sh})^2}} \tag{4.38}$$

$$\lambda_{el} = \frac{\alpha_{sh} - 1}{\alpha_{sh} + 1} \tag{4.39}$$

$$e_{el} = \frac{c_{el}}{h_c} = \sqrt{1 - \frac{1}{(\alpha_{sh})^2}} \tag{4.40}$$

The elliptical perimeter coefficient λ_{el} of Eq. (4.39) is used to determine the perimeter of an ellipse p_{el} which is given by:

$$p_{el} = \frac{\pi}{2} B_c (1 + \alpha_{sh}) \left[1 + \frac{3(\lambda_{el})^2}{10 + \sqrt{4 - 3(\lambda_{el})^2}} \right] \tag{4.41}$$

The eccentricity of the ellipse e_{el} of Eq. (4.40) measures the roundness of the ellipse. An eccentricity $e_{el} = 0$ indicates a circular section, whereas $e_{el} = 1.0$ indicates a flat (degenerate) ellipse or a line having a length of $2h_c = H_c$.

Confining Efficiency

The dilation of the elliptical FRP-confined concrete section depends on the hoop dilation of the FRP jacket; arching of the confining stresses does not occur as it takes place in rectangular and square FRP-confined concrete sections, as shown in **Figures 4.5** and **4.6**. Membrane action occurs in circular and elliptical sections but not in rectangular or square FRP-confined sections. In rectangular and square FRP jackets bending of the sides of the FRP jackets occurs, due to lateral dilation of the concrete core, as a result of the weak out-of-plane stiffness of the thin rectangular and square FRP jacket.

A circular section as shown in **Figure 4.8** is also a special case of an elliptical section, as shown in **Figure 4.9**, for a unity section aspect ratio (i.e., $\alpha_{sh} = 1.0$). In addition, an elliptical section can also be considered as a special case of an elongated (i.e., distorted) circular section for which $\alpha_{sh} \geq 1.0$. As a result, the confining efficiency $(k_e)_{el}$ of the elliptical FRP jacket is also given by Eq. (4.35); thus $(k_e)_{el} = (k_e)_{ci} = 1.0$.

Reinforcement Ratio

Using Eq. (4.12), the reinforcement ratio $(\rho_j)_{el}$ of the confining elliptical FRP jacket of **Figure 4.9** is given by:

$$(\rho_j)_{el} = \left(\frac{2t_j}{H_c}\right) C_{el} \tag{4.42}$$

$$C_{el} = (1+\alpha_{sh}) \left[1 + \frac{3(\lambda_{el})^2}{10 + \sqrt{4 - 3(\lambda_{el})^2}} \right] \tag{4.43}$$

where C_{el} is the reinforcement ratio coefficient of the confining elliptical FRP jacket. For a circular section for which $\alpha_{sh} = 1.0$, Eq. (4.43) yields $C_{ci} = C_{el} = 2.0$, which is identical to that given in Eq. (4.37).

Effective and Normalized Effective Confining Stiffness

The effective stiffness of an elliptical FRP jacket $(C_{je})_{el}$ can be found by setting $(C_{je})_{sh} = (C_{je})_{el}$ in Eq. (4.17) and substituting the confining efficiency $(k_e)_{el} = (k_e)_{ci} = 1.0$ and the reinforcement ratio coefficient C_{el} of Eq. (4.43) into Eq.

(4.17). The normalized effective confining stiffness $\left(K_{je}\right)_{el}$ of an elliptical FRP jacket, can be found by setting $\left(K_{je}\right)_{sh} = \left(K_{je}\right)_{el}$ and substituting $\left(C_{je}\right)_{sh} = \left(C_{je}\right)_{el}$ into Eq. (4.19).

Shape-Modified Sections

FRP jackets are effective in confining circular or elliptical concrete sections. However, in the case of square and rectangular concrete sections, the confinement provided by the FRP jacket is less effective due to the rectilinear FRP jacket shape which includes rounded corners and flat sides. The presence of steel ties in rectangular reinforced concrete sections limits corner rounding to small radii in the order of 25-76 mm.

One approach to increasing the confinement effectiveness and strain ductility of square and rectangular sections with chamfered corners, as shown in **Figure 4.10**, is to shape modify the cross section into either circular, oval or elliptical FRP-confined sections (Yan 2005).

When the presence of steel ties in square or rectangular reinforced concrete sections limits corner rounding to small radii, shapes other than rectangular FRP jackets may be used to improve the confining effectiveness of the FRP jacket while minimizing the size of the confining FRP jacket.

This can be accomplished by modifying the rectilinear (rectangular and square) section using either a circular FRP jacket to confined square sections or an elliptical or oval FRP jacket to confine rectangular sections. The use of shape-modifying elliptical FRP jackets (including circular) and oval FRP jackets are considered herein.

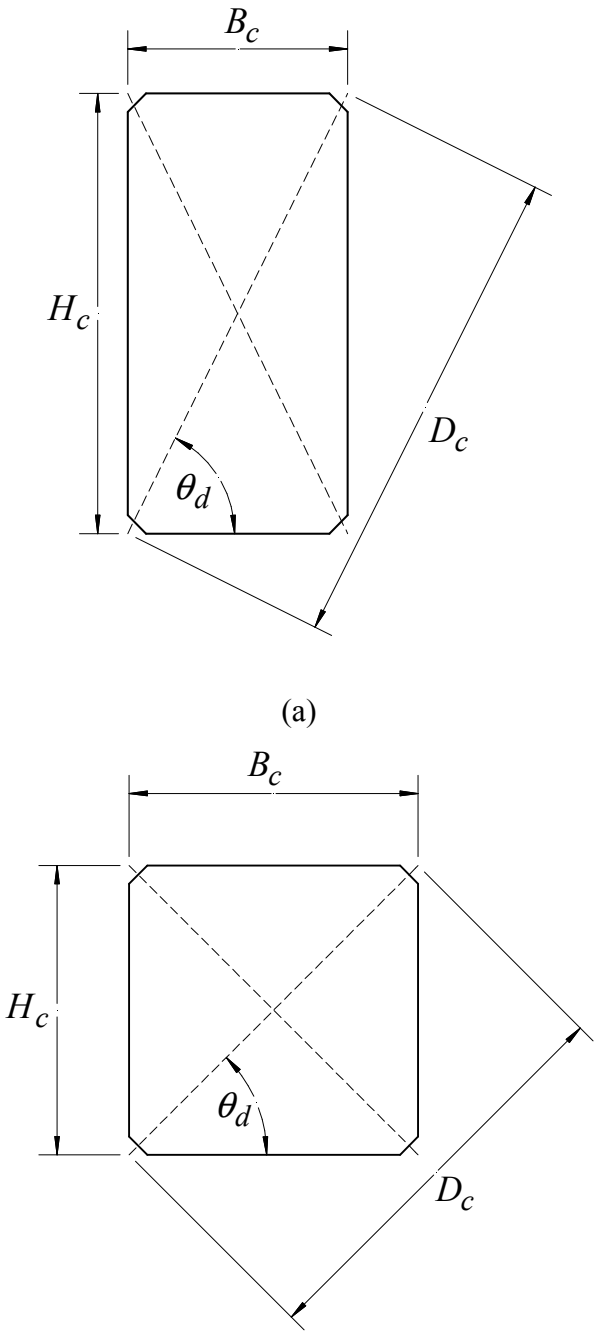

Figure 4.10 Geometry of existing (a) rectangular and (b) square sections.

In this section a rectangular shape-modified (RSM) section that is confined by either a shape-modifying oval (SMO) or a shape-modifying elliptical (SME) FRP jacket, as shown in **Figures 4.11** and **4.12**, is considered herein. In these figures a rectangular concrete section with major H_c and minor B_c dimensions, having a nonunity aspect ratio (i.e., $\alpha_{sh} > 1.0$) whose shape has been modified so that a minimum concrete cover c_{cor} is provided at the corners of the rectangular section, along the section's main diagonal is shown.

The dimensions of the dashed rectangle circumscribed within the elliptical FRP jacket shown in **Figure 4.11(a)** are given by:

$$H_{rsm} = H_c\left(1 + 2\alpha_{cor}\sin\theta_d\right) \;;\; \alpha_{cor} = \frac{c_{cor}}{H_c} \tag{4.44}$$

$$B_{rsm} = B_c\left(1 + 2\alpha_{cor}\alpha_{sh}\cos\theta_d\right) \tag{4.45}$$

$$D_{rsm} = \sqrt{\left(B_{rsm}\right)^2 + \left(H_{rsm}\right)^2} = H_{rsm}\sqrt{1 + \frac{1}{\left(\alpha_{sh}\right)^2}} \tag{4.46}$$

$$\alpha_{rsm} = \frac{H_{rsm}}{B_{rsm}} = \frac{h_{rsm}}{b_{rsm}} = \alpha_{sh} \;;\; h_{rsm} = \frac{H_{rsm}}{2} \;;\; b_{rsm} = \frac{B_{rsm}}{2} \tag{4.47}$$

The subscript rsm indicates a rectangular shape-modified (RSM) section confined by a shape-modifying elliptical or oval FRP jacket. In addition, α_{rsm} is the aspect ratio of the RSM section; H_{rsm}, B_{rsm}, and D_{rsm} are the overall major, minor, and main diagonal dimensions of the RSM section. Also, h_{rsm} and b_{rsm} are the major and minor axis of the RSM section, respectively, and θ_{rsm} is the angle of inclination of the main diagonal of the RSM section.

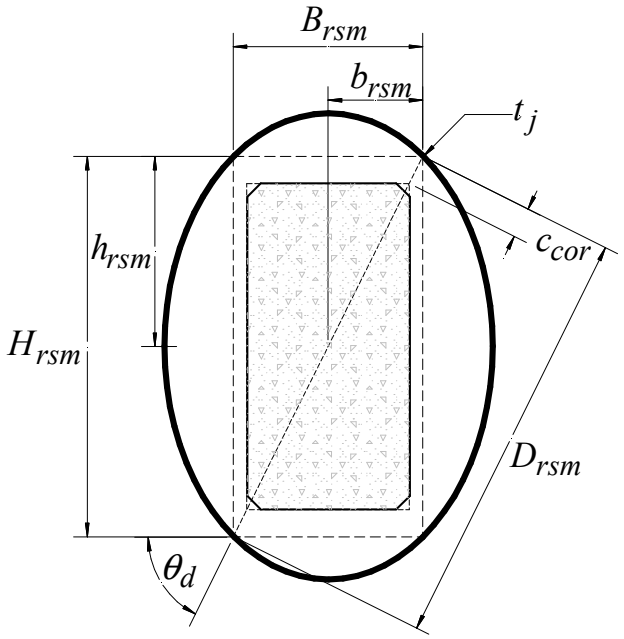

(a)

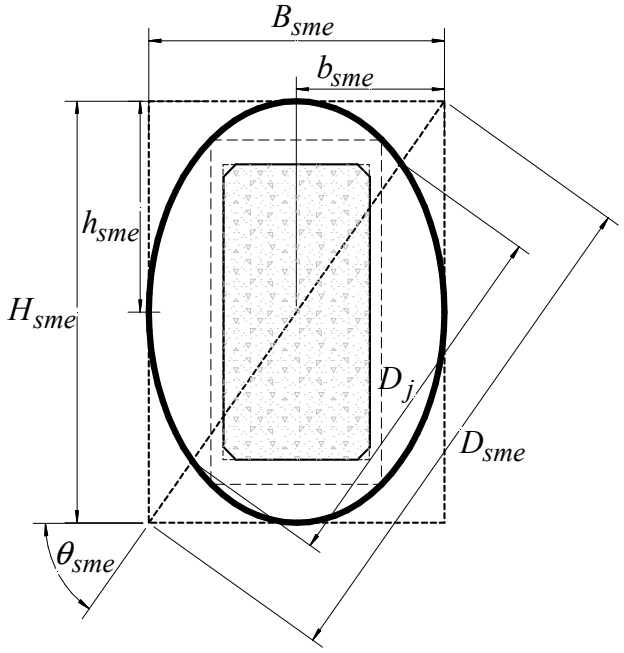

(b)

Figure 4.11 Geometry of shape-modified rectangular section: (a) rectangular section geometry and (b) elliptical FRP jacket geometry.

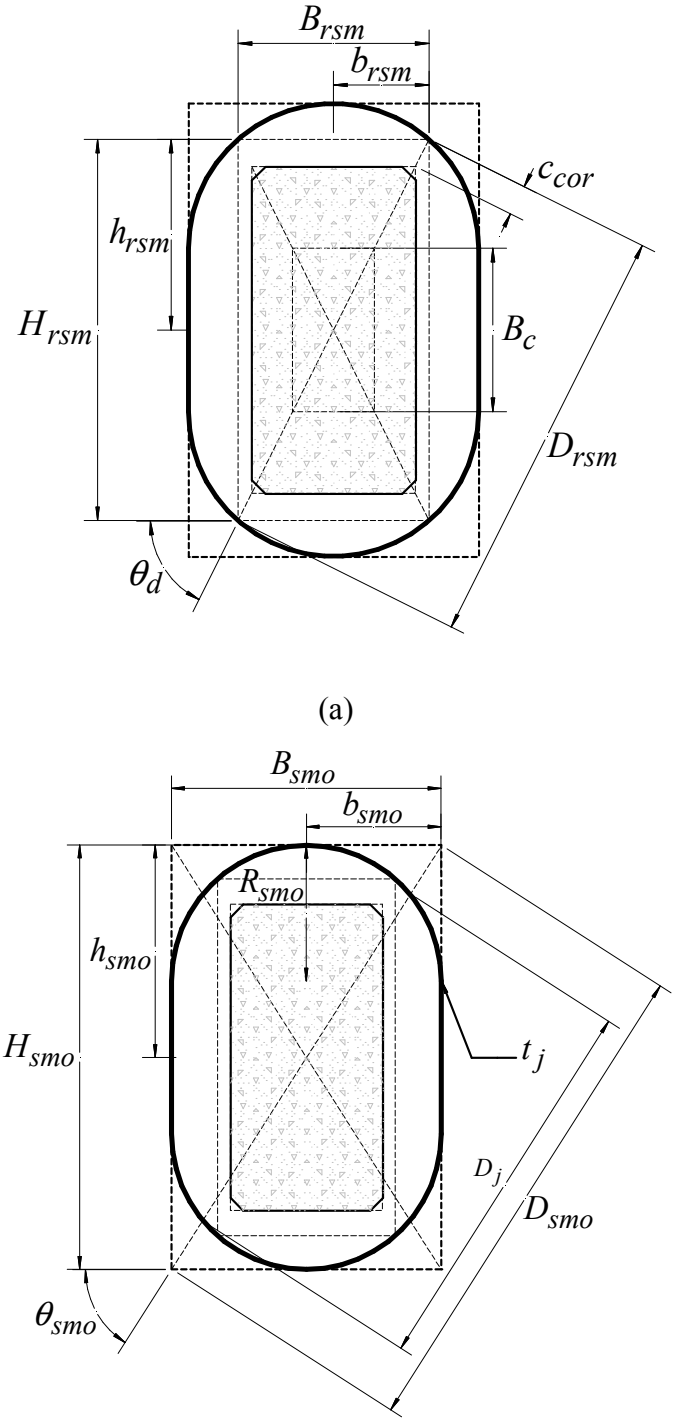

Figure 4.12 Geometry of shape-modified rectangular section: (a) rectangular section geometry and (b) oval FRP jacket geometry.

Elliptical Shape-Modified Sections

As shown in **Figure 4.11(b),** the rectangular section could be confined by an elliptical FRP jacket whose aspect ratio is minimized; this is accomplished by minimizing the distance of the foci c_{el} of Eq. (4.38) of an elliptical FRP jacket, which yields the following:

$$\alpha_{sme} = \left(\frac{H}{B}\right)_{sme} = \sqrt{\alpha_{sh}} = \tan(\theta_{sme}) \tag{4.48}$$

$$B_{sme} = B_{rsm}\sqrt{1+\alpha_{sh}} \;\; ; \;\; b_{sme} = \frac{B_{sme}}{2} \tag{4.49}$$

$$H_{sme} = H_{rsm}\sqrt{1+\frac{1}{\alpha_{sh}}} \;\; ; \;\; h_{sme} = \frac{H_{sme}}{2} \tag{4.50}$$

$$D_{sme} = \sqrt{(B_{sme})^2 + (H_{sme})^2} = H_{sme}\sqrt{1+\left(\frac{1}{\alpha_{sh}}\right)^2} \tag{4.51}$$

$$D_j = \frac{\sqrt{2}}{2} D_{sme} \tag{4.52}$$

where α_{sme} is the aspect ratio of the shape-modifying elliptical (SME) FRP jacket. Also, H_{sme}, B_{sme}, and D_{sme} are the overall major, minor, and main diagonal dimensions of the SME jacket, respectively. In addition, h_{sme} and b_{sme} are the major and minor axis of the SME jacket, respectively, and θ_{sme} is the angle of inclination of the FRP jacket diagonal D_j and D_{sme} of the SME jacket. The subscript *sme* indicates a rectangular concrete section confined by an SME jacket.

Using Eq. (4.12), the reinforcement ratio of the shape-modifying elliptical FRP jacket of **Figure 4.11**, $(\rho_j)_{sme}$ is given by:

$$(\rho_j)_{sme} = \left(\frac{2t_j}{H_c}\right) C_{sme} \tag{4.53}$$

$$C_{sme} = (1+\alpha_{sme}) \left[1 + \frac{3(\lambda_{sme})^2}{10+\sqrt{4-3(\lambda_{sme})^2}} \right] \tag{4.54}$$

where C_{sme} is the reinforcement ratio coefficient of the shape-modifying elliptical FRP jacket. The effective stiffness of the shape-modifying elliptical FRP jacket $(C_{je})_{sme}$ can be found by setting $(C_{je})_{sh} = (C_{je})_{sme}$ in Eq. (4.17) and substituting the confining efficiency $(k_e)_{sme} = (k_e)_{el} = (k_e)_{ci} = 1.0$ and the reinforcement ratio coefficient C_{sme} of Eq. (4.54) into Eq. (4.17). In addition, the normalized effective confining stiffness of the shape-modifying elliptical FRP jacket $(K_{je})_{sme}$ can be found by setting $(K_{je})_{sh} = (K_{je})_{sme}$ and substituting $(C_{je})_{sh} = (C_{je})_{sme}$ into Eq. (4.19).

Oval Shape-Modified Sections.

The rectangular concrete section of **Figure 4.10(a)**, whose shape has been modified by a shape-modifying oval (SMO) FRP jacket, as shown in **Figure 4.12,** is considered. Minimizing the aspect ratio of an SMO jacket α_{smo}, the minimum required aspect ratio $(\alpha_{smo})_{\min}$ of the SMO jacket is given by:

$$(\alpha_{smo})_{\min} = \left(\frac{H_{smo}}{B_{smo}}\right)_{\min} = \frac{B_c + 2R_{smo}}{2R_{smo}} = \tan\theta_{smo} \tag{4.55}$$

$$(R_{smo})_{\min} = \frac{H_c}{2\alpha_{sh}}\sqrt{(\alpha_{sh} + 2\alpha_{sh}\alpha_{cor}\sin\theta_d - 1)^2 + (1 + 2\alpha_{sh}\alpha_{cor}\cos\theta_d)^2} \tag{4.56}$$

$$B_{smo} = 2R_{smo} \;\; ; \;\; b_{smo} = R_{smo} \tag{4.57}$$

$$H_{smo} = 2\alpha_{smo}R_{smo} \;\; ; \;\; h_{smo} = \alpha_{smo}R_{smo} \tag{4.58}$$

$$D_{smo} = \sqrt{(B_{smo})^2 + (H_{smo})^2} = H_{smo}\sqrt{1 + \left(\frac{1}{\alpha_{smo}}\right)^2} \tag{4.59}$$

$$D_j = 2R_{smo}\csc\theta_{smo}\{\alpha_{smo} - [1 - \sin(\theta_a)_{smo}]\} \tag{4.60}$$

$$(\theta_a)_{smo} = \theta_{smo} - \sin^{-1}(\sin\theta_{smo} - \cos\theta_{smo}) \tag{4.61}$$

where B_{smo}, H_{smo}, and D_{smo} are the overall minor, major, and diagonal dimensions of the SMO jacket; D_j is the main diagonal of the confined core within the SMO jacket; θ_{smo} is the main diagonal angle of the SMO jacket, and $(\theta_a)_{smo}$ is the reference angle measured from the center of the jacket radius R_{smo} to the intercept of the main diagonal with the FRP jacket for a rectangular concrete section with a nonunity aspect ratio (i.e., $\alpha_{sh} > 1.0$) as shown in **Figure 4.12,** the subscript smo indicates a rectangular section confined by a SMO jacket. For the rectangular section confined by an SMO jacket, as shown in **Figure 4.12,** the confining efficiency $(k_e)_{smo}$ of the SMO jacket can be found by substituting $\alpha_{sh} = \alpha_{smo}$ and $\alpha_j = 1/(2\alpha_{smo})$ into Eq. (4.29) which yields $(k_e)_{smo} = 1.0$.

Using Eq. (4.12), the reinforcement ratio $(\rho_j)_{smo}$ of the SMO section as shown in **Figure 4.12** is found by substituting $\alpha_{sh} = \alpha_{smo}$ and $\alpha_j = 1/(2\alpha_{smo})$ into Eq. (4.30), which yields:

$$(\rho_j)_{smo} = \left(\frac{2t_j}{B_c}\right) C_{smo} \tag{4.62}$$

$$C_{smo} = \frac{4\alpha_{smo}(\alpha_{smo} - 1) + 2\pi\alpha_{smo}}{4(\alpha_{smo} - 1) + \pi} \tag{4.63}$$

where C_{smo} is the reinforcement ratio coefficient of the SMO jacket.

The effective stiffness $(C_{je})_{smo}$ of the SMO jacket can be found by setting $(C_{je})_{sh} = (C_{je})_{smo}$ in Eq. (4.17) and substituting the confining efficiency $(k_e)_{smo} = (k_e)_{ci} = 1.0$, the aspect ratio $\alpha_{sh} = \alpha_{smo}$, and the jacket reinforcement ratio coefficient $C_{sh} = C_{smo}$ into Eq. (4.17). In addition, the normalized effective confining stiffness of the shape-modifying circular FRP jacket $(K_{je})_{smo}$ can be found by setting $(K_{je})_{sh} = (K_{je})_{smo}$ and substituting $(C_{je})_{sh} = (C_{je})_{smo}$ into Eq. (4.19).

Circular Shape-Modified Sections

A square concrete section with chamfered corner having major H_c and minor B_c dimensions, and a unity aspect ratio (i.e., $\alpha_{sh} = 1.0$), whose shape has been modified so that a minimum cover c_{cor} is provided at the corners of the square section is shown in **Figure 4.13**. The dimensions of the dashed square circumscribed within the shape-modifying circular FRP jacket, as shown in **Figure 4.13(a)**, are given by:

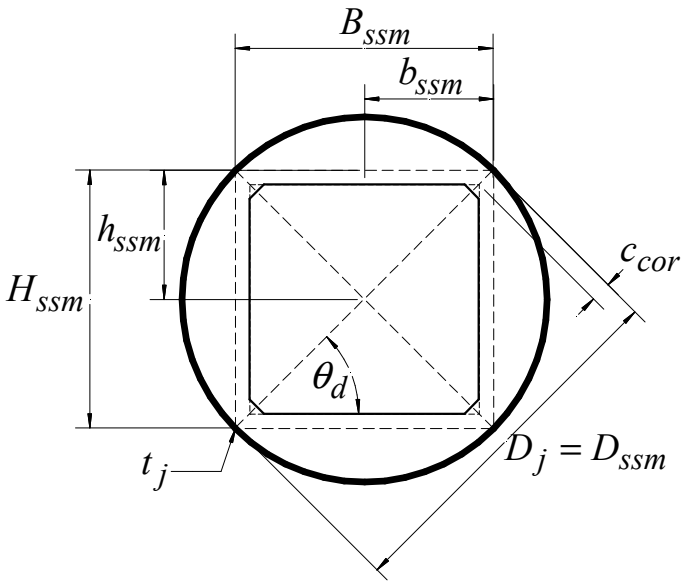

(a)

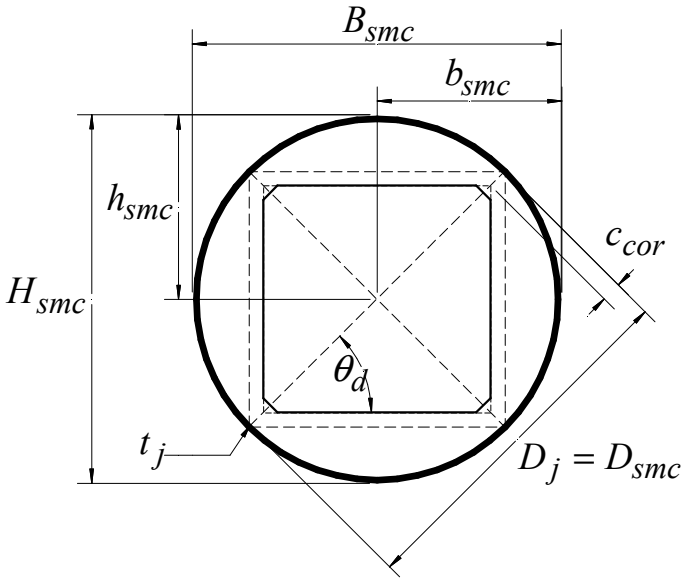

(b)

Figure 4.13 Geometry of shape-modified square section: (a) square section geometry and (b) circular FRP jacket geometry.

$$H_{ssm} = B_{ssm} = H_c\left[1+\sqrt{2}\,\alpha_{cor}\right] \tag{4.64}$$

$$D_{ssm} = \sqrt{(B_{ssm})^2 + (H_{ssm})^2} = \sqrt{2}\,H_{ssm} \tag{4.65}$$

$$h_{ssm} = b_{ssm} = \frac{H_{ssm}}{2} \tag{4.66}$$

The subscript ssm indicates a square shape-modified (SSM) section confined by a shape-modifying circular (SMC) FRP jacket. The size of the SMC jacket with a unity aspect ratio (i.e., $\alpha_{smc} = \alpha_{sh} = 1.0$) as shown in **Figure 4.13(b)** can be found as follows:

$$D_j = D_{smc} = H_{smc} = B_{smc} = \sqrt{2}H_{ssm} \;\; ; \;\; h_{smc} = b_{smc} = \frac{H_{smc}}{2} \tag{4.67}$$

where α_{smc} is the aspect ratio of the shape-modifying circular FRP jacket; H_{smc}, B_{smc}, D_{smc}, and D_j are the overall major, minor, and diagonal dimensions of the shape-modifying circular FRP jacket, respectively; h_{smc} and b_{smc} are the overall major and minor axis of the shape-modifying circular FRP jacket, respectively. The subscript smc indicates a section confined by a SMC jacket.

Using Eq. (4.12), the reinforcement ratio $(\rho_j)_{smc}$ of the SMC jacket as shown in **Figure 4.12** is given by:

$$(\rho_j)_{smc} = \left(\frac{2t_j}{H_c}\right)C_{smc} \;\; ; \;\; C_{smc} = 2.0 \tag{4.68}$$

where C_{smc} is the reinforcement ratio coefficient of the shape-modifying circular (SMC) FRP jacket.

The effective stiffness $\left(C_{je}\right)_{smc}$ of the SMC jacket, can be found by setting $\left(C_{je}\right)_{sh} = \left(C_{je}\right)_{smc}$ in Eq. (4.17) and substituting the confining efficiency $\left(k_e\right)_{smc} = \left(k_e\right)_{ci} = 1.0$, and the reinforcement ratio coefficient C_{smc} of Eq. (4.59) into Eq. (4.17). In addition, the normalized effective confining stiffness $\left(K_{je}\right)_{smc}$ of the SMC jacket, can be found by setting $\left(K_{je}\right)_{sh} = \left(K_{je}\right)_{smc}$ and substituting $\left(C_{je}\right)_{sh} = \left(C_{je}\right)_{smc}$ into Eq. (4.19).

The confinement efficiency k_e of Eq. (4.8) and the reinforcement ratio coefficient C_{sh} of Eq. (4.12) of the FRP-jacketed sections considered herein are summarized in **Table 4.1** and **Table 4.2**, respectively.

In this chapter a series of mathematical relationships were developed to describe the geometric and mechanical properties of FCC sections of various shapes, which include circular, elliptical, rectangular, square, and oval sections. These relationships are incorporated into Chapters 5-10 to describe the uniaxial compressive behavior and the axial strain-induced transverse and diagonal dilation behavior of FRP-confined concrete sections in compression.

Table 4.1 Summary of the confinement efficiency k_e of various FRP-confined concrete sections.

FRP jacket shape	Confinement Efficiency (k_e)	Ref. Eq.
Rectangular	$k_e = 1 - \frac{2}{3}\left[\frac{(1-2\alpha_{sh}\alpha_j)^2}{1-\alpha_{sh}(4-\pi)(\alpha_j)^2}\right]$	(4.29)
Square	$k_e = 1 - \frac{2}{3}\left[\frac{(1-2\alpha_j)^2}{1-(4-\pi)(\alpha_j)^2}\right]$	(4.32)
Oval	Same as rectangular with $2\alpha_j = 1/\alpha_{sh}$ or $k_e = 1.0$	N/A
Circular	Same as rectangular with $\alpha_{sh} = 1.0$ and $\alpha_j = 0.50$, or $k_e = 1.0$	N/A
Elliptical	$k_e = 1.0$	N/A

Table 4.2 FRP jacket shape dependent reinforcement ratio coefficient C_{sh} of various FRP-confined concrete sections.

FRP jacket shape	FRP jacket shape dependent reinforcement ratio coefficient C_{sh}	Ref. Eq.
Rectangular	$C_{sh} = \dfrac{(1+\alpha_{sh}) - (4-\pi)\alpha_j \alpha_{sh}}{1-\alpha_{sh}(4-\pi)(\alpha_j)^2}$	(4.30)
Square	$C_{sh} = \dfrac{2-(4-\pi)\alpha_j}{1-(4-\pi)(\alpha_j)^2}$	(4.34)
Oval	$C_{oval} = \dfrac{4\alpha_{sh}(\alpha_{sh}-1)+2\pi\alpha_{sh}}{4(\alpha_{sh}-1)+\pi}$	(4.36)
Circular	$C_{sh} = 2.0$	(4.37)
Elliptical	$C_{sh} = (1+\alpha_{sh})\left[1+\dfrac{3(\lambda_{sh})^2}{10+\sqrt{4-3(\lambda_{sh})^2}}\right]$ with $\lambda_{sh} = \dfrac{\alpha_{sh}-1}{\alpha_{sh}+1}$	(4.43)

CHAPTER 5

TRANSVERSE AND DIAGONAL EQUILIBRIUM OF CONCRETE SECTIONS CONFINED BY FIBER-REINFORCED POLYMER JACKETS

In this chapter a series of equilibrium relationships are developed from the transverse and diagonal equilibrium of the FRP-confined concrete (FCC) sections considered in this dissertation. In addition, a novel concept of diagonal equilibrium along the main diagonal of the FCC section is introduced. The mechanical and geometric properties of these FCC sections introduced in Chapter 4 are used to develop a series of diagonal equilibrium relationships for FCC sections.

The analytical equilibrium relationships introduced in what follows are used to determining the analytical strain compatibility relationships introduced in Chapter 6**.** Also, the concept of diagonal equilibrium is used in an analytical Mohr-Coulomb-based yield criterion for frictional-cohesive materials introduced in Chapter 9 and in an incremental damage-based stress-strain model introduced in Chapter 10.

In this investigation the following assumptions are made in the transverse and diagonal equilibrium analysis of FCC sections:

1. Perfect bond exists between the FRP jacket and the confined concrete core near the corners of rectangular and square FCC sections with surface-bonded FRP jackets or

bonded shape-modifying FRP jackets, referred to herein as bonded FRP-confined concrete (BFCC) sections.

2. At the corners of cast in place FRP jacketed concrete sections or what is typically referred to as concrete filled FRP tube (CFFT) sections, the coefficient of friction between the concrete core and the FRP jacket is assumed to be sufficiently high to suppress slippage between the FRP jacket and concrete core near the rounded corners of rectangular and square FCC sections and at the concrete-to-jacket interface of oval, circular, and elliptical CFFT sections, including shape-modifying FRP jackets.
3. Flexural stiffness of the confining rectangular jacket is assumed negligible, and arching action between the rounded corners is assumed to spread the resultant passive confining pressures along the faces of the rectangular and square BFCC and CFFT sections. As a result, the FRP jacket is considered as an element having only axial stiffness.
4. Flexure-induced strains at the extreme fibers of the FRP jacket due to lateral bulging of the confined core at the faces of the rectangular and square BFCC or CFFT sections are ignored. In addition, flexure-induced strains at the extreme fibers of elliptical FRP jackets due to lateral bulging of the confined core are also ignored.
5. Secondary effects due to combined axial shortening and transverse extension of the FRP jacket are ignored in the analysis of the FCC section.
6. The fibers of the FRP jacket are assumed oriented in the hoop or transverse direction.
7. Stress-concentrations at the concrete-to-jacket interface that can occur due to cracking of the confined concrete core near the surface of the FRP-jacketed concrete are ignored in the equilibrium analysis of the FCC section.

8. In determining the lateral confining pressure provided by the confining FRP jacket at a given transverse jacket strain, the concrete core within the FRP jacket is considered infinitely rigid when compared to the lateral stiffness of the FRP jacket.

In the analysis of confined concrete sections, be it concrete confined by transverse steel reinforcing, steel jackets, or FRP jackets, the equilibrium of the passively confined concrete is typically defined in terms of the transverse equilibrium of the confined concrete core, as shown in **Figures 5.1-5.5,** for FCC sections of various shapes. In this dissertation, a series of mathematical relationships are introduced using the concept of diagonal equilibrium of the FCC sections as shown in **Figures 5.6-5.10**.

Consider the transverse equilibrium of the half body of the concrete sections along the minor B_c dimension, as shown in **Figures 5.1(a), 5.2(a), 5.3(a), 5.4(a)** and **5.5(a),** and along the major H_c dimension as shown in **Figures 5.1(b), 5.2(b), 5.3(b), 5.4(b),** and **5.5(b)**. Equilibrium of the FCC sections along the minor B_c and major H_c dimension of **Figures 5.1-5.5**, yields:

$$2\left(f_j\right)_B t_j - f_B H_c = 0 \tag{5.1}$$

$$2\left(f_j\right)_H t_j - f_H B_c = 0 \tag{5.2}$$

The average stress in the linear elastic FRP jacket along the minor $\left(f_j\right)_B$ and major $\left(f_j\right)_H$ faces of the FRP jackets of **Figures 5.1-5.5** are given in terms of overall average transverse strains in the confined concrete core along the minor ε_B and major ε_H dimensions of the FRP jacket, respectively, as follows:

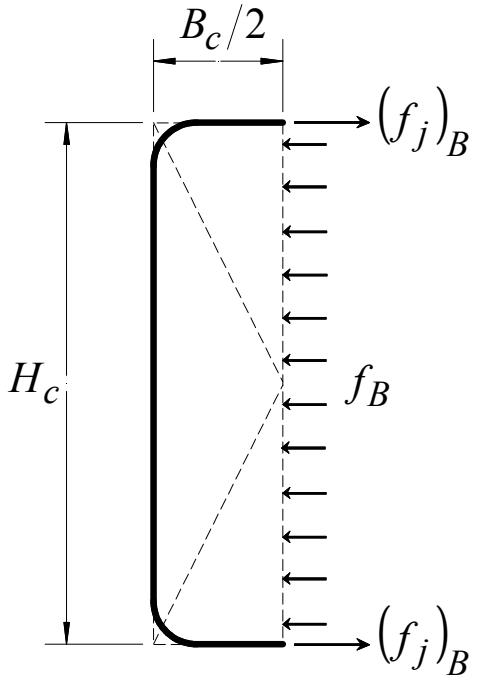

(a)

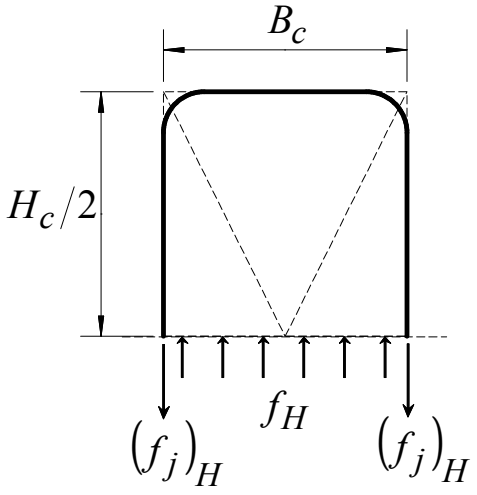

(b)

Figure 5.1 Transverse equilibrium of rectangular FRP-confined concrete section along the (a) minor and (b) major dimension.

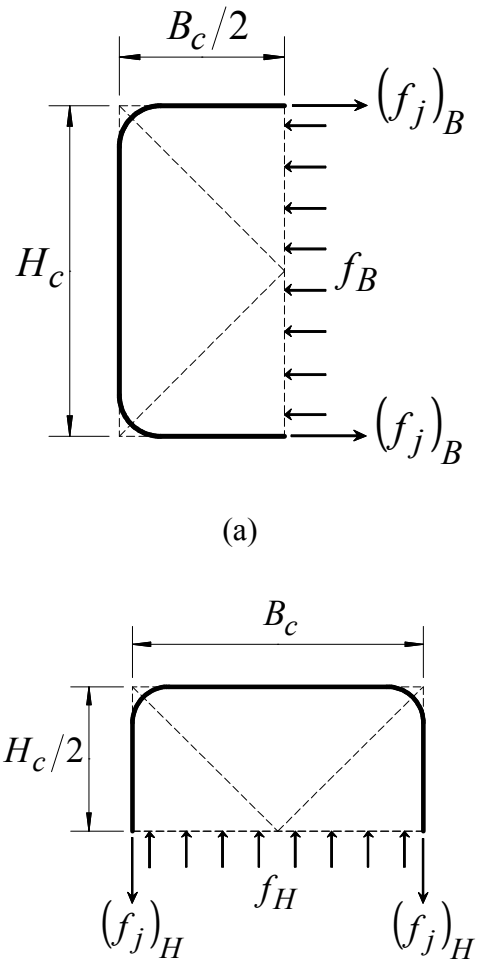

Figure 5.2 Transverse equilibrium of square FRP-confined concrete section: along the (a) minor and **(**b**)** major dimension.

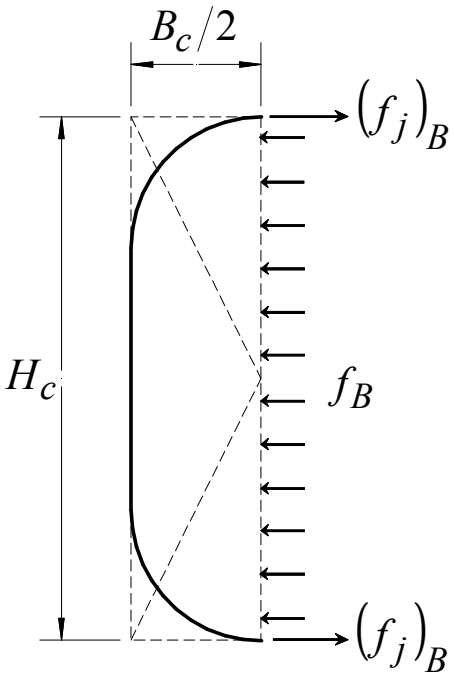

(a)

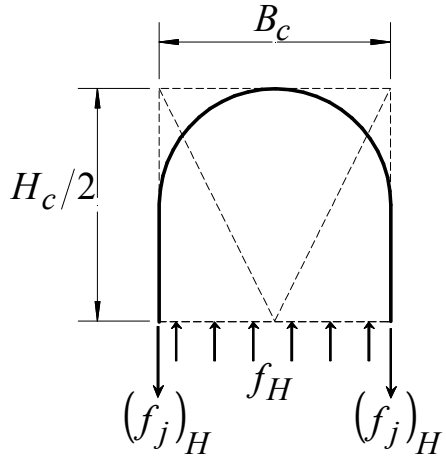

(b)

Figure 5.3 Transverse equilibrium of oval FRP-confined concrete sections: along the (a) minor and (b) major dimension.

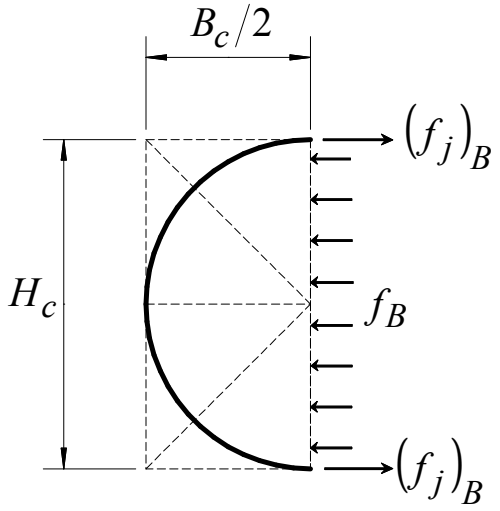

(a)

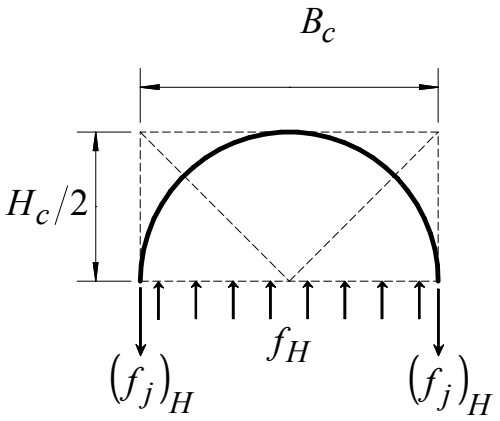

(b)

Figure 5.4 Transverse equilibrium of circular FRP-confined concrete sections: along the (a) minor and (b) major dimension.

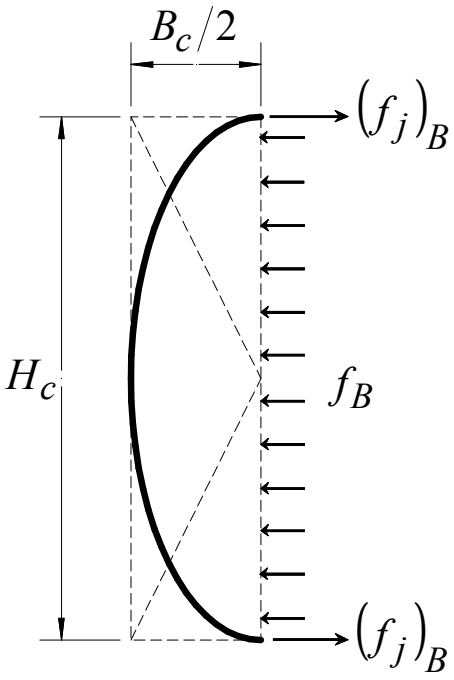

(a)

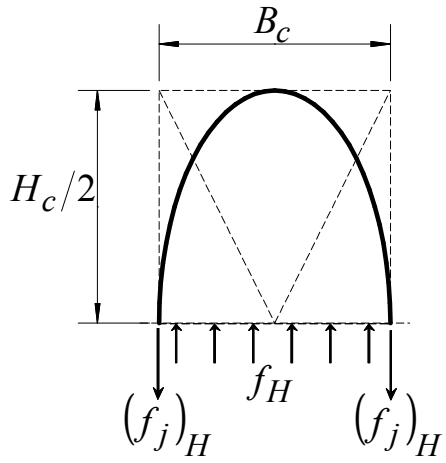

(b)

Figure 5.5 Transverse equilibrium of elliptical FRP-confined concrete sections: along the (a) minor and (b) major dimension.

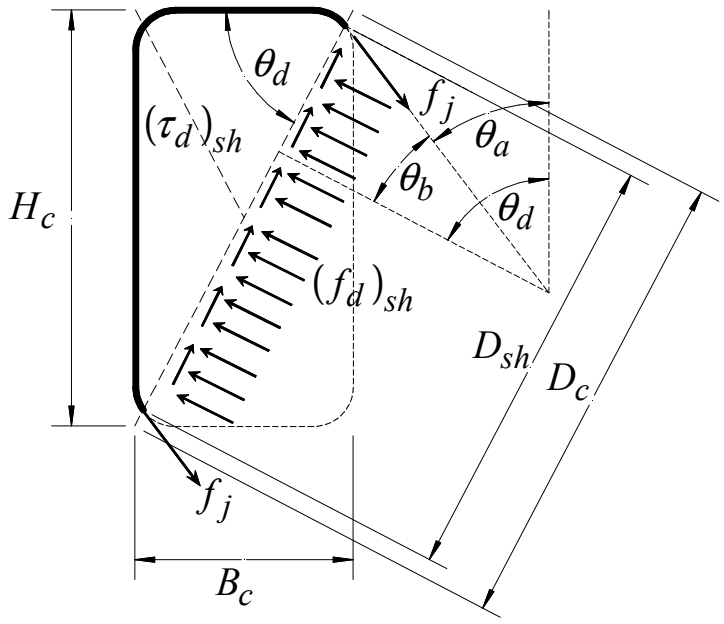

Figure 5.6 Diagonal equilibrium of a rectangular FRP-confined concrete section.

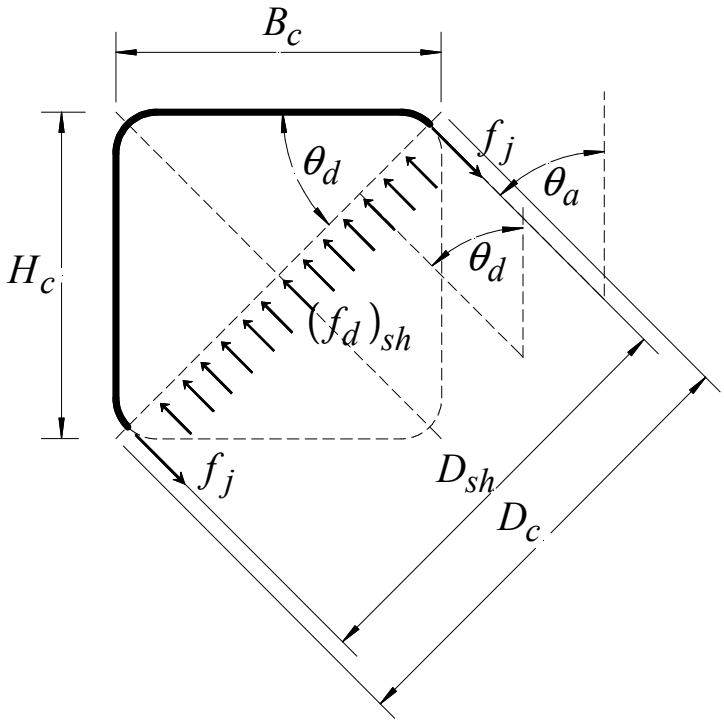

Figure 5.7 Diagonal equilibrium of a square FRP-confined concrete section.

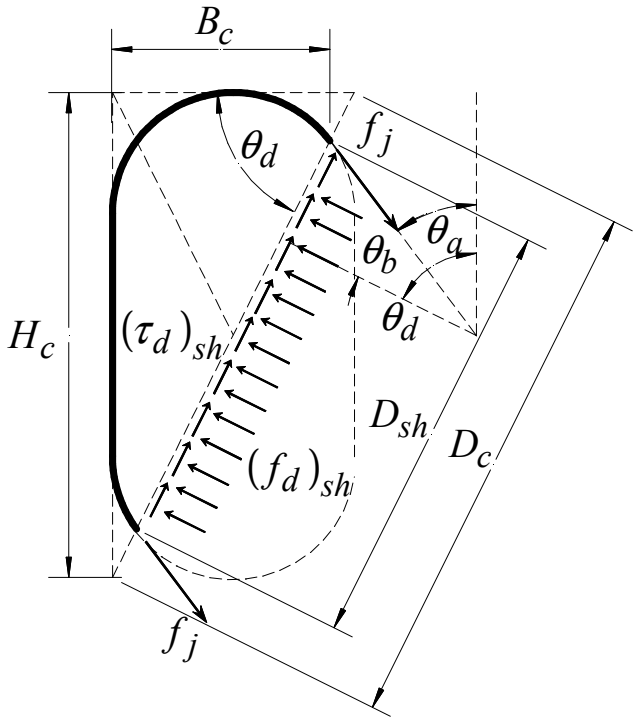

Figure 5.8 Diagonal equilibrium of an oval FRP-confined concrete section.

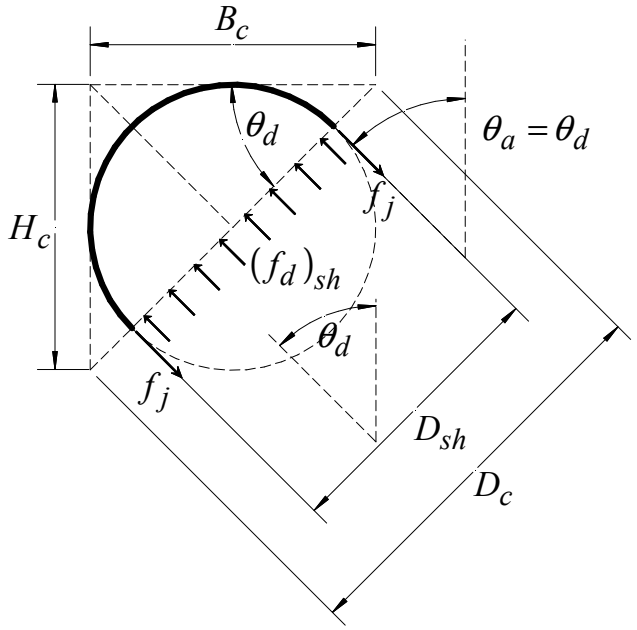

Figure 5.9 Diagonal equilibrium of a circular FRP-confined concrete section.

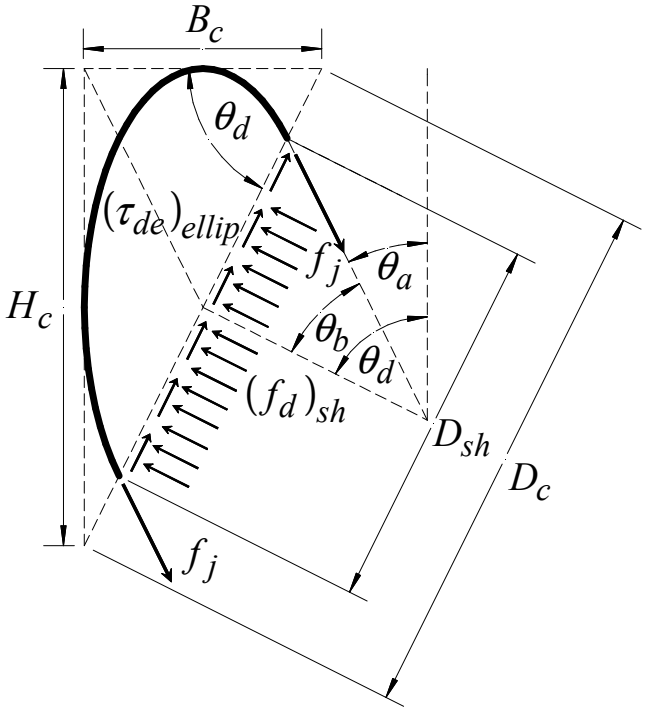

Figure 5.10 Diagonal equilibrium of an elliptical FRP-confined concrete section.

$$\left(f_j\right)_B = E_j \varepsilon_B \tag{5.3}$$

$$\left(f_j\right)_H = E_j \varepsilon_H \tag{5.4}$$

Solving for the average confining stress along the minor B_c and major H_c dimensions in Eqs. (5.1) and (5.2), and setting the effective confining stress as $\left(f_B\right)_e = k_e f_B$ and $\left(f_H\right)_e = k_e f_H$ and using Eqs. (5.3) and (5.4) yields:

$$\left(f_B\right)_e = \left(E_{je}\right)_B \varepsilon_B \tag{5.5}$$

$$\left(f_H\right)_e = \left(E_{je}\right)_H \varepsilon_H \tag{5.6}$$

where $\left(E_{je}\right)_B$ and $\left(E_{je}\right)_H$ are the effective transverse stiffness of the FRP jacket along the minor B_c and major H_c dimensions of the FCC section, given in Eqs. (4.15) and (4.16), respectively.

One of the difficulties associated with Eqs. (5.5) and (5.6) is that they are two equilibrium equations with two unknown transverse strains ε_B and ε_H and an unknown relationship between them. These challenges can be overcome by considering the diagonal equilibrium of the FCC sections shown in **Figures 5.6-5.10,** in combination with the transverse equilibrium of the FCC sections of **Figures 5.1-5.5** and the resulting transverse equilibrium relationships of Eqs. (5.5) and (5.6)**.**

The novel concept of diagonal equilibrium and dilation of the FCC sections introduced herein, to the knowledge of the author, has not been introduced in the analysis of FCC sections. From equilibrium of the FCC sections perpendicular to the main

concrete core diagonal D_{sh}, as shown in **Figures 5.6-5.10**, the average diagonal confining stress $(f_d)_{sh}$ can be found as:

$$(f_d)_{sh} = \left(\frac{2f_j t_j}{D_{sh}}\right)\cos\theta_b \tag{5.7}$$

From equilibrium of the FCC sections parallel to the main concrete core diagonal D_{sh}, as shown in **Figures 5.6-5.10**, the average shearing stress $(\tau_d)_{sh}$ is given by:

$$(\tau_d)_{sh} = \left(\frac{2f_j t_j}{D_{sh}}\right)\sin\theta_b \tag{5.8}$$

where f_j is the tensile stress in the FRP jacket at the intersection of the main diagonal, D_c of Eq. (4.3), with the FRP jacket having a thickness t_j, as shown in **Figures 5.6-5.10** which is given as:

$$f_j = E_j \varepsilon_j \tag{5.9}$$

This tensile stress in the FRP jacket is a result of the transverse dilation that the FCC core exhibits during axial deformation of the core. In addition, ε_j is the tensile strain in the FCC section at the intersection of the main diagonal D_c of Eq. (4.3) with the FRP jacket; E_j is the transverse or hoop modulus of elasticity of the FRP jacket. Also, the main concrete core diagonal D_{sh} and the FRP jacket strain/stress angles θ_a and θ_b depend on the shape and geometry of the FCC core.

Using Eqs. (5.7) and (5.8) the average effective shearing stress $(\tau_{de})_{sh}$ can be found in terms of the average effective diagonal confining stress $(f_{de})_{sh}$, as follows:

$$(\tau_d)_{sh} = (f_d)_{sh} \tan\theta_b \tag{5.10}$$

The main concrete core diagonal D_{sh} of the FRP-confined core is given in terms of the major dimension H_c of the FRP jacket, as follows:

$$D_{sh} = \chi_{sh} H_c \tag{5.11}$$

where χ_{sh} is a diagonal parameter that relates main concrete core diagonal D_{sh} to the major dimension H_c.

Substituting the effective transverse stiffness $(E_{je})_B$ of the FRP jacket along the minor jacket dimension B_c of Eq. (4.15) and the main concrete core diagonal D_{sh} of Eq. (5.11) into the definition of the average diagonal confining stress $(f_d)_{sh}$ of Eq. (5.7) and setting the effective diagonal confining stress as $(f_{de}) = k_e (f_d)_{sh}$ yield:

$$(f_{de})_{sh} = (E_{je})_B (\psi_d)_{sh} \varepsilon_j \tag{5.12}$$

$$(\psi_d)_{sh} = \frac{\cos\theta_b}{\chi_{sh}} \tag{5.13}$$

where k_e is the confinement efficiency of the FRP jacket, which is summarized in **Table 4.1** for the FRP-confined sections considered herein; $(\psi_d)_{sh}$ is a diagonal confinement equilibrium coefficient of the FCC section. This coefficient is included in the analytical

strain compatibility relationships introduced in Chapter 6, which relate the diagonal jacket strain ε_j to the strain along the minor ε_B, and major ε_H, dimensions of the FCC section.

Performing identical substitutions into the definition of the average diagonal shear stress $(\tau_d)_{sh}$ of Eqs. (5.8) and (5.10) and setting the effective diagonal shear stress (τ_{de}) as $(\tau_{de}) = k_e(\tau_d)_{sh}$ yield the following:

$$(\tau_{de})_{sh} = (E_{je})_B(\psi_\tau)_{sh}\varepsilon_j = (f_{de})_{sh}\tan\theta_b \tag{5.14}$$

$$(\psi_\tau)_{sh} = \frac{\sin\theta_b}{\chi_{sh}} = (\psi_d)_{sh}\tan\theta_b \tag{5.15}$$

where $(\psi_\tau)_{sh}$ is a diagonal shear equilibrium coefficient of the FCC section.

The normalized effective confining stress $(F_{de})_{sh}$ and the normalized diagonal shearing stress $(\mathrm{T}_{de})_{sh}$ of any given FRP jacket is defined as:

$$(F_{de})_{sh} = \frac{(f_{de})_{sh}}{f_{co}} \tag{5.16}$$

$$(\mathrm{T}_{de})_{sh} = \frac{(\tau_{de})_{sh}}{f_{co}} \tag{5.17}$$

where f_{co} is the unconfined peak compressive strength of the concrete core.

Using the effective transverse stiffness $(E_{je})_B$ of Eq. (4.15), the effective confining stiffness $(C_{je})_{sh}$ of Eq. (4.17), the normalized effective jacket stiffness K_{je} of Eq.

(4.18), and the effective diagonal confining stress $(f_{de})_{sh}$ of Eq. (5.12), the normalized effective confining stress $(F_{de})_{sh}$ of Eq. (5.16) can be rewritten as:

$$(F_{de})_{sh} = (K_{je})_{sh}(\gamma_d)_{sh}\varepsilon_j \tag{5.18}$$

$$(\gamma_d)_{sh} = \frac{2(\psi_d)_{sh}}{C_{sh}} \tag{5.19}$$

where $(\gamma_d)_{sh}$ is a normalized diagonal confinement equilibrium coefficient of the FCC section. In addition, C_{sh} is an FRP-jacket shape-dependent reinforcement ratio coefficient, summarized in **Table 4.2**.

The same can be done for the normalized diagonal shearing stress $(\mathrm{T}_{de})_{sh}$ of Eq. (5.17) where:

$$(T_{de})_{sh} = (K_{je})_{sh}(\gamma_\tau)_{sh}\varepsilon_j = (K_{je})_{sh}(\gamma_d)_{sh}\varepsilon_j \tan\theta_b \tag{5.20}$$

$$(\gamma_\tau)_{sh} = \frac{2(\psi_\tau)_{sh}}{C_{sh}} = (\gamma_d)_{sh}\tan\theta_b \tag{5.21}$$

where $(\gamma_\tau)_{sh}$ is a normalized diagonal shear equilibrium coefficient of the FCC section.

Using the geometry of **Figures 5.6-5.10**, the $\cos\theta_d$ and $\sin\theta_d$ terms included in the following relationships are given as:

$$\sin\theta_d = \frac{H_c}{\sqrt{(H_c)^2 + (B_c)^2}} = \frac{1}{\sqrt{1 + \frac{1}{(\alpha_{sh})^2}}} \tag{5.22}$$

$$\cos\theta_d = \frac{B_c}{\sqrt{(H_c)^2 + (B_c)^2}} = \frac{1}{\sqrt{1 + (\alpha_{sh})^2}} \tag{5.23}$$

where the angle of inclination θ_d of the main diagonal D_c and the section aspect ratio α_{sh} of the FCC sections shown in **Figures 5.6-5.10** are defined in Eqs. (4.1), (4.2), and (4.3), respectively.

In what follows, a series of relationships for the nondimensional shape-dependent parameter χ_{sh} of Eq. (5.11) and the FRP jacket shape-dependent angles θ_a and θ_b are introduced from the diagonal equilibrium of the FRP-jacketed concrete sections of the various shapes shown in **Figures 5.6-5.10**.

Rectangular Sections

A unit length rectangular FRP-confined concrete BFCC or CFFT section, as shown in **Figure 5.11(a),** is considered herein. From the geometry of the half body shown in **Figure 5.11,** the minor B_{sh} and major H_{sh} dimensions of the main diagonal D_{sh} of the rectangular FRP-confined concrete (RFCC) section can be found as:

$$H_{sh} = H_c\left[1 - 2\alpha_j\left(1 - \sin\theta_a\right)\right] \tag{5.24}$$

$$B_{sh} = B_c\left[1 - 2\alpha_j\left(1 - \sin\theta_a\right)\right] \tag{5.25}$$

where the corner aspect ratio of the FRP jacket α_j is defined in Eq.(4.4).

The main concrete core diagonal D_{sh} of the rectangular RFCC section, as shown in **Figure 5.11,** is given as:

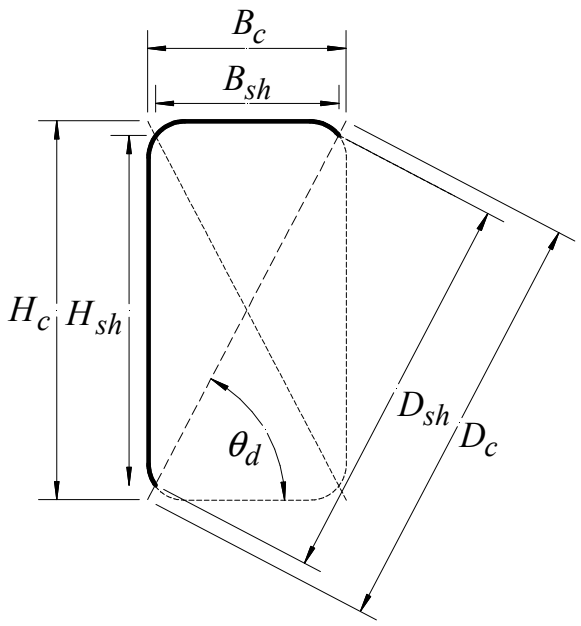

(a)

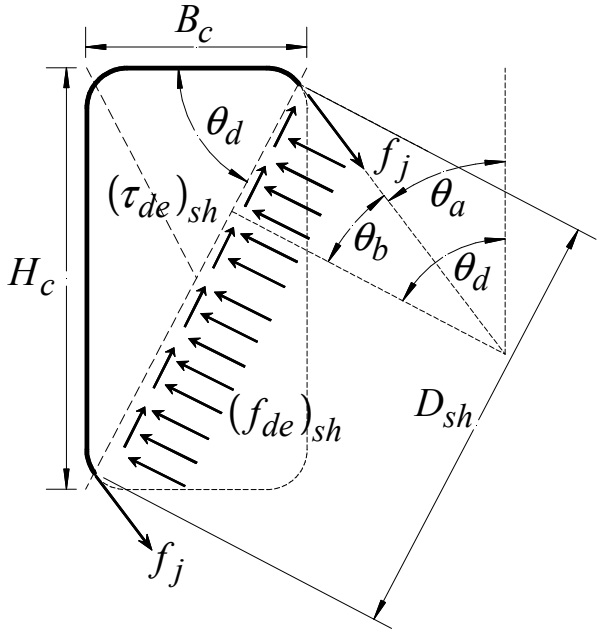

(b)

Figure 5.11 Rectangular FRP-confined concrete section: (a) typical section geometry, (b) diagonal equilibrium.

$$D_{sh} = \sqrt{(B_{sh})^2 + (H_{sh})^2} = \frac{H_{sh}}{\sin\theta_d} = \frac{B_{sh}}{\cos\theta_d} \tag{5.26}$$

The shape-dependent angles θ_a and θ_b of the rectangular FRP jacket are given by:

$$\theta_a = \theta_d - \theta_b \tag{5.27}$$

$$\theta_b = \sin^{-1}(\sin\theta_d - \cos\theta_d) \tag{5.28}$$

Substituting H_{sh} of Eq. (5.24) into the definition of D_{sh} of Eq. (5.26) and solving for the nondimensional shape-dependent parameter of the RFCC section χ_{sh} of Eq. (5.11) yields:

$$\chi_{sh} = \frac{1 - 2\alpha_j(1 - \sin\theta_a)}{\sin\theta_d} \tag{5.29}$$

Square Sections

A unit length square FRP-confined concrete BFCC or CFFT section, as shown in **Figure 5.12(a)**, is considered herein. From the geometry of the half body shown in **Figure 5.12,** the minor B_{sh} and major H_{sh} dimensions of the main diagonal D_{sh} of the square FRP-confined concrete (SFCC) section can be found as:

$$H_{sh} = H_c\left[1 - \alpha_j\left(2 - \sqrt{2}\right)\right] \tag{5.30}$$

$$B_{sh} = B_c\left[1 - \alpha_j\left(2 - \sqrt{2}\right)\right] \tag{5.31}$$

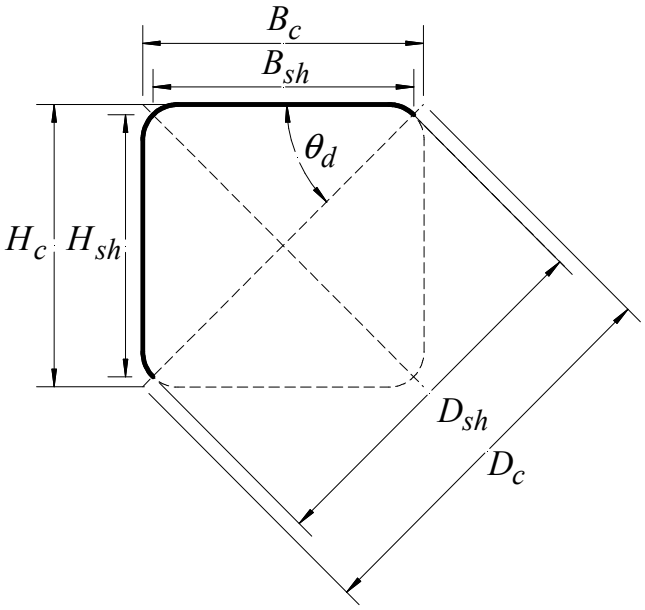

(a)

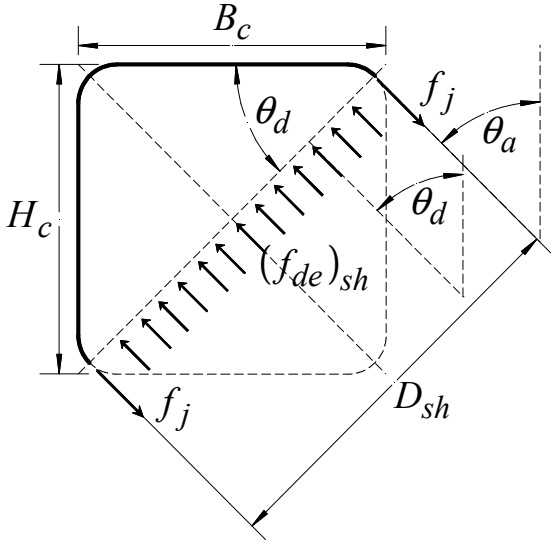

(b)

Figure 5.12 Square FRP-confined concrete section: (a) typical section geometry, (b) diagonal equilibrium.

For a square section $B_c = H_c$ (i.e., $\alpha_{sh} = 1.0$); hence the minor B_{sh} dimension is equal to the major H_{sh} dimension and can be used interchangeably given that $B_{sh} = H_{sh}$. The main concrete core diagonal D_{sh} of the SFCC section, as shown in **Figure 5.12,** is given as:

$$D_{sh} = \sqrt{(B_{sh})^2 + (H_{sh})^2} = \sqrt{2}\, H_{sh} \tag{5.32}$$

Substituting H_{sh} of Eq. (5.30) into D_{sh} of Eq. (5.32) and solving for the nondimensional shape-dependent parameter χ_{sh} of the SFCC section of Eq. (5.11) yield:

$$\chi_{sh} = \frac{1 - 2\alpha_j (1 - \sin\theta_d)}{\sin\theta_d} = \sqrt{2}\left[1 - \alpha_j \left(2 - \sqrt{2}\right)\right] \tag{5.33}$$

The nondimensional shape-dependent parameter χ_{sh} of the SFCC section of Eq. (5.33) is similar to that introduced in Eq. (5.29) for RFCC sections, since a SFCC section is the special case of a RFCC section with rounded corners with a unity section aspect ratio (i.e., $\alpha_{sh} = 1.0$ and $\theta_d = 45^\circ$).

As shown in **Figure 5.12(b)**, the shape-dependent angles θ_a and θ_b of the SFCC jacket are $\theta_a = \theta_d = 45^\circ$ and $\theta_b = 0$; these values can also be found by substituting $\alpha_{sh} = 1.0$ (i.e., $\theta_d = 45^\circ$) into θ_b of the RFCC section of Eq. (5.28).

Oval Sections

A unit length oval FRP-confined concrete BFCC or CFFT section, as shown in **Figure 5.13(a)**, is considered herein. From the geometry of the half body shown in

Figure 5.13, the minor B_{sh} and major H_{sh} dimensions of the main diagonal D_{sh} of an oval FRP-confined concrete (OFCC) section can be found as:

$$H_{sh} = \frac{H_c}{\alpha_{sh}}\left[\alpha_{sh} - (1 - \sin\theta_a)\right] \tag{5.34}$$

$$B_{sh} = \frac{H_c}{\alpha_{sh}^2}\left[\alpha_{sh} - (1 - \sin\theta_a)\right] \tag{5.35}$$

The main diagonal D_{sh} is given by Eq. (5.26). The shape-dependent angles θ_a and θ_b of the oval FRP jacket are given by Eqs. (5.27) and (5.28), respectively.

Substituting H_{sh} of Eq. (5.34) into the definition of D_{sh} of Eq. (5.26) and solving for the nondimensional shape-dependent parameter χ_{sh} of the OFCC section of Eq. (5.11) yield:

$$\chi_{sh} = \frac{\alpha_{sh} - (1 - \sin\theta_a)}{\alpha_{sh}\sin\theta_d} = \csc^2\theta_d\left[\sin\theta_d - \cos\theta_d(1 - \sin\theta_a)\right] \tag{5.36}$$

The nondimensional shape-dependent parameter χ_{sh} of the OFCC section of Eq. (5.36) is similar to that introduced in Eq. (5.29) for RFCC sections, since an OFCC section is the special case of a rectangular section with rounded corners with $\alpha_{sh} \geq 1.0$ and $\alpha_j = 1/(2\alpha_{sh})$. Also, an oval section with a unity aspect ratio $\alpha_{sh} = 1.0$ is a circular section, as shown in the following section, since a circular section is also a special case of a square section with rounded corners for which $R_j = D_j/2$ or $\alpha_j = 1/2$.

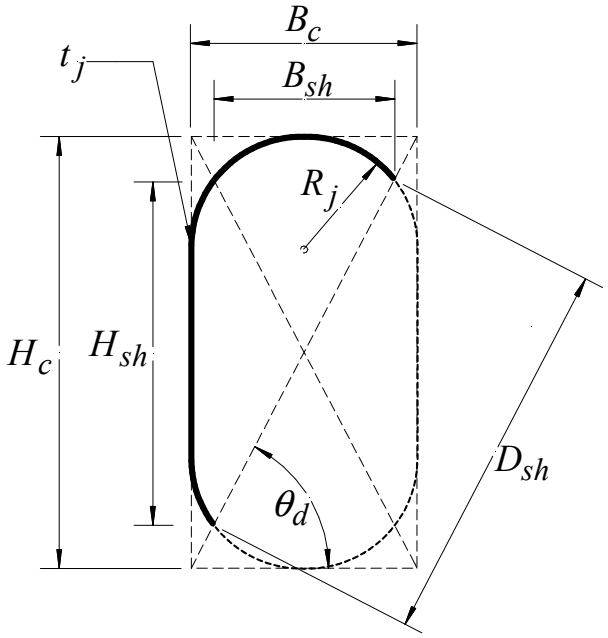

(a)

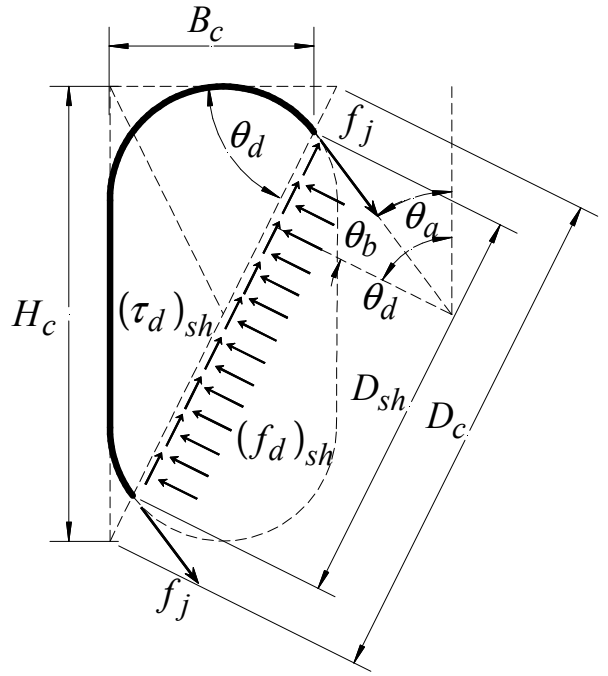

(b)

Figure 5.13 Oval FRP-confined concrete section: (a) typical section geometry, (b) diagonal equilibrium.

Circular Sections

In this section, the following analysis of circular FRP-confined concrete (CFCC) sections also includes square concrete sections confined by shape-modifying circular FRP jackets introduced in Chapter 4. A unit length CFCC section, as shown in **Figure 5.14(a)**, is considered herein.

From the geometry of the half body shown in **Figure 5.14,** the minor B_{sh} and major H_{sh} dimensions of the main diagonal D_{sh} of the CFCC section can be found as:

$$B_{sh} = B_c \sin\theta_d \tag{5.37}$$

$$H_{sh} = H_c \sin\theta_d \tag{5.38}$$

Considering that for a circular section $B_c = H_c$ (i.e., $\alpha_{sh} = 1.0$), the minor dimension B_{sh} of Eq. (5.37) is equal to the major dimension H_{sh} of Eq. (5.37), i.e., $B_{sh} = H_{sh}$. The $\sin\theta_d$ terms in Eq. (5.37) and (5.38) is equal to $\sqrt{2}/2$, determined by substituting $\alpha_{sh} = 1.0$ into $\sin\theta_d$ of Eq. (5.22). The main concrete core diagonal D_{sh} of the CFCC section, as shown **Figure 5.14,** is given by:

$$D_{sh} = \sqrt{(B_{sh})^2 + (H_{sh})^2} = \sqrt{2}\, H_{sh} \tag{5.39}$$

Substituting H_{sh} of Eq. (5.37) into D_{sh} of Eq. (5.39) and solving for the nondimensional shape-dependent parameter χ_{sh} of the CFCC section of Eq. (5.11) yield $\chi_{sh} = 1.0$ for a CFCC section.

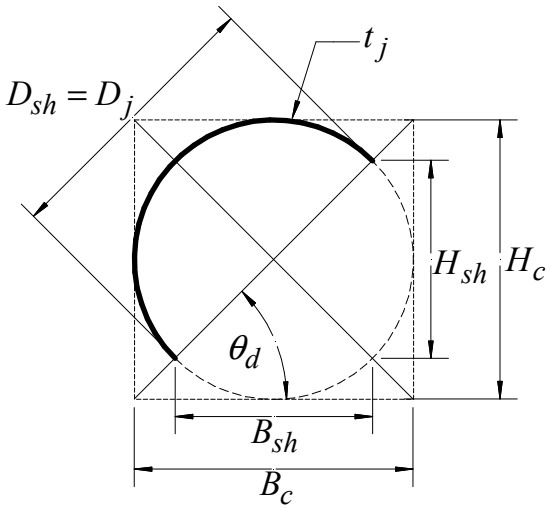

(a)

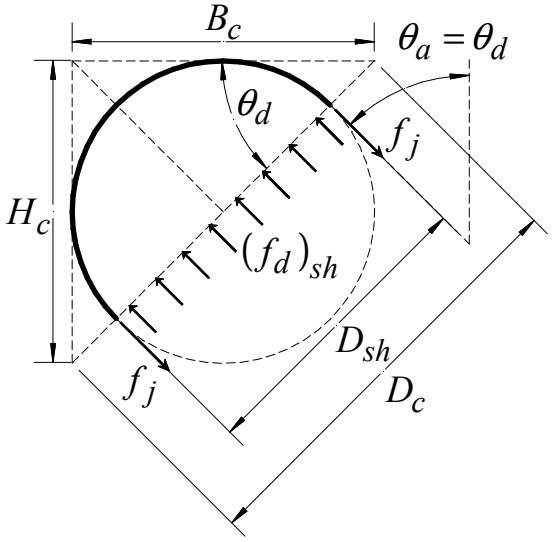

(b)

Figure 5.14 Circular FRP-confined concrete section: (a) typical section geometry; (b) diagonal equilibrium.

A value of $\chi_{sh} = 1.0$ can also be obtained by substituting $\alpha_j = 1/2$ (i.e., $R_j = D_j/2$), $\theta_b = 0^\circ$, and $\theta_d = 45^\circ$ for $\alpha_{sh} = 1.0$ (i.e., $B_c = H_c = D_j$) into χ_{sh} of Eq. (5.29), since a circular section is a special case of a rectangular section with rounded corners for which $\alpha_{sh} = 1.0$ and $\alpha_j = 1/2$ (i.e., $R_j = D_j/2$).

A value of $\chi_{sh} = 1.0$ can also be obtained by substituting $\alpha_j = 1/2$ (i.e., $R_j = D_j/2$) into χ_{sh} of Eq. (5.33), since a circular section is also a special case of a square section with rounded corners for which $R_j = D_j/2$ or $\alpha_j = 1/2$.

As shown in **Figure 5.14(b)**, the shape-dependent angles θ_a and θ_b of the CFCC jacket are $\theta_a = \theta_d = 45^\circ$ and $\theta_b = 0$; these values can also be found by substituting $\alpha_{sh} = 1.0$ into θ_b of the RFCC section of Eq. (5.28).

Elliptical Sections

In this section the analysis of elliptical FRP-confined concrete (EFCC) sections also includes rectangular sections confined by shape-modifying elliptical FRP jackets. A unit length EFCC section, as shown in **Figure 5.15,** is considered herein.

The main concrete core diagonal D_{sh} of the EFCC section is given by D_{sh} of Eq. (5.39). The shape-dependent angles θ_a and θ_b of the elliptical FRP jacket are given by:

$$\theta_a = 90^\circ - \theta_d \tag{5.40}$$

$$\theta_b = \theta_d - \theta_a = 2\theta_d - 90^\circ \tag{5.41}$$

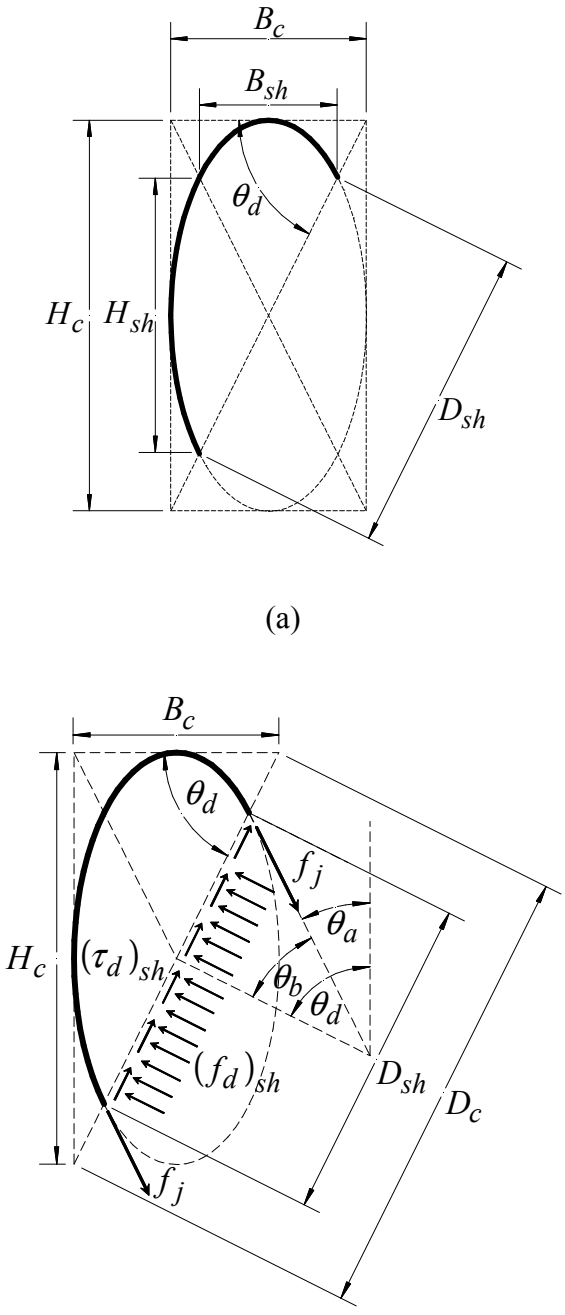

Figure 5.15 Elliptical FRP-confined concrete section: (a) typical section geometry, (b) diagonal equilibrium

Substituting H_{sh} of Eq. (5.38) into D_{sh} of Eq. (5.39) and solving for the nondimensional shape-dependent parameter χ_{sh} of the EFCC section of Eq. (5.11) yield:

$$\chi_{sh} = \frac{\sqrt{2}}{2\sin(\theta_d)} \tag{5.42}$$

As indicated in Chapter 4, a circular section is a special case of an ellipse with a unity aspect ratio ($\alpha_{sh} = 1.0$) for which $\theta_d = 45°$. As a result, the nondimensional shape-dependent parameter χ_{sh} of the EFCC section of Eq. (5.42) reduces to that of a circular section for which $\chi_{sh} = 1.0$.

The nondimensional shape-dependent parameter χ_{sh} of Eq. (5.11) of the FCC sections shown in **Figures 5.11-5.15** introduced in Eqs. (5.29)-(5.42) is summarized in **Table 5.1**. The shape-dependent angles θ_a and θ_b of the FCC sections shown in **Figures 5.5-5.8,** introduced in Eqs. (5.27)-(5.41), are summarized in **Table 5.2.**

Table 5.1 Summary of the nondimensional shape-dependent parameter χ_{sh} of various FRP-confined concrete sections.

FRP jacket shape	Nondimensional shape-dependent parameter χ_{sh}	Ref. Eq.
Rectangular	$\chi_{sh} = \dfrac{1 - 2\alpha_j (1 - \sin\theta_a)}{\sin\theta_d}$	(5.29)
Square	$\chi_{sh} = \sqrt{2}\left[1 - \alpha_j \left(2 - \sqrt{2}\right)\right]$	(5.33)
Oval	$\chi_{sh} = \dfrac{\alpha_{sh} - (1 - \sin\theta_a)}{\alpha_{sh} \sin\theta_d}$	(5.36)
Circular	$\chi_{sh} = 1.0$	N/A
Elliptical	$\chi_{sh} = \dfrac{\sqrt{2}}{2\sin\theta_d}$	(5.42)

Table 5.2 Summary of the shape-dependent angles θ_a and θ_b of various FRP-confined concrete sections.

FRP jacket shape	FRP jacket angle			
	θ_a	**Ref. Eq.**	θ_b	**Ref. Eq.**
Rectangular	$\theta_a = \theta_d - \theta_b$	(5.27)	$\theta_b = \sin^{-1}(\sin\theta_d - \cos\theta_d)$	(5.28)
Square	$\theta_a = \theta_d = 45^\circ$	N/A	$\theta_b = 0^\circ$	N/A
Oval	$\theta_a = \theta_d - \theta_b$	N/A	$\theta_b = \sin^{-1}(\sin\theta_d - \cos\theta_d)$	(5.28)
Circular	$\theta_a = \theta_d = 45^\circ$	N/A	$\theta_b = 0^\circ$	N/A
Elliptical	$\theta_a = 90^\circ - \theta_d$	(5.40)	$\theta_b = 2\theta_d - 90^\circ$	(5.41)

CHAPTER 6

STRAIN COMPATIBILITY OF CONCRETE SECTIONS CONFINED BY FIBER-REINFORCED POLYMER JACKETS

In this chapter, a series of analytical strain compatibility relationships are introduced from the analysis of the dilation behavior of rectangular, square, oval, circular and elliptical concrete columns confined by FRP jackets, using the concept of diagonal equilibrium of FRP-confined concrete (FCC) sections, introduced in Chapter 5.

The assumptions made in Chapter 5 are also applicable to the transverse and diagonal dilation analysis of FRP-confined concrete sections introduced herein. These strain compatibility relationships are then utilized in Chapters 7 and 8 to describe and model the transverse and diagonal dilation of FCC sections.

It is shown herein that due to the elastic properties of the confining FRP jacket, as introduced in Chapter 4, the geometry of the FRP jacket plays a significant role in determining a series of mathematical relationships between the axial strain and the transverse and diagonal dilation strains in the FRP-confined concrete core and FRP jacket.

These strain compatibility relationships are used in Chapters 7, 8, and 9 to describe how the section shape and geometry affect the transverse and diagonal dilation of the FCC section and the passive confinement provided by the restraining elastic FRP jacket.

Rectangular Sections

A rectangular FRP-confined concrete (RFCC) sections, with rounded corners that is confined with an FRP jacket having a corner radius R_j, a thickness t_j, and a hoop stiffness E_j, is shown in **Figure 6.1**.

From this figure, the minor $B_{sh}^{'}$ and major $H_{sh}^{'}$ dimensions of the diagonal $D_{sh}^{'}$ of the RFCC section are given by:

$$B_{sh}^{'} = B_c - R_j = B_c\left(1-\alpha_j\alpha_{sh}\right) \tag{6.1}$$

$$H_{sh}^{'} = H_c - R_j\tan(\theta_d) = H_c\left(1-\alpha_j\alpha_{sh}\right) \tag{6.2}$$

where the FRP jacket aspect ratio α_{sh} and the jacket corner aspect ratio α_j, are defined in Eqs.(4.2) and (4.4), respectively.

As shown in **Figure 6.1**, H_c and B_c are the major and minor dimensions of the FRP jacket, respectively; the diagonal angle θ_d is given in Eq. (4.1); the main jacket diagonal D_c is defined in Eq. (4.3); the FRP jacket shape-dependent angles θ_a and θ_b of an RFCC section are defined in Eqs. (5.27) and (5.28), respectively.

The main core diagonal D_{sh} of an FCC section is defined in Eq. (5.11) with the shape parameter χ_{sh} in Eq. (5.29). Also, ε_j is the diagonal FRP jacket strain, and ε_B and ε_H are the FRP jacket strains along the minor B_c and major H_c FRP jacket dimensions, respectively.

The diagonal $D_{sh}^{'}$ of an RFCC, as shown in **Figures 6.1**, is given by:

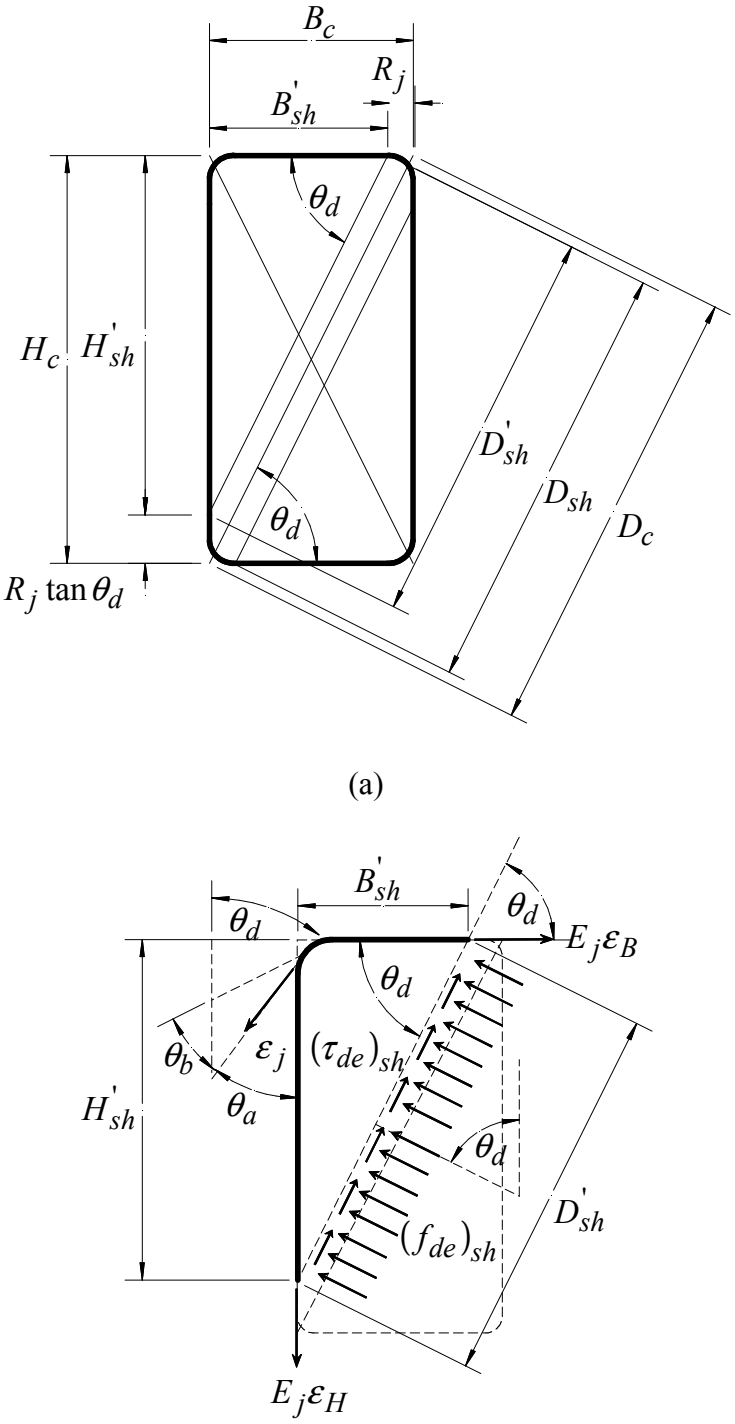

Figure 6.1 Rectangular FRP-confined concrete section: (a) section geometry, (b) offset diagonal equilibrium.

$$D_{sh}^{'} = \sqrt{\left(B_{sh}^{'}\right)^2 + \left(H_{sh}^{'}\right)^2} = \frac{H_{sh}^{'}}{\sin\theta_d} = \frac{B_{sh}^{'}}{\cos\theta_d} \tag{6.3}$$

where the $\cos\theta_d$ and $\sin\theta_d$ terms are defined in Eqs. (5.22) and (5.23), respectively.

A relationship between the diagonal $D_{sh}^{'}$ of Eq. (6.3) and the major jacket dimension H_c can be found by substituting $H_{sh}^{'}$ of Eq. (6.2) into Eq. (6.3), which yields:

$$D_{sh}^{'} = \lambda_{sh} H_c \tag{6.4}$$

$$\lambda_{sh} = \frac{\left(1 - \alpha_j \alpha_{sh}\right)}{\sin\theta_d} \tag{6.5}$$

where λ_{sh} is a diagonal shape coefficient that relates the diagonal $D_{sh}^{'}$ of the RFCC section to the major FRP jacket dimension H_c.

Using the horizontal jacket stress $\left(f_j\right)_B$ of Eq. (5.3), horizontal equilibrium of the half body of an RFCC section as shown in **Figure 6.1(b)** yields:

$$E_j \varepsilon_B t_j - \left(f_d\right)_{sh} D_{sh}^{'} \sin\theta_d + \left(\tau_d\right)_{sh} D_{sh}^{'} \cos\theta_d = 0 \tag{6.6}$$

Substituting the diagonal shearing stress $\left(\tau_d\right)_{sh}$ of Eq. (5.10) into the equilibrium relationship of Eq. (6.6), solving for the diagonal confining stress $\left(f_d\right)_{sh}$, setting the effective diagonal confining stress as $\left(f_{de}\right) = k_e \left(f_d\right)_{sh}$, using $\left(E_{je}\right)_B$ of Eq. (4.15) and $D_{sh}^{'}$ of Eq. (6.4) yield the following generalized relationship of the effective diagonal

confining stress $(f_{de})_{sh}$ in terms of the FRP jacket strain ε_B along the minor dimension B_c as follows:

$$(f_{de})_{sh} = (E_{je})_B (\psi_B)_{sh} \varepsilon_B \tag{6.7}$$

where $(\psi_B)_{sh}$ is the minor diagonal equilibrium coefficient of the FCC section. Using D'_{sh} of Eq. (6.4) with λ_{sh} of Eq. (6.5) for an RFCC section, this coefficient is given by:

$$(\psi_B)_{sh} = \frac{1}{2(1-\alpha_j \alpha_{sh})(1-\cot\theta_d \tan\theta_b)} \tag{6.8}$$

Equating the effective diagonal confining stress $(f_{de})_{sh}$ of Eqs. (5.12) and (6.7), yields the following generalized relationship between minor FRP jacket strain ε_B and the diagonal FRP jacket strain ε_j:

$$\varepsilon_B = (\gamma_B)_{sh} \varepsilon_j \tag{6.9}$$

$$(\gamma_B)_{sh} = \frac{\varepsilon_B}{\varepsilon_j} = \left(\frac{\psi_d}{\psi_B}\right)_{sh} \tag{6.10}$$

where $(\gamma_B)_{sh}$ is the FRP minor strain ratio that relates the minor strain ε_B to the diagonal FRP jacket strain ε_j and $(\psi_d)_{sh}$ is the diagonal confinement equilibrium coefficient of the FCC section of Eq. (5.13). In RFCC sections, the minor strain coefficient $(\gamma_B)_{sh}$ can be found by substituting $(\psi_d)_{sh}$ of Eq. (5.13) with χ_{sh} of Eq. (5.29) and $(\psi_B)_{sh}$ of Eq. (6.8) into $(\gamma_B)_{sh}$ of Eq. (6.10), which yields:

$$(\gamma_B)_{sh} = \frac{\varepsilon_B}{\varepsilon_j} = \frac{2(1-\alpha_j \alpha_{sh})\sin\theta_a}{1-2\alpha_j(1-\sin\theta_a)} \tag{6.11}$$

Using the vertical jacket stress $(f_j)_H$ of Eq. (5.4), the vertical equilibrium of the half body of the RFCC section of **Figure 6.1(b)** yields the following:

$$(f_d)_{sh} D'_{sh} \cos\theta_d + (\tau_d)_{sh} D'_{sh} \sin\theta_d - E_j \varepsilon_H t_j = 0 \tag{6.12}$$

Substituting the diagonal shearing stress $(\tau_d)_{sh}$ of Eq. (5.10) into the equilibrium relationship of Eq. (6.12), solving for the diagonal confining stress $(f_d)_{sh}$, and performing the same substitutions as in the horizontal equilibrium of the RFCC section yield the following generalized relationship between the effective diagonal confining stress $(f_{de})_{sh}$ and the major FRP jacket strain ε_H:

$$(f_{de})_{sh} = (E_{je})_B (\psi_H)_{sh} \varepsilon_H \tag{6.13}$$

where $(\psi_H)_{sh}$ is the major diagonal equilibrium coefficient of the FCC section. For an RFCC section, this coefficient is given by:

$$(\psi_H)_{sh} = \frac{1}{2(1-\alpha_j \alpha_{sh})(\cot\theta_d + \tan\theta_b)} \tag{6.14}$$

Equating the effective diagonal confining stress $(f_{de})_{sh}$ of Eqs. (5.12) and (6.14), yields the following generalized relationship between the major FRP jacket strain ε_H and the tangential jacket strain ε_j:

$$\varepsilon_H = (\gamma_H)_{sh}\,\varepsilon_j \tag{6.15}$$

$$(\gamma_H)_{sh} = \frac{\varepsilon_H}{\varepsilon_j} = \left(\frac{\psi_d}{\psi_H}\right)_{sh} \tag{6.16}$$

where $(\gamma_H)_{sh}$ is the major strain ratio that relates the major jacket strain ε_H to the tangential jacket strain ε_j.

In RFCC sections, the major strain ratio $(\gamma_H)_{sh}$ can be found by substituting $(\psi_d)_{sh}$ of Eq. (5.13) with χ_{sh} of Eq. (5.29) and $(\psi_H)_{sh}$ of Eq. (6.14) into $(\gamma_H)_{sh}$ of Eq. (6.16), which yields:

$$(\gamma_H)_{sh} = \frac{\varepsilon_H}{\varepsilon_j} = \frac{2(1-\alpha_j\alpha_{sh})\cos\theta_a}{1-2\alpha_j(1-\sin\theta_a)} \tag{6.17}$$

Solving for the diagonal jacket strain ε_j in Eqs. (6.9) and (6.15) yields the following generalized transverse strain ratio α_ε:

$$\alpha_\varepsilon = \frac{\varepsilon_H}{\varepsilon_B} = \frac{(\gamma_H)_{sh}}{(\gamma_B)_{sh}} \tag{6.18}$$

Substituting $(\gamma_B)_{sh}$ of Eq. (6.11) and $(\gamma_H)_{sh}$ of Eq. (6.17) into the above relationship yields the following transverse strain ratio α_ε:

$$\alpha_\varepsilon = \frac{\varepsilon_H}{\varepsilon_B} = \cot\theta_a \tag{6.19}$$

Square Sections

A square FRP-confined concrete (SFCC) section, with rounded corners that is confined with an FRP jacket having a corner radius R_j, a thickness t_j, and a hoop stiffness E_j is shown in **Figure 6.2**.

From this figure, the minor B'_{sh} and major H'_{sh} dimensions of the diagonal D'_{sh} of the SFCC section are given by:

$$B'_{sh} = B_c - R_j = B_c\left(1-\alpha_j\right) \tag{6.20}$$

$$H'_{sh} = H_c - R_j = H_c\left(1-\alpha_j\right) \tag{6.21}$$

Substituting H'_{sh} of Eq. (6.21) into (6.3) and (6.4) yields the following diagonal shape coefficient λ_{sh} for SFCC sections:

$$\lambda_{sh} = \frac{\left(1-\alpha_j\right)}{\sin\theta_d} = \sqrt{2}\left(1-\alpha_j\right) \tag{6.22}$$

The previous diagonal shape coefficient λ_{sh} can also be found by substituting $\alpha_{sh} = 1.0$ and $\theta_d = 45^\circ$ into λ_{sh} of an RFCC section of Eq. (6.5).

Using the horizontal jacket stress $\left(f_j\right)_B$ of Eq. (5.3), horizontal equilibrium of the half body of an SFCC section of **Figure 6.2(b)** yields:

$$E_j\varepsilon_B t_j - \left(f_d\right)_{sh} D'_{sh}\sin\theta_d = 0 \tag{6.23}$$

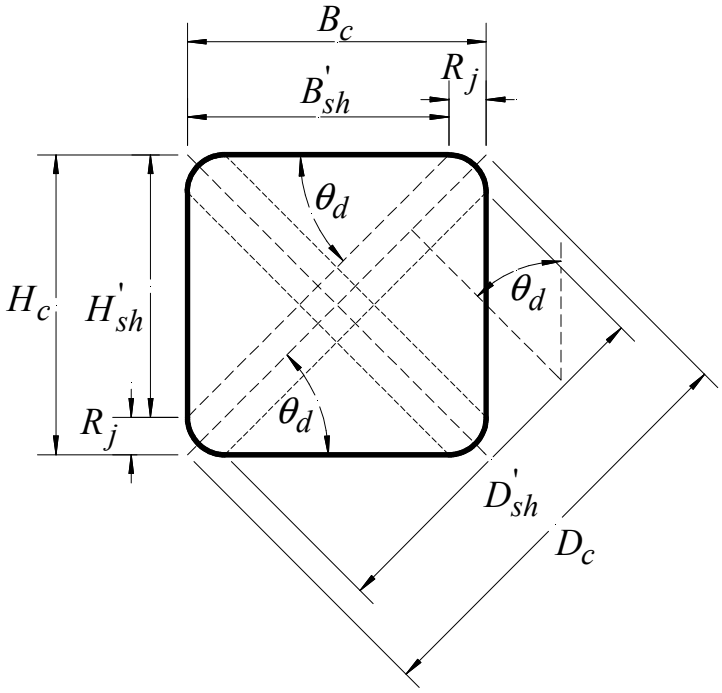

(a)

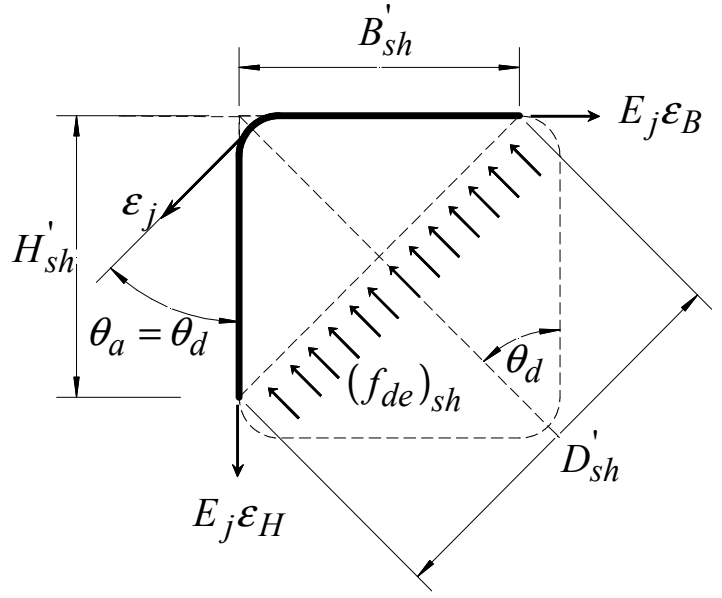

(b)

Figure 6.2 Square FRP-confined concrete sections: (a) section geometry, (b) offset diagonal equilibrium.

Solving for the diagonal confining stress $(f_d)_{sh}$ in the previous relationship, setting $(f_{de}) = k_e (f_d)_{sh}$, using $(E_{je})_B$ of Eq. (4.15), D'_{sh} of Eq. (6.4), λ_{sh} of Eq. (6.22), and using $(f_{de})_{sh}$ of Eq. (6.7) yield the following the minor diagonal equilibrium coefficient $(\psi_B)_{sh}$ of an SFCC section:

$$(\psi_B)_{sh} = \frac{1}{2(1-\alpha_j)} \tag{6.24}$$

The above minor diagonal equilibrium coefficient $(\psi_B)_{sh}$ can also be found by substituting $\alpha_{sh} = 1.0$, $\theta_d = \theta_a = 45^\circ$, and $\theta_b = 0$ into $(\psi_B)_{sh}$ of an RFCC section of Eq. (6.6).

In SFCC sections, the minor strain coefficient $(\gamma_B)_{sh}$ of Eq. (6.10) can be found by substituting $(\psi_d)_{sh}$ of Eq. (5.13) with χ_{sh} of Eq. (5.33) and $(\psi_B)_{sh}$ of Eq. (6.24) into Eq. (6.10), which yield:

$$(\gamma_B)_{sh} = \frac{\varepsilon_B}{\varepsilon_j} = \frac{\sqrt{2}(1-\alpha_j)}{1-\alpha_j(2-\sqrt{2})} \tag{6.25}$$

The above minor strain coefficient $(\gamma_B)_{sh}$ can also be found by substituting $\alpha_{sh} = 1.0$, $\theta_d = \theta_a = 45^\circ$ and $\theta_b = 0$ into the $(\gamma_B)_{sh}$ of an RFCC section of Eq. (6.11).

Using the vertical jacket stress $(f_j)_H$ of Eq. (5.4), the vertical equilibrium of the half body of a RFCC section of **Figure 6.1(b)** yields the following:

$$(f_d)_{sh} D'_{sh} \cos\theta_d - E_j \varepsilon_H t_j = 0 \tag{6.26}$$

Solving for the diagonal confining stress $(f_d)_{sh}$ in the above relationship and performing the same substitutions as in the horizontal equilibrium of the SFCC section yield the following the major diagonal equilibrium coefficient $(\psi_H)_{sh}$ of SFCC sections:

$$(\psi_H)_{sh} = \frac{1}{2(1-\alpha_j)} \tag{6.27}$$

The above major diagonal equilibrium coefficient $(\psi_H)_{sh}$ can also be found by substituting $\alpha_{sh} = 1.0$, $\theta_d = \theta_a = 45^\circ$, and $\theta_b = 0$ into $(\psi_H)_{sh}$ of an RFCC section of Eq. (6.14). The above relationship indicates that for SFCC sections $(\psi_H)_{sh} = (\psi_B)_{sh}$.

For an SFCC section, the major strain coefficient $(\gamma_H)_{sh}$ of Eq. (6.16) can be found by substituting $(\psi_d)_{sh}$ of Eq. (5.13) with χ_{sh} of Eq. (5.33) and $(\psi_H)_{sh}$ of Eq. (6.27) into Eq. (6.16), which yield:

$$(\gamma_H)_{sh} = \frac{\varepsilon_H}{\varepsilon_j} = \frac{\sqrt{2}(1-\alpha_j)}{1-\alpha_j(2-\sqrt{2})} \tag{6.28}$$

The above major strain coefficient $(\gamma_H)_{sh}$ can also be found by substituting $\alpha_{sh} = 1.0$, $\theta_d = \theta_a = 45^\circ$, and $\theta_b = 0$ into the major strain coefficient $(\gamma_H)_{sh}$ of an RFCC section of Eq. (6.17). The above relationship indicates that for an SFCC section $(\gamma_B)_{sh} = (\gamma_H)_{sh}$.

Substituting $(\gamma_B)_{sh}$ of Eq. (6.25) and $(\gamma_H)_{sh}$ of Eq.(6.28) into the transverse strain ratio α_ε of Eq. (6.18) yields:

$$\alpha_\varepsilon = \frac{\varepsilon_H}{\varepsilon_B} = \frac{(\gamma_H)_{sh}}{(\gamma_B)_{sh}} = 1.0 \tag{6.29}$$

The above strain ratio α_ε can also be found by substituting $\theta_d = \theta_a = 45^\circ$ into the strain ratio α_ε of Eq. (6.19) of an RFCC section, since an SFCC section is a special case of an RFCC section with a unit aspect ratio, i.e., $\alpha_{sh} = 1.0$. This indicates that the strain ratio α_ε of Eq. (6.19) also applies to SFCC sections.

Oval Sections

An oval FRP-confined concrete (OFCC) section, with rounded corners that is confined with an FRP jacket having a corner radius $R_j = B_c/2$, a thickness t_j, and a hoop stiffness E_j is shown in **Figure 6.3.** The oval sections considered herein also include rectangular section confined by shape-modifying oval FRP jackets, i.e., oval shape-modified (OSM) sections.

The minor B'_{sh} and major H'_{sh} dimensions of the diagonal D'_{sh}, shown in the OFCC section of **Figure 6.3,** are given by:

$$B'_{sh} = B_c - R_j = \frac{B_c}{2} \tag{6.30}$$

$$H'_{sh} = H_c - R_j \tan\theta_d = \frac{H_c}{2} \tag{6.31}$$

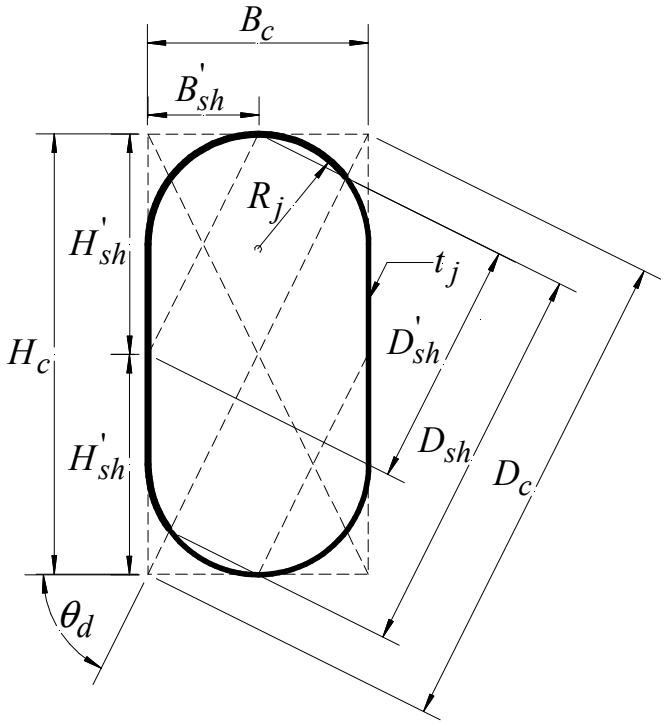

(a)

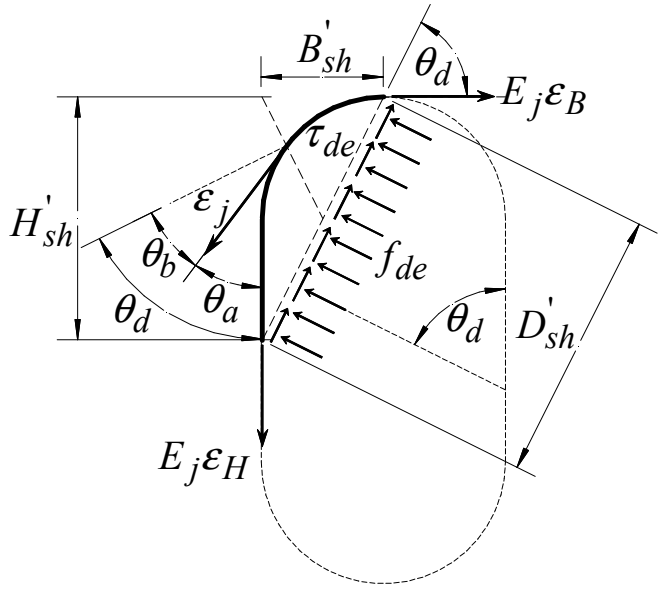

(b)

Figure 6.3 Oval FRP-confined concrete sections: (a) section geometry, (b) offset diagonal equilibrium.

Substituting H'_{sh} of Eq. (6.30) into (6.3) and (6.4) yields the following diagonal-shape coefficient λ_{sh} of Eq. (6.4) for OFCC sections:

$$\lambda_{sh} = \frac{1}{2\sin\theta_d} \tag{6.32}$$

The above diagonal equilibrium coefficient λ_{sh} can also be found by substituting $\alpha_j = 1/(2\alpha_{sh})$ into λ_{sh} of an RFCC section of Eq. (6.5).

Using the horizontal jacket stress $(f_j)_B$ of Eq. (5.3), horizontal equilibrium of the half body of an OFCC section of **Figure 6.3(b)** yields the equilibrium relationship of Eq. (6.6). Solving for the diagonal confining stress $(f_d)_{sh}$ in Eq. (6.6), setting the effective diagonal confining stress as $(f_{de}) = k_e(f_d)_{sh}$, using $(E_{je})_B$ of Eq. (4.15), D'_{sh} of Eq. (6.4), λ_{sh} of Eq. (6.32), and using $(f_{de})_{sh}$ of Eq. (6.7) yield the following the minor diagonal equilibrium coefficient $(\psi_B)_{sh}$ of an OFCC section:

$$(\psi_B)_{sh} = \frac{\alpha_{sh}}{(\alpha_{sh} - \tan\theta_b)} \tag{6.33}$$

The previous minor diagonal equilibrium coefficient $(\psi_B)_{sh}$ can also be found by substituting $\alpha_j = 1/(2\alpha_{sh})$ into the $(\psi_B)_{sh}$ of an RFCC section of Eq. (6.8).

In OFCC sections, the minor strain coefficient $(\gamma_B)_{sh}$ of Eq. (6.10) can be found by substituting $(\psi_d)_{sh}$ of Eq. (5.13) with χ_{sh} of Eq. (5.32) and $(\psi_B)_{sh}$ of Eq. (6.33), which yield:

$$\gamma_B = \frac{\varepsilon_B}{\varepsilon_j} = \frac{\alpha_{sh} \sin\theta_a}{\alpha_{sh} - (1 - \sin\theta_a)} \tag{6.34}$$

Using the vertical jacket stress $(f_j)_H$ of Eq. (5.4), the vertical equilibrium of the half body of an RFCC section of **Figure 6.3(b)** yields the equilibrium relationship of Eq. (6.12). Solving for the diagonal confining stress $(f_d)_{sh}$ in Eq. (6.26) and performing the same substitutions as in the horizontal equilibrium of the SFCC section yield the following major diagonal equilibrium coefficient $(\psi_H)_{sh}$ of OFCC sections:

$$(\psi_H)_{sh} = \frac{\alpha_{sh}}{(1 + \alpha_{sh} \tan\theta_b)} \tag{6.35}$$

The above major diagonal equilibrium coefficient $(\psi_H)_{sh}$ can also be found by substituting $\alpha_j = 1/(2\alpha_{sh})$ into $(\psi_H)_{sh}$ of an RFCC section of Eq. (6.14).

In OFCC sections, the major strain coefficient $(\gamma_H)_{sh}$ of Eq. (6.16) can be found by substituting $(\psi_d)_{sh}$ of Eq. (5.13) with χ_{sh} of Eq. (5.32) and $(\psi_H)_{sh}$ of Eq. (6.35) into Eq. (6.16), which yields:

$$(\gamma_H)_{sh} = \frac{\varepsilon_H}{\varepsilon_j} = \frac{\alpha_{sh} \cos\theta_a}{\alpha_{sh} - (1 - \sin\theta_a)} \tag{6.36}$$

The above major strain coefficient $(\gamma_H)_{sh}$ can also be found by substituting $\alpha_j = 1/(2\alpha_{sh})$ into $(\gamma_H)_{sh}$ of an RFCC section of Eq. (6.17). Substituting $(\gamma_B)_{sh}$ of

Eq. (6.34) and $(\gamma_H)_{sh}$ of Eq.(6.36) into the transverse strain ratio α_ε of Eq. (6.18) yields the transverse strain ratio of Eq. (6.19) for OFCC sections.

Circular Sections

The circular FRP-confined concrete (CFCC) sections included herein, also applies to square sections confined by shape-modifying circular FRP jackets. An CFCC section that is confined with a circular FRP jacket having radius R_j or diameter $D_j = 2R_j$, a thickness t_j, and a hoop stiffness E_j is shown in **Figure 6.4**.

From these figures, the minor $B'_{sh} = B_{sh}/2$, and major $H'_{sh} = H_{sh}/2$ dimensions of the diagonal D'_{sh}. The circular section dimensions B_{sh}, H_{sh}, and D_{sh} are given in Eqs. (5.37), (5.38), and (5.39), respectively. As a result, for an CFCC section, the diagonal shape coefficient λ_{sh} of Eq. (6.4) is given by:

$$\lambda_{sh} = \frac{1}{2\sin\theta_d} = \frac{\sqrt{2}}{2} \tag{6.37}$$

The previous diagonal equilibrium coefficient λ_{sh} can be found by substituting $\alpha_{sh} = 1.0$, $\alpha_j = 1/2$, and $\theta_d = 45^\circ$ into λ_{sh} of an RFCC section of Eq. (6.5). The diagonal equilibrium coefficient λ_{sh} of Eq. (6.37) can also be found by substituting $\alpha_j = 1/2$ and $\theta_d = 45^\circ$ into λ_{sh} of an SFCC section of Eq. (6.22), since a circular section is a special case of a square section with a radius equal to one half its overall jacket dimension, i.e., $R_j = H_c/2$ or $\alpha_j = 1/2$.

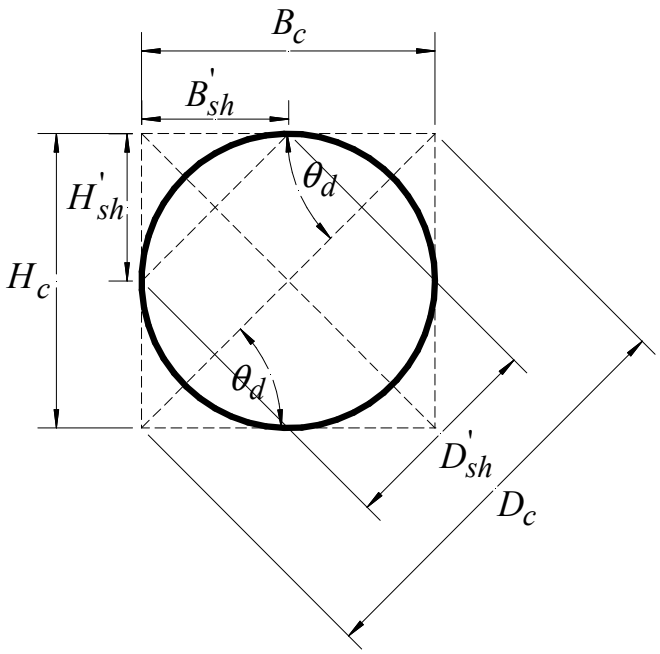

(a)

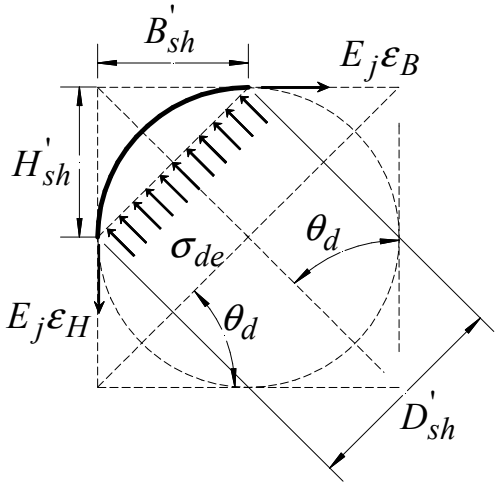

(b)

Figure 6.4 Circular FRP-confined concrete sections: (a) typical geometry, (b) offset diagonal equilibrium.

Using the FRP jacket stress f_j of Eq. (5.9), the horizontal equilibrium of the half body of the CFCC section of **Figure 6.4(b)** yields the equilibrium relationship of Eq. (6.23). Solving for the diagonal confining stress $(f_d)_{sh}$, setting $(f_{de}) = k_e (f_d)_{sh}$, using $(E_{je})_B$ of Eq. (4.15), D'_{sh} of Eq. (6.4), λ_{sh} of Eq. (6.37), and using $(f_{de})_{sh}$ of Eq. (6.7) yield a unity minor diagonal equilibrium coefficient, $(\psi_B)_{sh} = 1.0$. A unity minor diagonal equilibrium coefficient $(\psi_B)_{sh}$ can also be found by substituting $\alpha_{sh} = 1.0$, $\alpha_j = 1/2$, $\theta_a = \theta_d = 45^\circ$, and $\theta_b = 0^\circ$ into $(\psi_B)_{sh}$ of an RFCC section of Eq. (6.8) and by setting $\alpha_j = 1/2$ into $(\psi_B)_{sh}$ of an SFCC section of Eq. (6.24).

For an CFCC section, the minor strain coefficient $(\gamma_B)_{sh}$ of Eq. (6.10) also has a unity value, i.e., $(\gamma_B)_{sh} = 1.0$, which indicates that for CFCC section $\varepsilon_B = \varepsilon_j$, as occurs in SFCC sections. This unity minor strain coefficient $(\gamma_B)_{sh}$ can be found by substituting $(\psi_d)_{sh}$ of Eq. (5.13) with $\chi_{sh} = 1.0$ of Eq. (6.37) and $\theta_b = 0^\circ$, and $(\psi_B)_{sh} = 1.0$ into $(\gamma_B)_{sh}$ of an RFCC section of Eq. (6.11). A unity minor strain coefficient $(\gamma_B)_{sh}$ can also be found by substituting $\alpha_j = 1/2$ into $(\gamma_B)_{sh}$ for an SFCC section of Eq. (6.25).

Solving for the diagonal confining stress $(f_d)_{sh}$ in Eq. (6.26) and performing the same substitutions as in the horizontal equilibrium of the CFCC section yield $(\psi_H)_{sh} = 1.0$ and $(\gamma_H)_{sh} = 1.0$, which indicates that for an CFCC section $\varepsilon_H = \varepsilon_j$, as occurs in an SFCC section . For CFCC sections the strain ratio α_ε of Eq. (6.18) also has a unity value, $\alpha_\varepsilon = 1.0$ or $\varepsilon_H = \varepsilon_B = \varepsilon_j$. This indicates that the strain ratio α_ε of Eq.

(6.19) also applies to CFCC sections since for an CFCC section $\theta_a = \theta_d = 45^\circ$; this is proven in the following equilibrium analysis of elliptical FRP-confined concrete sections.

Circular and Elliptical Sections

Circular FRP-confined sections (CFCC), including square sections confined by shape-modifying circular (SMC) FRP jackets and elliptical FRP-confined concrete (EFCC) sections, including rectangular sections confined by shape-modifying elliptical (SME) FRP jackets, are considered in this section.

A typical elliptical and circular FRP-confined concrete section is shown in **Figure 6.5.** As was previously established**,** a circular section is a special case of an elliptical section with a unity aspect ratio α_{sh} of Eq. (4.2), i.e., $\alpha_{sh} = 1.0$. A portion of the elliptical FRP jacket at a given diagonal angle θ_i is shown in **Figure 6.6(b)**; the following equilibrium relationships can be found:

Equilibrium in the y-direction of **Figure 6.6(b)** yields:

$$(f_B)_\theta h_\theta - E_j t_j (\varepsilon_j)_\theta \cos(\theta_j)_\theta = 0 \tag{6.38}$$

$$(\theta_j)_\theta = \tan^{-1}\left(\frac{\alpha_{sh}^{\,2}}{\tan\theta_i}\right) \tag{6.39}$$

where $(\varepsilon_j)_\theta$ is the tangential jacket strain in the elliptical FRP jacket at a given angle θ_i and corresponding jacket tangent angle $(\theta_j)_\theta$ of Eq. (6.39); $(f_B)_\theta$ is the average confining stress in the confined concrete core jacket at the minor jacket dimension B_c at a given angle θ_i.

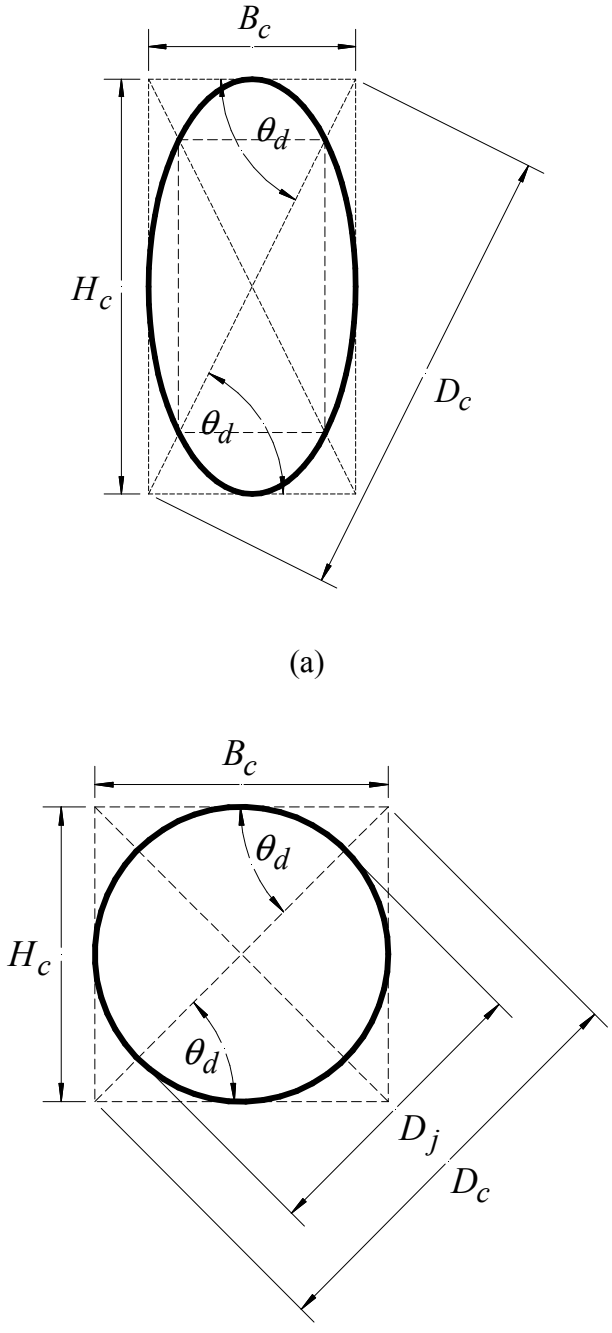

Figure 6.5 Typical geometry of (a) an elliptical and (b) a circular FRP-confined concrete section.

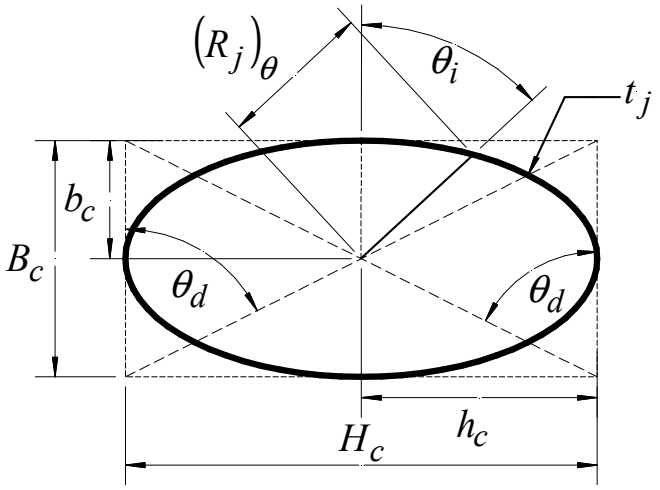

(a)

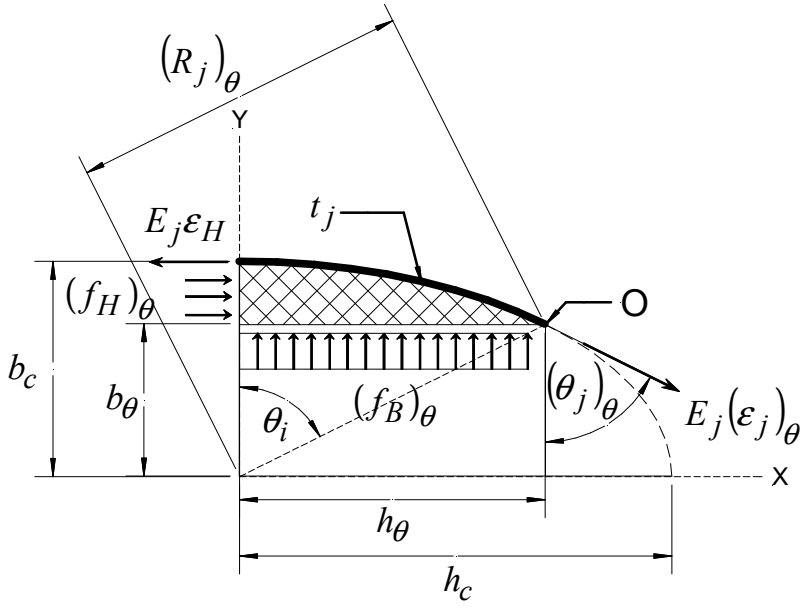

(b)

Figure 6.6 Elliptical FRP-confined concrete section: (a) section geometry and (b) equilibrium of a portion of an elliptical section.

From the geometry of **Figure 6.6** it can be established that $(\theta_j)_\theta = 0^\circ$ when $\theta_i = 90^\circ$. Equilibrium in the x-direction of **Figure 6.6(b)** yields:

$$E_j t_j (\varepsilon_j)_\theta \sin(\theta_j)_\theta + (f_H)_\theta (b_c - b_\theta) - E_j t_j \varepsilon_H = 0 \tag{6.40}$$

where b_c is the minor axis dimension of the EFCC section, where $b_c = B_c/2$; $(f_H)_\theta$ is the average confining stress in the confined concrete core along the major jacket dimension H_c, at a given angle θ_i; and h_c is the major axis dimension of the EFCC section, where $h_c = H_c/2$.

Rotational equilibrium with respect to the point O of **Figure 6.6(b)** with counterclockwise moment being positive, yields the following equilibrium relationship:

$$E_j t_j \varepsilon_H (b_c - b_\theta) - \frac{1}{2}(f_H)_\theta (b_c - b_\theta)^2 - \frac{1}{2}(f_B)_\theta (h_\theta)^2 = 0 \tag{6.41}$$

This equilibrium analysis is similar to the analysis of EFCC sections introduced by Campione and Cuchiara (2007).

The elliptical radius $(R_j)_\theta$, at a given diagonal angle θ_i can be determined from the geometry of **Figure 6.6** as follows:

$$(R_j)_\theta = \sqrt{(b_\theta)^2 + (h_\theta)^2} = \sqrt{\frac{(b_c h_c)^2}{(b_c \sin\theta_i)^2 + (h_c \cos\theta_i)^2}} = h_c \sqrt{\frac{1}{{\alpha_{sh}}^2 \cos^2\theta_i + \sin^2\theta_i}} \tag{6.42}$$

Based on the analysis of **Figure 6.6**, the elliptical radius $(R_j)_\theta$ has a minimum value of $(R_j)_\theta = (R_j)_{\min} = b_c$ when $\theta_i = 0°$ and a maximum value of $(R_j)_\theta = (R_j)_{\max} = h_c$ when $\theta_i = 90°$. These minimum $(R_j)_{\min}$ and maximum $(R_j)_{\max}$ radii values can also be obtained analytically by substituting $\theta_i = 0°$ and $\theta_i = 90°$ into $(R_j)_\theta$ of Eq. (6.42), respectively.

The major $(h_j)_\theta$ and minor $(b_j)_\theta$ core dimensions, measured from the centroid of the elliptical FRP-confined concrete to the perimeter of the FRP jacket at a given diagonal angle θ_i, as shown in **Figure 6.6(b)**, are given by:

$$(h_j)_\theta = (R_j)_\theta \sin\theta_i \;\; ; \;\; (b_j)_\theta = (R_j)_\theta \cos\theta_i \tag{6.43}$$

Solving for $(f_B)_\theta$ in Eq. (6.38), solving for $(f_H)_\theta$ in Eq. (6.40), substituting them into Eq. (6.41), using $(R_j)_\theta$ of Eq. (6.42) and the major $(h_j)_\theta$ and minor $(b_j)_\theta$ dimensions of Eq. (6.43) yield the following tangential jacket strain ratio $(\alpha_\varepsilon)_\theta$ of an EFFC section:

$$(\alpha_\varepsilon)_\theta = \frac{\varepsilon_H}{(\varepsilon_j)_\theta} = \left[\frac{(R_j)_\theta \sin\theta_i}{b_c - (R_j)_\theta \cos\theta_i}\right]\cos(\theta_j)_\theta - \sin(\theta_j)_\theta \tag{6.44}$$

The previous relationship is plotted in **Figure 6.7** versus the diagonal angle θ_i for a quadrant of an elliptical section, i.e., for $0° \le \theta_i \le 90°$.

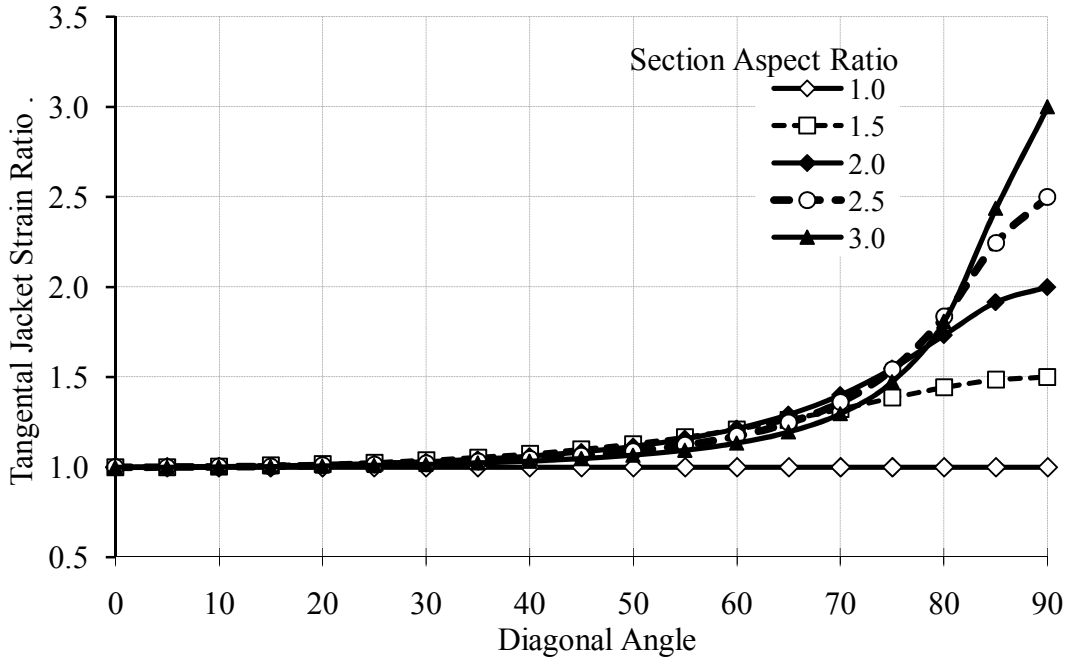

Figure 6.7 Tangential jacket strain ratio versus diagonal angle of elliptical FRP-confined concrete sections of various section aspect ratios.

The elliptical sections considered in **Figure 6.7** have an aspect ratio of $\alpha_{sh} = 1.0$ (i.e., circular sections), $\alpha_{sh} = 1.50$, $\alpha_{sh} = 2.0$, $\alpha_{sh} = 2.50$, and $\alpha_{sh} = 3.0$. From Eq. (6.44) and **Figure 6.7** it can be established that a nonlinear variation of the transverse strain in the FRP jacket occurs along the perimeter of the elliptical FRP jacket for elliptical sections having an aspect ratio greater than one, i.e., for $\alpha_{sh} > 1.0$.

For an elliptical section with a unity aspect ratio ($\alpha_{sh} = 1.0$), i.e., a circular section, Eq. (6.44) and **Figure 6.7** indicate that the strain along the perimeter of the FRP jacket remains constant, $\alpha_{\varepsilon} = 1.0$, i.e., $\left(\varepsilon_j\right)_{\theta} = \varepsilon_j = \varepsilon_H = \varepsilon_B$, as demonstrated in the preceding section.

The nonlinear variation of the transverse jacket strain $\left(\varepsilon_j\right)_{\theta}$ of elliptical jackets having an aspect ratio greater than one, i.e., for $\alpha_{sh} > 1.0$, as shown in **Figure 6.7**, can also be attributed to the change in the radius of curvature of the FRP jacket $\left(\Phi_j\right)_{\theta}$, at a given diagonal angle θ_i, that is defined as:

$$\begin{aligned}\left(\Phi_j\right)_{\theta} &= \frac{\left(R_j\right)_{\theta}^{3}}{\left(\alpha_{sh}^{2} b_c\right)^2} \left[\alpha_{sh}^{4} \cos^2\theta_i + \sin^2\theta_i\right]^{3/2} \\ &= \frac{\left(R_j\right)_{\theta}^{3}}{\left(\alpha_{sh} h_c\right)^2} \left[\alpha_{sh}^{4} \cos^2\theta_i + \sin^2\theta_i\right]^{3/2}\end{aligned} \tag{6.45}$$

The maximum radius of curvature $\left(\Phi_j\right)_{\max}$ of the elliptical jacket occurs along the minor axis dimension b_c, and the minimum $\left(\Phi_j\right)_{\min}$ occurs along the major axis dimension h_c of the elliptical jacket. These curvatures are given by:

$$\left(\Phi_j\right)_{\max} = \frac{(h_c)^2}{b_c} = {\alpha_{sh}}^2 b_c = \alpha_{sh} h_c \tag{6.46}$$

$$\left(\Phi_j\right)_{\min} = \frac{(b_c)^2}{h_c} = \frac{b_c}{\alpha_{sh}} = \frac{h_c}{{\alpha_{sh}}^2} \tag{6.47}$$

Using the radius of curvature $\left(\Phi_j\right)_\theta$ of Eq. (6.45) and the maximum radius of curvature $\left(\Phi_j\right)_{\max}$ of Eq. (6.46), the following tangential jacket strain ratio $(\alpha_\varepsilon)_\theta$ can also be established:

$$(\alpha_\varepsilon)_\theta = \frac{\varepsilon_H}{\left(\varepsilon_j\right)_\theta} = \sqrt[3]{\frac{\left(\Phi_j\right)_{\max}}{\left(\Phi_j\right)_\theta}} = \sqrt[3]{\frac{\alpha_{sh} h_c}{\left(\Phi_j\right)_\theta}} \tag{6.48}$$

For a circular section having a unity aspect ratio ($\alpha_{sh} = 1.0$), the radius of the ellipse $\left(R_j\right)_\theta$ of Eq. (6.42) and the radius of curvature $\left(\Phi_j\right)_\theta$ of Eq. (6.45) are a constant where $\left(R_j\right)_\theta = \left(\Phi_j\right)_\theta = R_j = b_c = h_c$.

Thus for an CFCC section the tangential jacket strain ratio $(\alpha_\varepsilon)_\theta$ of Eqs. (6.44) and (6.48) is also a constant with a unity value, i.e., $(\alpha_\varepsilon)_\theta = 1.0$ or $\left(\varepsilon_j\right)_\theta = \varepsilon_j = \varepsilon_H = \varepsilon_B$, as pointed out earlier. For an EFCC section for which $\alpha_{sh} > 1.0$, a strain ratio $(\alpha_\varepsilon)_\theta$ of unity occurs only when $\theta_i = 0°$ is substituted into Eqs. (6.42), (6.44), and (6.48), i.e., $\left(\varepsilon_j\right)_\theta = \varepsilon_H$.

At the major axis, for which $\left(\varepsilon_j\right)_\theta = \varepsilon_B$, the tangential jacket strain ratio of $(\alpha_\varepsilon)_\theta = \alpha_\varepsilon = \varepsilon_H / \varepsilon_B$ is found to occur only when $\theta_i = 90°$ is substituted into Eq.

(6.39), which yields $\left(\theta_j\right)_\theta = 0°$; further substituting $\theta_i = 90°, \left(R_j\right)_\theta = h_c$ into Eqs. (6.44), (6.45), and (6.48) yields the following transverse strain ratio α_ε for an EFCC section:

$$\alpha_\varepsilon = \frac{\varepsilon_H}{\varepsilon_B} = \tan\theta_d = \alpha_{sh} \tag{6.49}$$

In reference to **Figure 6.8**, the main core diagonal D_{sh} or main diagonal radius $R_{sh} = D_{sh}/2$, at the main diagonal angle $\theta_i = \theta_d$, can be determined from the geometry of **Figure 6.8,** by setting $\theta_i = \theta_d$, which yields $\left(R_j\right)_\theta = R_{sh} = D_{sh}/2$ in Eq. (6.42), where for an EFCC section:

$$R_{sh} = \frac{D_{sh}}{2} = \chi_{sh} h_c \tag{6.50}$$

$$\chi_{sh} = \frac{D_{sh}}{H_c} = \sqrt{\frac{1}{{\alpha_{sh}}^2 \cos^2\theta_d + \sin^2\theta_d}} = \frac{\sqrt{2}}{2}\csc\theta_d \tag{6.51}$$

where the above χ_{sh} is also given in Eq. (5.42) for EFCC sections.

In reference to **Figure 6.6**, the tangential jacket angle θ_j of the FRP jacket at the main diagonal can be found by substituting angle of inclination θ_d of the main diagonal of Eq. (4.1) and setting $\theta_i = \theta_d$ in $\left(\theta_j\right)_\theta$ of Eq. (6.39), which yields:

$$\theta_j = \tan^{-1}\left[\frac{{\alpha_{sh}}^2}{\tan\theta_d}\right] = \theta_d \tag{6.52}$$

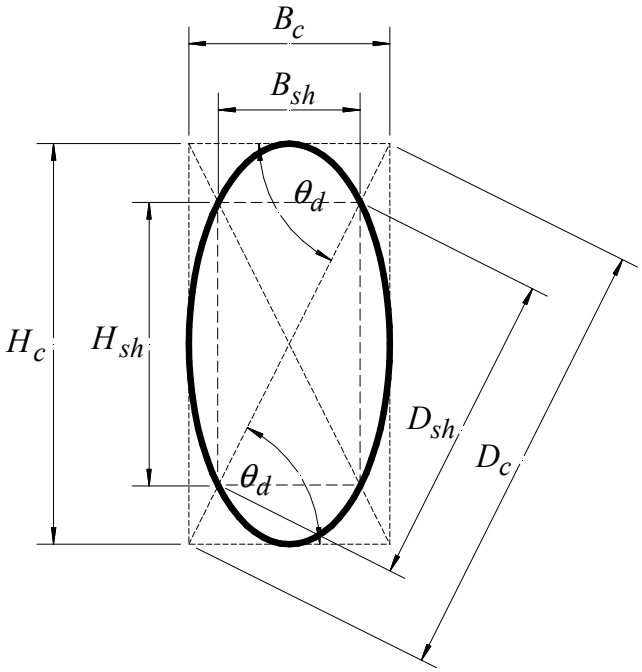

(a)

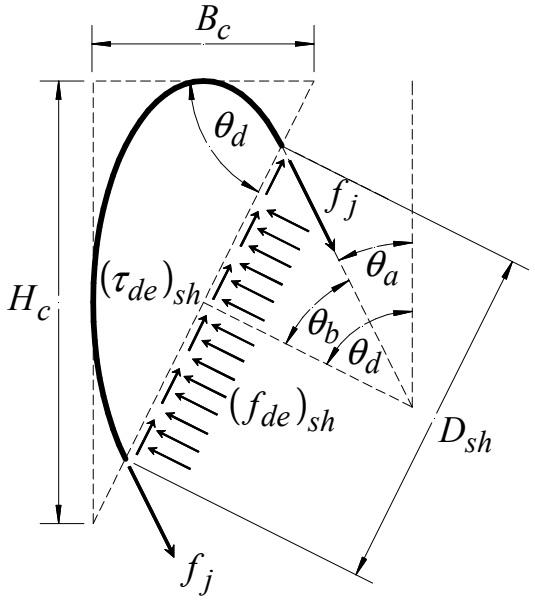

(b)

Figure 6.8 Elliptical FRP-confined concrete section: (a) section geometry; (b) diagonal equilibrium.

Setting $(\varepsilon_j)_\theta = \varepsilon_j$, substituting $\theta_i = \theta_d$, $(R_j)_\theta = R_{sh}$, and $\theta_i = \theta_d$ into $(\varepsilon_j)_\theta$ of Eq. (6.44), yield the following major strain ratio $(\gamma_H)_{sh}$ of Eq. (6.16) of an EFCC section:

$$(\gamma_H)_{sh} = \frac{\varepsilon_H}{\varepsilon_j} = \left[\frac{R_{sh}\sin\theta_d}{b_c - R_{sh}\cos\theta_d}\right]\cos\theta_d - \sin\theta_d = \sqrt{2}\sin\theta_d \tag{6.53}$$

Substituting the shape-dependent diagonal confinement equilibrium coefficient $(\psi_d)_{sh}$ of Eq. (5.13) with the shape parameter χ_{sh} of Eq. (5.40) or (6.51) into $(\gamma_H)_{sh}$ of Eqs. (6.16) and (6.53), solving for the major diagonal equilibrium coefficient $(\psi_H)_{sh}$, yields:

$$(\psi_H)_{sh} = \cos\theta_b \tag{6.54}$$

Solving for the major transverse strain ε_H in Eq. (6.49), substituting it into Eq. (6.53), and solving for the generalized minor strain ratio $(\gamma_B)_{sh}$ of Eq. (6.10) yield:

$$(\gamma_B)_{sh} = \frac{\varepsilon_B}{\varepsilon_j} = \left(\frac{\psi_d}{\psi_B}\right)_{sh} = \sqrt{2}\cos\theta_d \tag{6.55}$$

Substituting the shape-dependent diagonal confinement equilibrium coefficient $(\psi_d)_{sh}$ of Eq. (5.13) with the shape parameter χ_{sh} of Eq. (5.42) or (6.51) into $(\gamma_B)_{sh}$ of Eqs. (6.10) and (6.55) and solving for the minor diagonal equilibrium coefficient $(\psi_B)_{sh}$, yield:

$$(\psi_B)_{sh} = \frac{(\psi_H)_{sh}}{\alpha_{sh}} \tag{6.56}$$

Substituting $(\gamma_H)_{sh}$ of Eq. (6.53) and $(\gamma_B)_{sh}$ of Eq. (6.55) into the generalized transverse strain ratio α_ε of Eq. (6.18) and using the shape-dependent angles θ_a and θ_b of Eqs. (5.40) and (5.41), respectively, yield the following transverse jacket strain ratio α_ε for an EFCC section:

$$\alpha_\varepsilon = \frac{\varepsilon_H}{\varepsilon_B} = \frac{(\gamma_H)_{sh}}{(\gamma_B)_{sh}} = \cot(\theta_a) \tag{6.57}$$

The previous strain ratio indicates that the relationship for the transverse jacket strain ratio α_ε of Eq. (6.19) introduced from the diagonal equilibrium analysis of rectangular $(\alpha_{sh} \geq 1.0)$ and square $(\alpha_{sh} = 1.0)$ FCC sections with rounded corners is also applicable to both elliptical ($\alpha_{sh} \geq 1.0$ and $\theta_d \geq 45^\circ$) and circular ($\alpha_{sh} = 1.0$ and $\theta_d = 45^\circ$) FCC sections.

The previous relationship indicates that for rectangular, oval, square, elliptical, and circular FCC sections, the transverse strain ratio α_ε of the FCC section is given by α_ε of Eq. (6.19) with the angle θ_a listed in **Table 5.2.**

Using the strain relationship of Eq. (6.9), using $(\gamma_B)_{sh}$ of Eq. (6.10), and solving for the FRP jacket strain ε_j yield:

$$\varepsilon_j = \beta_j \varepsilon_B \tag{6.58}$$

$$\beta_j = \frac{\varepsilon_j}{\varepsilon_B} = \frac{1}{(\gamma_B)_{sh}} \tag{6.59}$$

where β_j is the diagonal strain coefficient, which is the inverse of the minor strain ratio $(\gamma_B)_{sh}$ of Eq. (6.10).

Using the transverse strain ratio α_ε of Eq. (6.18), solving for the minor strain ε_B, and substituting it into Eq. (6.58) yield:

$$\varepsilon_j = \left(\frac{\beta_j}{\alpha_\varepsilon}\right)\varepsilon_H = \varepsilon_H \beta_j \tan(\theta_a) \tag{6.60}$$

In this chapter it was determined that the geometry of the FRP-confined concrete section, which includes the FRP jacket shape, the section aspect ratio α_{sh}, and the jacket corner aspect ratio α_j (rectangular and square sections only), introduced in Chapter 4, influences the diagonal dilation, the diagonal equilibrium, introduced in Chapter 5, and the transverse dilation of FRP-confined concrete core introduced in this chapter.

The diagonal strain coefficient β_j of Eq. 6.59 is summarized in **Table 6.1** for the FRP jacket shapes considered herein. Both the transverse strain ratio α_ε of Eq. (6.19) and the diagonal strain coefficient β_j of Eq. 6.59 will be used in determining the transverse and diagonal dilation relationships introduced in Chapters 7 and 8, the transverse confinement relationships introduced in Chapter 9, and the design of FRP jackets introduced in Chapter 11.

Table 6.1 Summary of the nondimensional jacket shape-dependent transverse strain coefficient β_j of various FRP-confined concrete sections.

FRP jacket shape	Transverse strain coefficient β_j	Reference Eqs.
Rectangular	$\beta_j = \dfrac{1-2\alpha_j\left[1-\sin(\theta_a)\right]}{2\left(1-\alpha_j\alpha_{sh}\right)\sin(\theta_a)}$	(6.11) and (6.59)
Square	$\beta_j = \dfrac{\sqrt{2}\left[1-\alpha_j\left(2-\sqrt{2}\right)\right]}{2\left(1-\alpha_j\right)}$	(6.25) and (6.59)
Oval	$\beta_j = \dfrac{\alpha_{sh}-\left(1-\sin\theta_a\right)}{\alpha_{sh}\sin\theta_a}$	(6.34) and (6.59)
Circular	Same as elliptical with $\theta_d = 45^\circ$ or $\beta_j = 1.0$	N/A
Elliptical	$\beta_j = \dfrac{\sqrt{2}}{2\cos\theta_d}$	(6.55) and (6.59)

CHAPTER 7

TRANSVERSE AND DIAGONAL STRAIN RELATIONSHIPS FOR CONCRETE SECTIONS CONFINED BY FIBER-REINFORCED POLYMER JACKETS

In this chapter a series of strain compatibility relationships are introduced from analysis of the dilation behavior of rectangular, square, oval (including rectangular sections confined by a shape-modifying oval FRP jacket), circular (including square section confined by shape-modifying circular jacket), and elliptical (including rectangular sections confined by a shape-modifying elliptical FRP jacket) FRP-confined concrete (FCC) sections in compression. The strain compatibility relationships introduced in Chapter 6 are incorporated herein into a series of analytical diagonal and transverse strain relationships for the aforementioned FRP-jacketed shapes.

The damage-based stress-strain model for FCC sections developed herein, requires defining a series of strain compatibility relationships that describe the increase in damage in the cross section in terms of the geometric and mechanical properties of the confining elastic FRP jacket, introduced in Chapter 4, and the mechanical properties of the concrete core. In addition to the assumptions made in Chapter 5, the following assumptions are also made in the strain compatibility relationships developed herein:

1. Prior to cracking of the passively confined concrete core, both the concrete core and FRP jacket are assumed to behave elastically. In the elastic regime the confined

concrete core is idealized as an isotropic, homogeneous elastic material, whereas the FRP material is idealized as a unidirectional isotropic elastic material.

2. Poisson effects due to shortening of the FRP jacket along the length of the FCC section are considered negligible and are ignored in the analysis.
3. Tensile stresses and strains are considered negative, and compressive stresses and strains are considered positive.

FRP-Confined Concrete Sections-Elastic Regime

Prior to cracking of the passively confined concrete core, both the concrete core and FRP jacket behave elastically. Thus, the concrete is treated as an isotropic, homogeneous elastic material prior to cracking and the FRP jacket as an elastic material that passively confines the concrete core during the application of a uniform axial compressive load and resultant axial compressive stress f_c and strain ε_c.

Using Hooke's law for a linear homogeneous isotropic concrete material, the normal strain ε_m, for which the subscript m indicates an arbitrary transverse strain direction where $m = x, y,$ or z, is directly proportional to the applied normal stress σ_m as follows:

$$\varepsilon_z = \frac{\sigma_z - \nu_{ci}(\sigma_x + \sigma_y)}{E_{ci}} \tag{7.1}$$

$$\varepsilon_x = \frac{\sigma_x - \nu_{ci}(\sigma_y + \sigma_z)}{E_{ci}} \tag{7.2}$$

$$\varepsilon_y = \frac{\sigma_y - \nu_{ci}(\sigma_x + \sigma_z)}{E_{ci}} \tag{7.3}$$

where E_{ci} is the elastic modulus of the unconfined concrete core; ν_{ci} is the initial Poisson's ratio of the unconfined concrete core; σ_x, σ_y, and σ_z are the axial stresses along the X, Y, and Z coordinates, respectively; ε_x, ε_y, and ε_z, are the axial strains along the X, Y, and Z coordinates, respectively. For known strains ε_x, ε_y, and ε_z, the axial σ_x, σ_y, and σ_z stresses can be solved simultaneously utilizing Eqs. (7.1)-(7.3), which yield:

$$\sigma_z = \frac{E_{ci}}{(1+\nu_{ci})(1-2\nu_{ci})}\left[(1-\nu_{ci})\varepsilon_z + \nu_{ci}(\varepsilon_x + \varepsilon_y)\right] \tag{7.4}$$

$$\sigma_x = \frac{E_{ci}}{(1+\nu_{ci})(1-2\nu_{ci})}\left[(1-\nu_{ci})\varepsilon_x + \nu_{ci}(\varepsilon_y + \varepsilon_z)\right] \tag{7.5}$$

$$\sigma_y = \frac{E_{ci}}{(1+\nu_{ci})(1-2\nu_{ci})}\left[(1-\nu_{ci})\varepsilon_y + \nu_{ci}(\varepsilon_x + \varepsilon_z)\right] \tag{7.6}$$

The secant Poisson's ratio ν of the concrete core is defined as the secant slope of the transverse strains (ε_r, ε_θ, ε_d, $\varepsilon_x = \varepsilon_B$, and $\varepsilon_y = \varepsilon_H$) versus the axial strain, $\varepsilon_z = \varepsilon_c$, curves.

The dilation rate μ of the concrete core is defined as the tangent slope of the transverse strain versus axial strain curves as follows:

$$\nu_m = -\left(\frac{\varepsilon_m}{\varepsilon_c}\right) \;;\; \mu_m = -\left(\frac{\partial \varepsilon_m}{\partial \varepsilon_c}\right) \tag{7.7}$$

where the subscript m indicates an arbitrary transverse strain direction, where $m = r, \theta, d, H,$ or B. In addition, at the initiation of loading the initial dilation rate $(\mu_m)_o$ and the initial secant Poisson's ratio $(\nu_m)_o$ of the confined concrete core are equal to each other, such that:

$$(\nu_m)_o = -\left(\frac{\varepsilon_m}{\varepsilon_c}\right)_o = (\mu_m)_o = -\left(\frac{\partial \varepsilon_m}{\partial \varepsilon_c}\right)_o \tag{7.8}$$

where the subscript o in the relationships introduced herein indicates an initial confined condition and the subscript i indicates an initial unconfined condition.

Circular Concrete Sections

A circular concrete column, shown in **Figure 7.1**, having an unconfined compressive strength f_{co}, an initial tangent modulus of elasticity E_{ci}, an initial Poisson's ratio ν_{ci}, and an initial dilation rate μ_{ci}, where $\mu_{ci} = \nu_{ci}$, that is confined by a thin elastic circular FRP jacket of thickness t_j, having an average hoop or transverse modulus of elasticity E_j, and a hoop or transverse stiffness $(C_{je})_{ci}$ of Eq. (4.17), with the volumetric ratio $(\rho_j)_{ci}$ of Eq. (4.37), is considered herein.

Considering the transverse equilibrium of the half circles of **Figure 7.2** and considering that for a circular section $\varepsilon_r = \varepsilon_\theta = \varepsilon_d = \varepsilon_x = \varepsilon_y$, and setting $\varepsilon_x = \varepsilon_B$, $\varepsilon_y = \varepsilon_H$, $\varepsilon_z = \varepsilon_c$, and $\sigma_z = f_c$, setting $(E_{je})_x = (E_{je})_B$ in Eq. (4.15) and $(E_{je})_y = (E_{je})_H$ in Eq. (4.16), the applied axial stress f_c can be found by solving for $\sigma_z = f_c$ in Eq. (7.1), which yields:

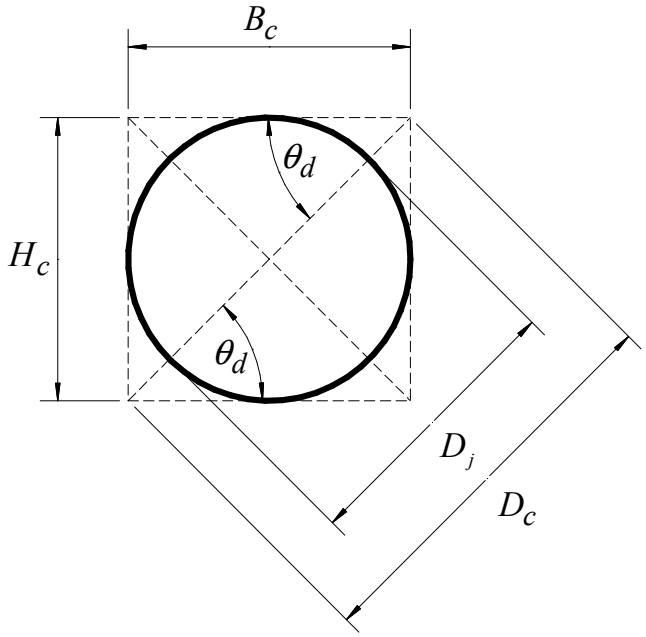

Figure 7.1 Geometry of a circular FRP-confined concrete section.

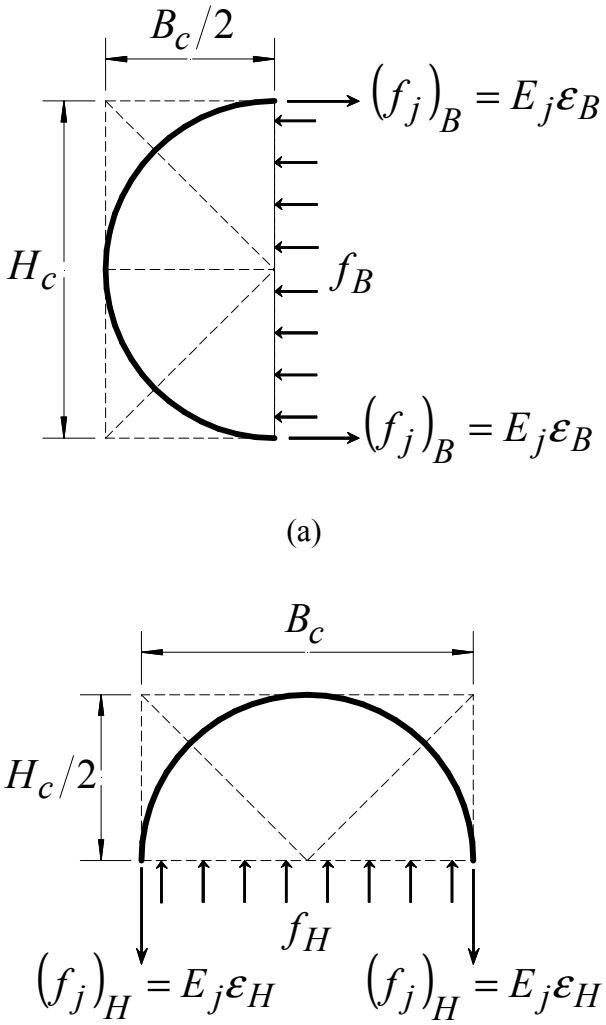

Figure 7.2 Equilibrium of a circular FRP-confined concrete section: (a) along the minor axis and (b) along the major axis.

$$\begin{aligned} f_c &= E_{co}\varepsilon_c \\ &= E_{ci}\varepsilon_c - \nu_{ci}\left[\left(E_{je}\right)_B \varepsilon_x + \left(E_{je}\right)_H \varepsilon_y\right] \\ &= E_{ci}\varepsilon_c - 2\nu_{ci}\left(E_{je}\right)_B \varepsilon_r \\ &= E_{ci}\varepsilon_c\left[1 + 2\alpha_E \nu_{ci}\left(\nu_r\right)_o\right] \end{aligned} \tag{7.9}$$

$$\alpha_E = \frac{\left(E_{je}\right)_B}{E_{ci}} \tag{7.10}$$

where ε_r, ε_θ, and ε_d are the average radial, hoop, and diagonal strains in the circular FRP-confined concrete (CFCC) section, respectively.

In addition $\left(E_{je}\right)_H$ and $\left(E_{je}\right)_B$ are the effective transverse modulus of the FRP jacket along its major and minor dimensions, respectively; α_E is the transverse modular ratio of the FRP jacket; and $\left(\nu_r\right)_o$ is the initial secant Poisson's ratio of the FCC section. At the initiation of loading $\left(\nu_r\right)_o = \left(\mu_r\right)_o$, with $\left(\mu_r\right)_o$ being the initial dilation rate or tangent Poisson's ratio of the CFCC section.

Solving for the initial modulus of elasticity of the CFCC section E_{co} in Eq. (7.9) yields:

$$E_{co} = E_{ci}\left[1 + 2\alpha_E \nu_{ci}\left(\mu_r\right)_o\right] \tag{7.11}$$

The above indicates that the initial modulus of elasticity of the CFCC section increases as the hoop stiffness $\left(C_{je}\right)_{ci}$ of the FRP jacket increases. It also demonstrates that E_{co} is directly proportional to the transverse modular ratio of the FRP jacket α_E of Eq. (7.10).

Using Eqs. (7.7) and (7.8), realizing that for a circular section $\varepsilon_r = \varepsilon_\theta = \varepsilon_d = \varepsilon_x = \varepsilon_y$, substituting Eqs. (7.9)-(7.11) into Eq. (7.4), and solving for the initial dilation rate $(\mu_r)_o$ of the CFCC section yield:

$$(\mu_r)_o = -\left(\frac{\partial \varepsilon_r}{\partial \varepsilon_c}\right)_o = \frac{E_{co}}{E_{ro}} = \frac{\nu_{ci}}{1+\alpha_E(1+\nu_{ci})(1-2\nu_{ci})} \tag{7.12}$$

where E_{ro} is the initial radial or transverse modulus of elasticity of the CFCC section. The previous relationship reveals that the initial dilation rate $(\mu_r)_o$ of the CFCC section decreases as the hoop or transverse stiffness $(C_{je})_{ci}$ of the circular FRP jacket increases.

Using the initial axial modulus E_{co} of Eq. (7.11) and solving for the initial transverse modulus E_{ro} in Eq. (7.12) yield:

$$E_{ro} = \frac{E_{co}}{(\mu_r)_o} = E_{ci}\left[\frac{1}{(\mu_r)_o} + 2\alpha_E \nu_{ci}\right] \tag{7.13}$$

FRP-Confined Concrete Sections

In this analysis the FCC sections shown in **Figure 7.3** are considered herein. A given FCC sections is considered to have an unconfined compressive strength f_{co}, an initial tangent modulus of elasticity E_{ci}, an initial Poisson's ratio ν_{ci}, and an initial dilation rate μ_{ci}, for which $\mu_{ci} = \nu_{ci}$ that is confined by thin elastic FRP jackets of thickness t_j and having a transverse or hoop modulus of elasticity E_j and a transverse or hoop stiffness $(C_{je})_{sh}$ of Eq. (4.14).

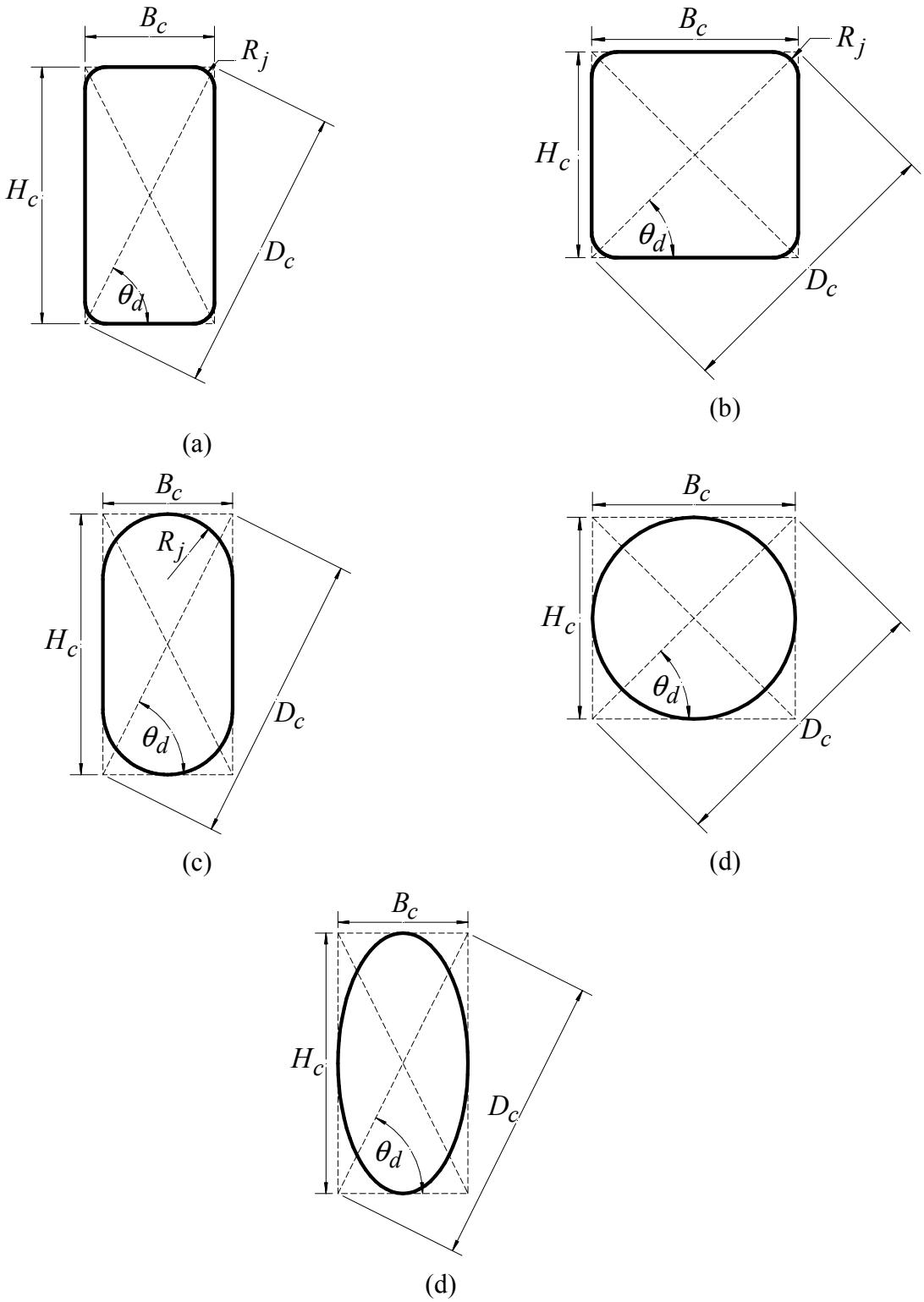

Figure 7.3 FRP-confined concrete sections: (a) rectangular; (b) square, (c) oval, (d) circular, and (e) elliptical.

The transverse equilibrium along the minor B_c and major H_c dimensions of the FCC sections of a rectangular (RFCC) section of **Figure 5.1,** a square (SFCC) section of **Figure 5.2,** an oval (OFCC) section of **Figure 5.3**, a circular (CFCC) section of **Figure 5.4,** and an elliptical (EFCC) section of **Figure 5.5** for which $\varepsilon_B = \varepsilon_x \le \varepsilon_y$ and $\varepsilon_H = \varepsilon_y \ge \varepsilon_x$; by setting $\varepsilon_z = \varepsilon_c$, setting $\left(E_{je}\right)_x = \left(E_{je}\right)_B$ of Eq. (4.15), $\left(E_{je}\right)_y = \left(E_{je}\right)_H$ of Eq. (4.16), and setting $\sigma_z = f_c$, and by using the aspect ratio α_{sh} of Eq. (4.2), and the strain ratio α_ε of Eq. (6.19), the applied axial stress f_c in the FCC section can be found by solving for $\sigma_z = f_c$ in Eq. (7.1), which yields:

$$\begin{aligned} f_c &= E_{co}\varepsilon_c \\ &= E_{ci}\varepsilon_c - \nu_{ci}\left[\left(E_{je}\right)_B \varepsilon_B + \left(E_{je}\right)_H \varepsilon_H\right] \\ &= E_{ci}\varepsilon_c\left[1 + \beta_{sh}\alpha_E \nu_{ci}\left(\nu_B\right)_o\right] \end{aligned} \tag{7.14}$$

$$\beta_{sh} = 1 + \alpha_{sh}\alpha_\varepsilon \tag{7.15}$$

where $\left(\nu_B\right)_o$ is the initial secant Poisson's ratio along the minor B_c dimension of the FCC section. As previously indicated, at the initiation of loading the initial secant and tangent slopes are equal, such that $\left(\nu_B\right)_o = \left(\mu_B\right)_o$, where $\left(\mu_B\right)_o$ is the initial dilation rate along the minor B_c dimension of the FCC section and β_{sh} is a transverse strain coefficient. Solving for the initial modulus of elasticity E_{co} of the FCC section in Eq. (7.14) yields:

$$E_{co} = E_{ci}\left[1 + \alpha_E \beta_{sh} \nu_{ci}\left(\mu_B\right)_o\right] \tag{7.16}$$

This indicates that the initial modulus of elasticity of the FCC section increases with an increase in the transverse stiffness $(E_{je})_B$ of Eq. (4.15), the section aspect ratio α_{sh} of Eq. (4.2) and the strain ratio α_ε of Eq. (6.19) of the FCC section. For a circular section for which $\alpha_{sh} = \alpha_\varepsilon = 1.0$, the initial modulus of elasticity E_{co} of Eq. (7.16) yields E_{ro} of Eq. (7.13), i.e., $E_{co} = E_{ro}$.

Substituting Eqs. (7.14) and (7.16) into Eq. (7.4) and solving for the initial dilation rate $(\mu_B)_o$, along the minor dimension B_c of the FCC section yield:

$$(\mu_B)_o = -\left(\frac{\partial \varepsilon_B}{\partial \varepsilon_c}\right)_o = \frac{E_{co}}{E_{Bo}} = \frac{\nu_{ci}}{1 + \alpha_E(1+\nu_{ci})(1-\beta_{sh}\nu_{ci})} \tag{7.17}$$

where E_{Bo} is the initial modulus of elasticity along the minor B_c dimension of the FCC section. This dilation rate is the initial tangent slope of the transverse strain ε_B along the minor B_c dimension of the FCC section versus the axial strain ε_c in the section. The above relationship indicates that the initial minor dilation rate μ_{Bo} decreases as the hoop or transverse stiffness $(E_{je})_B$ of the FRP jacket increases and increases as the aspect ratio α_{sh} and strain ratio α_ε increase.

Using E_{co} of Eq. (7.16), and solving for the initial modulus of elasticity along the minor dimension E_{Bo} in Eq. (7.17) yield:

$$E_{Bo} = E_{ci}\left[\frac{1}{(\mu_B)_o} + \alpha_E \beta_{sh} \nu_{ci}\right] \tag{7.18}$$

The initial dilation rate $(\mu_H)_o$ along the major H_c dimension of the FCC section can be found using the strain ratio α_ε of Eq. (6.19) and the initial minor dilation rate μ_{Bo} of (7.17), which yield:

$$(\mu_H)_o = -\left(\frac{\partial \varepsilon_H}{\partial \varepsilon_c}\right)_o = \frac{E_{co}}{E_{Ho}} = \alpha_\varepsilon (\mu_B)_o \tag{7.19}$$

where E_{Ho} is the initial modulus of elasticity along the major H_c dimension of the FCC section.

The initial dilation rate μ_{jo} along the main diagonal of the FCC sections shown in **Figure 7.3** is found using the strain relationships of Eqs. (6.57)-(6.59) and the initial dilation rates along the minor $(\mu_B)_o$ of Eq. (7.17) and major $(\mu_H)_o$ of Eq. (7.19) dimensions, which yield:

$$\mu_{jo} = -\left(\frac{\partial \varepsilon_j}{\partial \varepsilon_c}\right)_o = \beta_j (\mu_B)_o = \left(\frac{\beta_j}{\alpha_\varepsilon}\right)(\mu_H)_o \tag{7.20}$$

where β_j is the diagonal strain coefficient of Eq. (6.58).

Using E_{co} of Eq. (7.16) and E_{Bo} of (7.18) and solving for the initial modulus of elasticity along the major H_c dimension E_{Ho} in (7.19), yield:

$$E_{Ho} = \alpha_\varepsilon E_{Bo} = E_{ci}\left[\frac{1}{(\mu_H)_o} + \alpha_E\left(\frac{\beta_{sh}}{\alpha_\varepsilon}\right)\nu_{ci}\right] \tag{7.21}$$

At the initiation of loading or deformation the initial secant slope is equal to the initial tangent slope such that $(\mu_H)_o = (\nu_H)_o$, where $(\nu_H)_o$ is the initial secant Poisson's ratio along the major H_c dimension of the FCC section. For a circular section for which $\alpha_{sh} = \alpha_\varepsilon = 1.0$, the initial moduli of elasticity E_{Ho} of Eq. (7.21) and E_{Bo} of Eq. (7.18) yield E_{co} of Eq. (7.15) and E_{ro} of Eq. (7.13), i.e., $E_{Bo} = E_{Ho} = E_{co} = E_{ro}$.

Plastic Properties of FRP-Confined Concrete

In this investigation, plastic compressive behavior of FRP-confined concrete is assumed to occur at axial compressive strains $\varepsilon_c = \varepsilon_{cp}$, greater than the peak compressive strain ε_{co} of the unconfined concrete core, where $\varepsilon_{co} < \varepsilon_{cp} \le \varepsilon_{cu}$ and where ε_{cu} is the axial compressive strain at failure of the confining elastic FRP jacket.

Circular Concrete Sections

As a result of the constant kinematic restraint provided by elastic circular FRP jacket, the plastic dilation behavior, as measured by the dilation rate μ_r, of a circular concrete section confined by a high stiffness circular FRP jacket reaches an asymptotic value which is referred to herein as the plastic dilation rate μ_{rp}. This asymptotic plastic dilation rate μ_{rp} can be established based on the following hyperbolic relationship:

$$\mu_{rp} = -\left(\frac{\partial \varepsilon_r}{\partial \varepsilon_c}\right)_p \cong \mu_{ci} + \frac{\mu_u - \mu_{ci}}{\left(1 + \dfrac{K_{je}}{(K_{je})_{ref}}\right)^n} \tag{7.22}$$

where μ_u is the dilation rate of a circular unconfined concrete section and $\left(K_{je}\right)_{ref}$ is a reference FRP jacket stiffness. Using an initial dilation rate of $\mu_{ci} = \nu_{ci} = 0.20$ and performing a regression analysis of uniaxial compression tests of FRP-confined concrete cylinders yield:

$$\mu_{rp} = -\left(\frac{\partial \varepsilon_r}{\partial \varepsilon_c}\right)_p \cong \mu_{ci} + \frac{\sqrt{2} - \mu_{ci}}{\left(1 + \frac{K_{je}}{35}\right)^2} \tag{7.23}$$

The above empirical relationship was determined from the analysis of the transverse dilation behavior of circular concrete cylinders confined by bonded (Xiao and Wu 2000, Saenz 2004, Tamuzs et al. 2007) and unbonded FRP jackets (Mirmiran 1997). The above relationship indicates that an unconfined circular concrete section will experience a maximum dilation rate of $\left(\mu_{rp}\right)_{\max} = \mu_u = \sqrt{2}$, whereas highly confined concrete will experience a minimum dilation rate equal to the initial dilation rate of the unconfined concrete, i.e., $\left(\mu_{rp}\right)_{\min} = \mu_{ci} = \nu_{ci} = 0.20$. The plastic dilation rate μ_{rp} of the afore-mentioned CFCC cylinder tests is plotted versus the effective stiffness of the FRP jacket in **Figure 7.4.** The previous equation has a coefficient of correlation of 82.9 %, i.e., $R^2 = 0.829$, and a standard deviation of $6.27x10^{-3}$, i.e., $\sigma = 6.27x10^{-3}$.

In this figure, the asymptotic plastic dilation rate μ_{rp} of Eq. (7.23) is plotted as a solid curve, and the dashed curves indicate the prediction with a plus or minus two standard deviations.

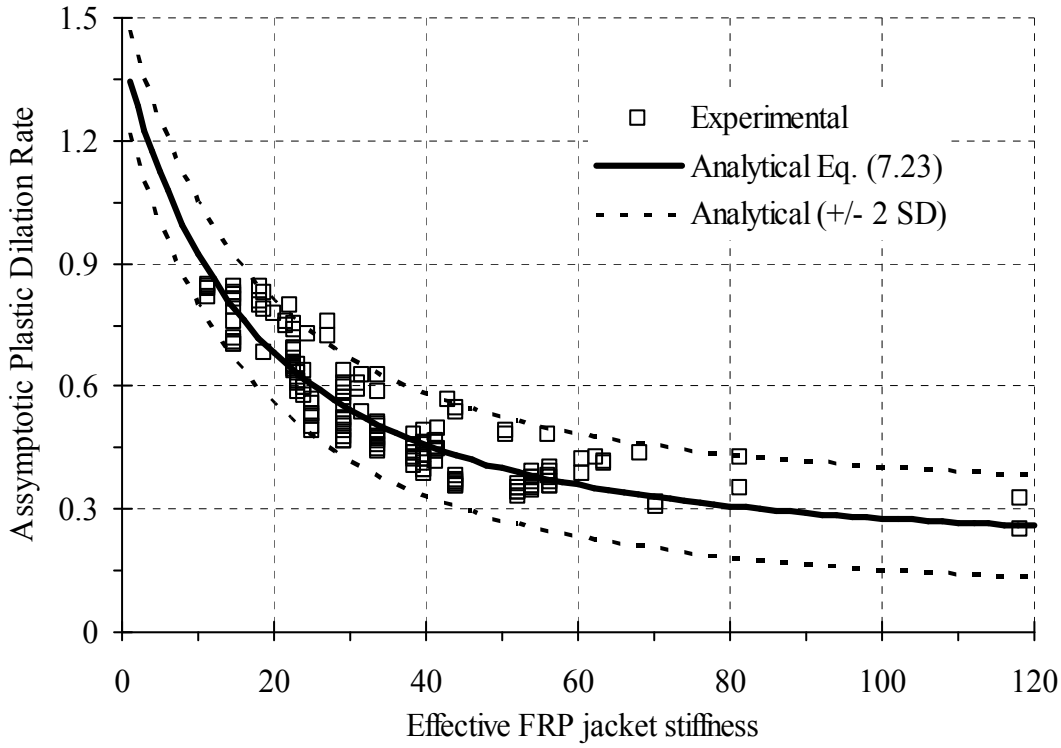

Figure 7.4 Plot of plastic dilation rate versus effective jacket stiffness of FRP-confined concrete.

For a circular concrete section the secant Poisson's ratio ν_m and the dilation rate μ_m of the section remain essentially constant along the perimeter of the section, as was demonstrated in Chapter 6. In Chapters 4 and 5, it was demonstrated that a CFCC section is a special case of a rectangular (RFCC) section for which $\alpha_{sh} = 1.0$ and $\alpha_j = 1/2$, and a special case of an elliptical (EFCC) section with a unit aspect ratio, i.e., $\alpha_{sh} = 1.0$. In addition, α_j is the jacket corner aspect ratio of Eq. (4.4).

FRP-Confined Concrete Sections

The diagonal dilation rate μ_j of the rectangular (RFCC), square (SFCC), oval (OFCC), circular (CFCC), and elliptical (EFCC) FRP-confined concrete sections can be found in terms of the dilation rate μ_r of an equivalent circular concrete section confined by a continuous circular FRP jacket as follows:

$$\mu_j = \beta_j \mu_r \tag{7.24}$$

Thus, in the plastic regions of the compressive behavior of the FCC sections shown in **Figure 7.3**, the plastic diagonal dilation rate μ_{jp} can be found in terms of the plastic dilation rate μ_{rp} of Eq. (7.23) of an equivalent circular concrete section confined by a continuous circular FRP jacket having the same effective FRP jacket stiffness K_{je} of Eq. (4.19) of the FCC sections considered herein as follows:

$$\mu_{jp} = \beta_j \mu_{rp} \tag{7.25}$$

General Transverse Strain Relationships for FRP-Confined Concrete Sections

A typical compressive stress-strain curve of normal weight, normal strength, unconfined concrete cylinder is plotted in **Figure 7.5.** In this figure, the stress-strain curves are plotted versus the axial strain ε_c on the right side of the vertical axis and versus the transverse dilation strain ε_r on the left hand side. The peak axial compressive strain ε_{co} and peak transverse strain ε_{ro} occur when the unconfined concrete reaches its peak compressive strength f_{co}, i.e., when $f_c / f_{co} = 1.0$.

Secant Poisson's Ratio

As indicated in Eq. (7.7), the secant Poisson's ratio ν_m of an unconfined or FRP-confined concrete section is the secant slope of the transverse strain ε_m versus axial strain ε_c curve of the FRP-confined section in compression.

In the following sections, a series of secant Poisson ratio formulations are introduced from the analysis of the dilation of unconfined and FRP-confined circular concrete sections in compression. Using the strain compatibility relationships introduced in Chapter 6, these formulations are expanded to include other FCC cross-sectional shapes (i.e., rectangular, square, oval, and elliptical) in compression.

Circular Concrete Sections

The absolute transverse strain of the concrete cylinder stress-strain curve shown in **Figure 7.5** is plotted versus the axial strain in **Figure 7.6(a)**.

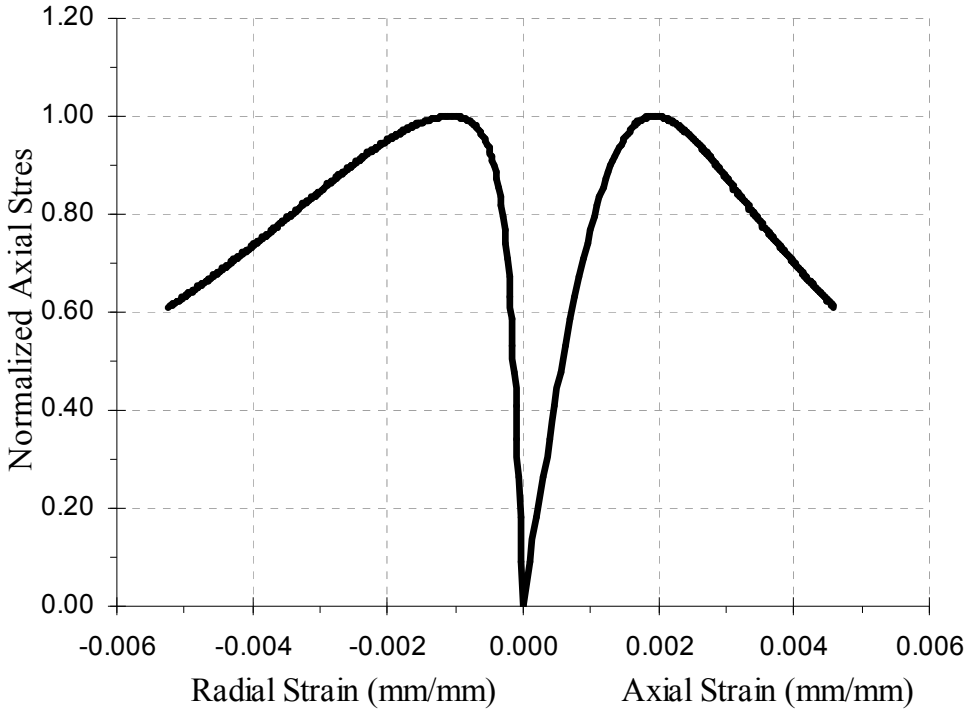

Figure 7.5 Plot of normalized axial stress versus radial and axial strain curve of unconfined concrete in compression.

The initial slope of the curve in this figure is the initial Poisson's ratio ν_{ci} of the concrete material, which is in the range of $0.15 \le \nu_{ci} \le 0.22$; a value of $\nu_{ci} = 0.20$ is used herein.

From analysis of **Figure 7.6(a)**, the secant Poisson's ratio ν_r of the circular concrete section is defined as:

$$\nu_r = -\left(\frac{\varepsilon_r}{\varepsilon_c}\right) \tag{7.26}$$

The Poisson's ratio of a circular concrete section is plotted versus the axial strain in **Figure 7.6(b)**. From **Figure 7.6,** it can be observed that as the axial compressive strain ε_c reaches the peak compressive strain ε_{co} of the unconfined concrete (i.e., as $\varepsilon_c \to \varepsilon_{co}$) the concrete section experiences a significant increase in the Poisson's ratio with a small increase in axial strain. This results in an uncontrolled increase in the area strain ε_a, in the concrete core (i.e., increase in area per unit of initial cross-sectional area). For a circular section, the area strain ε_a is defined as:

$$\varepsilon_a = \varepsilon_x + \varepsilon_y = \varepsilon_r + \varepsilon_\theta = 2\varepsilon_r = 2\varepsilon_\theta \tag{7.27}$$

Considering that for a circular section $\varepsilon_r = \varepsilon_\theta = \varepsilon_d = \varepsilon_x = \varepsilon_y$, as demonstrated in Chapter 6, the above Poisson's ratio of circular concrete section can be rewritten as:

$$\nu_r = -\left(\frac{\varepsilon_r}{\varepsilon_c}\right) = -\left(\frac{\varepsilon_\theta}{\varepsilon_c}\right) = -\left(\frac{\varepsilon_a}{2\varepsilon_c}\right) \tag{7.28}$$

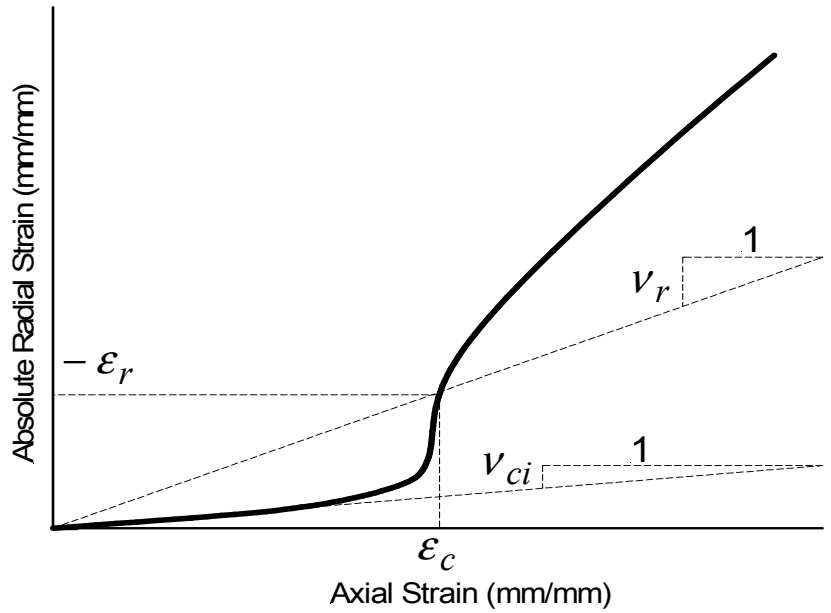

(a)

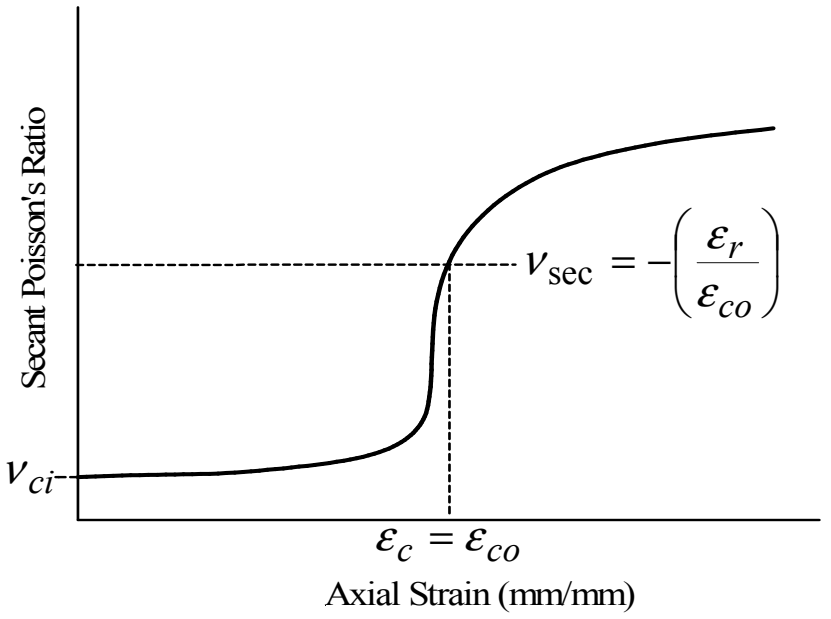

(b)

Figure 7.6 Plot of (a) absolute transverse strain versus axial strain and (b) secant Poisson's ratio versus axial strain of unconfined concrete in compression.

As can be observed in **Figure 7.6(b)**, deviation from a linear elastic material behavior occurs almost immediately after loading as a result of an increase in damage in the concrete's structure due to axial strain-induced transverse dilation which generates material discontinuities, such as internal micro- and macro-crack formation and compaction or nucleation of existing voids within the concrete's structure.

The area strain ε_a in a concrete member in compression measures the amount of damage in response to the applied axial load or deformation in the cross-sectional area supporting the load (Pantazopoulou and Mills 1995). As the area strain ε_a increases, i.e., an increase in damage, the net effective area supporting the load decreases and results in a decrease in the resistance of the concrete material as damage progresses (Pantazopoulou 1995). Pantazopoulou and Mills (1995) and Pantazopoulou (1995) recognized that the initiation of the descending branch of unconfined and confined concrete can be attributed to the drastic increase in the rate of growth (i.e., slope) of the area strain ε_a curve of **Figure 7.7(a)**. This sudden increase is a result of unrestrained crack propagation (i.e., increase in damage) near the peak compressive strength of the unconfined concrete core.

The secant slope of the area strain ε_a versus axial strain ε_c curve of **Figure 7.7(a)** is defined herein as the secant area Poisson's ratio ν_a and is given by:

$$\nu_a = -\left(\frac{\varepsilon_a}{\varepsilon_c}\right) \tag{7.29}$$

A typical secant area Poisson's ratio ν_a of Eq. (7.29) curve is plotted in **Figure 7.7(b)** versus the axial strain ε_c in a circular concrete section in compression.

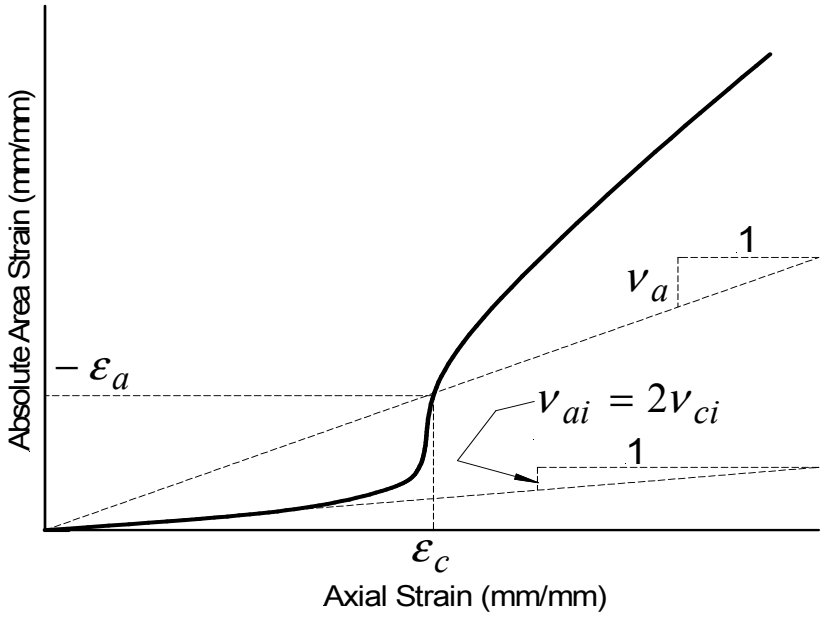

(a)

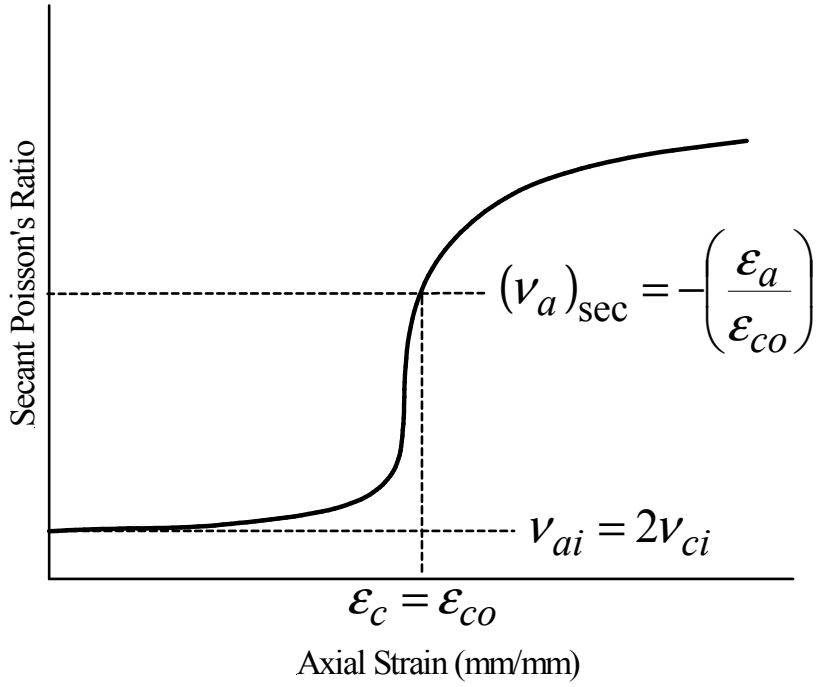

(b)

Figure 7.7 Plot of typical (a) absolute area strain and (b) secant area Poisson's ratio versus axial strain curve of unconfined concrete in compression.

Using Eqs. (7.28) and (7.29), the secant area Poisson's ratio ν_a can be obtained in terms of the secant Poisson's ratio ν_r of Eq. (7.26) as follows:

$$\nu_a = -\left(\frac{\varepsilon_a}{\varepsilon_c}\right) = -2\left(\frac{\varepsilon_r}{\varepsilon_c}\right) = 2\nu_r \tag{7.30}$$

For an unconfined circular section the initial area Poisson's ratio ν_{ai} is given by $\nu_{ai} = 2\,\nu_{ci}$, as shown in the typical Poisson's ratio curve plotted in **Figure 7.7(b)**.

In **Figure 7.8**, the axial strain ε_c curve is potted versus the absolute transverse strain $|\varepsilon_r|$. The initial inverse secant Poisson's ratio $1/\nu_{ci}$ of the unconfined concrete is given by:

$$\frac{1}{\nu_{ci}} = -\left(\frac{\varepsilon_c}{\varepsilon_r}\right)_i = \frac{1}{\mu_{ci}} = -\left(\frac{\partial\varepsilon_c}{\partial\varepsilon_r}\right)_i \tag{7.31}$$

The inverse secant Poisson's ratio $1/\nu_r$ or secant slope of the axial strain ε_c versus absolute transverse strain $|\varepsilon_r|$ curve of **Figure 7.8**, is given by:

$$\frac{1}{\nu_r} = -\left(\frac{\varepsilon_c}{\varepsilon_r}\right) \tag{7.32}$$

FRP-Confined Concrete Sections

The rectangular, square, oval, circular and elliptical FRP-confined concrete sections shown in **Figure 7.3** are considered herein**.**

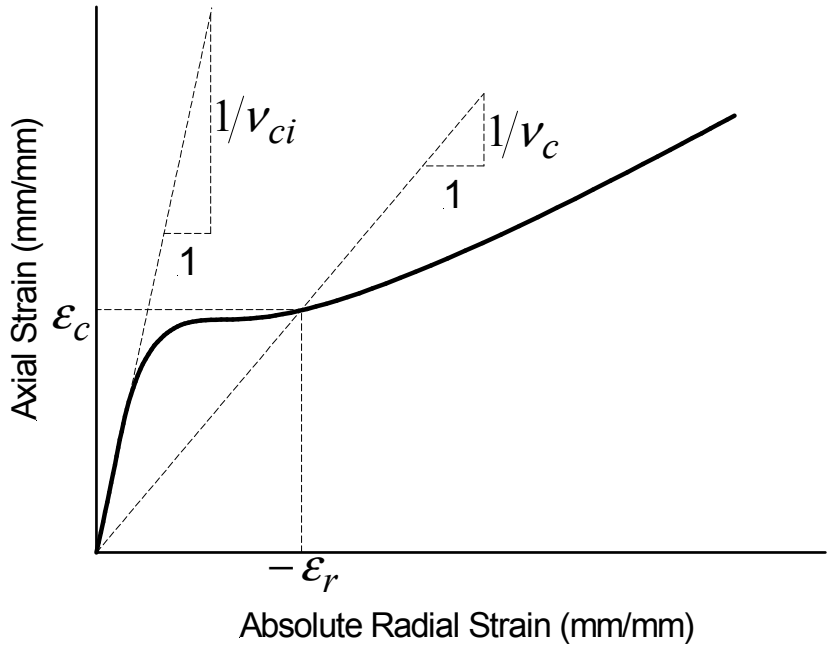

Figure 7.8 Plot of typical axial strain versus absolute transverse strain curve of unconfined concrete in compression.

Using the general strain relationships introduced in Chapter 6 that relate the minor ε_B and major ε_H transverse strains of the FRP-confined concrete sections of **Figure 7.3** to the diagonal jacket strain ε_j, introduced in Eqs. (6.58)-(6.60); the following strain transformation relationships are introduced.

Defining the secant jacket diagonal Poisson's ratio ν_j as:

$$\nu_j = -\left(\frac{\varepsilon_j}{\varepsilon_c}\right) \tag{7.33}$$

where ν_j represents the secant slope of the diagonal jacket strain along the main diagonal ε_j introduced in Chapter 5 versus the average axial strain ε_c in the FCC section.

Using the transverse strain ratio α_ε of Eq. (6.19) and the diagonal transverse strain coefficient β_j of Eq. (6.59), the average secant Poisson's ratio along the minor ν_B and major ν_H dimension of FCC sections shown in **Figure 7.3** yields:

$$\nu_B = -\left(\frac{\varepsilon_B}{\varepsilon_c}\right) = \left(\frac{1}{\beta_j}\right)\nu_j \tag{7.34}$$

$$\nu_H = -\left(\frac{\varepsilon_H}{\varepsilon_c}\right) = \alpha_\varepsilon \nu_B \tag{7.35}$$

where ν_B and ν_H represent the secant slopes of the minor ε_B and major ε_H transverse strains versus the average axial strain ε_c in the FCC section, respectively. Using Eqs.

(7.28), (7.30), (7.34), and (7.35), and setting $\varepsilon_B = \varepsilon_x$ and $\varepsilon_H = \varepsilon_y$, the average area strain ε_a and the average secant area Poisson's ratio ν_a in an FCC section are given by:

$$\varepsilon_a = \varepsilon_B + \varepsilon_H \tag{7.36}$$

$$\nu_a = -\frac{\varepsilon_a}{\varepsilon_c} = -\frac{(\varepsilon_B + \varepsilon_H)}{\varepsilon_c} = \nu_B + \nu_H \tag{7.37}$$

Using the strain ratio α_ε of Eq. (6.19), the average area strain ε_a of Eq. (7.36) can be given in terms of the diagonal jacket strain ε_j as follows:

$$\varepsilon_a = (\varepsilon_B + \varepsilon_H) = \varepsilon_B(1 + \alpha_\varepsilon) = \beta_a \varepsilon_j \tag{7.38}$$

$$\beta_a = \left(\frac{1 + \alpha_\varepsilon}{\beta_j}\right) \tag{7.39}$$

where β_a is the area strain coefficient of the FCC section. Using Eqs. (7.34)-(7.39), the average secant area Poisson's ratio ν_a of Eq. (7.37) can be given in terms of the diagonal jacket Poisson's ratio ν_j of Eq. (7.33) as follows:

$$\nu_a = -\frac{\varepsilon_a}{\varepsilon_c} = \beta_a \nu_j \tag{7.40}$$

Dilation Rate

As indicated in Eq. (7.7), the dilation rate μ_m of an unconfined or FCC section is the tangent slope of the transverse strain ε_m versus axial strain ε_c curve of the section in compression. In what follows, a series of dilation rate formulations are introduced from

the analysis of the dilation of unconfined and FRP-confined circular concrete sections in compression. These formulations are then expanded to include the FRP-confined cross-sectional shapes considered in this dissertation.

Circular Concrete Sections

The tangent slope of the transverse strain ε_r versus axial strain ε_c curve of **Figure 7.6(a)** is defined herein as the dilation rate μ_r, where:

$$\mu_r = -\left(\frac{\partial \varepsilon_r}{\partial \varepsilon_c}\right) \tag{7.41}$$

The dilation rate μ_r of the concrete section is also typically referred to as the tangent Poisson's ratio $(\nu_r)_t$. A typical dilation rate curve is plotted in **Figure 7.9(a)**.

The tangent slope of the area strain ε_a versus axial strain ε_c curve of **Figure 7.7(a)** is defined herein as the area dilation rate μ_a and is given by:

$$\mu_a = -\left(\frac{\partial \varepsilon_a}{\partial \varepsilon_c}\right) \tag{7.42}$$

In **Figure 7.9 (b)** a typical area dilation rate μ_a is plotted versus the axial strain in the concrete section. Setting $\varepsilon_r = \varepsilon_\theta = \varepsilon_d = \varepsilon_x = \varepsilon_y = \varepsilon_B = \varepsilon_H$ in the area strain ε_a of Eq. (7.27) and substituting it into μ_a of Eq. (7.42), yield the following:

$$\mu_a = -\left(\frac{\partial \varepsilon_a}{\partial \varepsilon_c}\right) = -2\left(\frac{\partial \varepsilon_r}{\partial \varepsilon_c}\right) = 2\mu_r \tag{7.43}$$

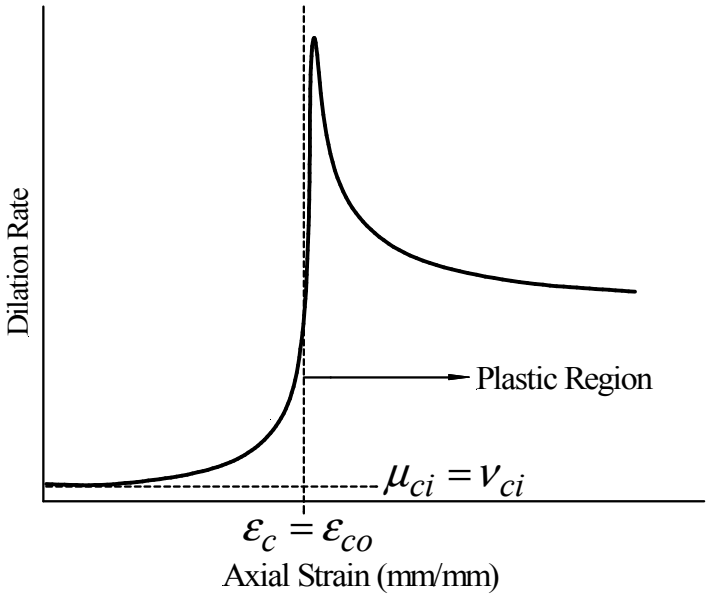

(a)

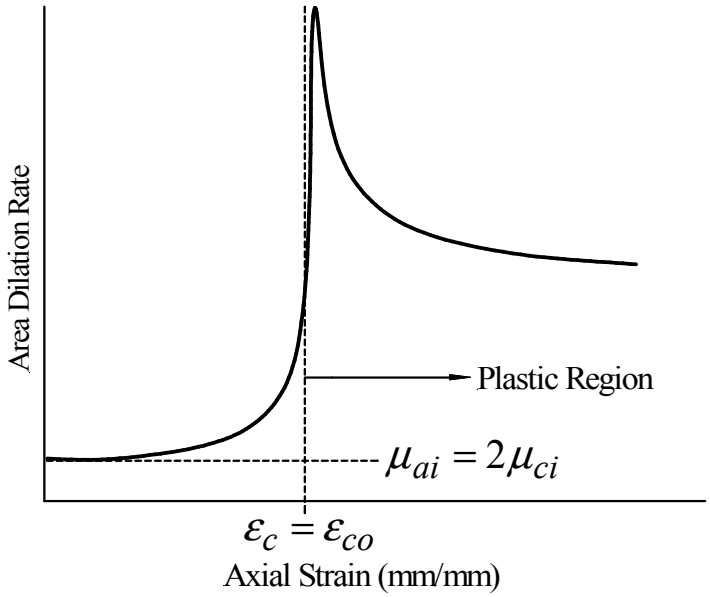

(b)

Figure 7.9 Plot of typical (a) dilation rate and (b) axial dilation rate versus axial strain curve of unconfined concrete in compression.

As can be observed in **Figure 7.9**, the unconfined circular concrete core approaches its unconfined peak compressive strain ε_{co} and strength f_{co}, as both the dilation rate μ_r of Eq. (7.40) and the area dilation rate μ_a of Eq. (7.41) approach their maximum value.

The inverse dilation rate $1/\mu_r$ is defined as the tangent slope of the axial strain ε_c versus absolute transverse strain $|\varepsilon_r|$ curve of **Figure 7.8** where:

$$\frac{1}{\mu_r} = -\left(\frac{\partial \varepsilon_c}{\partial \varepsilon_r}\right) \tag{7.44}$$

FRP-Confined Concrete Sections

For the FCC sections shown in **Figure 7.3**, the average dilation rates along the minor μ_B and major μ_H dimensions of the FCC section can be found using the general strain transformation relationships introduced in Chapter 6, which relate the transverse strain along the minor ε_B and major ε_H dimensions to the diagonal jacket strain ε_j. [refer to Eqs. (6.53)-(6.55)] as follows:

$$\mu_B = -\left(\frac{\partial \varepsilon_B}{\partial \varepsilon_c}\right) \tag{7.45}$$

$$\mu_H = -\left(\frac{\partial \varepsilon_H}{\partial \varepsilon_c}\right) = \alpha_\varepsilon \mu_B \tag{7.46}$$

where μ_B and μ_H represent the tangent slopes of the minor ε_B and major ε_H transverse strains versus the average axial strain ε_c in the FCC section, respectively.

Substituting μ_B of Eq. (7.45) and μ_H of Eq. (7.46) into the area dilation rate μ_a of Eq. (7.42) and using the area strain ε_a of Eqs. (7.36) and (7.38) yield:

$$\mu_a = -\frac{\partial \varepsilon_a}{\partial \varepsilon_c} = -\frac{\partial(\varepsilon_B + \varepsilon_H)}{\partial \varepsilon_c} = \mu_B + \mu_H = \mu_B(1+\alpha_\varepsilon) \tag{7.47}$$

As in circular unconfined and confined concrete sections, the area dilation rate μ_a of Eqs. (7.42) and (7.47) determines the average rate of change (i.e., slope) of the area strain ε_a versus the axial strain ε_c curve of an FCC section in compression.

The plastic dilation rate along the minor μ_{Bp} for $|\varepsilon_{Bo}| \le |\varepsilon_{Bp}| \le |\varepsilon_{Bu}|$ and major μ_{Hp} for $|\varepsilon_{Ho}| \le |\varepsilon_{Hp}| \le |\varepsilon_{Hu}|$ dimensions of an FCC section and the average plastic area dilation rate μ_{ap} in the plastic region of its compressive stress-strain behavior (i.e., when $\varepsilon_{co} \le \varepsilon_{cp} \le \varepsilon_{cu}$) are defined as:

$$\mu_{Bp} = -\left(\frac{\partial \varepsilon_B}{\partial \varepsilon_c}\right)_p \tag{7.48}$$

$$\mu_{Hp} = -\left(\frac{\partial \varepsilon_H}{\partial \varepsilon_c}\right)_p = \alpha_\varepsilon \mu_{Bp} \tag{7.49}$$

$$\mu_{ap} = -\left(\frac{\partial \varepsilon_a}{\partial \varepsilon_c}\right)_p = -\left(\frac{\partial(\varepsilon_B + \varepsilon_H)}{\partial \varepsilon_c}\right)_p = \mu_{Bp} + \mu_{Hp} = \mu_{Bp}(1+\alpha_\varepsilon) \tag{7.50}$$

where ε_{Bo} and ε_{Ho} are the average dilation strains along the minor and major dimensions of the FCC section, corresponding to the peak unconfined compressive strain, ε_{co}; ε_{Bp} and ε_{Hp} are the average plastic dilation strains along the minor and major

dimensions of the FCC section, corresponding to an arbitrary plastic compressive strain, ε_{cp}; ε_{Bu} and ε_{Hu} are the average ultimate dilation strains along the minor and major directions of the FCC section, corresponding to the ultimate compressive strain ε_{cu} at failure of the FRP jacket.

Define the diagonal jacket dilation rate μ_j, of the FRP-confined concrete section as:

$$\mu_j = -\left(\frac{\partial \varepsilon_j}{\partial \varepsilon_c}\right) \tag{7.51}$$

Using the strain transformation relationships introduced in Eqs. (6.58)-(6.60), the transverse dilation rates μ_B of Eq. (7.45) and μ_H of Eq. (7.46) can be written in terms of the diagonal dilation rate μ_j of Eq. (7.51) as follows:

$$\mu_B = -\left(\frac{\partial \varepsilon_B}{\partial \varepsilon_c}\right) = \left(\frac{1}{\beta_j}\right)\mu_j \tag{7.52}$$

$$\mu_H = -\left(\frac{\partial \varepsilon_H}{\partial \varepsilon_c}\right) = \left(\frac{\alpha_\varepsilon}{\beta_j}\right)\mu_j \tag{7.53}$$

Using Eqs. (7.34)-(7.39), the average area dilation rate μ_a of Eq. (7.47) can be given in terms of the diagonal jacket dilation rate μ_j of Eq. (7.51), or vice versa as follows:

$$\mu_a = -\frac{\partial \varepsilon_a}{\partial \varepsilon_c} = -\frac{\partial\left(\varepsilon_B + \varepsilon_H\right)}{\partial \varepsilon_c} = \beta_a \mu_j \tag{7.54}$$

The jacket diagonal plastic dilation rate μ_{jp} for $|\varepsilon_{do}| \le |\varepsilon_{dp}| \le |\varepsilon_{du}|$ of an FCC section in the plastic region of its compressive stress-strain behavior when $\varepsilon_{co} \le \varepsilon_{cp} \le \varepsilon_{cu}$ is given by:

$$\mu_{jp} = -\left(\frac{\partial \varepsilon_j}{\partial \varepsilon_c}\right)_p \tag{7.55}$$

Using Eqs. (7.52) and (7.53), the plastic dilation rate μ_{Bp} of Eq. (7.48), and μ_{Hp} of (7.49) and the average plastic area dilation rate μ_{ap} of Eq. (7.50) can be found in terms of the plastic diagonal dilation rate μ_{jp} of Eq. (7.55) as follows:

$$\mu_{Bp} = -\left(\frac{\partial \varepsilon_B}{\partial \varepsilon_c}\right)_p = \left(\frac{1}{\beta_j}\right)\mu_{jp} \tag{7.56}$$

$$\mu_{Hp} = -\left(\frac{\partial \varepsilon_H}{\partial \varepsilon_c}\right)_p = \left(\frac{\alpha_\varepsilon}{\beta_j}\right)\mu_{jp} \tag{7.57}$$

$$\mu_{ap} = \left(\frac{\partial \varepsilon_a}{\partial \varepsilon_c}\right)_p = \beta_a \mu_{jp} \tag{7.58}$$

Volumetric Strain

Another means of measuring the amount of damage in the concrete material is the volumetric strain of concrete in a uniaxial, biaxial, or triaxial compression state of stress. In the analysis of concrete sections in compression, the volumetric strain ε_v is typically defined as:

$$\varepsilon_v = \sum_{m=1}^{3} \varepsilon_m = \varepsilon_1 + \varepsilon_2 + \varepsilon_3 \tag{7.59}$$

where ε_m is the principal strain in the orthogonal principal m^{th} direction.

As the imposed axial deformation or strain in the concrete section increases, damage of the internal structure of the concrete material starts to accumulate. Deviation from a linear elastic response of the concrete material initiates in the axial stress-axial strain, axial stress-transverse strain, axial strain-transverse strain, volumetric strain-axial strain, volumetric strain-transverse and the axial stress-volumetric strain curves of concrete in a uniaxial, biaxial or triaxial compression state of stress occurs as a result of axial strain-induced damage, i.e.. micro-crack growth at the paste-aggregate interface.

In this dissertation, the axial stress-volumetric strain, volumetric strain-axial strain, and the volumetric strain-transverse strain curves of the concrete in a uniaxial and triaxial compression state of stress typical of unconfined concrete sections and FCC sections are studied in order to describe the nonlinear compressive behavior of unconfined and concrete sections confined by the FRP jacket, as shown in **Figure 7.3**.

A negative volumetric strain indicates that the concrete section experiences volumetric contraction, whereas, a positive volumetric strain indicates volumetric expansion.

Circular Concrete Sections

The normalized axial stress f_c / f_{co} versus axial and radial strain curve plotted in **Figure 7.5** is plotted in **Figure 7.10(a)** versus the volumetric strain ε_v of Eq. (7.59). For confined and unconfined circular concrete sections the volumetric strain ε_v, is given as:

$$\varepsilon_v = -(\varepsilon_c + \varepsilon_r + \varepsilon_\theta) = -(\varepsilon_c + 2\varepsilon_r) = -(\varepsilon_c + \varepsilon_a) \tag{7.60}$$

Using ν_r of Eq. (7.26) and ν_a of Eq. (7.30), the above volumetric strain ε_v can be rewritten as:

$$\varepsilon_v = -(\varepsilon_c + 2\varepsilon_r) = \varepsilon_c(2\nu_r - 1) = \varepsilon_c(\nu_a - 1) \tag{7.61}$$

It can be observed from **Figure 7.10(a)** that the unconfined concrete core approaches its unconfined compressive strength, $f_c \to f_{co}$ as the volumetric strain $\varepsilon_v \to 0$. This is a result of unrestrained volumetric expansion of the unconfined concrete cores when $\varepsilon_v > 0$ as $f_c \to f_{co}$ and as $\varepsilon_c \to \varepsilon_{co}$. For a circular section, a value of $\varepsilon_v > 0$ occurs as $\nu_r \to 1/2$, $\varepsilon_r \to \varepsilon_c/2$, $\nu_a \to 1.0$ and $\varepsilon_a \to \varepsilon_c$ as can be seen from Eqs. (7.28) and (7.59). In **Figure 7.10(b)**, the volumetric strain curve of an unconfined concrete section is plotted versus the axial strain and radial strain in the section.

FRP-Confined Concrete Sections

Using the strain relationships of Eqs. (6.19) and (6.54)-(6.55), the average volumetric strain ε_v of Eq. (7.59) in the FCC section can be determined from the average transverse strains ε_B and ε_H and the average area strain ε_a of Eq. (7.36) as follows:

$$\varepsilon_v = -(\varepsilon_c + \varepsilon_B + \varepsilon_H) = -[\varepsilon_c + \varepsilon_B(1 + \alpha_\varepsilon)] = -(\varepsilon_c + \varepsilon_a) \tag{7.62}$$

Using Eqs. (7.38) and (7.39), the previous relationship can be rewritten in terms of the diagonal jacket strain ε_j as follows:

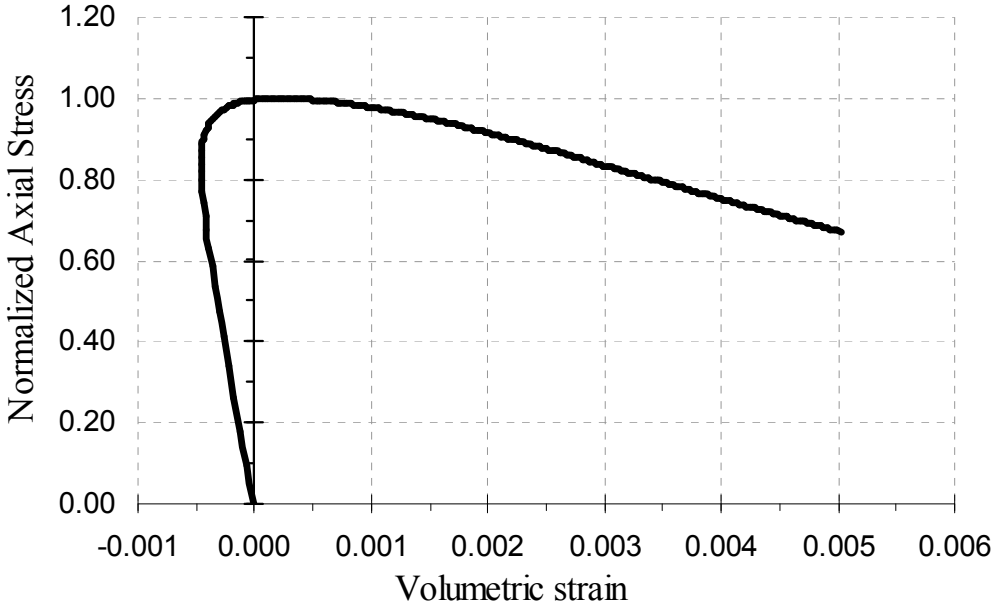

(a)

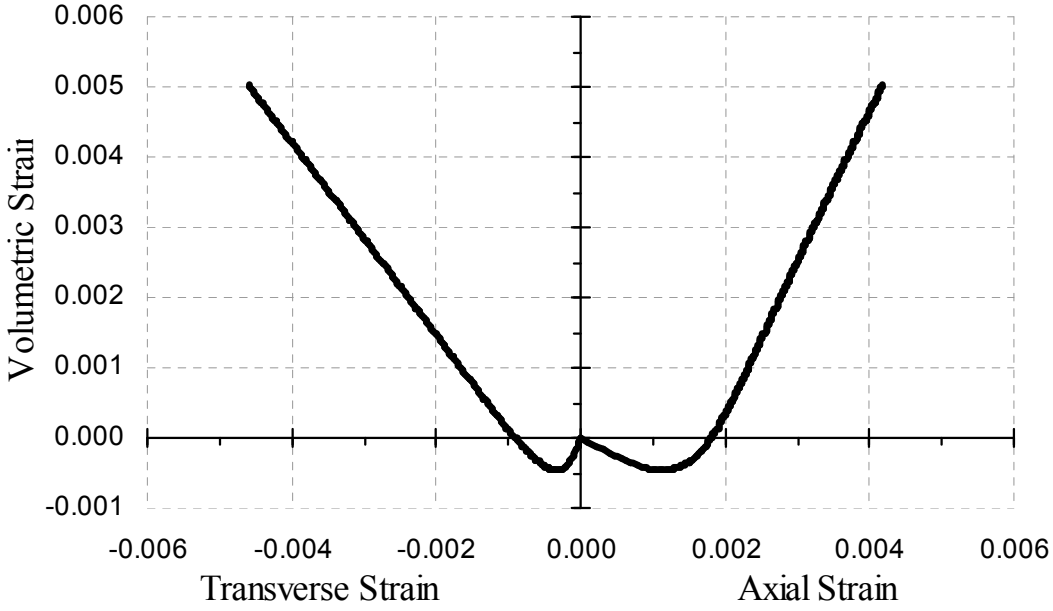

(b)

Figure 7.10 Plot of a typical (a) normalized axial stress versus volumetric strain and (b) volumetric strain versus axial and transverse strain of unconfined concrete in compression.

$$\varepsilon_v = -\left(\varepsilon_c + \beta_a \varepsilon_j\right) = \varepsilon_c \left[\beta_a \nu_j - 1\right] \tag{7.63}$$

The diagonal jacket strain ε_j, at the instant of zero volumetric strain (i.e., $\varepsilon_v = 0$) is defined herein as the average volumetric diagonal jacket strain $\left(\varepsilon_j\right)_{vol}$ and is found by setting $\varepsilon_v = 0$ and $\varepsilon_c = \left(\varepsilon_c\right)_{vol}$ for $\varepsilon_c \neq 0$ in Eqs. (7.62) and (7.63), which yield:

$$\left(\varepsilon_j\right)_{vol} = -\frac{\left(\varepsilon_c\right)_{vol}}{\beta_a} \tag{7.64}$$

Using the strain relationships on Eqs. (6.58)-(6.60), the minor $\left(\varepsilon_B\right)_{vol}$ and major $\left(\varepsilon_H\right)_{vol}$ dilation strains of the FCC section at the instant of zero volumetric strain can be given in terms of the jacket volumetric strain ε_v of Eq. (7.64) as follows:

$$\left(\varepsilon_B\right)_{vol} = \frac{1}{\beta_j}\left(\varepsilon_j\right)_{vol} \tag{7.65}$$

$$\left(\varepsilon_H\right)_{vol} = \left(\frac{\alpha_\varepsilon}{\beta_j}\right)\left(\varepsilon_j\right)_{vol} \tag{7.66}$$

The diagonal Poisson's ratio ν_j, at the instant of zero volumetric strain, is defined as the volumetric diagonal Poisson's ratio $\left(\nu_j\right)_{vol}$.

This Poisson's ratio can be determined by setting $\varepsilon_v = 0$, $\varepsilon_j = \left(\varepsilon_j\right)_{vol}$, and $\varepsilon_c = \left(\varepsilon_c\right)_{vol}$ in Eq. (7.63), which yield:

$$\left(\nu_j\right)_{vol} = -\left(\frac{\varepsilon_j}{\varepsilon_c}\right)_{vol} = \frac{1}{\beta_a} \tag{7.67}$$

Using Eqs. (7.34) and (7.35), the volumetric Poisson's ratio along the minor $\left(\nu_B\right)_{vol}$ and major $\left(\nu_H\right)_{vol}$ dimensions of the FCC section is given in terms of the volumetric diagonal Poisson's ratio $\left(\nu_j\right)_{vol}$ of Eq. (7.67) as follows:

$$\left(\nu_B\right)_{vol} = -\left(\frac{\varepsilon_B}{\varepsilon_c}\right)_{vol} = \frac{1}{\beta_j}\left(\nu_j\right)_{vol} = \frac{1}{\beta_j \beta_a} \tag{7.68}$$

$$\left(\nu_H\right)_{vol} = -\left(\frac{\varepsilon_B}{\varepsilon_c}\right)_{vol} = \frac{\alpha_\varepsilon}{\beta_j}\left(\nu_j\right)_{vol} = \frac{\alpha_\varepsilon}{\beta_a \beta_j} \tag{7.69}$$

Volumetric Dilation Rate

The volumetric dilation rate ψ_n of an unconfined or FRP-confined concrete section is defined as the tangent slope of the volumetric strain ε_v versus the ε_n strain curve of the section in compression, and is given by:

$$\psi_n = \frac{\partial \varepsilon_v}{\partial \varepsilon_n} \tag{7.70}$$

where the subscript n indicates an arbitrary strain direction, where $n = c, r, \theta, d, H,$ or B.

Circular Concrete Sections

In **Figure 7.11**, the tangent slope of the volumetric strain ε_v curves plotted in **Figure 7.10(b)** is plotted versus the axial ε_c and transverse strain ε_r of a typical concrete member in compression.

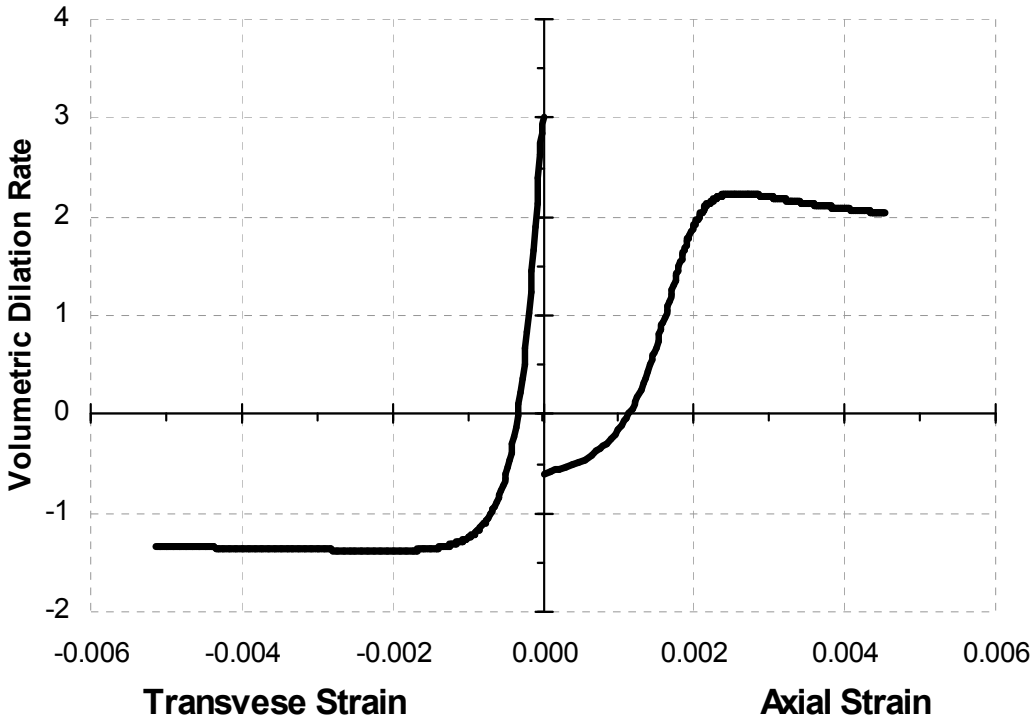

Figure 7.11 Plot of a typical volumetric dilation rate versus axial and transverse strains of an unconfined concrete in compression.

These tangent slopes in the axial and transverse strain direction of the volumetric curves of **Figure 7.10(b)** of a circular concrete section are defined as the axial ψ_c and transverse ψ_r volumetric dilation rates, respectively, and are given by:

$$\psi_c = \frac{\partial \varepsilon_v}{\partial \varepsilon_c} = -\frac{\partial(\varepsilon_c + \varepsilon_r + \varepsilon_\theta)}{\partial \varepsilon_c} = 2\mu_c - 1 = \mu_a - 1 \tag{7.71}$$

$$\psi_r = \frac{\partial \varepsilon_v}{\partial \varepsilon_r} = -\frac{\partial(\varepsilon_c + \varepsilon_r + \varepsilon_\theta)}{\partial \varepsilon_r} = \frac{1}{\mu_c} - 2 = 2\left(\frac{1}{\mu_a} - 1\right) \tag{7.72}$$

As can be observed in **Figure 7.11**, the axial volumetric dilation rate ψ_c of Eq. (7.71), of the circular unconfined concrete section approaches its maximum value at axial strains near the peak axial compressive strain ε_{co} of the concrete core. The minimum transverse volumetric dilation rate ψ_r of Eq. (7.72) tends to occur near the peak transverse strain ε_{ro}.

FRP-Confined Concrete Sections

For the FRP-confined cross-sections shown in **Figure 7.3**, the axial ψ_c and transverse volumetric dilation rates along the minor ψ_B and major ψ_H dimensions of the FRP-confined concrete sections are given by:

$$\psi_c = \frac{\partial(\varepsilon_v)}{\partial \varepsilon_c} = \frac{-\partial(\varepsilon_c + \varepsilon_H + \varepsilon_B)}{\partial \varepsilon_c} = \mu_H + \mu_B - 1 = \mu_B(1 + \alpha_\varepsilon) - 1 \tag{7.73}$$

$$\psi_B = \frac{\partial(\varepsilon_v)_{avg}}{\partial \varepsilon_B} = \frac{-\partial(\varepsilon_c + \varepsilon_H + \varepsilon_B)}{\partial \varepsilon_B} = \frac{1}{\mu_B} - (1 + \alpha_\varepsilon) \tag{7.74}$$

$$\psi_H = \frac{\partial(\varepsilon_v)_{avg}}{\partial \varepsilon_H} = \frac{-\partial(\varepsilon_c + \varepsilon_H + \varepsilon_B)}{\partial \varepsilon_H} = \left(\frac{1}{\alpha_\varepsilon}\right)\psi_B \tag{7.75}$$

where the axial ψ_c and transverse volumetric dilation rates ψ_B and ψ_H are the tangent slopes of the volumetric strain ε_v versus the axial ε_c, and the minor ε_B, and major ε_H, transverse strain curves, respectively.

The diagonal jacket volumetric dilation rate ψ_j is defined as the tangent slope of the volumetric strain ε_v versus the diagonal jacket strain ε_j, and is given by:

$$\psi_j = \frac{\partial(\varepsilon_v)_{avg}}{\partial \varepsilon_j} = \frac{-\partial(\varepsilon_c + \varepsilon_H + \varepsilon_B)}{\partial \varepsilon_j} = \frac{1}{\mu_j} - \beta_a \tag{7.76}$$

Using Eqs. (7.52)-(7.54), (7.60)-(7.63), and (7.76), the volumetric dilation rates ψ_c of Eq. (7.73), ψ_B of Eq. (7.74), and ψ_H of Eq. (7.75) can be found in terms of the diagonal jacket dilation rate μ_j of Eq. (7.51) as follows:

$$\psi_c = \frac{\partial(\varepsilon_v)_{avg}}{\partial \varepsilon_c} = \beta_a \mu_j - 1 \tag{7.77}$$

$$\psi_B = \frac{\partial(\varepsilon_v)_{avg}}{\partial \varepsilon_B} = \frac{\beta_j}{\mu_j} - (1 + \alpha_\varepsilon) \tag{7.78}$$

$$\psi_H = \frac{\partial \varepsilon_v}{\partial \varepsilon_H} = \frac{\partial \varepsilon_v}{\alpha_\varepsilon \partial \varepsilon_B} = \frac{\beta_j}{\alpha_\varepsilon \mu_j} - (1 + \frac{1}{\alpha_\varepsilon}) \tag{7.79}$$

In this chapter it was determined that the geometry of the FCC section and stiffness of the FRP jacket, introduced in Chapters 4-6, influence the Poisson's ratio (ν_j, ν_B, and

ν_H), the dilation rate or tangent Poisson's ratio (μ_j, μ_B, and μ), the area strain ε_a, the area Poisson's ratio ν_a, and dilation rate μ_a, the volumetric strain ε_v, and volumetric dilation rates (ψ_c, ψ_r, ψ_H, ψ_B, and ψ_j) of the FRP-jacketed section shapes considered in this dissertation.

CHAPTER 8

TRANSVERSE AND DIAGONAL DILATION MODEL OF CONCRETE SECTIONS CONFINED BY FIBER-REINFORCED POLYMER JACKETS

In this chapter, a series of damage-based strain relationships are introduced for modeling the dilation behavior of rectangular, square, circular, and elliptical concrete columns confined by FRP jackets. The dilation model requires the definition of a series of dilation relationships that describe the increase in damage in the cross section in terms of the geometric and mechanical properties of the FRP jacket and concrete core, as discussed in Chapters 4-7. The assumptions made in Chapters 5 and 7 are also applicable to the analytical dilation model introduced herein.

Dilation Behavior of Concrete in Compression

A series of typical compressive stress-strain curves of normal weight, normal strength, FRP-confined concrete (FCC) cylinders are plotted in **Figure 8.1** of FRP jacket having low, moderate, and high effective jacket stiffness C_{je} of Eq. (4.13) or normalized stiffness K_{je} of Eq. (4.18). In this figure, the stress-strain curves of concrete are plotted versus the axial strain ε_c on the right side of the vertical axis, and versus the transverse dilation strain ε_r on the left-hand side.

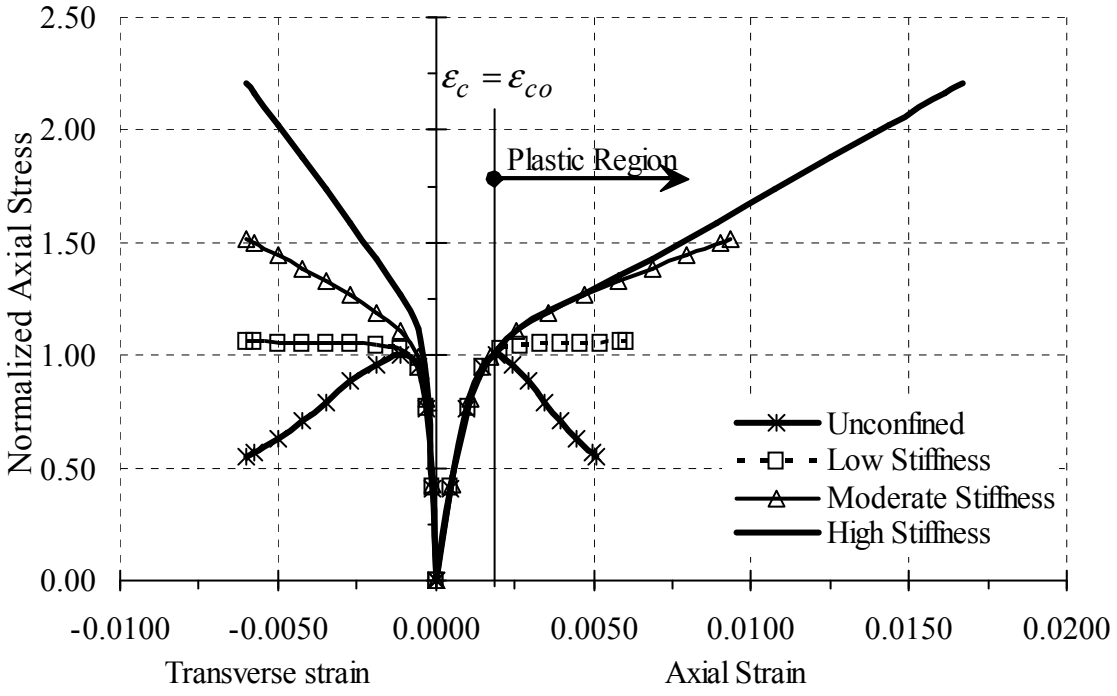

Figure 8.1 Plot of typical normalized axial stress versus transverse and axial strains curves of FRP-confined concrete cylinders section in compression.

In **Figure 8.2**, a typical absolute transverse strain $|\varepsilon_r|$ of the concrete cylinder stress-train curves, shown in **Figure 8.1**, is plotted versus the axial strain ε_c. The initial slope shown in **Figure 8.2** up to an axial strain of 0.001 is the initial dilation rate μ_{ro} of Eq. (7.8) or Eq. (7.12) of the circular FRP-confined concrete (CFCC) section. As can be observed from both **Figures 8.1** and **8.2**, the second slope of the bilinear stress-strain curves of the FCC section increases as the relative stiffness of the confining elastic FRP jacket increases. This bilinear behavior is a result of the increase in the lateral kinematic restraint provided by the restraining (confining) elastic FRP jacket, as measured by the transverse effective stiffness $(C_{je})_{sh}$ of Eq. (4.14) or the normalized effective stiffness $(K_{je})_{sh}$ of Eq. (4.19).

At high levels of axial compressive strains, i.e., at $\varepsilon_c >> \varepsilon_{co}$, the slope of the absolute transverse strain versus axial strain curves of **Figure 8.2** decreases as the FRP jacket stiffness increases. This effect is also a result of an increase in the lateral restraint provided by the confining elastic FRP jacket. Unconfined and confined concrete is considered to be in a plastic compressive behavior when the axial compressive strain ε_c in the concrete is greater than the unconfined peak compressive strain ε_{co}, i.e., when $\varepsilon_c > \varepsilon_{co}$, as shown in **Figures 8.1** and **8.2**.

In **Figure 8.3(a)**, a typical absolute diagonal jacket strain $|\varepsilon_j|$ versus axial strain ε_c curve (the $|\varepsilon_j|$-ε_c dilation curve) of a section confined by a moderate stiffness FRP jacket is shown.

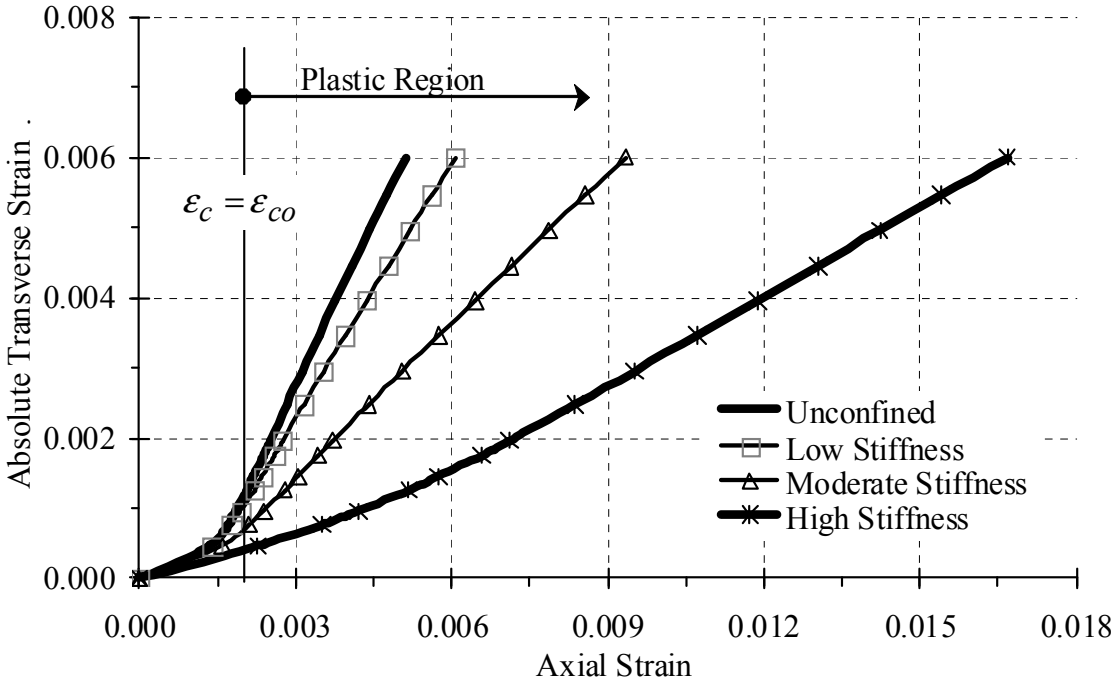

Figure 8.2 Plot of typical absolute transverse strain versus axial strain curves of FRP-confined concrete cylinder sections in compression.

In **Figure 8.3(b)** the axial strain ε_c versus absolute diagonal jacket strain $|\varepsilon_j|$ curve (the ε_c-$|\varepsilon_j|$ dilation curve) is shown, i.e., the inverse of the dilation curve of **Figure 8.3(a)**. In this figure the curve shown is the inverse transverse strain-axial strain curve. For a circular section, the inverse Poisson's ratio $1/\nu_r$ is defined as:

$$\frac{1}{\nu_r} = \frac{1}{\nu_j} = -\frac{\varepsilon_c}{\varepsilon_j} = -\frac{\varepsilon_c}{\varepsilon_r} = -\frac{\varepsilon_c}{\varepsilon_\theta} \tag{8.1}$$

where ν_j is the secant Poisson's ratio of an FCC section of Eq. (7.33) and ν_r is the secant Poisson's ratio of a circular concrete section of Eq. (7.28). For unconfined and confined circular concrete sections $\varepsilon_r = \varepsilon_\theta = \varepsilon_B = \varepsilon_H = \varepsilon_j = \varepsilon_a/2$, where ε_r, ε_θ, ε_B, ε_H, ε_j and ε_a are the radial, hoop, minor, major, diagonal jacket and area strains, respectively, which are terms previously introduced in Chapters 6 and 7.

The inverse secant Poisson's ratio along the minor $1/\nu_B$ and major $1/\nu_H$ dimensions of the FCC section and the inverse jacket diagonal secant Poisson's ratio $1/\nu_j$ of rectangular (RFCC), square (SFCC), oval (OFCC), including oval shape-modified (OSM) sections, circular (CFCC), including circular shape-modified (CSM) sections, and elliptical (EFCC), including elliptical shape-modified (ESM) sections, are given by:

$$\frac{1}{\nu_B} = -\frac{\varepsilon_c}{\varepsilon_B} \;\; ; \;\; \frac{1}{\nu_H} = -\frac{\varepsilon_c}{\varepsilon_H} \;\; ; \;\; \frac{1}{\nu_j} = -\frac{\varepsilon_c}{\varepsilon_j} \tag{8.2}$$

where ν_B, ν_H, and ν_j are the minor, major, and jacket diagonal Poisson's ratios of the FRP-confined concrete section, introduced in Eqs. (7.34), (7.35), and (7.33), respectively.

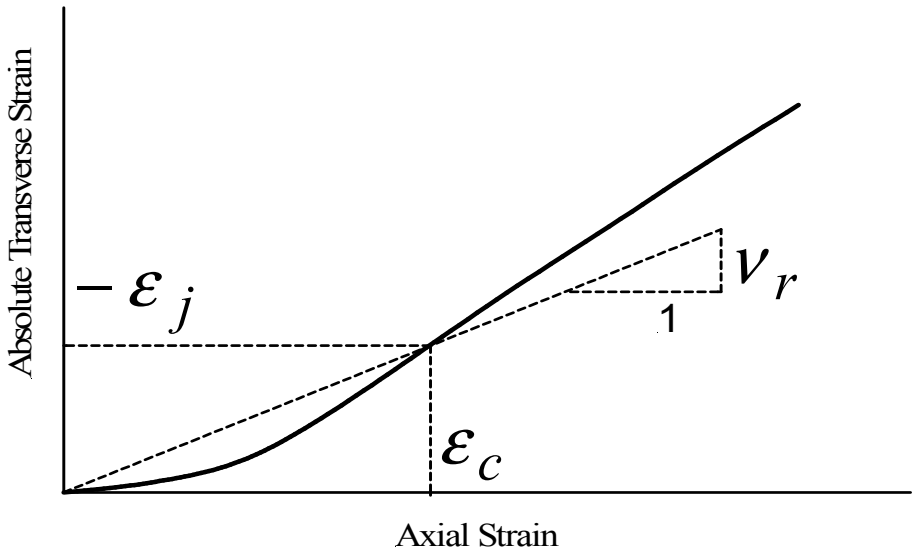

(a)

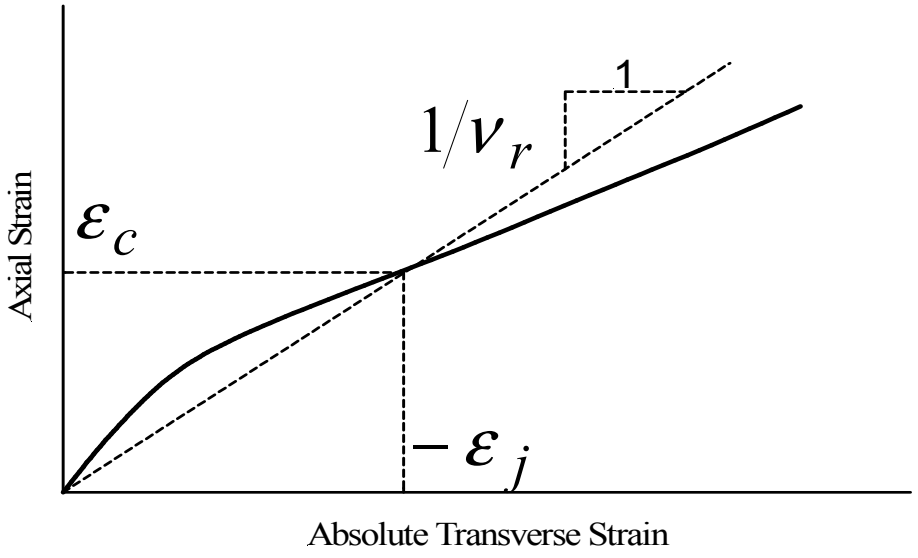

(b)

Figure 8.3 Plot of a typical (a) absolute transverse strain versus axial strain and (b) axial strain versus transverse strain curves of an FRP-confined concrete cylinder section in compression.

In Chapters 5 and 6 it was established that for a circular concrete section $\varepsilon_r = \varepsilon_\theta = \varepsilon_B = \varepsilon_H = \varepsilon_j = \varepsilon_a/2$; this chapter is concerned only with modeling the diagonal dilation of the FCC section shown in **Figure 7.3**. As a result, the strain transformation relationships introduced in Chapters 6 and 7 are applicable to rectangular, square, oval , circular, and elliptical FCC sections.

A typical axial strain ε_c versus absolute jacket diagonal strain $|\varepsilon_j|$ curve (the ε_c-$|\varepsilon_j|$ curve) of an FRP-confined concrete member is shown in **Figure 8.4(a).** This curve is subdivided into a linear and a nonlinear component. The nonlinear component of the ε_c-$|\varepsilon_j|$ curve, which is shown as a cross-hatched area in **Figure 8.4(a),** represents the amount of degradation that the internal structure of the FRP-confined concrete core exhibits as a result of a remolding of its internal structure, as it undergoes unrestrained axial strain-induced extension, growth and nucleation of micro-cracks and/or voids (as damage progresses) prior to fully engaging the lateral kinematic restraint provided by the confining elastic FRP jacket. The linear component of the ε_c-$|\varepsilon_j|$ curve, which is shown as a vertically hatched area in **Figure 8.4(a),** represents the amount of degradation of the concrete's internal structure that is restrained by the confining elastic FRP jacket as the axial strain-induced damage in the confined concrete core progresses.

The effective axial strain $\varepsilon_c^{'}$ at a given jacket diagonal strain ε_j can be found from the geometry of the ε_c-$|\varepsilon_j|$ curve of **Figure 8.4(a)**, and using the inverse jacket diagonal secant Poisson's ratio $1/\nu_j$ of Eq. (8.2) and the plastic dilation rate μ_{jp} of Eq. (7.25), as follows:

$$\varepsilon_c^{'} = -\left(\frac{\varepsilon_j}{\nu_j^{'}}\right) = \varepsilon_c + \frac{\varepsilon_j}{\mu_{jp}} = \varepsilon_j\left(\frac{1}{\mu_{jp}} - \frac{1}{\nu_j}\right) \tag{8.3}$$

where $1/\nu_j^{'}$ is the inverse effective jacket diagonal secant Poisson's ratio at a given effective axial strain $\varepsilon_c^{'}$ and corresponding jacket diagonal strain ε_j; it represents the secant slope of the effective axial strain $\varepsilon_c^{'}$ versus the absolute jacket diagonal strain ε_j curve (the $\varepsilon_c^{'}$-$|\varepsilon_j|$ curve) shown in **Figure 8.4(b).** Using Eq. (8.3), the inverse effective jacket diagonal secant Poisson's ratio $1/\nu_j^{'}$ is given by:

$$\frac{1}{\nu_j^{'}} = \frac{\mu_{jp} - \nu_j}{\nu_j \mu_{jp}} \tag{8.4}$$

Graphically, the inverse effective secant Poisson's ratio $1/\nu_j^{'}$ of Eq. (8.4) is the difference in slope between the inverse Poisson's ratio $1/\nu_j$ and the asymptotic plastic slope $1/\mu_{jp}$, as shown in the ε_c-$|\varepsilon_j|$ curve of **Figure 8.4(a)**. Solving for the effective Poisson's ratio $\nu_j^{'}$ in Eq. (8.4) yields:

$$\nu_j^{'} = \left(\frac{\nu_j \mu_{jp}}{\mu_{jp} - \nu_j}\right) \text{ for } \nu_j \neq \mu_{jp} \tag{8.5}$$

As shown in **Figure 8.4** when $\nu_j \to \mu_{jp}$ plastic dilation commences and $\nu_j^{'} \to 0$. As a result, the limit of $\nu_j \neq \mu_{jp}$ is imposed in Eq. (8.5).

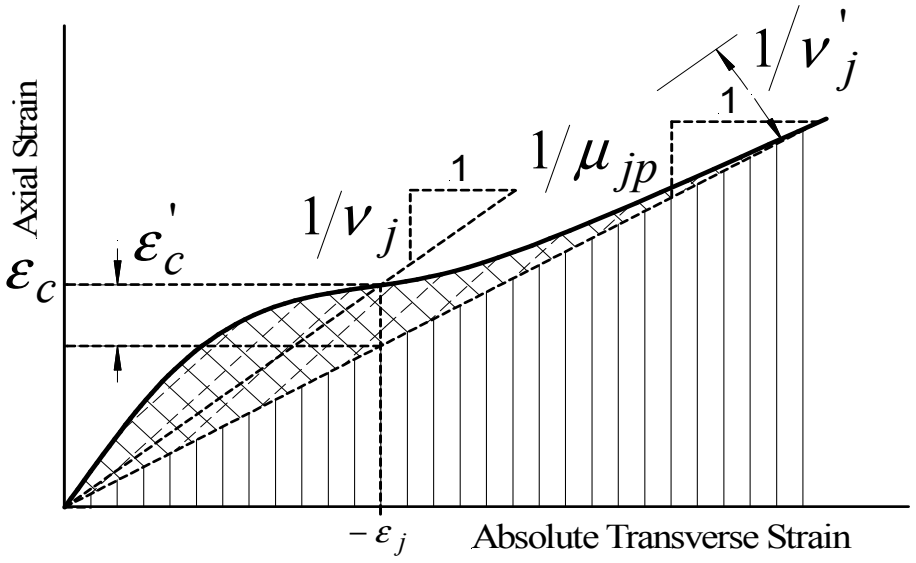

(a)

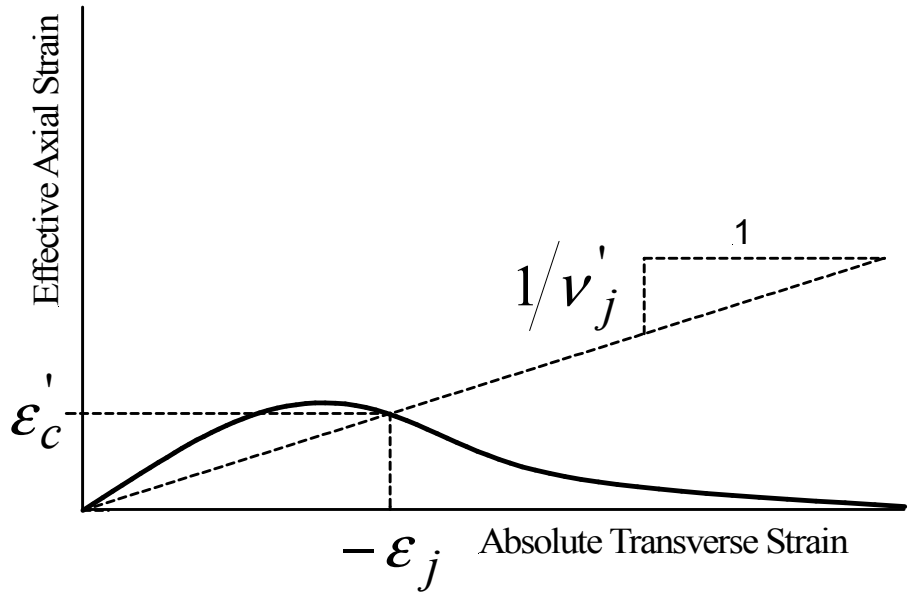

(b)

Figure 8.4 Plot of a typical (a) axial strain versus absolute transverse strain versus axial strain curve and (b) nonlinear component of FRP-confined concrete section in compression.

The geometric terms that are used to describe the shape of the ε_c-$|\varepsilon_j|$ curve of **Figure 8.4(a)** are plotted in **Figure 8.5.** In this figure μ_{jo} is the initial diagonal dilation rate of Eq. (7.19); μ'_{jo} is the effective initial jacket diagonal dilation rate; $(\nu_j)_{\text{sec}}$ is the jacket diagonal secant Poisson's ratio evaluated at the axial strain ε_{co} and corresponding diagonal strain ε_{jo}; $(\nu'_j)_{\text{sec}}$ is the effective jacket diagonal secant Poisson's ratio; $(\nu_j)_{pk}$ is the localized jacket diagonal peak Poisson's ratio evaluated at the localized peak axial strain $(\varepsilon_c)_{pk}$ and corresponding jacket diagonal strain $(\varepsilon_j)_{pk}$; $(\nu'_j)_{pk}$ is the effective jacket diagonal peak Poisson's ratio. The mathematical relationships of these geometric terms of the diagonal strain-axial strain curve of **Figure 8.5** are introduced in what follows.

The initial inverse diagonal dilation rate $1/\mu_{jo}$ is the initial tangent slope of the ε_c-$|\varepsilon_j|$ curve of **Figure 8.5(a)**, which can be found using the initial inverse diagonal dilation rate μ_{jo} of Eq. (7.20) as follows:

$$\frac{1}{\mu_{jo}} = -\left(\frac{\varepsilon_c}{\varepsilon_d}\right)_o = \frac{1}{\beta_j(\mu_B)_o} = \frac{\alpha_\varepsilon}{\beta_j(\mu_H)_o} \tag{8.6}$$

where $(\mu_B)_o$ and $(\mu_H)_o$ are the minor and major initial dilation rate of the FRP-confined concrete section of Eqs. (7.17) and (7.19), respectively; β_j is the shape diagonal strain coefficient of Eq. (6.59), summarized in **Table 6.1**.

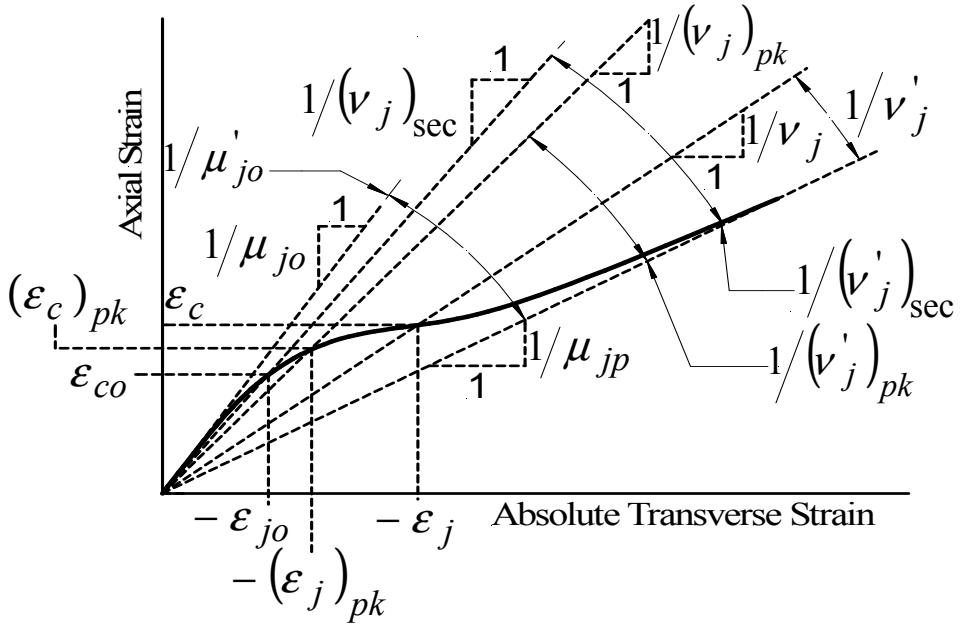

(a)

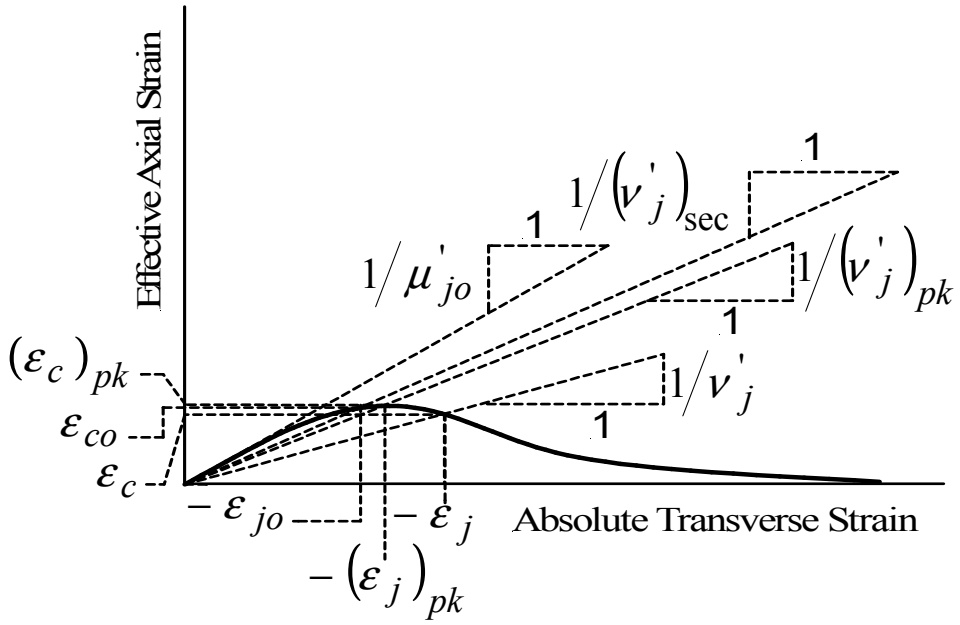

(b)

Figure 8.5 Geometry of a typical (a) axial strain versus absolute transverse strain versus axial strain curve and (b) its nonlinear component of FRP-confined concrete sections in compression.

From analysis of ε_c-$\left|\varepsilon_j\right|$ curve of **Figure 8.6(a)**, using the definition of the effective Poisson's ratio $1/\left(\nu_j\right)'$ of Eq. (8.5), and recognizing that in the elastic regime prior to cracking $\nu_{jo} = \mu_{jo}$, the effective inverse initial dilation rate $1/\mu'_{jo}$ is the difference in slope, between the initial tangent slope $1/\mu_{jo}$, and the final plastic slope $1/\mu_{jp}$. In addition, the inverse effective initial jacket dilation rate $1/\mu'_{jo}$ is the initial tangent slope of the nonlinear portion of the typical ε'_c-$\left|\varepsilon_j\right|$ curve of the FRP-confined concrete section shown in **Figure 8.6(b)**. As a result, the effective initial jacket dilation rate μ'_{jo} is given by:

$$\mu'_{jo} = -\left(\frac{\varepsilon_j}{\varepsilon'_c}\right)_o = \frac{\mu_{jo}\mu_{jp}}{\mu_{jp} - \mu_{jo}} \quad \text{for } \mu_{jp} > \left(\mu_j\right)_o \tag{8.7}$$

The jacket diagonal secant Poisson's ratio $\left(\nu_j\right)_{sec}$ of the typical axial stress-axial strain and axial stress-diagonal strain curves of FRP-confined concrete sections shown in **Figure 8.7(a)**, is defined as:

$$\left(\nu_j\right)_{sec} = -\left(\frac{\varepsilon_{jo}}{\varepsilon_{co}}\right) \tag{8.8}$$

From analysis of the ε_c-$\left|\varepsilon_d\right|$ and ε'_c -$\left|\varepsilon_d\right|$ curves of **Figure 8.7**, the effective peak axial strain ε'_{co} is given by:

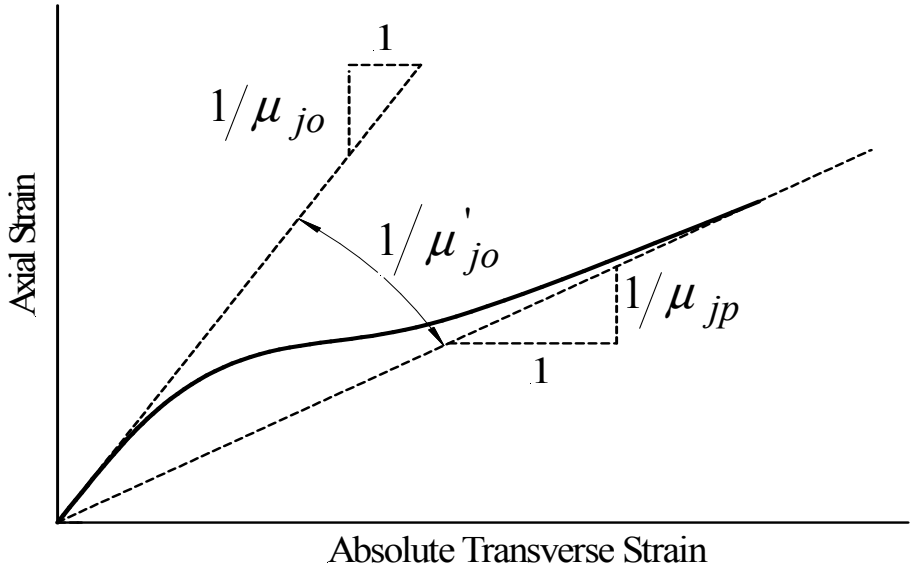

(a)

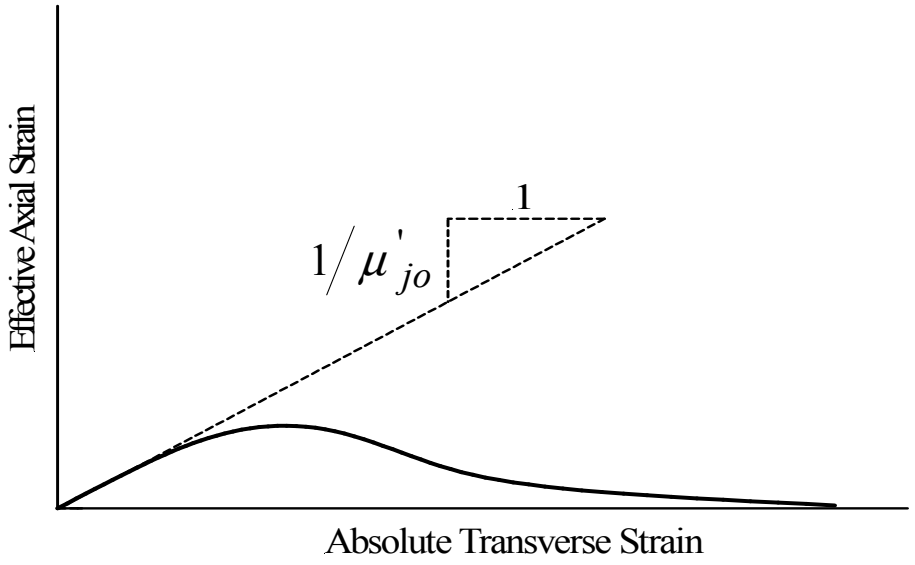

(b)

Figure 8.6 Definition of (a) the initial dilation rate and (b) initial effective dilation rate of the dilation curve of an FRP-confined concrete section in compression.

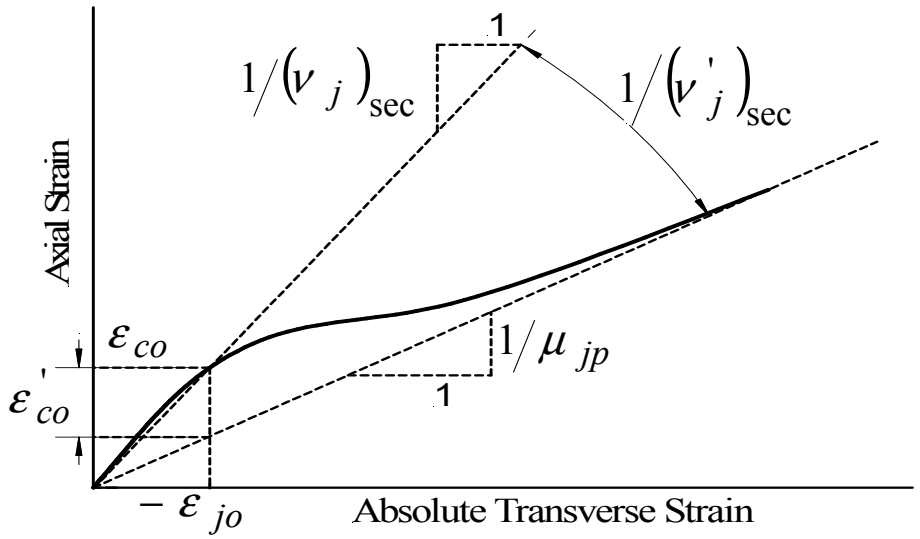

(a)

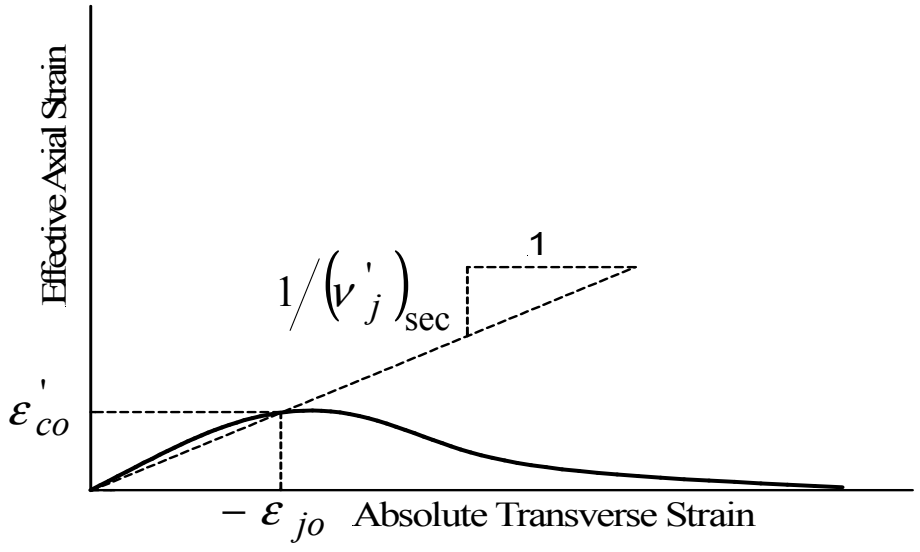

(b)

Figure 8.7 Definition of (a) the secant Poisson's ratio and (b) the effective secant Poisson's ratio of the dilation curve of an FRP-confined concrete section.

$$\varepsilon_{co}^{'} = -\frac{\varepsilon_{jo}}{\left(\nu_j^{'}\right)_{\text{sec}}} = \varepsilon_{co} + \frac{\varepsilon_{jo}}{\mu_{jp}} = \varepsilon_{jo}\left(\frac{1}{\mu_{jp}} - \frac{1}{\left(\nu_j\right)_{\text{sec}}}\right) \tag{8.9}$$

where the inverse effective secant Poisson's ratio $1/\left(\nu_j^{'}\right)_{\text{sec}}$ of Eq. (8.9) is the difference between the inverse secant Poisson's ratio $1/\left(\nu_j\right)_{\text{sec}}$ and the inverse plastic dilation rate $1/\mu_{jp}$, as can be observed in the ε_c-$\left|\varepsilon_j\right|$ curve of **Figure 8.7(a)**.

Graphically, the inverse effective secant Poisson's ratio $1/\left(\nu_j^{'}\right)_{\text{sec}}$ is the difference in slope between the secant slope $1/\left(\nu_j\right)_{sec}$ and the final plastic slope $1/\mu_{jp}$, as shown in the ε_c-$\left|\varepsilon_j\right|$ curve of **Figure 8.7(a)** at the instant when $\varepsilon_c = \varepsilon_{co}$ and $\varepsilon_j = \varepsilon_{jo}$. In addition, the inverse effective secant Poisson's ratio $1/\left(\nu_j^{'}\right)_{\text{sec}}$ is the secant slope of the $\varepsilon_c^{'}$-$\left|\varepsilon_j\right|$ curve of **Figure 8.7(b)** at the instant when $\varepsilon_c^{'} = \varepsilon_{co}^{'}$ and $\varepsilon_j = \varepsilon_{jo}$.

Using Eq. (8.9), the effective secant Poisson's ratio $\left(\nu_j^{'}\right)_{\text{sec}}$ is given by:

$$\left(\nu_j^{'}\right)_{\text{sec}} = -\left(\frac{\varepsilon_{jo}}{\varepsilon_{co}^{'}}\right) = \frac{\left(\nu_j\right)_{sec}\mu_{jp}}{\mu_{jp} - \left(\nu_j\right)_{\text{sec}}} \text{ for } \left(\nu_j\right)_{sec} \neq \mu_{jp} \tag{8.10}$$

The localized peak diagonal Poisson's ratio $\left(\nu_j\right)_{pk}$ of the typical axial stress-axial strain and axial stress-diagonal strain curves of an FRP-confined concrete section, shown in **Figure 8.8(a)**, is defined as:

$$\left(\nu_j\right)_{pk} = -\left(\frac{\varepsilon_j}{\varepsilon_c}\right)_{pk} \tag{8.11}$$

where $\left(\varepsilon_c\right)_{pk}$ is the localized peak axial strain; $\left(\varepsilon_j\right)_{pk}$ is the corresponding peak diagonal strain. From analysis of the ε_c-$\left|\varepsilon_j\right|$ and $\varepsilon_c^{\cdot}-\left|\varepsilon_d\right|$ curves of **Figure 8.8,** the effective localized peak axial strain $\left(\varepsilon_c^{'}\right)_{pk}$ is given by:

$$\left(\varepsilon_c^{'}\right)_{pk} = -\left(\frac{\varepsilon_j}{\nu_j^{'}}\right)_{pk} = \left(\varepsilon_c\right)_{pk} + \frac{\left(\varepsilon_j\right)_{pk}}{\mu_{dp}} = \left(\varepsilon_j\right)_{pk}\left(\frac{1}{\mu_{jp}} - \frac{1}{\left(\nu_j\right)_{pk}}\right) \tag{8.12}$$

As shown in of **Figure 8.8, t**he inverse effective localized peak Poisson's ratio $1/\left(\nu_j^{'}\right)_{pk}$ of Eq. (8.12) is the difference between the inverse jacket peak Poisson's ratio $1/\left(\nu_j\right)_{pk}$ and the inverse jacket plastic dilation rate $1/\mu_{jp}$. Graphically, the inverse effective peak Poisson's ratio $1/\left(\nu_j^{'}\right)_{pk}$ is the difference in slope between the peak slope $1/\left(\nu_j\right)_{pk}$ and the final plastic slope $1/\mu_{jp}$ of the ε_c-$\left|\varepsilon_j\right|$ curve shown in **Figure 8.8(a)** at the instant when $\varepsilon_c = \left(\varepsilon_c\right)_{pk}$ and $\varepsilon_j = \left(\varepsilon_j\right)_{pk}$. In addition, the inverse effective secant Poisson's ratio $1/\left(\nu_j^{'}\right)_{pk}$ is the slope of the $\varepsilon_c^{'}$-$\left|\varepsilon_j\right|$ curve of **Figure 8.8(b)** at the instant when $\varepsilon_c^{'} = \left(\varepsilon_c^{'}\right)_{pk}$ and $\varepsilon_j = \left(\varepsilon_j\right)_{pk}$.

Using Eq. (8.12), the effective peak Poisson's ratio $\left(\nu_j^{'}\right)_{pk}$ is given by:

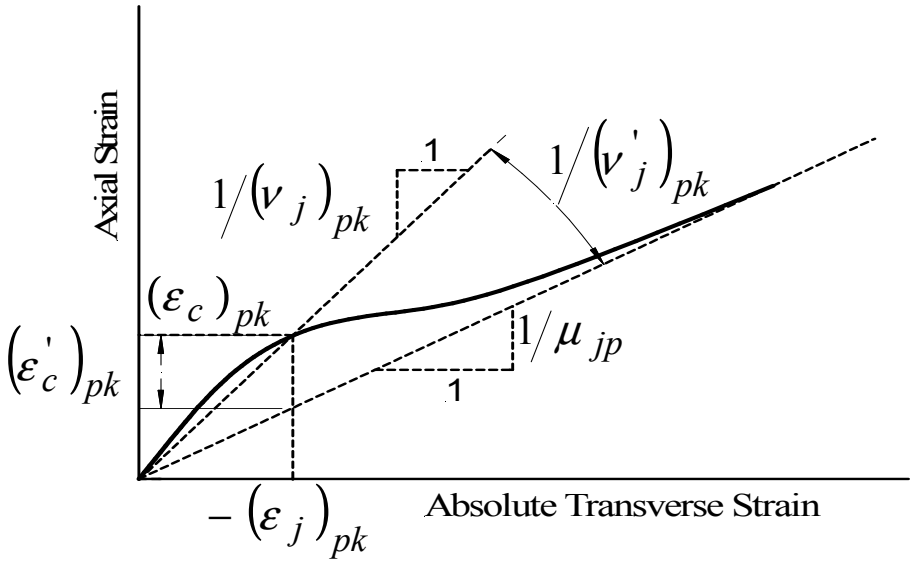

(a)

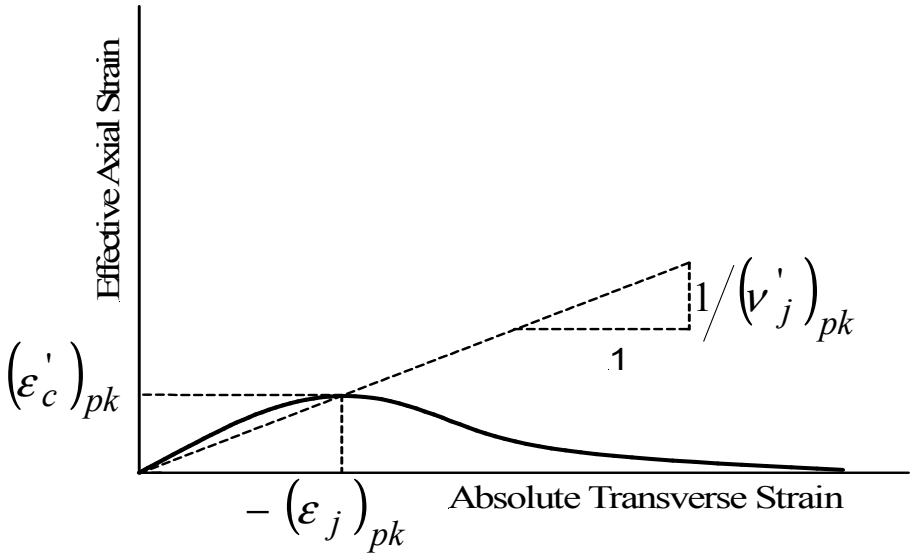

(b)

Figure 8.8 Definition of (a) the localized peak Poisson's ratio and (b) the effective peak Poisson's ratio of the dilation curve of an FRP-confined concrete section.

$$\left(\nu_j^{'}\right)_{pk} = -\left(\frac{\varepsilon_j}{\varepsilon_c^{'}}\right)_{pk} = \frac{\left(\nu_j\right)_{pk}\mu_{jp}}{\mu_{jp} - \left(\nu_j\right)_{pk}} \quad \text{for } \mu_{jp} > \left(\nu_j\right)_{pk} \tag{8.13}$$

For FCC sections confined by low to moderate stiffness FRP jackets that exhibit volumetric expansion during their loading history, the volumetric diagonal Poisson's ratio $\left(\nu_j\right)_{vol}$ of Eq. (7.67), which is defined as the Poisson's ratio of the FRP-confined concrete section at the instant of zero volumetric strain, e.g., $\varepsilon_v = 0$, can be found from analysis of the ε_c-$\left|\varepsilon_j\right|$ curve of **Figure 8.9(a)** [refer to Eqs. (7.59)-(7.69)]**.** In this figure the effective volumetric axial strain $\left(\varepsilon_c^{'}\right)_{vol}$ at the instant of zero volumetric strain $\varepsilon_v = 0$ is given by:

$$\left(\varepsilon_c^{'}\right)_{vol} = -\left(\frac{\varepsilon_j}{\nu_j^{'}}\right)_{vol} = \left(\varepsilon_c\right)_{vol} + \frac{\left(\varepsilon_j\right)_{vol}}{\mu_{jp}} = \left(\varepsilon_j\right)_{vol}\left(\frac{1}{\mu_{jp}} - \frac{1}{\left(\nu_j\right)_{vol}}\right) \tag{8.14}$$

where $\left(\varepsilon_c\right)_{vol}$ and $\left(\varepsilon_j\right)_{vol}$ are the axial and corresponding diagonal volumetric strains at the instant of zero volumetric strain, respectively. The volumetric strain ε_v is defined in Eqs. (7.62) and (7.63) and $\left(\varepsilon_j\right)_{vol}$ in Eq. (7.64).

The inverse effective volumetric Poisson's ratio $1/\left(\nu_j^{'}\right)_{vol}$ of Eq. (8.14) is the difference between the inverse volumetric Poisson's ratio $1/\left(\nu_j\right)_{vol}$ and the inverse plastic dilation rate $1/\mu_{jp}$, as shown in **Figure 8.9**.

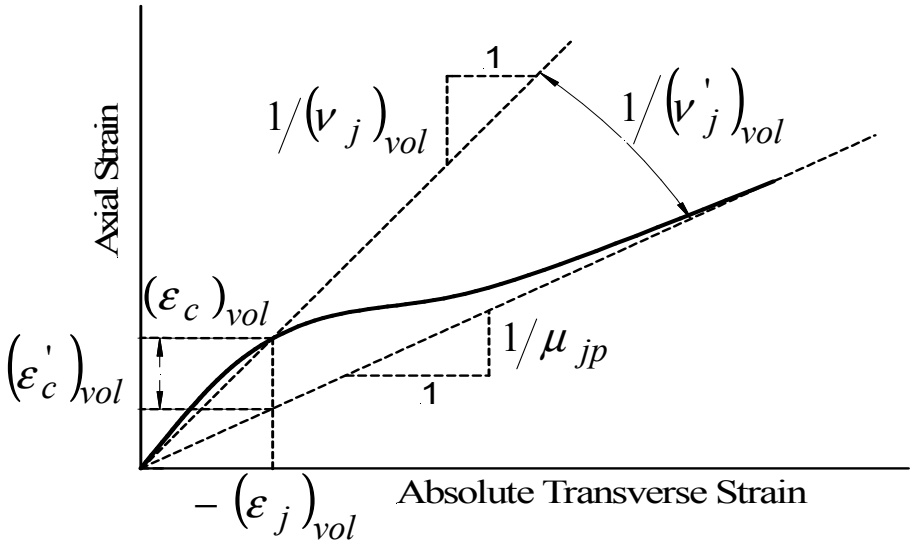

(a)

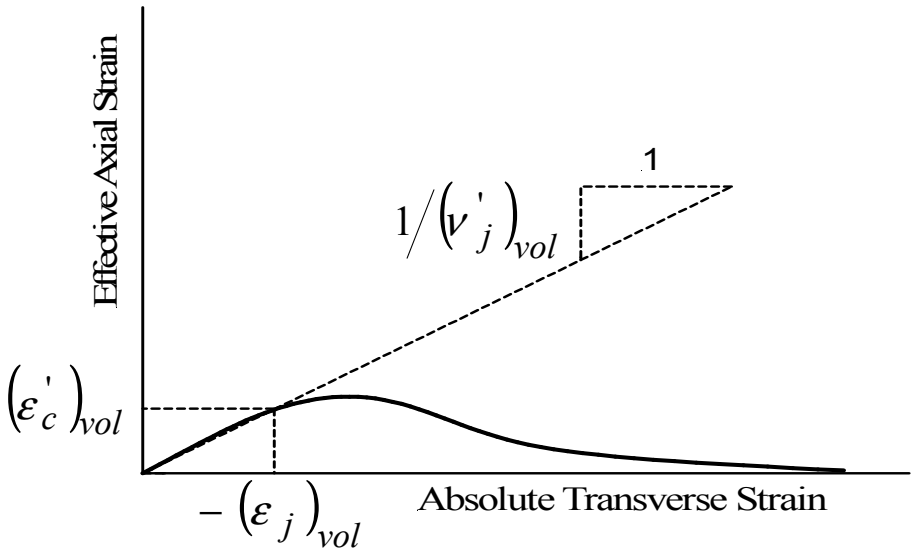

(b)

Figure 8.9 Definition of (a) the volumetric Poisson's ratio and (b) the effective volumetric Poisson's ratio of the dilation curve of an FRP-confined concrete section.

Graphically, the inverse effective volumetric Poisson's ratio $1/\left(\nu_j^{'}\right)_{vol}$ is the difference in slope between the volumetric slope $1/\left(\nu_j\right)_{vol}$ and the final plastic slope $1/\mu_{jp}$, as shown in the ε_c-$\left|\varepsilon_j\right|$ curve of **Figure 8.9(a)** at the instant when $\varepsilon_c = \left(\varepsilon_c\right)_{vol}$ and $\varepsilon_j = \left(\varepsilon_j\right)_{vol}$. In addition, the inverse effective volumetric Poisson's ratio $1/\left(\nu_j^{'}\right)_{vol}$ is the secant slope of the $\varepsilon_c^{'}$-$\left|\varepsilon_j\right|$ curve of an FRP-confined concrete section shown in Figure 8.9(b) at the instant when $\varepsilon_c^{'} = \left(\varepsilon_c^{'}\right)_{vol}$ and $\varepsilon_j = \left(\varepsilon_j\right)_{vol}$. Using Eq. (8.14), the effective volumetric Poisson's ratio $\left(\nu_j^{'}\right)_{vol}$ is given by:

$$\left(\nu_j^{'}\right)_{vol} = -\left(\frac{\varepsilon_j}{\varepsilon_c^{'}}\right)_{vol} = \frac{\mu_{jp}\left(\nu_j\right)_{vol}}{\mu_{jp} - \left(\nu_j\right)_{vol}} \quad \text{for } \left(\nu_j\right)_{vol} \neq \mu_{jp} \tag{8.15}$$

Dilation Model for FRP-Confined Concrete Sections

Due to the nonlinearity of the ε_c-$\left|\varepsilon_j\right|$ and $\varepsilon_c^{'}$-$\left|\varepsilon_j\right|$ curves shown in **Figures 8.4-8.9**, a simple continuous mathematical relationship is sought for which the following geometrical conditions apply:

1. At very small axial and diagonal strains as $\varepsilon_c, \varepsilon_j \rightarrow 0$, the initial slope of $\varepsilon_c^{'}$-$\left|\varepsilon_j\right|$ is given by the effective initial dilation rate $1/\mu_{jo}^{'}$, where:

$$-\left(\frac{\partial \varepsilon_c^{'}}{\partial \varepsilon_j}\right)_{\varepsilon_j \rightarrow 0} = \frac{1}{\mu_{jo}^{'}} \tag{8.16}$$

2. When the diagonal jacket strain ε_j is equal to the localized peak diagonal jacket strain $(\varepsilon_j)_{pk}$, the slope of $\varepsilon_c^{'}$-$|\varepsilon_j|$ curve is equal to zero, where:

$$-\left(\frac{\partial \varepsilon_c^{'}}{\partial \varepsilon_j}\right)_{\varepsilon_j=(\varepsilon_j)_{pk}} = 0 \tag{8.17}$$

3. At infinitely large diagonal strains as $\varepsilon_j \to -\infty$, the effective axial strain $\varepsilon_c^{'}$ approaches the value of zero where:

$$(\varepsilon_c^{'})_{\varepsilon_j \to -\infty} \cong 0 \tag{8.18}$$

4. At infinitely large diagonal strains as $\varepsilon_j \to -\infty$, the slope of $\varepsilon_c^{'}$-$|\varepsilon_j|$ curve approaches the value of zero where:

$$-\left(\frac{\partial \varepsilon_c^{'}}{\partial \varepsilon_j}\right)_{\varepsilon_j \to -\infty} \cong 0 \tag{8.19}$$

A simple continuous mathematical relationship that can accurately model the nonlinearity of the $\varepsilon_c^{'}$-$|\varepsilon_j|$ curve as shown in **Figures 8.4-8.9** and which meets the conditions imposed in Eqs. (8.16)-(8.19) is the Popovics (1973) fractional model for concrete, modified herein in terms of the effective axial strain $\varepsilon_c^{'}$ and diagonal strain ε_j introduced in Eqs. (8.3)-(8.15), where the effective inverse effective jacket diagonal

Poisson's ratio $1/\nu_j^{'}$ or secant slope of the $\varepsilon_c^{'}$-$|\varepsilon_j|$ curve of **Figures 8.4(b)** and **8.5(b)** is given as:

$$\frac{1}{\nu_j^{'}} = -\left(\frac{\varepsilon_c^{'}}{\varepsilon_j}\right) = \frac{1}{\left(\nu_j^{'}\right)_{pk}}\left[\frac{\gamma_j}{\left(\gamma_j - 1\right) + \left(\dfrac{\varepsilon_j}{\left(\varepsilon_j\right)_{pk}}\right)^{\gamma_j}}\right] \tag{8.20}$$

where γ_j is the diagonal curvature parameter of the Popovics-based fractional model (1973). This curvature parameter determines both the rate of softening of the ascending portion and the rate of decay of the descending portion of the $\varepsilon_c^{'}$-$|\varepsilon_j|$ curve and is given by:

$$\gamma_j = \frac{\dfrac{1}{\mu_{jo}^{'}}}{\dfrac{1}{\mu_{jo}^{'}} - \dfrac{1}{\nu_{pk}^{'}}} = \frac{\left(\nu_j^{'}\right)_{pk}}{\left(\nu_j^{'}\right)_{pk} - \mu_{jo}^{'}} \quad \text{for } \left(\nu_j^{'}\right)_{pk} \neq \mu_{jo}^{'} \tag{8.21}$$

Graphically, the above diagonal curvature parameter γ_j of Eq. (8.21) is the ratio of the initial effective slope $1/\mu_{jo}^{'}$ and the difference between the initial effective slope $1/\mu_{jo}^{'}$ and effective peak slope $1/\left(\nu_j^{'}\right)_{pk}$ of the $\varepsilon_c^{'}$-ε_j curve, shown in of **Figures 8.4(b)** and **8.5(b)**.

The ratio of the effective peak Poisson's ratio $\left(\nu_j^{'}\right)_{pk}$ to the effective initial dilation rate $\mu_{jo}^{'}$ is defined as the peak dilation parameter γ_{pk} where:

$$\gamma_{pk} = \frac{\left(\nu_j^{'}\right)_{pk}}{\mu_{jo}^{'}} \tag{8.22}$$

Using the effective initial dilation rate $\mu_{jo}^{'}$ of Eq. (8.7) and the effective peak Poisson's ratio $\left(\nu_j^{'}\right)_{pk}$ of Eq. (8.13), the peak Poisson's ratio $\left(\nu_j\right)_{pk}$ of Eq. (8.11) can be rewritten in terms of the peak dilation parameter γ_{pk} of Eq. (8.22), as follows:

$$\left(\nu_j\right)_{pk} = -\left(\frac{\varepsilon_j}{\varepsilon_c}\right)_{pk} = \frac{\gamma_{pk}\mu_{jo}\mu_{jp}}{\mu_{jp} + \mu_{jo}\left(\gamma_{pk} - 1\right)} \tag{8.23}$$

Using the peak dilation parameter γ_{pk} of Eq. (8.22), the diagonal curvature parameter γ_j of Eq. (8.21) can be rewritten as:

$$\gamma_j = \frac{\gamma_{pk}}{\gamma_{pk} - 1} \tag{8.24}$$

Using the diagonal curvature parameter γ_j of Eqs. (8.21) and (8.24) and the peak dilation parameter γ_{pk} of Eq. (8.22), the fractional dilation model of Eq. (8.20) can be rewritten as:

$$\frac{1}{\nu_j^{'}} = -\left(\frac{\varepsilon_c^{'}}{\varepsilon_j}\right) = \frac{1}{\mu_{jo}^{'}}\left(\frac{1}{\gamma_{pk}-1}\right)\left[\frac{1}{(\gamma_j-1)+\left(\frac{\varepsilon_j}{(\varepsilon_j)_{pk}}\right)^{\gamma_j}}\right] \tag{8.25}$$

In the development of the diagonal dilation model introduced in Eqs. (8.5)-(8.25), both the axial volumetric strain $(\varepsilon_c)_{vol}$ and the localized peak axial strain $(\varepsilon_c)_{pk}$ have not been determined; this is accomplished as follows.

The ratio of the axial volumetric strain $(\varepsilon_c)_{vol}$ to the unconfined peak compressive strain ε_{co} is defined as the volumetric strain ratio α_{vol} where:

$$\alpha_{vol} = \frac{(\varepsilon_c)_{vol}}{\varepsilon_{co}} \tag{8.26}$$

The ratio of the localized peak axial strain $(\varepsilon_c)_{pk}$ to the unconfined peak compressive strain ε_{co} is defined as the peak strain ratio α_{pk} where:

$$\alpha_{pk} = \frac{(\varepsilon_c)_{pk}}{\varepsilon_{co}} \tag{8.27}$$

From analysis of the ε_c-$|\varepsilon_j|$ curve of **Figure 8.10(a)** of a typical concrete section confined by a low stiffness FRP jacket for which $(\nu_j)_{vol} < \mu_{jp} \le \beta_j \mu_u$, and using α_{pk} of Eq. (8.27), the intercept peak axial strain $(\varepsilon_o)_{pk}$ is given by:

$$(\varepsilon_o)_{pk} = (\varepsilon_c)_{pk} + \frac{(\varepsilon_j)_{pk}}{\mu_{jp}} = \alpha_{pk}\varepsilon_{co}\left(\frac{\mu_{jp} - (\nu_j)_{pk}}{\mu_{jp}}\right) \tag{8.28}$$

From analysis of **Figure 8.10(b)** and using α_{vol} of Eq. (8.26), the intercept volumetric axial strain $(\varepsilon_o)_{vol}$ is given by:

$$(\varepsilon_o)_{vol} = (\varepsilon_c)_{vol} + \frac{(\varepsilon_j)_{vol}}{\mu_{dp}} = \alpha_{vol}\varepsilon_{co}\left(\frac{\mu_{jp} - (\nu_j)_{vol}}{\mu_{jp}}\right) \tag{8.29}$$

Assuming that for concrete sections confined by a low stiffness FRP jacket, the peak strain ratio α_{pk} of Eq. (8.27) is approximately equal to one ($\alpha_{pk} \approx 1.0$), and equating Eqs. (8.28) and (8.29), where $(\varepsilon_o)_{pk} \approx (\varepsilon_o)_{vol}$, the volumetric strain ratio α_{vol} of Eq. (8.26) can be approximated by:

$$\alpha_{vol} = \frac{(\varepsilon_c)_{vol}}{\varepsilon_{co}} \cong \left(\frac{\mu_{jp}}{\mu_{jp} - (\nu_j)_{vol}}\right)\left(\frac{\mu_{jp} - \mu_{jo}}{\mu_{jp} + \mu_{jo}(\gamma_{pk} - 1)}\right) \tag{8.30}$$

Substituting the inverse effective diagonal Poisson's ratio model $1/\nu_j'$ of Eq. (8.25) into Eq. (8.5), solving for the inverse diagonal Poisson's ratio $1/\nu_j$ of Eq. (8.2), setting $\nu_j = (\nu_j)_{vol}$, setting $\varepsilon_j = (\varepsilon_j)_{vol} = -\alpha_{vol}\varepsilon_{co}(\nu_j)_{vol}$ using α_{vol} of Eq. (8.30), setting $(\varepsilon_j)_{pk} = -\alpha_{pk}\varepsilon_{co}(\nu_j)_{pk}$ using α_{pk} of Eq. (8.27), and solving for the peak strain ratio α_{pk}, yield:

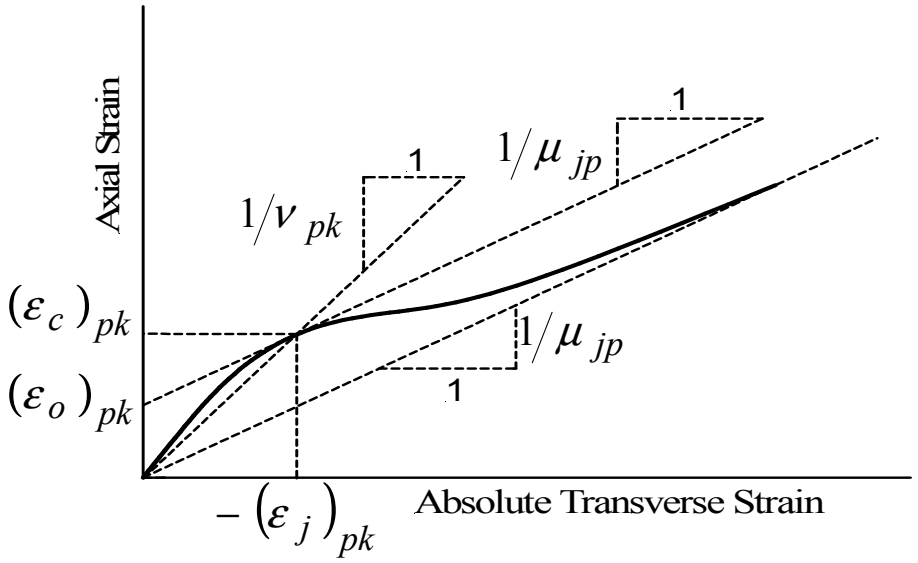

(a)

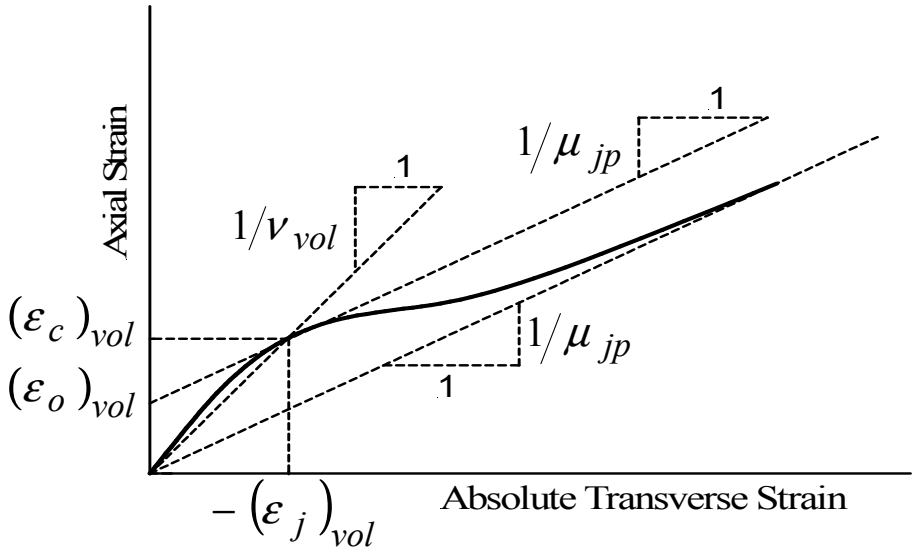

(b)

Figure 8.10 Definition of (a) the peak intercept axial strain and (b) volumetric intercept axial strain of the dilation curve of an FRP-confined concrete section.

$$\alpha_{pk} = \frac{(\varepsilon_c)_{pk}}{\varepsilon_{co}} \cong \alpha_D \alpha_{vol} \tag{8.31}$$

$$\alpha_A = \frac{(\nu_j)_{vol}}{(\nu_j)_{pk}} \;\; ; \;\; \alpha_B = \gamma_{pk} \mu'_{jo} (1 + \alpha_\varepsilon) \left[\mu_{jp} - (\nu_j)_{vol} \right] \tag{8.32}$$

$$\alpha_C = \gamma_j \sqrt{\frac{\alpha_B}{\gamma_j \beta_j \mu_{jp} - \alpha_B (\gamma_j - 1)}} \;\; ; \;\; \alpha_D = \alpha_A \alpha_C \tag{8.33}$$

where the coefficients α_A, α_B, α_B, and α_D are used to simplify the solution for the peak strain ratio α_{pk} of Eqs. (8.27) and (8.31).

Considering that the effective initial diagonal dilation rate μ'_{jo} of Eq. (8.7) and the effective peak Poisson's ratio $(\nu'_j)_{pk}$ of Eq. (8.13), both depend on the diagonal plastic dilation rate μ_{jp} of Eq. (7.25) of the FCC section; the peak dilation parameter γ_{pk} of Eq. (8.22) can be approximated by:

$$\gamma_{pk} = \frac{(\nu'_j)_{pk}}{\mu'_{jo}} = \frac{(\nu_j)_{pk}}{\mu_{jo}} \left(\frac{\mu_{jp} - \mu_{jo}}{\mu_{jp} - (\nu_j)_{pk}} \right) \approx \frac{\mu_u - \mu_{ci}}{\mu_{ci}(2\mu_u - 1)} \tag{8.34}$$

Based on the definition of the asymptotic diagonal plastic dilation rate μ_{rp} of Eq. (7.23) and the unconfined dilation rate $\mu_u = 1.40$ of Eq. (7.23), the above approximation indicates that the effective stiffness $(K_{je})_{sh}$ of Eq. (4.19) or the transverse stiffness $(C_{je})_{sh}$ of Eq. (4.17) of the FRP jacket and the Poisson's ratio of the unconfined concrete core, i.e., μ_{ci} and μ_u, are solely responsible for the dilation behavior of the

FRP-jacketed concrete throughout its compression loading history. In addition, for an unconfined circular concrete section for which $\left(K_{je}\right)_{sh} = 0$, Eq. (7.23) yields $\mu_{rp} = \mu_u = 1.40$, Eq. (8.30) yields $\alpha_{vol} = 1.0$, and Eq. (8.31) yields $\alpha_{pk} = 1.0$ when γ_{pk} of Eq. (8.34) is used. As a result, the proposed dilation relationships introduced herein indicate that volumetric expansion of the unconfined concrete begins to occur, i.e., $\varepsilon_v \geq 0$, as the unconfined concrete approaches its peak unconfined compressive strength f_{co} and strain ε_{co}, which is in agreement with Pantazopoulou and Mills(1995) and Pantazopoulou (1995) for the general concrete model.

The curvature coefficient γ_{pk} of Eq. (8.34) is considered a material constant that is affected by the initial Poisson's ratio or dilation rate of the unconfined concrete material $\mu_{ci} = \nu_{ci}$. This indicates that the dilation behavior (Poisson's ratio ν_c and dilation rate μ_j) of the concrete material is significantly affected by the initial elastic properties of the concrete material, i.e., ν_{ci}.

For normal-strength concrete ν_{ci} is influenced by the water-cement and aggregate-cement ratio (Anon 1964, Imran 1994) of the concrete material and can range between $0.15 \leq \nu_{ci} \leq 0.30$. Based on this range of ν_{ci}, the curvature parameter γ_{pk} of Eq. (8.34) can range between $2.03 \leq .\gamma_{pk} \leq 4.63$, with the higher value corresponding to the lower value of ν_{ci}, and viceversa. For $\nu_{ci} = 0.20$ and $\mu_u = 1.40$, Eq. (8.34) yields $\gamma_{pk} = 3.33$. For convenience a value of $\gamma_{pk} = \pi$ is used herein. For cases in which the

initial Poisson's ratio ν_{ci} of the concrete material is known, the curvature parameter γ_{pk} of Eq. (8.34) can be evaluated and substituted for π in the following relationships.

Using $\gamma_{pk} = \pi$ in Eq. (8.24), indicates that that the diagonal curvature parameter γ_j of Eq. (8.21) can be rewritten as:

$$\gamma_j = \frac{\pi}{\pi - 1} \tag{8.35}$$

The ratio of the diagonal volumetric Poisson's ratio $(\nu_j)_{vol}$ to the plastic dilation rate μ_{jp} is defined as the volumetric dilation parameter γ_{vol} where:

$$\gamma_{vol} = \frac{(\nu_j)_{vol}}{\mu_{jp}} \tag{8.36}$$

Using the peak dilation parameter γ_{pk} of Eq. (8.34) and the volumetric dilation parameter γ_{vol} of Eq. (8.36), the peak Poisson's ratio $(\nu_j)_{pk}$ of Eq. (8.23) and the volumetric strain ratio α_{vol} of Eq. (8.30) can be rewritten as:

$$\alpha_{vol} = \frac{(\varepsilon_c)_{vol}}{\varepsilon_{co}} \approx \left(\frac{1}{1-\gamma_{vol}}\right)\left(\frac{\mu_{jp} - \mu_{jo}}{\mu_{jp} + (\pi - 1)\ \mu_{jo}}\right) \tag{8.37}$$

For an unconfined circular concrete section that above relationships assumes that volumetric expansion of the unconfined concrete core occurs when $(\varepsilon_c)_{vol} = \varepsilon_{co}$ (i.e. $\alpha_{vol} = 1.0$), which is supported by experimental evidence (Imran 1994, Pantazopoulou and Mills 1995). For FRP-confined sections the above relationship predicts that the axial

strain at which volumetric expansion occurs increases, i.e. $\alpha_{vol} > 1.0$, as the confining stiffness of the restraining FRP jacket increases (an increase in confinement). This behavior is supported by experimental evidence of actively confined concrete (Imran 1994, Imran and Pantazopoulou 1996) and FCC sections (Mirmiran 1999, Saenz 2004, Yan 2007).

Substituting the peak dilation parameter γ_{pk} of Eq. (8.34) and the volumetric strain ratio α_{vol} of Eq. (8.37) into the peak strain ratio α_{pk} of Eq. (8.31) yields:

$$\alpha_{pk} = \frac{(\varepsilon_c)_{pk}}{\varepsilon_{co}} = \left(\frac{\gamma_{vol}}{1-\gamma_{vol}}\right)\left[\frac{\mu_{jp}}{(\nu_j')_{pk}}\right] \alpha_C \tag{8.38}$$

The previous relationships for the peak strain ratio α_{pk} of Eq. (8.31) and (8.38) are undefined when $\mu_{jp} \le (\nu_j)_{vol}$ or $\gamma_{vol} > 1.0$. A value of α_{pk} of Eq. (8.38), evaluated at a volumetric dilation parameter γ_{vol} of Eq. (8.36) approximately equal to one $\gamma_{vol} \approx 1.0$ or within the range $0.95 \le \gamma_{vol} \le 0.98$ can be used without incurring a significant loss in accuracy of the nonlinear component of the proposed dilation model of Eq. (8.25).

Solving for the inverse jacket diagonal Poisson's ratio $1/\nu_j$ in (Eq. 8.5) yields:

$$\frac{1}{\nu_j} = -\left(\frac{\varepsilon_c}{\varepsilon_j}\right) = \frac{1}{\nu_j'} + \frac{1}{\mu_{jp}} \tag{8.39}$$

The term $1/\nu_j'$ of Eq. (8.39) is governed by the dilation model of Eq. (8.25), this term represents the degradation that the FCC core experiences as a result of the remolding

process that its internal structure endures, due to unrestrained axial strain-induced damage prior to full activation of the kinematic restraint provided by the confining elastic FRP jacket. The term $1/\mu_{jp}$ of Eq. (8.39) represents the amount of degradation of the concrete's internal structure that is restrained by the confining elastic FRP jacket.

Substituting the inverse effective diagonal Poisson's ratio $1/\nu'_j$ model of Eq. (8.25) into the inverse diagonal Poisson's ratio $1/\nu_j$ of (Eq. 8.39) the whole axial strain ε_c versus jacket diagonal strain ε_j curve (the ε_c-ε_j curve) of the FCC section of **Figures 8.4** and **8.5** can be modeled using the following fractional dilation model:

$$\frac{1}{\nu_j} = -\left(\frac{\varepsilon_c}{\varepsilon_j}\right) = \frac{1}{\mu'_{jo}}\left(\frac{1}{\pi - 1}\right)\left[\frac{1}{\left(\frac{1}{\pi-1}\right) + \left(\frac{\varepsilon_j}{(\varepsilon_j)_{pk}}\right)^{\pi/(\pi-1)}}\right] + \frac{1}{\mu_{jp}} \tag{8.40}$$

Defining the inverse diagonal dilation rate of the FRP-confined concrete $1/\mu_j$ as:

$$\frac{1}{\mu_j} = -\left(\frac{\partial \varepsilon_c}{\partial \varepsilon_j}\right) \tag{8.41}$$

Taking the derivative of the inverse diagonal secant Poisson's ratio $1/\nu_j$ of Eq. (8.40), with respect to the diagonal jacket strain ε_j, yields the inverse diagonal dilation rate $1/\mu_j$, as follows:

$$\left(\frac{1}{\mu_j}\right)=-\left(\frac{\partial\varepsilon_c}{\partial\varepsilon_j}\right)=\frac{1}{\mu_{jo}^{'}}\left(\frac{1}{\pi-1}\right)^2\left\{\frac{1-\left(\dfrac{\varepsilon_j}{(\varepsilon_j)_{pk}}\right)^{\pi/(\pi-1)}}{\left[\left(\dfrac{1}{\pi-1}\right)+\left(\dfrac{\varepsilon_j}{(\varepsilon_j)_{pk}}\right)^{\pi/(\pi-1)}\right]^2}\right\}+\frac{1}{\mu_{jp}} \tag{8.42}$$

Manipulation of Eq. (8.40) and (8.42) yields the diagonal jacket Poisson's ratio ν_j and the diagonal dilation rate μ_j of the FRP-confined concrete section, as follows:

$$\nu_j=-\left(\frac{\varepsilon_j}{\varepsilon_c}\right)=\frac{\mu_{jo}^{'}\mu_{jp}\left[1+(\pi-1)\left(\dfrac{\varepsilon_j}{(\varepsilon_j)_{pk}}\right)^{\pi/(\pi-1)}\right]}{\mu_{jp}+\mu_{jo}^{'}\left[1+(\pi-1)\left(\dfrac{\varepsilon_j}{(\varepsilon_j)_{pk}}\right)^{\pi/(\pi-1)}\right]} \tag{8.43}$$

$$\mu_j=-\left(\frac{\partial\varepsilon_j}{\partial\varepsilon_c}\right)=\frac{\mu_{jp}\mu_{jo}^{'}(\pi-1)\left[1+(\pi-1)\left(\dfrac{\varepsilon_j}{(\varepsilon_j)_{pk}}\right)^{\pi/(\pi-1)}\right]^2}{\mu_{jp}\left[1-\left(\dfrac{\varepsilon_j}{(\varepsilon_j)_{pk}}\right)^{\pi/(\pi-1)}\right]+\mu_{jo}^{'}(\pi-1)\left[1+(\pi-1)\left(\dfrac{\varepsilon_j}{(\varepsilon_j)_{pk}}\right)^{\pi/(\pi-1)}\right]^2} \tag{8.44}$$

The jacket diagonal peak strain $(\varepsilon_j)_{pk}$ can be found using the peak strain ratio α_{pk} of Eqs. (8.38), the peak dilation parameter γ_{pk} of Eq. (8.34)**,** and the diagonal peak Poisson's ratio $(\nu_j)_{pk}$ of Eq. (8.23), as follows:

$$\left(\varepsilon_j\right)_{pk} = -\pi\alpha_{pk}\varepsilon_{co}\left[\frac{\mu_{jo}\mu_{jp}}{\mu_{jp}+\mu_{jo}(\pi-1)}\right] \tag{8.45}$$

The previous dilation model assumes that the dilation of FCC sections is a function of the kinematic restraint provided by the confining elastic FRP jacket and the initial dilation properties (ν_{ci} and μ_{ci}) of the concrete core. (Also, refer to the strain relationships introduced in Chapters 6 and 7.)

In the diagonal dilation rate model μ_j of Eq. (8.44), the maximum diagonal jacket dilation rate $\left(\mu_j\right)_{\max}$ of the FCC section is obtained by taking the derivative of the jacket diagonal dilation rate μ_j of Eq. (8.44) with respect to the diagonal strain ε_j, i.e., $\delta\mu_j/\delta\varepsilon_j$, and setting $\delta\mu_j/\delta\varepsilon_j = 0$ for $\varepsilon_j \neq 0$. As a result, the maximum diagonal dilation rate $\left(\mu_j\right)_{\max}$ can be found when $\varepsilon_j/\left(\varepsilon_j\right)_{pk} = \sqrt{1+\gamma_{pk}}$ is substituted into the diagonal dilation rate μ_j of Eq. (8.44).

The proposed analytical transverse dilation model introduced in this dissertation is unlike the empirical dilation models introduced by other researchers in the past, which include: the empirical fractional dilation model introduced by Mirmiran and Shahawy (1997b); the empirical trilinear model introduced by Carey (2002); the transverse confining stress-dependent empirical models introduced by Fam and Rizkalla (2001), Fujikake et al. (2004), Binici and Mosalam (2007) and Teng et al. (2007); and the empirical volumetric strain-dependent dilation model introduced by Monti and Nistico (2007).

The distinguishing feature for the proposed analytical dilation model is that it uses the concept of diagonal dilation of the FRP-confined concrete core and describes the increase in damage (dilation) in the cross-section in terms of the mechanical and geometric properties of both the concrete core and the confining FRP jacket.

In this dissertation, the confined concrete core is considered to be a restraint sensitive material rather than a pressure sensitive material, as is typically assumed in the analysis of confined concrete. As a result, the proposed dilation model considers that the dilation behavior of the FRP-confined concrete depends only on the lateral kinematic restraint provided by the thin elastic FRP jacket at the surface of the confined concrete core, rather than on the passive confining pressure provided by the restraining FRP jacket that results from transverse dilation of the FRP-confined concrete core.

CHAPTER 9

AN EXTENDED MOHR-COULOMB FAILURE CRITERION FOR CONFINED CONCRETE

One of the goals of this research is to introduce a theoretically sound mechanics-based stress-strain model, applicable to rectangular, square, oval, circular, and elliptical concrete beam-columns confined by bonded FRP jackets (BFCC sections) or cast in place FRP tubes (CFFT sections). This model requires an analytical yield surface or failure envelope that defines the confinement effectiveness of actively or passively confined concrete in a triaxial compression state of stress.

The geometric and mechanical properties of the aforementioned FRP-jacketed sections introduced in Chapter 4, the transverse and diagonal equilibrium relationships introduced in Chapter 5, and the strain compatibility relationships introduced in Chapter 6 are included in the development of a Mohr-Coulomb-based failure criterion for confined concrete, FRP-confined concrete in particular.

Confinement Effectiveness of FRP-Confined Concrete

Currently, there is a lack of stress-strain models that can accurately model the non-linear compressive behavior of rectangular, square, oval, circular, and elliptical concrete

sections confined by bonded FRP jackets (BFCC) or cast in place FRP tubes (CFFT), generally referred to as FRP-confined concrete (FCC) sections in this review.

In the analysis of laterally confined concrete members, it is assumed that the increase in strength due to passive confinement provided by the restraining transverse reinforcement or jacket is governed by an experimentally determined confinement effectiveness of the confining element k_{cc}, given as:

$$k_{cc} = \frac{f_{cc}}{f_{co}} \tag{9.1}$$

where f_{co} and f_{cc} are the peak compressive strength of the unconfined and confined concrete core, respectively. The increase in the compressive strength of the actively or passively confined concrete is typically assumed to be governed by the following Richart et al. (1928) relationship:

$$f_{cc} = f_{co} + k_1(f_r) \tag{9.2}$$

$$k_1 = \frac{f_{cc} - f_{co}}{f_r} \tag{9.3}$$

where f_r is the average transfer confining stress provided by the confining element and k_1 is the average confinement effectiveness coefficient.

The confinement effectiveness k_{cc} of Eq. (9.1) can be rewritten in terms of the average confinement stress ratio $k_r = f_r / f_{co}$ and the confinement effectiveness coefficient k_1 by dividing Eq. (9.2) and Eq. (9.3) by the unconfined compressive strength f_{co} as:

$$k_{cc} = \frac{f_{cc}}{f_{co}} = 1 + k_1 k_r \tag{9.4}$$

$$k_1 = \frac{k_{cc} - 1}{k_r} \tag{9.5}$$

The above relationship correlates well with experimental test data of plain and reinforced concrete sections actively confined by hydrostatic fluid pressure and passively confined concrete sections confined by transverse steel reinforcement, steel jackets, as well as FRP jackets.

For plain concrete sections in a uniform triaxial compression state of stress (i.e., biaxially confined concrete), for which $\sigma_1 > \sigma_2 = \sigma_3 = f_r$, Richart, et al. (1928) found that the value of the confinement effectiveness coefficient k_1 is in the range of $3.50 \le k_1 \le 5.50$. The upper value corresponding to concrete subjected to low confining stresses f_r and the lower value corresponds to highly confined concrete, with an average value of $(k_1)_{avg} = 4.10$. σ_1, , σ_2 and σ_3 are the major, intermediate and minor compressive stresses in the confined concrete, for which shearing stresses vanish and compression is considered positive.

In the analysis of biaxially confined concrete cylinder tests performed by Imran (1994), the range of the confinement effectiveness coefficient k_1 was $2.50 \le k_1 \le 6.50$. The higher values of k_1 occur at low levels of confinement, and the lower values at high levels of confinement, with an average value of $(k_1)_{avg} = 4.10$, which is in agreement with Richart et al. (1928).

In the past, many investigators described the variation of the confinement effectiveness coefficient k_1 of Eq. (9.3), in terms of the applied confining stress f_r, while mostly ignoring the contributions of the applied axial compressive stress f_c at failure of the confined concrete core (i.e., f_{cc}).

The confinement effectiveness coefficient k_1 of the confined concrete is typically plotted versus the applied transverse confining stress f_r, as shown in **Figures 9.1-9.3**, or versus the confinement ratio $k_r = f_r / f_{co}$ as shown in **Figures 9.4-9.6.** This behavior is a result of the inherent decreasing nonlinear relationship between the confinement effectiveness coefficient k_1, with respect to the confining stress f_r or confinement stress ratio k_r, as shown in **Figures 9.1-9.6**. Several researchers in the past have introduced empirical relationships for k_1 in the form of a decreasing power relationship as follows:

$$k_1 = a_1 (f_r)^{-a_2} \tag{9.6}$$

$$k_1 = a_3 (k_r)^{-a_4} \tag{9.7}$$

where a_1, a_2, a_3 , and a_4 are empirical constants that have no physical meaning. Eq. (9.6) was introduced by Saatcioglu (1992) and Eq. (9.7) by Newman and Newman (1971). Both Eqs. (9.6) and (9.7) with $a_2 = a_4 = 0$ are the special case for a constant confinement effectiveness coefficient k_1, a concept first introduced by Richart et al. (1928), an assumption that is not supported by experimental data, as can be observed in **Figures 9.1-9.6**, which reflect the experimental fact that for confined concrete, k_1 decreases with increasing axial and transverse confining stress f_r or stress ratio k_r.

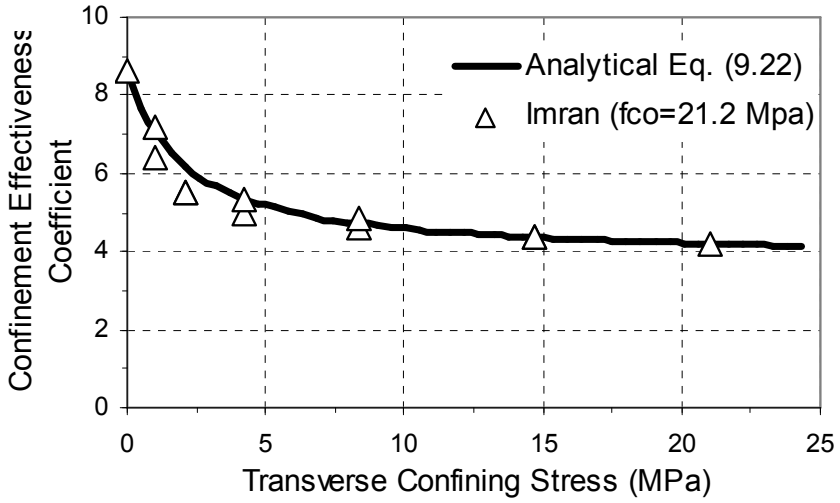

(a)

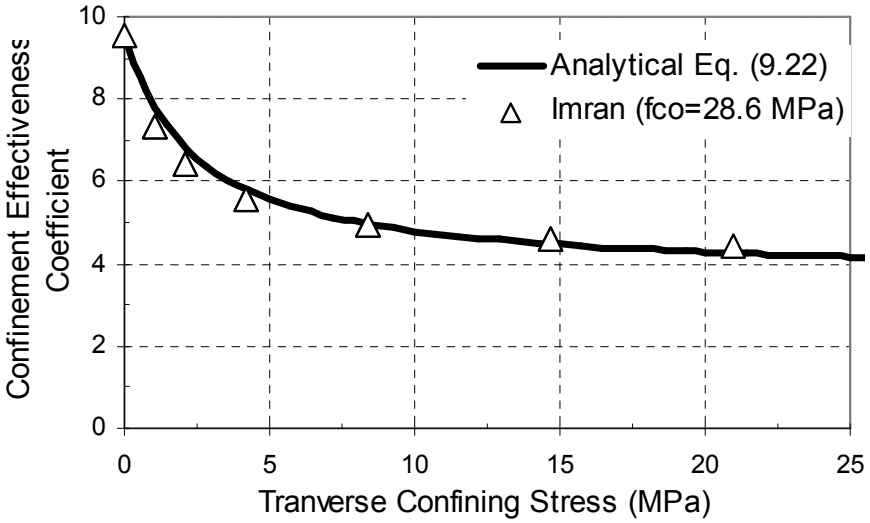

(b)

Figure 9.1 Experimental and analytical confinement effectiveness coefficient versus transverse confining stress of biaxially confined low-strength concrete cylinders performed by Imran (1994).

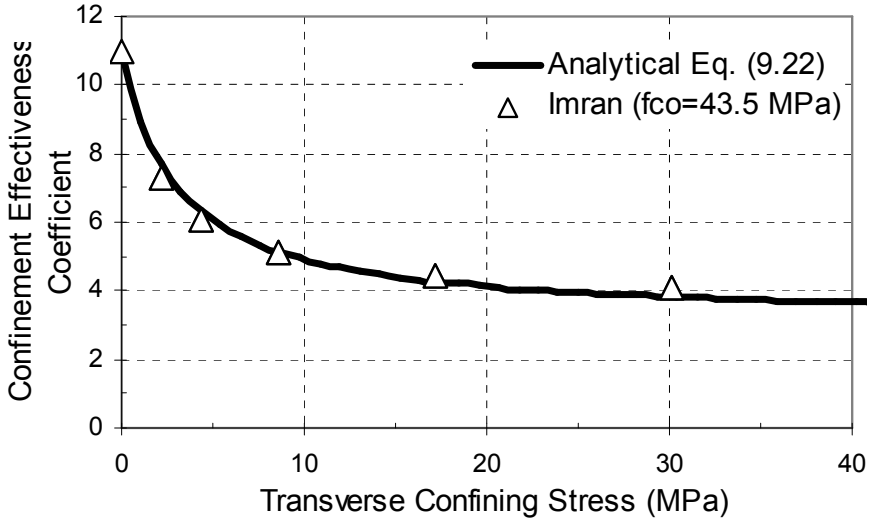

(a)

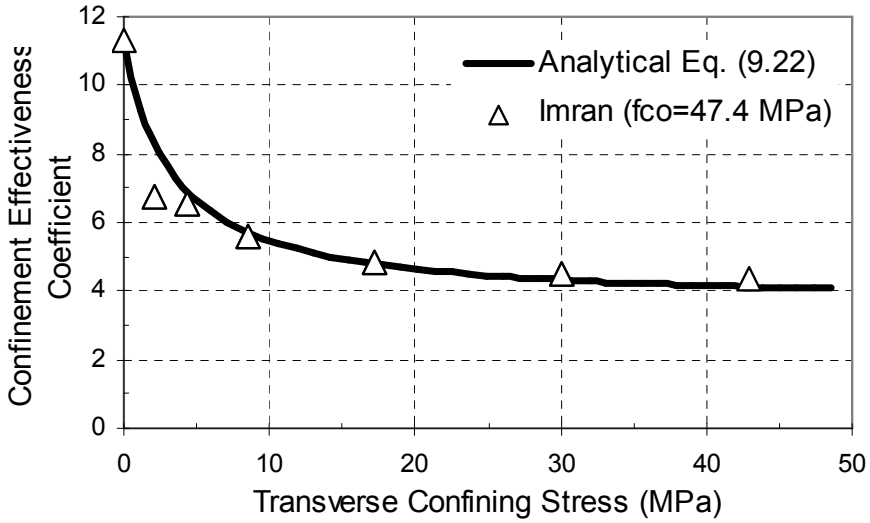

(b)

Figure 9.2 Experimental and analytical confinement effectiveness coefficient versus transverse confining stress of biaxially confined medium-strength concrete cylinders performed by Imran (1994).

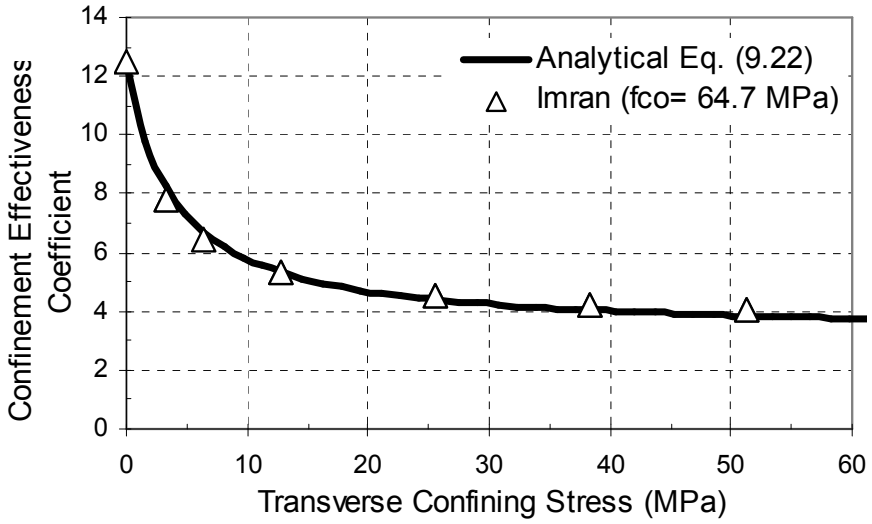

(a)

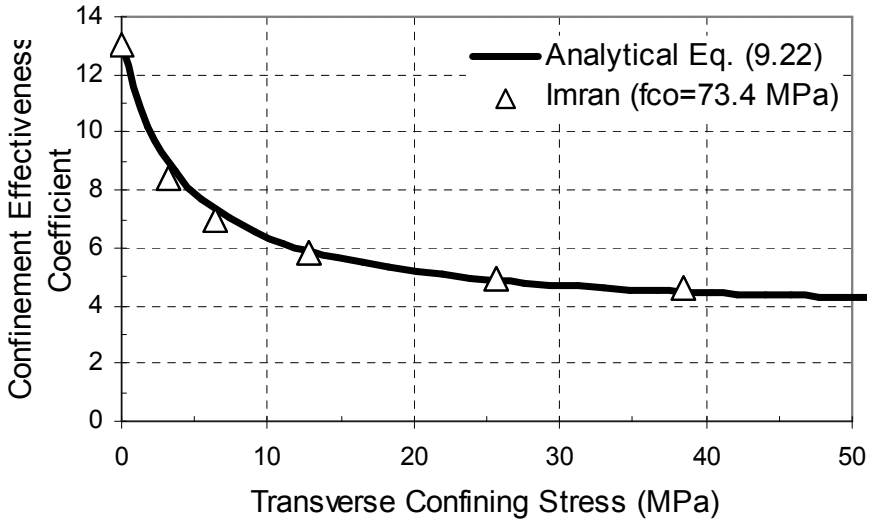

(b)

Figure 9.3 Experimental and analytical confinement effectiveness coefficient versus transverse confining stress of biaxially confined high-strength concrete cylinders performed by Imran (1994).

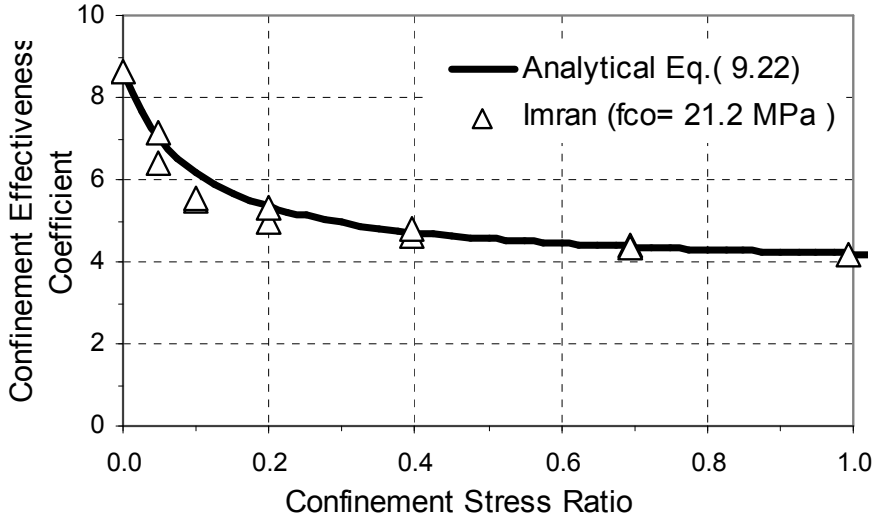

(a)

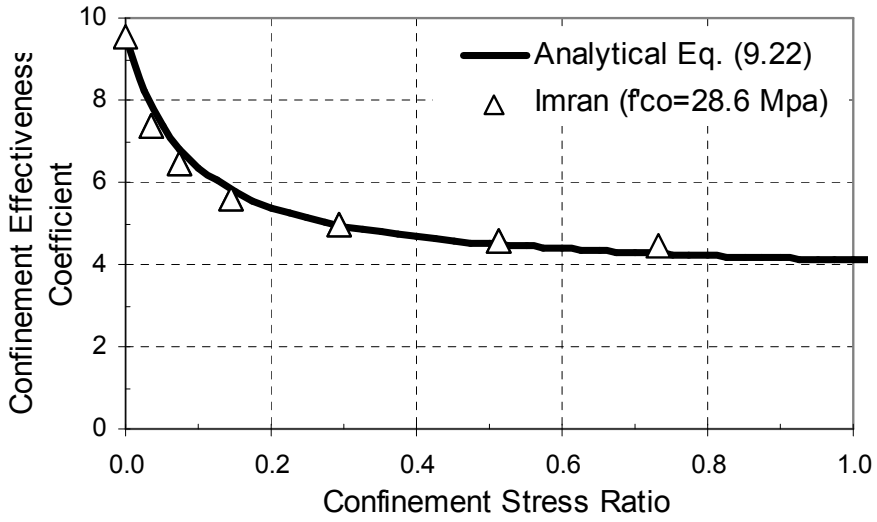

(b)

Figure 9.4 Experimental and analytical confinement effectiveness coefficient versus confinement stress ratio of biaxially confined low-strength concrete cylinders performed by Imran (1994).

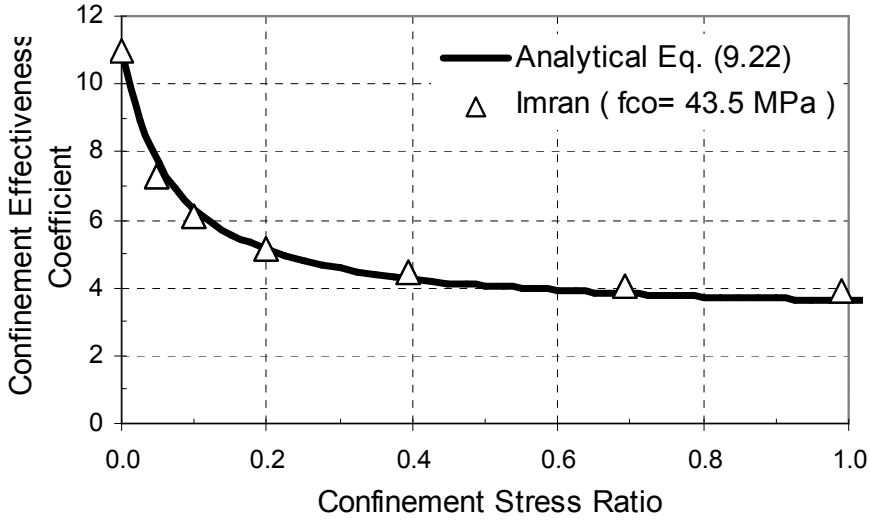

(a)

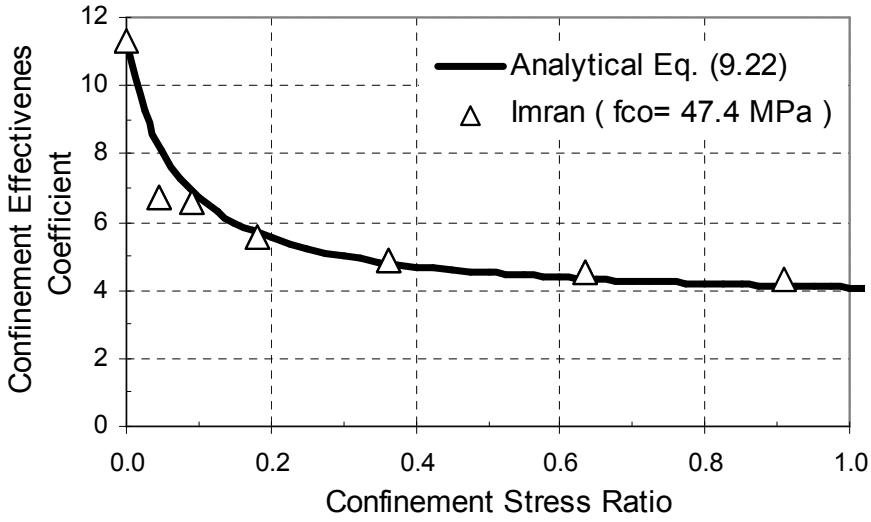

(b)

Figure 9.5 Experimental and analytical confinement effectiveness coefficient versus confinement stress ratio of biaxially confined medium-strength concrete cylinders performed by Imran (1994).

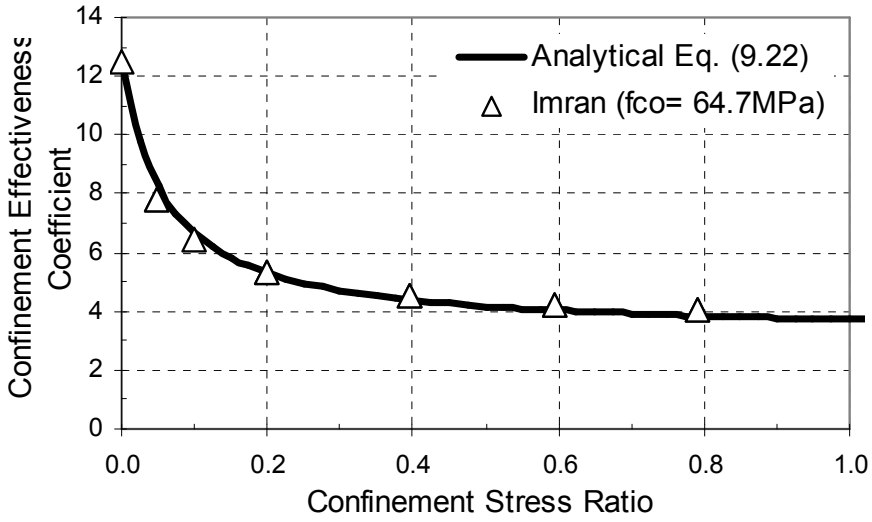

(a)

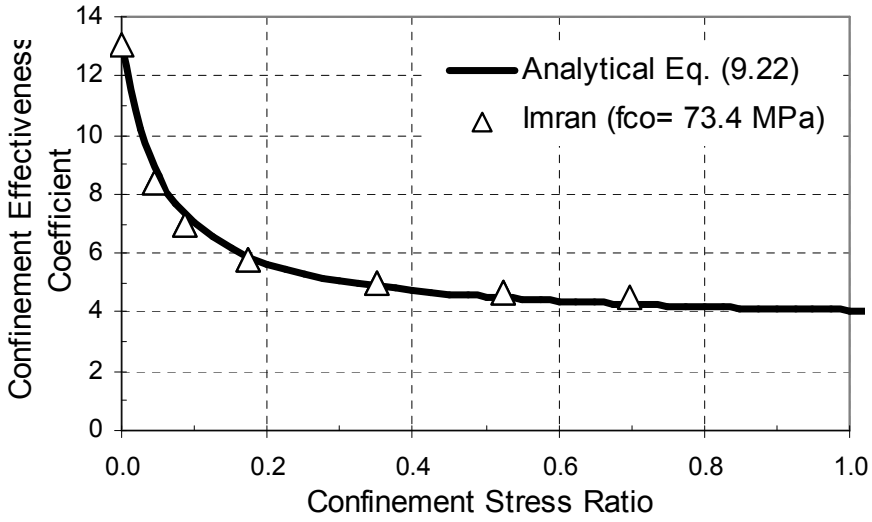

(b)

Figure 9.6 Experimental and analytical confinement effectiveness coefficient versus confining stress of biaxially confined high-strength concrete cylinders performed by Imran (1994).

The data points plotted in **Figures 9.1-9.6** are the experimental data of biaxially confined concrete cylinder tests performed by Imran (1994) for which $\sigma_1 > \sigma_2 = \sigma_3 = f_r$. From these figures, it can be observed that the confinement effectiveness coefficient k_1 decreases nonlinearly as the transverse confining stress f_r or stress ratio k_r increases. This is the basis for utilizing the negative a_2 and a_4 exponents in the empirical relationships of Eqs. (9.6) and (9.7).

The compressive stress at failure of the confined concrete core f_{cc} is plotted versus the transverse confining stress f_r in **Figures 9.7-9.9**. The confinement effectiveness k_{cc} is plotted versus the confinement stress ratio k_r as shown in **Figures 9.10-9.12**. The data points plotted in **Figures 9.7-9.12** are the experimental data points of biaxially confined concrete cylinder tests performed by Imran (1994). From these figures, it can be observed that at high levels of transverse confinement, the compressive stress f_{cc} and the confinement effectiveness k_{cc} appear to be a linear function of the confining stress f_r and the confinement stress ratio k_r, respectively. As a result of the nonlinear relationship between the confinement effectiveness coefficient k_1 and the transverse confining stress f_r of **Figures 9.1-9.3**, or the confinement stress ratio k_r of **Figures 9.4-9.6**, an analytical failure criterion for confined concrete must capture the nonlinear relationships between k_1 and f_r or k_1 and k_r at low confinement levels and also capture the essentially linear relationship between the compressive strength f_{cc} and the transverse confining stress f_r at high confinement levels, as shown in **Figures 9.7-9.9**.

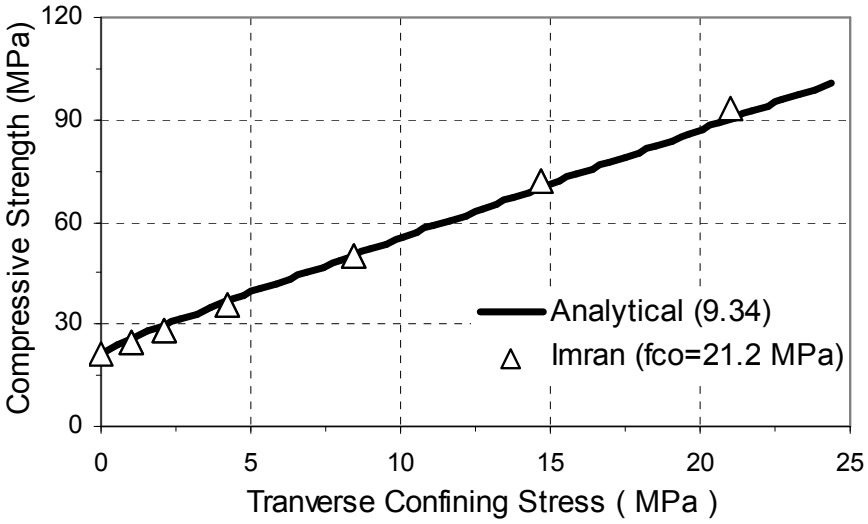

(a)

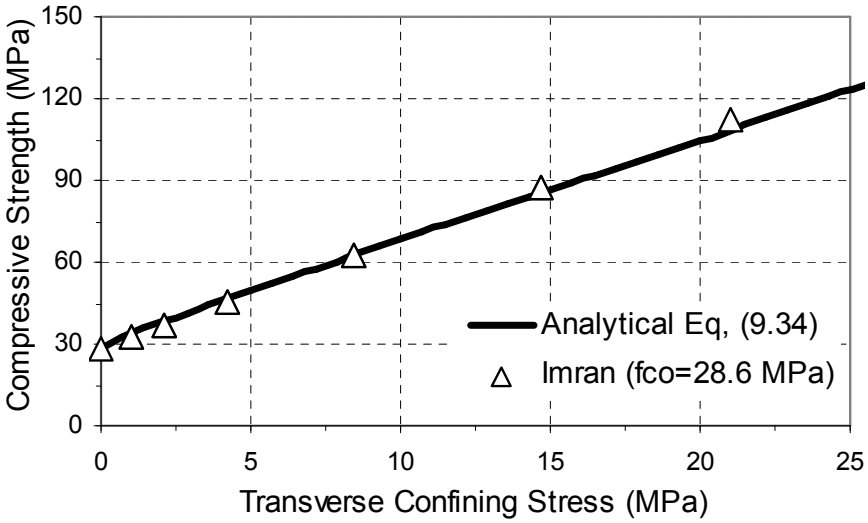

(b)

Figure 9.7 Experimental and analytical compressive strength versus confining stress of biaxially confined low-strength concrete cylinders performed by Imran (1994).

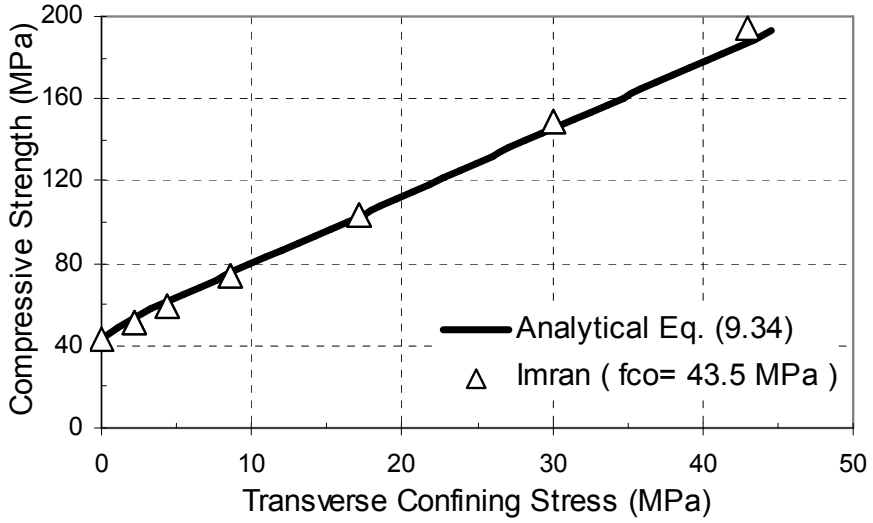

(a)

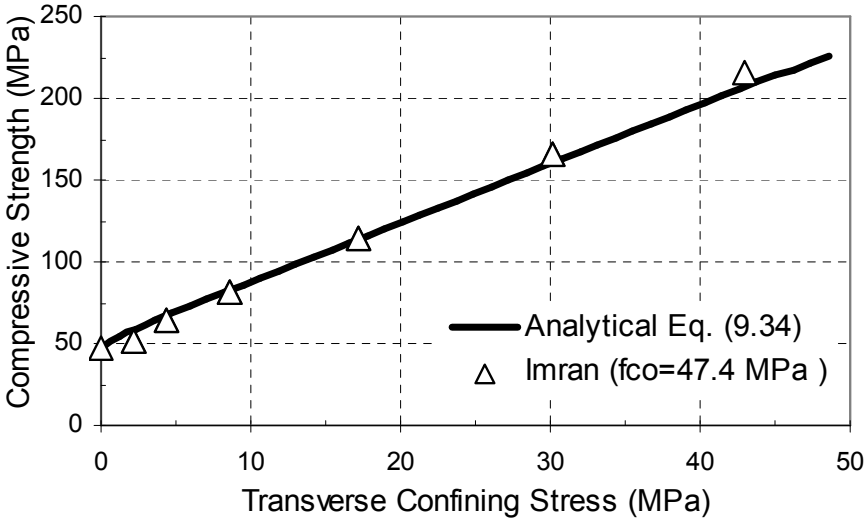

(b)

Figure 9.8 Experimental and analytical compressive strength versus confining stress of biaxially confined medium-strength concrete cylinders performed by Imran (1994).

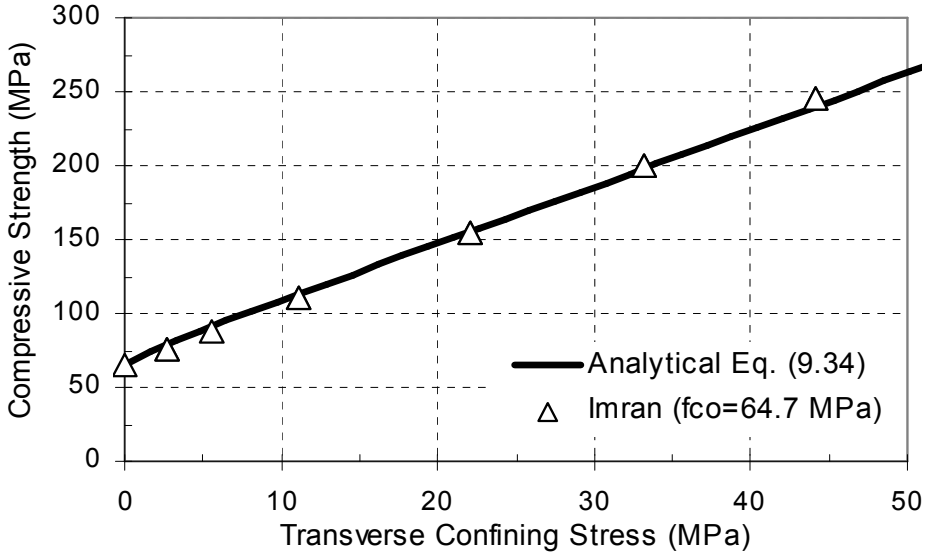

(a)

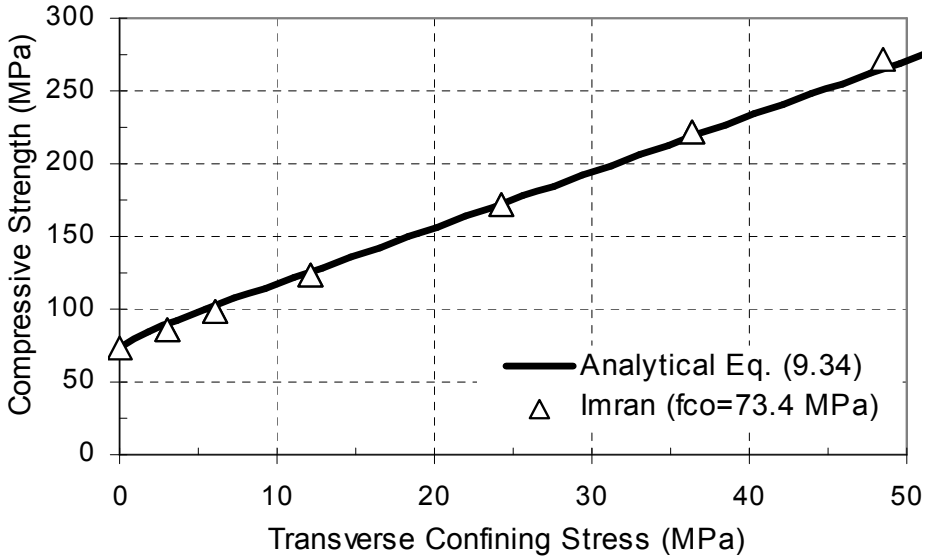

(b)

Figure 9.9 Experimental and analytical compressive strength versus confining stress of biaxially confined high-strength concrete cylinders performed by Imran (1994).

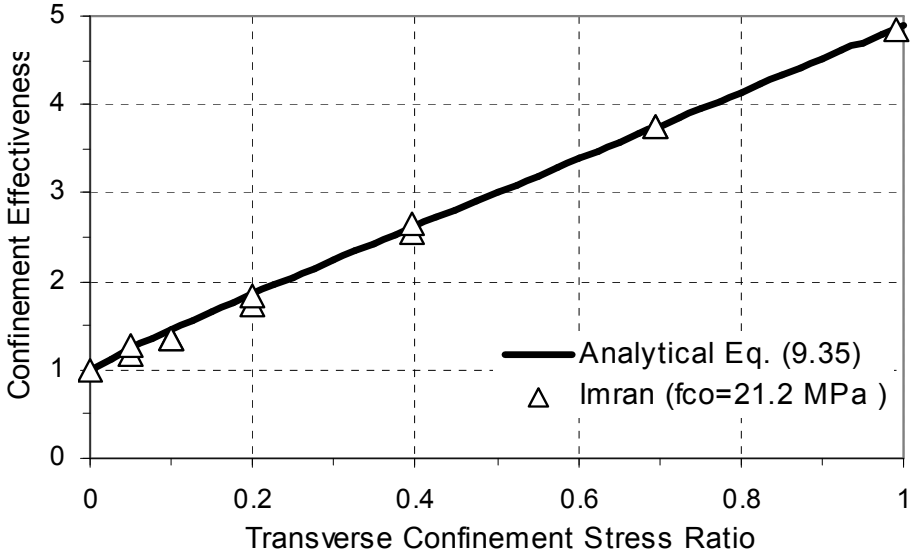

(a)

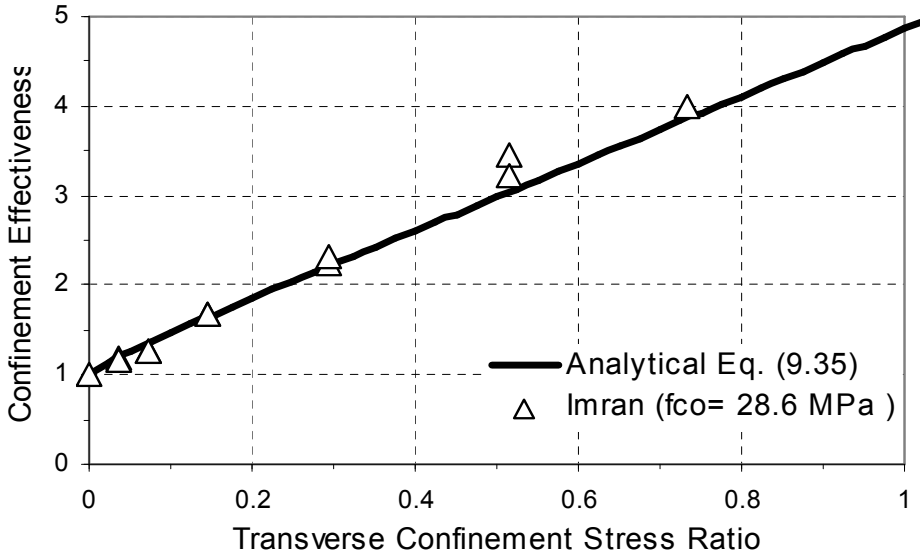

(b)

Figure 9.10 Experimental and analytical confinement effectiveness versus confinement stress ratio of biaxially confined low-strength concrete cylinders performed by Imran (1994).

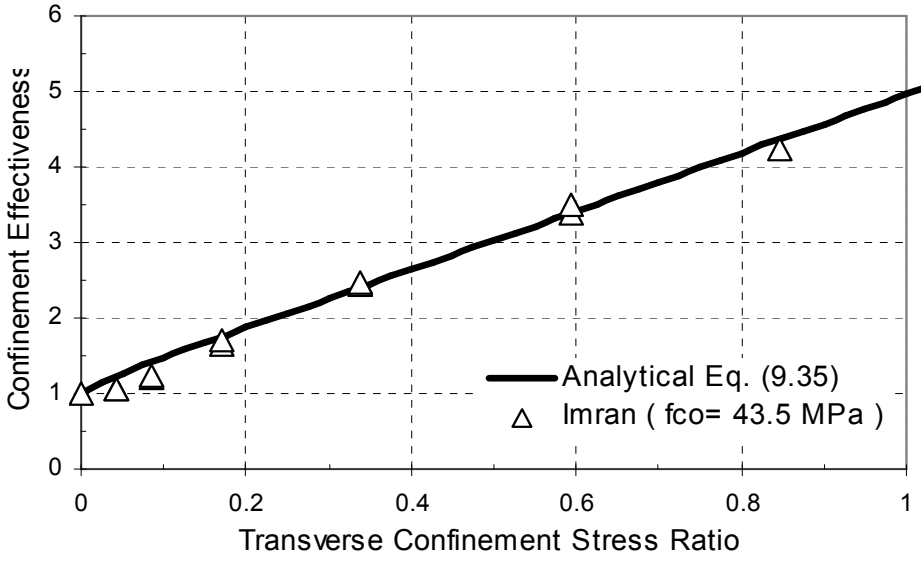

(a)

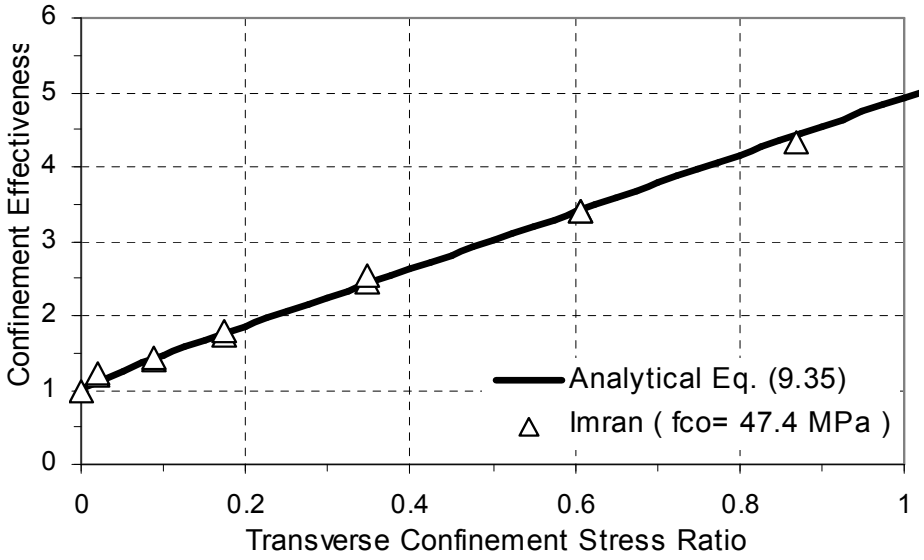

(b)

Figure 9.11 Experimental and analytical confinement effectiveness versus confinement stress ratio of biaxially confined medium-strength concrete cylinders performed by Imran (1994).

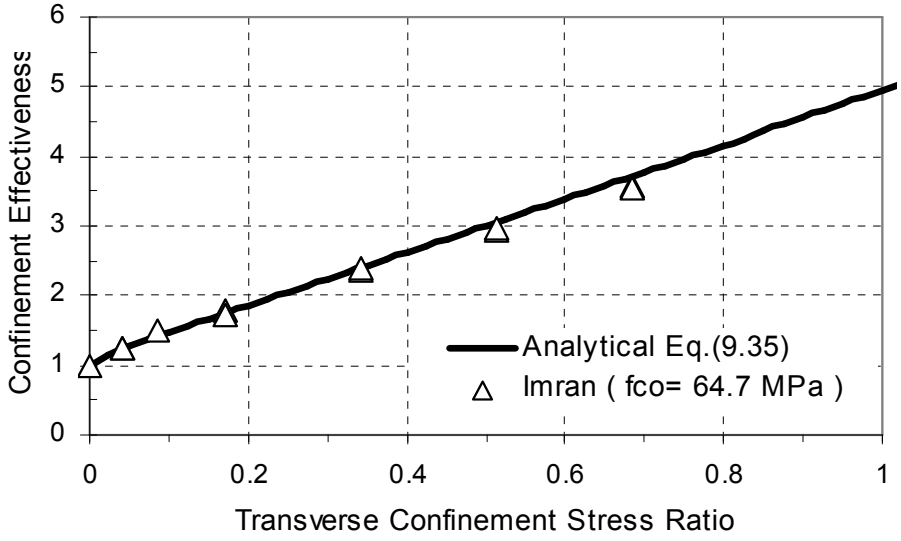

(a)

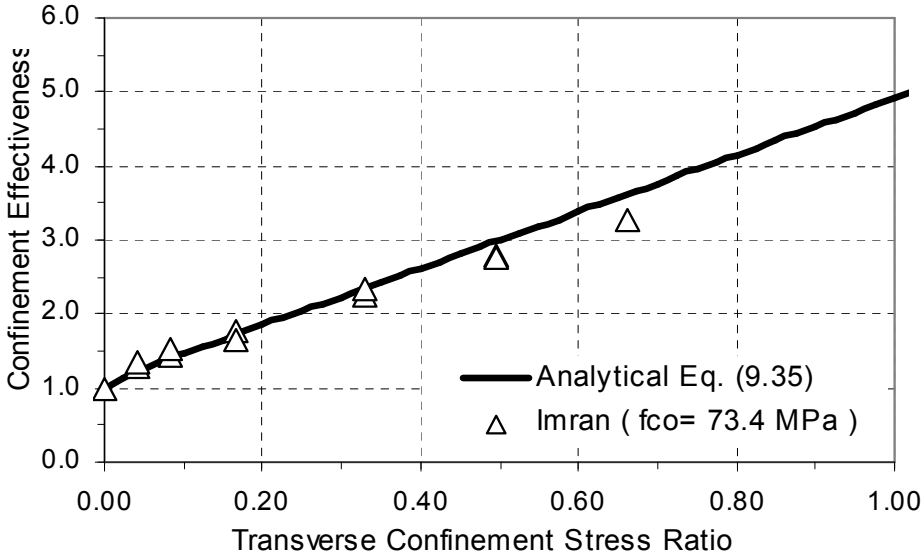

(b)

Figure 9.12 Experimental and analytical confinement effectiveness versus confinement stress ratio of biaxially confined high-strength concrete cylinders performed by Imran (1994).

The analytical failure criterion must also capture the linear relationship between the confinement effectiveness k_{cc} and the confinement stress ratio k_r, as shown in **Figures 9.10-9.12**, and the combined effects of the applied axial stress f_c and applied or resultant transverse confining stress f_r, in order to describe the compressive behavior of uniaxially and biaxially confined concrete.

Pramono and Willam (1989), Menetrey and Willam (1995), Xie et al. (1995) and Fujikake et al. (2004) introduced a series of relationships based on the Leon (Romano 1969) or the Hoek and Brown (1980) parabolic model for the failure envelope of concrete in a triaxial compression state of stress. This includes the cases of uniaxial tension, tension-compression, and tension-tension stress states given by the following three-parameter parabolic relationship:

$$\left(\frac{\sigma_1^{'}-\sigma_3^{'}}{f_{co}}\right)^2 + a_3\left(\frac{\sigma_1^{'}-\sigma_3^{'}}{f_{co}}\right) + a_4\left(\frac{\sigma_1^{'}}{f_{co}}\right) + a_5 = 0 \tag{9.8}$$

where $\sigma_1^{'}$ and $\sigma_3^{'}$ are the minor and major principal stresses in the concrete core with tension considered positive. When compared to the principal compressive stresses σ_1, σ_2, and σ_3, $\sigma_1^{'}=-\sigma_3$, $\sigma_2^{'}=-\sigma_2$, and $\sigma_3^{'}=-\sigma_1$. Also, $\sigma_2^{'}$ is the intermediate principal stress.

Pramono and Willam (1989) found that the ultimate strength envelope of concrete can be described by considering that the constants in the parabolic model of Eq. (9.8) are $a_3=0$, $a_4=\left(k_t{}^2-1\right)\!/k_t$, and $a_5=-1.0$. k_t is defined as the ratio of the uniaxial tensile strength f_{to} to the uniaxial compressive strength f_{co} of the concrete core as:

$$k_t = \left| \frac{f_{to}}{f_{co}} \right| \tag{9.9}$$

Menetrey and Willam (1995) found that the ultimate strength envelope of concrete can be described by considering that the constants in the parabolic model of Eq. (9.8) are $a_3 = 0$, $a_4 = \left(k_t{}^2 - 1\right) \big/ k_t \left[3e/(e+1)\right]$, and $a_5 = -1.0$, where e is the eccentricity of an elliptical function which is further discussed in this chapter. Fujikake et al. (2004) used Pramono and Willam's (1989) model to describe the ultimate strength envelope of FRP-confined concrete with $k_t = 0.08$.

Xie et al. (1995) found that for the case of high-strength concrete, the terms a_3 and a_5 in Eq. (9.8) are empirical constants of the concrete core which were found to depend on the unconfined compressive strength of the concrete core f_{co}, and the term a_4 is an empirical constant that depends on both the unconfined compressive f_{co} and tensile strength f_{to} of the concrete material.

In the modified Leon (Romano 1969) or Hoek and Brown (1980) parabolic failure criterion of Eq. (9.8), the influence of the intermediate principal compressive stress σ_2 is omitted similar to the Tresca and Mohr-Coulomb condition of maximum shear. In addition, the three-parameter parabolic formulation for the ultimate strength envelope of Eq. (9.8) combines the two-parameter Mohr-Coulomb friction law and the one-parameter tension cut-off condition of Rankine. Although the parabolic type ultimate strength envelope of Eq. (9.8) can accurately describe the cases of uniaxial tension, tension-compression, tension-tension stress, and triaxial compression stress states, a direct

solution for the minor principal stress $\sigma_3^{'}$ cannot be obtained in terms of the major principal stress $\sigma_1^{'}$ without iteration.

In this research a noniterative ultimate strength envelope of the concrete material is obtained by treating the restraint sensitive concrete material as a frictional-cohesive material whose ultimate strength criterion is governed by a Mohr-Coulomb type failure envelope for frictional-cohesive materials subjected to uniform biaxial confinement, i.e., $\sigma_3 = \sigma_2$ or $\sigma_1^{'} = \sigma_2^{'}$. For confined concrete, the kinematic restraint is provided by either active hydrostatic compressive stresses or passive confining stresses provided by a transverse confining element, such as FRP jackets.

In what follows, a series of mathematical relationships are introduced to describe the variation of the confinement effectiveness coefficient k_1 and the confinement effectiveness k_{cc}, with respect to the applied axial stress f_c and the applied transverse confining stress f_r, while minimizing or eliminating the number of empirical coefficients such as those introduced in Eqs. (9.1)-(9.9).

Confinement Effectiveness of Confined Concrete: A Soil Mechanics Approach

The structure of the concrete material within the confined concrete core can be considered a heterogeneous material consisting of granular aggregates (i.e., crushed stone aggregate or gravel and sand), a binding material (i.e., cement paste), and pores. The concrete material in a uniaxial tension, tension-compression, and tension-tension, biaxial or triaxial compression state of stress behaves as a cohesive-frictional material and

exhibits similar compressive and dilation behavior as that exhibited by granular cemented soils, i.e., soils that exhibit a uniaxial tensile capacity.

The confined concrete core is a restraint sensitive material that is composed of granular materials (i.e., angular crushed rocks, well-graded gravels, and dense sands) plus a binding agent (i.e., cement paste). As the internal structure of the confined concrete core is subjected to very large compressive strains, it becomes damaged as a result of internal crack growth, aggregate crushing and shifting, void compaction, and nucleation.

As damage in the internal structure of the concrete core increases, it undergoes a remolding process in which its internal structure essentially degrades to that of its constituent materials. This is a result of the degradation of the adhesion provided by the binding cement paste from internal crack growth, void compaction, and nucleation (i.e., as damage progresses).

At high levels of axial and transverse deformations, the mechanical response of the remolded concrete core depends on the resistance provided by a combination of aggregate sliding, shifting, rolling, and crushing that develops during the axial and transverse deformation of the concrete core.

The concrete material is treated as an isotropic, homogenous Mohr-Coulomb frictional-cohesive granular material with some interparticle attraction or cohesion that is provided by the binding cement, whose resistance to deformation is contingent upon the shear strength of the material τ_c. This shear strength depends on the average interparticle attraction or apparent cohesion c_c of the concrete core and the resistance to interparticle slip called the coefficient of friction of the concrete core υ_c, that is given by:

$$\tau_c = c_c + \sigma_n \upsilon_c \tag{9.10}$$

$$\upsilon_c = \frac{\partial \tau_c}{\partial \sigma_n} = \tan \phi_c \tag{9.11}$$

where σ_n is the normal stress on the failure shear plane, as shown in **Figures 9.13** and **9.14**; υ_c is the coefficient of internal friction of the concrete core; ϕ_c is the average angle of internal friction of the concrete core. The above relationships describe a maximum shear strength failure envelope of the concrete material as shown in **Figures 9.13** and **9.14.**

For a Mohr-Coulomb-based maximum shear strength envelope to properly model the behavior of concrete in a triaxial compression state of stress, it must also include the cases of uniaxial tension, tension-compression, and tension-tension stress states and shall satisfy the following conditions:

1. It should represent a close fit to the experimental data
2. It should have simple identification of the model parameters
3. It should pass through the point of uniaxial tension, i.e., when $\sigma_3 = -|f_{to}|$, $\sigma_1 = 0$
4. It should pass through the point of uniaxial compression, i.e., when $\sigma_3 = 0$, $\sigma_1 = f_{co}$
5. It should fit the failure envelope of concrete in a triaxial compression state of stress, as shown in **Figure 9.15** in which $\sigma_3 \geq 0$, $\sigma_1 \geq f_{co}$.

This is accomplished herein by considering that the concrete material behaves similar to similar compressive and dilation behavior as that exhibited by granular cemented soils.

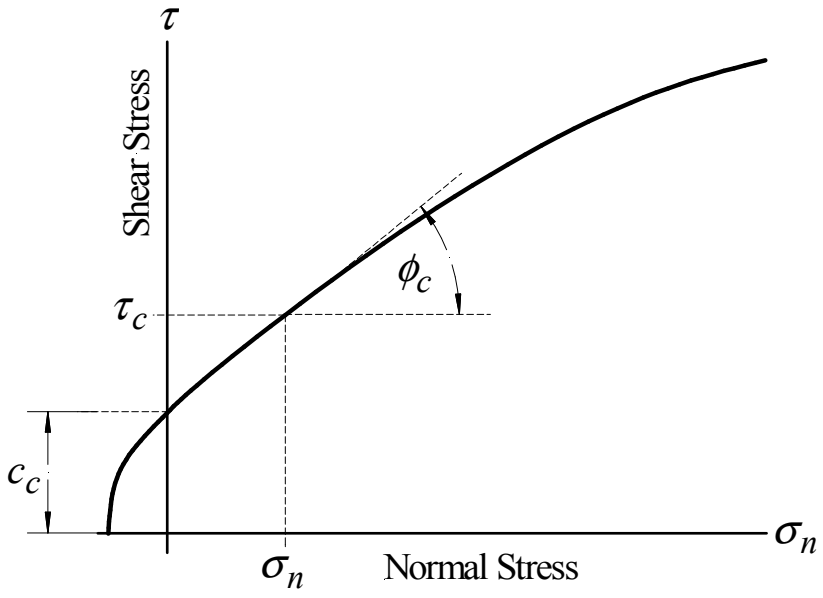

Figure 9.13 Plot of typical Mohr-Coulomb failure envelope of a frictional cohesive material.

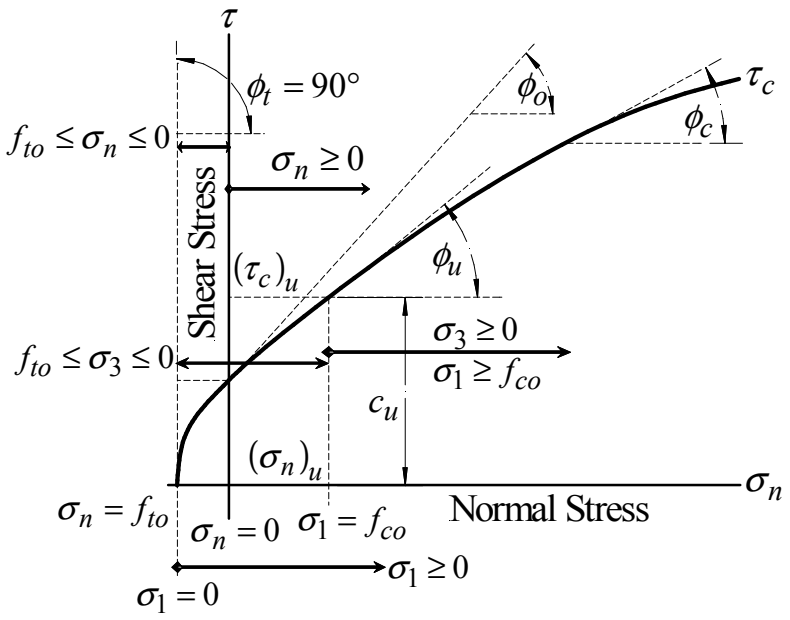

(a)

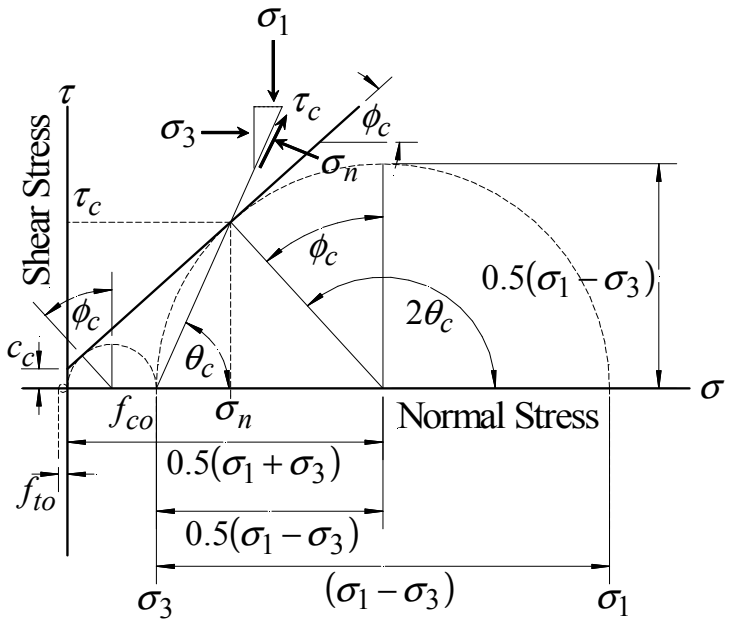

(b)

Figure 9.14 Plot of (a) typical Mohr-Coulomb failure envelope of a frictional cohesive material showing pertinent terms, (b) Mohr's circle and definition of σ_1, σ_3 and the angle of inclination of the failure shear plane θ_c.

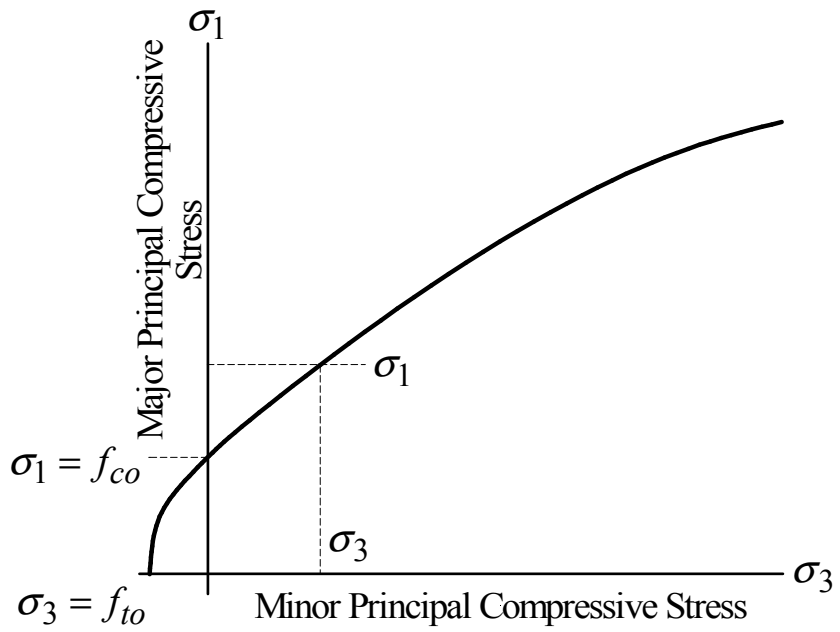

Figure 9.15 Plot of typical failure envelope of a frictional cohesive material in the major principal and minor principal compressive stress region.

A concrete prism subjected to a triaxial compression state of stress for which $\sigma_1 > \sigma_2 \geq \sigma_3$, uniaxial compression tests for which $\sigma_1 \geq 0$ and $\sigma_2 = \sigma_3 = 0$, uniaxial tension tests for which $\sigma_1 = \sigma_2 = 0$, and $\sigma_3 \leq 0$, and uniform biaxial confinement for which $\sigma_2 = \sigma_3 = f_r$ is considered herein.

Referring to the Mohr's circle of **Figure 9.14(b),** the normal stress σ_n and the shear stress τ_c on the failure shear plane are given in terms of the minor σ_3 and major σ_1 principal compressive stresses in the concrete core as follows:

$$\tau_c = \frac{\sigma_1 - \sigma_3}{2}\sin(2\theta_c) \tag{9.12}$$

$$\sigma_n = \frac{\sigma_1 + \sigma_3}{2} + \frac{\sigma_1 - \sigma_3}{2}\cos(2\theta_c) \tag{9.13}$$

$$\theta_c = 45° + \frac{\phi_c}{2} \tag{9.14}$$

where θ_c and ϕ_c are the average angle of inclination of the failure shear plane and the angle of internal friction of the confined concrete, respectively, as shown in **Figure 9.14(b)**. In this research, a relationship is sought for concrete subjected to a triaxial compression state of stress in which the major principal compressive stress σ_1 is determined in terms of the minor principal compressive stress σ_3. This is accomplished using the following trigonometric relationships:

$$\tan^2(\theta_c) = \tan^2\left(45° + \frac{\phi_c}{2}\right) = \frac{1+\sin\phi_c}{1-\sin\phi_c} \tag{9.15}$$

$$\tan(\theta_c) = \tan\left(45^\circ + \frac{\phi_c}{2}\right) = \frac{1+\sin\phi_c}{\cos\phi_c} = \frac{\cos\phi_c}{1-\sin\phi_c} \tag{9.16}$$

$$\tan^2(\vartheta_c) = \tan^2\left(45^\circ - \frac{\phi_c}{2}\right) = \cot^2(\theta_c) = \frac{1-\sin\phi_c}{1+\sin\phi_c} \tag{9.17}$$

$$\tan(\vartheta_c) = \tan\left(45^\circ - \frac{\phi_c}{2}\right) = \cot(\theta_c) = \frac{\cos\phi_c}{1+\sin\phi_c} = \frac{1-\sin\phi_c}{\cos\phi_c} \tag{9.18}$$

Thus setting the minor $\sigma_3 = f_r$ and major $\sigma_1 = f_{cc}$ compressive stresses in Eqs. (9.10)-(9.13), using the previous trigonometric relationships and solving for σ_1 yields:

$$\begin{aligned}\sigma_1 &= 2c_c\left(\frac{\cos\phi_c}{1-\sin\phi_c}\right) + \sigma_3\left(\frac{1+\sin\phi_c}{1-\sin\phi_c}\right) \\ &= 2c_c\left(\frac{\cos\phi_c}{1-\sin\phi_c}\right) + f_r\left(\frac{1+\sin\phi_c}{1-\sin\phi_c}\right) \\ &= 2c_c\tan(\theta_c) + f_r\tan^2(\theta_c)\end{aligned} \tag{9.19}$$

Setting the $\sigma_1 = f_{cc}$ and $\sigma_3 = f_r$, the above relationships can be rewritten as a generalized two-parameter modified Mohr-Coulomb (MMC) failure envelope for confined as follows:

$$\gamma_f\sigma_1 - \beta_f\sigma_3 - 1 = 0 \tag{9.20}$$

where γ_f and β_f are material parameters that measure the cohesive and frictional strength of the concrete subjected to a biaxial or triaxial compression state of stress. The Richart et al. (1928) failure criterion of Eq. (9.2) is the case for which $\gamma_f = 1/f_{co}$ and $k_1 = \beta_f/\gamma_f = 4.10$. The material parameters γ_f and β_f of the concrete material are

determined as follows. The apparent cohesion of the confined concrete core c_c of Eqs. (9.10) and (9.19) can be determined from the uniaxial unconfined compression test. Setting $\sigma_1 = f_{cc} = f_{co}$ and $\sigma_3 = f_r = 0$ and substituting $f_{cc} = f_{co}$ and $f_r = 0$ into Eq. (9.19) yield:

$$c_c = \frac{1}{2} f_{co} \left(\frac{1 - \sin \phi_c}{\cos \phi_c} \right) = \frac{1}{2} f_{co} \cot(\theta_c) \tag{9.21}$$

Substituting Eq. (9.21) into Eq. (9.19) yields a relationship for the peak compressive strength f_{cc} similar to the Richart et al. (1928) relationship of Eq. (9.2) or a confinement effectiveness k_{cc} relationship similar to that of Eq. (9.4). Utilizing Eqs. (9.2), (9.19), and (9.21), the confinement effectiveness coefficient k_1 of Eqs. (9.2) and (9.6) can be rewritten in terms of the angle of internal friction of the concrete core ϕ_c or the angle of inclination of the failure shear plane θ_c and the coefficient of friction υ_c of the concrete core as follows:

$$\begin{aligned} k_1 &= \frac{1 + \sin \phi_c}{1 - \sin \phi_c} \\ &= \tan^2(\theta_c) \\ &= \left(\frac{1 + \sin \phi_c}{\cos \phi_c} \right)^2 \\ &= \left(\frac{\cos \phi_c}{1 - \sin \phi_c} \right)^2 \\ &= \left[\sqrt{1 + (\upsilon_c)^2} + \upsilon_c \right]^2 \end{aligned} \tag{9.22}$$

The previous confinement effectiveness coefficient k_1 also applies to concrete in a triaxial compression state of stress for which $\sigma_1 > \sigma_2 > \sigma_3$, which corresponds to the case of rectangular, oval, and elliptical FCC sections, since the MMC criterion introduced herein ignores the effects of the intermediate compressive stress σ_2.

The angle of internal friction of the confined concrete core ϕ_c can be determined in terms of the confinement effectiveness coefficient k_1 of Eq. (9.22) as follows:

$$\phi_c = \sin^{-1}\left(\frac{k_1 - 1}{k_1 + 1}\right) \tag{9.23}$$

In the analysis of concrete in a biaxial or triaxial compression state of stress, the combined effects of the applied axial stress f_c and transverse confining stress f_r are typically ignored in the development of maximum or ultimate strength criterion for confined concrete. In order to capture these combined effects, a series of analytical relationships are introduced using a MMC failure envelope, that combines the two-parameter Mohr-Coulomb friction law of limited shear stress and the one-parameter Rankine tension cut-off condition as follows.

As shown in Eqs. (9.10) and (9.11), shear failure of the confined concrete core τ_c occurs when the normal stress in concrete σ_n and the angle of internal friction ϕ_c reach a critical combination. Based on the definition of the normal stress on the failure shear plane σ_n of Eq. (9.13), failure of the concrete core in a triaxial compression state of stress occurs due to shear failure of the concrete, i.e., when $\tau = \tau_c$ or when equality of Eqs. (9.2) and (9.12) occurs. The occurrence of higher values of k_1 at low levels of

confinement, as evidenced in the Richart et al. (1928) and Imran (1994) investigations, can be attributed to the following.

The uniaxial compression case for which $\sigma_3 = 0$ and $\sigma_1 = f_{co}$ and the uniaxial tension case for which $\sigma_3 = -f_t$ and $\sigma_1 = 0$ are considered herein. For these cases Eqs. (9.10)-(9.19) predict that the uniaxial shear strength τ_u, the apparent uniaxial cohesion c_u, the uniaxial coefficient of internal friction υ_u, the uniaxial angle of internal friction ϕ_u, and the uniaxial confinement effectiveness coefficient $(k_1)_u$ are given by:

$$\tau_u = c_u + (\sigma_n)_u \upsilon_u \tag{9.24}$$

$$c_u = -\frac{f_{to}}{2\sqrt{k_t}} = \frac{f_{co}}{2}\sqrt{k_t} \tag{9.25}$$

$$(\sigma_n)_u = \frac{1}{2} f_{co}[1 + \cos(2\theta_u)] \tag{9.26}$$

$$\upsilon_u = \frac{\partial \tau_u}{\partial \sigma_n} = \tan\phi_u \tag{9.27}$$

$$\phi_u = 90° - 2\tan^{-1}\sqrt{k_t} \quad ; \quad \theta_u = 45° + \frac{\phi_u}{2} \tag{9.28}$$

$$(k_1)_u = \frac{1 + \sin\phi_u}{1 - \sin\phi_u} = \frac{1}{k_t} \tag{9.29}$$

$$f_{to} \cong -0.32(f_{co})^{2/3} \tag{9.30}$$

where the uniaxial tensile strength of the concrete f_{to} can be determined by uniaxial tensile tests or it can be estimated using Eq. (9.30) with f_{co} in MPa units (Raphael 1984) with compression being positive.

For an unconfined concrete compressive strength ranging between $17 \text{ MPa} \le f_{co} \le 55 \text{ MPa}$, using f_{to} of Eq. (9.30) and k_t of Eq. (9.9), k_t ranges between $0.08 \le k_t \le 0.12$. Also, for this range of concrete compressive strengths $0.15 \le c_u / f_{co} \le 0.18$, $51.1° \le \phi_u \le 57.7°$, $1.24 \le \upsilon_u \le 1.58$ and $8.06 \le (k_1)_u \le 11.90$. This indicates that at low levels of confinement, as $k_r \to 0$, the confined concrete core behaves similar to unconfined concrete, and the confinement effectiveness coefficient k_1 approaches the value of the uniaxial confinement effectiveness coefficient $(k_1)_u$ of Eq. (9.29), [i.e., as $k_r \to 0$, $k_1 \to (k_1)_u = 1/k_t$].

As previously indicated and as shown in **Figures 9.1-9.6**, the assumption of a constant confinement effectiveness coefficient k_1 at all levels of confinement is not supported by the experimental data. The experimental data of triaxial compression tests by Richart et al. (1928) and Imran (1994) suggest that at low levels of confinement k_1 approaches the value of the uniaxial confinement effectiveness coefficient $(k_1)_u$ of Eq. (9.29). At high levels of confinement k_1 approaches an asymptotic value, which will be referred to herein as the basic confinement effectiveness coefficient $(k_1)_b$ of the dry concrete material. This indicates that for concrete in a uniaxial or triaxial compression state of stress, k_1 is bounded by the following range $(k_1)_b \ge k_1 \ge (k_1)_u$.

The nonlinearity of the confinement effectiveness coefficient k_1, as can be observed in **Figures 9.1-9.6,** can be attributed to the inherent nonlinearity of the Mohr-Coulomb failure envelope for granular frictional-cohesive materials. The curvature of this failure envelope can be attributed to remolding of the concrete's internal structure as axial strain-

induced damage progresses. As a result, the shear strength τ_c of the confined concrete core is a nonlinear function of the normal stress σ_n of Eq. (9.13) (or of the major σ_1 and minor σ_3 principal compressive stresses), where the shear strength τ_c of Eqs. (9.10) and (9.12) can be rewritten as:

$$\tau_c = c_c + \sigma_n \tan\phi_c = \frac{\sigma_1 - \sigma_3}{2}\sin(2\theta_c) \tag{9.31}$$

In Eq. (9.31), the apparent cohesion c_c (i.e., apparent intercept shear stress) of the concrete material is given by the unconfined cohesion, c_u of Eq. (9.25). Using σ_n of Eqs. (9.13), c_u of Eq. (9.25), τ_c of Eq. (9.31) and solving for both the major σ_1 and minor σ_3 principal compressive stresses in terms of the normal stress σ_n yield:

$$\sigma_1 = 2c_u\sqrt{k_1} + \sigma_3 k_1 \tag{9.32}$$

$$\sigma_3 = \frac{2\sigma_n - f_{co}\sqrt{k_t k_1}(1+\cos\theta_c)}{(k_1+1)+(k_1-1)\cos(2\theta_c)} \tag{9.33}$$

Setting the major principal compressive stress σ_1 in the confined concrete core equal to the ultimate strength of the confined concrete core f_{cc} (i.e., $\sigma_1 = f_{cc}$), the confined concrete strength f_{cc} of Eq. (9.2) can be found in terms of minor principal compressive stress σ_3 by substituting the uniaxial cohesion intercept c_u of Eq. (9.25) into Eq. (9.32) and setting $\sigma_1 = f_{cc}$ in Eq. (9.32), which yields:

$$f_{cc} = f_{co}\sqrt{k_t k_1} + \sigma_3 k_1 \tag{9.34}$$

The previous analytical compressive strength of biaxially confined concrete is plotted as a solid curved versus the confining stress in **Figures 9.7-9.9** of actively confined concrete cylinders performed by Imran (1994). From these figures it can be observed that the analytical compressive strength of Eq. (9.34) can accurately predict the compressive strength f_{cc} of biaxially confined concrete, for which $\sigma_1 > \sigma_2 = \sigma_3 = f_r$, of varying uniaxial compressive strengths f_{co} at all confinement levels.

Substituting the confined concrete strength f_{cc} of Eq. (9.34) into the confinement effectiveness of the confined concrete core k_{cc} of Eq. (9.4) yields:

$$k_{cc} = \frac{f_{cc}}{f_{co}} = \sqrt{k_t k_1} + k_3 k_1 \tag{9.35}$$

$$k_3 = \frac{\sigma_3}{f_{co}} \tag{9.36}$$

where k_3 is the minor principal compressive stress ratio. The previous relationship indicates that confinement effectiveness k_{cc} can be found in terms of the uniaxial tensile-uniaxial compressive strength ratio k_t of Eq. (9.9), with f_{to} estimated using Eq. (9.30) and k_1 of Eq. (9.22).

The confinement effectiveness k_{cc} of biaxially confined concrete of Eq. (9.35) is plotted versus the confining stress in **Figures 9.10-9.12** of actively confined concrete cylinders performed by Imran (1994). From these figures it can be observed that the analytical confinement effectiveness k_{cc} of Eq. (9.35) can accurately predict the

confinement effectiveness of biaxially confined concrete of various uniaxial compressive strengths f_{co}.

The confinement effectiveness k_{cc} of Eq. (9.35) is somewhat similar to that introduced in Eq. (9.4); k_{cc} of Eq. (9.35) yields k_{cc} of Eq. (9.4) for unconfined concrete only, i.e., only when $k_3 = \sigma_3 = 0$ and when $k_1 = (k_1)_u$. As a result, it can be stated that for confined concrete in a triaxial compression state of stress, for which $\sigma_1 > \sigma_2 = \sigma_3 = f_r$, the confinement effectiveness k_{cc} of Eq. (9.35) can be considered to be the lower bound value of k_{cc} and k_{cc} of Eq. (9.4) its upper bound value.

Solving for the MMC concrete material parameters γ_f and β_f of Eq. (9.20) in Eq. (9.34) yields:

$$\gamma_f = \frac{1}{f_{co}\sqrt{k_t k_1}} \tag{9.37}$$

$$\beta_f = k_1 \gamma_f = \frac{1}{f_{co}} \sqrt{\frac{k_1}{k_t}} \tag{9.38}$$

The above material parameters also apply to plain concrete in a triaxial compression state of stress for which $\sigma_1 > \sigma_2 > \sigma_3$, which corresponds to the case of rectangular, oval, and elliptical FCC sections which have an aspect ratio α_{sh} of Eq. (4.2) greater than unity, i.e., $\alpha_{sh} > 1.0$.

Solving for the confinement effectiveness coefficient k_1 of biaxially confined concrete in Eqs. (9.32) and (9.34) yields:

$$k_1 = \left[\frac{\sqrt{4(c_u)^2 + 4\sigma_1\sigma_3} - 2c_u}{2\sigma_3} \right]^2 = \left(\frac{\sqrt{k_t + 4k_{cc}k_3} - \sqrt{k_t}}{2k_3} \right)^2 \qquad (9.39)$$

The above solution applies to cylindrical concrete section for which $\sigma_1 > \sigma_2 = \sigma_3 = f_r$**.** In addition, the above solution was determined using the fact for unconfined and confined concrete in compression k_1 is bounded by $(k_1)_b \le k_1 \le (k_1)_u$.

The experimental data points shown in **Figures 9.1-9.6** are the experimental confinement effectiveness coefficients k_1 calculated using Eq. (9.39)**.** The experimental values of the angle of internal friction of the confined concrete core ϕ_c of Eq. (9.23), determined using the experimental k_1 data points previously mentioned, are plotted in **Figures 9.16-9.18** versus the transverse confining stress $f_r = \sigma_3$, and in **Figures 9.19-9.21** versus the confinement stress ratio $k_r = k_3$.

Angle of Internal Friction of Plain Concrete

The nonlinearly decreasing relationship between the angle of internal friction of the confined concrete core ϕ_c and the minor principal confining stress σ_3 or stress ratio k_3, as shown in **Figures 9.16-9.21**, is a result of remolding of the concrete's internal structure, that results from axial strain-induced damage (i.e., dilation). At very large axial compressive stresses and strains, the concrete's internal structure becomes damaged as a result of internal crack growth, aggregate crushing and shifting, void compaction and nucleation, and decohesion (loss of adhesion provided by the binding cement paste) as it essentially degrades to that of its constituent granular materials.

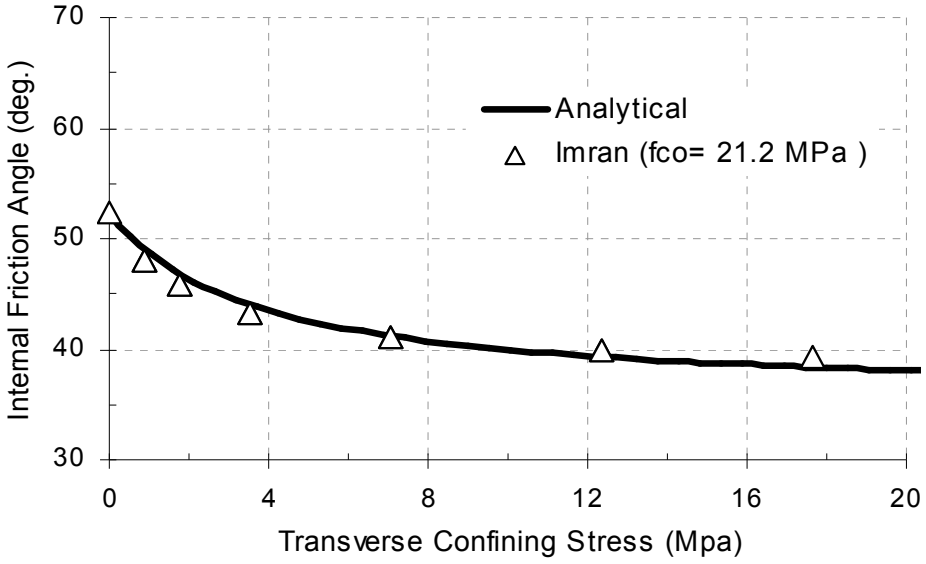

(a)

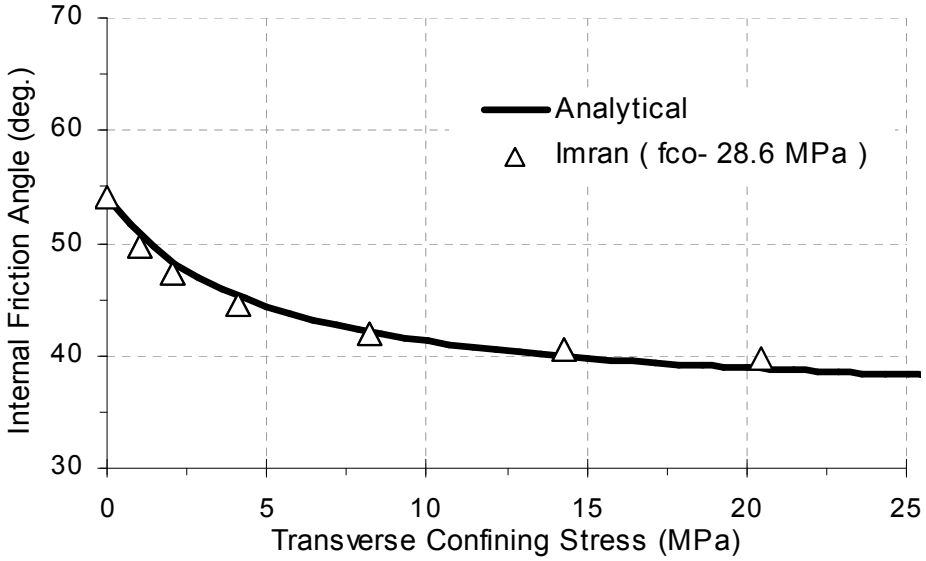

(b)

Figure 9.16 Experimental and analytical internal friction angle versus confining stress of biaxially confined low-strength concrete cylinders performed by Imran (1994).

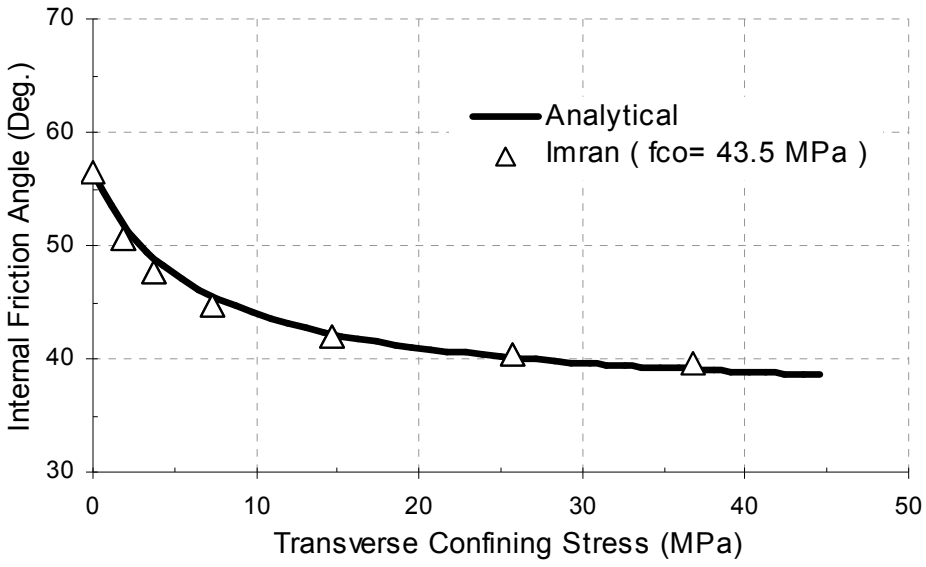

(a)

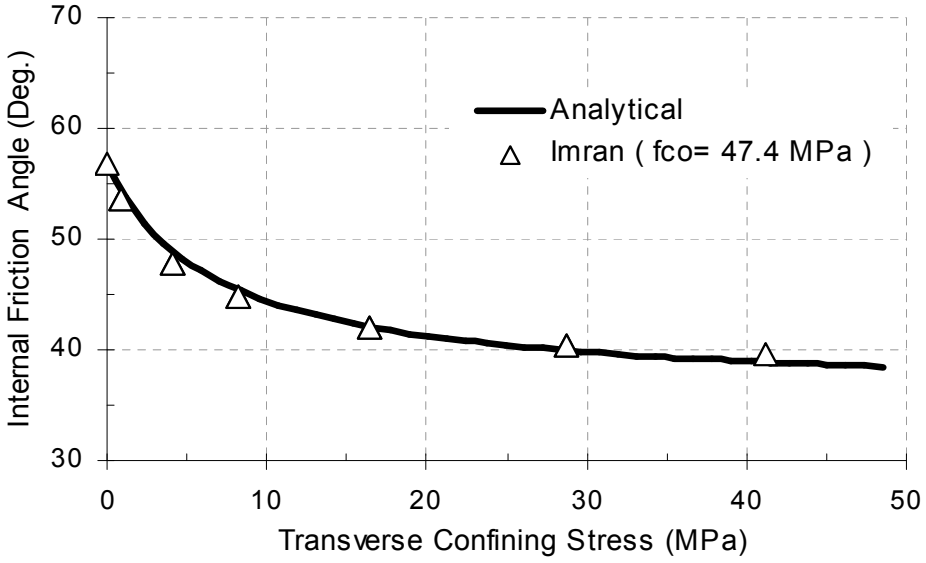

(b)

Figure 9.17 Experimental and analytical internal friction angle versus confining stress of biaxially confined medium-strength concrete cylinders performed by Imran (1994).

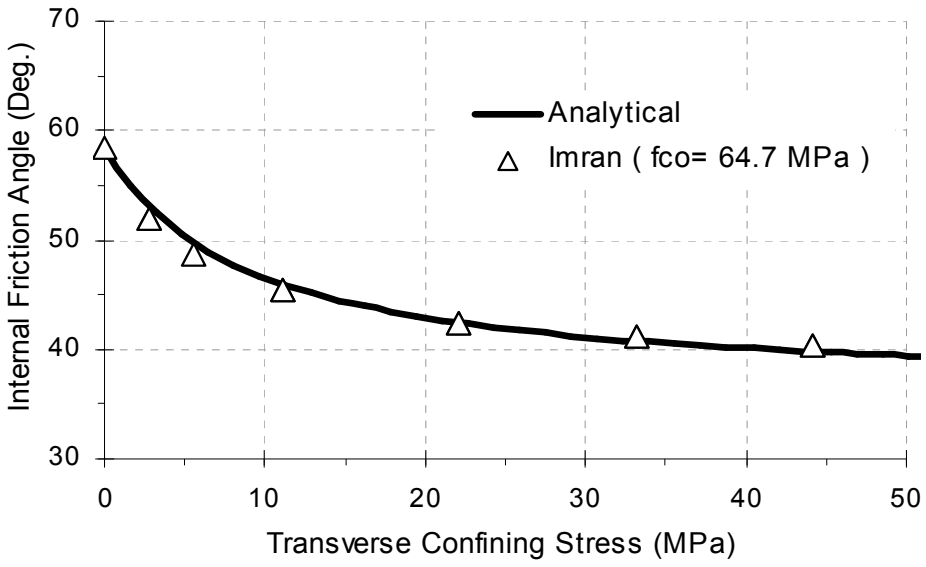

(a)

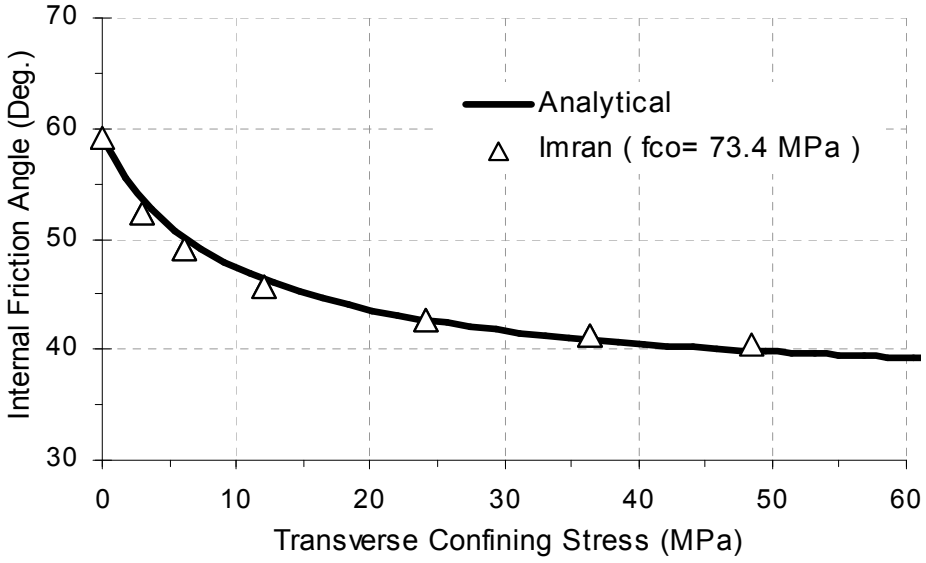

(b)

Figure 9.18 Experimental and analytical internal friction angle versus confining stress of biaxially confined high-strength concrete cylinders performed by Imran (1994).

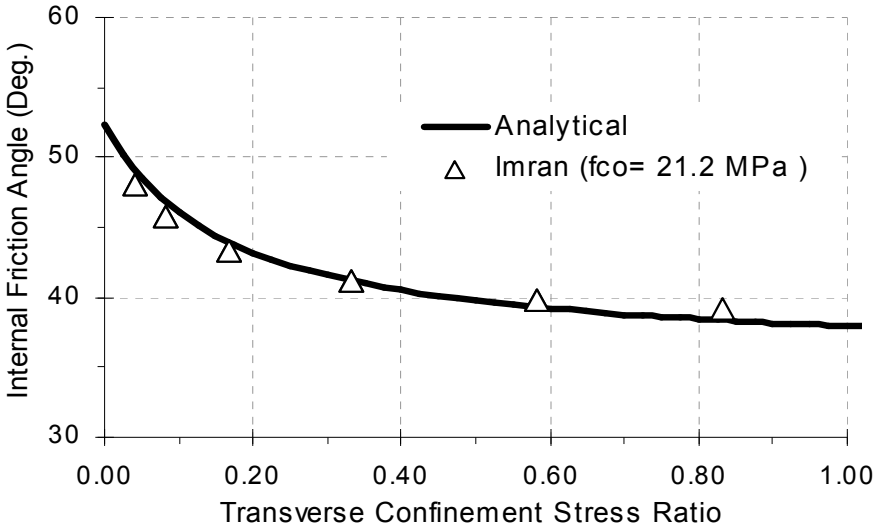

(a)

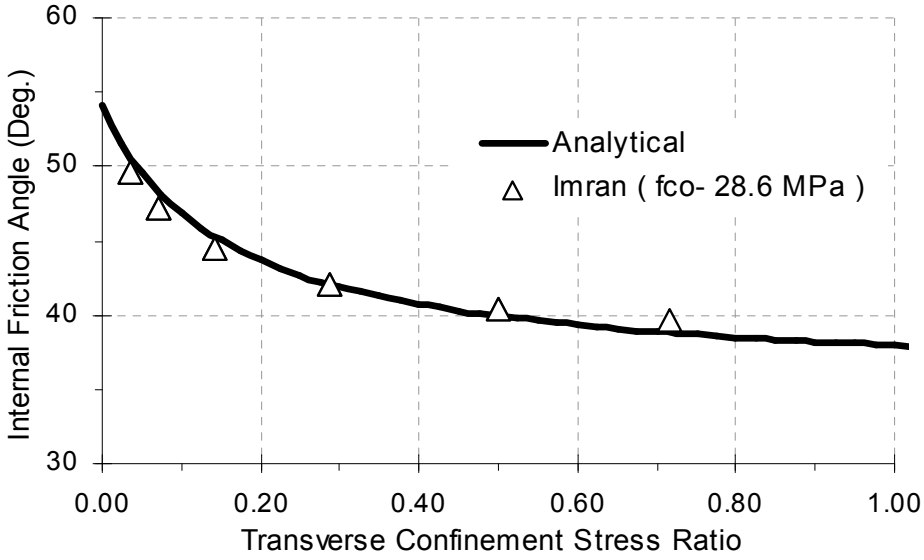

(b)

Figure 9.19 Experimental and analytical internal friction angle versus confinement stress ratio of biaxially confined low-strength concrete cylinders performed by Imran (1994).

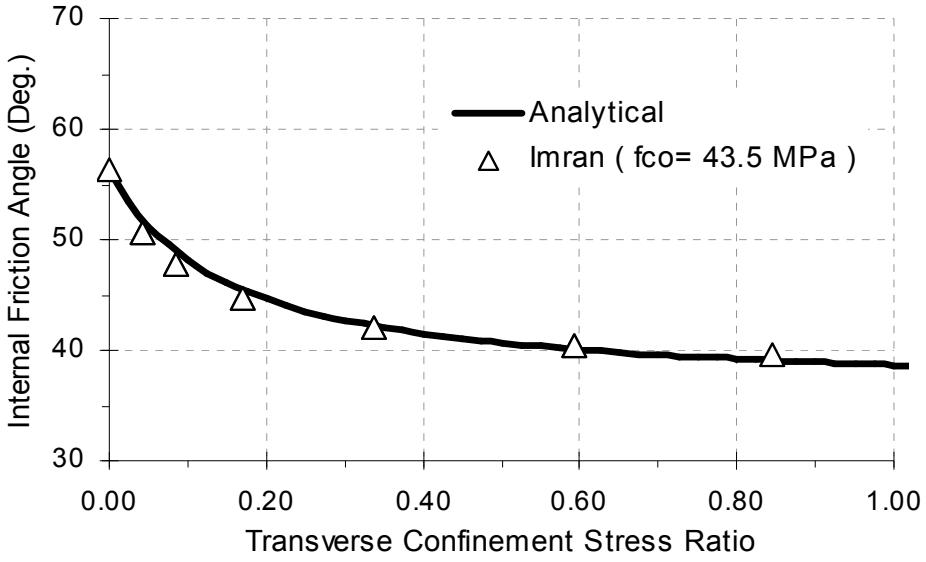

(a)

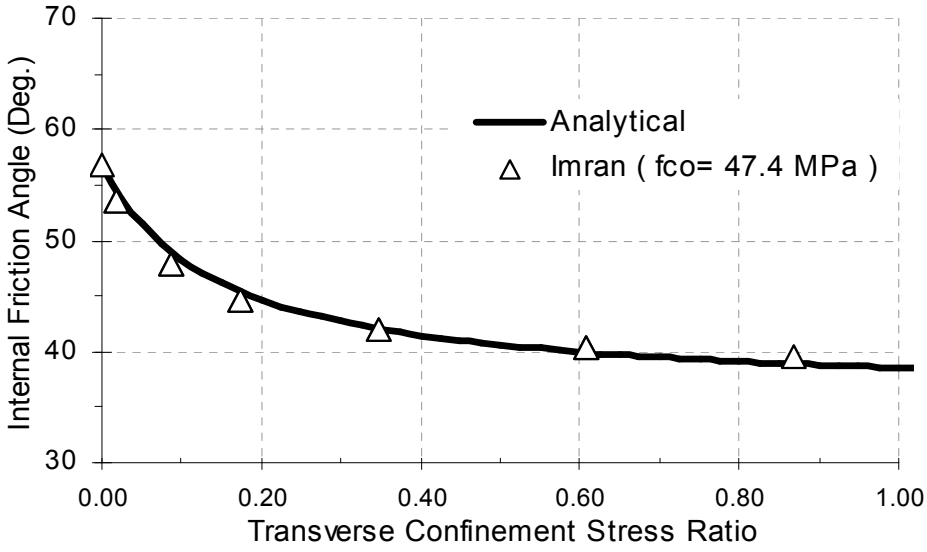

(b)

Figure 9.20 Experimental and analytical internal friction angle versus confinement stress ratio of biaxially confined medium-strength concrete cylinders performed by Imran (1994).

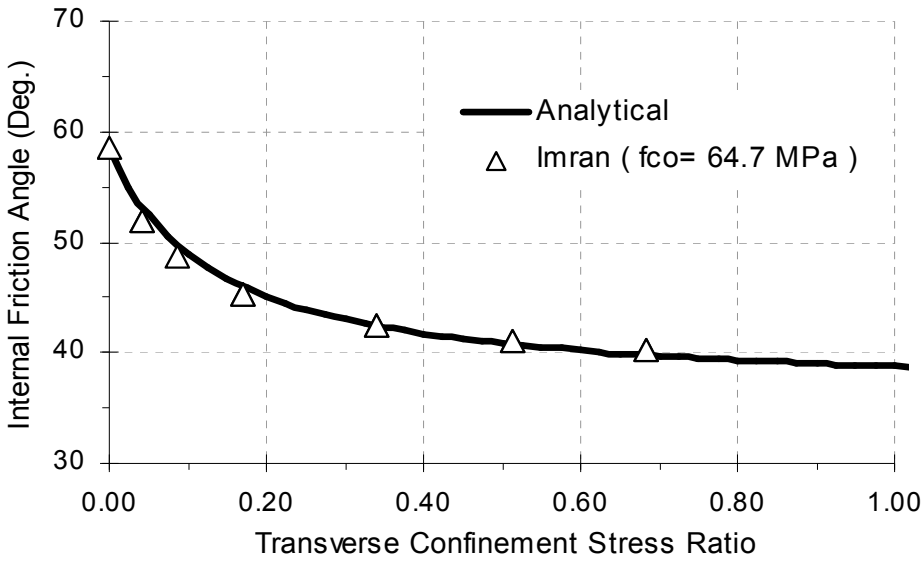

(a)

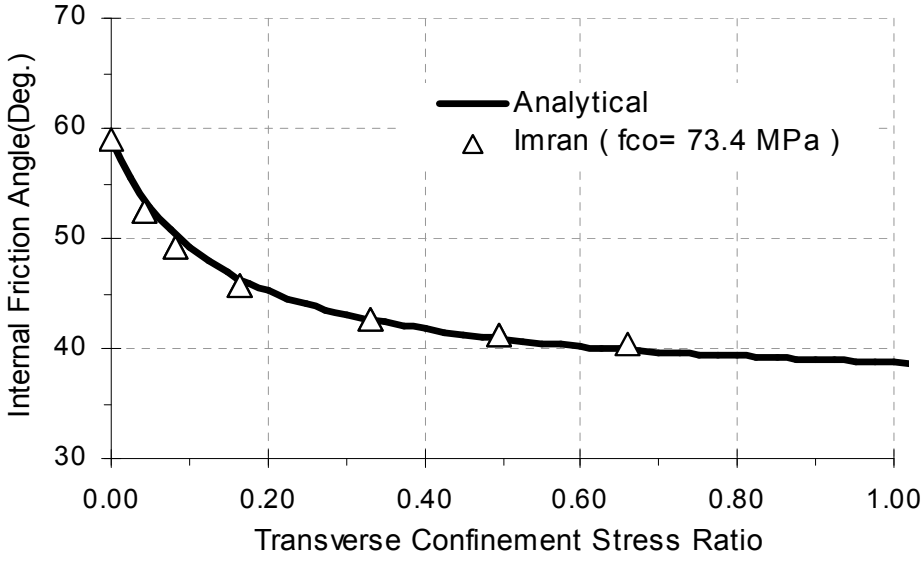

(b)

Figure 9.21 Experimental and analytical internal friction angle versus confinement stress ratio of biaxially confined high-strength concrete cylinders performed by Imran (1994).

At high levels of axial and transverse deformations, the mechanical response of the remolded confined and unconfined concrete core depends on the resistance provided by a combination of aggregate sliding, shifting, rolling, and crushing that develops during the axial and transverse deformation of the concrete core.

The nonlinearity of the Mohr-Coulomb shear strength τ_c, as shown in **Figures 9.13** and **9.15,** is due to de-cohesion of the concrete's rock-like structure as axial strain-induced damage accumulates, as is evident in the experimental confinement effectiveness coefficient k_1 and the angle of internal friction ϕ_c plots of **Figures 9.1-9.6** and **9.16-9.21**, respectively.

Both the shear strength of the concrete core τ_c of Eq. (9.12) and the normal stress σ_n of Eq. (9.13) are a function of the angle of inclination of the failure shear plane θ_c of Eq. (9. 14) and the angle of internal friction ϕ_c of the concrete core that has a nonlinear relationship with respect to the applied stresses, as shown in **Figures 9.16-9.21**.

In order to properly capture the compressive behavior of confined concrete, this nonlinear relationship is taken into consideration in the extended Mohr-Coulomb (EMC) failure criterion for concrete, presented herein, which combines the modified Mohr-Coulomb (MMC) failure criterion previously discussed with a degrading friction angle model presented in what follows.

Degrading Friction Angle Model for Confined Concrete

A nonlinear variation of the angle of internal friction ϕ_c versus the applied transverse confining stress f_r was observed of **Figures 9.16-9.18** or versus the transverse stress ratio k_r in **Figures 9.19-9.21.** From these figures it can be observed that the angle of

internal friction ϕ_c of the concrete core is a nonlinear stress-path dependent material property that depends on the magnitude of the applied stresses (σ_n, σ_1 or σ_3), where the angle of internal friction ϕ_c is separated into two distinct components: (1) a constant basic angle of internal friction ϕ_b considered a material constant, and (2) a stress-dependent angle of dilatancy ϕ_{dil} (Maksimovic 1989,1996) as follows:

$$\phi_c = \phi_b + \phi_{dil} \tag{9.40}$$

The basic angle of internal friction of the concrete material ϕ_b of Eq. (9.40) is considered to be a stress-path-independent material constant (i.e., ϕ_b is independent of σ_1, σ_3, and σ_n). At very high confining stresses, the behavior of the confined concrete core is mostly governed by friction and aggregate particle breakage occurring at existing micro- and macro-crack interfaces. The basic angle of internal friction of the concrete core ϕ_b represents the residual angle of shearing resistance of the rock-like concrete material, which is mobilized at very high normal stresses at which dilatancy effects are suppressed (Maksimovic 1989,1996).

For uniaxially and biaxially confined concrete, the confinement effectiveness coefficient k_1 of the confined concrete falls within the range of $(k_1)_b \le k_1 \le (k_1)_u$. Using the definition of the angle of internal friction ϕ_c of Eq. (9.23), the range of the angle of internal friction ϕ_c of Eq. (9.40) indicates that for unconfined and confined concrete ϕ_c should be in the range of $\phi_b \le \phi_c \le \phi_u$. This range for the angle of internal friction ϕ_c applies to a minor principal compressive stress σ_3 in the range of

$0 \le \sigma_3 \le \infty$ and a resultant major principal compressive stress σ_1 in the range of $f_{co} \le \sigma_1 \le \infty$. For this range of stresses, the lower bound value of $\phi_c = \phi_b$ in Eqs. (9.23) and (9.40) is the basic angle of friction ϕ_b of the concrete core, whereas the upper bound value is $\phi_c = \phi_u$, where ϕ_u is the uniaxial angle of internal friction of Eq. (9.28).

At very low levels of confinement, as $\sigma_3 = f_r \to 0$, the angle of dilatancy ϕ_{dil} of Eq. (9.40) approaches the value of $\phi_{dil} = (\phi_u - \phi_b)$ (i.e., as $\sigma_3 \to 0$, $\phi_{dil} \to (\phi_u - \phi_b)$, and $\phi_c \to \phi_u$). At very high levels of confinement, i.e., as $\sigma_3 \to \infty$, the angle of dilatancy ϕ_{dil} diminishes and approaches the value of $\phi_{dil} = 0$, i.e., as $\sigma_3 \to \infty$, $\phi_{dil} \to 0$, and $\phi_c \to \phi_b$.

The angle of dilatancy ϕ_{dil} of Eq. (9.40) represents the degradation of the concrete's internal structure that occurs as a result of de-cohesion of the rock-like structure of the concrete material as axial strain-induced damage accumulates. This increase in internal damage contributes to an apparent degradation of the angle of internal friction ϕ_c of the concrete.

At low and moderate levels of active confinement, $k_r = k_3 \le 0.40$, the angle of dilatancy ϕ_{dil} represents the effects of dilatancy of the confined concrete as damage in the internal structure of the partially restrained concrete core is dominated by a combination of internal micro-crack growth at the paste-aggregate interface, macro-crack growth through the aggregate, fine and coarse aggregate crushing and rolling, and de-cohesion provided by the cement paste (Imran 1994, Sfer et al. 2002). At high levels of active confinement, $k_r = k_3 > 0.40$, the angle of dilatancy ϕ_{dil} represents the effects of

alterations in the microstructure of the highly restrained concrete core that are dominated by collapse and compaction of the pore structure of the concrete (Imran 1994, Imran and Pantazopoulou 1996, Sfer et al. 2002).

For passively confined concrete, the angle of dilatancy ϕ_{dil} represents the effects of alterations to the internal structure (de-cohesion and internal cracking) of the concrete core due to axial strain-induced damage, which depends on the lateral kinematic restraint provided by the confining element, be it closely spaced transverse steel reinforcement or steel jacket (Pantazopoulou 1995) or an FRP jacket (Moran and Pantelides 2002a,b, Yan and Pantelides 2006, Saenz and Pantelides 2007).

The curvature of the failure envelope of confined concrete can be attributed to remolding of the concrete's internal structure as the axial strain-induced damage (de-cohesion and internal cracking) progresses. As a result of this process, the angle of internal friction of the concrete core ϕ_c of Eq. (9.40) is assumed to be a nonlinear function of the applied stress (σ_n, σ_1, or σ_3), in which ϕ_{dil} of Eq. (9.40) is assumed to be governed by the following hyperbolic-type degrading friction angle model, as shown in **Figure 9.22**, similar to the Maksimovic (1989,1996) hyperbolic model, where ϕ_{dil} is given by:

$$\phi_{dil} = \frac{\phi_i - \phi_b}{1 + \left[\dfrac{\sigma_k - (\sigma_k)_i}{(\sigma_k)_{m_{ib}} - (\sigma_k)_i} \right]} \tag{9.41}$$

$$(\phi_m)_{ib} = \frac{\phi_i + \phi_b}{2} \tag{9.42}$$

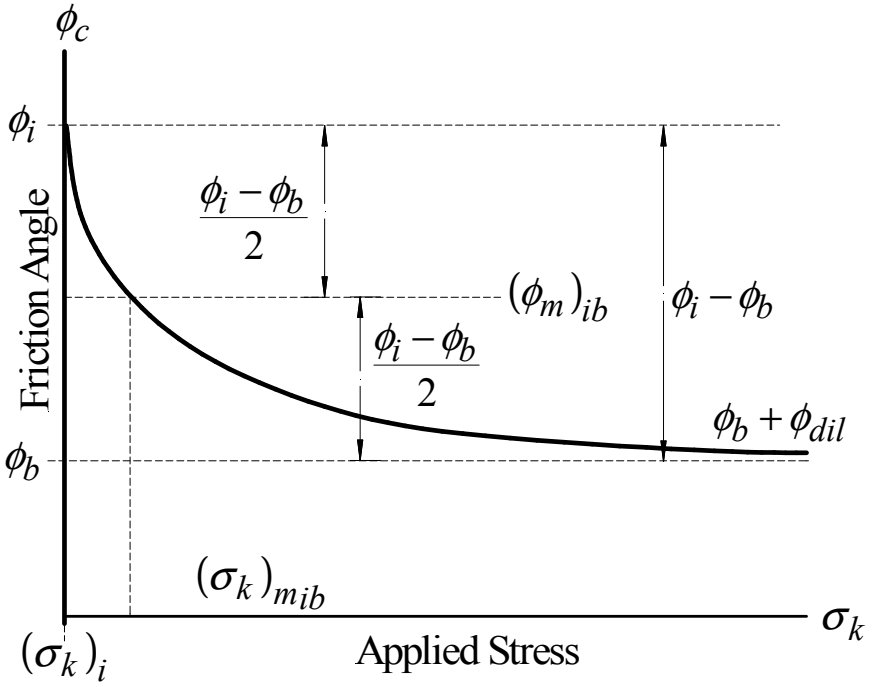

Figure 9.22 Geometry of generalized degrading friction angle model for concrete.

where ϕ_i is the reference initial angle of friction at the instant when the applied stress σ_k is equal to the initial reference stress $(\sigma_k)_i$ (i.e., $\sigma_k = (\sigma_k)_i$); $(\sigma_k)_{m_{ib}}$ is the median-angle stress corresponding to the median-angle of internal friction $(\phi_m)_{ib}$ of Eq. (9.42).

The above dilatancy angle model applies to concrete subjected to an applied stress σ_k in the range of $(\sigma_k)_i \le \sigma_k \le \infty$, as shown in **Figure 9.22**. In what follows it is demonstrated that the proposed degrading frictional model of Eqs. (9.40)-(9.42) reduces to the normal stress-dependent Maksimovic (1989, 1996) hyperbolic degrading friction angle model previously mentioned.

Normal Stress-Dependent Dilatancy Angle Model

The degrading dilatancy angle model of Eqs. (9.41) and (9.42) in combination with Eq. (9.40) yield the Maksimovic (1989, 1996) model only when the reference initial angle of friction ϕ_i occurs at the instant of zero normal stress, i.e., when $(\sigma_k)_i = (\sigma_n)_i = 0$, i.e., cohesionless soils. The dilatancy angle model of Eqs. (9.41) and (9.42), applies to cohensionless frictional materials such as noncemented sands, silts, or gravels, and to frictional cohesive materials such as concrete since the concrete exhibits a uniaxial tensile capacity $|f_{to}| > 0$, and it exhibits a positive apparent uniaxial cohesion intercept, $c_u > 0$, as indicated in Eq. (9.25).

For concrete in a tension-compression, uniaxial compression, and triaxial compression state of stress, the resultant normal stress σ_n in the concrete core is in the range of $0 \le \sigma_n \le \infty$, as shown in **Figure 9.23.** For this range of normal stresses the angle of dilatancy of the concrete material ϕ_{dil} of Eq. (9.41) can be rewritten as:

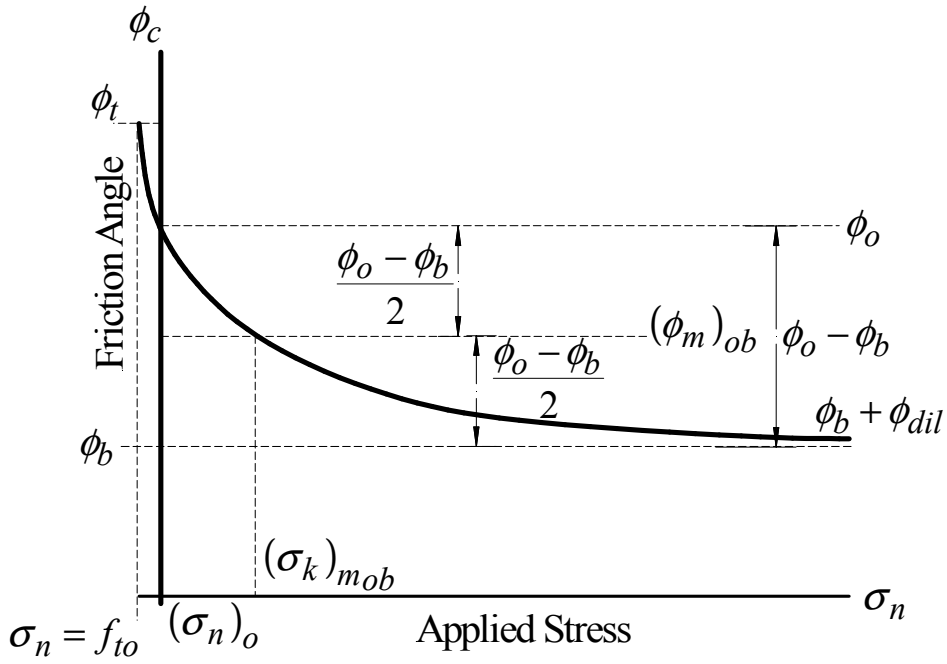

Figure 9.23 Geometry of normal stress-dependent degrading friction angle model for concrete.

$$\phi_{dil} = \frac{\phi_o - \phi_b}{1 + \dfrac{\sigma_n}{(\sigma_n)_{m_{ob}}}} \tag{9.43}$$

$$(\phi_m)_{ob} = \frac{\phi_o + \phi_b}{2} \tag{9.44}$$

where $(\sigma_n)_{m_{ob}}$ is the median-angle normal stress corresponding to the median-angle of internal friction $(\phi_m)_{ob}$ for a normal stress σ_n in the range of $0 \le \sigma_n \le \infty$; ϕ_o is the initial angle of internal friction at the instant of zero normal stress, i.e., when $\sigma_n = 0$.

The normal stress-dependent degrading angle model of Eqs. (9.43) and (9.44), in combination with Eq. (9.40), is similar to the model originally proposed by Maksimovic (1989,1996) for cohesionless soils and rock discontinuities, i.e., for granular materials that exhibit little or no tensile capacity (i.e., $f_{to} \cong 0$ and for which $c_u \cong 0$).

The median-angle normal stress $(\sigma_n)_{m_{ob}}$ of Eq. (9.43) can be found in terms of the normal stress at failure of the unconfined concrete $(\sigma_n)_u$ of Eq. (9.26) by setting $\phi_c = \phi_u$ and $\sigma_n = (\sigma_n)_u$ in Eq. (9.43), using Eq. (9.40), and solving for the median-angle normal stress $(\sigma_n)_{m_{ob}}$, which yields:

$$(\sigma_n)_{m_{ob}} = (\sigma_n)_u \left(\frac{\phi_u - \phi_b}{\phi_o - \phi_u} \right) \tag{9.45}$$

The median-angle normal stress $(\sigma_n)_{m_{ob}}$ of Eqs. (9.43) and (9.45) is considered to be a function of the unconfined cohesion c_u of Eq. (9.25) as follows:

$$k_\sigma = \frac{c_u}{(\sigma_n)_{m_{ob}}} \tag{9.46}$$

where k_σ is a normal stress parameter, which is determined as follows. Solving for the unconfined cohesion c_u in both Eqs. (9.32) and (9.46) and recognizing that for unconfined concrete $\sigma_1 = f_{co}$, $\sigma_3 = 0$ and $k_1 = (k_1)_u = 1/k_t$, and solving for the median-angle normal stress $(\sigma_n)_{m_{ob}}$ of Eqs. (9.43) and (9.46) yield:

$$(\sigma_n)_{m_{ob}} = \frac{1}{2} f_{co} \sqrt{\frac{k_t}{(k_\sigma)^2}} \tag{9.47}$$

Equating the median-angle normal stress $(\sigma_n)_{m_{ob}}$ of Eqs. (9.45) and (9.47), using $(\sigma_n)_u$ of Eq. (9.26), and solving for the initial angle of friction ϕ_o at the instant of zero normal stress yield:

$$\phi_o = \phi_u + (\phi_u - \phi_b)[1 + \cos(2\theta_u)]\sqrt{\frac{(k_\sigma)^2}{k_t}} \tag{9.48}$$

Substituting the median-angle normal stress $(\sigma_n)_{m_{ob}}$ of Eq. (9.47) and the initial angle of friction ϕ_o of Eq. (9.48) into the angle of internal friction ϕ_c of Eq. (9.43) yields:

$$\phi_c = \phi_b + \gamma_{dil}(\phi_u - \phi_b) \tag{9.49}$$

$$\gamma_{dil} = \frac{1 + [1 + \cos(2\theta_u)]\sqrt{\frac{(k_\sigma)^2}{\mathrm{k_t}}}}{1 + 2\sqrt{\frac{(k_n k_\sigma)^2}{\mathrm{k_t}}}} \tag{9.50}$$

$$k_n = \frac{\sigma_n}{f_{co}} \tag{9.51}$$

where γ_{dil} is a dilatancy parameter and k_n is the normalized normal stress.

The normal stress parameter k_σ of Eqs. (9.46)-(9.48) and (9.50) can be found based on the uniaxial tensile strength of the concrete material f_{to} as follows. For concrete in a uniaxial tension state of stress $\sigma_1 = 0$, $\sigma_3 = -|f_{to}|$, $\phi_c = \phi_t = 90°$, and $\theta_c = 45° + \phi_c/2 = \theta_t = 90°$, as shown in **Figure 9.15.** Substituting these values into the relationships for the normal stress on the failure shear plane σ_n of Eq. (9.13) and the failure shear stress τ_c of Eq. (9.12) yields $\sigma_n = (\sigma_n)_t = -|f_{to}|$ and $\tau_c = \tau_t = 0$, respectively.

Substituting $\sigma_n = (\sigma_n)_t = -|f_{to}|$ into the relationship for the angle of internal friction ϕ_c of Eq. (9.43), setting $\phi_c = \phi_t = 90°$, and solving for the initial angle of internal friction ϕ_o yield:

$$\phi_o = \phi_b + \left[1 - \frac{|f_{to}|}{(\sigma_n)_{m_{ob}}}\right](\phi_t - \phi_b) \tag{9.52}$$

where $\phi_t = 90°$ is the tensile angle of separation of the concrete material.

Substituting the mean angle normal stress $(\sigma_n)_{m_{ob}}$ of Eq. (9.47) into Eq. (9.52), equating Eqs. (9.52) and (9.48), and solving for the mean angle normal stress parameter k_σ yield:

$$k_\sigma = \frac{c_u}{(\sigma_n)_{m_{ob}}} = \frac{\sqrt{k_t}(\phi_t - \phi_u)}{2k_t(\phi_t - \phi_b) + (\phi_u - \phi_b)[1 + \cos(2\theta_u)]} \tag{9.53}$$

The above mean angle normal stress parameter k_σ can be substituted into Eq. (9.48) to find the initial angle of friction ϕ_o at the instant of zero normal stress, when $\sigma_n = 0$. In addition, ϕ_o can also be found by substituting $(\sigma_n)_{m_{ob}}$ of Eq. (9.45) and f_{to} of Eq. (9.30) into Eq. (9.52). In the development of the ultimate failure envelope of the concrete material of Eqs. (9.40)-(9.53), the basic angle of friction ϕ_b is the only unknown term in the extended Mohr-Coulomb (EMC) criterion developed herein, which combines the modified Mohr-Coulomb (MMC) criterion previously discussed with the degrading friction angle models presented herein. This basic friction angle ϕ_b is determined in what follows.

At very large confining stress and at high levels of axial and transverse deformations, the confined concrete material is expected to behave similar to sandy and gravelly soils subjected to very large confining stresses. Maksimovic (1996) has shown that for coarse granular soils like limestone sand $\phi_b \cong 36°$; $32.7° \le \phi_b \le 34°$ for crushed Basalt (an aggregate used in normal-weight concrete Attard and Setunge 1996); $\phi_b \approx 32.7°$ for gravel; $\phi_b \approx 36.4°$ for sand and gravelly soil; and $\phi_b \approx 37.8°$ for very dense sand. This would indicate that the type of large aggregate used (be it crushed stone or gravel), the

aggregate size and gradation, and gravel-to-sand ratio can have a significant influence on the basic angle of internal friction ϕ_b of normal-weight dry concrete; based on the previous values, this basic angle of internal friction ϕ_b is expected to range between $33° \le \phi_b \le 37°$, with an average value of $(\phi_b)_{avg} \cong 35°$.

Based on the analysis of tests of plain concrete in a triaxial compression state of stress performed by Imran (1994), an average value of the basic angle of internal friction of $\phi_b = (\phi_b)_{avg} = 35°$ is used in Eqs. (9.39)-(9.52) and is plotted as solid curves in **Figures 9.1-9.6** and **9.16-9.21.** Based on these findings and the typical range of the basic angle of granular soils given by Maksimovic (1996) previously listed and the stress path independency of the concrete core (Imran 1994), it is assumed that the basic angle of internal friction ϕ_b of normal-weight concrete in a triaxial compression state of stress, be it active confinement provided by fluid pressure or passive confinement provided by a restraining transverse reinforcement, including transverse steel, steel jacket, or FRP jackets, can be approximated by $\phi_b = 35°$.

The extended Mohr-Coulomb (EMC) failure envelope as developed in Eqs. (9.10)-(9.39) in combination with the hyperbolic degrading friction model of Eqs (9.40)-(9.53) can accurately capture the ultimate failure envelopes of normal-weight concrete in a triaxial compression state of stress. This EMC ultimate strength model developed herein satisfies the following conditions:

1. It passes through the point of uniaxial compression
2. It passes through the point of uniaxial tension

3. It describes the typical nonlinear failure envelope of concrete in a triaxial compression state of stress, as shown in **Figures 9.1-9.12**
4. It approaches the hydrostatic state at very large confining stresses (i.e., as $\sigma_2 = \sigma_3 \to \infty$, $\sigma_1 \to \sigma_2 = \sigma_3$).

One of the drawbacks of the Maksimovic (1989, 1996)-type normal stress degrading friction angle model of Eqs. (9.43)-(9.53) in combination with Eq. (9.40), is that it describes the EMC ultimate strength failure envelope in terms of the normal stress σ_n on the failure shear plane. As shown in Eq. (9.13), this depends on a critical combination of the major σ_1 and minor σ_3 principal compressive stresses and the normal stress-dependent angle of inclination of the failure shear plane θ_c of Eq. (9.19). As a result, a direct solution for the major principal compressive stress σ_1 cannot be obtained in terms of the minor principal compressive stress σ_3, thus requiring an indirect iterative or incremental solution as follows.

Solving for the resultant normal stress on the shear plane σ_n and defining the normalized normal stress as $k_n = \sigma_n / f_{co}$ yield a relationship between the normalized normal stress and the minor principal stress ratio k_3 of Eq. (9.36) as follows:

$$k_n = \frac{\sigma_n}{f_{co}} = -\frac{k_3}{2}\left[(k_1+1)+(k_1-1)\cos(2\theta_c)+\frac{\sqrt{k_t k_1}}{k_3}(1+\cos\theta_c)\right] \qquad (9.54)$$

Solving for the normal stress on the shear plane σ_n in Eq. (9.43), using the median-angle normal stress $(\sigma_n)_{m_{ob}}$ of Eqs. (9.45), the normalized normal stress k_n of Eq. (9.54), and equating both relationships yield the following equality which can be solved

in terms of the applied minor principal compressive stress σ_3 and the angle of internal friction ϕ_c:

$$(k_n)_u\left(\frac{\phi_c-\phi_o}{\phi_o-\phi_u}\right)\left(\frac{\phi_u-\phi_b}{\phi_o-\phi_b}\right)-\frac{k_3}{2}\left[(k_1+1)+(k_1-1)\cos(2\theta_c)+\frac{\sqrt{k_t k_1}}{k_3}(1+\cos\theta_c)\right]=0 \quad (9.55)$$

where $(k_n)_u=(\sigma_n)_u/f_{co}$ is the normalized unconfined normal stress. The above equality indicates that for a normal stress-dependent degrading friction angle model an iterative (indirect) solution for the angle of internal friction ϕ_c is required. A noniterative (direct) solution for ϕ_c can be found in terms of the applied minor principal compressive stress σ_3 as follows.

Minor Principal Compressive Stress-Dependent Dilatancy Angle Model

In the analysis of concrete sections in a triaxial compression state of stress, it is best to describe the ultimate strength envelope of the confined concrete in terms both the major σ_1 and minor σ_3 principal compressive stresses in the confined concrete core, as shown in Eqs. (9.20) and (9.34)-(9.39); this is preferable to describing the ultimate strength in terms of the normal stress σ_n, since it leads to a rather simple degrading friction angle model, introduced in what follows.

The variation of the angle of dilatancy as described in ϕ_{dil} of Eq. (9.39) throughout the compressive loading history of the confined concrete core can be found in terms of the minor principal compressive stress σ_3 or compressive stress ratio k_3 of Eq. (9.36).

Solving for the applied minor principal compressive stress σ_3 in Eq. (9.33) and using k_3 of Eq. (9.36) yield a relationship between the normalized normal stress defined as $k_n = \sigma_n / f_{co}$ and the minor principal stress ratio k_3 as follows:

$$k_3 = \frac{\sigma_3}{f_{co}} = \frac{2(k_n) - \sqrt{k_t k_1}(1 + \cos\theta_c)}{[k_1 + 1] + [k_1 - 1]\cos(2\theta_c)} \tag{9.56}$$

Both Eqs. (9.54) and (9.56) indicate that at failure of the confined concrete, the normal stress σ_n on the failure shear plane and the applied minor principal compressive stress σ_3 are proportional to each other, i.e., $\sigma_n \propto \sigma_3$ or $k_n \propto k_3$ and vice versa. Thus, the hyperbolic-type degrading friction model of Eqs. (9.41) and (9.42) can also be written in terms of the minor principal compressive stress σ_3 or stress ratio k_3, which is accomplished in what follows.

Substituting the minor stress ratio terms k_3, $(k_3)_i$, and $(k_3)_{m_{ib}}$ in place of the applied stress terms σ_k, $(\sigma_k)_i$ and $(\sigma_k)_{m_{ib}}$, respectively, in Eq. (9.41), yields a relationship for the angle of dilatancy ϕ_{dil} in terms the minor compressive stress ratio k_3 of Eq. (9.36) as follows:

$$\phi_{dil} = \frac{\phi_i - \phi_b}{1 + \left[\dfrac{k_3 - (k_3)_i}{(k_3)_{m_{ib}} - (k_3)_i}\right]} \tag{9.57}$$

where $(k_3)_{m_{ib}}$ is the reference median-confinement ratio corresponding to the median-angle of internal friction $(\phi_m)_{ib}$ of Eq. (9.42), as shown in **Figure 9.24**.

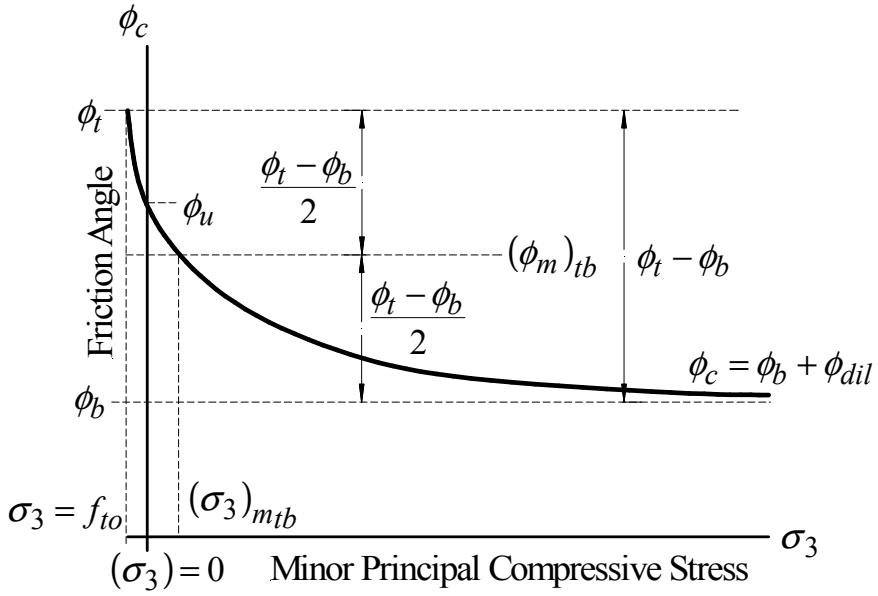

(a)

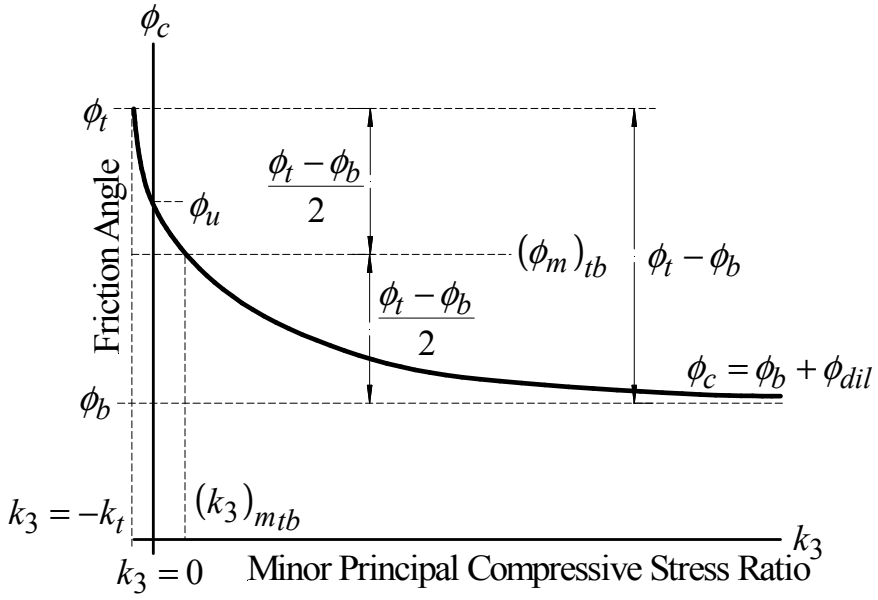

(b)

Figure 9.24 Plot of angle of internal friction versus (a) minor principal compressive stress and (b) minor principal compressive stress ratio, including geometry.

For unconfined concrete in uniaxial tension and compression, and confined concrete in a triaxial compression state of stress, the minor principal compressive stress σ_3 is in the range of $f_{to} \le \sigma_3 \le \infty$ or $-k_t \le k_3 \le \infty$, as shown in **Figure 9.24**. Thus setting the reference minor principal compressive stress ratio $(k_3)_i = -k_t$ and setting the reference initial angle of friction ϕ_i as $\phi_i = \phi_t$ and the reference median-confinement ratio $(k_3)_{m_{ib}}$ as $(k_3)_{m_{ib}} = (k_3)_{m_{tb}}$ in Eq. (9.57) yield:

$$\phi_{dil} = \frac{\phi_t - \phi_b}{1 + \left[\dfrac{k_3 + k_t}{(k_3)_{m_{tb}} + k_t} \right]} \tag{9.58}$$

$$(\phi_m)_{tb} = \frac{\phi_t + \phi_b}{2} \tag{9.59}$$

$$(k_3)_{m_{tb}} = k_t \left(\frac{2\phi_u - \phi_b - \phi_t}{\phi_t - \phi_u} \right) \tag{9.60}$$

where $(k_3)_{m_{tb}}$ is the median angle minor principal stress ratio at the median angle of internal friction $(\phi_m)_{tb}$, as shown in **Figure 9.24.** Eqs. (9.58)-(9.60) apply when σ_3 is in the range of $f_{to} \le \sigma_3 \le \infty$ or $-k_t \le k_3 \le \infty$.

For low-to-medium-strength normal-weight concrete with f_{co} ranging between $17 \text{ MPa} \le f_{co} \le 55$, with a tensile strength ratio k_t, determined using f_{to} of Eq. (9.30) and k_t of Eq. (9.9), in the range of $0.084 \le k_t \le 0.124$, with a uniaxial angle of internal friction ϕ_u in the range of $51.2° \le \phi_u \le 57.7°$, the median angle minor principal stress ratio ratio $(k_3)_{m_{tb}}$ of Eq. (9.60) is in the range of $0.048 \le (k_3)_{m_{tb}} \le 0.056$.

The combination of the modified Mohr-Coulomb (MMC) criterion introduced in Eqs. (9.12)-(9.39) and the minor principal compressive stress-dependent degrading friction angle model ϕ_c of Eqs. (9.40) and Eqs. (9.56)-(9.61), yields what is referred to herein as the extended Mohr-Coulomb (EMC) criterion for actively and passively confined, FRP-confined concrete in particular.

Excess Pore Water Pressure Effects

For the case of normal-weight FRP-confined concrete (FCC) cylinders, an average value of $(k_1)_{avg} \approx 4.10$ (i.e., $(\phi_c)_{avg} = 37.4°$) was found to apply to bonded FRP-confined concrete (BFCC) cylindrical sections (Nanni and Bradford 1995, Wu and Xiao 2000, Moran and Pantelides 2002a) at high levels of confinement, i.e., when $0.4 \le k_3 \le 1.0$. From the analysis of concrete-filled FRP tube (CFFT) cylinders tests performed by Mirmiran (1997) and Saafi et al. (1999), an average value of $(k_1)_{avg} \approx 2.33$ was found (i.e., $(\phi_c)_{avg} = 23.5°$).

The lower values of $(k_1)_{avg}$ or $(\phi_c)_{avg}$ of CFFT sections in comparison to that of BFCC sections can be attributed to the presence of excess pore water in the concrete core. For BFCC sections, the FRP-wrapped concrete is typically allowed to dry to its natural moisture content, whereas for CFFT sections the cast-in-place FRP jacket serves as a barrier against evaporation of the nonhydrated water (i.e., bleed water) at the perimeter surface of the concrete member. As a result, in CFFT sections, the remaining bleed water remains in suspension in the concrete mix and may become trapped within the voids of the concrete's structure. The presence of pore water has a significant weakening

influence on the strength of the concrete material, which increases as the confining stress increases (Imran 1994).

For FCC sections, this weakening influence is a result of an increase in the pore water pressure which acts against the concrete's internal structure and weakens the effectiveness of the concrete core in sustaining the applied load. An increase in the pore water pressure results from an increase in the passive confining stresses provided by the restraining elastic FRP jacket as dilation of the confined concrete core progresses; this weakening effect increases as the passive confining stress provided by the retraining FRP jacket increases.

The presence of excess pore water can be accounted for in the analysis of FCC in Eqs. (9.39) and Eqs. (9.42)-(9.58), with the use of an effective confinement effectiveness coefficient $(k_1)_{PW}$, given as:

$$(k_1)_{PW} = n_{PW} + (1 - n_{PW})k_1 \tag{9.61}$$

where n_{PW} is the pore water pressure parameter of the granular concrete core where $0 \le n_{PW} \le 1.0$, which is somewhat analogous to the degree of saturation of the concrete material. The lower value of $n_{PW} = 0$ corresponds to dry concrete and $n_{PW} = 1.0$ to saturated concrete, and for $0 < n_{PW} < 1.0$ corresponds to partially saturated concrete.

The pore water pressure parameter of the concrete material can be found based on the confinement effectiveness coefficient of the confined concrete core by solving for n_{PW} in Eq. (9.61), which yields:

$$n_{PW} = 1 - \frac{(\sigma_3)_{PW}}{\sigma_3} \cong \frac{(k_1)_{PW} - k_1}{1 - k_1} \tag{9.62}$$

where $(\sigma_3)_{PW}$ is the effective confining stress including the effects of excess pore water pressure and $(k_1)_{PW}$ is the effective confinement effectiveness including pore water pressure effects.

The average pore water pressure parameter of FRP-confined concrete sections can be determined from the average effective confinement coefficients of BFCC and CFTT sections by evaluating the angle of internal friction of dry normal-weight concrete with f_{co} ranging between $17 \text{ MPa} \le f_{co} \le 55 \text{ MPa}$, k_t of Eq. (9.9) ranging between $0.084 \le k_t \le 0.124$, and ϕ_u of Eq. (9.28) ranging between $51.1° \le \phi_u \le 57.7°$.

Using these values of k_t and ϕ_u, a basic angle of friction of dry concrete of $\phi_b = 33^\circ$ and a unity minor principal stress ratio, i.e., $k_3 = 1.0$, in the degrading friction angle model of Eqs. (9.58)-(9.60), yield a friction angle ϕ_c in the range of $37.8^\circ \le \phi_c \le 38.6^\circ$ and a confinement effectiveness coefficient k_1 in the range of $4.17 \le k_1 \le 4.32$.

Substituting these values of k_1 and the average confinement effectiveness of BFCC sections of $(k_1)_{PW} = (k_1)_{avg} \approx 4.10$ into Eq. (9.62) yields a pore water pressure parameter of the FCC section n_{PW} in the range of $2.2\% \le n_{PW} \le 6.6\%$. Substituting $(k_1)_{PW} = (k_1)_{avg} \approx 2.33$ into Eq. (9.63) and the aforementioned range of k_1 values yields n_{PW} in the range of $58.1\% \le n_{PW} \le 59.9\%$ for CFFT sections.

The lower value of pore water pressure parameter n_{PW} of the surface applied or bonded FRP jackets is because prior to the application of the FRP jacket, the concrete is typically allowed to dry to its natural moisture content, as previously mentioned. The higher value of n_{PW} for CFFT sections is because the FRP jacket serves as a barrier against evaporation of the nonhydrated water, which increases the degree of saturation of the concrete material and, hence, results in increasing the presence of excess pore water within the voids of the concrete, which has a significantly detrimental effect in decreasing the apparent strength of an FCC section due to the presence of excess pore water pressure.

The pore water pressure parameter n_{PW} of the confined concrete section depends on the water-cement ratio and can range between $0.01 < n_{PW} \leq 0.20$ for dry to partially saturated concrete. When concrete is not allowed to dry to its natural water content, such as submerged concrete, wet or fog-cured concrete, or concrete exposed to a high humidity environment, the pore water pressure parameter n_{PW} is in the range of $0.20 < n_{PW} < 1.0$. This indicates that under a triaxial compression state of stress, FCC sections behave more like dry and low partially saturated concrete and CFFT sections more like highly saturated concrete.

In the analysis of BFCC sections, an average value of $n_e = 3.0\%$ is recommended for surface applied or bonded FRP-jacketed concrete in which the natural moisture content of is low. For cast in place FRP-jacketed (CFFT) sections, an average value of $n_e = 59.0\%$ is recommended.

The effective basic confinement effectiveness $(k_1)_{be}$ can be found by substituting $(k_1) = (k_1)_{PW} = (k_1)_{be}$ and $\phi_b = \phi_{be}$ into Eqs. (9.23) and (9.61), which yield:

$$(k_1)_{be} = n_{PW} + (1 - n_{PW})(k_1)_b \tag{9.63}$$

$$\phi_{be} = \sin^{-1}\left[\frac{(k_1)_{be} - 1}{(k_1)_{be} + 1}\right] = \sin^{-1}\left[\frac{(n_{PW} - 1) + (1 - n_{PW})(k_1)_b}{(1 + n_{PW}) + (1 - n_{PW})(k_1)_b}\right] \tag{9.64}$$

where ϕ_{be} is the effective basic angle of internal friction, including pore water pressure effects. The effects of excess pore water pressure on the compressive behavior of the confined concrete core must be considered; this can be accomplished by substituting $\phi_b = \phi_{be}$ of Eq. (9.64) in the degrading friction angle model introduced in Eqs. (9.40) through (9.60).

In **Figure 9.25** the variation of the angle of internal friction of a circular concrete section having a compressive strength of 40 MPa is plotted versus the minor principal compressive stress ratio k_3 of Eq. (9.36) for $-k_t \le k_3 \le 1.5$ and pore water pressure parameters of $n_{PW} = 5.0\,\%$, $n_{PW} = 30.0\,\%$, and $n_{PW} = 60.0\,\%$.

The detrimental effects of excess pore water pressure is more evident on the increase in compressive strength of confined concrete, as is shown in the plot of the confinement effectiveness k_{cc} of Eq. (9.35) versus the transverse confinement stress ratio, as shown in **Figure 9.26.**

From these figures it can be observed that the value of the pore water parameter has no significant effect on the friction angle ϕ_c and the confinement effectiveness coefficient at low levels of transverse confinement.

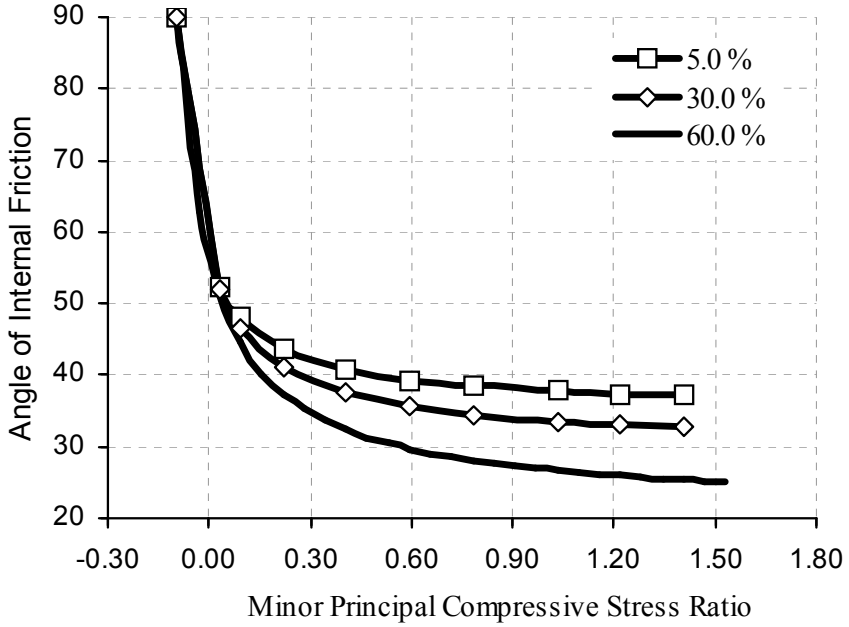

(a)

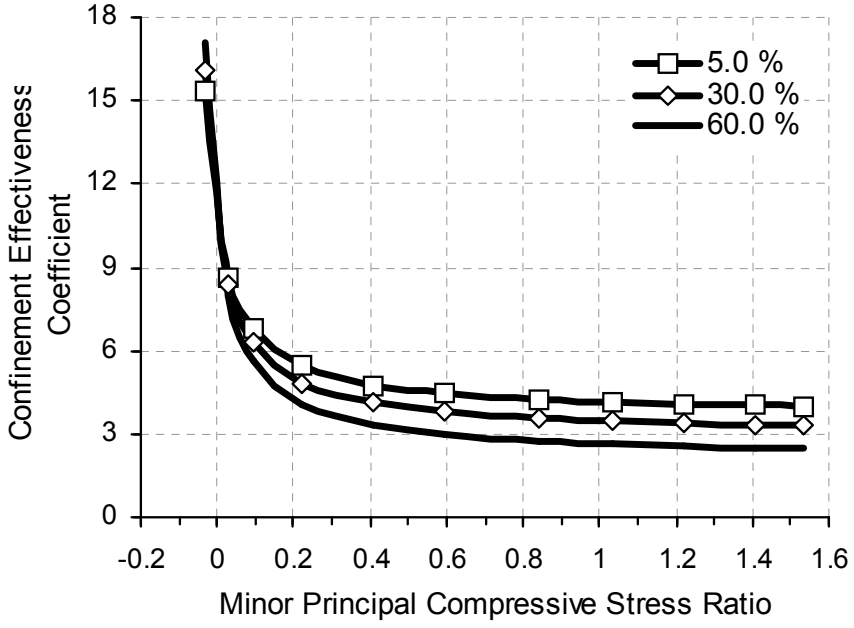

(b)

Figure 9.25 Plot of the (a) friction angle and (b) confinement effectiveness coefficient versus minor principal compressive stress ratio of concrete with varying pore water pressure parameters.

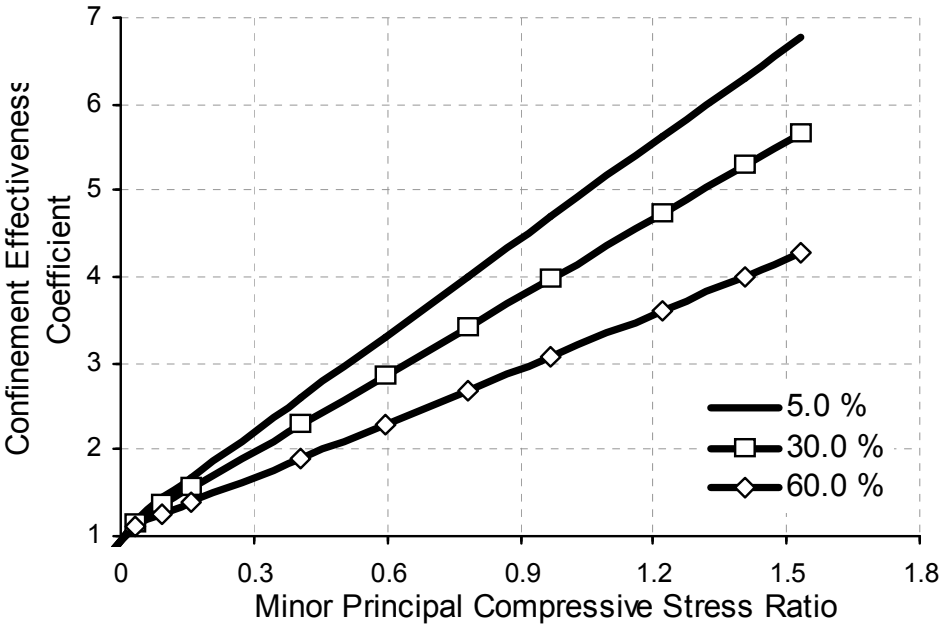

Figure 9.26 Plot of confinement effectiveness coefficient versus minor principal compressive stress ratio of concrete with varying pore water pressure parameters.

At high levels of transverse confinement, an increase in the pore water parameter (degree of saturation) has a significant detrimental effect on the friction angle ϕ_c and confinement effectiveness coefficient k_1, and the confinement effectiveness k_{cc} as the confining pressure becomes large.

Triaxial Extended Mohr-Coulomb Failure Criterion for Concrete

The failure surface of a Mohr-Coulomb material in principal stress space is plotted in **Figure 9.27**; from this figure it can be observed that the Mohr-Coulomb criterion models the failure envelope of concrete as a conical failure surface with an irregular hexagonal base section with sharp corners, which is not supported by experimental evidence. The typical failure surface of concrete in principal stress space is a cone with a noncircular base section, as is plotted in **Figure 9.28**.

In this research a mathematical model is developed in which the minor principal compressive stress-dependent two-parameter extended Mohr-Coulomb criterion (EMC) for concrete is incorporated into a triaxial failure surface for concrete with a noncircular base section, such as that shown in **Figure 9.28,** rather than an irregular hexagon base section as shown in **Figure 9.27**.

The proposed two-parameter EMC model, which is an extension of the modified Mohr-Coulomb (MMC) criterion of Eq. (9.20) with a degrading friction angle, is dependent upon the major σ_1 and minor σ_3 principal compressive stresses and *ignores the effects of the intermediate compressive principal stress* σ_2 on the strength of the confined concrete in a nonuniform triaxial compression state of stress.

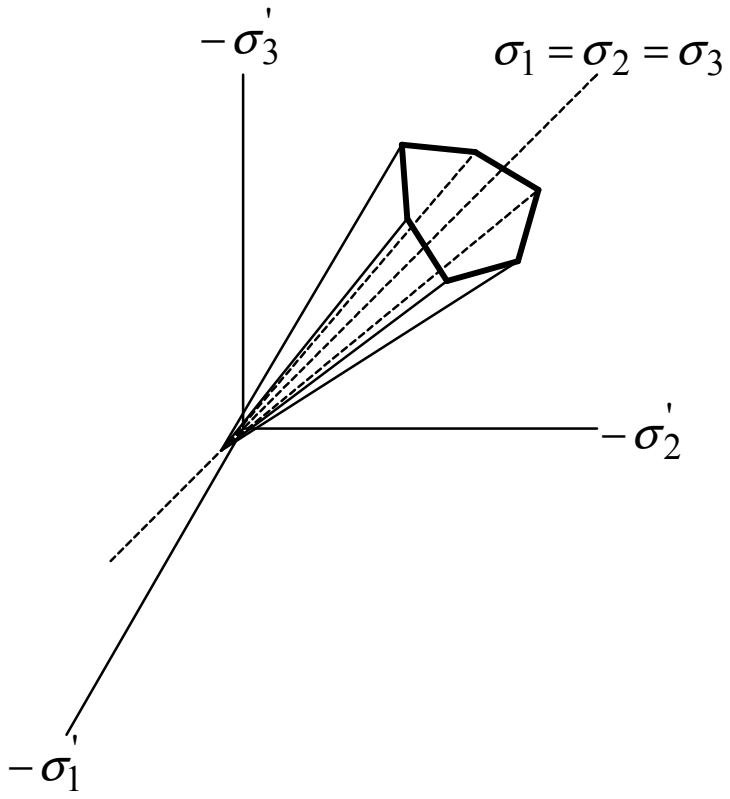

Figure 9.27 Plot of typical Mohr-Coulomb-type triaxial failure surface of concrete in principal stress space.

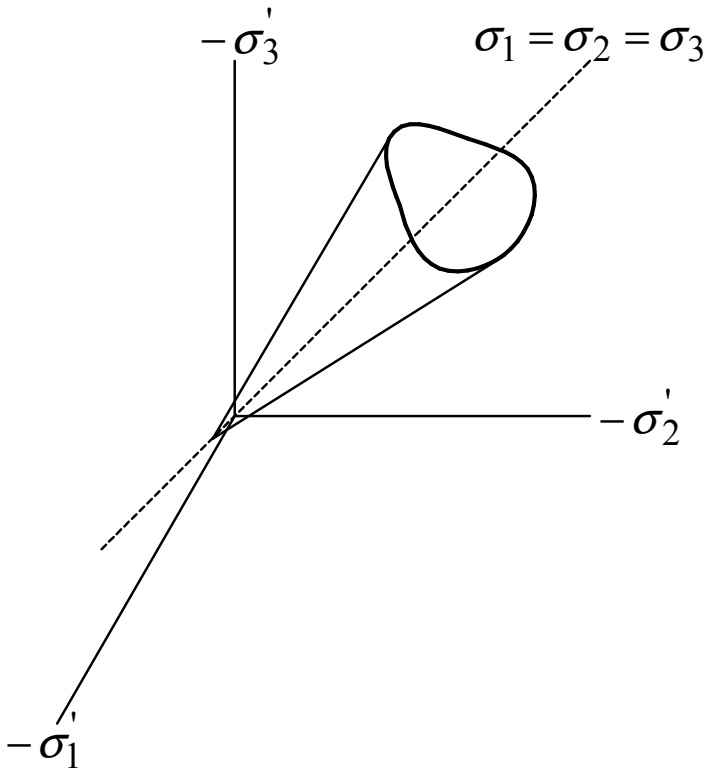

Figure 9.28 Plot of typical triaxial failure surface of concrete in principal stress space.

This is the main weakness of a Mohr-Coulomb-base criterion, including the MMC and EMC yield criteria. This obstacle can be easily overcome by transforming the Mohr-Coulomb-type principal stress-criterion into a yield surface or yield function with a noncircular base section as follows:

$$f\left(\sigma_1^{'},\sigma_2^{'},\sigma_3^{'}\right)=0 \tag{9.65}$$

where $\sigma_1^{'}$, $\sigma_2^{'}$, and $\sigma_3^{'}$ are the principal stresses, for which tensile stresses are considered positive. The principal compressive stresses σ_1, σ_2, and σ_3, and the principal stresses $\sigma_1^{'}$, $\sigma_2^{'}$, and $\sigma_3^{'}$ depend only on the load being applied and are not influenced by the choice of coordinate axis (x,y,z) or any particular orthogonal coordinate system, and as a result they are considered as stress invariants.

The principal stress yield surface of Eq. (9.65) can be written in terms of the three basic invariants of the stress tensor I_1, I_2, I_3 and the second J_2 and third J_3 deviatoric stress invariants as follows:

$$f\left(I_1,J_2,J_3\right)=0 \tag{9.66}$$

where the first I_1, second I_2, and third I_3 basic invariants of the stress tensor also have the same magnitudes for all choices of coordinate axis (x,y,z). These invariants are given in terms of the principal stresses $\sigma_1^{'}$, $\sigma_2^{'}$, and $\sigma_3^{'}$ as follows:

$$I_1=\frac{\sigma_1^{'}+\sigma_2^{'}+\sigma_3^{'}}{3} \tag{9.67}$$

$$I_2 = -\left(\sigma_1^{'}\sigma_2^{'} + \sigma_2^{'}\sigma_3^{'} + \sigma_3^{'}\sigma_1^{'}\right) \tag{9.68}$$

$$I_3 = \sigma_1^{'}\sigma_2^{'}\sigma_3^{'} \tag{9.69}$$

The second J_2 and third J_3 deviatoric stress invariants can also be given in terms of the principal stresses $\sigma_1^{'}$, $\sigma_2^{'}$, and $\sigma_3^{'}$ and the three basic invariants of the stress tensor I_1, I_2, I_3 as follows:

$$\begin{aligned} J_2 &= \frac{1}{6}\left[\left(\sigma_1^{'} - \sigma_2^{'}\right)^2 + \left(\sigma_2^{'} - \sigma_3^{'}\right)^2 + \left(\sigma_3^{'} - \sigma_1^{'}\right)^2\right] \\ &= \frac{(I_1)^2}{3} + I_2 \end{aligned} \tag{9.70}$$

$$\begin{aligned} J_3 &= \frac{1}{27}\left[\left(2\,\sigma_1^{'} - \sigma_2^{'} - \sigma_3^{'}\right) + \left(2\,\sigma_2^{'} - \sigma_3^{'} - \sigma_1^{'}\right) + \left(2\,\sigma_3^{'} - \sigma_1^{'} - \sigma_2^{'}\right)\right] \\ &= I_3 + \frac{I_1\, I_2}{3} + \frac{2(I_1)^3}{27} \end{aligned} \tag{9.71}$$

The principal stress invariants $\sigma_1^{'}$, $\sigma_2^{'}$, and $\sigma_3^{'}$ can also be transformed into the Haigh-Westergaard coordinates as follows:

$$\begin{Bmatrix} \sigma_1^{'} \\ \sigma_2^{'} \\ \sigma_3^{'} \end{Bmatrix} = \frac{1}{\sqrt{3}}\begin{Bmatrix} \xi \\ \xi \\ \xi \end{Bmatrix} + \sqrt{\frac{2}{3}}\rho\begin{Bmatrix} \cos(\theta) \\ \cos\left(\theta - \frac{2\pi}{3}\right) \\ \cos\left(\theta + \frac{2\pi}{3}\right) \end{Bmatrix} \tag{9.72}$$

where ξ is the hydrostatic stress invariant which represents the distance of the hydrostatic projection from the origin, ρ is the deviatoric stress invariant that represents the polar radius or orthogonal distance of the stress point from the hydrostatic axis, and θ

is the deviatoric polar radius, which is often referred to as the angle of similarity or the polar angle.

This polar angle describes the direction of the deviatoric stress invariant ρ from the projection of the principal axis onto the deviatoric plane, as is shown in **Figure 9.29**. $\theta = 0$ corresponds to triaxial extension, biaxial compression, or uniaxial tension stress states, and $\theta = 2\pi/3$ corresponds to uniaxial/triaxial compression and biaxial tension stress states.

These Haigh-Westergaard coordinates are given in terms of the first basic stress invariant I_1 and the second J_2 and third J_3 deviatoric stress invariants as follows:

$$\xi = \frac{I_1}{\sqrt{3}} \tag{9.73}$$

$$\rho = \sqrt{2J_2} \tag{9.74}$$

$$\theta = \frac{1}{3}\cos^{-1}\left[\frac{3\sqrt{3}\,J_3}{2(J_2)^{3/2}}\right] \tag{9.75}$$

The principal stress yield surface of Eq. (9.65) can be written in terms of the above Haigh-Westergaard coordinates as follows:

$$f(\xi, \rho, \theta) = 0 \tag{9.76}$$

The principal stress invariants σ_1', σ_2', and σ_3' can be written in terms of the Haigh-Westergaard coordinates using the transformation relationship of Eq. (9.72) as follows:

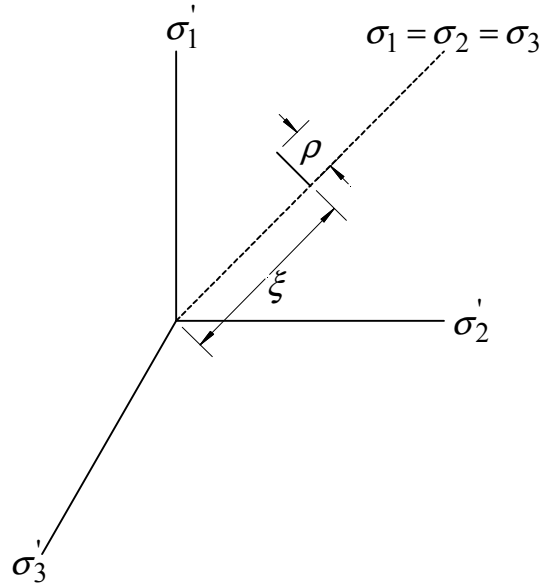

(a)

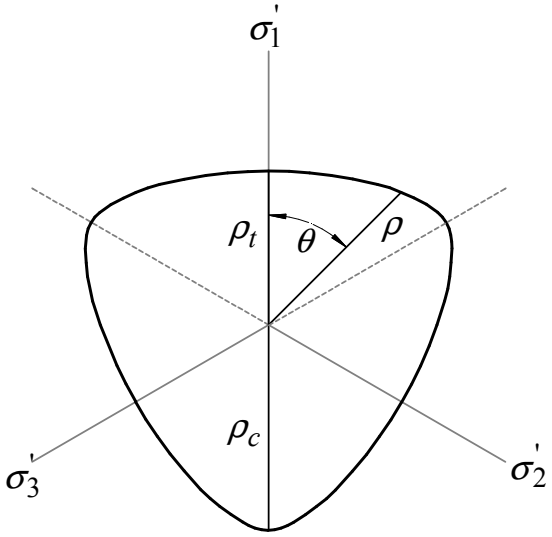

(b)

Figure 9.29 Plot of (a) Haigh-Westergaard coordinate system, (b) deviatoric plane or section.

$$\sigma_1^{'} = \frac{\xi}{\sqrt{3}} + \sqrt{\frac{2}{3}}\rho\cos(\theta) \tag{9.77}$$

$$\sigma_2^{'} = \frac{\xi}{\sqrt{3}} + \sqrt{\frac{2}{3}}\rho\cos\left(\theta - \frac{2\pi}{3}\right) \tag{9.78}$$

$$\sigma_3^{'} = \frac{\xi}{\sqrt{3}} + \sqrt{\frac{2}{3}}\rho\cos\left(\theta + \frac{2\pi}{3}\right) \tag{9.79}$$

The yield function of a Mohr-Coulomb-type criterion, including the MMC and EMC criteria introduced herein, can be expressed in terms of the major $\sigma_1^{'}$ and minor $\sigma_3^{'}$ principal stresses using Eq. (9.65) as follows:

$$\frac{\left(\sigma_1^{'} - \sigma_3^{'}\right)}{2} + \frac{\left(\sigma_1^{'} + \sigma_3^{'}\right)}{2}\sin(\phi_c) - c_u\cos(\phi_c) = 0 \tag{9.80}$$

The previous yield function can also be expressed using Eq. (9.25) as:

$$\left(\frac{\sigma_1^{'}}{f_{co}\sqrt{k_t}}\right)\left[\frac{1+\sin(\phi_c)}{\cos(\phi_c)}\right] - \left(\frac{\sigma_3^{'}}{f_{co}\sqrt{k_t}}\right)\left[\frac{1-\sin(\phi_c)}{\cos(\phi_c)}\right] - 1 = 0 \tag{9.81}$$

Substituting the Haigh-Westergaard transformation relationships for $\sigma_1^{'}$ of Eq. (9.77) and $\sigma_3^{'}$ of Eq. (9.79) into the above yield function yields:

$$\sqrt{\frac{2}{3k_t}}\left\{\left(\frac{\rho}{f_{co}}\right)\left[\sqrt{3}\sin\left(\theta + \frac{\pi}{3}\right)\sec(\phi_c) + \cos\left(\theta + \frac{\pi}{3}\right)\tan(\phi_c)\right] + \sqrt{2}\left(\frac{\xi}{f_{co}}\right)\tan(\phi_c)\right\} - 1 = 0 \tag{9.82}$$

The above Haigh-Westergaard representation of a Mohr-Coulomb-type criterion also yields a deviatoric section with an irregular hexagon shape as shown in **Figure 9.30**.

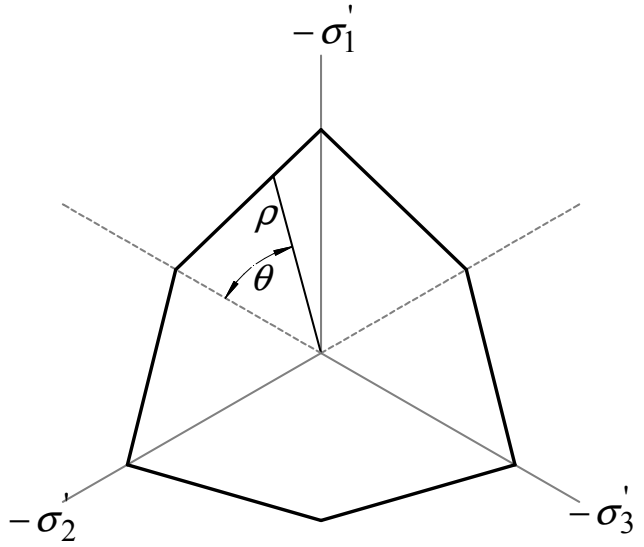

Figure 9.30 Plot of typical deviatoric section of a Mohr-Coulomb-type yield criterion.

The Mohr-Coulomb-type criterion of Eq. (9.82) can be transformed into a yield surface with a smooth noncircular deviatoric section (Menetrey 1994), modified herein using c_u of Eq. (9.25), that matches the Mohr-Coulomb deviatoric section only at the compressive ρ_c and tensile ρ_t meridians as shown in **Figure 9.31** as follows:

$$\left(\frac{\rho}{f_{co}}\right)\sqrt{\frac{2}{3k_t}}\left[\frac{3-\sin(\phi_c)}{r(\theta,e)}\right]+\left(\frac{\xi}{f_{co}}\right)\left[\frac{2\tan(\phi_c)}{\sqrt{3k_t}}\right]-1=0 \tag{9.83}$$

The term $r(\theta,e)$ of Eq. (9.83) is a radial function that describes the shape of the deviatoric trace and the radial distance from the hydrostat. The radial function $r(\theta,e)$ utilized herein is that introduced by Papanikolopoulos and Papadrakakis (2006), which transforms the circular trace of the deviatoric polar radius $\rho(\theta)$ into a triple symmetric smooth deviatoric trace of the yield function.

This radial function is defined in the sextant $0\le\theta\le\pi/3$ and extends to all polar directions $0\le\theta\le2\pi$ due to symmetry and is given by:

$$r(\theta,e)=\frac{e+\cos\theta-1}{\cos\theta\ \ [4(1-e)(\cos\theta-1)+1)]} \tag{9.84}$$

where e defines the eccentricity or out-of-roundness of the deviatoric trace where $0.50\le e\le1.0$.

For a pressure sensitive material such as concrete, the eccentricity e introduced in Eqs. (9.83) and 9.84) is defined as the ratio between the polar radius of the tensile ρ_t and the compressive ρ_c meridian as follows:

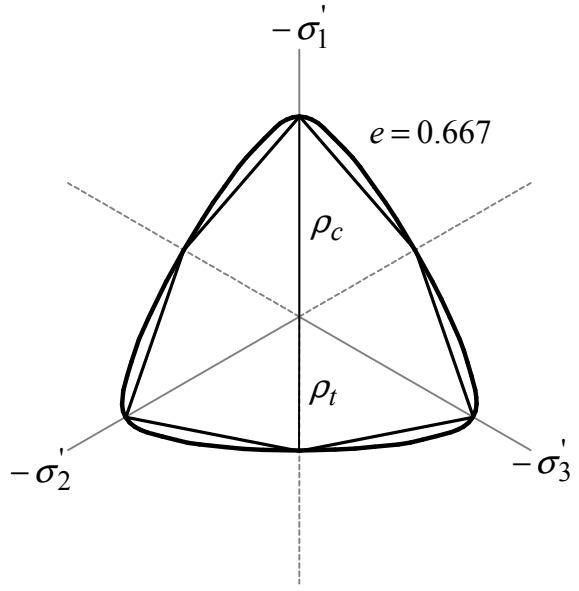

(a)

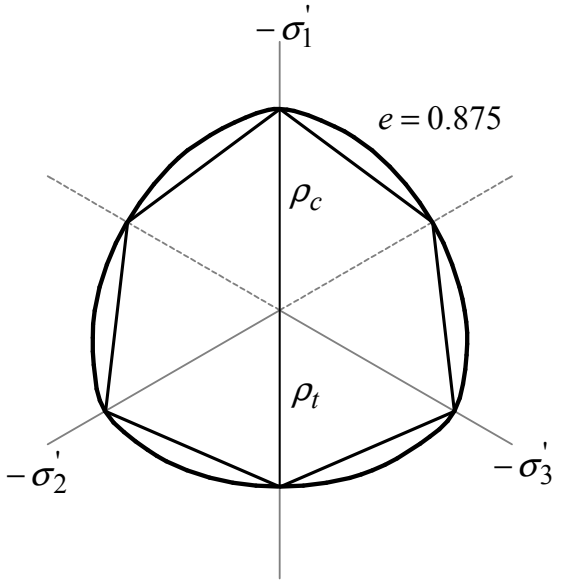

(b)

Figure 9.31 Plot of deviatoric stress projections of eccentricity: (a) $e = 0.667$ and (b) $e = 0.875$.

$$e = \frac{\rho_t}{\rho_c} \tag{9.85}$$

The radial deviatoric function $r(\theta, e)$ of Eq. (9.84) cannot exactly trace the irregular hexagonal shape of the Mohr-Coulomb-type deviatoric section, but it can exactly match the tensile ρ_t and compressive ρ_c polar radius by using the above definition of eccentricity e, as shown in **Figure 9.31**, which is plotted, or a deviatoric section described by $\rho_c\, r(\theta, e)$, with a unity compression meridian (i.e., $\rho_c = 1.0$), and the irregular hexagonal deviatoric section of the Mohr-Coulomb criterion having an eccentricity $e = 0.667$ and $e = 0.875$.

In **Figures 9.32** and **9.33** the shape of the deviatoric section of a Mohr-Coulomb-type criterion of various eccentricities with a unity compression meridian (i.e., $\rho_c = 1.0$) is shown. From these figures it can be observed that at low eccentricities the deviatoric section becomes triangular as $e \to 0.50$ (see **Figure 9.32)**, and hexagonal as $e \to 1.0$ (see **Figure 9.33)**.

As shown in **Figure 9.32(a)**, when $e = 0.50$, the shape of the deviatoric section is that of the Rankine yield criteria for tensile cracking; when $e = 1.0$ it describes the hexagonal deviatoric section of the Tresca maximum shear stress criterion for materials exhibiting insensitivity to hydrostatic pressure, as shown in **Figure 9.33(b)**.

For eccentricities e ranging between $0.50 < e < 1.0$, the shape of the deviatoric section becomes an irregular hexagon that resembles a distorted triangular shape at small eccentricities as $e \to 0.50$.

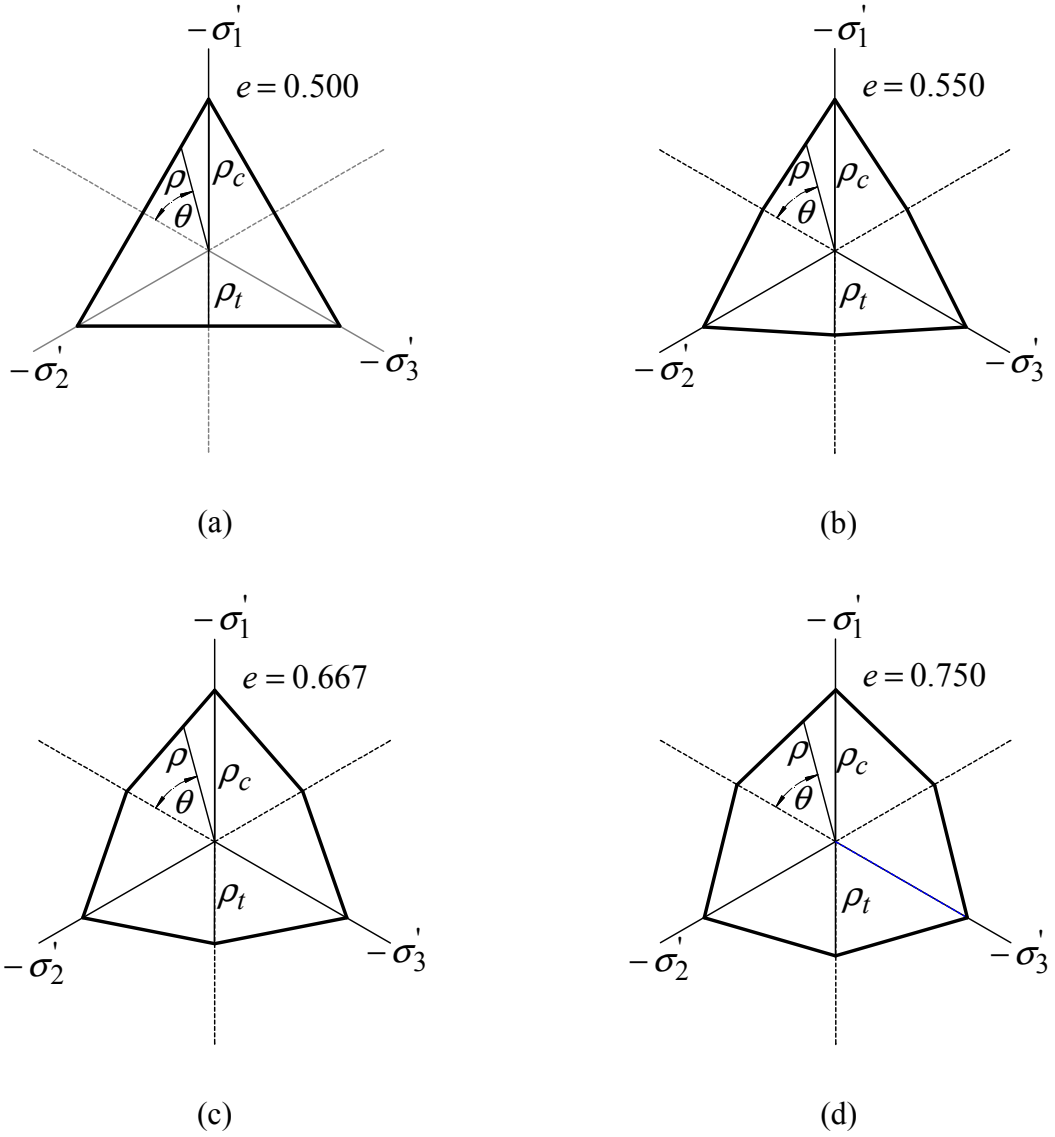

Figure 9.32 Plot of deviatoric stress projections of the Mohr-Coulomb yield criterion of various eccentricities: (a) $e = 0.500$, (b) $e = 0.550$, (c) $e = 0.667$, and (d) $e = 0.750$.

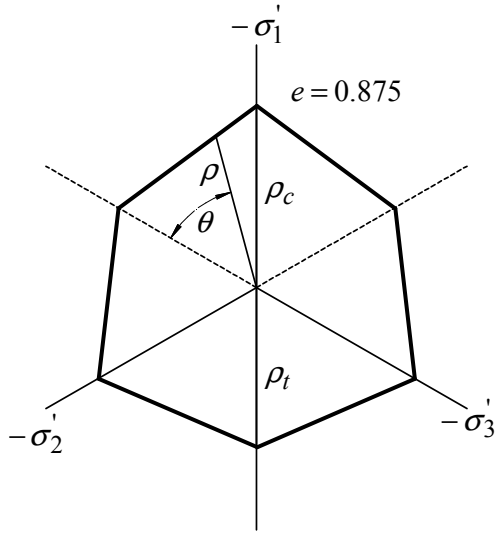

(a)

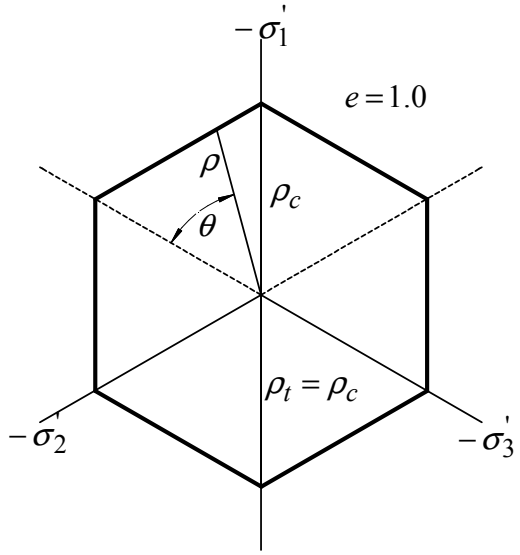

(b)

Figure 9.33 Plot of deviatoric stress projections of the Mohr-Coulomb yield criterion various eccentricities: (a) $e = 0.875$ and (b) $e = 1.0$.

As the eccentricity increases, the essentially triangular deviatoric section achieves an irregular hexagonal shape that becomes more uniform as $e \to 1.0$, as shown in **Figures 9.32** and **9.33**.

In reference to **Figures 9.34** and **9.35**, it can be observed that at low eccentricities the deviatoric section described by $\rho_c \, r(\theta, e)$, with a unity compression meridian (i.e., $\rho_c = 1.0$) becomes triangular as $e \to 0.50$ and circular as $e \to 1.0$. When $e = 0.50$, the deviatoric trace function $r(\theta, e)$ of Eq. (9.84) describes the deviatoric section of the Rankine yield criteria for tensile cracking.

When $e = 1.0$, the radial function $r(\theta, e)$ of Eq. (9.84) describes the deviatoric section of the Huber-Mises yield criteria for materials exhibiting insensitivity to hydrostatic pressure, since for $e = 1.0$, $\phi_c = 0^\circ$, which corresponds to a frictionless material.

The radial function $r(\theta, e)$ of Eq. (9.84) cannot exactly trace the irregular hexagon shape of the Mohr-Coulomb deviatoric section, but it can be calibrated to exactly match the tensile ρ_t and compressive ρ_c polar radius when the eccentricity is given by (Menetrey 1994):

$$e = \frac{\rho_t}{\rho_c} = \frac{3 - \sin(\phi_c)}{3 + \sin(\phi_c)} \tag{9.86}$$

In reference to **Figures 9.34** and **9.35** and Eq. (9.86), it can be observed that for low eccentricities the deviatoric section of a Mohr-Coulomb-type criterion becomes triangular as $e \to 0.50$, i.e., when $\phi_c = \phi_t = 90^\circ$, and hexagonal as $e \to 1.0$, i.e., when $\phi_c = 0^\circ$.

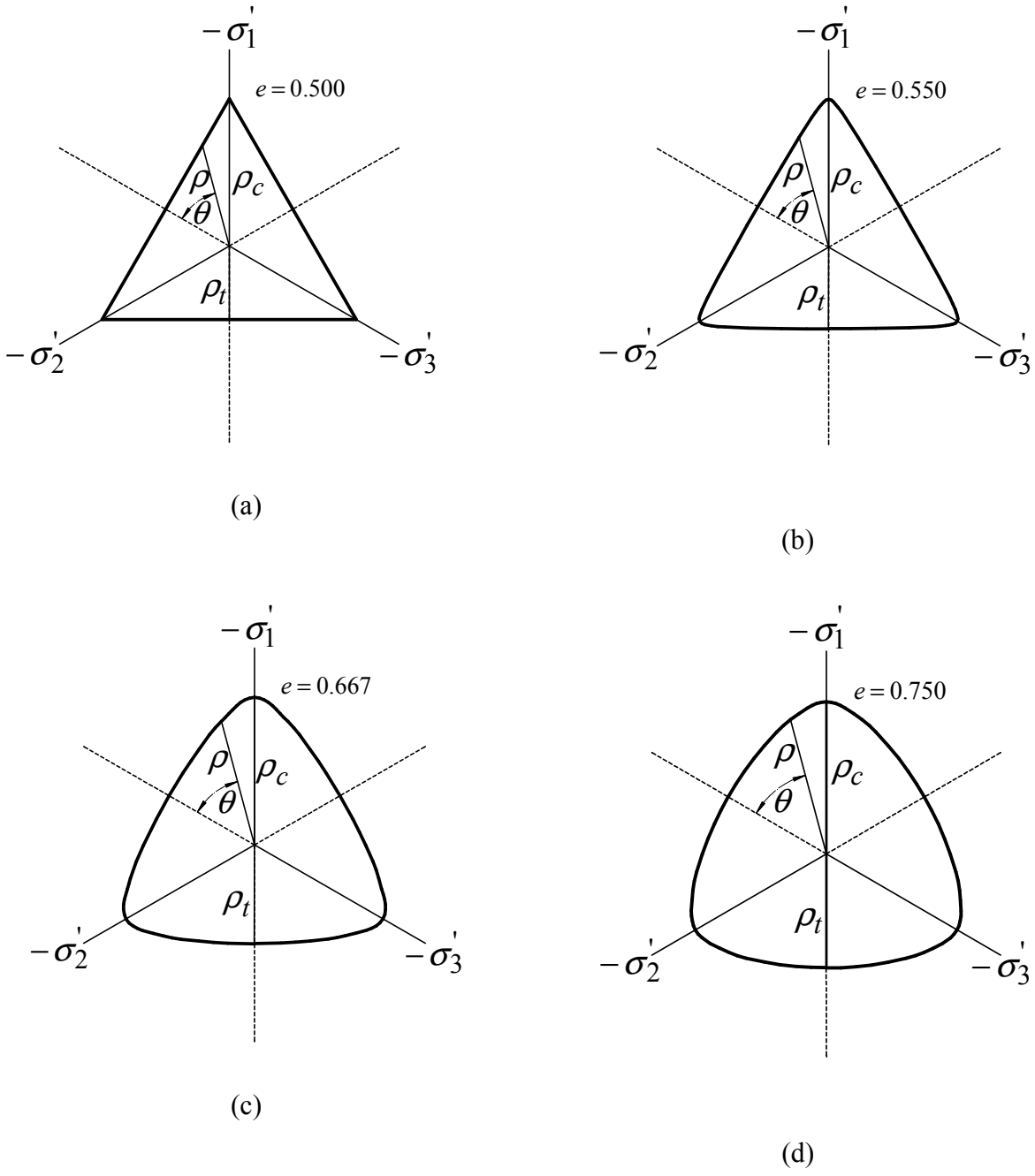

Figure 9.34 Plot of deviatoric stress projections of various eccentricities: (a) $e = 0.500$, (b) $e = 0.550$, (c) $e = 0.667$, and (d) $e = 0.750$.

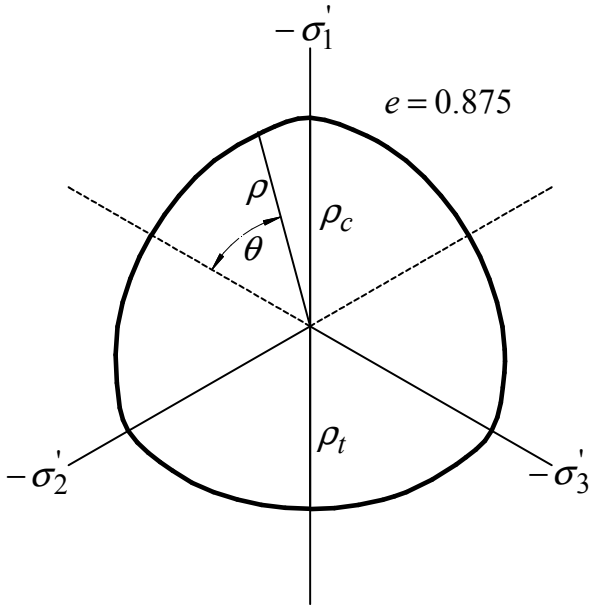

(a)

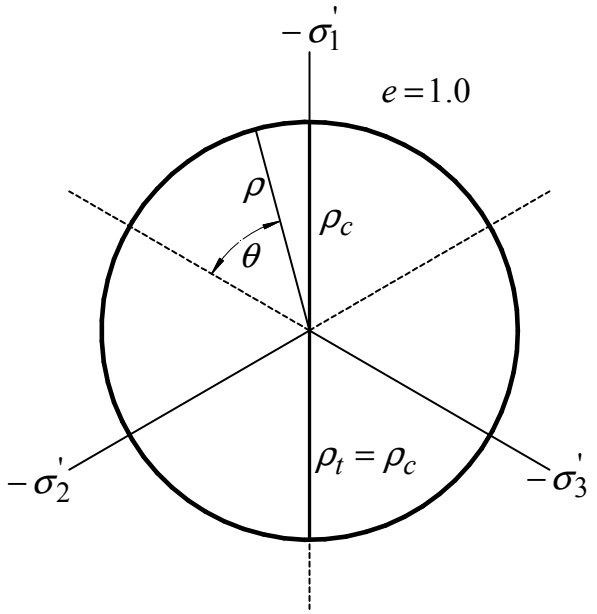

(b)

Figure 9.35 Plot of deviatoric stress projections of various eccentricities: (a) $e = 0.875$ and (b) $e = 1.0$.

When $0.50 < e < 1.0$, the deviatoric section of the Mohr-Coulomb-type criterion can evolve from a distorted triangular section to an irregular hexagon, since $0^\circ < \phi_c < 90°$.

As shown in **Figure 9.36** for the MMC criterion, the deviatoric section of the concrete material evolves from a triangular section to an irregular hexagonal section having a constant eccentricity e as a result of the assumption of a constant angle of internal friction ϕ_c of the concrete material, which as previously indicated, is not supported by the experimental evidence.

As shown in **Figure 9.37** for the EMC criterion, the deviatoric section of the concrete material evolves from a triangular section to an irregular hexagon section having a variable eccentricity e as a result of the hydrostatic stress-dependent angle of internal friction ϕ_c of the concrete material assumption included in the EMC criterion.

For dry normal-weight concrete the angle of internal friction ϕ_c is in the range of $\phi_t \le \phi_c \le \phi_b$, where ϕ_t is the angle of separation with a value of $\phi_t = 90^\circ$ and ϕ_b is the basic or residual angle of shearing resistance of dry concrete with an average value of $\phi_b = 35^\circ$.

This indicates that for dry normal-weight concrete, the eccentricity e of Eq. (9.86), included in the radial function $r(\theta, e)$ of Eq. (9.84), varies between $0.50 \le e \le 0.68$ for $\phi_t \le \phi_c \le \phi_b$. The lower value of $e = 0.50$ corresponds to $\sigma_1' = f_{to}$, $\phi_c = \phi_t = 90^\circ$, and $\xi = f_{to}/\sqrt{3}$, and the upper value $e = e_b = 0.68$ corresponds to $\xi = \sigma_1' = \sigma_3 = \infty$, $\phi_c = \phi_b = 35^\circ$. e_b is the basic eccentricity of dry normal-weight concrete.

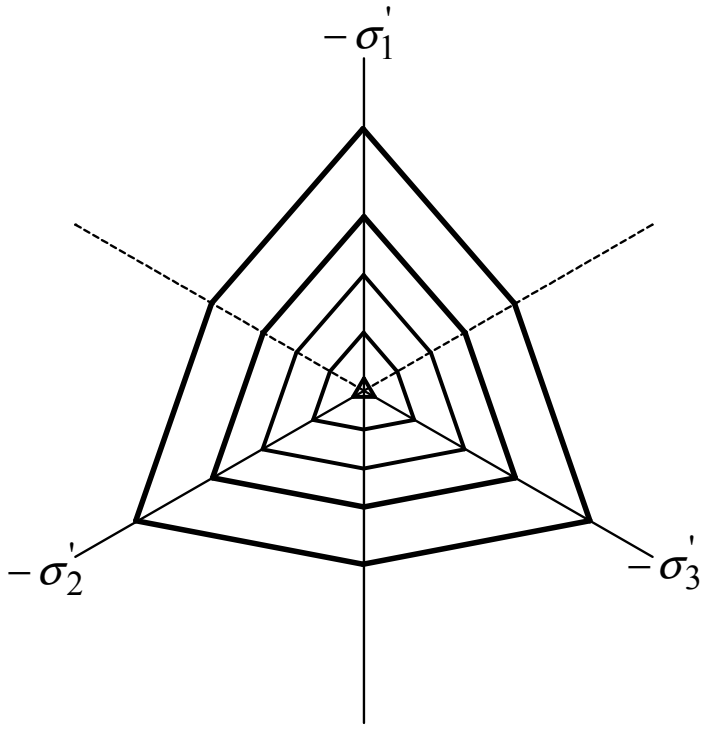

Figure 9.36 Plot of deviatoric stress projections of the MMC criterion for concrete.

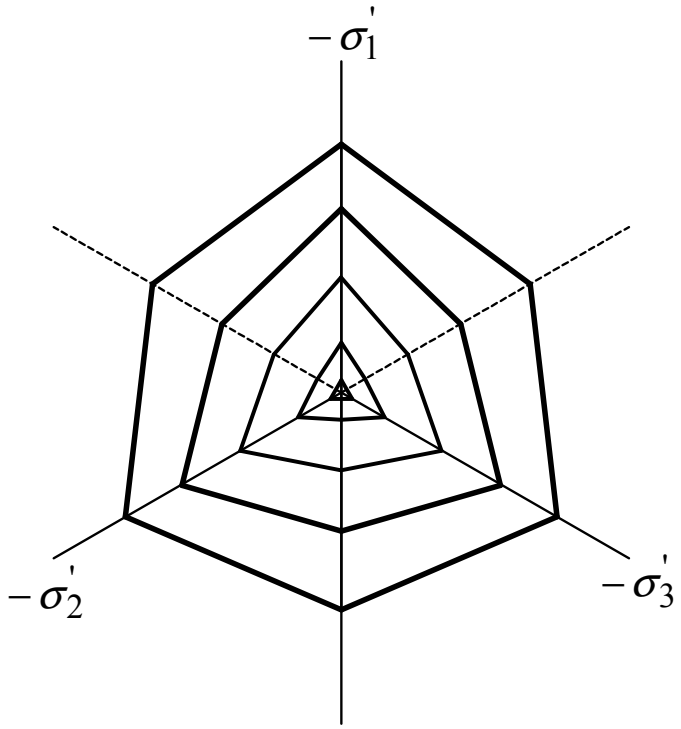

Figure 9.37 Plot of deviatoric stress projections of the EMC criterion for concrete.

For normal-weight concrete having an unconfined compressive strength ranging between $17\ \text{MPa} \le f_{co} \le 55\ \text{MPa}$, the uniaxial angle of internal friction ϕ_u of Eq. (9.28) is in the range of $51.2° \le \phi_u \le 57.7°$. For this range of compressive strengths the eccentricity e_u of the unconfined concrete (i.e., for $\xi = -f_{co}/\sqrt{3}$) varies between $0.56 \le e_u \le 0.59$, which is also obtained by substituting $\phi_c = \phi_u$ into e of Eq. (9.86). The lower value of $e = e_u = 0.56$ corresponds to the higher strength concrete and $e = e_u = 0.59$ to low strength concrete.

At high levels of confinement, the eccentricity of highly confined normal-weight wet concrete with a pore water pressure parameter n_{PW} of 50% is $e = e_{be} = 0.78$. Essentially dry concrete having a pore water pressure parameter n_{PW} of 5% has an eccentricity of $e = e_{be} = 0.678$ at high levels of confinement. This indicates that for high moisture content concrete at high levels of confinement, the deviatoric section of the concrete has a more rounded triangular shape when compared to that of dry concrete, as is shown in **Figure 9.34(c)** and **(d)**, respectively. e_{be} is the effective eccentricity of highly confined wet concrete, which is found by substituting the pore pressure parameter n_{PW} into Eq. (9.63), substituting $(k_1)_{be}$ of Eq. (9.63) into Eq. (9.64), and substituting ϕ_{be} of Eq. (9.64) into Eq. (9.86) with $\phi_c = \phi_{be}$.

The smooth Mohr-Coulomb-type criterion of Eqs. (9.83)-(9.86) can be further simplified using the following generalized two-parameter triaxial extended Mohr-Coulomb (TEMC)-type failure criterion for concrete as follows:

$$\bar{\gamma}_f \rho + \bar{\beta}_f \xi - 1 = 0 \tag{9.87}$$

The above two-parameter TEMC criterion simplifies the Mohr-Coulomb failure criterion of Eqs. (9.82) and (9.83), as it broadens the applicability of the MMC and EMC criterion by including the sensitivity of the concrete's behavior to the intermediate principal stress $\sigma_2^{'}$ for concrete subjected to a triaxial compression state of stress, as well as the sensitivity of the angle of internal friction ϕ_c of the EMC model.

The above material parameters $\bar{\gamma}_f$ and $\bar{\beta}_f$ apply to plain concrete in a triaxial compression state of stress for which $\sigma_1 \geq \sigma_2 \geq \sigma_3$ or $\sigma_1^{'} \geq \sigma_2^{'} \geq \sigma_3^{'}$ with $\sigma_1^{'} = -\sigma_3$, $\sigma_2^{'} = -\sigma_2$, and $\sigma_3^{'} = -\sigma_1$. The case of $\sigma_1^{'} > \sigma_2^{'} > \sigma_3^{'}$ corresponds to rectangular, oval, and elliptical FCC sections which have an aspect ratio α_{sh} of Eq. (4.2) greater than unity, i.e., $\alpha_{sh} > 1.0$; the case of $\sigma_1^{'} = \sigma_2^{'} > \sigma_3^{'}$ corresponds to circular and square FRP-confined concrete sections which have a unity aspect ratio, i.e., $\alpha_{sh} = 1.0$

The effects of the intermediate principal stress $\sigma_2^{'}$ on the compressive strength of the confined concrete are considered herein for rectangular, oval, and elliptical FCC sections, which have an aspect ratio α_{sh} of Eq. (4.2) greater than unity (i.e., $\alpha_{sh} > 1.0$ or $H_c > B_c$). For these sections, the effectively confined concrete core is in a nonuniform biaxial confinement state of stress, i.e., $\sigma_1^{'} > \sigma_2^{'} > \sigma_3^{'}$, as a result of the nonuniform effective transverse stiffness of the FRP jacket, since for these sections $\left(E_{je}\right)_B > \left(E_{je}\right)_H$; $\left(E_{je}\right)_B$ was defined in Eq. (4.15) and $\left(E_{je}\right)_H$ in Eq. (4.16).

The nonuniform transverse stiffness of the FRP jacket affects the transverse and diagonal dilation of the FCC section, as measured by the diagonal ε_j, minor ε_B, and major ε_H transverse dilation strains in the FCC section, as indicated in Chapters 4-6.

The material parameters $\bar{\gamma}_f$ and $\bar{\beta}_f$ of the proposed two-parameter TEMC criterion of Eq. (9.87) are given in terms of the material parameters γ_f of Eq. (9.37) and β_f of Eq. (9.38) of the generalized two-parameter MMC yield criteria of Eq. (9.20) as follows:

$$\bar{\gamma}_f = \frac{\gamma_f}{r(\theta,e)}\left(\frac{\sqrt{6}}{6}\right)\left[\frac{3-\sin(\phi_c)}{1-\sin(\phi_c)}\right] \tag{9.88}$$

$$\bar{\beta}_f = \beta_f\left(\frac{2\sqrt{3}}{3}\right)\left[\frac{\sin(\phi_c)}{1+\sin(\phi_c)}\right] = \gamma_f\left(\frac{2\sqrt{3}}{3}\right)\left[\frac{\sin(\phi_c)}{1-\sin(\phi_c)}\right] \tag{9.89}$$

The deviatoric section of the generalized two-parameter TEMC criterion of Eq. (9.87)-(9.89), using the radial function $r(\theta,e)$ of Eq. (9.84) and the eccentricity e of Eq. (9.86) is plotted in **Figure 9.38.**

When the confined concrete core is subjected to uniform biaxial confinement, i.e. when $\sigma_1' = \sigma_2' > \sigma_3'$, the generalized two-parameter TEMC criterion of Eq. (9.87) reduces to the EMC criterion, which combines the generalized two-parameter MMC criterion of Eq. (9.20) and the minor principal compressive stress σ_3 dependent degrading friction angle model of Eq. (9.40) and Eqs. (9.56)-(9.61).

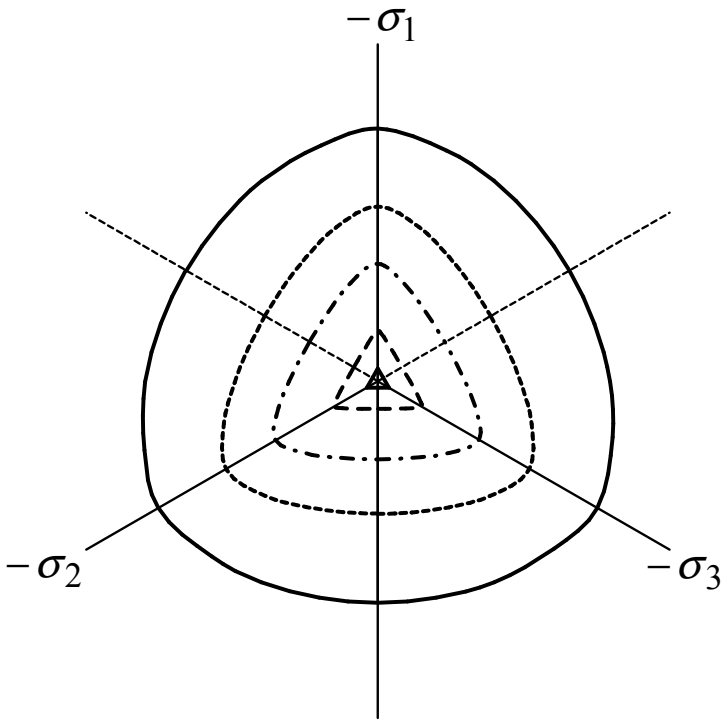

Figure 9.38 Plot of deviatoric stress projections of the TEMC criterion for concrete.

The smooth Mohr-Coulomb-type criterion of Eqs. (9.83)-(9.85) is similar to the Menetrey (1994) smooth coulomb yield criterion, in which the eccentricity e of Eq. (9.89) is considered a constant throughout its loading history, as shown in **Figure 9.39,** i.e, a constant angle of internal friction which is in disagreement with the experimental evidence, as was demonstrated in **Figures 9.16-9.21**. Kang and Willam (1999) considered that the eccentricity e of Eq. (9.86) is a hyperbolic empirical function of the hydrostatic stress invariant ξ of Eq. (9.73), i.e., $e = f(\xi)$, which allows the shape of the deviatoric section to expand from triangular to circular shapes with increasing compressive hydrostatic pressure.

In the TEMC criterion for concrete in a triaxial compression state of stress, introduced herein, the eccentricity e of Eq. (9.86) is considered to be a nonlinear function of the minor principal compressive stress σ_3. This is a direct result of the hyperbolic relationship introduced in the minor principal compressive stress-dependent degrading friction angle model of Eq. (9.40) and Eqs. (9.58)-(9.60). As a result, the proposed TEMC model allows the shape of the deviatoric section to expand from triangular to rounded triangular shapes with increasing compressive hydrostatic pressure, as shown in **Figure 9.38**.

The detrimental effects of excess pore water on the compressive behavior of the concrete in a triaxial compression state of stress are included in the TEMC model, as shown in **Figures 9.25, 9.26,** and **9.34(d)** as $\phi_c \rightarrow \phi_{be}$, with ϕ_{be} being the effective basic angle of internal friction of Eqs. (9.63) and (9.64). Excess pore water pressure affects the roundness of the deviatoric section due to the reduction in the angle of internal friction ϕ_c, as demonstrated in **Figures 9.25** and **9.26**.

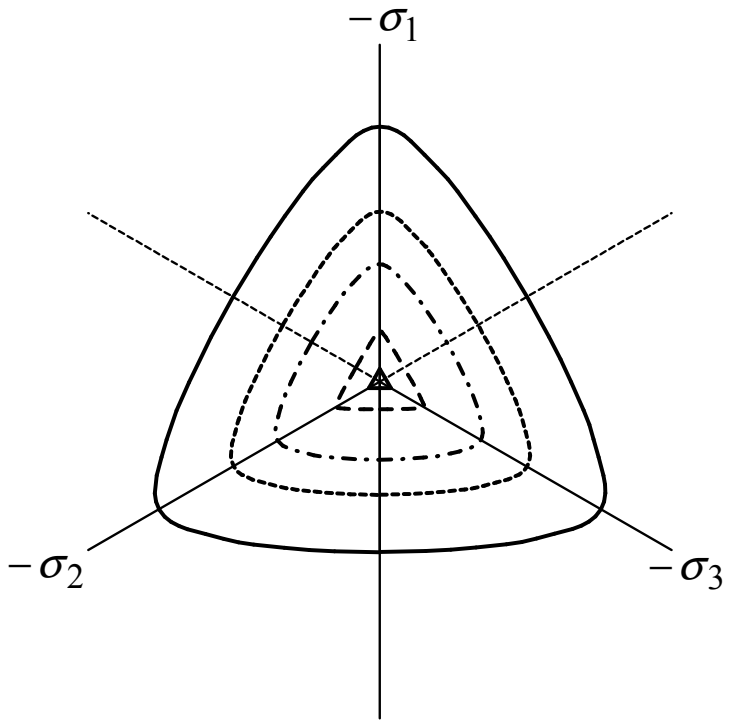

Figure 9.39 Plot of deviatoric stress projections of the smooth Mohr-Coulomb criterion with a constant eccentricity e.

Determination of the Intermediate and Minor Compressive Stress in FRP-Confined Concrete Sections

The proposed EMC and TEMC models for plain concrete in a triaxial compression state of stress require the determination of the minor σ_3 and intermediate σ_2 principal compressive stresses in the biaxially confined concrete section. Thus far this chapter has included a generalized Mohr-Coulomb model for confined plain concrete; its applicability is extended herein for the cases of rectangular (RFCC), square (SFCC), oval (SFCC), circular (CFCC), and elliptical (EFCC) FRP-confined concrete (FCC) sections in compression confined by a continuous linear elastic FRP jacket.

As was demonstrated in Chapters 4-6, the transverse and diagonal equilibrium of the FRP-confined concrete depends on the effective transverse stiffness of the FRP jacket, $\left(E_{je}\right)_B$ of Eq. (4.15), and the shape of the FRP-jacketed section.

For the aforementioned FCC sections, the minor σ_3 and intermediate σ_2 principal compressive stresses can be found from the vertical and horizontal equilibrium of the confined concrete core bounded by the major H_{sh}, minor B_{sh}, and diagonal D_{sh} core dimensions of the confined concrete and the diagonal equilibrium of the FCC section as shown in **Figures 9.40-9.44**.

The main core diagonal D_{sh} can be found using Eqs. (5.11) or (5.16), with the diagonal parameter χ_{sh} of Eq. (5.11) summarized in **Table 5.1.** The major H_{sh} and minor B_{sh} core dimensions can be found using Eq. (5.26), using the angle of inclination θ_d of the main diagonal D_c of Eq. (4.1).

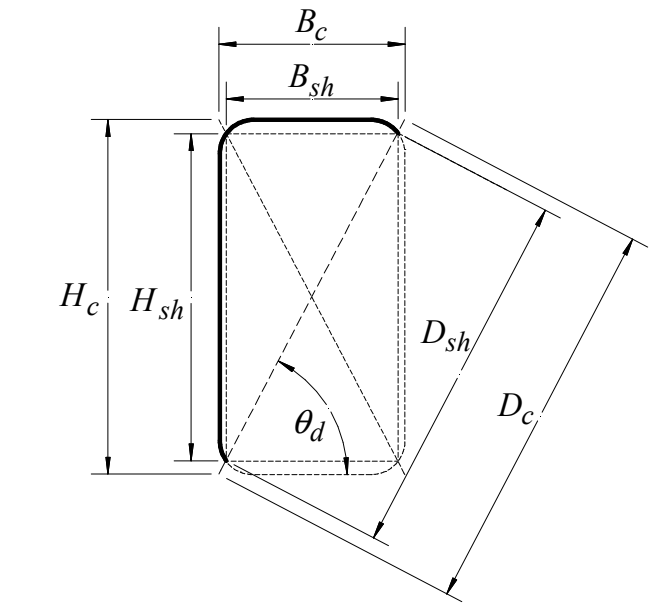

(a)

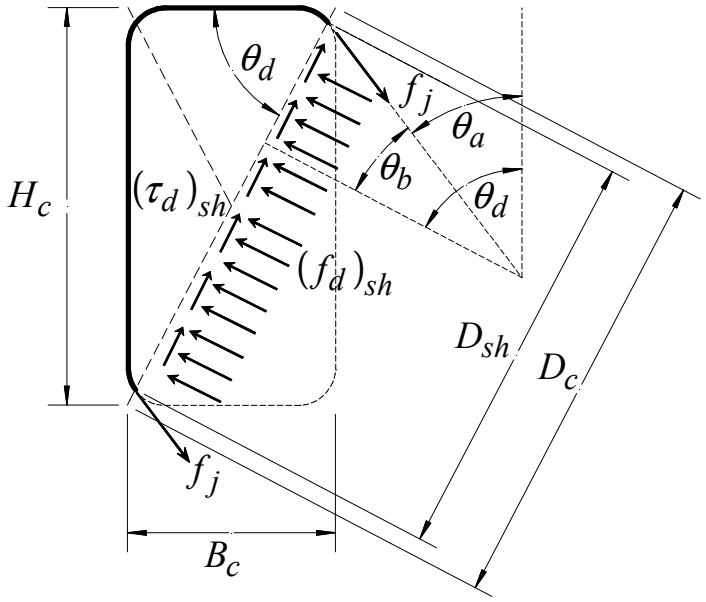

(b)

Figure 9.40. Main FRP-confined concrete core in a rectangular section: (a) typical section geometry and (b) diagonal equilibrium.

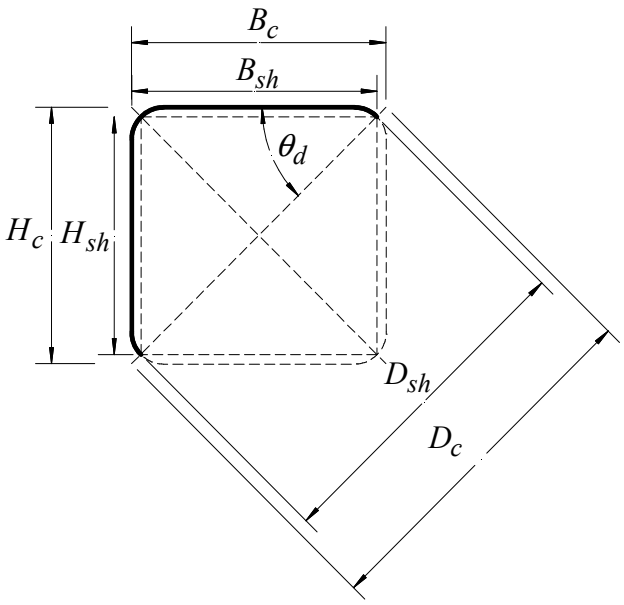

(a)

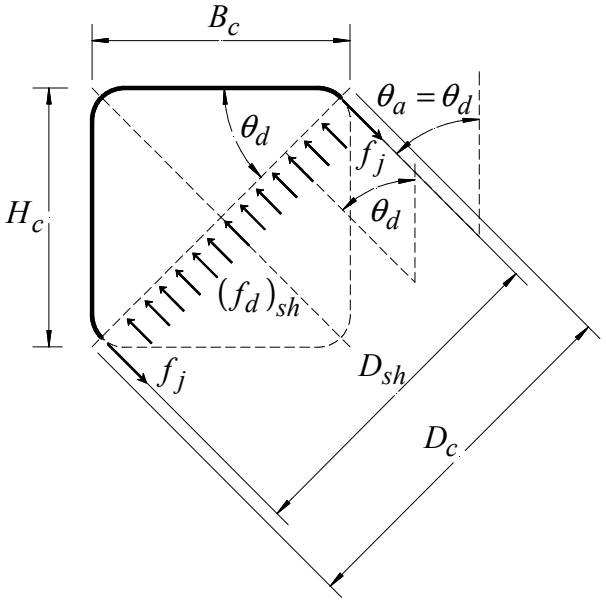

(b)

Figure 9.41 Main FRP-confined concrete core in a square section: (a) section geometry and (b) diagonal equilibrium.

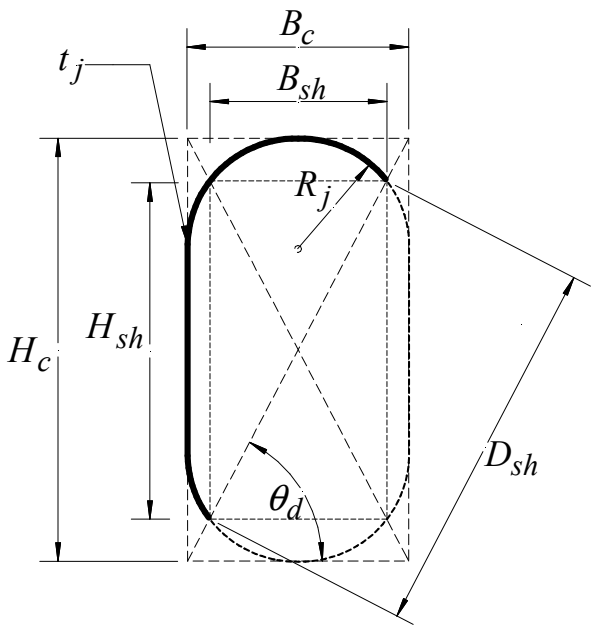

(a)

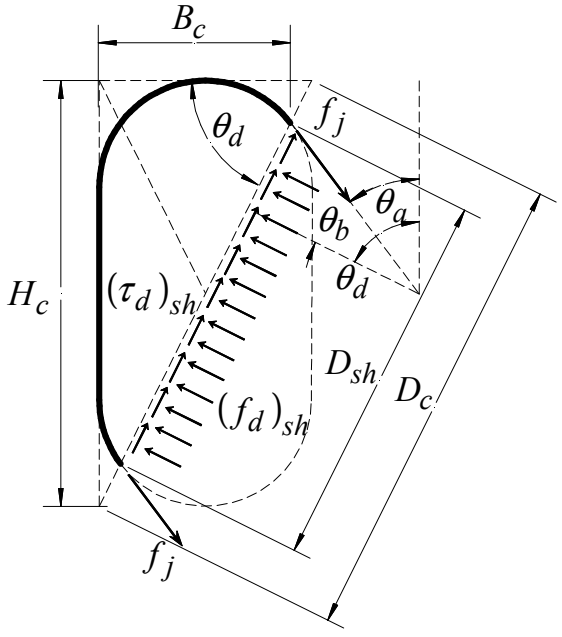

(b)

Figure 9.42 Main FRP-confined concrete core in an oval section: (a) section geometry and (b) diagonal equilibrium.

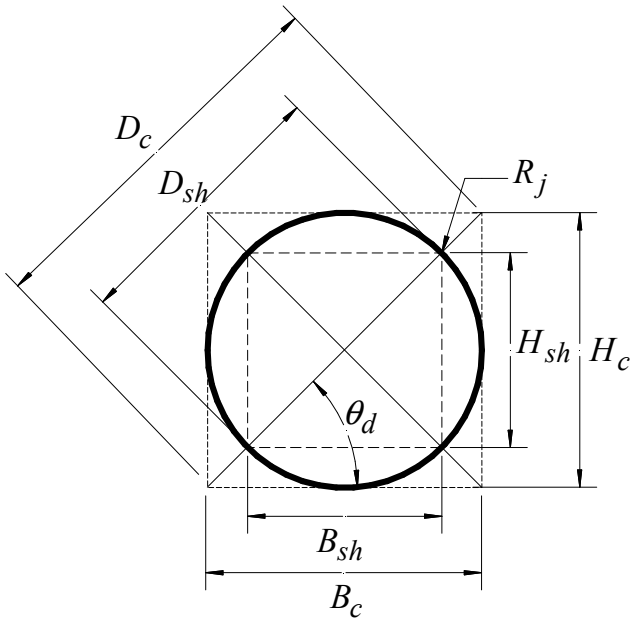

(a)

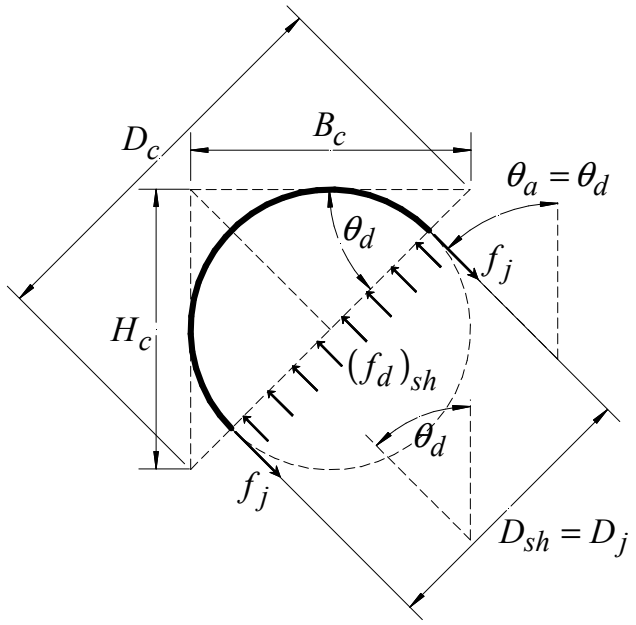

(b)

Figure 9.43 Main FRP-confined concrete core in a circular section: (a) section geometry and (b) diagonal equilibrium.

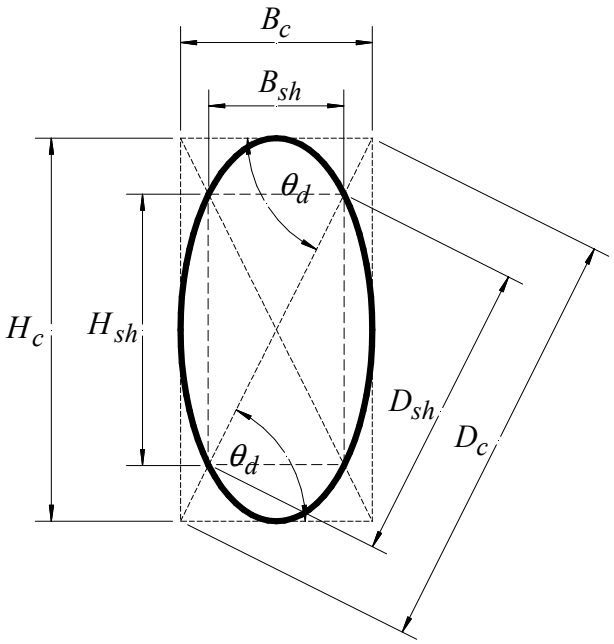

(a)

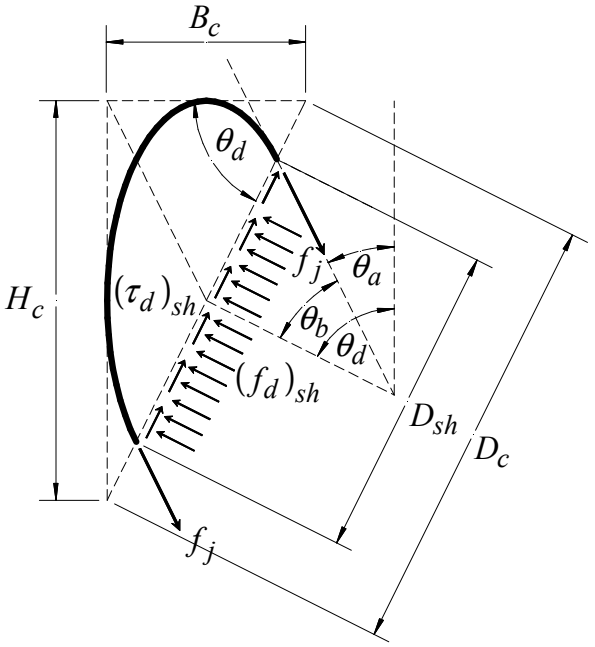

(b)

Figure 9.44 Main FRP-confined concrete core in an elliptical: (a) section geometry and (b) diagonal equilibrium.

As shown in these figures, the aspect ratio α_{sh} of rectangular FCC sections is $\alpha_{sh} = H_c / B_c > 1.0$, for square and circular sections $\alpha_{sh} = 1.0$, and for elliptical sections $\alpha_{sh} > 1.0$. For rectangular sections H_{sh}, B_{sh}, and D_{sh} can be found using Eqs. (5.24), (5.25) and (5.26), respectively; for square FCC sections using Eqs. (5.30), (5.31), and 5.32, respectively; for oval sections using Eqs. (5.34), (5.35), and (5.26), respectively; and for both circular and elliptical FCC sections using Eqs. (5.37), (5.38), and (5.39), respectively. As shown in **Figures 9.40-9.44**, H_c, B_c, and D_c are the *overall* major, minor, and diagonal dimensions of the FCC section, respectively. In addition, θ_d is the angle of inclination of the main diagonal D_c as given by Eq. (4.1).

In these figures $(f_d)_{sh}$ is the diagonal confining stress perpendicular to the main diagonal D_{sh}, at a given diagonal jacket strain ε_j, which can be found using Eqs. (5.7) and (5.12). In addition, $(\tau_d)_{sh}$ is the diagonal shear stress along the main diagonal, which can be found using Eqs. (5.8), (5.10), and (5.14).

The effectively confined concrete core within the elastic FRP jacket concrete, as shown in **Figure 9.45,** has a generalized rectangular shape as shown by the dashed lines in **Figures 9.40-9.44.** This generalized rectangle shown in **Figure 9.45(a)** can be separated into four triangular wedges having the dimensions shown in **Figure 9.45(b)**.

From **Figure 9.45(b)**, H_{sh}, $B_{sh}/2$, and $D_{sh}/2$ are the vertical, horizontal, and diagonal dimensions, respectively, of the triangular wedges on the right- and left-hand sides. For the top and bottom triangular wedges, $H_{sh}/2$, B_{sh}, and $D_{sh}/2$ are its vertical, horizontal, and diagonal dimensions, respectively.

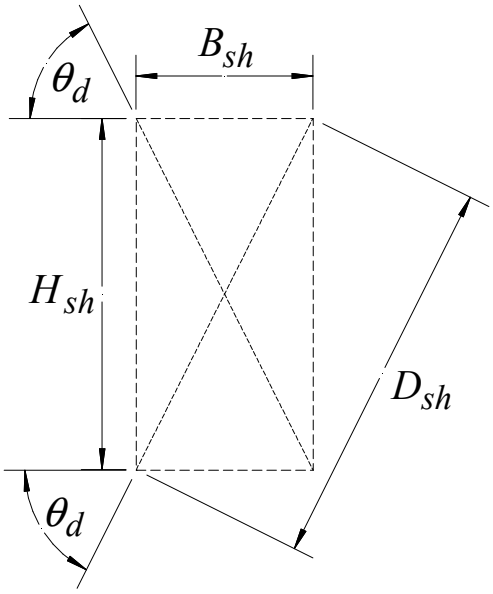

(a)

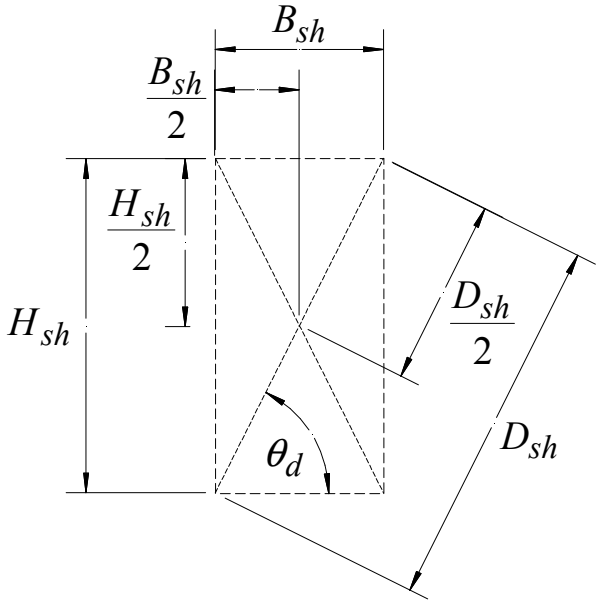

(b)

Figure 9.45 Main FRP-confined concrete core: (a) typical geometry and (b) triangular wedge geometry.

As shown in **Figure 9.46**, the diagonals in the effectively confined triangular wedges are subjected to a diagonal effective confining stress $(f_{de})_{sh} = k_e(f_d)_{sh}$ perpendicular to the diagonal of the triangular wedges and an effective shear stress $(\tau_{de})_{sh} = k_e(\tau_d)_{sh}$ along the main diagonal $D_{sh}/2$. k_e is the confinement effectiveness of the FRP jacket, as defined in Eq. (4.8) and summarized in **Table 4.2**. For rectangular sections k_e is given by Eq. (4.29), Eq. (4.32) for square sections, and $k_e = 1.0$ for oval, circular, and elliptical sections.

As shown in **Figure 9.46,** the vertical faces of the left and right triangular wedges are subjected to an effective minor principal stress $\sigma_{3e} = k_e\sigma_3$, and the horizontal faces of the top and bottom wedges are subjected to an effective intermediate principal stress $\sigma_{2e} = k_e\sigma_2$.

The effective intermediate principal stress σ_{2e} can be found from the vertical equilibrium of the top or bottom wedge shown in **Figure 9.47**, where:

$$D_{sh}\left[(f_{de})_{sh}\cos(\theta_d) + (\tau_{de})_{sh}\sin(\theta_d)\right] - \sigma_{2e}B_{sh} = 0 \tag{9.90}$$

The effective diagonal shearing stress $(\tau_{de})_{sh}$ of Eqs. (5.10) and (5.14) can be found by recognizing that in Eq. (5.26) $B_{sh} = D_{sh}\cos(\theta_d)$ and using $(f_{de})_{sh}$ of Eq. (5.12), the diagonal equilibrium coefficient $(\psi_d)_{sh}$ of Eq. (5.13), and the diagonal shear equilibrium cioefficient $(\psi_\tau)_{sh}$ of Eq. (5.15). Substituting this effective diagonal shearing stress $(\tau_{de})_{sh}$ into Eq. (9.90) and solving for the effective intermediate principal stress σ_{2e} yields:

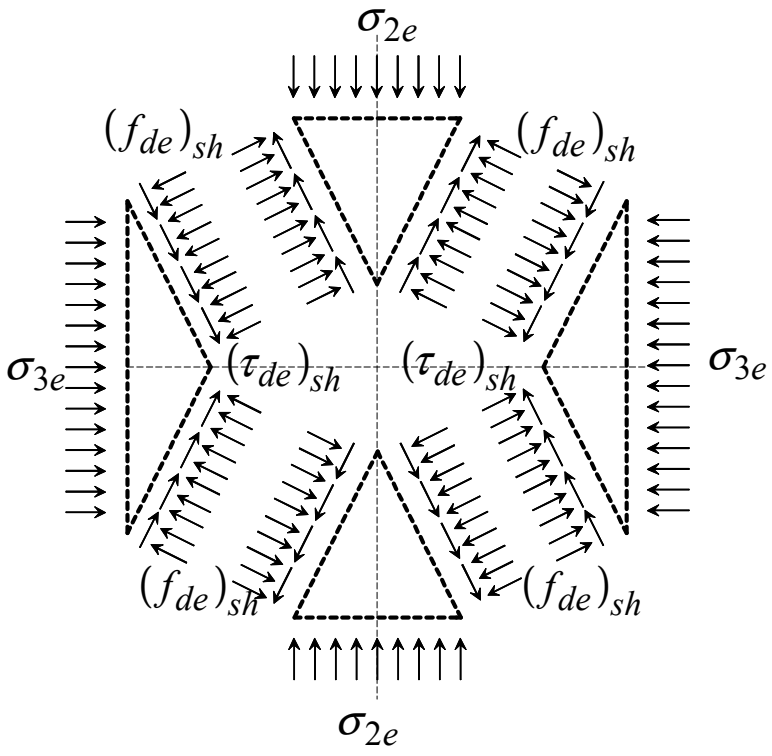

Figure 9.46 Definition of stresses on the triangular wedges of the effectively confined concrete core in an FRP-confined concrete section.

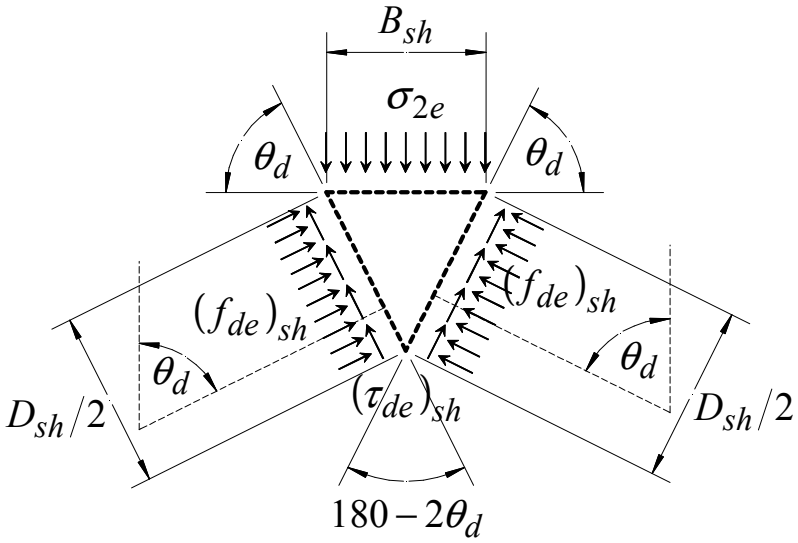

Figure 9.47 Geometry and stresses on the top triangular wedge of the effectively confined concrete core in an FRP-confined concrete section.

$$\sigma_{2e} = (f_{de})_{sh}[1 + \tan(\theta_d)\tan(\theta_b)] \tag{9.91}$$

where θ_b is an FRP jacket shape-dependent angle, which can be found using Eq. (5.27), using both the jacket angle θ_a and the diagonal angle θ_d. In addition, both θ_a and θ_b are summarized in **Table 5.2,** and are shown in **Figures 5.6-5.10** and **9.40-9.44**.

Using $(f_{de})_{sh}$ of Eq. (5.12) and $(\psi_d)_{sh}$ of Eq. (5.13) in the above relationship yields:

$$\sigma_{2e} = (E_{je})_B(\psi_2)_{sh}\varepsilon_j \tag{9.92}$$

$$(\psi_2)_{sh} = (\psi_d)_{sh}[1 + \alpha_{sh}\tan(\theta_b)] \tag{9.93}$$

where $(\psi_2)_{sh}$ is the intermediate principal stress coefficient. This coefficient is evaluated using $(\psi_d)_{sh}$ of Eq. (5.13) using χ_{sh} of Eq. (5.11) and is summarized in **Table 5.1.** This intermediate principal stress coefficient is summarized in **Table 9.1** for the FCC sections considered in this dissertation.

The diagonal jacket strain in the FRP-confined concrete section ε_j of Eq. (9.92) can be found in terms of the axial compressive strain ε_c, using the FRP jacket stiffness-dependent diagonal dilation model introduced in Chapter 8, using the diagonal Poisson's ratio model of Eq. (8.43).

Defining the normalized effective intermediate principal stress as $K_{2e} = \theta_{2e}/f_{co}$; using σ_{2e} of Eq. (9.92), $(E_{je})_B$ of Eq. (4.15), $(C_{je})_{sh}$ of Eq. (4.17), and K_{je} of Eq. (4.18) yield:

Table 9.1 Summary of the nondimensional intermediate principal stress coefficient $(\psi_2)_{sh}$ of various FRP-confined concrete sections.

FRP jacket shape	**Intermediate Principal Stress Coefficient $(\psi_2)_{sh}$**
Rectangular	$(\psi_2)_{sh} = \dfrac{[\alpha_{sh} + \tan(\theta_a)]\cos(\theta_d)\cos(\theta_b)}{1 - 2\alpha_j[1 - \sin(\theta_a)]}$
Oval	Same as rectangular with $2\alpha_j = \dfrac{1}{\alpha_{sh}}$ or $(\psi_2)_{sh} = \dfrac{[\alpha_{sh} + \tan(\theta_a)]\sin(\theta_d)\cos(\theta_b)}{\alpha_{sh} + \sin(\theta_a) - 1}$
Square	$(\psi_2)_{sh} = \dfrac{\sqrt{2}}{2\left[1 - \alpha_j\left(2 - \sqrt{2}\right)\right]}$
Circular	$(\psi_2)_{sh} = 1.0$ (Same as elliptical with $\theta_d = 45^\circ$ and $\alpha_{sh} = 1.0$)
Elliptical	$(\psi_2)_{sh} = \sqrt{2}\cos(\theta_d)\cos(\theta_b)[\alpha_{sh} + \tan(\theta_b)]$

$$K_{2e} = \frac{\sigma_{2e}}{f_{co}} = \left(K_{je}\right)_{sh} \left(\gamma_2\right)_{sh} \varepsilon_j \tag{9.94}$$

$$\left(\gamma_2\right)_{sh} = \frac{2\left(\psi_2\right)_{sh}}{C_{sh}} = \left(\gamma_d\right)_{sh} \left[1 + \alpha_{sh} \tan\left(\theta_b\right)\right] \tag{9.95}$$

where $\left(\gamma_2\right)_{sh}$ is the normalized intermediate stress coefficient, $\left(\gamma_d\right)_{sh}$ is the diagonal equilibrium coefficient of Eq. (5.19), and C_{sh} is the jacket reinforcement ratio coefficient of Eq. (4.12), summarized in **Table 4.1.**

The effective minor principal stress σ_{3e} can be found from the horizontal equilibrium of the left or right wedge, shown in **Figure 9.48**, where:

$$D_{sh}\left[\left(f_{de}\right)_{sh} \sin\left(\theta_d\right) - \left(\tau_{de}\right)_{sh} \cos\left(\theta_d\right)\right] - \sigma_{3e} H_{sh} = 0 \tag{9.96}$$

Recognizing that $H_{sh} = D_{sh} \sin\left(\theta_d\right)$ (see Eq. (5.26)), and using $\left(f_{de}\right)_{sh}$ of Eq. (5.12), $\left(\psi_d\right)_{sh}$ of Eq. (5.13), $\left(\tau_{de}\right)_{sh}$ of Eqs. (5.10) and (5.14), $\left(\psi_\tau\right)_{sh}$ of Eq. (5.15), and solving for effective minor principal stress σ_{3e} in the previous relationship yield:

$$\sigma_{3e} = \left(f_{de}\right)_{sh} \left[1 - \cot\left(\theta_d\right) \tan\left(\theta_b\right)\right] \tag{9.97}$$

Using $\left(f_{de}\right)_{sh}$ of Eq. (5.12) and $\left(\psi_d\right)_{sh}$ of Eq. (5.13) in the above relationship yields:

$$\sigma_{3e} = \left(E_{je}\right)_B \left(\psi_3\right)_{sh} \varepsilon_j \tag{9.98}$$

$$\left(\psi_3\right)_{sh} = \left(\psi_d\right)_{sh} \left[1 - \cot\left(\theta_d\right) \tan\left(\theta_b\right)\right] \tag{9.99}$$

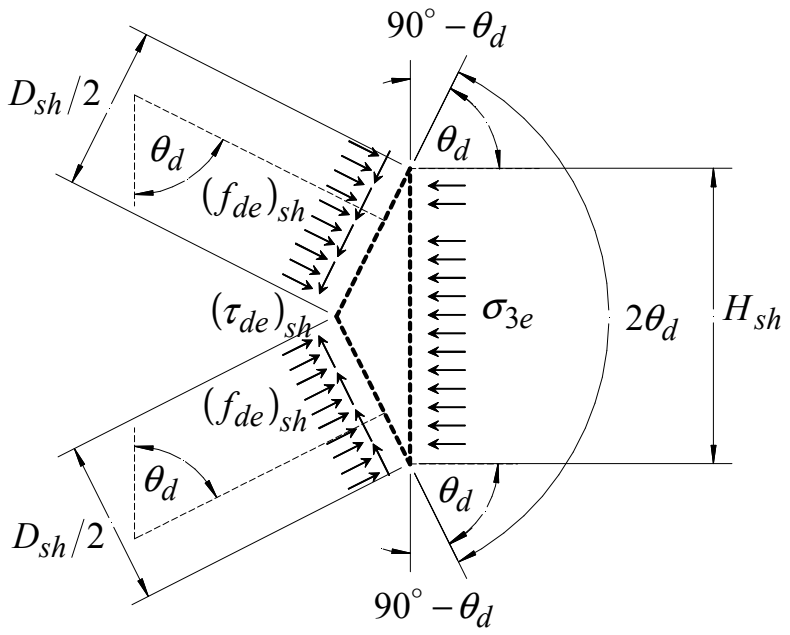

Figure 9.48 Geometry and stresses on the right triangular wedge of the effectively confined concrete core in an FRP-confined concrete section; left wedge similar.

where $(\psi_3)_{sh}$ is the minor principal stress coefficient.

Defining the normalized effective minor principal stress as $K_{3e} = \sigma_{3e}/f_{co}$ and using σ_{3e} of Eq. (9.98), $(E_{je})_B$ of Eq. (4.15), $(C_{je})_{sh}$ of Eq. (4.17) and K_{je} of Eq. (4.18) yield:

$$K_{3e} = \frac{\sigma_{3e}}{f_{co}} = (K_{je})_{sh}(\gamma_3)_{sh}\varepsilon_j \tag{9.100}$$

$$(\gamma_3)_{sh} = \frac{2(\psi_3)_{sh}}{C_{sh}} = (\gamma_d)_{sh}[1 - \cot(\theta_d)\tan(\theta_b)] \tag{9.101}$$

where $(\gamma_3)_{sh}$ is the normalized minor principal stress coefficient..

Using the intermediate σ_{2e} and minor σ_{3e} effective principal stresses of Eqs. (9.92) and (9.98), the principal stress ratio $\alpha_\sigma = \sigma_{2e}/\sigma_{3e}$ is given by:

$$\alpha_\sigma = \frac{\sigma_{2e}}{\sigma_{3e}} = \frac{(\psi_2)_{sh}}{(\psi_3)_{sh}} = \frac{(\gamma_2)_{sh}}{(\gamma_3)_{sh}} = \alpha_{sh}\alpha_\varepsilon = \beta_{sh} - 1 \tag{9.102}$$

The previous relationship indicates that the principal stress ratio α_σ of an FCC section is a function of the section aspect ratio α_{sh} of Eq. (4.2) and the transverse strain ratio α_ε of Eq. (6.19). Because both α_{sh} and α_ε are a function of the geometry of the FRP-confined concrete section, it can also be stated that the principal stress ratio α_σ is a function of the geometry of the confining elastic FRP jacket. In addition, the principal stress ratio α_σ is greater than or equal to unity, i.e., $\alpha_\sigma \geq 1.0$, since both $\alpha_{sh} \geq 1.0$ and $\alpha_\varepsilon \geq 1.0$. Furthermore, the effective minor principal stress σ_{3e} in the FCC section can

be found in terms of the effective intermediate principal stress σ_{2e} using the principal stress ratio α_σ of Eq. (9.102) or vice versa.

For the FCC sections considered herein that are confined by an elastic FRP jacket having an effective transverse confining stiffness of the FRP jacket $\left(E_{je}\right)_B$ of Eq. (4.15) that are subjected to an axial compressive stress ε_c, and resultant diagonal jacket strain ε_j, determined using the FRP jacket stiffness-dependent diagonal dilation model introduced in Chapter 8, the minor principal compressive stress σ_{3e} in the FRP-confined concrete section can be determined using Eq. (9.98). The intermediate principal compressive stress σ_{2e} can then be determined using the principal stress ratio α_σ of Eq. (9.102).

In reference to Eq. (9.102) and to FCC sections subjected to equibiaxial confinement, i.e., sections with a unity aspect ratio $\alpha_{sh} = 1.0$, such as square and circular FCC sections, the major principal compressive stress σ_1 can be found using the extended Mohr-Coulomb (EMC) criterion for concrete with the effective minor principal σ_{3e} of Eq. (9.98). This indicates that for circular (CFCC) and square (SFCC) sections, the EMC model can be used to find a direct (noniterative) solution for the major principal compressive stress σ_1 in terms of the effective minor principal compressive stress σ_{3e}.

For concrete sections subjected to nonuniform biaxial confinement, i.e., sections with an aspect ratio $\alpha_{sh} > 1.0$ such as rectangular (RFCC), oval (OFCC), and elliptical (EFCC) sections [refer to α_σ of Eq. (9.102)], an indirect (iterative) solution for the major principal compressive stress σ_1 can be found using the TEMC criterion for

concrete with the effective minor principal σ_{3e} of Eq. (9.98) and the intermediate principal stress σ_{2e} of Eq. (9.92) determined using the principal stress ratio α_σ of Eq. (9.102).

Unlike the EMC criterion, the TEMC criterion requires an iterative solution for the major principal compressive stress σ_1; this solution can be easily implemented in a spreadsheet-type program or incorporated into a finite element analysis program. In this dissertation a spreadsheet solution is used in the analysis of FCC sections in compression.

CHAPTER 10

UNIAXIAL COMPRESSIVE CONSTITUTIVE MODEL FOR CONCRETE SECTIONS CONFINED BY FIBER-REINFORCED POLYMER JACKETS

In this chapter, a series of stress-strain relationships are introduced for modelling the uniaxial compressive stress-strain behavior of rectangular, square, circular, and elliptical concrete columns confined by fiber-reinforced polymer (FRP) jackets. The stress-strain model introduced herein takes into consideration the effects that the FRP jacket shape has:

1. On the mechanical properties of the confining elastic FRP jacket introduced in Chapter 4
2. On the transverse and diagonal equilibrium of the FRP-confined concrete section, introduced in Chapter 5
3. On the strain compatibility relationships introduced in Chapter 6
4. On the transverse and diagonal dilation of FRP-confined concrete section, as discussed in Chapters 7 and 8
5. On the passive transverse confining stresses provided by the confining FRP jacket as introduced in Chapter 9.

Uniaxial Stress-Strain Model for FRP-Confined Concrete

The compressive stress-strain behavior of the FRP-confined concrete (FCC) sections considered herein is modeled by an incremental Popovics (1973)-type fractional secant modulus model for FRP-confined concrete, which will be developed in what follows.

For a given FCC section subjected to a uniform axial compressive strain ε_c and resultant transverse jacket diagonal strain ε_j, the average compressive stress f_c in the confined concrete core can be determined as follows:

$$f_c = E_c \varepsilon_c = -\left(\frac{1}{\nu_j}\right) E_c \varepsilon_j \tag{10.1}$$

where E_c is the average axial secant modulus of the confined concrete and ν_j is the diagonal Poisson's ratio of the FRP-confined concrete section, which is determined using the diagonal dilation model introduced in Chapter 8.

At a given axial compressive strain ε_c in the FCC section, the diagonal Poisson's ratio ν_j can be found iteratively by solving for the resultant diagonal expansive strain ε_j in the FRP jacket in Eq. (8.43), with the pertinent terms defined in Eqs. (8.20)-(8.45). A noniterative solution for the diagonal Poisson's ratio ν_j can be found using the Poisson's ratio model of Eq. (8.43) by assuming a diagonal expansive strain ε_j in the FRP jacket and finding the corresponding axial compressive strain ε_c in the FCC section using Eq. (7.32).

The average axial secant modulus of the FRP-confined concrete E_c can be found based on the applied axial compressive strain ε_c, using the following incremental

Popovics (1973)-type fractional secant modulus model for FRP-confined concrete. The average axial compressive stress-strain behavior of FRP-confined concrete sections considered herein, that exhibit either strain-softening or strain-hardening behavior as shown in the normalized axial stress versus normalized axial strain **Figure 10.1(a)** and **Figure 10.1(b),** respectively, is governed by the following fractional model**:**

$$E_c = \frac{f_c}{\varepsilon_c} = E_{cc}\left\{\frac{n_{cc}}{n_{cc} - 1 + \left(\frac{\varepsilon_c}{\varepsilon_{cc}}\right)^{n_{cc}}}\right\} \tag{10.2}$$

$$E_{cc} = \frac{f_{cc}}{\varepsilon_{cc}} \tag{10.3}$$

$$n_{cc} = \frac{1}{1 - \frac{E_{cc}}{E_{co}}} \tag{10.4}$$

where E_{cc} is the secant modulus of the confined concrete at the ultimate compressive strength f_{cc} and strain ε_{cc} of the confined concrete core; n_{cc} is the curvature parameter of the Popovics (1973)-type fractional model of Eq. (10.2).

In the above model, compressive stresses and strains are considered positive. In addition, E_{co} is the initial modulus of elasticity of the FRP-confined concrete section of Eq. (7.16), determined using the initial Poisson's ratio ν_{ci} and modulus of elasticity E_{ci} of the unconfined concrete core, and the initial dilation rate along the minor dimension of the FCC section, $(\mu_B)_o$ of Eq. (7.17).

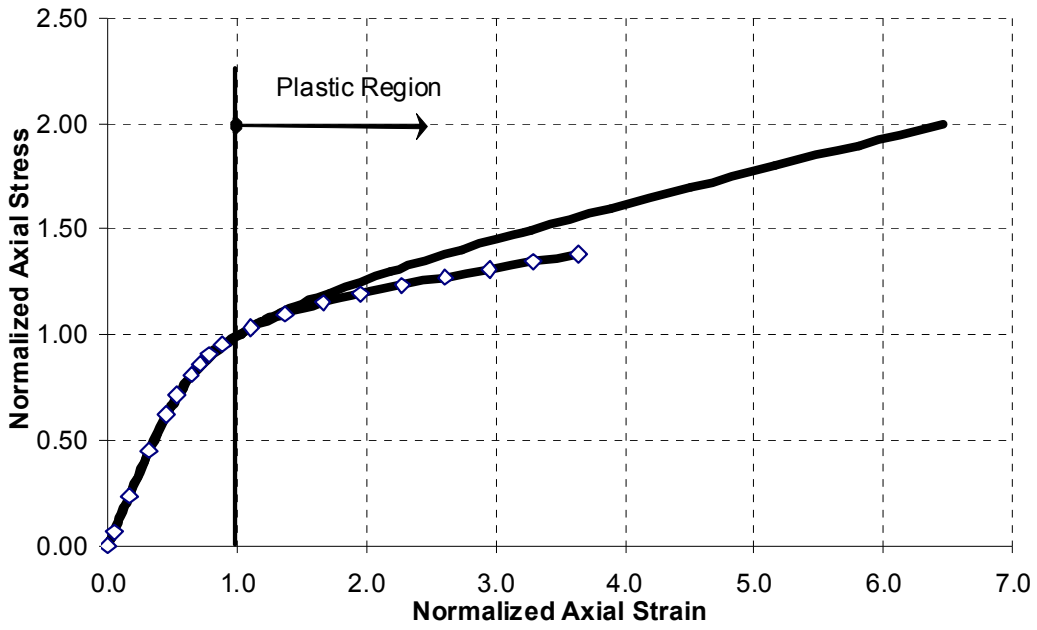

(a)

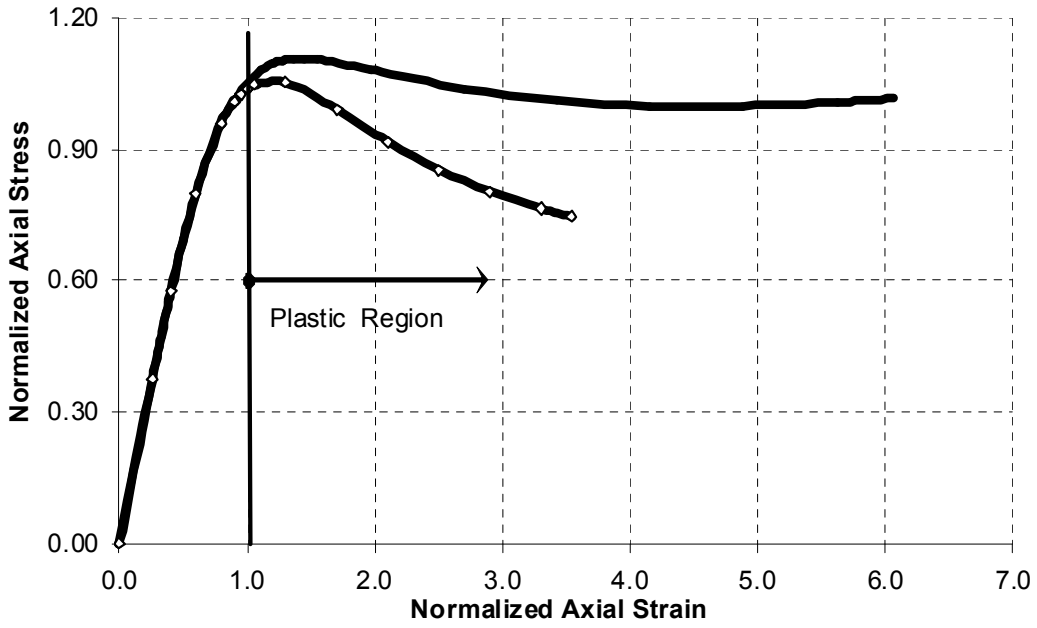

(b)

Figure 10.1 Plot of normalized axial stress versus normalized axial strain curves of sections exhibiting (a) strain-hardening and (b) strain-softening compressive behavior.

When the experimental values of unconfined concrete are unknown, the tangent modulus of elasticity E_{ci} and the peak compressive strain ε_{co} of the unconfined concrete can be estimated based on the unconfined compressive strength f_{co} as follows (Collins et al. 1993):

$$E_{ci} = 3320\sqrt{f_{co}} + 6900 \tag{10.5}$$

$$\varepsilon_{co} = \frac{f_{co}}{E_{ci}}\left(\frac{n_u}{n_u - 1}\right) \tag{10.6}$$

$$n_u = 0.80 + \left(\frac{f_{co}}{17}\right) \tag{10.7}$$

where n_u is a curvature parameter of the unconfined concrete core. In the above relationships, E_{ci} and f_{co} are expressed in MPa units. When the experimental values of unconfined concrete are known (E_{ci}, f_{co} and ε_{co}), the curvature parameter of the unconfined concrete core n_u can be determined as:

$$n_u = \frac{1}{1 - \dfrac{E_{\text{sec}}}{E_{ci}}} \quad ; \quad E_{\text{sec}} = \frac{f_{co}}{\varepsilon_{co}} \tag{10.8}$$

For the case of equi-biaxially confined concrete sections, square and circular FRP-confined concrete sections in particular, the ultimate compressive strength of the FRP-confined section can be found using the two-parameter extended Mohr-Coulomb (EMC) model introduced in Chapter 9 and setting $f_{cc} = \sigma_1$, where σ_1 is the major principal

compressive stress in the confined concrete core, in which compressive stresses and strain are considered positive.

For concrete in a nonuniform biaxial confinement state of stress, which is the case of rectangular and elliptical FRP-confined concrete sections, the ultimate compressive strength of the FRP-confined section f_{cc} can be found by utilizing the two-parameter triaxial extended Mohr-Coulomb (TEMC) model introduced in Chapter 9**,** and setting $f_{cc} = -\sigma_3^{'} = \sigma_1$, where $\sigma_3^{'}$ is the minor principal stress with tension considered positive.

Recently, Fujikake et al. (2004) recognized that an ultimate strength criterion for actively confined concrete, such as the parabolic Leon criterion (Pramono and Willam 1989) of Eq. (9.8), cannot accurately describe the uniaxial stress-strain behavior of concrete under a continuously increasing confining stress, which occurs in FRP-confined concrete sections. As a result, Fujikake et al. (2004) introduced a reduced maximum strength criterion after the FRP-confined concrete first reaches the Leon criterion.

In this dissertation, a different approach is taken by applying the EMC or TEMC failure criterion for confined concrete to the case of passively confined concrete, FRP-confined concrete sections in particular. It is assumed that the axial stress f_c or normalized axial stress $k_c = f_c / f_{co}$ in FRP-confined concrete asymptotically approaches the analytical ultimate strength f_{cc} or confinement effectiveness $k_{cc} = f_{cc} / f_{co}$ when the axial strains in the confined concrete reaches the peak compressive strain ε_{cc} or $\varepsilon_c = \varepsilon_{cc}$, in which f_{cc} is determined using either the proposed EMC (circular and square FCC sections) or the TEMC (rectangular, square,

oval, elliptical and circular FCC sections) ultimate strength criterion introduced in Chapter 9**.**

At the instant when $f_c = f_{cc}$ or $k_c = k_{cc}$**,** it is assumed that the axial compressive strain ε_c in the confined concrete reaches the peak compressive strain ε_{cc} or $\varepsilon_c = \varepsilon_{cc}$. The ultimate compressive strain ε_{cc} occurring at the ultimate compressive strength f_{cc} is determined as follows (Mander et al. 1988):

$$\varepsilon_{cc} = \varepsilon_{co}\left[1 + R\left(k_{cc} - 1\right)\right] \tag{10.9}$$

where R is the strain ductility ratio of concrete under constant (biaxial or uniaxial) confinement, which is defined as:

$$R = \frac{k_{cc} - 1}{k_{\varepsilon c} - 1} \tag{10.10}$$

$$k_{\varepsilon c} = \frac{\varepsilon_{cc}}{\varepsilon_{co}} \tag{10.11}$$

where $k_{\varepsilon c}$ is the strain effectiveness of the confined concrete core. In the definition of the strain ductility ratio R of Eq. (10.10), the terms $\left(k_{cc} - 1\right)$ and $\left(k_{\varepsilon c} - 1\right)$ represent the percentage increase in ultimate compressive strength and peak compressive strain in the confined concrete, respectively.

The strain ductility ratio of the confined concrete R of Eq. (10.10) is considered equal to $R = 5.0$ (Richart et al. 1928), when the section is subjected to uniform equibiaxial confinement, which will be referred to as the equi-biaxial confinement ductility ratio $R_{bc} = 5.0$. This is the case of concrete cylinders actively confined by

hydrostatic fluid pressure or passively confined concrete in which the confining element provides an essentially uniform equi-biaxial confining stress, typical of circular FRP-confined concrete (CFCC) sections (i.e., when $\alpha_{sh} \to 1.0$ and $k_e = 1.0$). When the confined concrete core is subjected to a uniform uniaxial confining stress, i.e., $\sigma_1 \geq \sigma_3$ with $\sigma_2 \cong 0$, the strain ductility ratio of the uniaxially confined concrete $R = 3.0$ (Darwin and Pecknold 1977), which will be referred to as the uniaxial confinement ductility ratio $R_{uc} = 3.0$. Due to the shape of rectangular FRP-confined concrete (RFCC) sections with rounded corners, including square FRP-confined concrete (SFCC) sections, the FRP-confined concrete core is subjected to nonuniform transverse confining stress; as the confining efficiency of the FRP jacket $k_e \to 1/3$ which occurs as the aspect ratio α_{sh} increases and/or the jacket corner aspect ratio α_j decreases. For high aspect ratio $\alpha_{sh} >> 2$, RFCC sections with small corner radii for which $\alpha_j \to 0$ and $k_e \to 1/3$, both the confinement effectiveness k_{cc} and strain effectiveness k_ε approach a unity value, i.e., $k_{cc}, k_\varepsilon \to 1.0$. In addition, for high aspect ratio RFCC sections, the minor principal stress $\sigma_{3e} \to 0$ and the principal stress ratio α_σ of Eq. (9.102) increase nonlinearly as α_{sh} increases. For high aspect ratio RFCC sections the strain ductility ratio of the lightly confined or essentially unconfined concrete approaches a unity value, with $R_u \to 1.0$, where R_u is the strain ductility ratio of the unconfined concrete. This also occurs in high aspect ratio, $\alpha_{sh} >> 2$ and $k_e = 1.0$, elliptical FRP-confined concrete (EFCC). In reference to the strain ratio α_ε of Eq. (6.52), the aspect ratio α_{sh} of Eq. (4.2) and the principal stress ratio α_σ of Eq. (9.102), for an EFCC section with

$\alpha_{sh} \geq 1.0$, the principal stress ratio is given by $\alpha_{\sigma} = \alpha_{sh}{}^{2}$ and $\alpha_{\sigma} = 1.0$ for circular sections.

For RFCC sections with low-aspect ratios, the confining efficiency of the FRP jacket $k_e \rightarrow 1.0$, which occurs as the RFCC section becomes more rounded, as the aspect ratio α_{sh} decreases and approaches a unity value (i.e., as $\alpha_{sh} \rightarrow 1.0$) and as the jacket corner aspect ratio α_j increases and approaches a value of 0.50 (i.e., as $\alpha_j \rightarrow 0.50$); hence the strain ductility ratio of the RFCC section approaches the value of the equi-biaxial confinement ductility ratio $R_{bc} = 5.0$. In addition, for low-aspect ratio RFCC sections, as the section aspect ratio approaches a unity value (i.e., as $\alpha_{sh} \rightarrow 1.0$), the intermediate principal stress σ_{2e} approaches the value of the minor principal stress $\sigma_{2e} \rightarrow \sigma_{3e}$ (i.e., $\sigma_{2e} \rightarrow \sigma_{3e}$), and the principal stress ratio α_{σ} of Eq. (9.102) approaches a unity value $\alpha_{\sigma} = \sigma_{2e}/\sigma_{3e} \rightarrow 1.0$. This indicates that the strain ductility ratio of FCC sections R_{sh}, depends on the FRP jacket shape. As a result, R_{sh} is assumed to be governed by the following hyperbolic relationship:

$$R_{sh} = R_u + \frac{(R_{bc} - R_u)}{\psi_R} \;\; ; \;\; \psi_R = \frac{\alpha_{\sigma}}{k_e} \tag{10.12}$$

where ψ_R is an FRP jacket shape-dependent ductility coefficient that measures the effect that the FRP jacket shape has on the strain ductility of the confined concrete; the strain ductility ratio R_{sh} of Eq. (10.12) is plotted in **Figure 10.2** versus the ductility coefficient ψ_R.

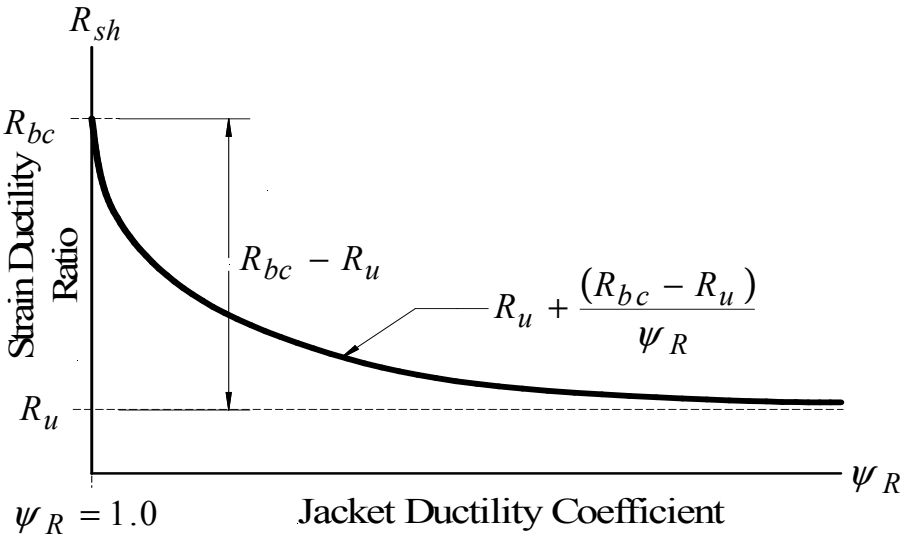

Figure 10.2 Plot of strain ductility ratio versus jacket ductility coefficient of FRP-confined concrete.

The previous relationship indicates that R_{sh} is proportional to the confinement efficiency k_e of the confining FRP jacket and inversely proportional to the principal stress ratio α_σ of Eq. (9.102). This strain ductility ratio is applicable to FRP-confined concrete subjected to uniform biaxial confinement (circular sections and low-aspect ratio elliptical sections) and to sections subjected to nonuniform biaxial confinement (square, rectangular and high aspect ratio elliptical sections).

For rectangular (including square and circular) FRP-confined concrete sections, and elliptical (including circular) FRP-confined concrete sections, $R_u \cong 1.0$. Substituting $R_u = 1.0$ and $R_{bc} = 5.0$ into R_{sh} of Eq. (10.12) yields the following for RFCC, SFCC, CFCC, and EFCC sections:

$$R_{sh} = 1 + 4\left(\frac{k_e}{\alpha_\sigma}\right) = 1 + 4\left(\frac{k_e}{\beta_{sh} - 1}\right) \tag{10.13}$$

For EFCC (including CFCC) sections for which $k_e = 1.0$ and $\alpha_\sigma = {\alpha_{sh}}^2$, Eq. (10.13) can be rewritten as:

$$R_{sh} = 1 + \left(\frac{4}{{\alpha_{sh}}^2}\right) \tag{10.14}$$

For circular sections for which $k_e = 1.0$, $\alpha_{sh} = 1.0$, and $\alpha_\sigma = 1.0$, R_{sh} of Eqs. (10.13) and (10.14) yield the equi-biaxial confinement ductility ratio of $R_{bc} = 5.0$, whereas for very high aspect ratio RFCC and EFCC sections, it approaches the unconfined ductility ratio of $R_u = 1.0$.

For the FCC sections considered herein, the ultimate compressive strain ε_{cc} in the FCC section is found by substituting $R = R_{sh}$ into Eq. (10.9) which yields:

$$\varepsilon_{cc} = \varepsilon_{co}\left[1 + R_{sh}\left(k_{cc} - 1\right)\right] \tag{10.15}$$

The plastic strain ductility ratio R_p of the FCC section is defined as:

$$R_p = \frac{k_{\varepsilon p} - 1}{k_{cp} - 1} \tag{10.16}$$

$$k_{cp} = \frac{f_{cp}}{f_{co}} \tag{10.17}$$

$$k_{\varepsilon p} = \frac{\varepsilon_{cp}}{\varepsilon_{co}} \tag{10.18}$$

In the plastic strain ductility ratio R_p of Eq. (10.15), the terms $\left(k_{cp} - 1\right)$ and $\left(k_{\varepsilon p} - 1\right)$ represent the percentage increase in plastic compressive strength and strain, respectively. Plastic compressive behavior is assumed to occur at any given plastic compressive strength f_{cp} and strain ε_{cp}, where $\varepsilon_{co} \le \varepsilon_{cp} \le \varepsilon_{cu}$, and corresponding plastic diagonal expansive jacket strain ε_{jp} in the FCC section, where $\left|\varepsilon_{jo}\right| \le \left|\varepsilon_{jp}\right| \le \left|\varepsilon_{ju}\right|$. In addition, k_{cp} is the plastic confinement effectiveness; $k_{\varepsilon p}$ is the plastic strain effectiveness; ε_{jo} is the jacket dilation strain corresponding to the unconfined peak compressive strain ε_{co}; and ε_{ju} is the ultimate jacket dilation strain corresponding to the ultimate compressive strain ε_{cu}, at failure of the FRP jacket.

The difference between R_{sh} of Eq. (10.12) and R_p of Eq. (10.16) is that the latter is applicable to any plastic axial compressive stress f_{cp} and strain ε_{cp} in the FCC section, whereas R_{sh} is defined only when $f_c = f_{cc}$ or $k_c = k_{cc}$ and when $\varepsilon_c = \varepsilon_{cc}$ of Eq. (10.11).

The plastic strain ductility coefficient α_R is defined herein as the ratio between the FRP jacket shape-dependent strain ductility ratio R_{sh} of Eq. (10.11) and the plastic strain ductility ratio R_p of Eq. (10.16):

$$\alpha_R = \frac{R_{sh}}{R_p} \tag{10.19}$$

When $\alpha_R = 1.0$ the stress ratio k_c in the FCC section asymptotically approaches the analytical confinement coefficient k_{cc}. This is illustrated in **Figures 10.3-10.5**, in which the normalized axial stress k_c is plotted versus the effective minor principal stress ratio k_{3e}.

The cases shown are for sections concrete exhibiting strain-softening compressive behavior, as shown in **Figures 10.3** and **10.4,** and sections which exhibit strain-hardening as shown in **Figure 10.5**. From these figures it can be observed that at a very small plastic strain ε_{cp}, in the FCC section near the peak unconfined strain ε_{co}, i.e., when $\varepsilon_{cp} \cong \varepsilon_{co}$, the plastic strain ductility coefficient α_R of Eq. (10.19) has a very large value as a result of the low value of the plastic strain ductility ratio R_p of Eq. (10.16), i.e., a low plastic strain effectiveness $k_{\varepsilon p}$ of Eq. (10.18).

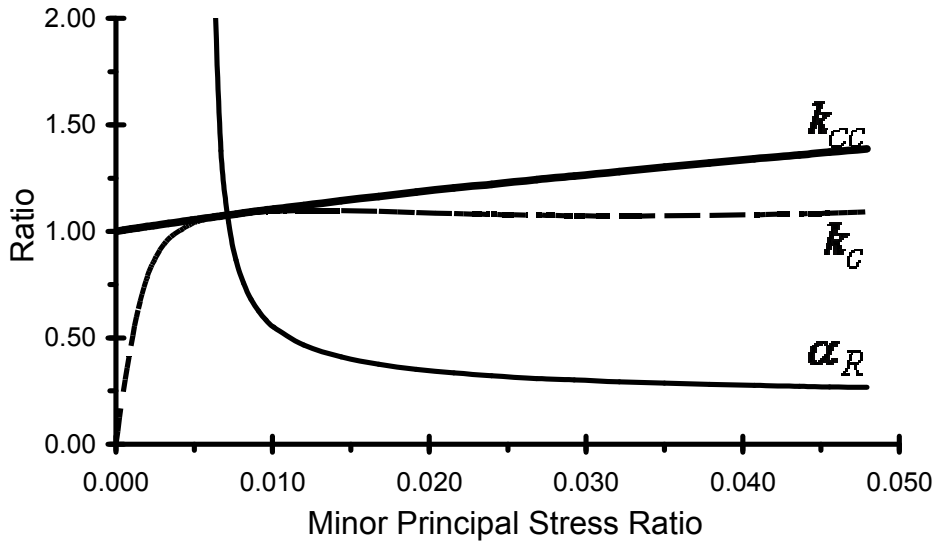

Figure 10.3 Axial stress ratio and strain ductility ratio versus minor principal stress ratio of an FRP section confined by a low stiffness FRP jacket exhibiting strain-softening compressive behavior.

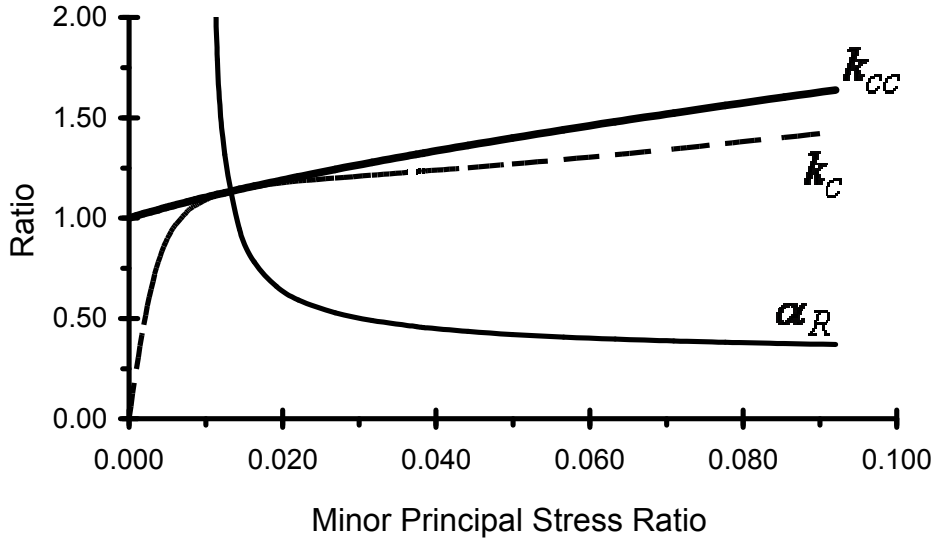

Figure 10.4 Axial stress ratio and strain ductility ratio versus minor principal stress ratio of an FRP section confined by a moderate stiffness FRP jacket exhibiting strain-hardening compressive behavior.

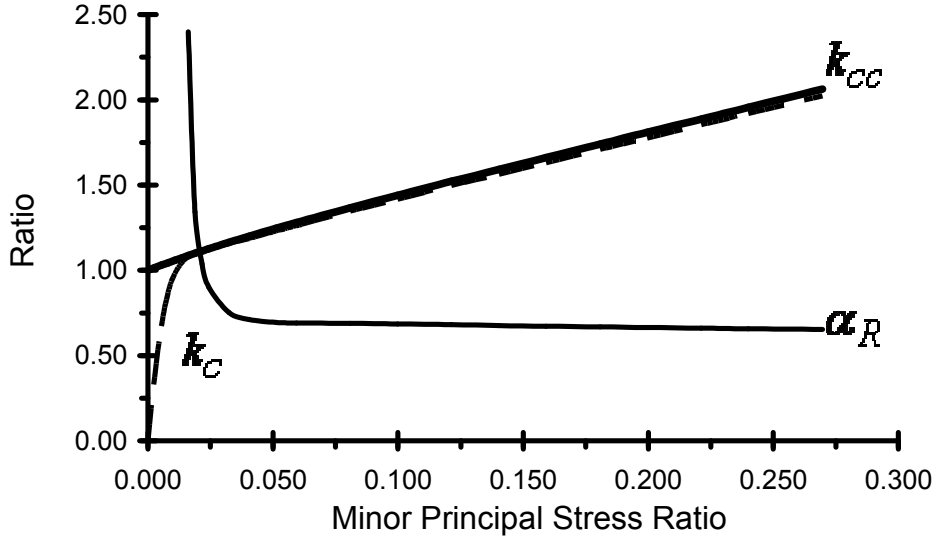

Figure 10.5 Axial stress ratio and strain ductility ratio versus minor principal stress ratio of an FRP section confined by a high stiffness FRP jacket exhibiting strain-hardening compressive behavior.

When the axial strain ratio k_ε strain approaches a unity value, i.e., when $k_\varepsilon = k_{\varepsilon p} = 1.0$ or when $\varepsilon_{cp} \cong \varepsilon_{co}$, the strain ductility coefficient α_R decreases as the FRP jacket stiffness increases; this is due to an increase in the kinematic restraint provided by the confining elastic FRP jacket which curtails the dilation behavior of the concrete core as it approaches its peak unconfined compressive strain ε_{co}, corresponding jacket dilation strain ε_{jo}, and confinement stress σ_{3e}.

At a high plastic compressive strain ε_{cp}, jacket strain ε_{jp}, and confinement stress σ_{3e}, the resultant plastic strain ductility coefficient α_R decreases at a smaller rate; i.e., the plastic strain ductility ratio R_p increases at a larger rate, as the stiffness of the FRP jacket increases. This increase in the plastic strain ductility ratio R_p is also a result of an increase in the jacket's ability to control the dilation of the confined concrete core, thus resulting in a larger increase in the plastic compressive strain ε_{cp} with respect to an increase in the plastic compressive strength f_{cp} and confinement effectiveness k_{cp}, due to a reduction in the FRP jacket strain ε_j at a given axial strain ε_c. The rate of increase of the plastic compressive strength f_{cp} is proportional to the rate of increase in the FRP jacket strain ε_j, the plastic dilation rate μ_{jp} of Eq. (7.25), and the plastic Poisson's ratio ν_{jp} of the FCC section.

Both the plastic dilation rate μ_{jp} (i.e., the slope of the Poisson's ratio curve) or plastic Poisson's ratio ν_{jp} decrease as the FRP jacket stiffness increases. As indicated in Chapter 7, the plastic dilation rate μ_{jp} of Eq. (7.25) is inversely proportional to the FRP

jacket stiffness. The FRP jacket stiffness also affects the plastic Poisson's ratio ν_{jp} of the FCC section. As the jacket Poisson's ratio ν_j decreases, either the jacket dilation strain ε_j decreases or the axial compressive strain ε_c increases [refer to v_j of Eq. (7.32)].

The incremental stress-strain model of Eqs. (10.1)-(10.18) can capture the strain-softening behavior of low FRP jacket stiffness confined concrete, the essentially elasto-plastic behavior of moderate FRP jacket stiffness confined concrete, and the strain-hardening behavior of high FRP jacket stiffness confined concrete, as shown in **Figures 10.3-10.5**. The increase in compressive strength and strain ductility of FRP-confined concrete is attributed to the lateral kinematic restraint provided by the confining FRP jacket and is evaluated using the triaxial extended Mohr-Coulomb (TEMC) criterion introduced in Chapter 9.

The axial strain-induced dilation of FCC sections is assumed to be governed by the FRP jacket stiffness-dependent fractional dilation model of Chapter 8. In the stress-strain model developed in this dissertation, the only experimentally obtained coefficients in the proposed TEMC criterion are the average values of the basic angle of friction of dry concrete, $\phi_b = 35°$ included in the degrading friction angle model introduced in Chapter 9**,** the diagonal plastic dilation rate μ_{jp} of Eq. (7.24), and the pore water pressure parameter n_{PW} of Eq. (9.62).

Stress-Strain Model Implementation

The damage-based stress-strain model can be implemented using the following steps shown in summarized in the flow charts of **Figures 10.6-10.9**, and **Tables 10.1-10.3:**

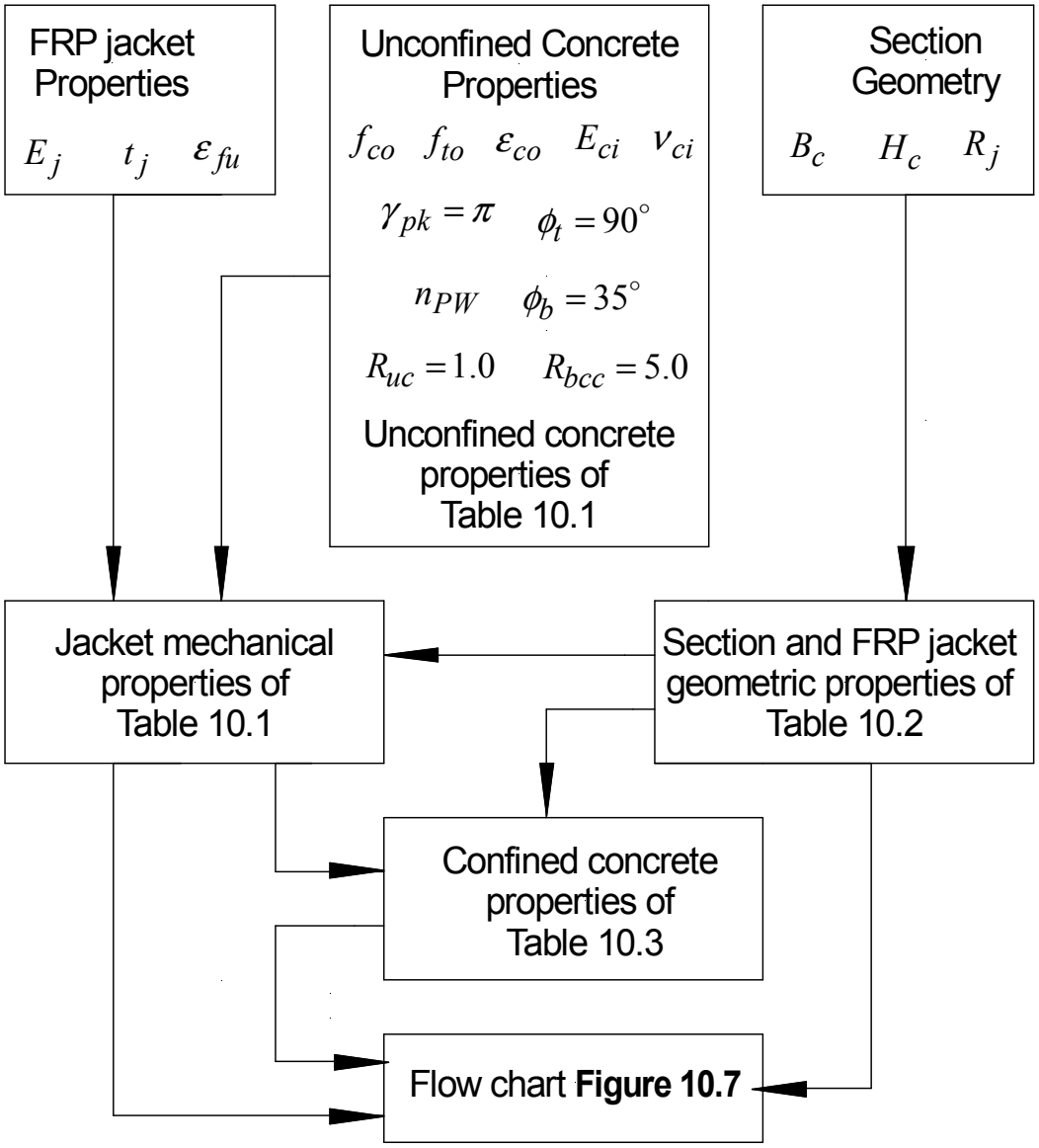

Figure 10.6 Flow chart of the proposed uniaxial stress-strain model-Part I.

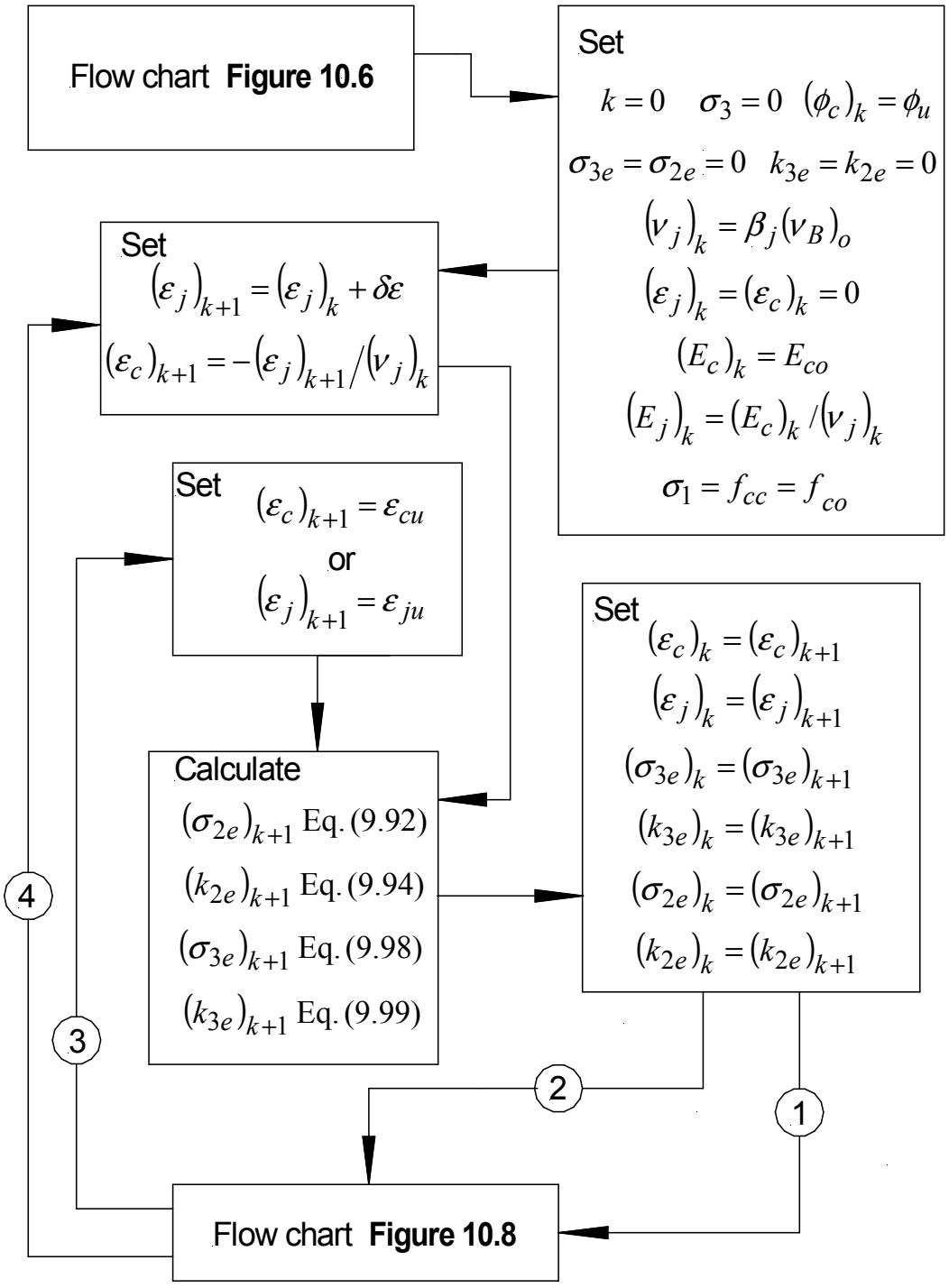

Figure 10.7 Flow chart of the proposed uniaxial stress-strain model-Part II.

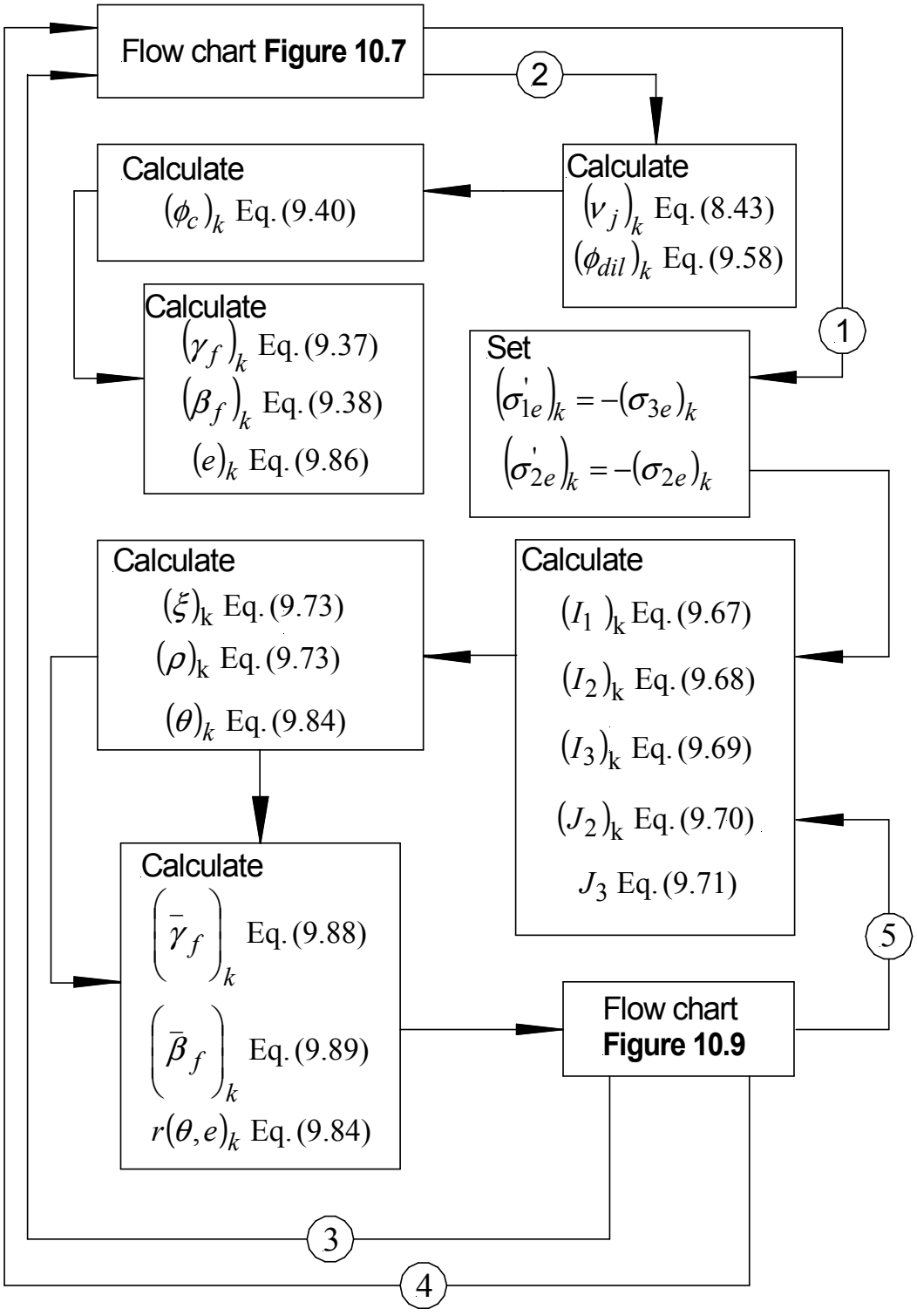

Figure 10.8 Flow chart of proposed uniaxial stress-strain model-Part III.

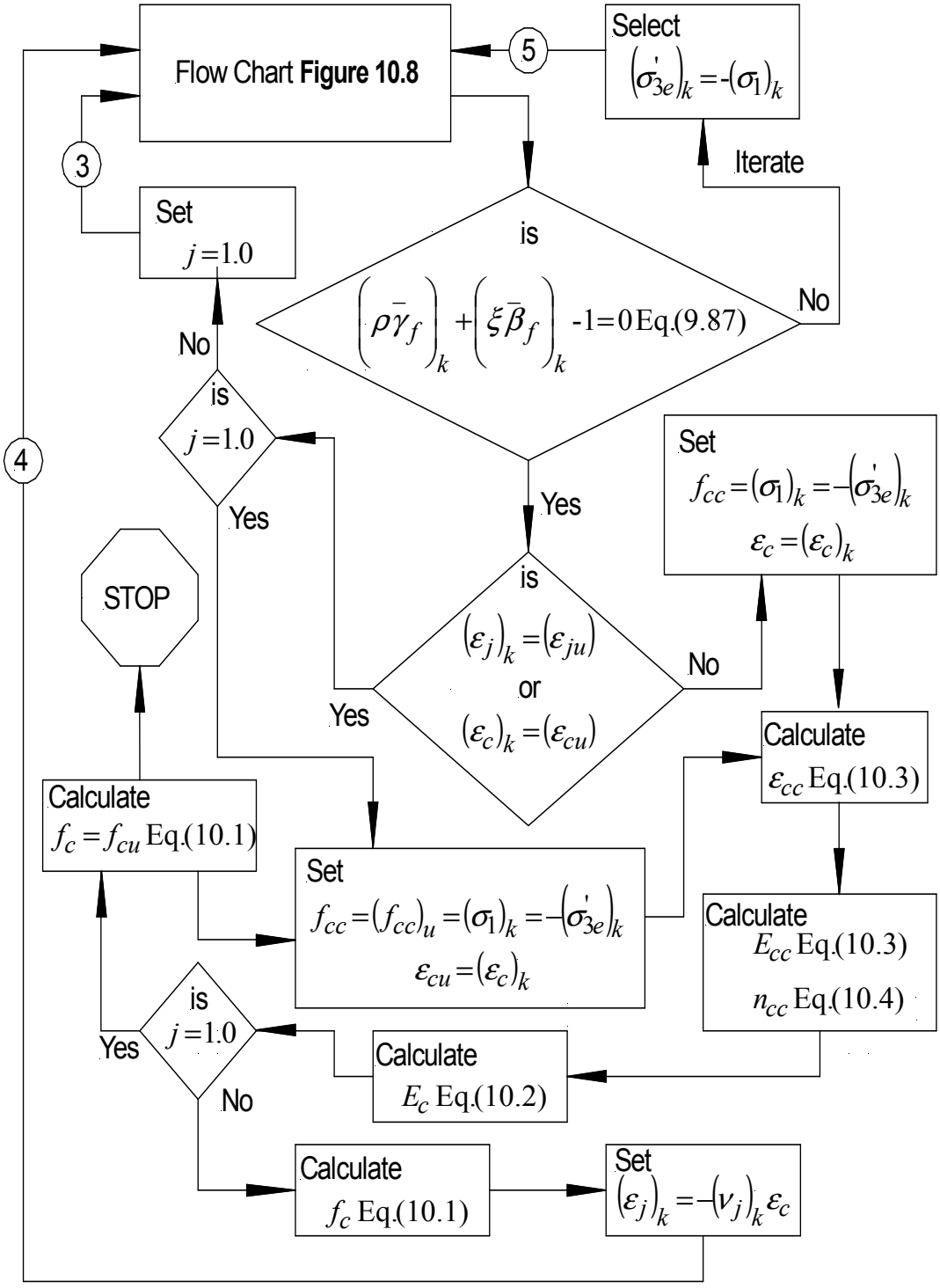

Figure 10.9 Flow chart of proposed uniaxial stress-strain model-Part IV.

Table 10.1 Summary of geometric properties of the FRP-confined concrete section required in the stress-strain model.

Properties	Term	Reference
Unconfined concrete	k_t	Eq. (9.9)
	c_u	Eq. (9.25)
	ϕ_u	Eq. (9.28)
	ϕ_{be}	Eq. (9.64)
	$(\phi_m)_{tb}$	Eq. (9.59)
	$(k_{3m})_{tb}$	Eq. (9.60)
	E_{sec}	Eq. (10.8)
	n_u	Eq. (10.8)
FRP jacket	$(E_{je})_B$	Eq. (4.15)
	$(C_{je})_{sh}$	Eq. (4.17)
	$(K_{je})_{sh}$	Eq. (4.18)
	α_E	Eq.(7.10)

Table 10.2 Summary of geometric properties of the FRP-confined concrete section required in the stress-strain model.

Term	Reference	Term	Reference
D_c	Eq. (4.3)	θ_d	Eq. (4.1)
α_{sh}	Eq. (4.2)	α_j	Eq. (4.2)
k_e	Table 4.2	C_{sh}	Table 4.1
D_{sh}	Eq. 5.11	χ_{sh}	Table 5.1
θ_a	Table 5.2	θ_b	Table 5.2
α_ε	Eq. (6.19)	β_j	Table 6.1
β_{sh}	Eq. (7.15)	β_a	Eq. (7.39)
$(\psi_2)_{sh}$	Table 9.1	α_σ	Eq. (9.102)
$(\psi_3)_{sh}$	Eq. (9.102)	R_{sh}	Eq. (10.12)
ψ_R	Eq. (10.12)		

Table 10.3 Summary of FRP-confined concrete properties.

Term	Reference	Term	Reference
E_{co}	Eq. (7.16)	$(\mu_B)_o$	Eq. (7.17)
μ_{jo}	Eq. (7.20)	μ_{rp}	Eq. (7.23)
μ_{jp}	Eq. (7.25)	$(\nu_j)_{vol}$	Eq. (7.67)
μ'_{jo}	Eq. (8.7)	α_C	Eq.(8.33)
γ_j	Eq. (8.35)	γ_{vol}	Eq. (8.36)
α_{vol}	Eq. (8.37)	α_{pk}	Eq. (8.38)
$(\varepsilon_j)_{pk}$	Eq. (8.45)		

Step (1) Input the material (FRP jacket and concrete) properties and FRP-confined section geometry, and calculate the mechanical and geometric terms shown in the flow diagram of **Figure 10.6**

Step (2) Utilize the flow diagram of **Figure 10.7-10.9** to model the uniaxial stress-strain behavior of FRP-confined concrete sections.

Parametric Study

The purpose of this parametric study is to examine how the proposed constitutive stress-strain model introduced herein responds to variations in the values of the various parameters including material properties, geometric and mechanical properties of the FCC section, and shape-dependent dilation and stress-strain parameters.

This includes the effects of the concrete material properties, such as the initial Poisson's ratio ν_{ci}, the initial modulus of elasticity E_{ci} of Eq. (10.5), the peak unconfined compressive strain ε_{co} and strength f_{co}, and the effective basic angle of internal friction ϕ_{be} of the concrete material are considered.

Variation of the FRP jacket properties such as jacket stiffness K_{je} of Eq. (4.18), the aspect ratio α_{sh} of the rectangular (RFCC) and elliptical (EFCC) FCC section of Eq. (4.2), the jacket corner ratio α_j of the RFCC section of Eq. (4.4), and the plastic dilation rate μ_{jp} of Eq. (7.24) are studied.

Variation of the strain ductility ratio R_{sh} of Eq. (10.12), a stress-strain model specific parameter, is considered in this parametric study. The FCC sections that serve as a basis of this parametric study are the following:

Case 1: A circular FRP-confined concrete section (CFCC) confined by a circular FRP jacket having a 305 mm diameter section.

Case 2: A rectangular FRP-confined concrete (RFCC) section with a minor dimension B_c of 305 mm, a unit aspect ratio $\alpha_{sh} = H_c / B_c = 1.0$ (i.e., a square section), and a jacket corner ratio $\alpha_j = R_j / H_c = 5.0\,\%$, where H_c is the major jacket dimension and R_j is the jacket corner radius.

The aforementioned FCC sections have an unconfined compressive strength of 41.4 MPa, an elastic modulus calculated using E_{ci} of Eq. (10.5), an unconfined peak compressive strain using ε_{co} of 0.002 mm/mm, i.e., $\varepsilon_{co} = 0.002$, with the curvature parameter n_u of Eq. (10.7), a tensile strength ratio $k_t = \left| f_{to} / f_{co} \right|$ of Eq. (9.9), with f_{to} of Eq. (9.30), a basic angle of friction of $\phi_b = 35^\circ$, a pore water pressure parameter n_{PW} of Eq. (9.62) and (9.63) of $n_{PW} = 5.0$ percent, an effective basic angle of friction $\phi_{be} = 34.1^\circ$ found using Eq. (9.64), and an initial Poisson's ratio of $\nu_{ci} = 0.20$. These sections are assumed to be confined by an FRP jacket having a transverse modulus E_j of 82.7 MPa and a jacket rupture strain of $\varepsilon_{ju} = 8.50$ mm/m.

Unless otherwise noted, the cases considered in the parametric study include sections confined by low stiffness FRP jackets with $K_{je} = 10.0$ and high stiffness jackets with $K_{je} = 30.0$. In the parametric study of the proposed model, the only parameters that change in value are those that are affected by the parameter being considered.

Concrete Material Properties

Initial Poisson's Ratio

The effects that the initial Poisson ratio ν_{ci} has on the stress-strain model introduced herein for the CFCC section of **Case 1** is plotted in the axial stress-strain curves shown in **Figure 10.10; Figure 10.11** shows the axial stress-strain curves for the RFCC section of **Case 2**. The Poisson's ratios considered in this parametric analysis are $\nu_{ci} = 0.15$ and $\nu_{ci} = 0.30$, which are considered to be the lower and upper bound values, respectively, of the initial Poisson's ratio of concrete materials. As can be observed in these figures, the initial Poisson's ratio ν_{ci}, is predicted to have no significant effect on the stress-strain curve of the CFCC or RFCC section.

The most noticeable influence predicted by the model is that as ν_{ci} increases, the ultimate axial strain ratio $(k_\varepsilon)_u$ (i.e., at $\varepsilon_c = \varepsilon_{cu}$) experiences a slight decrease; this results in a decrease in the strain ductility of the confined concrete core. This is apparent for both low and high stiffness FRP-jacketed sections and is predicted to be independent of the FRP jacket shape. A slight decrease in the ultimate stress ratio $(k_c)_u$ or ultimate axial stress f_{cu} is predicted to occur as ν_{ci} increases. This effect is more apparent in RFCC sections confined by high stiffness FRP jackets, than in circular sections.

The analytical model predicts that for a given plastic strain ratio $k_{\varepsilon p}$, the normalized plastic stress ratio value k_{cp} slightly increases as the initial Poisson's ratio ν_{ci} increases. This indicates that a slight increase in the strain energy in the FRP-confined concrete is predicted to occur at any given plastic strain ratio $k_{\varepsilon p}$, as ν_{ci} doubles in value.

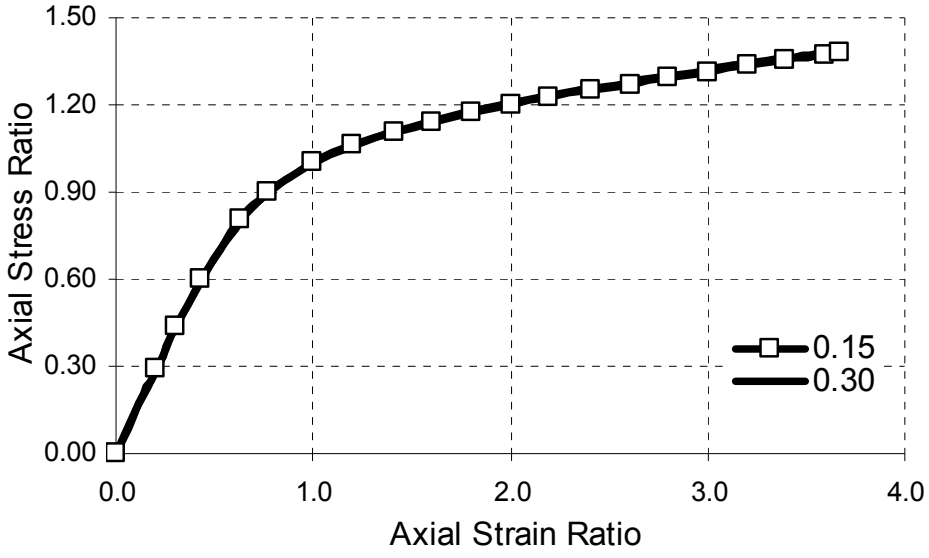

(a)

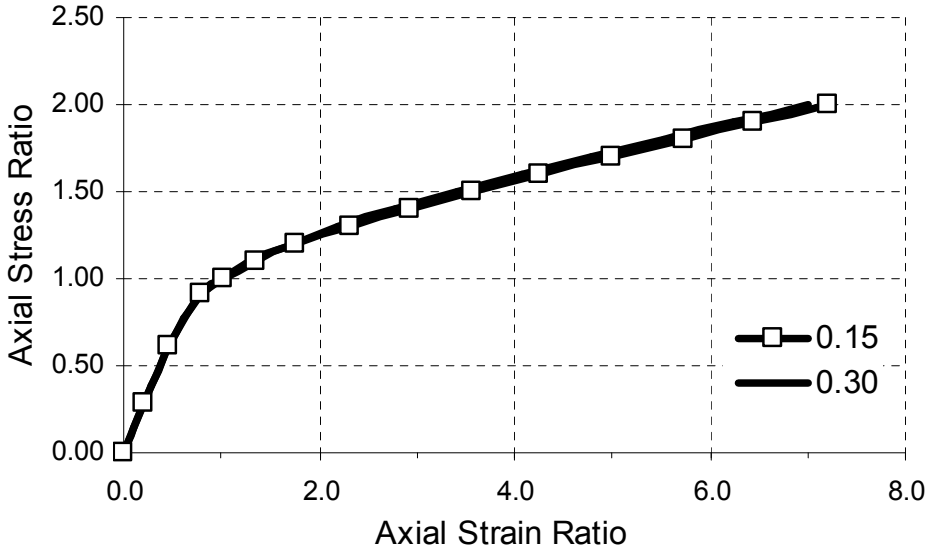

(b)

Figure 10.10 Axial stress-axial strain ratio curves of a circular concrete section confined by a (a) low stiffness and (b) high stiffness FRP jacket with various initial Poisson's ratio.

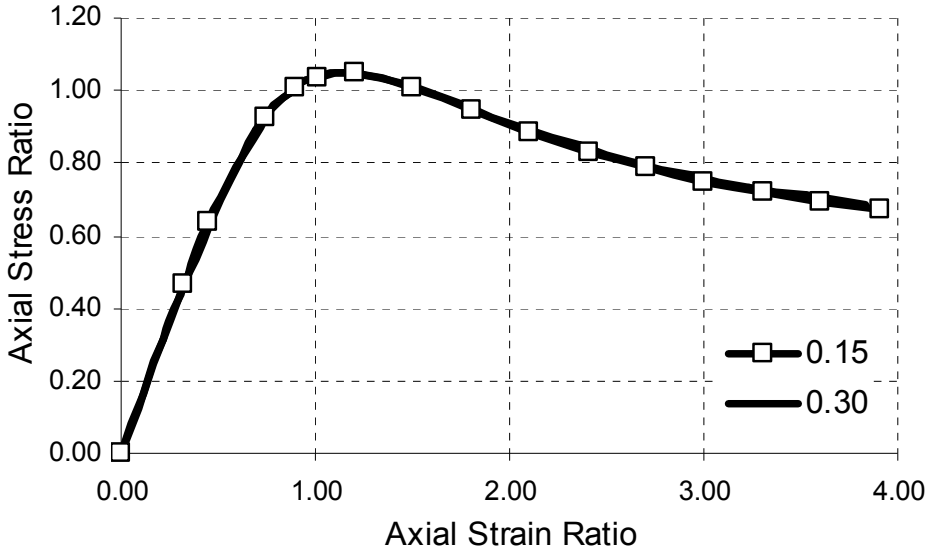

(a)

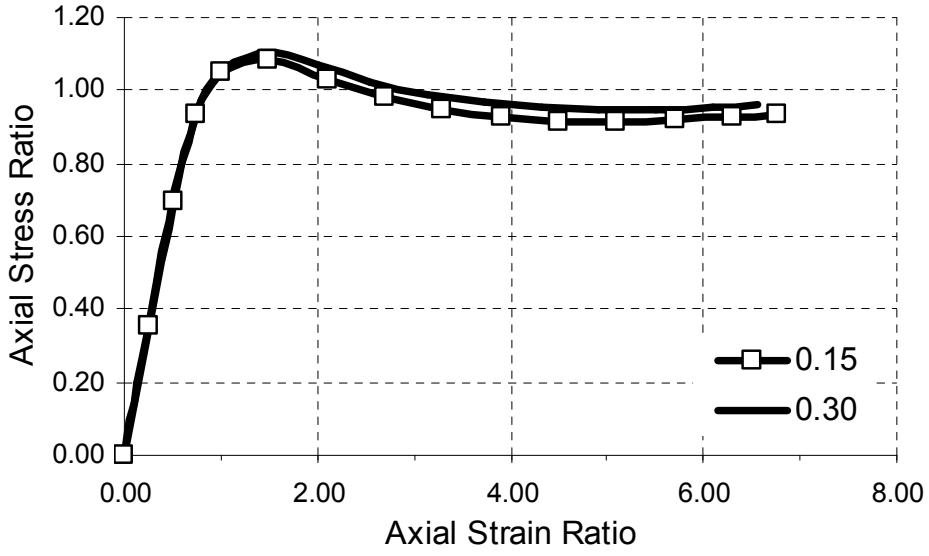

(b)

Figure 10.11 Axial stress-axial strain ratio curves of a rectangular concrete section confined by a (a) low stiffness and (b) high stiffness FRP jacket with various initial Poisson's ratio.

Initial Modulus of Elasticity

The effects that the initial modulus of elasticity E_{ci} of the concrete core has on the proposed stress-strain model for the CFCC section of **Case 1** is plotted in the axial stress-strain ratio curves shown in **Figure 10.12.** and in **Figure 10.13** for the RFCC section of **Case 2**. The initial modulus of elasticity E_{ci} values considered in this section of the parametric analysis is multiples of E_{ci} of Eq. (10.5), which are $0.75E_{ci}$, E_{ci}, and $1.25E_{ci}$.

As can be observed in **Figure 10.12**, a slight increase in the axial failure strain ratio $(k_\varepsilon)_u$ (i.e., at $\varepsilon_c = \varepsilon_{cu}$) and ultimate stress ratio k_{cu} is predicted to occur as the initial modulus of elasticity E_{ci} increases for both low and high stiffness CFCC sections. This results in a small increase in strain ductility of the confined concrete as both $(k_\varepsilon)_u$ and $(k_c)_u$ increase.

The analytical model predicts that for FCC sections exhibiting an essentially bilinear strain-hardening compressive stress-strain behavior, such as those shown in **Figure 10.12**, the initial slope and the slope of the plastic strain curve increases slightly as E_{ci} increases. This indicates that the model predicts a proportional relationship between the plastic slope of the sections exhibiting a bilinear strain-hardening behavior and the initial modulus of elasticity E_{ci} of the concrete core.

In RFCC sections, the analytical model predicts that an increase in the initial modulus of elasticity E_{ci} results in a significant decrease in the ultimate strength ratio k_{cu}, as shown **Figure 10.13**, for both high stiffness and low stiffness rectangular FRP-jacketed sections.

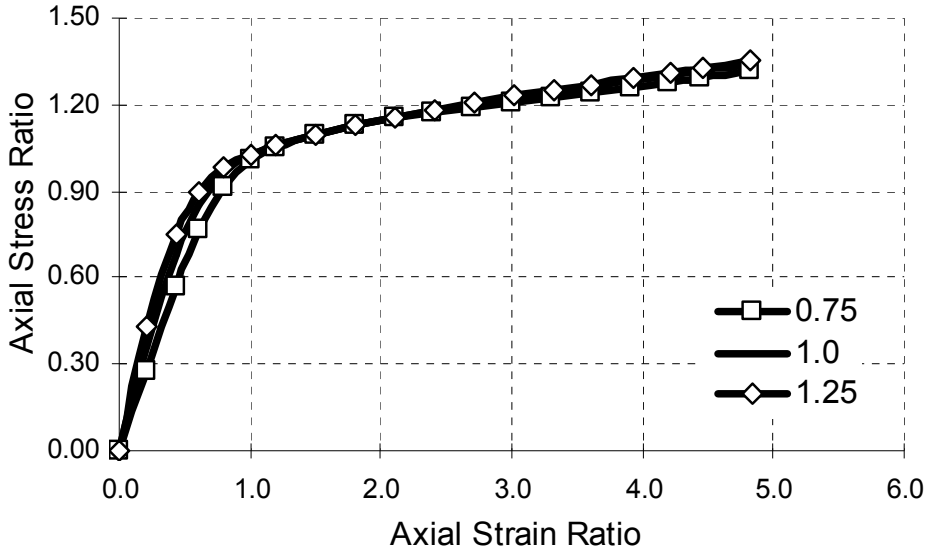

(a)

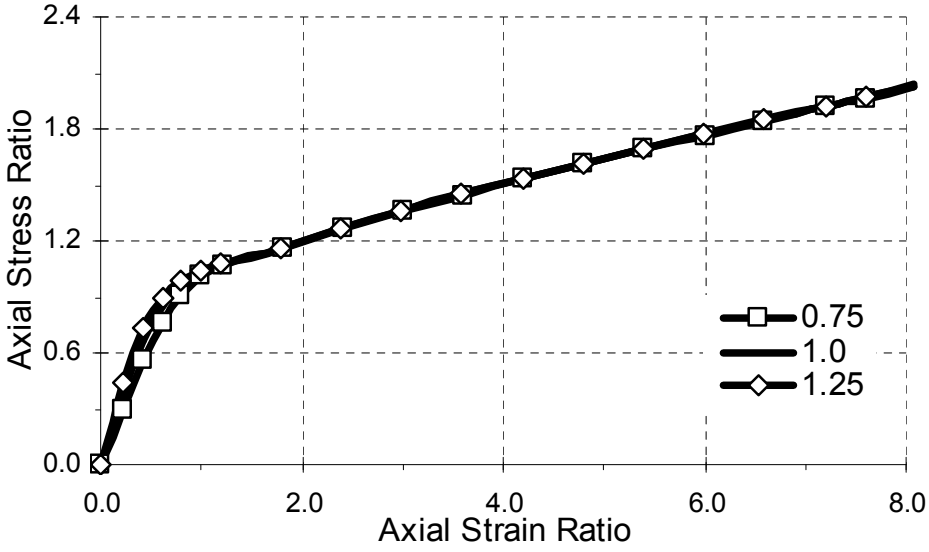

(b)

Figure 10.12 Axial stress-axial strain ratio curves of a circular concrete section confined by a (a) low stiffness and (b) high stiffness FRP jacket with various initial modulus of elasticity.

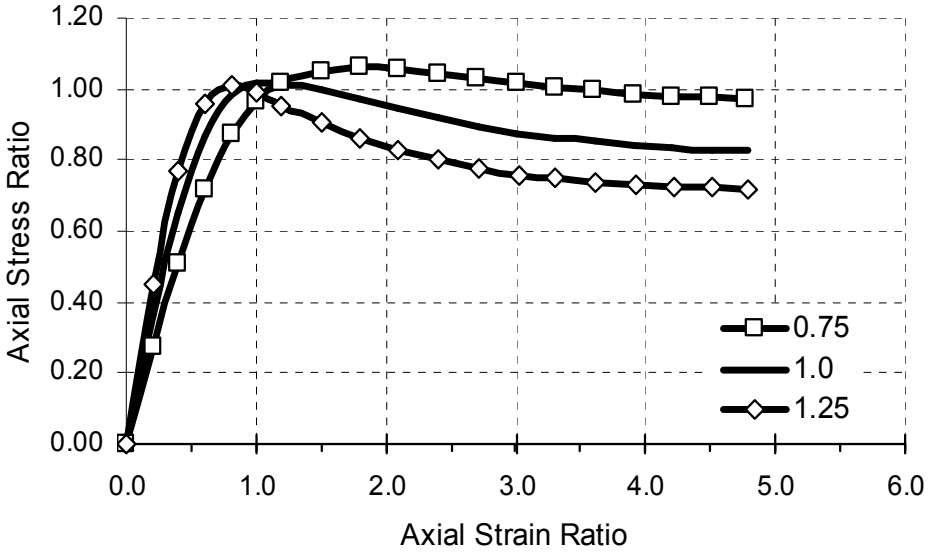

(a)

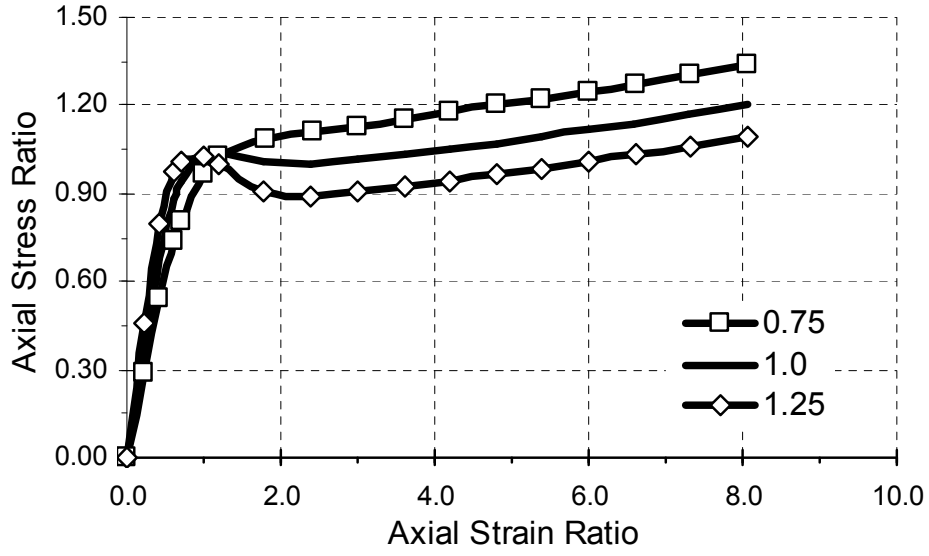

(b)

Figure 10.13 Axial stress-axial strain ratio curves of a rectangular concrete section confined by a (a) low stiffness and (b) high stiffness FRP jacket with various initial modulus of elasticity.

For sections exhibiting a strain-softening compressive behavior, typical of RFCC sections with a small corner radius, as shown in **Figure 10.13**, the model predicts that in the plastic region of the stress-strain curve (i.e., when $k_{\varepsilon} > 1.0$) and the axial stress ratio k_c at a given plastic axial strain ratio $k_{\varepsilon p}$ decreases as E_{ci} increases. This implies that an inversely proportional relationship is predicted between the axial plastic stress f_{cp} and the initial modulus E_{ci} for sections exhibiting strain-softening compressive behavior. This also indicates that the model predicts a decrease in the strain energy in the RFCC section at a given plastic axial strain ratio $k_{\varepsilon p}$ as E_{ci} increases. Analysis of **Figures 10.12** and **10.13** indicates that the effects that initial modulus of elasticity E_{ci} has on the analytical stress-strain curve of an FCC section is shape-dependent.

The effects of the elastic modulus E_{ci} on the analytical stress-strain curve of elliptical sections with an aspect ratio of $\alpha_{sh} = 1.5$ and $\alpha_{sh} = 2.0$ that are confined by a high stiffness $K_{je} = 30.0$; FRP jacket are investigated in **Figures 10.14(a)** and **(b)**, respectively. From these figures it can be observed that as both the aspect ratio α_{sh} of the elliptical section and E_{ci} increase, the ultimate stress ratio k_{cu} is predicted to decrease at a faster rate. An increase in the strain ductility of the FRP-confined concrete section is forecasted to occur as E_{ci} increases, due to an increase in the ultimate stress ratio k_{cu}. This effect is predicted to be independent of the elliptical section aspect ratio.

In **Figures 10.15(a)** and **(b)** the effects that the elastic modulus E_{ci} has on the analytical stress-strain curve of rectangular sections with aspect ratios of $\alpha_{sh} = 1.25$ and $\alpha_{sh} = 1.50$ confined by high stiffness FRP jackets are investigated.

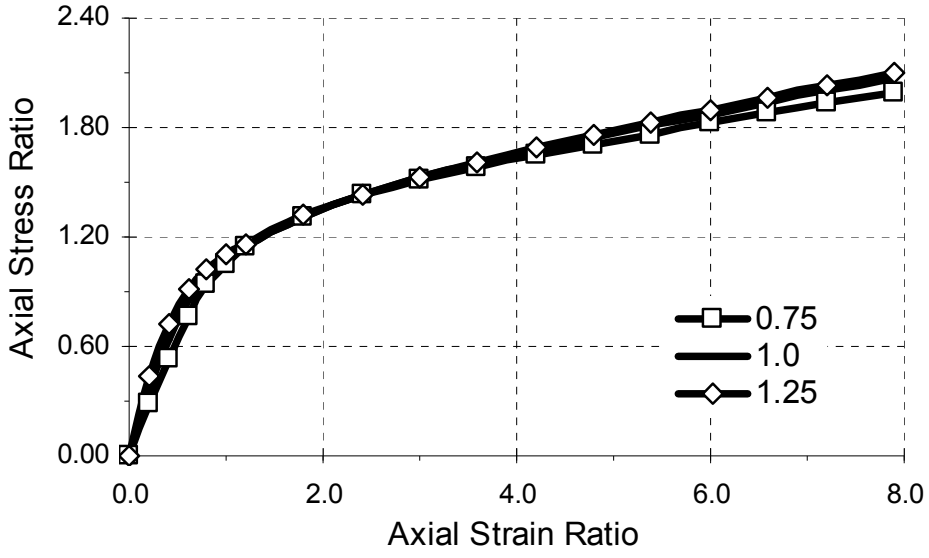

(a)

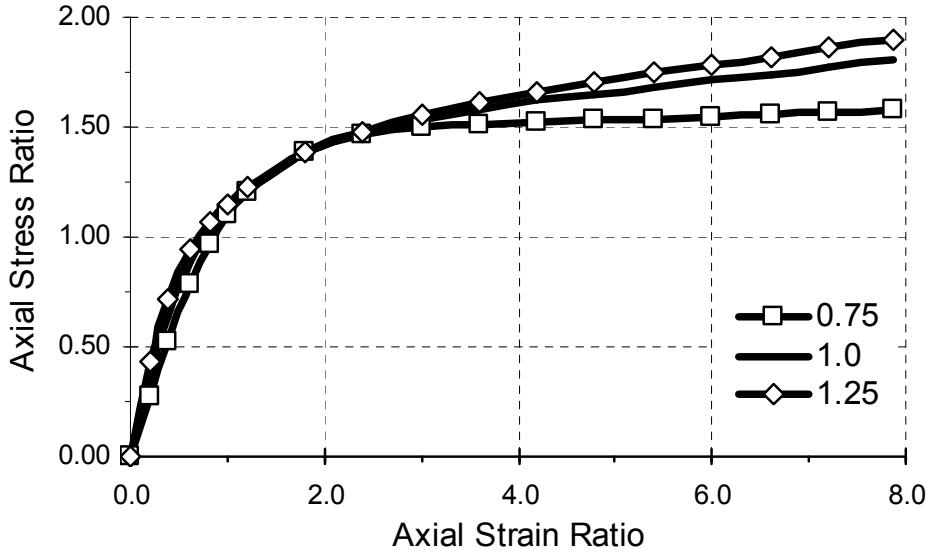

(b)

Figure 10.14 Axial stress-axial strain ratio curves of elliptical concrete section confined by a high stiffness FRP jacket with a section aspect ratio of (a) 1.50 and (b) 2.00 and various initial modulus of elasticity.

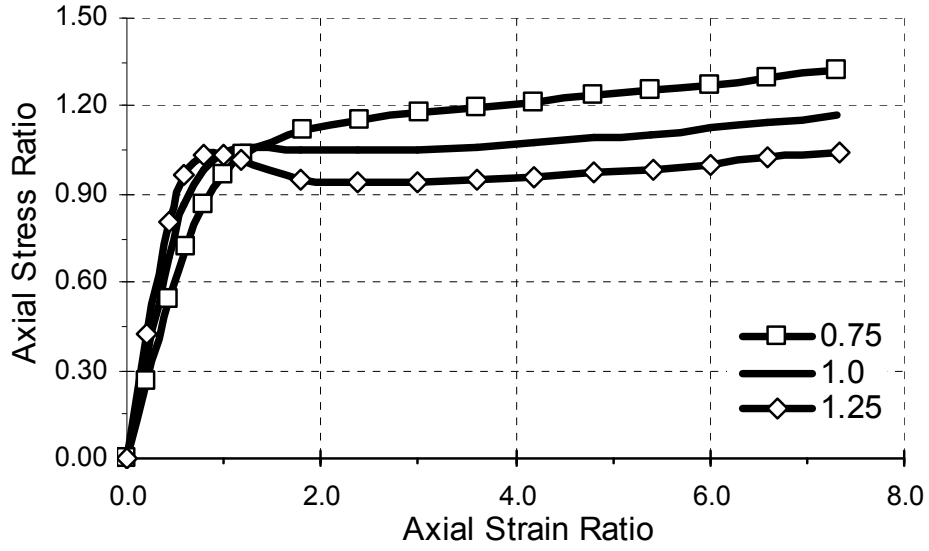

(a)

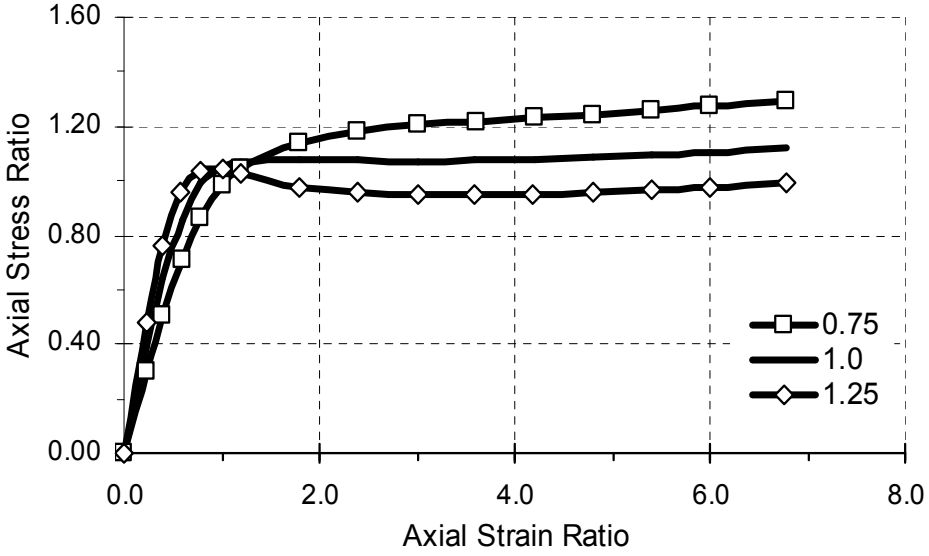

(b)

Figure 10.15 Axial stress-axial strain ratio curves of rectangular sections confined by stiffness FRP jacket having a section aspect ratio of (a) 1.25 and (b) 1.50 with various initial modulus of elasticity.

The analytical model predicts that as both the aspect ratio α_{sh} of the RFCC section and E_{ci} of the concrete increases, the ultimate stress ratio k_{cu} decreases at a faster rate; this effect is in contradiction with that predicted for EFCC sections. The decrease in strain ductility of RFCC sections is predicted to be dependent on the section aspect ratio.

Based on analysis of **Figures 10.12-10.15,** it can be stated that the analytical model predicts that the shape of the FRP-jacketed section has a significant effect on the shape of the axial compressive stress-strain curve of the FRP-jacketed section; this is supported by experimental evidence.

Unconfined Peak Compressive Strain

The effects that the unconfined peak compressive strain ε_{co} has on the stress-strain behavior predicted by the analytical stress-strain model introduced herein is plotted in the axial stress-strain ratio curves shown in **Figure 10.16** for the CFCC section of **Case 1** and in **Figure 10.17** for the RFCC section of **Case 2**. The unconfined peak compressive strain ε_{co} considered in this section of the parametric analysis are multiples of $\varepsilon_{co} = 0.002$, which are $0.75\varepsilon_{co}$, ε_{co}, and $1.25\varepsilon_{co}$.

As shown in **Figure 10.16**, the model predicts that for CFCC sections an increase in the unconfined peak compressive strain ε_{co} results in a decrease of the ultimate strain ratio $(k_\varepsilon)_u$ (i.e., at $\varepsilon_c = \varepsilon_{cu}$) and a slight increase in ultimate axial stress ratio k_{cu}, for both high stiffness and low stiffness CFCC sections. This effect is most notable in low stiffness circular FRP-jacketed sections. This indicates that a decrease in the strain ductility of the confined concrete is predicted to occur as ε_{co} increases.

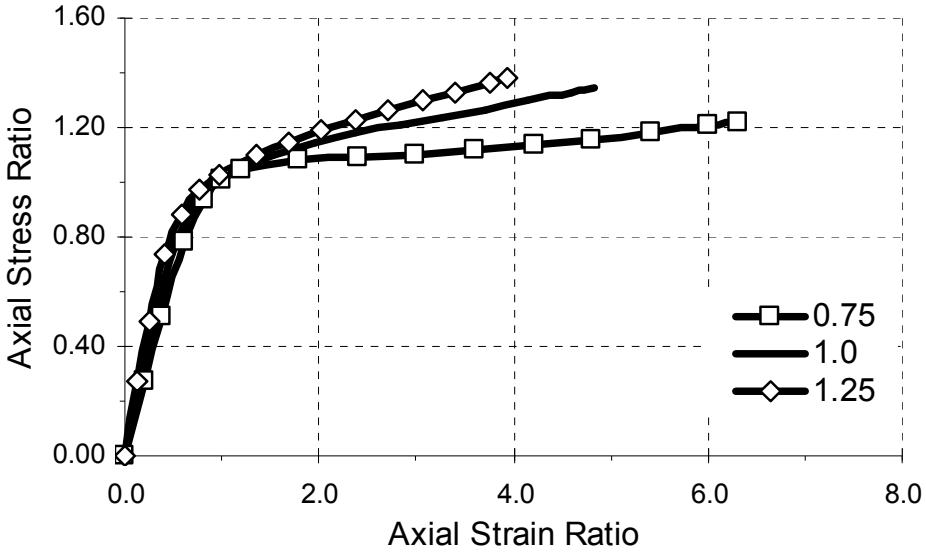

(a)

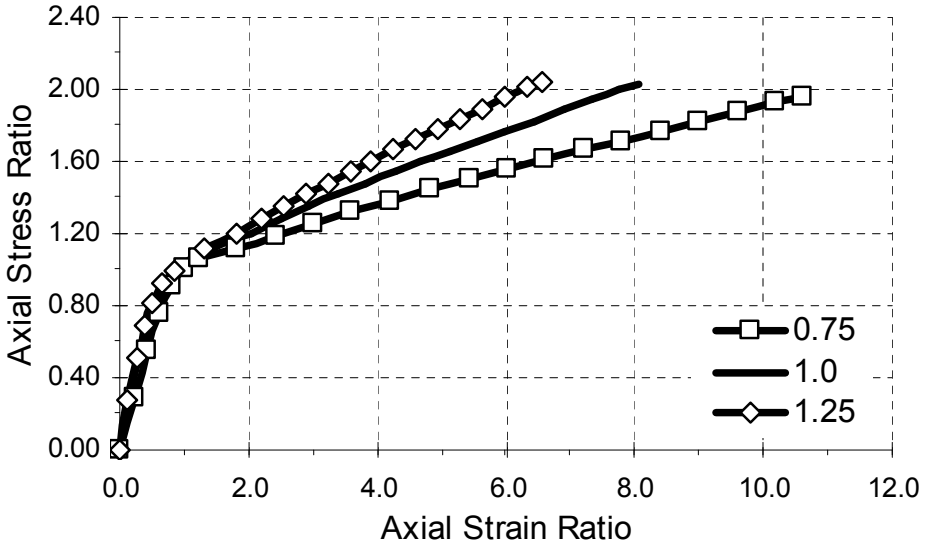

(b)

Figure 10.16 Axial stress-axial strain ratio curves of a circular concrete section confined by (a) low and (b) high stiffness FRP jacket with various peak unconfined compressive strains.

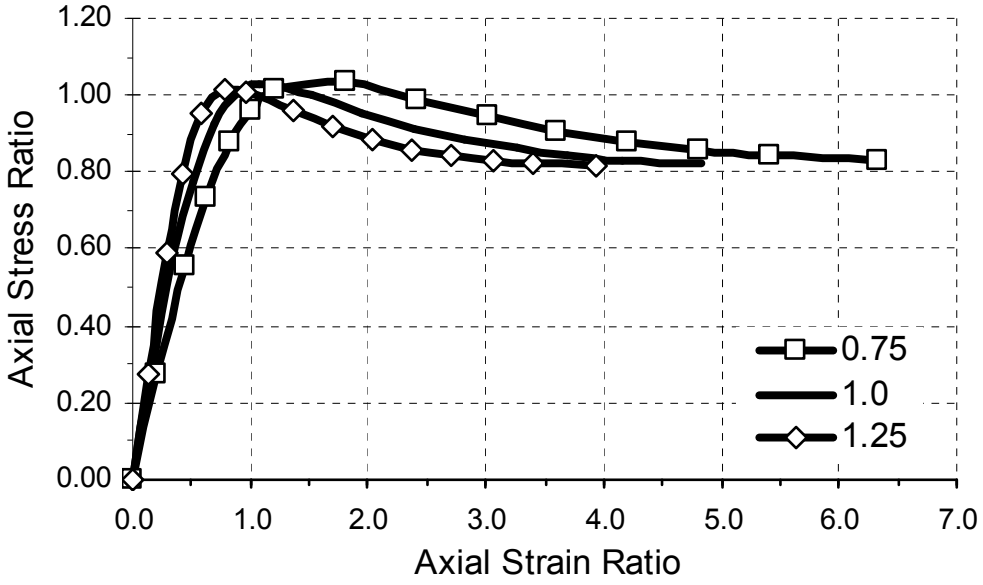

(a)

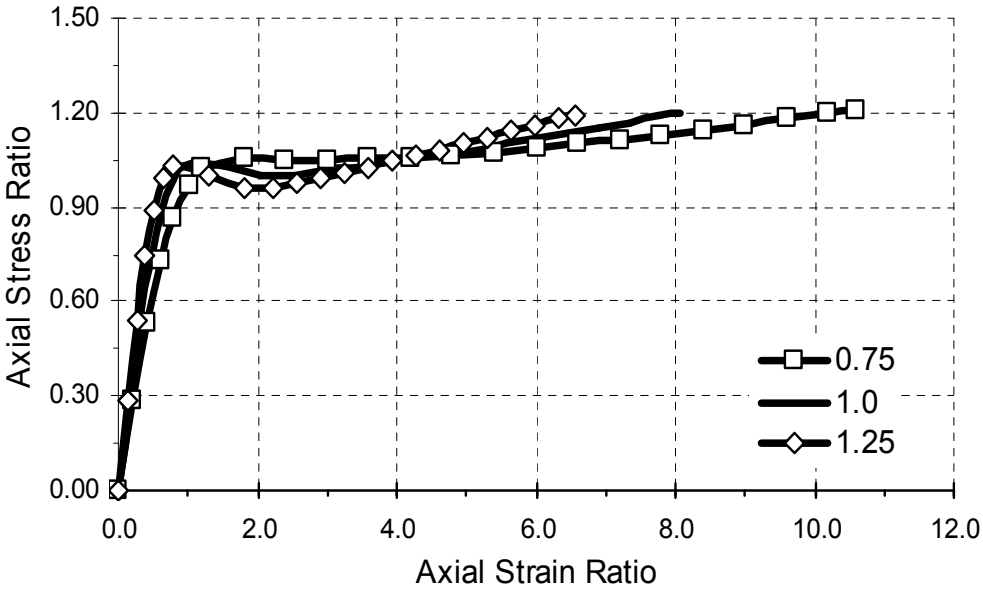

(b)

Figure 10.17 Axial stress-axial strain ratio curves of a rectangular concrete section confined by (a) low and (b) high stiffness FRP jacket with various unconfined peak compressive strains.

For an FCC section exhibiting an essentially bilinear strain-hardening compressive stress-strain behavior, such as those shown in **Figure 10.16**, the slope of the plastic strain ratio curve is predicted to increase as ε_{co} increases; this indicates that a proportional relationship exists between the plastic slope of the stress-strain curve and the peak unconfined compressive strain ε_{co} of the concrete core. For FCC sections experiencing a bilinear strain-hardening behavior, the plastic slope of the analytical stress-strain curve is proportional to the FRP jacket stiffness and can be affected by the unconfined peak compressive strain e_{co} of the concrete core, as shown in **Figure 10.16**.

In rectangular sections, the model predicts that as ε_{co} increases, the ultimate axial strain ratio $(k_{\varepsilon})_u$ decreases, as shown in **Figure 10.17**, whereas the ultimate axial stress ratio k_{cu} slightly increases for high stiffness rectangular FRP-jacketed sections. For low plastic strain ratios $k_{\varepsilon p}$, a decrease in the energy of the RFCC section is predicted to occur for both low and high stiffness FRP jackets. At high plastic strain ratios $k_{\varepsilon p}$, a decrease in the strain energy of the RFCC section is predicted to occur for a low stiffness RFCC section and a slight increase for high stiffness RFCC sections, as ε_{co} increases. The model predicts that for FCC sections exhibiting a strain-softening compressive behavior, as shown in **Figure 10.17** for rectangular sections, an increase in the unconfined peak compressive strain ε_{co} significantly affects the shape of the analytical plastic stress-strain curve of the RFCC section.

Based on analysis of **Figures 10.16** and **10.17,** it can be stated that the analytical model predicts that the shape of the FRP-jacketed section has a significant effect on the

shape of the axial compressive stress-strain curve of the FRP-jacketed section; this is supported by experimental evidence.

Unconfined Peak Compressive Strength

The effects that the unconfined peak compressive strength f_{co} has on the stress-strain behavior predicted by the analytical stress-strain model introduced herein is plotted in the axial stress-strain ratio curves shown in **Figure 10.18** for the CFCC section of **Case 1** and in **Figure 10.19** for the RFCC section of **Case 2**. The unconfined peak compressive strengths considered in this section of the parametric analysis are $f_{co} = 13.8$ MPa, $f_{co} = 27.6$ MPa, and $f_{co} = 41.4$ MPa.

As shown in **Figure 10.18**, the model predicts that for CFCC sections an increase in the unconfined peak compressive strength f_{co} has no significant effect on the stress-strain behavior of the circular sections confined by either high or low stiffness FRP jackets. This indicates that no significant increase in strain energy occurs in CFCC sections exhibiting strain-hardening compressive behavior.

In RFCC sections, the model predicts that as f_{co} increases both the ultimate axial strain $(k_\varepsilon)_u$ and strength k_{cu} ratio decrease, as shown in **Figure 10.19**, which indicates a decrease in strain energy in the RFCC section as f_{co} increases. This effect is in contradiction with the effects predicted in CFCC sections exhibiting strain-hardening behavior, as shown in **Figure 10.18.** As a result, it can be stated that the analytical model predicts that the effect of the peak unconfined compressive strength f_{co} is FRP jacket shape-dependent and appears to be independent of the FRP jacket stiffness.

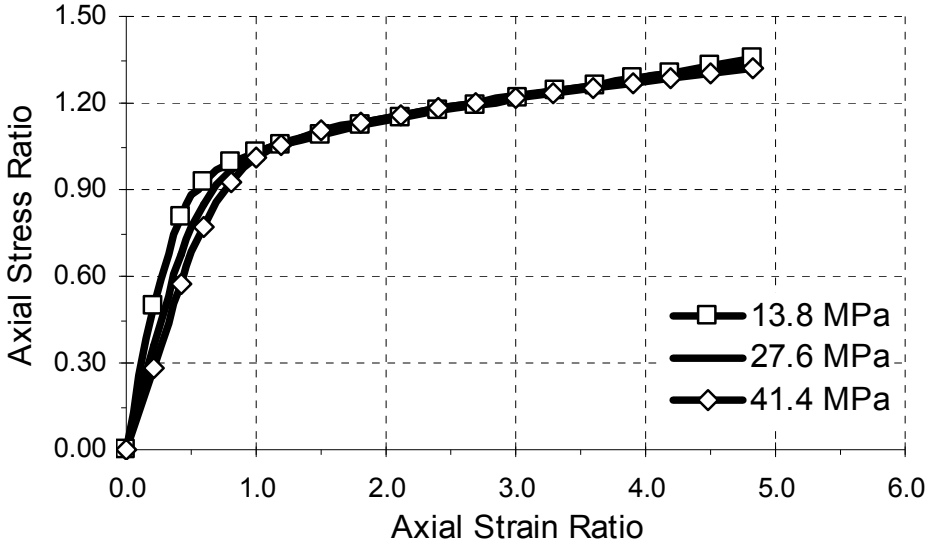

(a)

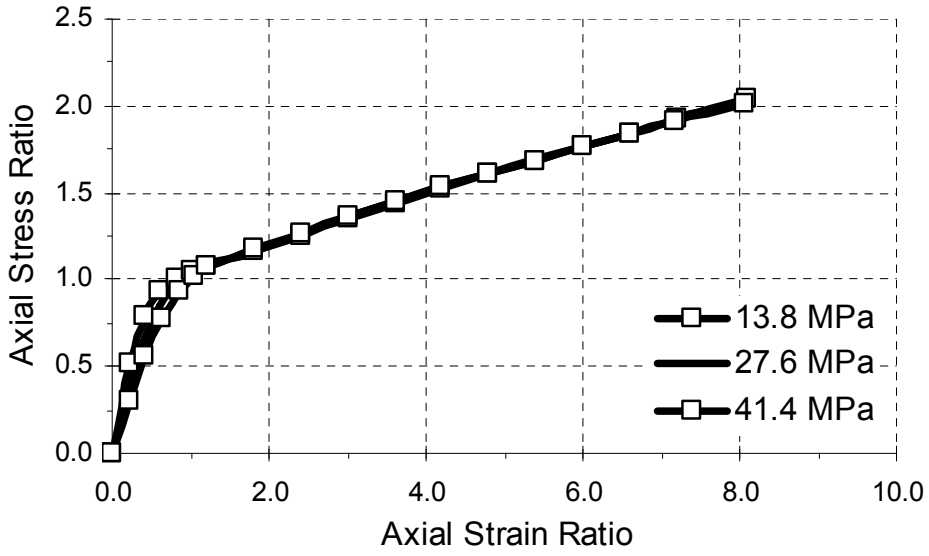

(b)

Figure 10.18 Axial stress-axial strain ratio curves of a circular concrete section confined by (a) low and (b) high stiffness FRP jacket with various unconfined peak compressive strengths.

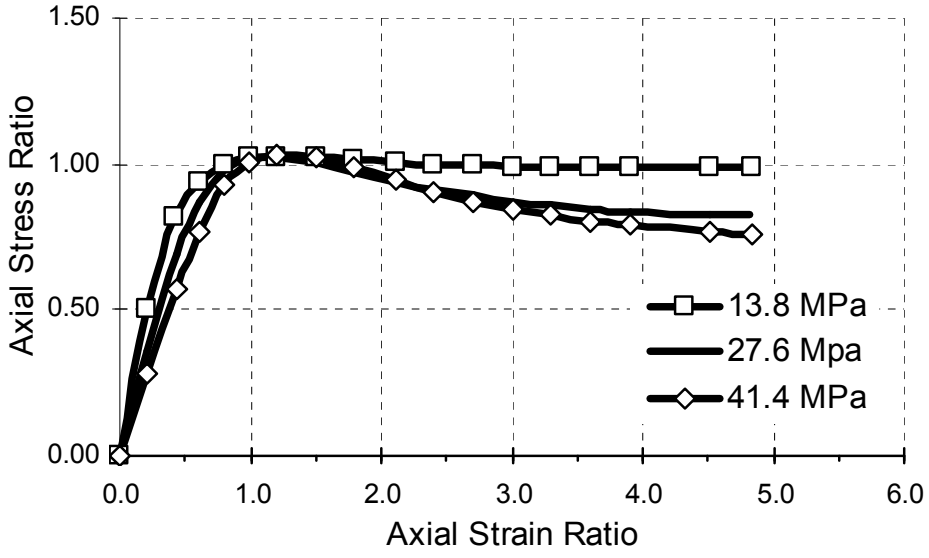

(a)

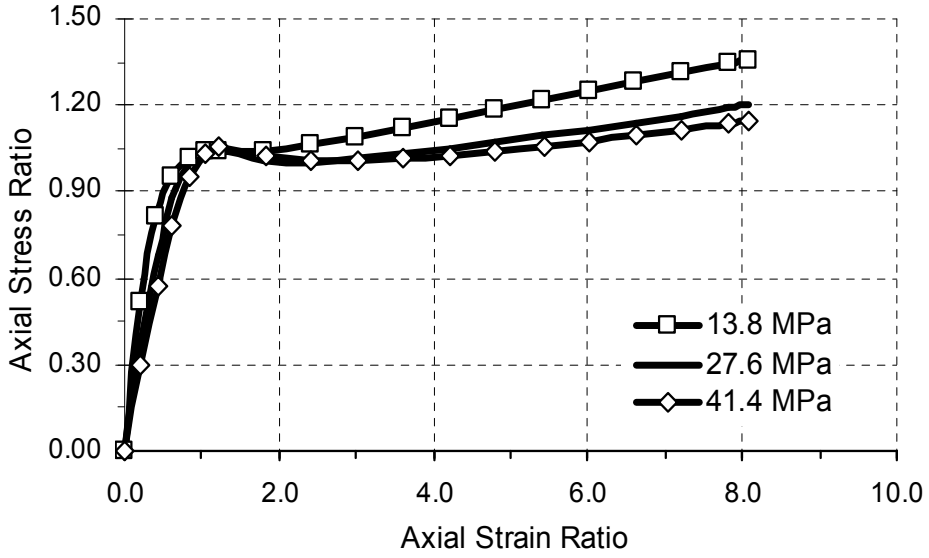

(b)

Figure 10.19 Axial stress-axial strain ratio curves of a rectangular concrete section confined by (a) low and (b) high stiffness FRP jacket with various unconfined peak compressive strengths.

Effective Basic Angle of Internal Friction

The effects of the effective basic angle of internal friction ϕ_{be} of the concrete core on the stress-strain behavior of FCC sections predicted by the analytical stress-strain model introduced herein are plotted in the axial stress-strain ratio curves shown in **Figure 10.20** for the CFCC section of **Case 1** and in **Figure 10.21** for the RFCC section of **Case 2**.

The effective basic angles of internal friction ϕ_{be} considered in this section of the parametric analysis are determined using a pore water pressure parameter n_{PW} of Eqs. (9.62) and (9.63) of $n_{PW} = 12.5$ %, $n_{PW} = 25.0$ and $n_{PW} = 50.0$, which result in $\phi_{be} = 32.7^{\circ}$, $\phi_{be} = 30.2^{\circ}$, and $\phi_{be} = 23.7^{\circ}$, respectively, found using ϕ_{be} of Eq. (9.64).

As can be observed in **Figures 10.20** and **10.21**, the model predicts that for CFCC and RFCC sections a decrease in the effective angle of internal friction ϕ_{be}, i.e., as the pore water pressure parameter n_{PW} increase, results in a decrease in the ultimate axial stress ratio k_{cu} (i.e., at $f_c = f_{cu}$).

For the CFCC sections that exhibit an essentially bilinear strain-hardening compressive behavior and RFCC sections that exhibit a strain-softening behavior, such as those shown in **Figures 10.20** and **10.21**, the slope of the plastic strain curve is predicted to decrease as the pore water pressure parameter n_{PW} increases, i.e., when ϕ_{be} decreases. This indicates that an inversely proportional relationship between the plastic slope of the stress-strain curve and the effective basic angle of internal friction ϕ_{be} of the concrete core is predicted.

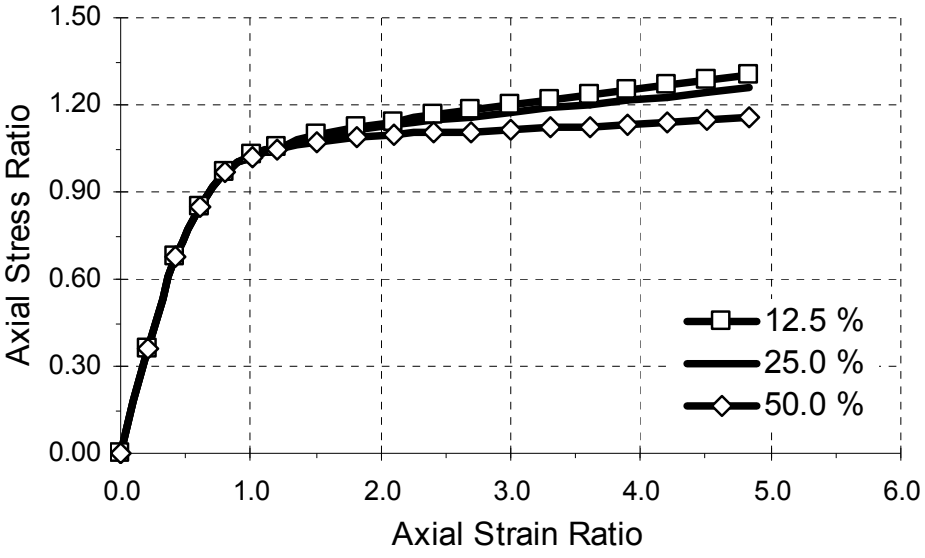

(a)

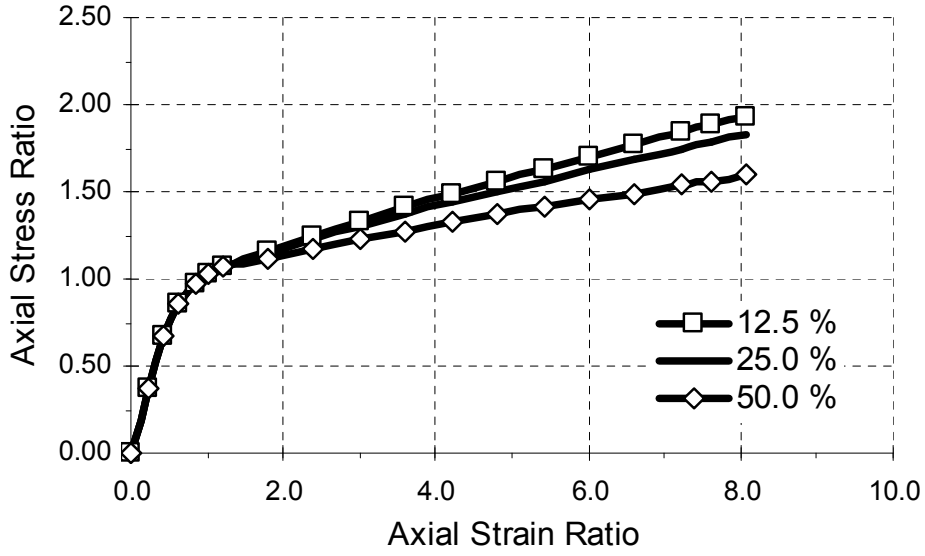

(b)

Figure 10.20 Axial stress-strain ratio curves of a circular concrete section confined by (a) low and (b) high stiffness FRP jacket with various pore water pressure parameters.

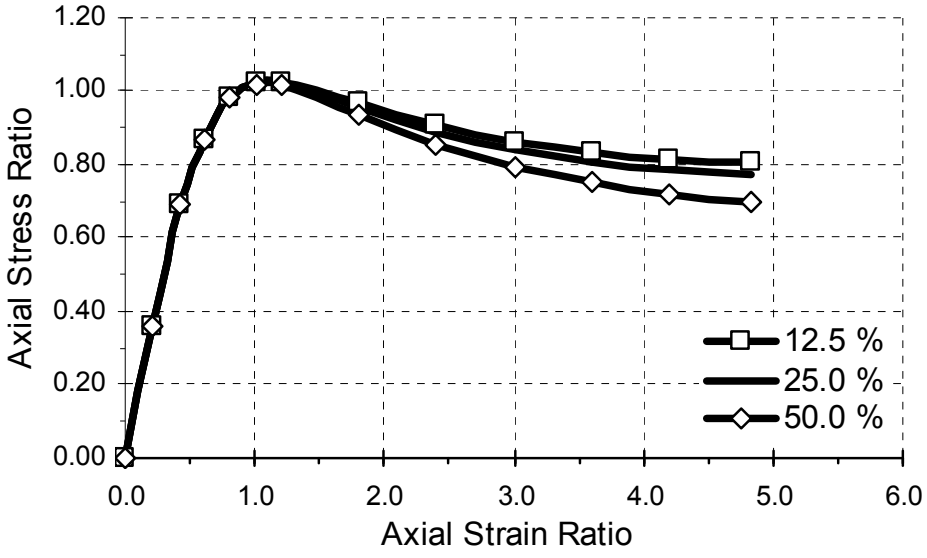

(a)

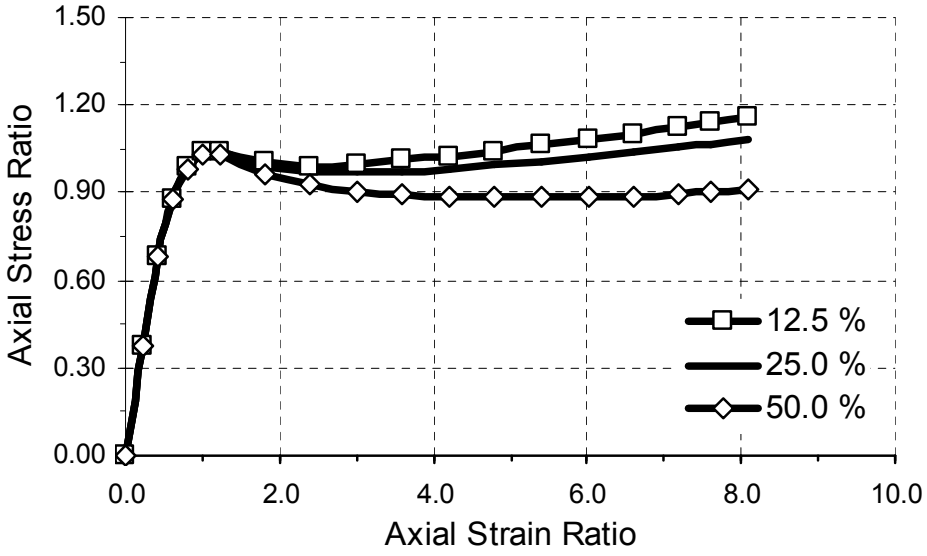

(b)

Figure 10.21 Axial stress-strain ratio curves of a rectangular concrete section confined by (a) low and (b) high stiffness FRP jacket with various pore water pressure parameters.

As a result, the plastic stress ratio k_{cp} at a given plastic axial strain ratio $k_{\varepsilon p}$ increases as ϕ_{be} increases, which indicates an increase in strain energy in the CFCC and RFCC sections is predicted to occur regardless of the FRP jacket stiffness.

This forecasted behavior is supported by experimental evidence, as concrete-filled FRP tubes (CFFT) exhibit a decrease in the plastic slope in comparison with bonded FRP-jacketed (BFCC) sections with similar FRP jacket stiffness, as will be demonstrated in the comparison with experimental results.

FRP Jacket Properties

FRP Jacket Stiffness

The effect that the FRP jacket stiffness K_{je} of Eq. (4.18) has on the stress-strain model introduced herein is plotted as an axial stress-strain ratio curve in **Figure 10.22(a)** for the CFCC section of **Case 1**, and in **Figure 10.22(b)** for the RFCC section of **Case 2**.

From analysis of **Figure 10.22(a)** it can be observed that for CFCC sections the model predicts that as the FRP jacket stiffness increases, both the ultimate stress ratio k_{cu} and strain ratio $(k_{\varepsilon})_u$ increase. The model makes similar predictions for RFCC sections, as shown in **Figure 10.22(b)**. An increase in the FRP jackets stiffness results in an increase in the ultimate axial strain ratio $(k_{\varepsilon})_u$ and stress ratio k_{cu}, which results in an increase in the strain ductility of the FRP-jacketed section.

At high axial plastic strains (i.e., at $k_{\varepsilon} = k_{\varepsilon p} > 2.0$), the slope of the stress-strain curve increases as the FRP jacket stiffness increases for a section experiencing a strain-hardening behavior, as shown in **Figure 10.22(a)** for CFCC sections.

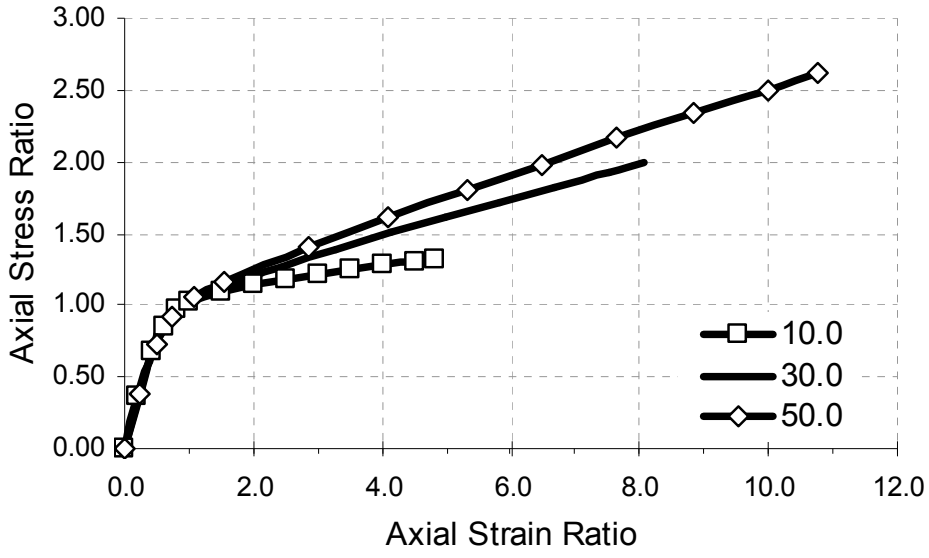

(a)

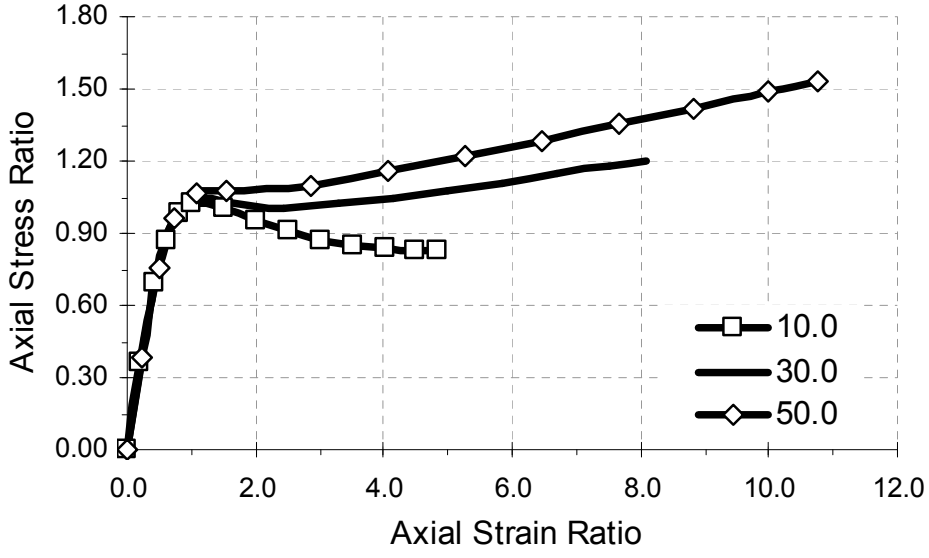

(b)

Figure 10.22 Axial stress-strain ratio curves of (a) circular and (b) rectangular concrete sections confined by FRP jackets of various jacket stiffness.

For sections experiencing a strain-softening behavior, as shown in **Figure 10.22(b)** for RFCC sections**,** the model predicts that the plastic slope can change from a negative plastic slope to a positive slope as the FRP jacket stiffness increases. Thus, at high axial plastic strains, the model forecasts that that the stress-strain behavior of the FCC section can change from that of a section exhibiting a strain-softening behavior to that of a section exhibiting strain-hardening as the stiffness of the FRP jacket increases.

As a result, it can be stated that the analytical model predicts that the effect that the FRP jacket stiffness K_{je} of Eq. (4.18) has on the compressive behavior of FRP-confined concrete sections is independent of the FRP jacket shape.

In order to accurately predict the shape of the uniaxial stress-strain curve of the FCC sections the model must adequately predict the effect that the FRP jacket stiffness K_{je} of Eq. (4.18) has on the compressive behavior of the FCC sections considered in this dissertation; this will be demonstrated in the comparison with experimental test results.

Jacket Aspect Ratio

The effect that the section aspect ratio α_{sh} of Eq. (4.2) has on the stress-strain behavior of FCC sections predicted by the analytical model introduced herein is plotted in the axial stress-strain ratio curves shown in **Figure 10.23** for an EFCC section of **Case 1,** and in **Figure 10.24** for an RFCC section of **Case 2**.

The cases considered in this parametric study are for sections with aspect ratios of $\alpha_{sh} = 1.0$, $\alpha_{sh} = 1.5$, and $\alpha_{sh} = 2.0$, with a constant jacket corner radius for the RFCC sections considered.

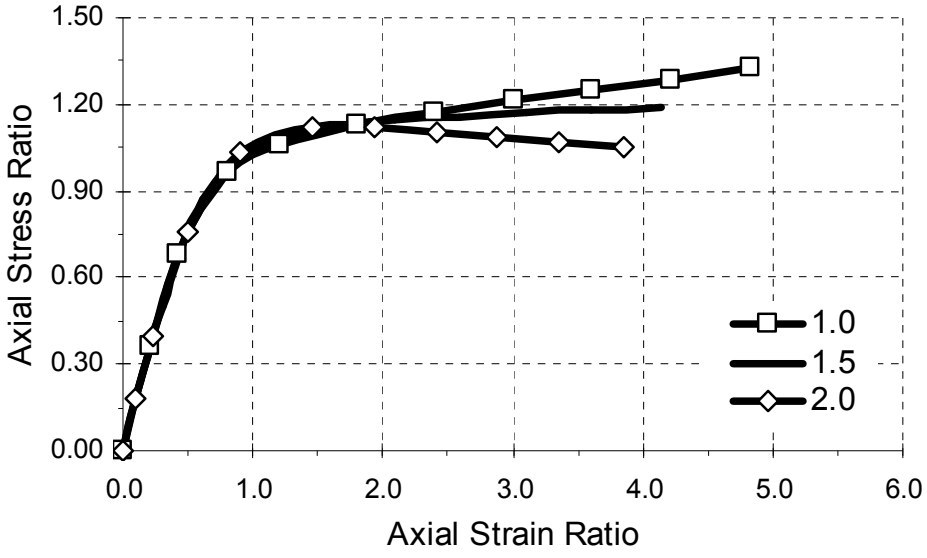

(a)

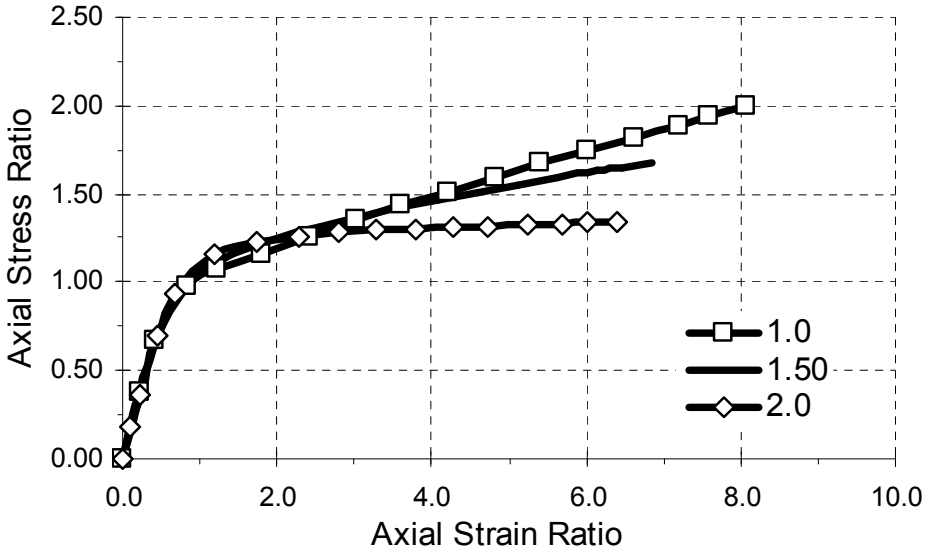

(b)

Figure 10.23 Axial stress-strain ratio curves of an elliptical concrete section confined by (a) low and (b) high stiffness FRP jacket with various section aspect ratios.

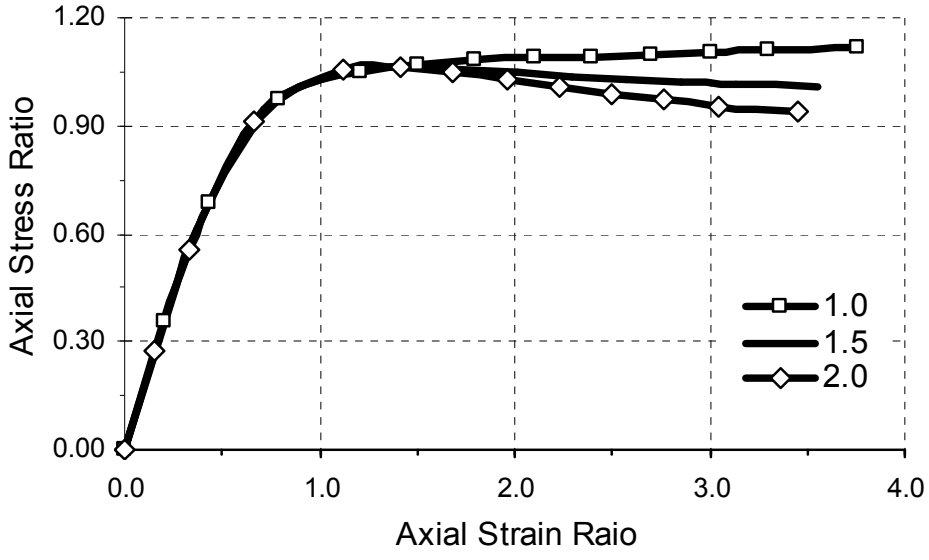

(a)

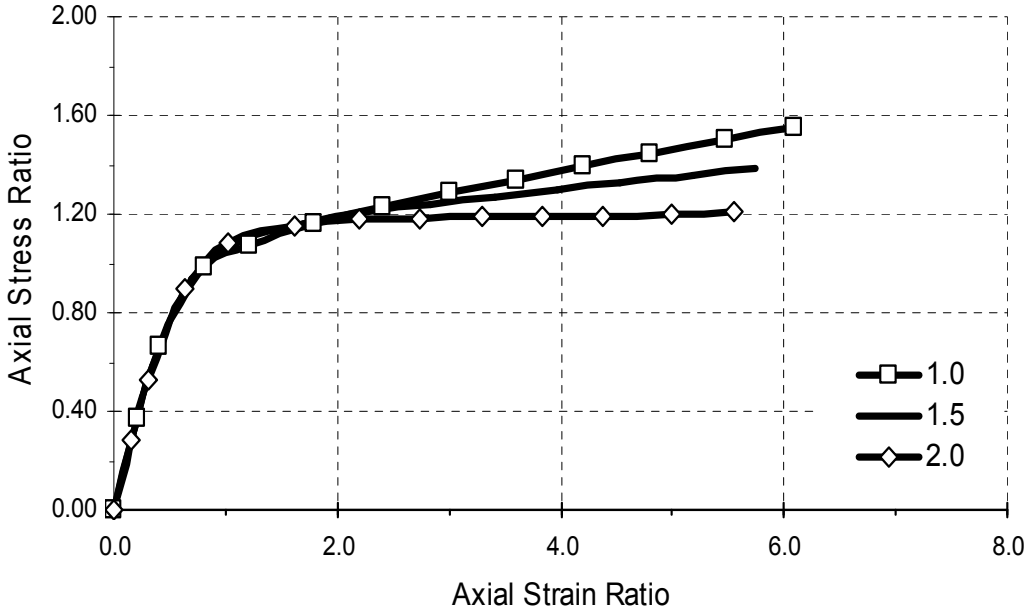

(b)

Figure 10.24 Axial stress-strain ratio curves of a rectangular concrete section confined by (a) low and (b) high stiffness FRP jacket with various section aspect ratios.

From these figures it can be observed that the analytical model predicts that an increase in the jacket aspect ratio α_{sh} results in a decrease in both the ultimate stress k_{cu} and strain $(k_{\varepsilon})_u$ ratio. This indicates that a decrease in the strain ductility of the confined concrete is predicted for both EFCC and RFCC sections as α_{sh} increases. As shown in **Figures 10.23** and **10.24**, this effect is more pronounced as the stiffness of the FRP jacket increases. This forecasted behavior is supported by the experimental evidence of RFCC and EFCC sections, as will be demonstrated in the comparison with experimental compressive tests. Analysis of **Figures 10.23** and **10.24** indicates that for a given plastic axial strain ratio $k_{\varepsilon p}$, a decrease in the strain energy of the confined concrete is predicted to occur as α_{sh} increases. This is due to the decrease in the plastic stress ratio k_{cp} at any given plastic axial plastic strain ratio $k_{\varepsilon p}$. This effect is predicted to be independent of the stiffness and shape of the FRP jacket. In order to accurately predict the shape of the uniaxial stress-strain curve of the FCC sections, the model must adequately capture the effects that the FRP jacket aspect ratio α_{sh} of Eq. (4.2) has on the compressive behavior of the FCC sections considered in this dissertation.

Jacket Corner Aspect Ratio

The effect that the jacket corner aspect ratio α_j of Eq. (4.4) has on the stress-strain behavior of RFCC sections predicted by the analytical stress-strain model introduced herein for **Case 2** is plotted in the axial stress-strain ratio curves shown in **Figure 10.25,** and for a RFCC section of **Case 2** with a section aspect ratio $\alpha_{sh} = 2.0$ is plotted in **Figure 10.26**.

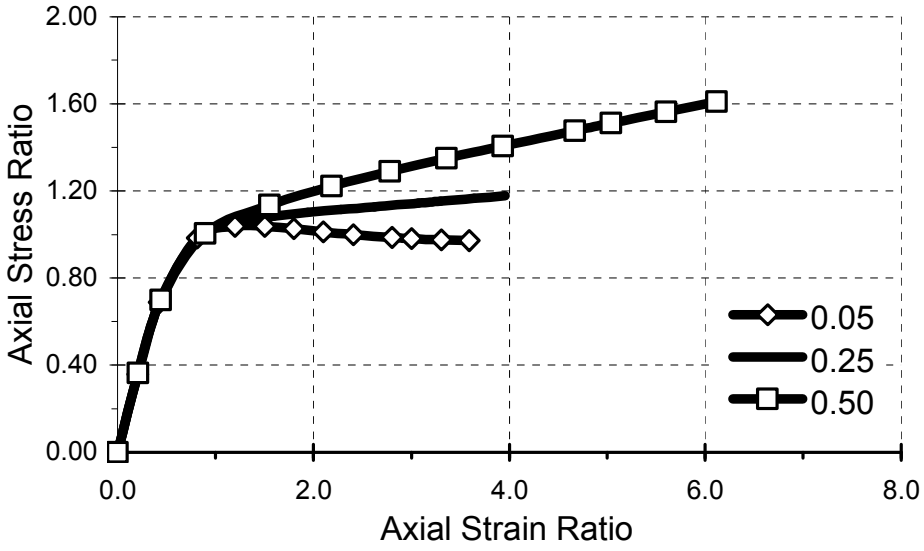

(a)

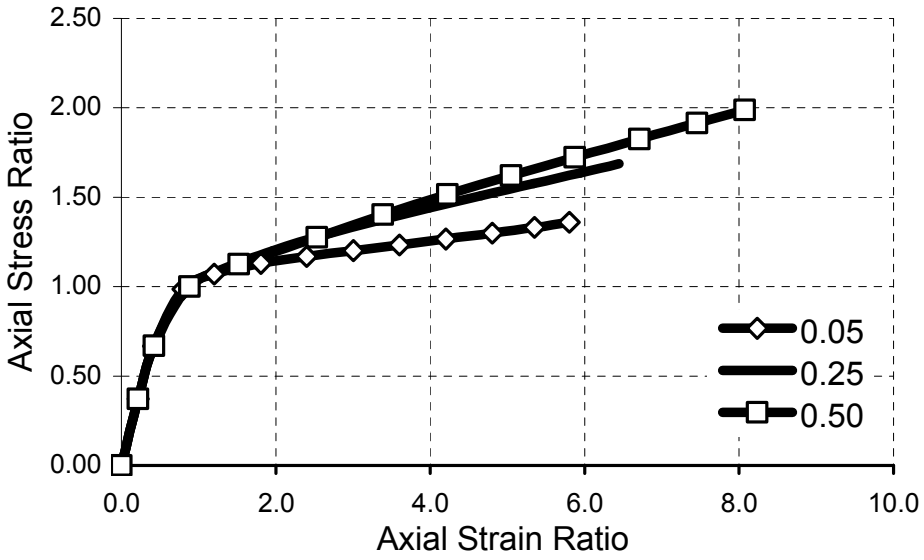

(b)

Figure 10.25 Axial stress-strain ratio curves of a square concrete section confined by (a) low and (b) high stiffness FRP jacket with various jacket corner aspect ratios.

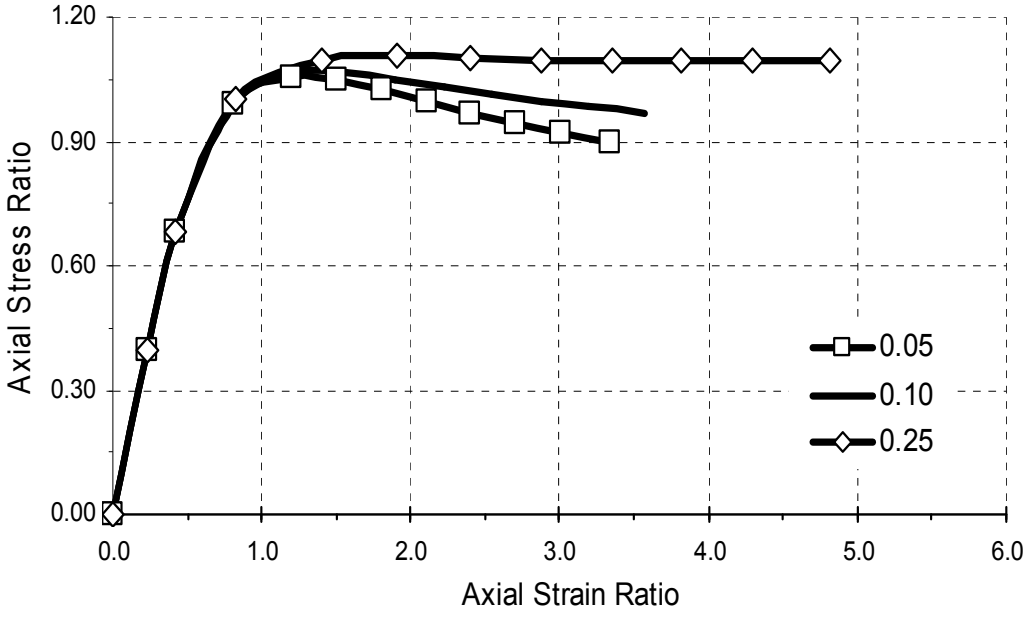

(a)

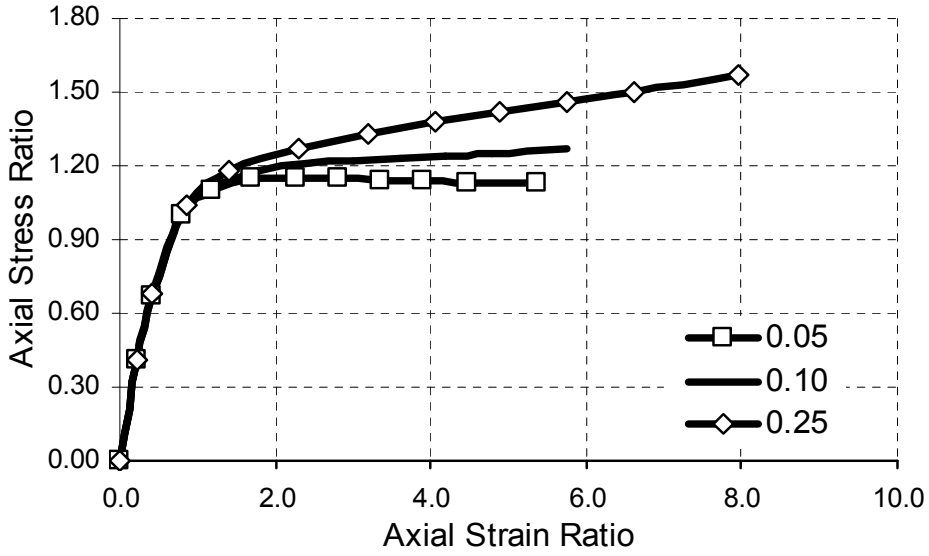

(b)

Figure 10.26 Axial stress-strain ratio curves of a rectangular concrete section confined by (a) low and (b) high stiffness FRP jacket with various jacket corner aspect ratios.

The cases shown in these figures are for RFCC sections confined by an FRP jacket having jacket corner aspect ratios α_j of $\alpha_j = 0.05$, $\alpha_j = 0.25$, and $\alpha_j = 0.50$, which is $\alpha_j = 0.50$ for the SFCC section and $\alpha_j = 0.05$, $\alpha_j = 0.15$, and $\alpha_j = 0.25$ for the RFCC section considered in this parametric study.

From these figures it can be observed that the analytical model predicts that an increase in the jacket corner aspect ratio α_j results in an increase in the ultimate strength ratio k_{cu} and a slight increase in the ultimate axial strain ratio $(k_\varepsilon)_u$, which indicates an increase in the strain ductility of the confined concrete is predicted for SFCC and RFCC sections. This predicted compressive stress-strain behavior is supported by the experimental evidence of SFCC and RFCC sections, as will be demonstrated in the comparison with experimental results.

The analytical model forecasts that the shape of the analytical plastic stress-strain curve of the FCC section can shift from that of a section exhibiting a strain-softening behavior to that of a section exhibiting strain-hardening behavior by increasing the jacket corner aspect ratios α_j, as shown in **Figures 10.25** and **10.26;** this effect is predicted to be independent of the rectangular FRP jacket aspect ratio and stiffness. In the plastic region of the stress-strain curve, the model predicts that the plastic stress ratio k_{cp} at a given plastic axial strain ratio $k_{\varepsilon p}$ increases as α_j increases. This indicates that an increase in strain energy at a given plastic axial strain ratio $k_{\varepsilon p}$ is predicted to occur as α_j increases and was found to be independent of the rectangular FRP jacket aspect ratio and stiffness.

In order to accurately predict the shape of the uniaxial stress-strain curve of the FCC sections, the model must adequately predict the effects that the jacket corner aspect ratio α_j of Eq. (4.4) has on the compressive behavior of RFCC sections.

Plastic Diagonal Dilation Rate

The effect that the plastic diagonal dilation rate μ_{jp} of Eq. (7.25) has on the stress-strain behavior of FCC predicted by the analytical stress-strain model introduced herein for an CFCC section of **Case 1** is plotted in the stress ratio-strain curves shown in **Figure 10.27** and for an RFCC section of **Case 2** in **Figure 10.28**. The plastic diagonal dilation rates μ_{jp} considered in this section of the parametric study are $0.75\mu_{jp}$, μ_{jp}, and $1.25\mu_{jp}$. As can be observed in **Figures 10.27** and **10.28**, the model predicts that for CFCC and RFCC sections an increase in the plastic diagonal dilation rate μ_{jp} results in a decrease of the axial failure strain ratio $(k_\varepsilon)_u$ (i.e., at $\varepsilon_c = \varepsilon_{cu}$), which results in a decrease in the strain ductility of the FRP-confined concrete.

An increase in the ultimate strength ratio k_{cu} (i.e., at $f_c = f_{cu}$) is predicted for both high stiffness and low stiffness CFCC and RFCC sections. The increase is smaller for CFCC sections with high stiffness FRP jackets. The analytical model forecasts that for a CFCC section exhibiting an essentially bilinear strain-hardening compressive behavior, such as those shown in **Figure 10.27** for CFCC sections, the slope of the plastic strain curve increases as μ_{jp} increases. This indicates that a proportional relationship is predicted between the plastic slope of the stress-strain curve and plastic diagonal dilation rate μ_{jp}, this effect is supported by the experimental evidence.

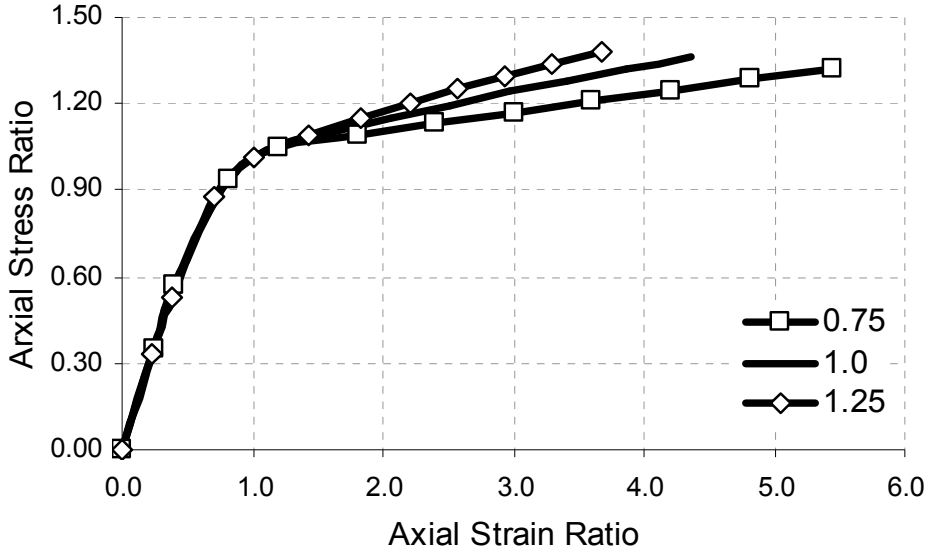

(a)

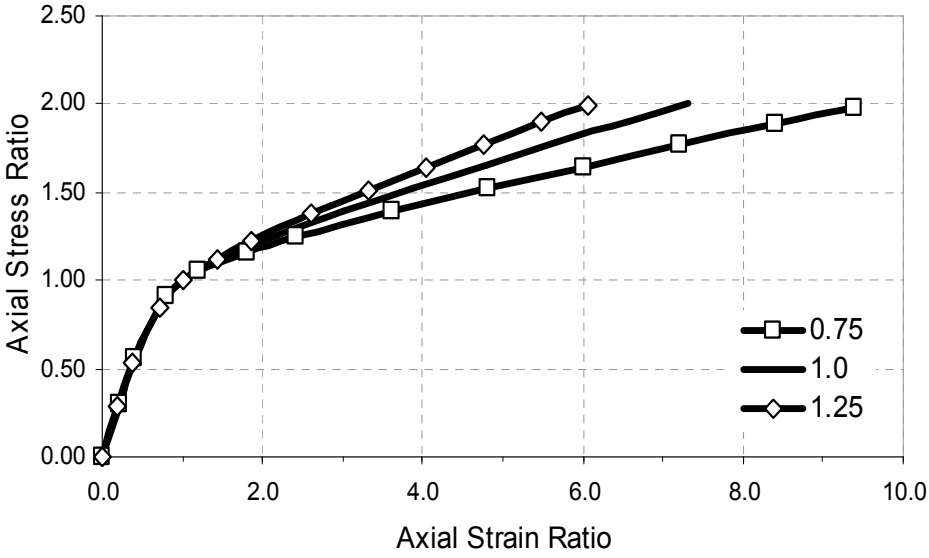

(b)

Figure 10.27 Axial stress-strain ratio curves of a circular concrete section confined by (a) low and (b) high stiffness FRP jacket with various plastic dilation rates.

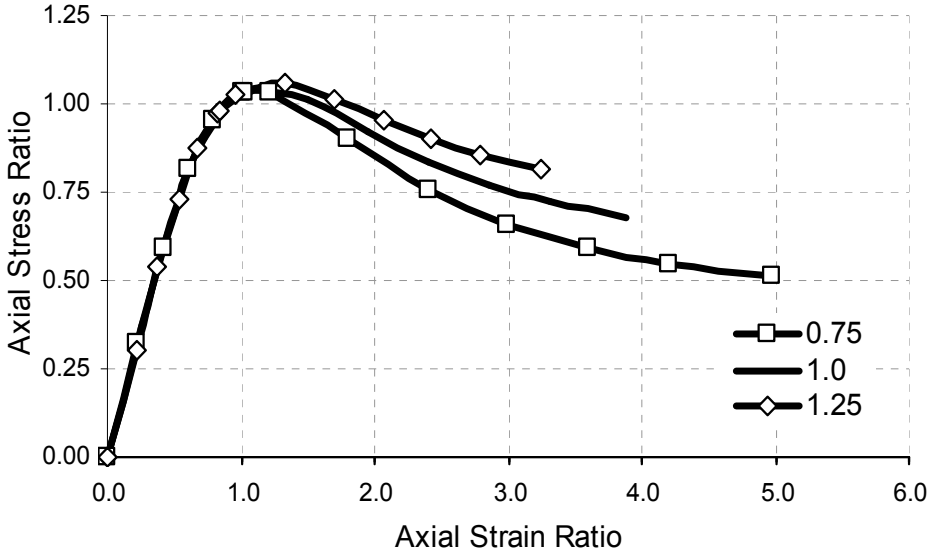

(a)

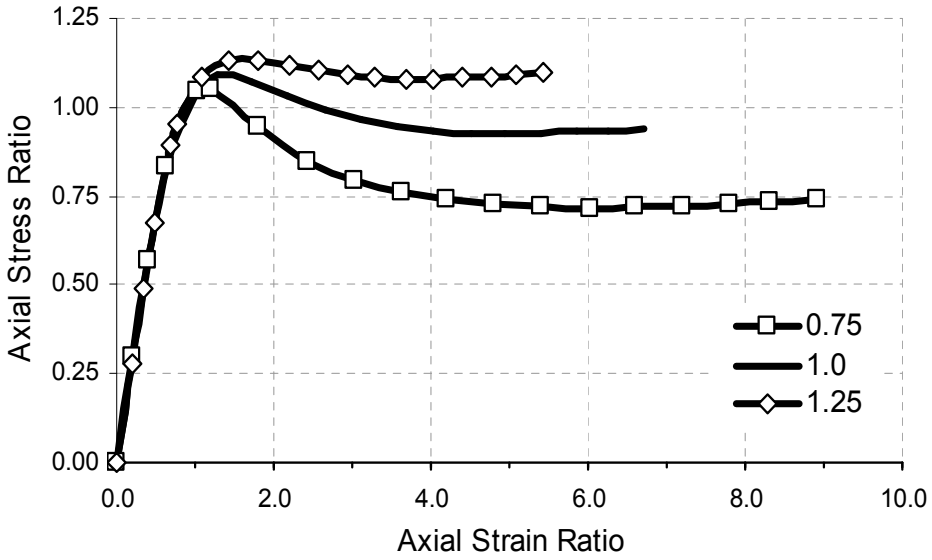

(b)

Figure 10.28 Axial stress-strain ratio curves of a rectangular concrete section confined by (a) low and (b) high stiffness FRP jacket with various plastic dilation rates.

For sections exhibiting a strain-softening compressive behavior, as shown in **Figure 10.28** for rectangular sections, the model predicts that an increase in μ_{jp} affects the shape of the analytical plastic stress-strain curve of the RFCC section.

From these figures it can be observed that in the plastic region of the stress-strain curve, the axial stress ratio k_c at a given plastic axial strain ratio $k_{\varepsilon p}$ increases as μ_{jp} increases, independent of the FRP jacket shape or stiffness. This implies that a proportional relationship is predicted between the axial plastic stress f_{cp} and μ_{jp}; this is a result of an increase in the corresponding FRP jacket strain ε_j [refer to Eqs. (7.32) and (7.54)], and diagonal confining stress $(f_{de})_{sh}$ of Eq. (5.12), which results in an increase in the confinement effectiveness k_{cc} of Eq. (9.35) with σ_{3e} of Eq. (9.100).

An increase in f_{cp} at a given $k_{\varepsilon p}$ implies that an increase in strain energy is predicted to occur by the proposed analytical model as μ_{jp} increases; this effect is also predicted to be independent of the FRP jacket shape and stiffness. This explains why the diagonal dilation is used in this dissertation as a basic model.

Stress-Strain Model Parameters

Strain Ductility Ratio

The effect that the strain ductility ratio R_{sh} of Eq. (10.12) has on the stress-strain behavior of FCC sections predicted by the analytical stress-strain model introduced herein are examined. The stress ratio-strain curves of the CFCC section of **Case 1** is plotted in **Figure 10.29** and in **Figure 10.30** for the RFCC section of **Case 2**.

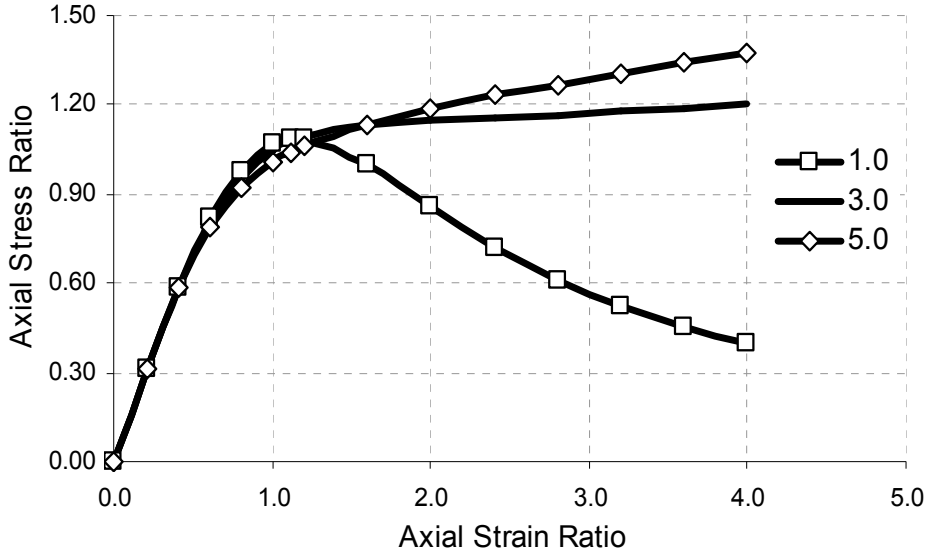

(a)

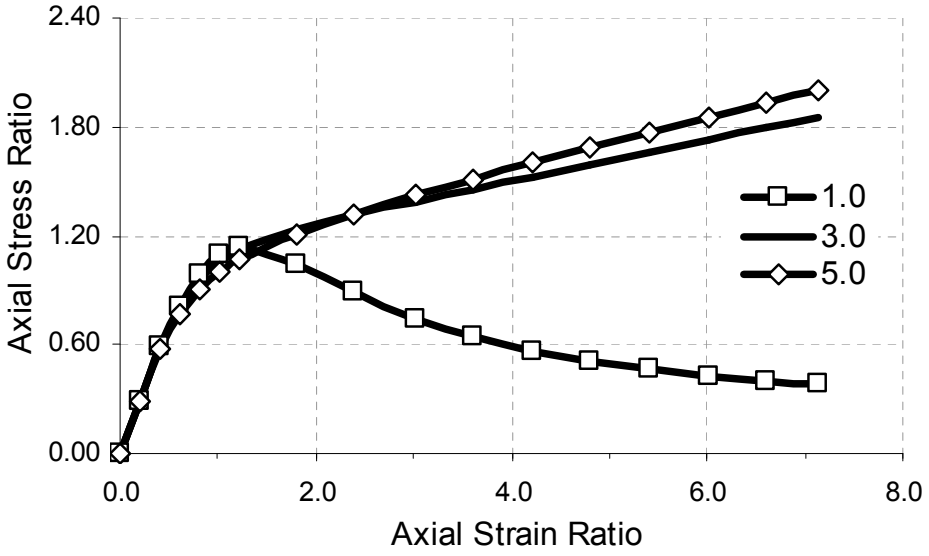

(b)

Figure 10.29 Axial stress-strain ratio curves of a circular concrete section confined by (a) low and (b) high stiffness FRP jacket with various strain ductility ratios.

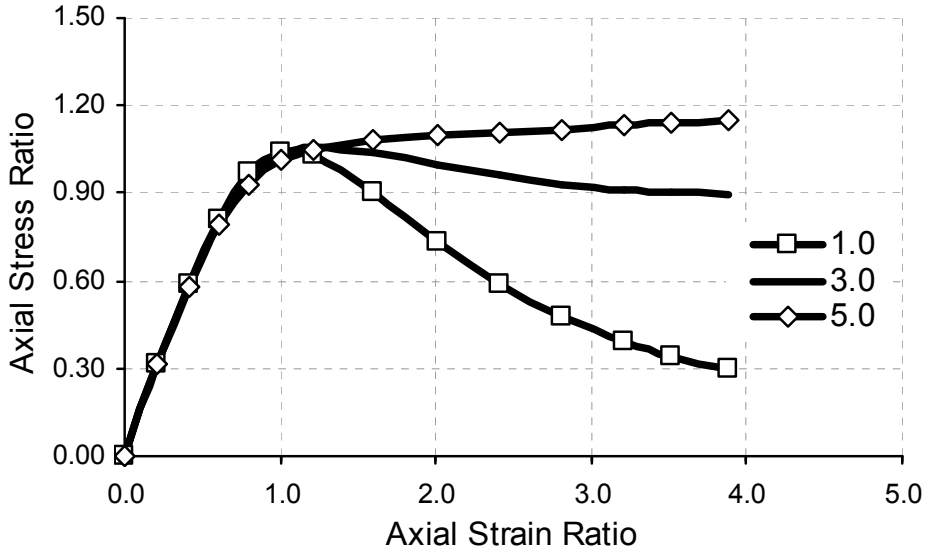

(a)

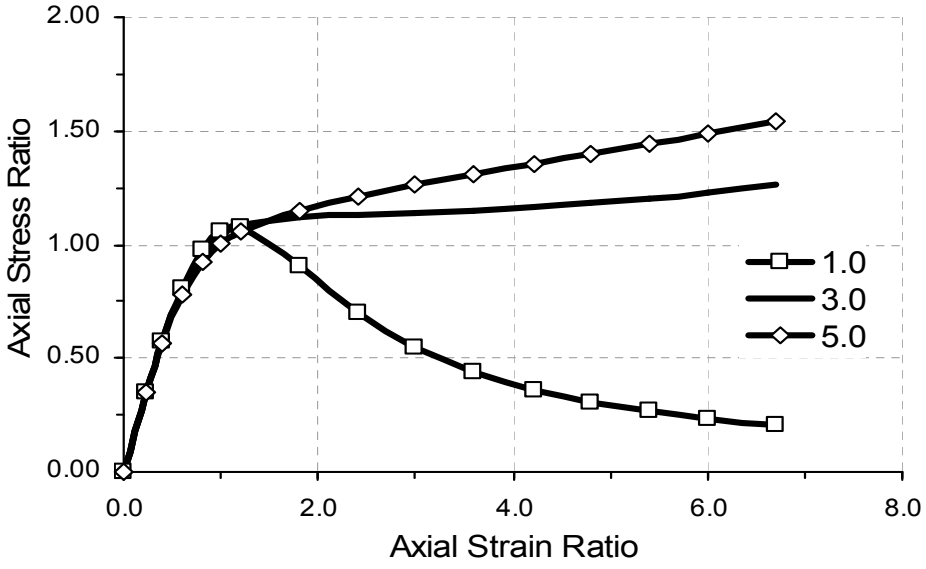

(b)

Figure 10.30 Axial stress-strain ratio curves of a rectangular concrete section confined by (a) low and (b) high stiffness FRP jacket with various strain ductility ratios.

It is apparent in these figures that the strain ductility ratio R_{sh} of the proposed analytical stress-strain model has a significant effect on the plastic region of the predicted axial stress-strain ratio curve. The model predicts that as R_{sh} increases, the normalized plastic stress k_{cp} at a given normalized plastic axial strain $k_{\varepsilon p}$ increases. This effect is less pronounced as the strain ductility ratio R_{sh} of the model approaches the value of the equi-biaxial confinement ductility ratio R_{bc} (i.e., as $R_{sh} \rightarrow R_{bc} = 5.0$) and as the FRP jacket stiffness increases.

The analytical model forecasts that the shape of the analytical plastic stress-strain curve of the FCC section can shift from that of section exhibiting a strain-softening behavior to that of a section exhibiting strain-hardening behavior by increasing the strain ductility ratio R_{sh}, as shown in **Figures 10.29** and **10.30.**

The amount of strain-hardening is predicted to be independent of the FRP jacket shape, aspect ratio, and stiffness. In order to accurately predict the shape of the uniaxial stress-strain curve of the FCC section the model must adequately predict the value of the strain ductility ratio R_{sh} of Eq. (10.11) for all the FCC jacket shapes considered in this dissertation.

The following is a ranking of the parameters that were predicted to affect the compressive behavior of FCC section the most:

1. The FRP jacket stiffness K_{je}, which is affected by the jacket transverse modulus E_j, the jacket thickness t_j, and the unconfined concrete compressive strength f_{co}
2. The plastic dilation rate μ_{jp}, which depends on the FRP jacket stiffness K_{je}

3. The FRP jacket shape, which includes the effects of the section aspect ratio α_{sh} and jacket corner aspect ratio α_j

4. The strain ductility ratio R_{sh} of the FCC section, which affects the slope of the plastic region of the FCC section and appears to depend on the FRP jacket shape

5. The pore water pressure parameter n_{PW}, which is affected by the type of FRP jacket application, bonded (BFCC) or unbonded (CFFT) FRP jackets, and the degree of saturation (moisture content) of the confined concrete core, which influences the effective basic angle of internal friction ϕ_{be} of the concrete core.

This ranking will be demonstrated in the following comparison with experimental tests of elliptical (EFCC), circular (CFCC), rectangular (RFCC), and square (SFCC), FRP-confined concrete sections.

Comparison with Experimental Tests

The effectiveness that the proposed uniaxial stress-strain model has in predicting the compressive behavior of the FCC section will depend on the model's ability to predict the effects that the concrete material properties such as initial modulus of elasticity E_{ci}, initial Poisson's ratio ν_{ci} and peak unconfined compressive strength f_{co} and train ε_{co}, and effective basic angle of internal friction ϕ_{be} have on the stress-strain curve of the FRP-confined concrete section.

Due to the analytical nature of the proposed model, it should be able to accurately predict the effects that the FRP jacket properties, such as the FRP jacket stiffness K_{je} (including the plastic dilation rate μ_{jp}), jacket aspect ratio α_{sh}, jacket corner aspect

ratio α_j, the FRP jacket shape (elliptical, circular, oval, square, or rectangular) and FRP jacket construction, i.e., bonded (BFCC) or unbonded (CFFT) FRP jacket, have on the compressive behavior of the FRP-confined concrete section.

The first goal of this dissertation as outlined in Chapter 3 was to develop an analytical unified damage-based model for the analysis of rectangular, square, oval, circular, and elliptical FCC sections that can capture their dilation and compressive behavior. This is accomplished herein with the introduction of a minimal number of empirical curve-fitting parameters, limited to three parameters:

1. The empirical plastic dilation μ_{rp} of Eq. (7.23) which was determined from the transverse dilation and axial deformation of CFFT and BFCC concrete cylinder tests, as described in Chapter 7
2. The pore water pressure parameter n_{PW} of Eq. (9.62) that was found to have an average value of $n_{PW} = 59.0\%$ for CFFT sections, determined from the analysis of CFFT cylinder tests performed by Mirmiran (1997), as described in Chapter 9
3. The basic angle of internal friction ϕ_b of Eq. (9.40), a material property of normal-strength normal-weight concrete, with an average value of $\phi_b = 35^\circ$ for dry concrete, determined from the analysis of hydrostatically confined concrete cylinder tests performed by Imran (1994), as described in Chapter 9.

In what follows, the results of the analytical uniaxial stress-strain model developed herein are compared to the experimental stress-strain and dilation behavior of FRP-confined concrete sections of different FRP jacket shapes, confined by FRP jacket of varying stiffness, varying unconfined concrete compressive strength, varying section aspect ratios α_{sh} (EFCC and RFCC sections), varying jacket corner aspect ratios α_j

(RFCC and SFCC sections only), and different FRP jacket construction (bonded or unbonded). The stress-strain model introduced in this dissertation has not been calibrated to match the compressive stress-strain behavior or dilation behavior of the FCC sections previously mentioned. This indicates that the model predictions are blind predictions of the compressive and dilation behavior of the FCC sections considered in these comparisons.

The predictions presented herein are based on the reported section and FRP jacket geometry, the mechanical properties of the FRP jacket, i.e., jacket modulus E_j and thickness t_j, and the unconfined concrete properties, i.e., f_{co}. The initial modulus of elasticity $E_{ci} \approx E_{co}$ used in the analysis was selected to match the experimental modulus. The unconfined peak compressive strain ε_{co} of Eq. (10.6) was determined based on matching the experimental compressive stress in the FCC section at an axial strain ε_c within the range of $0.0012 \le \varepsilon_c \le 0.0016$. The unconfined curvature parameter n_u was then calculated from Eq. (10.8) using the estimated initial modulus E_{ci} and unconfined peak compressive strain ε_{co}. This was done in order to ensure that the influences that both E_{ci} and ε_{co} have on the predicted stress-strain behavior, outlined in the parametric study and shown in **Figures 10.12-10.17**, are minimized in the stress-strain curves predicted by the analytical model.

Circular FRP-Confined Concrete Sections

The compressive stress-strain behavior predicted by the analytical stress-strain model is compared with the uniaxial compressive tests of circular concrete cylinders tests confined by either bonded (BFCC sections) or unbonded (CFFT sections) FRP jackets

performed by several investigators. The BFCC sections that are part of this comparison include the tests performed by Picher et al. (1996), Xiao and Wu (2000), Rochette and Labossiérre (2000), and Teng and Lam (2004) of medium-strength normal-weight concrete cylinders confined by circular FRP jackets. The CFFT sections with FRP jackets that are part of this comparison include the tests performed by Mirmiran (1997).

The results of the analytical model introduced herein are first compared to experimental stress-strain behavior and dilation behavior of the concrete cylinder tests perform by Xiao and Wu (2000). The CFCC section considered in this comparison is specimen H3-3P-3. In **Figure 10.31** the results of the analytical model are compared to the axial stress-axial strain shown in the right-hand quadrant and axial stress-transverse strain curve in the left-hand quadrant. From this figure it can be observed that the analytical model can accurately predict the experimental compressive stress-strain behavior.

In **Figure 10.32** the analytical axial strain-absolute transverse strain curves predicted by the transverse dilation model of Eq. (8.43) and pertinent terms introduced in Chapter 8 are compared to the experimental test results of specimen H3-3P-3. As can be observed in this figure, the analytical transverse dilation model of Chapter 8 can accurately predict the shape of the transverse dilation curve of this circular FCC cylinder test. In **Figure 10.33** the analytical and experimental Poisson's ratio ν_j of Eq. (7.33) is plotted versus the axial and transverse strain of specimen H3-3P-3. In **Figure 10.34** the analytical and experimental dilation rate μ_j of Eq. (7.51) is plotted versus the axial and transverse strain of specimen H3-3P-3, where the analytical dilation rate curve is that predicted by Eq. (8.44).

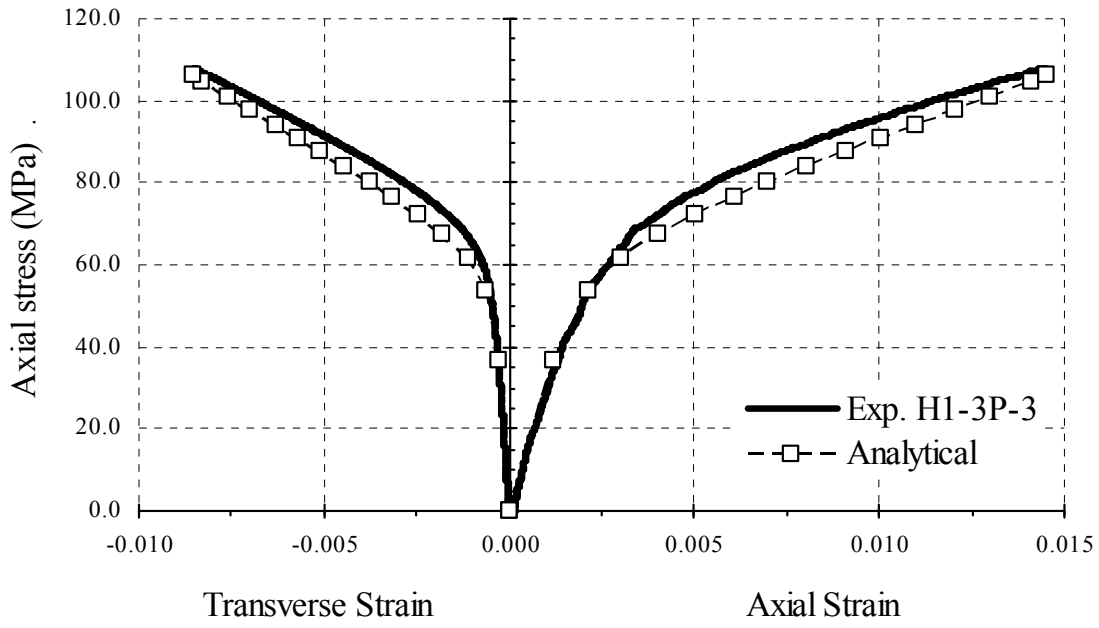

Figure 10.31 Analytical and experimental axial stress versus axial and transverse strain curves of concrete cylinder test specimen H3-3P-3 performed by Xiao and Wu (2000).

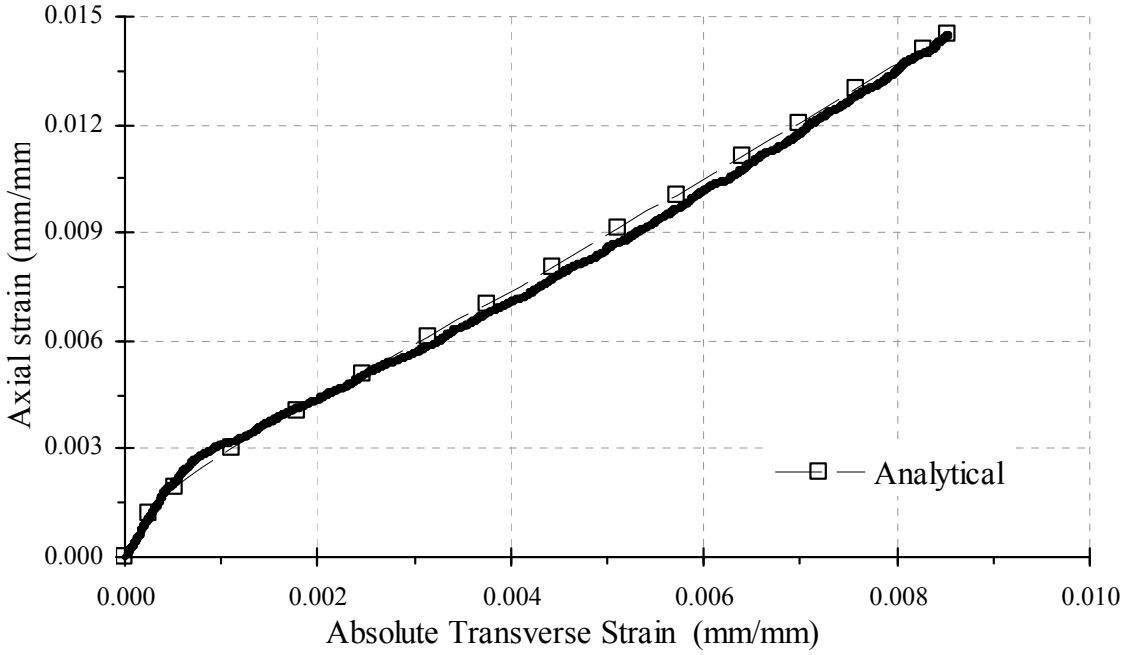

Figure 10.32 Analytical and experimental axial stress versus absolute transverse strain curves of concrete cylinder test specimen H3-3P-3 performed by Xiao and Wu (2000).

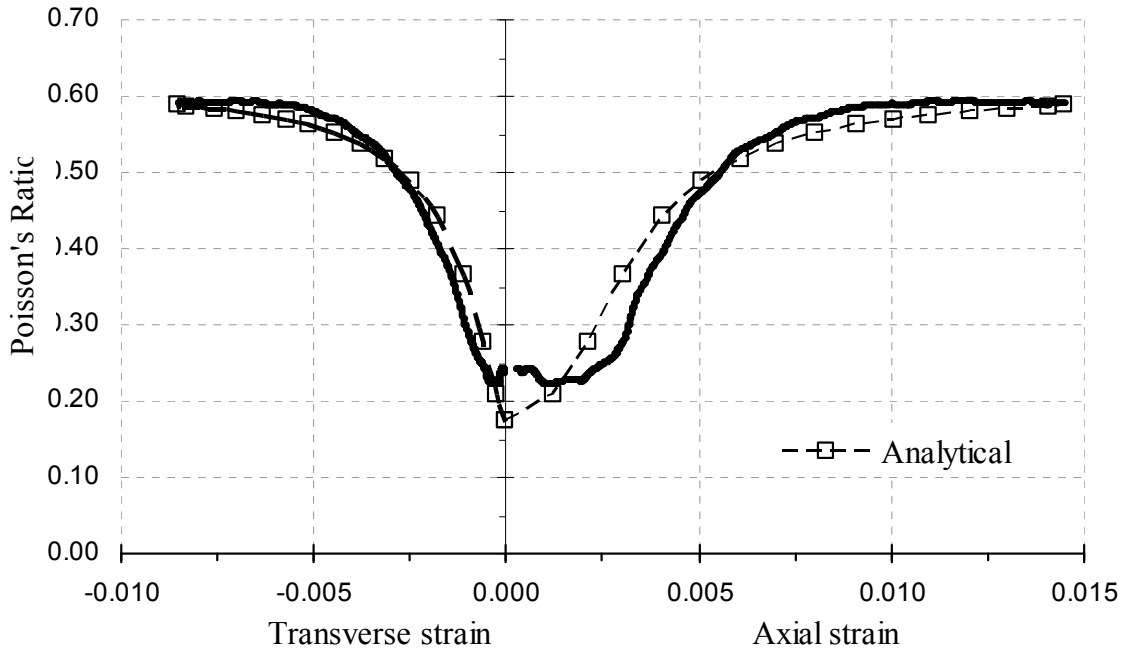

Figure 10.33 Analytical and experimental Poisson's ratio versus axial and transverse strain curves of concrete cylinder test specimen H3-3P-3 performed by Xiao and Wu (2000).

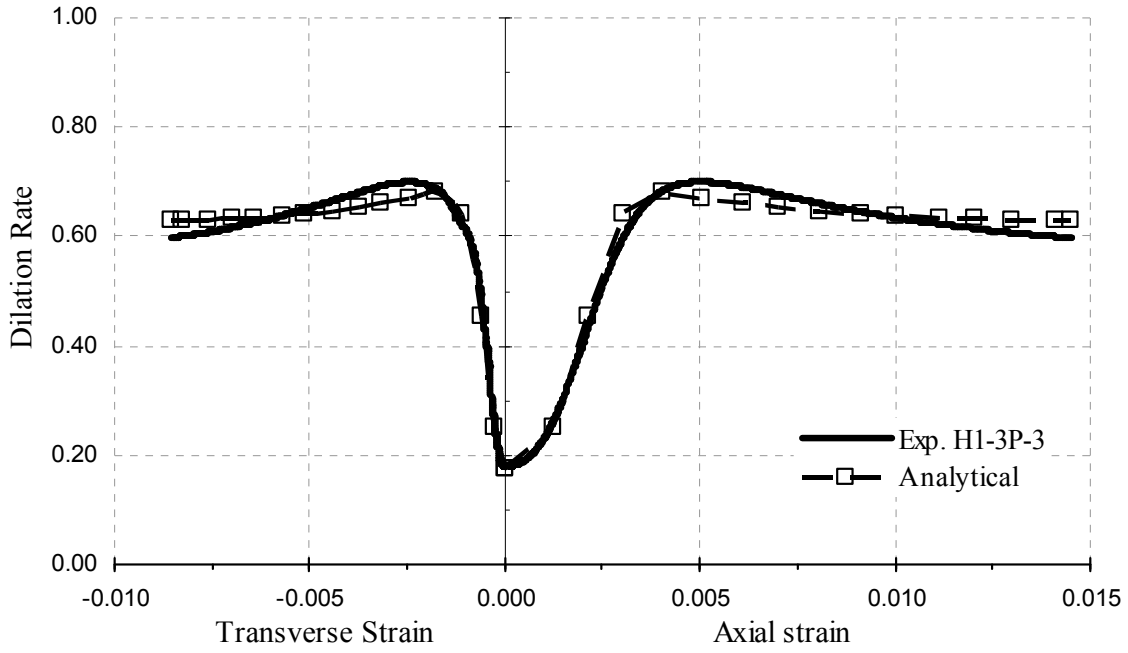

Figure 10.34 Analytical and experimental dilation rate versus axial and transverse strain curves of concrete cylinder test specimen H3-3 performed by Xiao and Wu (2000).

From these figures it can be observed that the analytical transverse dilation model of Chapter 8 can accurately predict the shape of the Poisson's ratio and transverse dilation rate curves of cylindrical FRP-confined concrete sections. The experimental dilation rate curve shown in **Figure 10.34** is a smooth dilation rate curve that was developed from the experimental data in order to minimize the noise introduced by the data acquisition hardware used in these experiments.

Poisson's ratio is the secant slope of the axial versus transverse strain curve, and the dilation rate is the tangent slope of the axial versus transverse strain curve, as discussed in Chapter 7. The Poisson's ratio and dilation rate curves shown in **Figures 10.33** and **10.34** are the secant and tangent slopes of the transverse dilation curve shown in **Figure 10.32.**

In **Figure 10.35** the analytical and experimental volumetric strain ε_{vol} of Eq. (7.62) is plotted versus the axial and transverse strain of specimen H3-3P-3. In this figure it can be observed that the proposed analytical dilation model introduced in Chapter 8 can accurately predict the shape of the volumetric strain curves of cylindrical FCC sections. This figure demonstrates that the analytical model can accurately predict instant when volumetric expansion begins to occur, i.e., when $\varepsilon_{vol} \cong 0$ for $\varepsilon_c > 0$. Zero volumetric strain occurs when the volumetric strain curves cross the horizontal axis of **Figure 10.35**.

The analytical axial volumetric strain $(\varepsilon_c)_{vol}$ can be found using Eq. (8.37), the transverse volumetric strain $(\varepsilon_j)_{vol}$ using Eq. (7.63), with the volumetric Poisson's ratio $(\nu_j)_{vol}$ evaluated using Eq. (7.66).

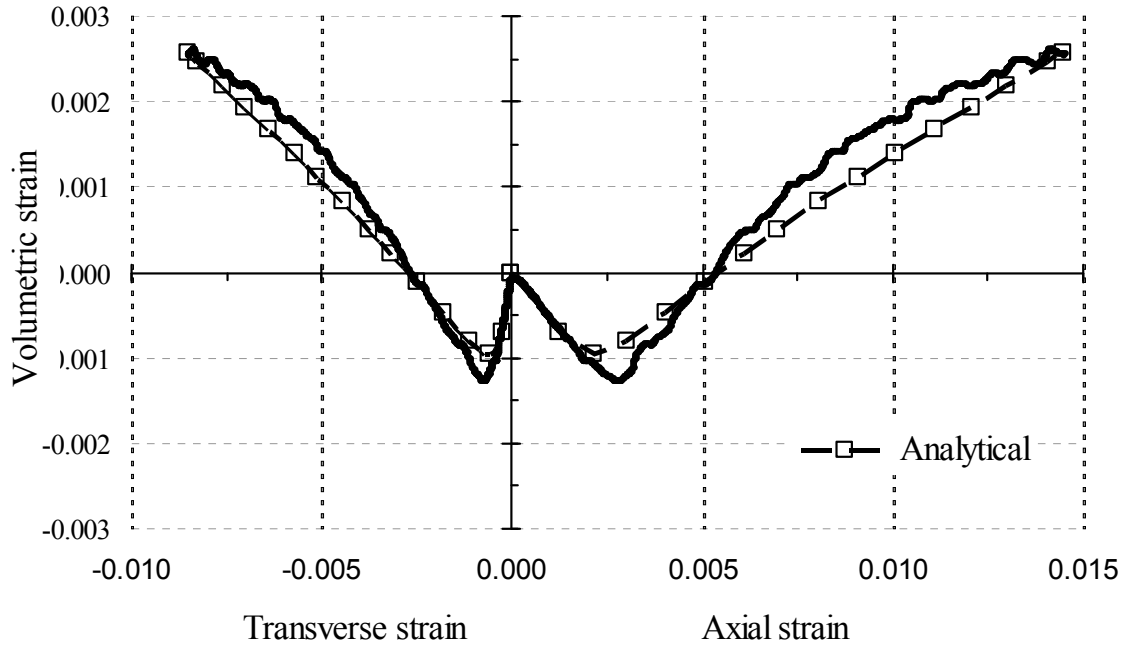

Figure 10.35 Analytical and experimental volumetric strain versus axial strain and transverse strain curves of concrete cylinder test specimen H3-3P-3 performed by Xiao and Wu (2000).

A negative volumetric strain indicates that the FRP-confined confined concrete core is experiencing volumetric contraction, whereas a positive volumetric strain indicates that it experiences volumetric expansion.

In **Figure 10.36** the analytical and experimental volumetric dilation rates ψ_m of Eq. (7.70) are plotted versus the axial and transverse strain of specimen H3-3P-3. The experimental and analytical axial volumetric dilation rate ψ_c of Eq. (7.7.) is plotted on the right-hand side of the vertical axis versus the axial compressive strain ε_c. In this figure the transverse volumetric dilation rate ψ_j of Eq. (7.76) is plotted on the left-hand side of the vertical axis versus the transverse jacket dilation strain ε_j. The experimental volumetric dilate rate curve shown in this figure is based on the smooth dilation rate curve of **Figure 10.34.**

The axial volumetric dilation rate ψ_c is the average tangent slope of the volumetric strain versus axial strain curve shown on the right-hand side of the vertical axis of **Figure 10.36.** In addition, the transverse volumetric dilation rate ψ_j is the tangent slope of the volumetric strain versus transverse strain curve plotted on the left-hand side of the vertical axial of **Figure 10.36**. From this figure it can be observed that the analytical transverse dilation model of Chapter 8 can accurately predict the shape of the volumetric dilation rate curves of cylindrical FRP-confined concrete sections.

In **Figure 10.37** the analytical and experimental plastic strain ductility ratio R_p of Eq. (10.16) is plotted versus the axial and transverse strain of specimen H3-3P-3. In this figure it can be observed that the proposed analytical stress-strain model can predict the shape of the plastic strain ductility ratio R_p curves of cylindrical FCC sections.

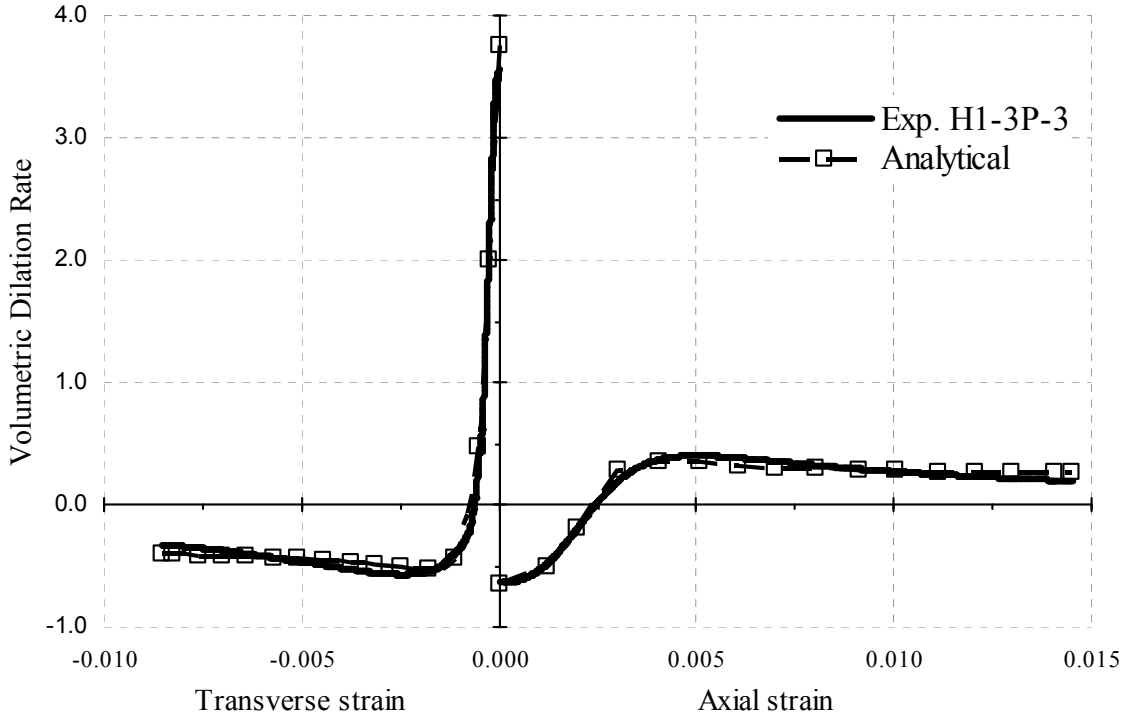

Figure 10.36 Analytical and experimental axial and transverse volumetric dilation rate curves of concrete cylinder test specimen H3-3P-3 performed by Xiao and Wu (2000).

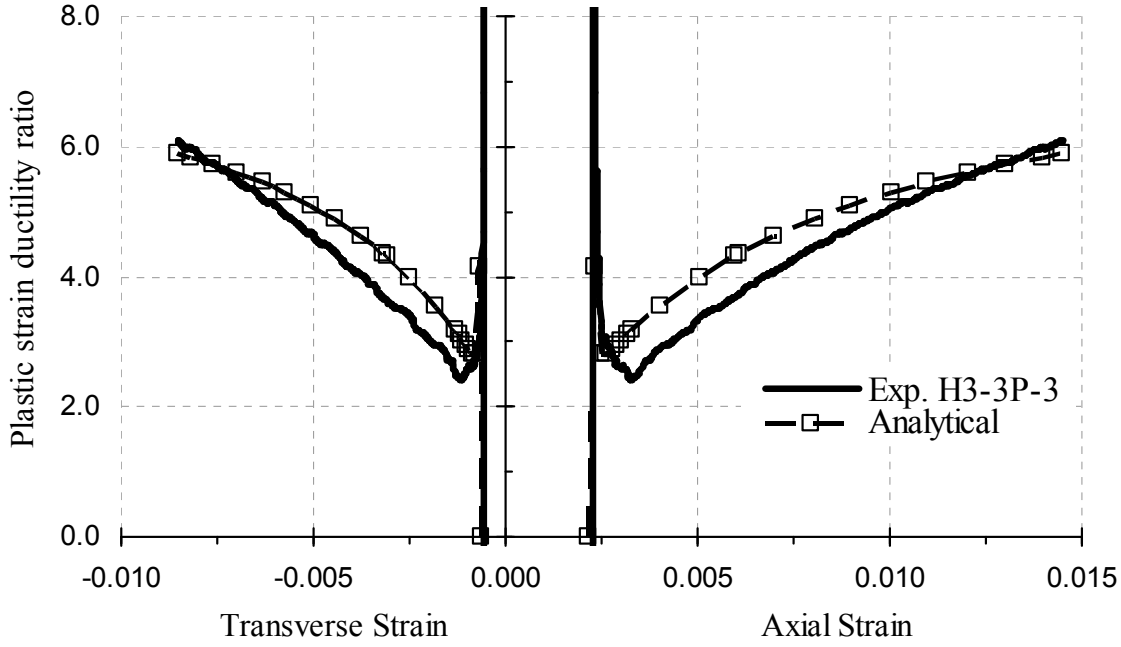

Figure 10.37 Analytical and experimental plastic strain ductility ratio versus axial strain and transverse strain curves of concrete cylinder test specimen H3-3P-3 performed by Xiao and Wu (2000).

From analysis of the analytical and experimental curves shown **Figures 10.31-10.37** it can be stated that the proposed incremental uniaxial stress-strain model can accurately predict the experimental stress-strain behavior and transverse dilation behavior of FRP-confined concrete cylinders.

The ability of the proposed stress-strain model in predicting the uniaxial compressive stress-strain behavior and transverse dilation behavior of circular FRP-confined sections is further demonstrated in the following comparisons with experimental tests of FRP-confined concrete cylinders.

The compressive stress-strain behavior predicted by the proposed analytical model introduced herein is compared to the experimental compressive stress-strain behavior of the concrete cylinder tests performed by Picher et al. (1996) for specimens C-0 and C-12 in **Figure 10.38**.

Comparisons of the analytical model predictions with the experimental stress-strain behavior of FRP-confined concrete cylinder tests performed by Xiao and Wu (2000) are shown in **Figures 10.39-10.41**.

The analytical and experimental axial stress-transverse strain and axial stress-axial strain curves plotted in **Figure 10.39** are for the concrete cylinder tests results of low-strength concrete specimens L1-1P-3 and L1-2P-3**.**

The stress-strain curves plotted in **Figure 10.40** are the concrete cylinder tests results and analytical predictions of medium-strength concrete specimens M1-2P-2 and M1-3P-1**.** The stress-strain curves plotted in **Figure 10.41** are the concrete cylinder tests results and analytical predictions of high-strength concrete specimen H1-3P-1.

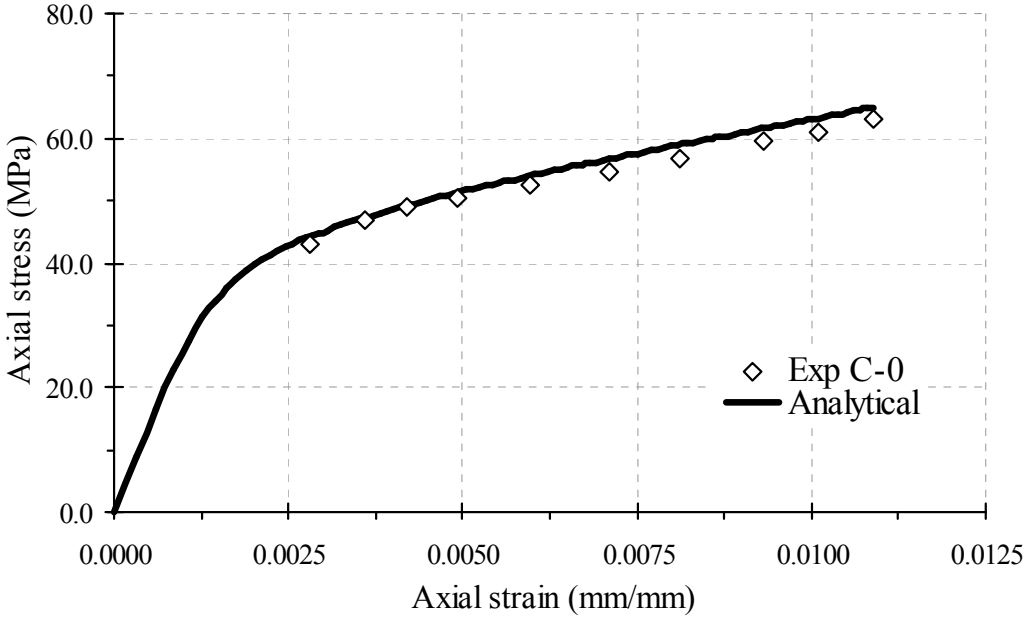

(a)

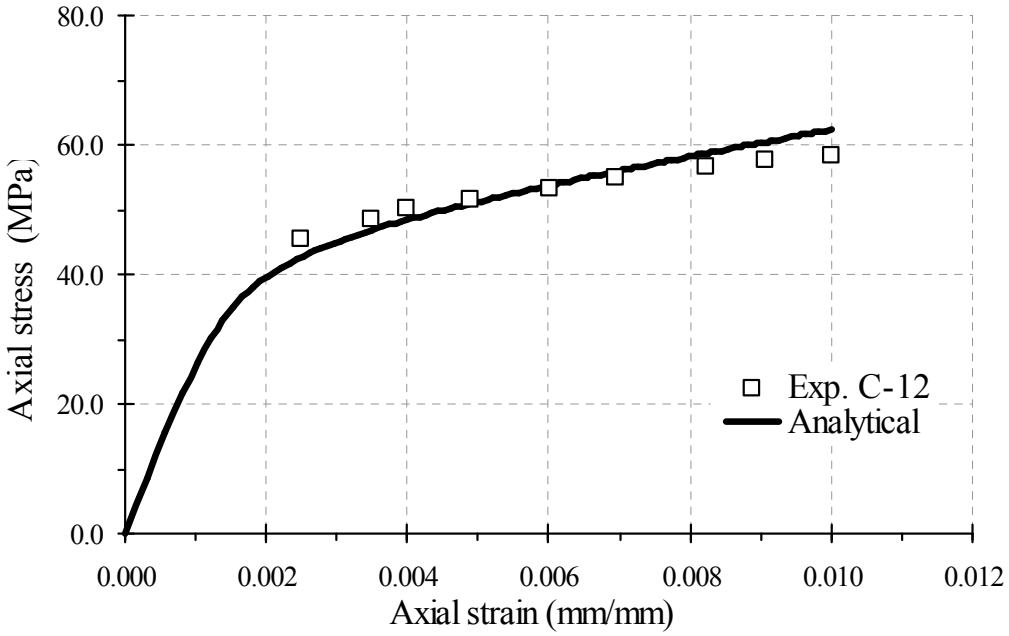

(b)

Figure 10.38 Analytical and experimental axial stress versus axial strain curves of concrete cylinder test specimen (a) C-0 and (b) C-12 performed by Pitcher et al. (1996).

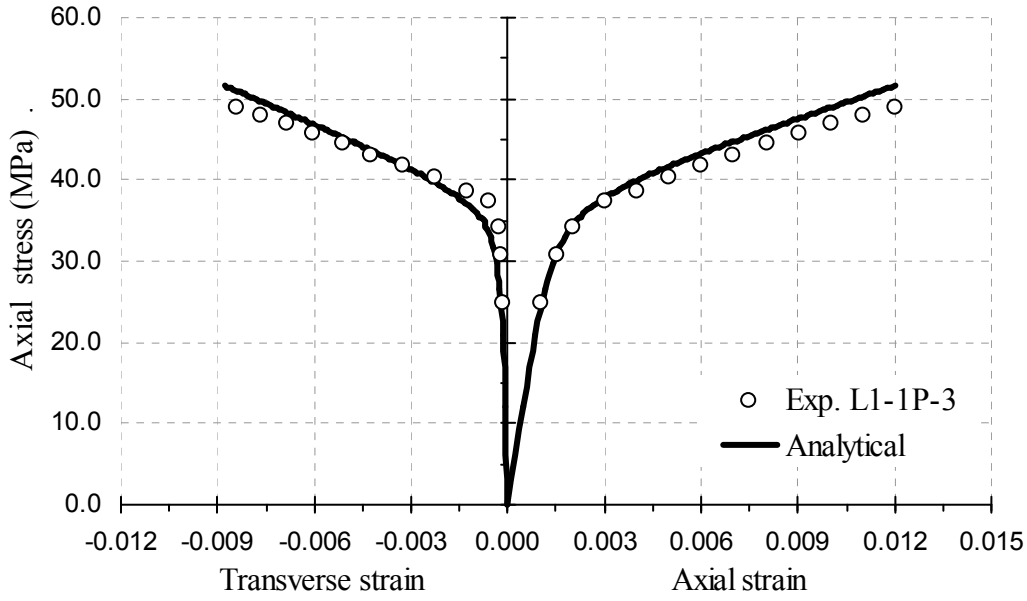

(a)

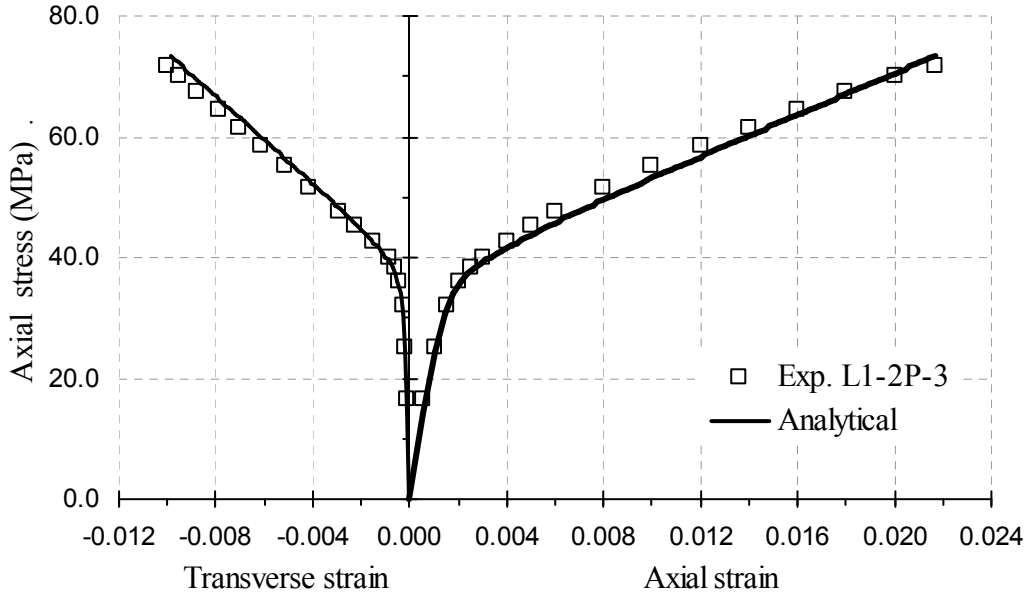

(b)

Figure 10.39 Analytical and experimental axial stress versus axial strain curves of low-strength concrete cylinder test specimen (a) L1-1P-3 and (b) L1-2P-3 performed by Xiao and Wu (2000).

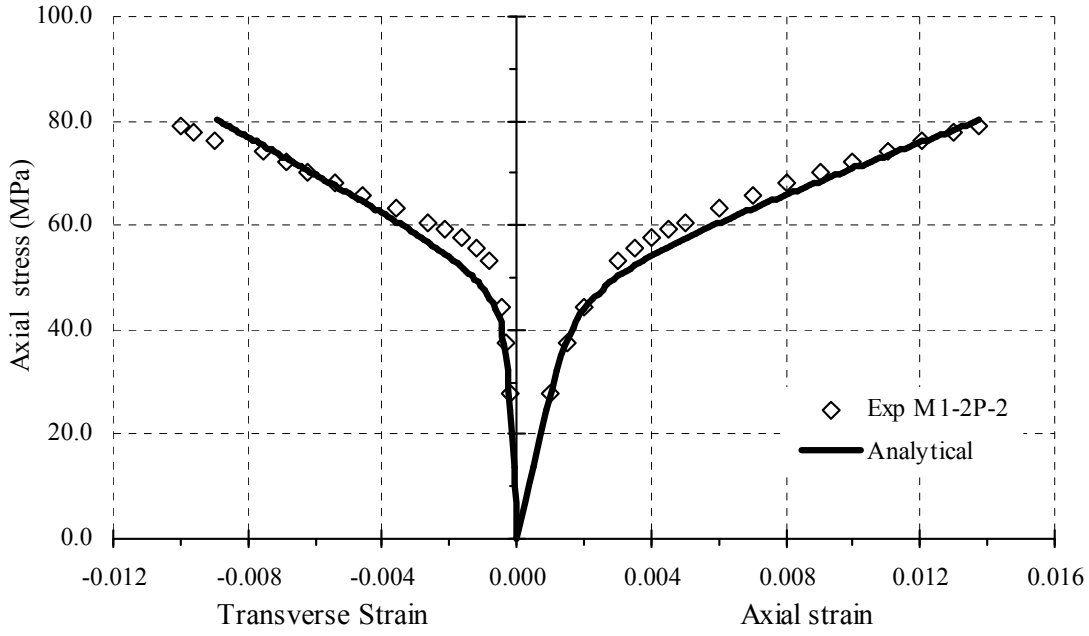

(a)

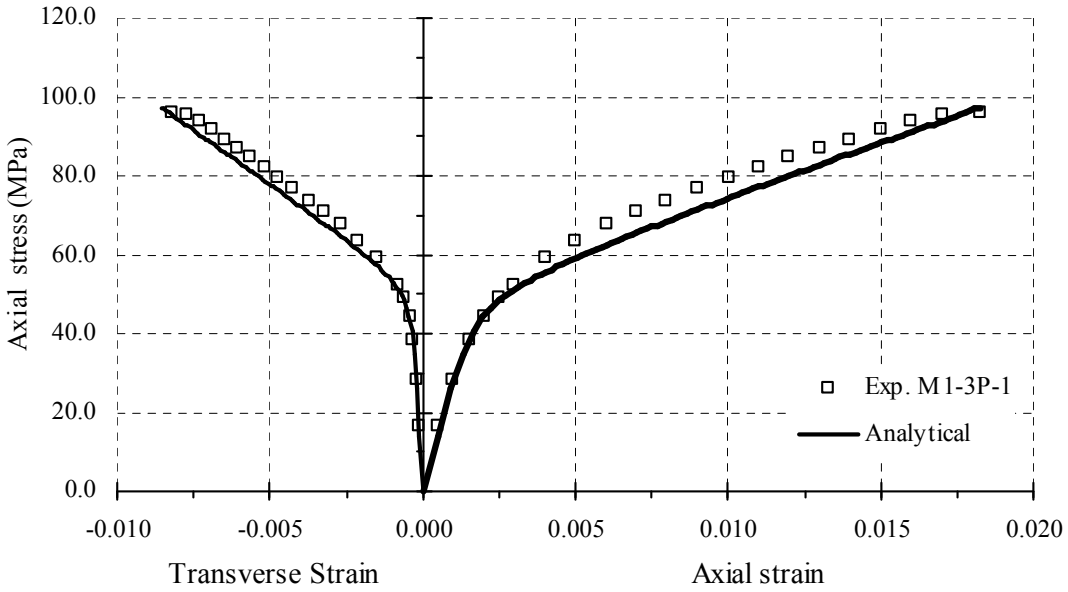

(b)

Figure 10.40 Analytical and experimental axial stress versus axial strain curves of medium-strength concrete cylinder test specimen (a) M1-2P-2 and (b) M1-3P-1 performed by Xiao and Wu (2000).

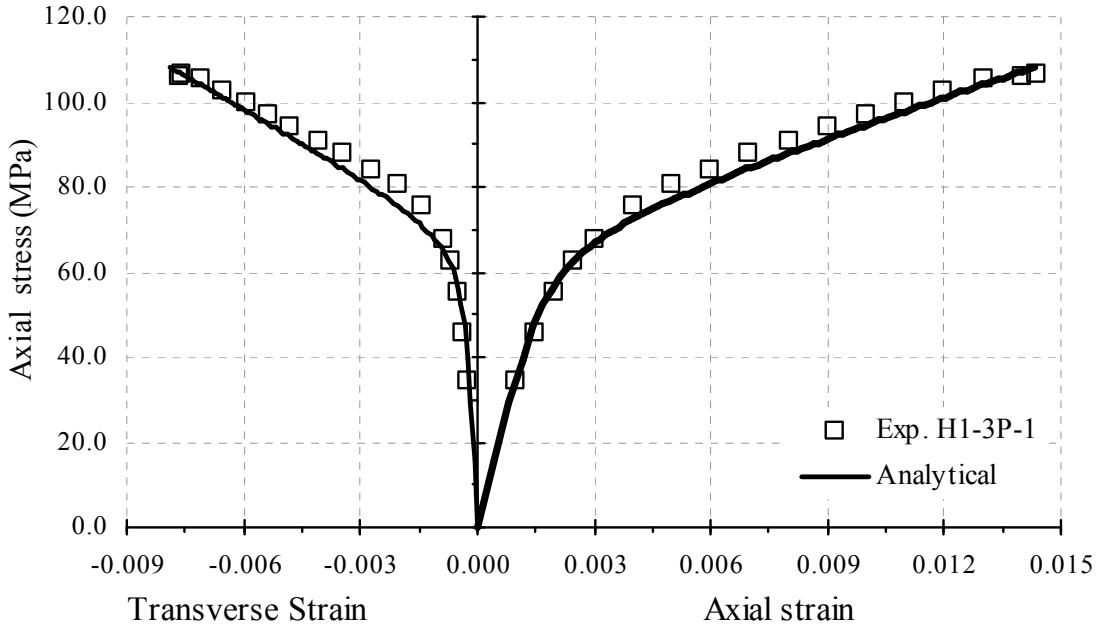

Figure 10.41 Analytical and experimental axial stress versus axial strain curves of high-strength concrete cylinder test specimen H1-3P-1 performed by Xiao and Wu (2000).

The first terms in the specimen designation indicates the concrete compressive strength where L1 indicates low-, M1 medium-, and H1 high-strength concrete; the second terms indicate the number of carbon FRP (CFRP) layers: 1P indicates one layer, 2P two layers, and 3P 3 layers**;** the third term indicates the specimen number in the tests series. For a given concrete strength, an increase in FRP jacket thickness indicates an increase in the FRP jacket stiffness K_{je} of Eq. (4.18).

The effects that the increase in the FRP jacket stiffness has on the compressive behavior of FRP-confined concrete cylinders are plotted in **Figure 10.42** for the low-strength concrete cylinders tests and in **Figure 10.43** for the medium-strength concrete cylinder tests. From these figures it can be observed that the proposed analytical model can predict and capture the beneficial effects that an increase in the stiffness of the confining FRP jacket has on the compressive behavior of cylindrical plain concrete sections as is evidenced by the experimental results shown in **Figure 10.42(a)** and **10.43(a)**. The effects that an increase in compressive strength of the concrete core has on the compressive behavior of FRP-confined concrete cylinders, having similar FRP jacket stiffness, is investigated in **Figure 10.44**. The medium-strength concrete cylinder test specimen M1-2P-2 is confined with an FRP jacket having an effective stiffness of $K_{je} = 30.4$ and with $K_{je} = 27.5$ for the high-strength concrete cylinder test specimen H1-3P-1.

Analysis of **Figure 10.44(b)** indicates that the proposed analytical stress-strain model can capture the effects that the increase in the compressive strength of the concrete core has on the compressive stress-strain behavior of cylindrical FRP-confined concrete sections, as evidenced by the experimental results shown in **Figure 10.44(a)**.

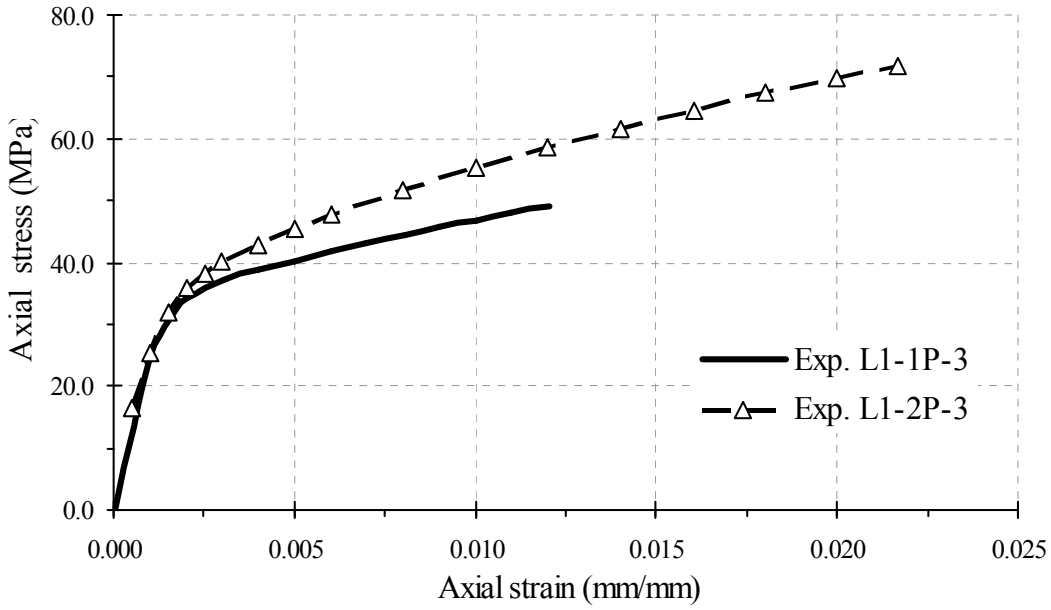

(a)

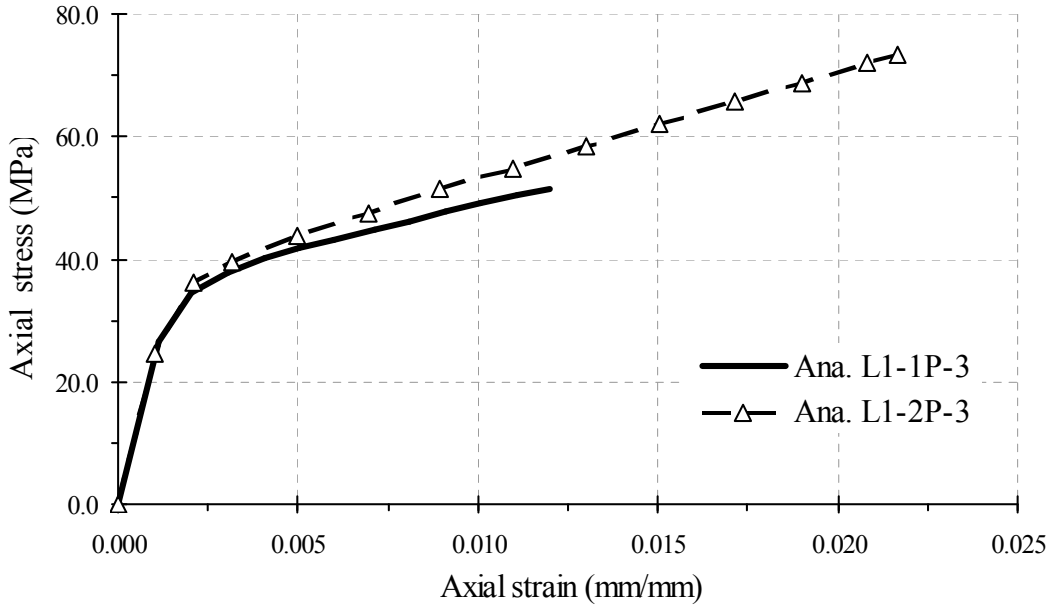

(b)

Figure 10.42 Axial stress-axial strain curves of low-strength concrete cylinder tests performed by Xiao and Wu (2000) with FRP jackets of various thicknesses: (a) experimental and (b) analytical.

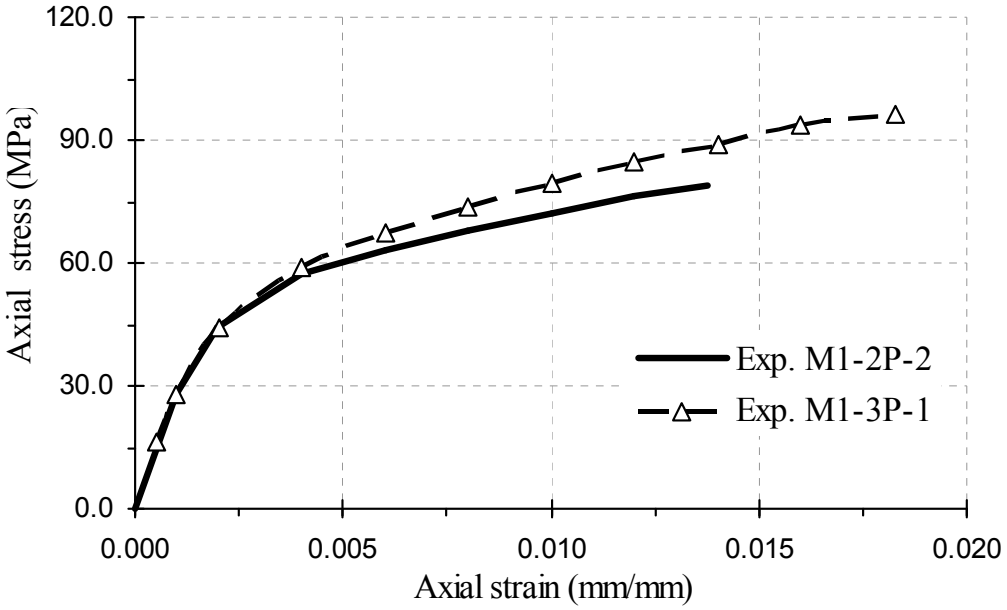

(a)

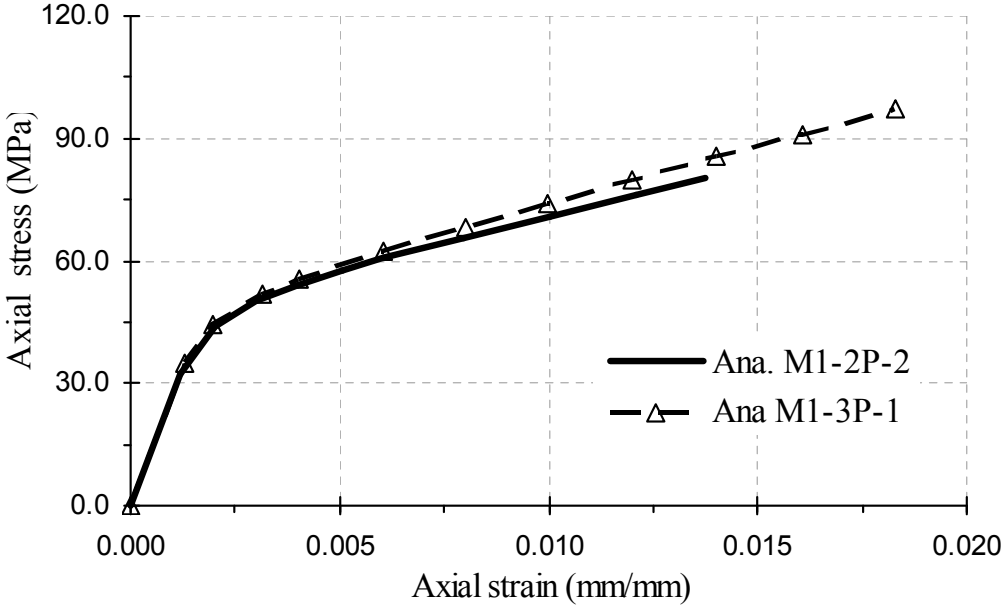

(b)

Figure 10.43 Axial stress-axial strain curves of medium-strength concrete cylinder tests performed by Xiao and Wu (2000) with FRP jackets of various thicknesses: (a) experimental and (b) analytical.

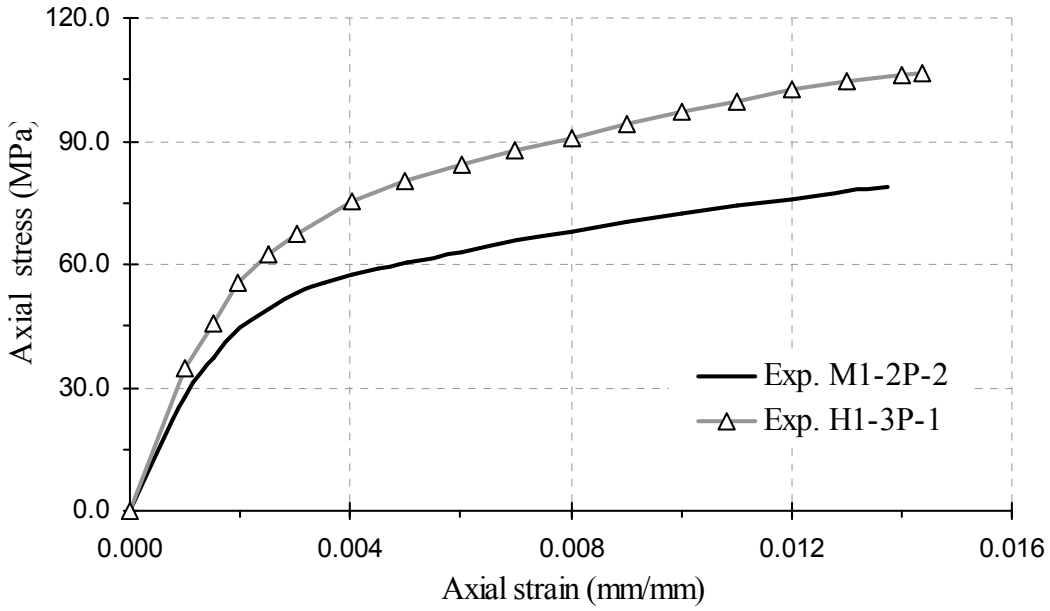

(a)

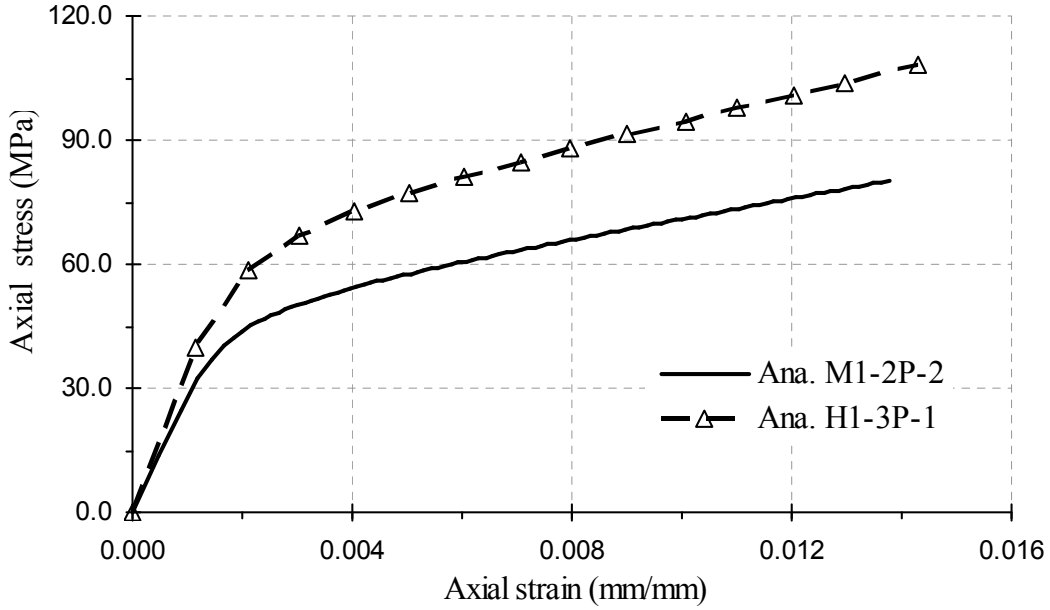

(b)

Figure 10.44 Axial stress-axial strain curves of medium- and high-strength concrete cylinder tests performed by Xiao and Wu (2000) with similar FRP jacket stiffness: (a) experimental and (b) analytical.

The plastic slopes of the axial stress-axial strain curves shown in **Figure 10.44** are essentially equal. This is because the specimens considered are confined by FRP jackets having similar FRP jacket stiffness K_{je}; this is evidenced by the plastic slopes of both the experimental and analytical stress-strain curves shown in **Figure 10.44**.

In **Figure 10.45**, the experimental compressive stress-strain behavior of the FRP-confined concrete cylinder tests performed by Rochette and Labossiérre (2000) for specimen C-100-2 is compared to the compressive stress-strain behavior predicted by the proposed analytical model introduced herein.

The compressive stress-strain behavior predicted by the proposed analytical model introduced herein is also compared to experimental stress-strain behavior of the FRP-confined concrete cylinder tests performed by Teng and Lam (2004) in **Figure 10.46**.

These figures indicate that the proposed analytical model can accurately predict the compressive behavior of circular concrete sections confined by both carbon (CFRP) and glass (GFRP) FRP jackets, as shown in **Figures 10.46(a)** and **10.46(b)**, respectively.

In **Figures 10.47** and **10.48**, the compressive stress-strain behavior predicted by the proposed analytical model introduced herein is compared to experimental compressive stress-strain behavior of cast in place FRP tubes (CFFT) cylinder tests performed by Mirmiran (1997).

These figures indicate that the proposed analytical model can accurately predict the compressive behavior of cylindrical plain concrete sections confined by an unbonded (CFFT) glass FRP jacket of low stiffness $K_{je} = 22.1$ of specimen DC-11 shown in **Figure 10.47(a).**

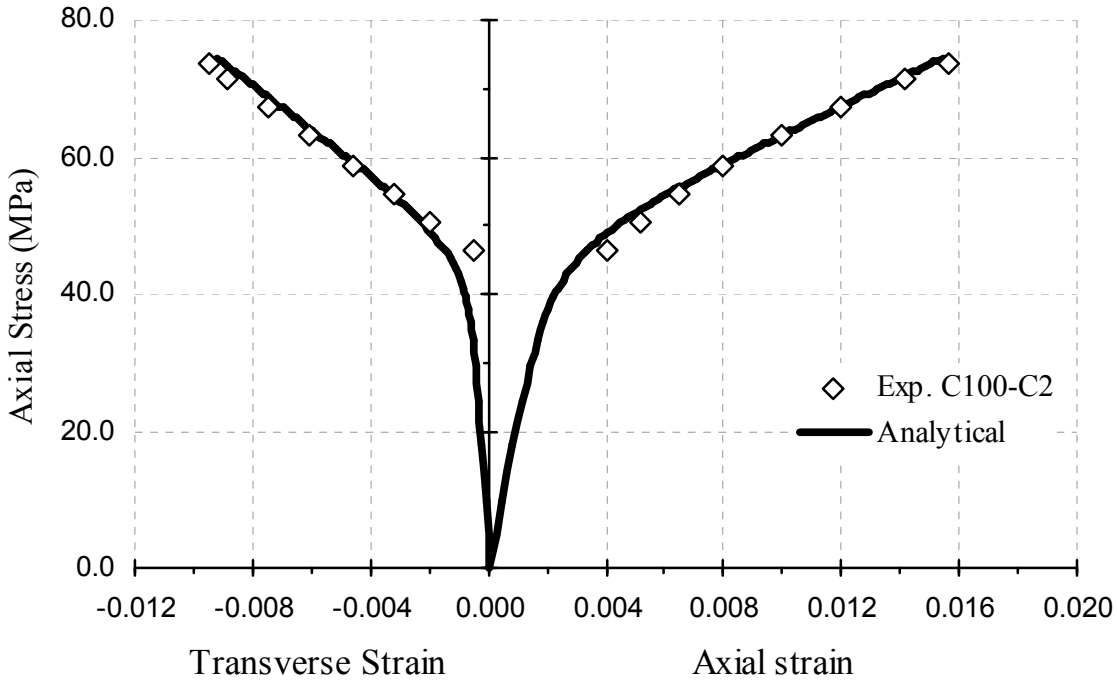

Figure 10.45 Analytical and experimental axial stress-axial strain curves of concrete cylinder test specimen C100-C2 performed by Rochette and Labossiérre (2000).

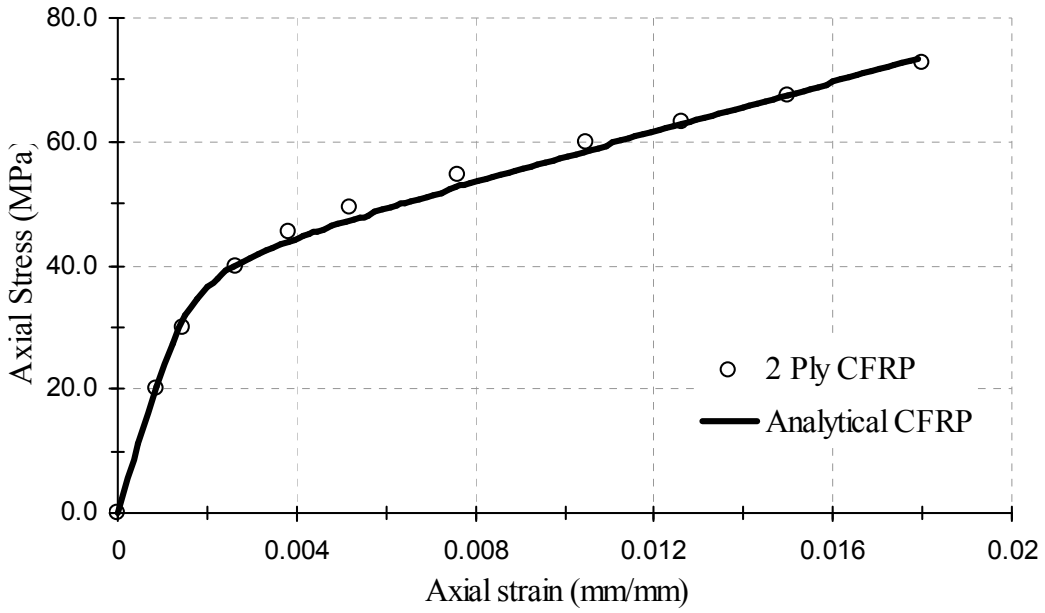

(a)

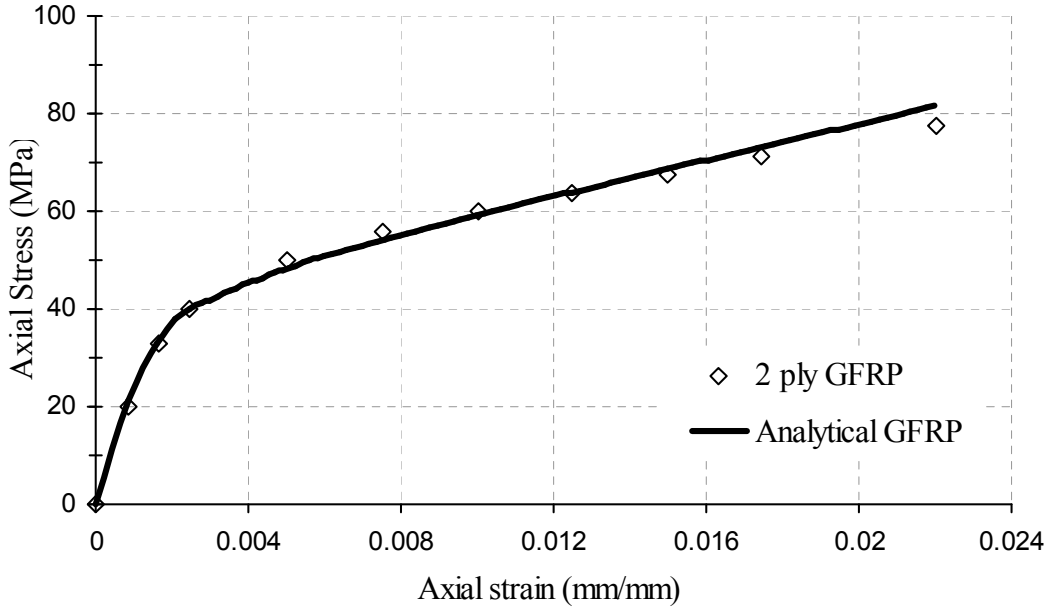

(b)

Figure 10.46 Analytical and experimental axial stress-axial strain curves of concrete cylinder tests performed by Teng and Lam (2004) of specimens confined by two plies of (a) carbon (CFRP) and (b) glass (GFRP) FRP jackets.

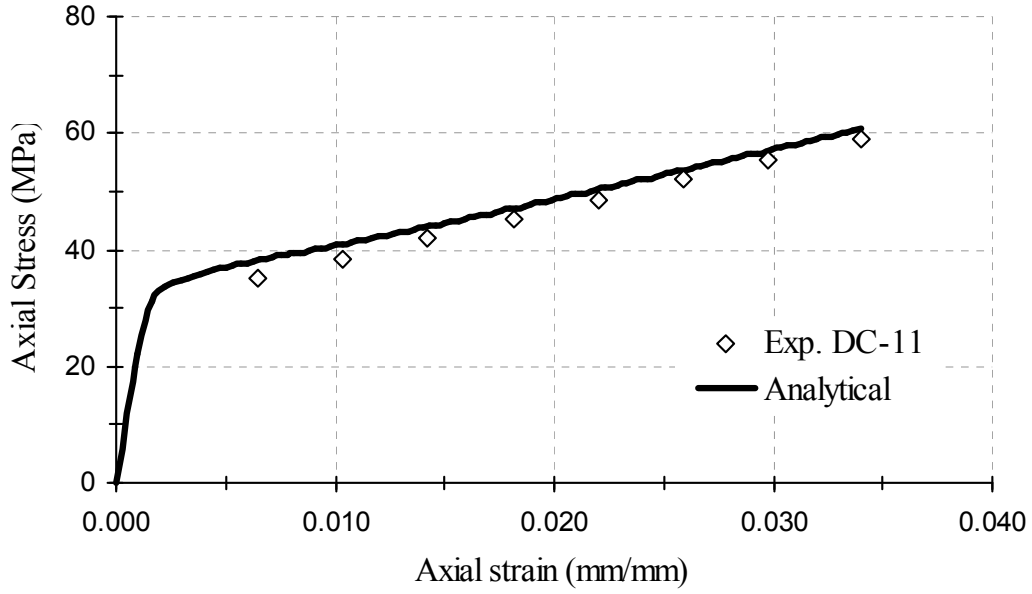

(a)

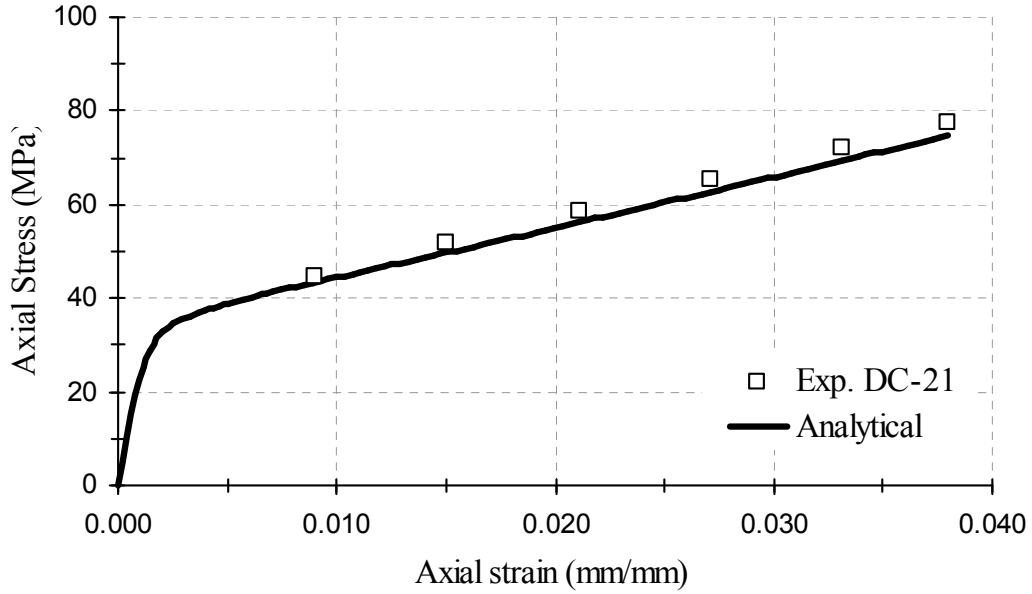

(b)

Figure 10.47 Analytical and experimental axial stress-axial strain curves of concrete cylinder tests performed by Mirmiran (1997) of specimens confined by (a) low stiffness and (b) moderate stiffness unbonded (CFFT) glass FRP jackets.

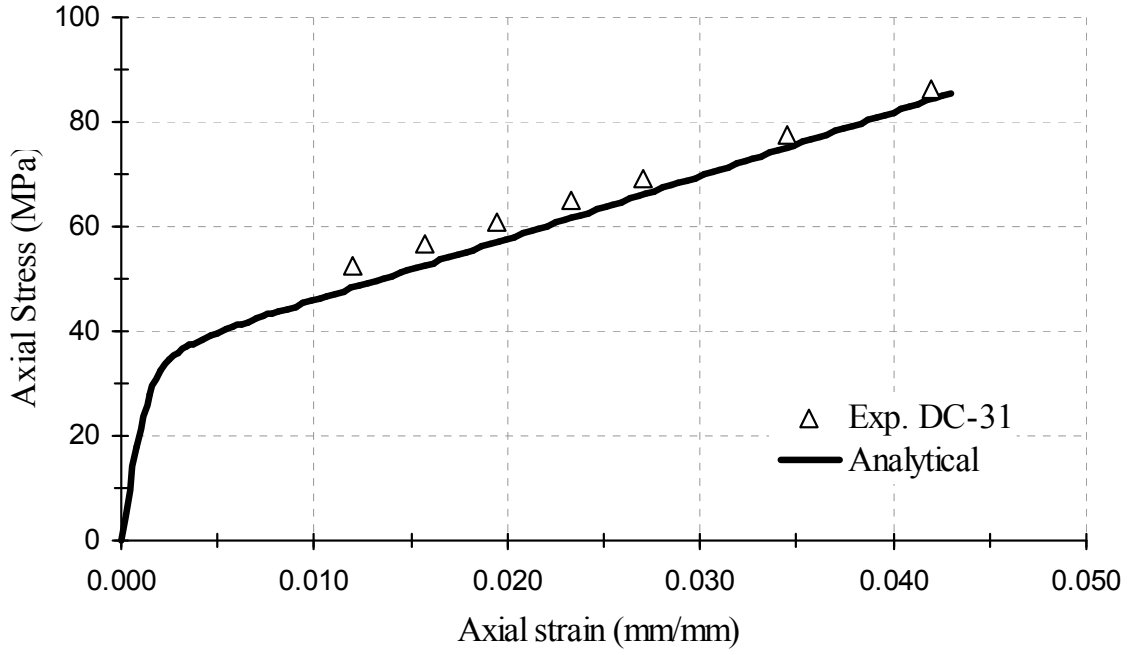

Figure 10.48 Analytical and experimental axial stress-axial strain curves of concrete cylinder test specimen performed by Mirmiran (1997) confined by a high stiffness unbonded (CFFT) glass FRP jacket.

The specimen DC-21 that is confined by a moderate stiffness $K_{je} = 36.6$ FRP jacket shown in **Figure 10.47(b)** and of specimen DC-31 that is confined by a high stiffness $K_{je} = 49.6$ FRP jacket shown in **Figure 10.48**.

These figures show that the proposed analytical stress-strain model can accurately predict the uniaxial stress-strain behavior of cylindrical plain concrete sections confined by cast in place (CFFT) FRP jackets, typically referred to as unbonded FRP jackets.

The effects that FRP jacket construction has on the compressive behavior of FRP-confined concrete is investigated in **Figure 10.49.** FRP jacket construction can be surface-bonded FRP-confined concrete (BFCC) or it can be cast in place concrete-filled FRP tubes (CFFT).

In this figure**,** the analytical axial stress ratio $k_c = f_c / f_{co}$ is plotted versus the axial strain ratio $k_\varepsilon = \varepsilon_c / \varepsilon_{co}$ of the FRP-confined concrete cylinder specimen M1-2P-2 tested by Xiao and Wu (2000) is compared to the analytical curve of the FRP-confined concrete cylinder specimen DC-11 tested by Mirmiran (1997) that is confined by a cast in place (CFFT) FRP tube.

These concrete cylinder tests were selected since they are confined by an FRP jacket having an identical stiffness; specimen M1-2P-2 has an effective stiffness of $K_{je} = 22.5$, and specimen DC-11 has $K_{je} = 22.1$.

From analysis of **Figure 10.49** it can be observed that at a given plastic axial compressive strain, i.e., when $k_\varepsilon >> 1.0$ or $\varepsilon_c >> \varepsilon_{co}$, the bonded FRP-jacketed cylindrical concrete section exhibits a greater increase in compressive strength, i.e., an increase in strain energy, than a cast-in-place FRP-jacketed section.

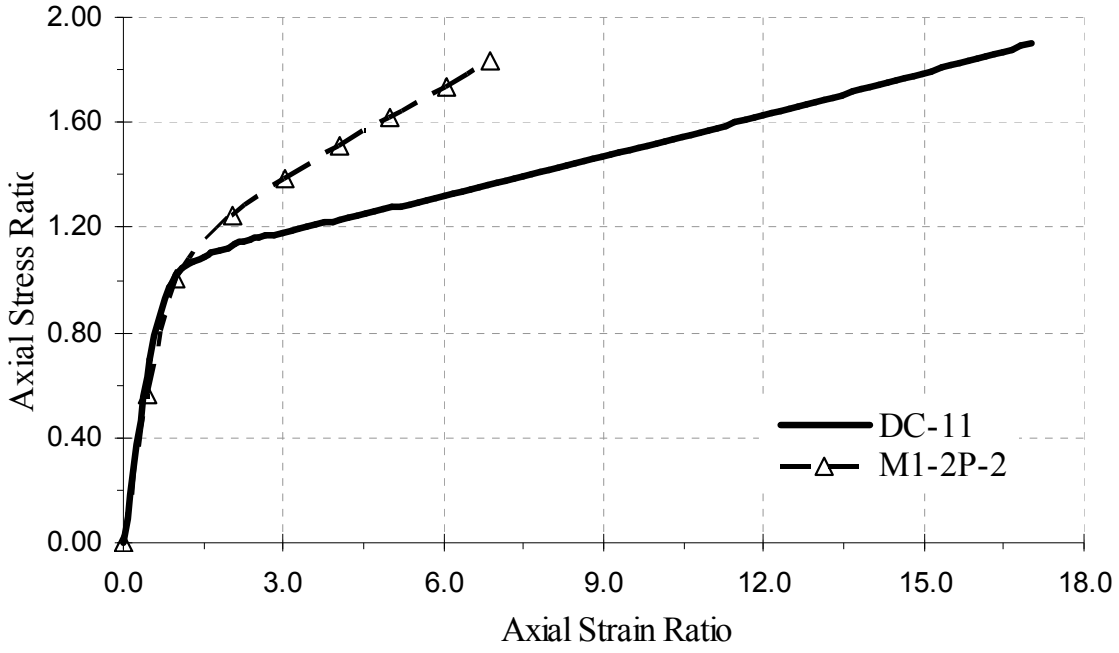

Figure 10.49 Comparison of analytical axial stress-axial strain ratio curves of concrete cylinders confined by cast in place FRP jacket (DC-11) tested by Mirmiran (1997) and by bonded (MP-2P-2) FRP jacket tested by Xiao and Wu (2000) that are confined by similar stiffness FRP jackets.

For a given axial plastic compressive stress for which $k_\varepsilon >> 1.0$ or $\varepsilon_c >> \varepsilon_{co}$, the cast-in-place (CFFT) FRP jacketed section exhibits a significant increase in plastic compressive strain, i.e., an increase in strain ductility, when compared to that experienced by the bonded (BFCC) FRP-jacketed section. As a result, for new construction, a cast-in-place concrete-filled FRP tube (CFFT) construction may be warranted when an increase in strain ductility is the desired feature in the FRP-confined concrete section.

For existing or new cast-in-place concrete sections, surface-bonded (BFCC) FRP jacket construction can provide a significant increase in strength and ductility. Care must be taken when selecting the required FRP jacket thickness or stiffness, since low stiffness FRP-jacketed sections can experience premature jacket rupture due to stress concentrations at the jacket-to-concrete interface, as a result of the axial strain-induced transverse dilation of the confined concrete core.

The difference in behavior between BFCC and CFFT can be attributed to the presence of excess pore water in the FRP-confined concrete core. For the case of BFCC sections, the FRP-wrapped concrete is typically allowed to dry to its natural moisture content.

For CFFT sections the cast-in-place FRP jacket serves as a barrier against evaporation of the nonhydrated water (i.e., bleed water) which can remain in suspension in the concrete mix and often becomes trapped within the voids of the concrete's structure. The presence of pore water has a significant weakening influence on the strength of the concrete material, which is a result of an increase in the pore water pressure, which acts against the concrete's internal structure and weakens the effectiveness of the concrete core in sustaining the applied load.

An increase in the pore water pressure results from an increase in the passive confining stresses provided by the restraining elastic FRP jacket as dilation of the confined concrete core progresses; this weakening effect increases as the passive confining stress provided by the retraining FRP jacket increases (Imran 1994).

As demonstrated in **Figures 10.31-10.49** the proposed uniaxial stress-strain model for FRP-confined concrete sections can accurately capture the essentially bilinear compressive stress-strain behavior that circular FRP-confined concrete sections experience throughout entire axial compressive loading or deformation. The bilinear behavior of the FRP-confined concrete section is a result of the constant kinematic restraint that is provided by the confining elastic FRP jacket, which curtails the transverse dilation of the confined concrete core.

As established in the parametric study [refer to **Figure 10.22**] and as supported by the experimental evidence introduced herein, as shown in **Figures 10.42-10.44,** an increase in the FRP jacket stiffness K_{je} of Eq. (4.14) can result in an increase in strain ductility and in strain energy. In addition, for FRP-confined concrete sections experiencing strain-hardening behavior, the plastic slope of the stress-strain curve is proportional to the FRP jacket stiffness as indicated in the parametric study, as demonstrated in **Figure 10.22** and as supported by the experimental evidence in **Figures 10.42-10.44**.

In what follows, shape effects are considered in the comparison of the proposed analytical model with the experimental compressive behavior of elliptical (EFCC), circular (CFCC), rectangular (RFCC), and square (SFCC) FRP-confined concrete sections.

Elliptical FRP-Confined Concrete Sections

The compressive stress-strain behavior predicted by the proposed analytical stress-strain model is compared with the uniaxial compressive tests of plain elliptical FRP-confined concrete (EFCC) tests confined by bonded (BFCC) FRP-jackets performed by several investigators. These include compressive tests of normal-strength normal-weight EFCC sections performed by Teng and Lam (2002) and shape-modified rectangular concrete sections confined by elliptical FRP jackets performed by Yan (2005).

In **Figures 10.50-10.53**, the compressive stress-strain behavior predicted by the proposed analytical model introduced herein is compared to experimental stress-strain behavior of elliptical FRP-confined concrete sections performed by Teng and Lam (2002).

The stress-strain curves shown in **Figure 10.50** correspond to the series I tests of circular (a/b=1.0) and elliptical (a/b=5/4) FRP-confined concrete sections, shown in **Figure 10.50(a)** and **(b)**, respectively.

The stress-strain curves shown in **Figure 10.51** correspond to the series II tests of circular (a/b=1.0) and elliptical (a/b=5/4) FRP-confined concrete sections, shown in **Figure 10.51(a)** and (**b)**, respectively.

The stress-strain curves shown in **Figure 10.52** and **Figure 10.53** correspond to the series V tests of circular (a/b=1.0) and elliptical (a/b=5/4) and (a/b-5/3) FRP-confined concrete sections, shown in **Figure 10.52(a), (b)**, and **Figure 10.53,** respectively.

From **Figures 10.50-10.53**, it can be observed that the proposed analytical stress-strain model can accurately predict the uniaxial stress-strain behavior of elliptical concrete sections confined with elliptical FRP jackets.

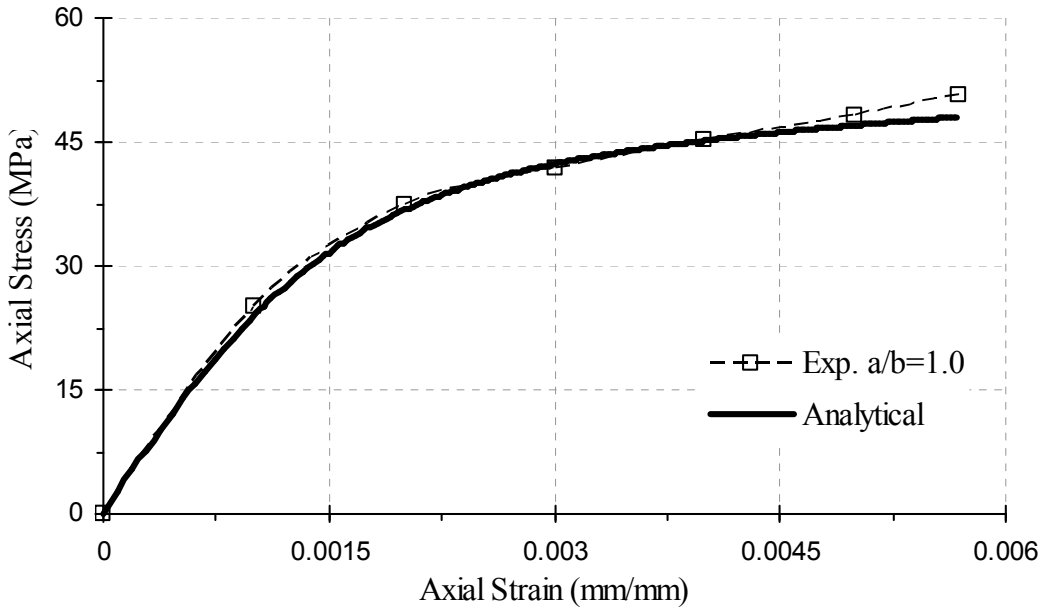

(a)

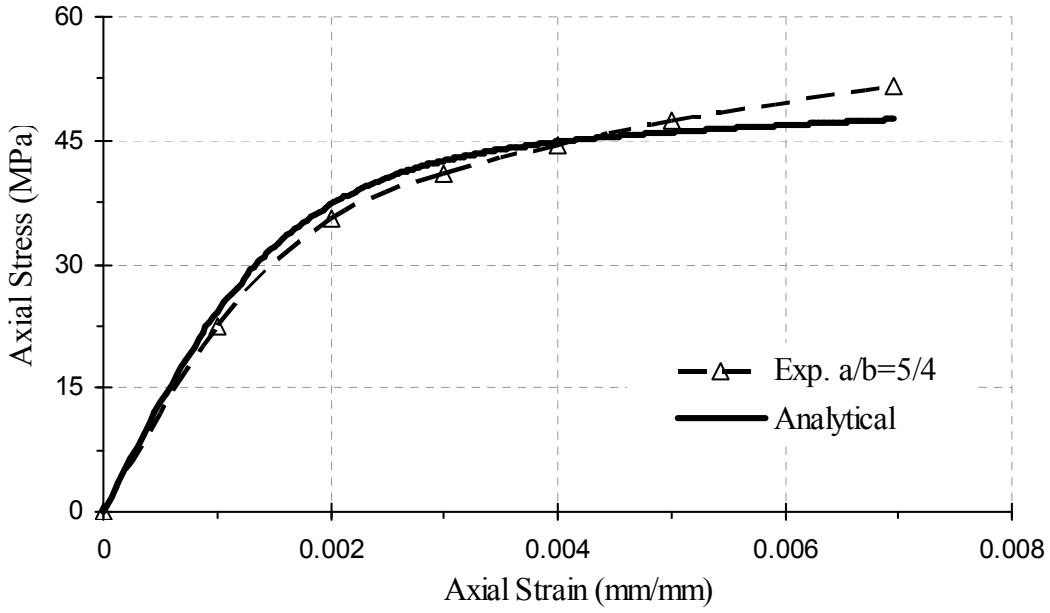

(b)

Figure 10.50 Analytical and experimental axial stress-axial strain curves of series I elliptical concrete section tests performed by Teng and Lam (2002).

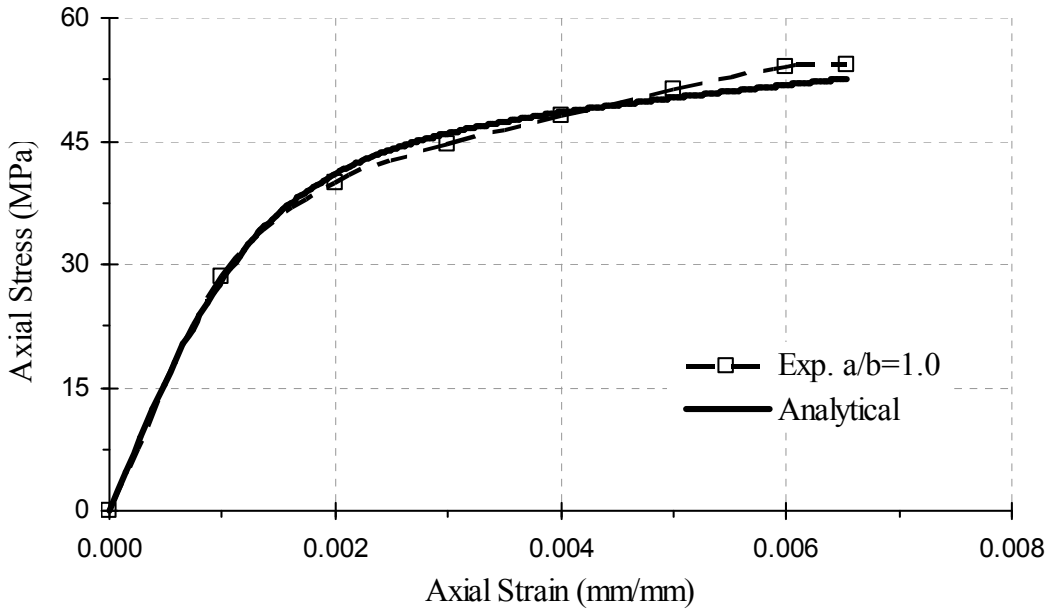

(a)

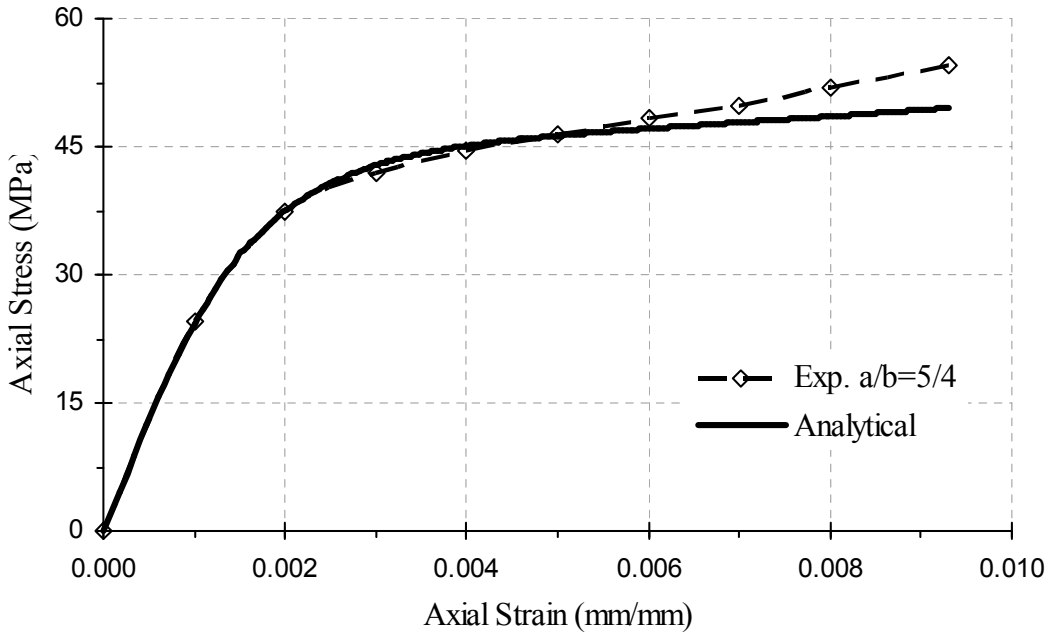

(b)

Figure 10.51 Analytical and experimental axial stress-axial strain curves of series II elliptical concrete section tests performed by Teng and Lam (2002).

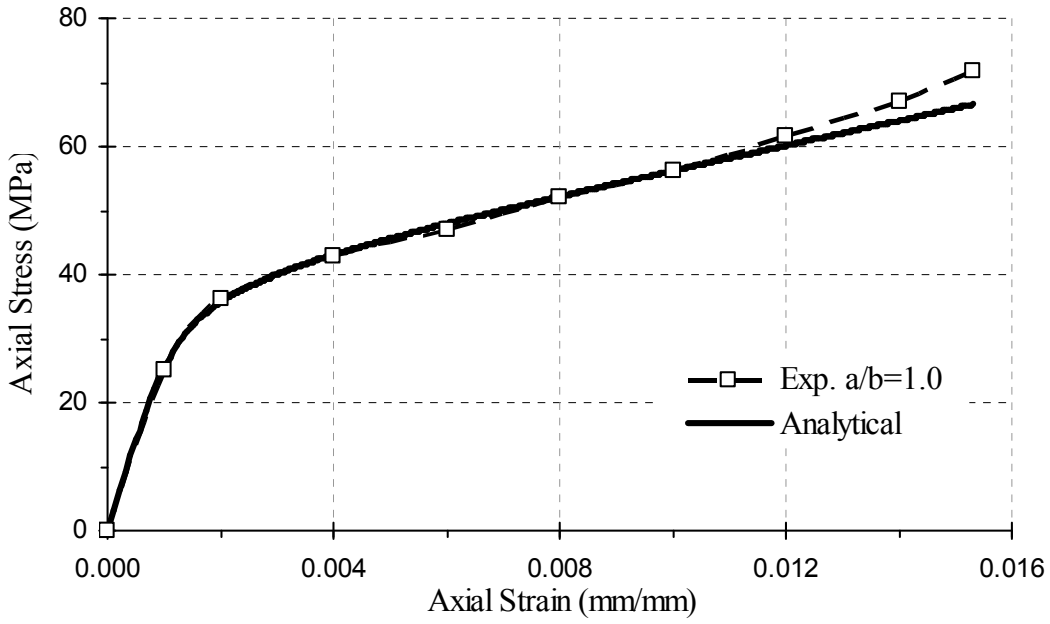

(a)

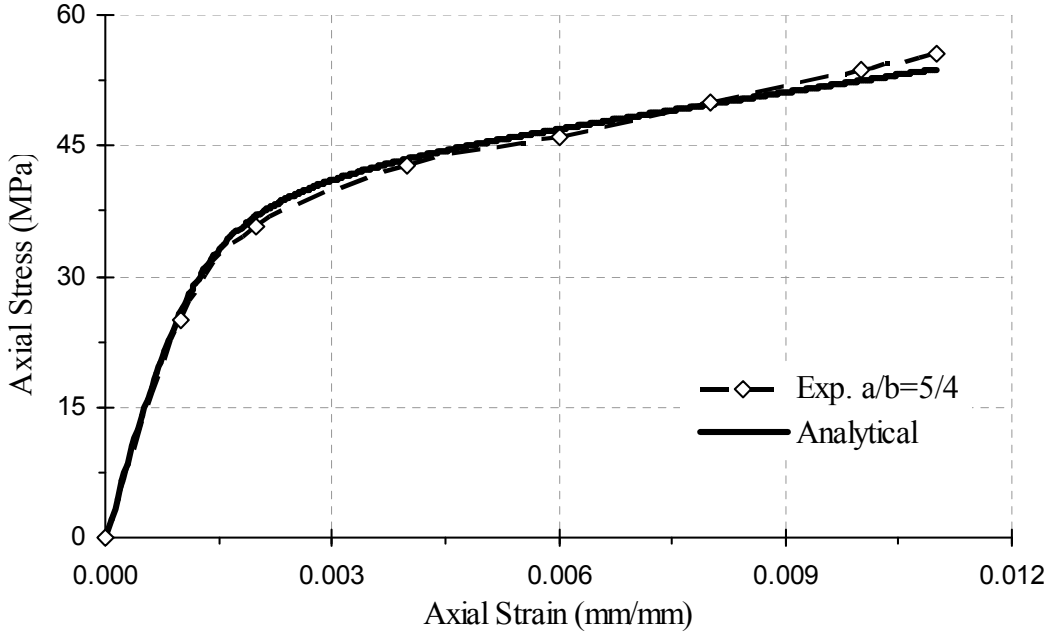

(b)

Figure 10.52 Analytical and experimental axial stress-axial strain curves of series V elliptical concrete section tests performed by Teng and Lam (2002).

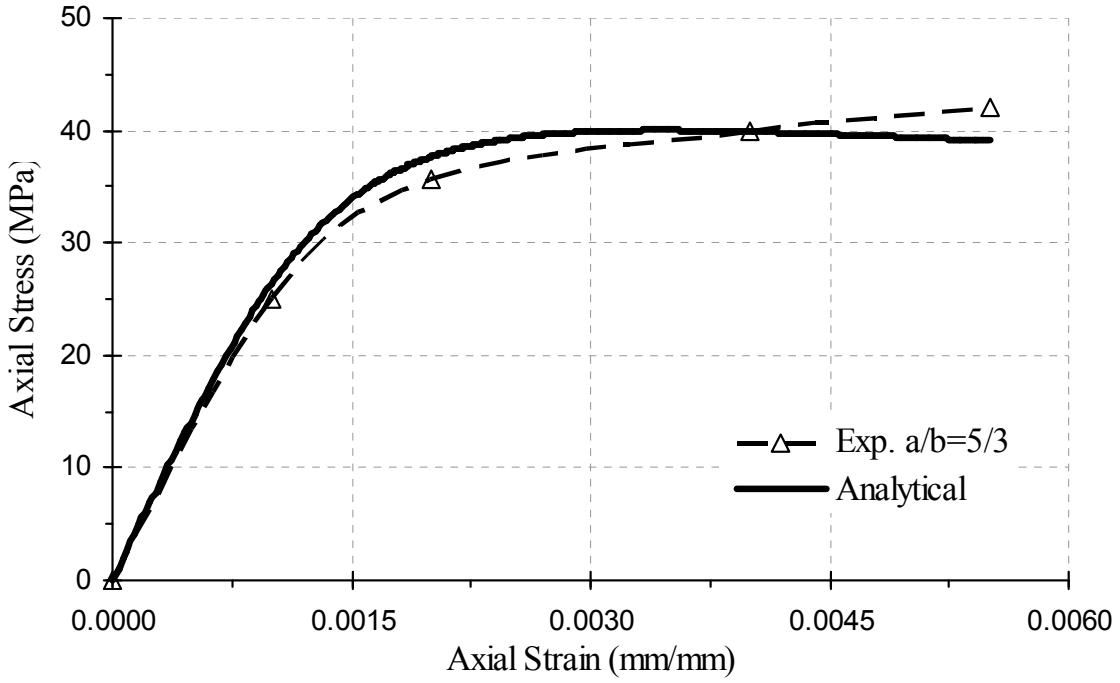

Figure 10.53 Analytical and experimental axial stress-axial strain curves of series V elliptical concrete section tests performed by Teng and Lam (2002).

The model also accurately predicts the effects that the elliptical FRP jacket aspect ratio α_{sh} of Eq. (4.2) has on the uniaxial compressive behavior of elliptical FRP-confined concrete sections.

The designation a/b of the elliptical specimens tested by Teng and Lam (2002), as shown in **Figures 10.50-10.53**, refers to the aspect ratio of the elliptical FRP-confined concrete section $\alpha_{sh} = H_c/B_c$ of Eq. (4.2), with $H_c = 2a$ and $B_c = 2b$.

In **Figure 10.54** and **10.55**, the compressive stress-strain behavior predicted by the proposed analytical model introduced herein is compared to the experimental stress-strain behavior of shape-modified rectangular concrete sections confined by carbon and glass elliptical FRP jackets performed by Yan (2005).

The stress-strain curves shown in **Figure 10.54** correspond to the shape-modified square concrete section confined by a circular carbon FRP jacket, as shown in **Figure 10.54(a)**, and a shape-modified rectangular concrete section with an aspect ratio of $\alpha_{sh} = 3.0$ confined an elliptical carbon FRP jacket, as shown in **Figure 10.52(b)**.

The stress-strain curves shown in **Figure 10.55** correspond to the shape-modified square concrete section confined by a circular glass FRP (GFRP) jacket, as shown in **Figure 10.55(a)** and a shape-modified rectangular concrete section with an aspect ratio of $\alpha_{sh} = 3.0$ confined by an elliptical glass FRP (GFRP) jacket, as shown in **Figure 10.55(b)**. From these figures it can be observed that the proposed analytical stress-strain model can accurately predict the uniaxial stress-strain behavior of shape-modified rectangular and square sections confined by elliptical FRP jackets.

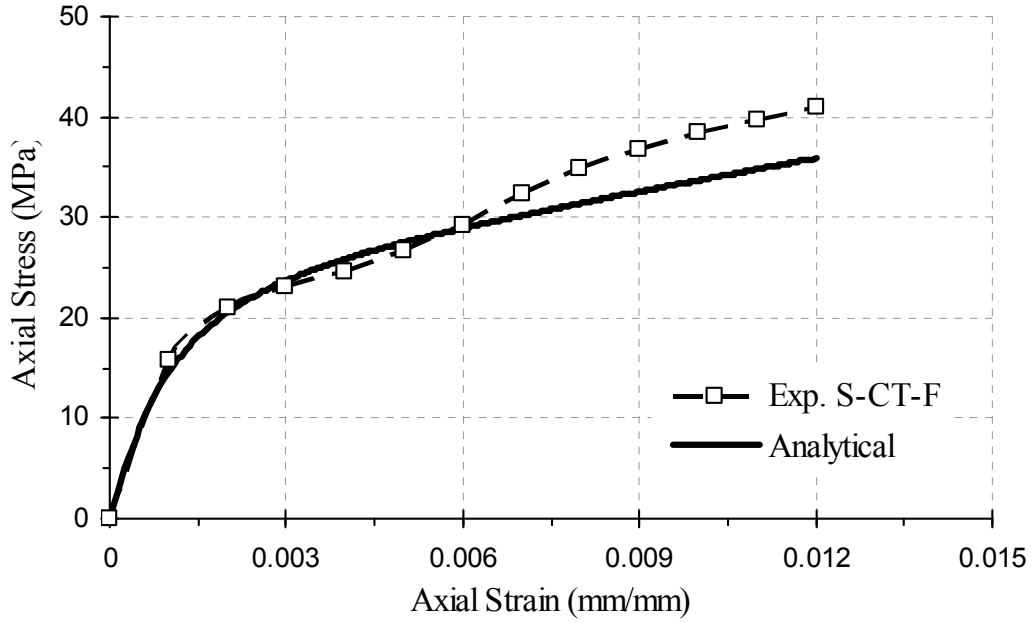

(a)

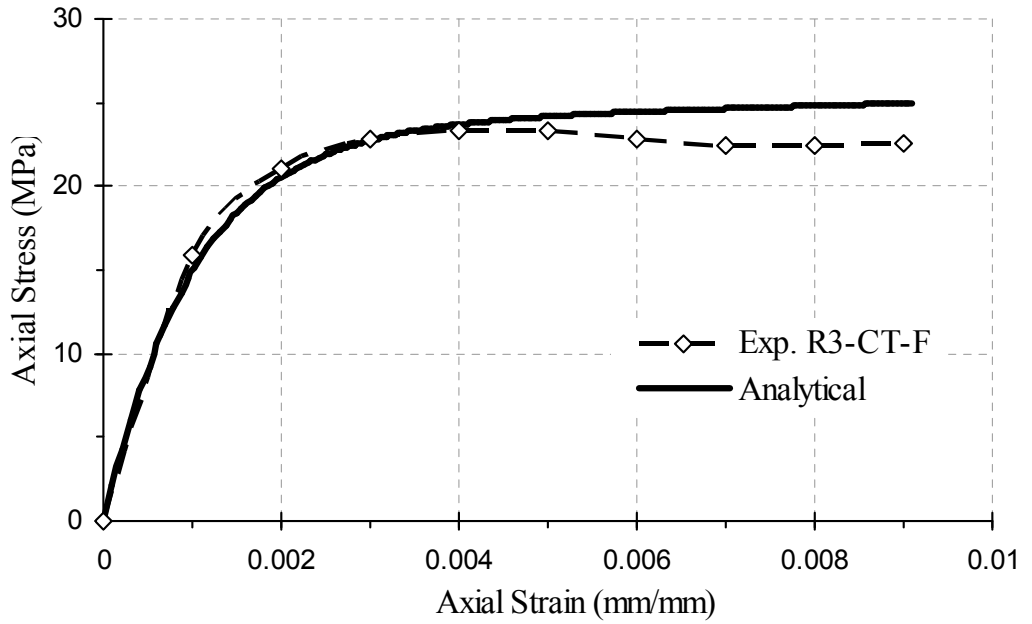

(b)

Figure 10.54 Analytical and experimental axial stress-axial strain curves of (a) square and (b) rectangular shape-modified concrete sections confined by carbon elliptical FRP jackets performed by Yan (2005).

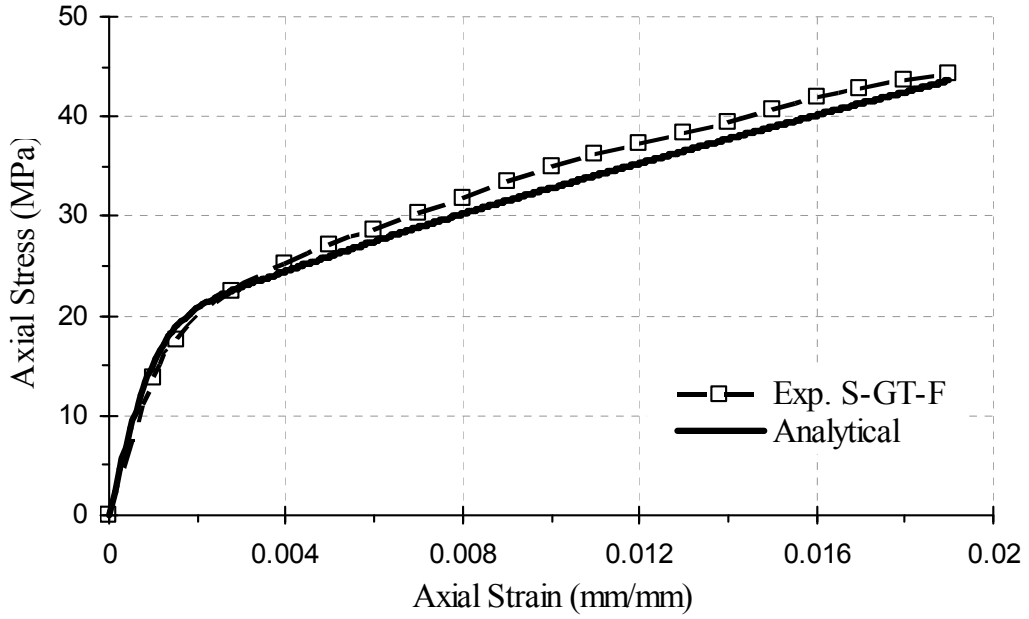

(a)

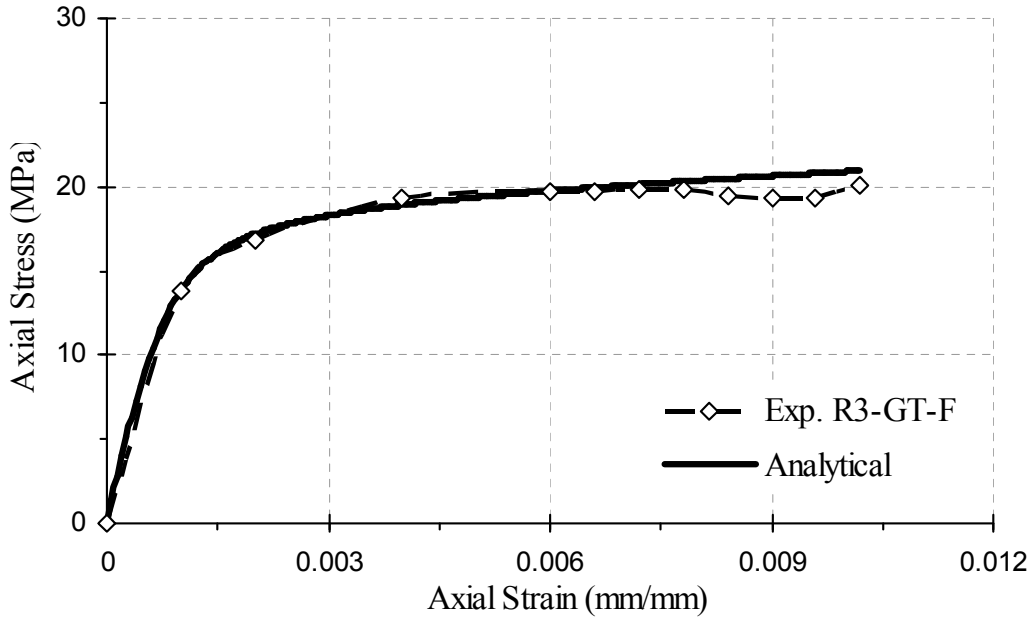

(b)

Figure 10.55 Analytical and experimental axial stress-axial strain curves of (a) square and (b) rectangular shape-modified concrete sections confined by glass elliptical FRP jackets performed by Yan (2005).

As shown in **Figures 10.54-10.55,** the proposed analytical model can predict the effects that the FRP jacket aspect ratio α_{sh} of Eq. (4.2) has on the uniaxial compressive behavior of shape-modified rectangular (SMR) (including square) sections confined by shape–modifying elliptical (ESM) and circular (CSM) FRP jackets.

Analysis of **Figures 10.50-10.55** indicates the proposed analytical model can predict the uniaxial compressive stress-strain behavior of elliptical FRP-confined concrete sections, be it surface-bonded FRP jacket construction (Teng and Lam 2002) or prefabricated circular or elliptical FRP jacket used as a cast-in-place FRP form that shape modifies rectangular (including square) sections (Yan 2005). Also, these figures demonstrate that the proposed analytical model can predict the FRP jacket's aspect ratio effects on the uniaxial compression behavior of EFCC sections, as was demonstrated in the parametric study of **Figure 10.23** and supported by the experimental evidence, as shown in **Figures 10.48-10.53**.

Square FRP-Confined Concrete Sections

The compressive stress-strain behavior predicted by the proposed analytical stress-strain model is compared with the uniaxial compressive tests of plain square FRP-confined concrete (SFCC) tests confined by bonded (BFCC) and unbonded (CFFT) FRP-jackets with rounded corners performed by several investigators. These include compressive tests of SFCC sections with bonded carbon FRP (CFRP) jackets performed by Rochette and Labossièrre (2000), Lam and Teng (2003b) and SFCC sections with cast-in-place (CFFT) rectangular glass FRP (GFRP) jackets performed by Mirmiran et al. (2000).

The compressive stress-strain behavior predicted by the proposed analytical model introduced herein is compared to the experimental stress-strain behavior of 152 mm square FRP-confined concrete sections performed by Rochette and Labossièrre (2000) in **Figure 10.56.**

The stress-strain curves plotted in **Figure 10.56(a)** are for a 152 mm square specimen with rounded corners having an average radius of 5 mm, with a jacket corner aspect ratio α_j of Eq. (4.4), of $\alpha_j = 3.3\%$, whereas the stress-strain curve of **Figure 10.56(b)** corresponds to a square section with 38 mm corner radius, with a jacket corner aspect ratio of $\alpha_j = 25.0\%$.

In **Figures 10.57-10.58**, the compressive stress-strain behavior predicted by the proposed analytical model introduced herein is compared to the experimental stress-strain behavior of 152 mm square FRP-confined concrete sections with rounded corners, performed by Lam and Teng (2003b)**.**

In **Figure 10.57**, the compressive stress-strain behavior predicted by the proposed analytical model introduced herein is compared to the experimental stress-strain behavior of 152 mm square sections confined by a single layer carbon FRP (CFRP) jacket with a corner radius of 15 mm corner radius ($\alpha_j = 9.9\%$), as shown in **Figure 10.57(a)**, and 25 mm corner radius ($\alpha_j = 16.5\%$), as shown in **Figure 10.57(b).**

In **Figure 10.58**, the analytical and experimental stress-strain curves of a 152 mm square section confined by a double layer carbon FRP (CFRP) jacket with a 15 mm corner radius ($\alpha_j = 9.9\%$) are shown.

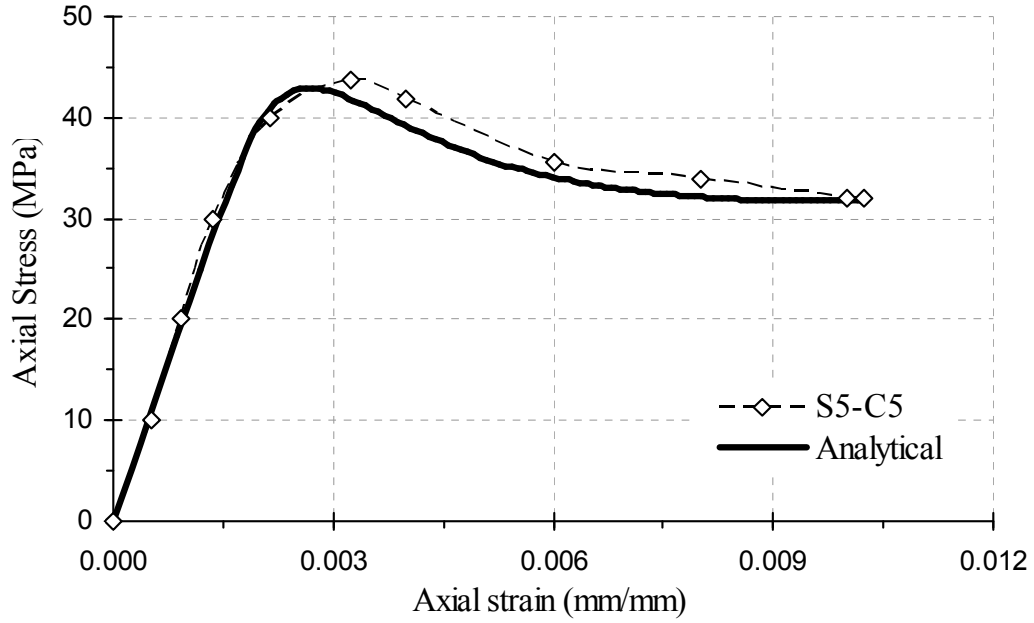

(a)

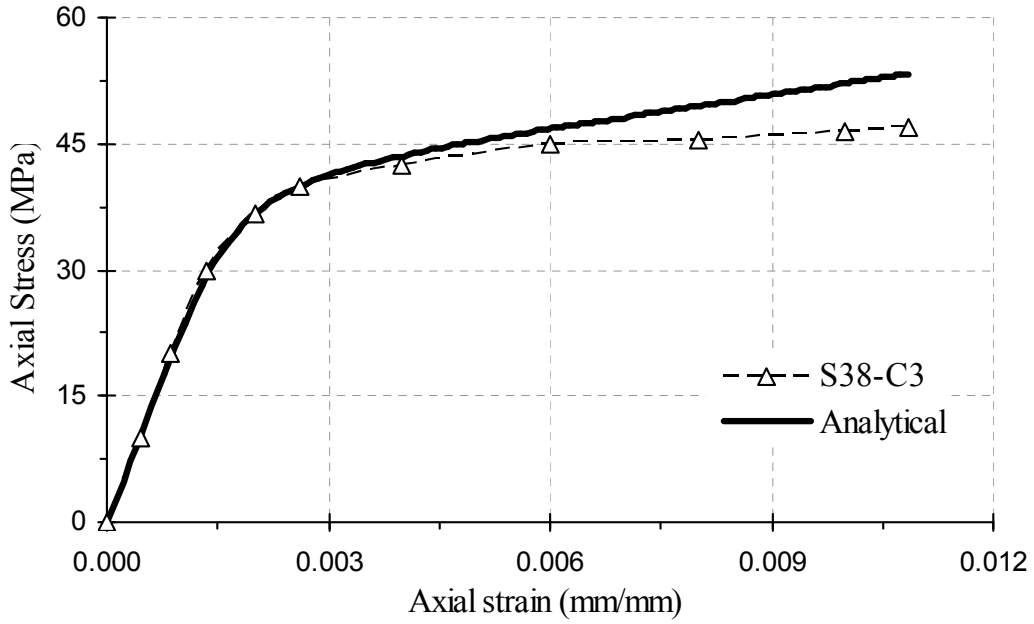

(b)

Figure 10.56 Analytical and experimental axial stress-axial strain curves of square FRP-confined concrete sections with corners having a radius of (a) 5 mm and (b) 38 mm performed by Rochette and Labossièrre (2000).

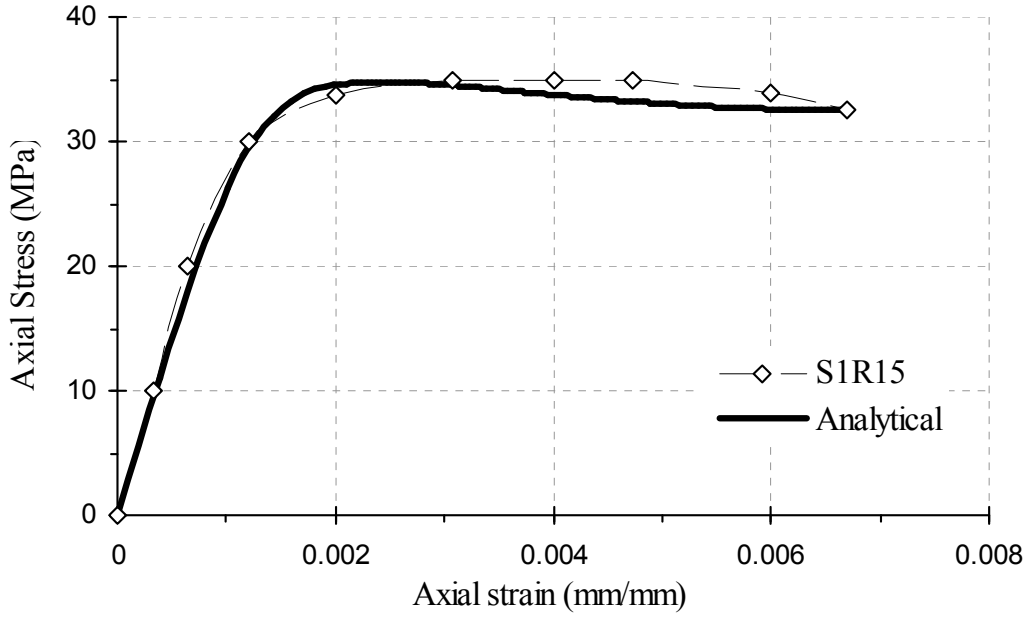

(a)

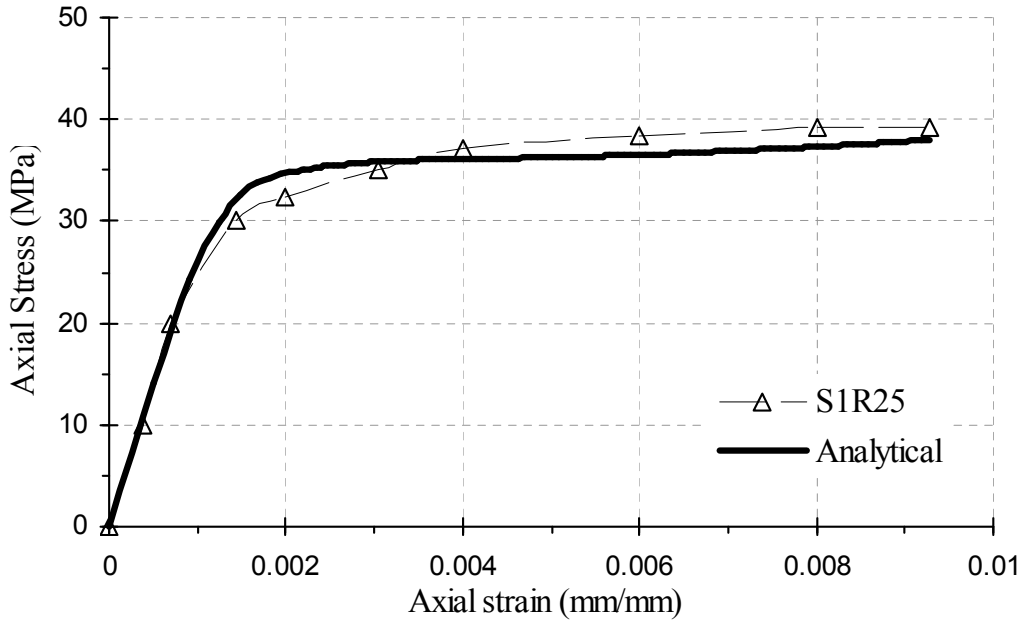

(b)

Figure 10.57 Analytical and experimental axial stress-axial strain curves of square concrete sections confined by a single layer carbon FRP jacket with (a) 15 mm and (b) 25 mm corner radius, performed by Lam and Teng (2003b).

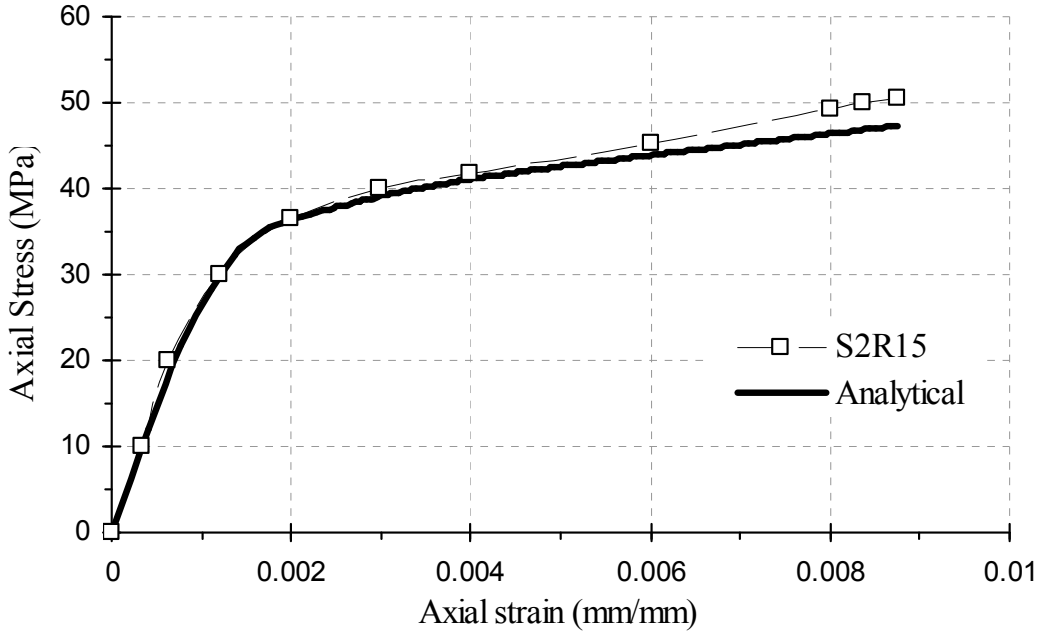

Figure 10.58 Analytical and experimental axial stress-axial strain curves of a square concrete section confined by a double layer carbon FRP jacket with 15 mm corner radius, performed by Lam and Teng (2003b).

The stress-strain curves shown in **Figures 10.56-10.58** indicate that analytical model can accurately predict the effects that an increase in the jacket corner aspect ratio α_j of Eq. (4.4) has on the uniaxial compressive behavior of square (SFCC) sections, as was demonstrated in **Figure 10.25**.

In **Figures 10.59** and **10.60,** the compressive stress-strain behavior predicted by the proposed analytical model is compared to the experimental stress-strain behavior of 152 mm square concrete filled FRP tube (CFFT) sections, with 6.35 mm corner radius ($\alpha_j = 4.2\,\%$), performed by Mirmiran et al. (2000).

The experimental stress-strain curves of the square concrete sections confined by a single- and double-layer bonded (BFCC) carbon FRP (CFRP) jacket, shown in **Figure 10.61(a)**, are compared to the analytical stress-strain predictions shown in **Figure 10.61(b)** of the tests performed by Lam and Teng (2003b)**.** In these figures it can be observed that the proposed stress-strain model can accurately predict that the stress-strain behavior of FCC sections having identical geometries can change from that of a section exhibiting a strain-softening behavior to that exhibiting strain-hardening as the FRP jacket stiffness K_{je} of Eq. (4.18) increases.

The experimental stress-strain curves of the square CFFT concrete sections confined by a 6 ply and 10 ply GFRP jackets performed by Mirmiran et al. (2000), shown in **Figure 10.62(a)**, are compared to the analytical stress-strain shown in **Figure 10.62(b).** These figures show that the proposed analytical stress-strain model can predict the effects that an increase in the FRP jacket stiffness K_{je} has on the compressive behavior of square CFFT concrete sections with identical section geometries.

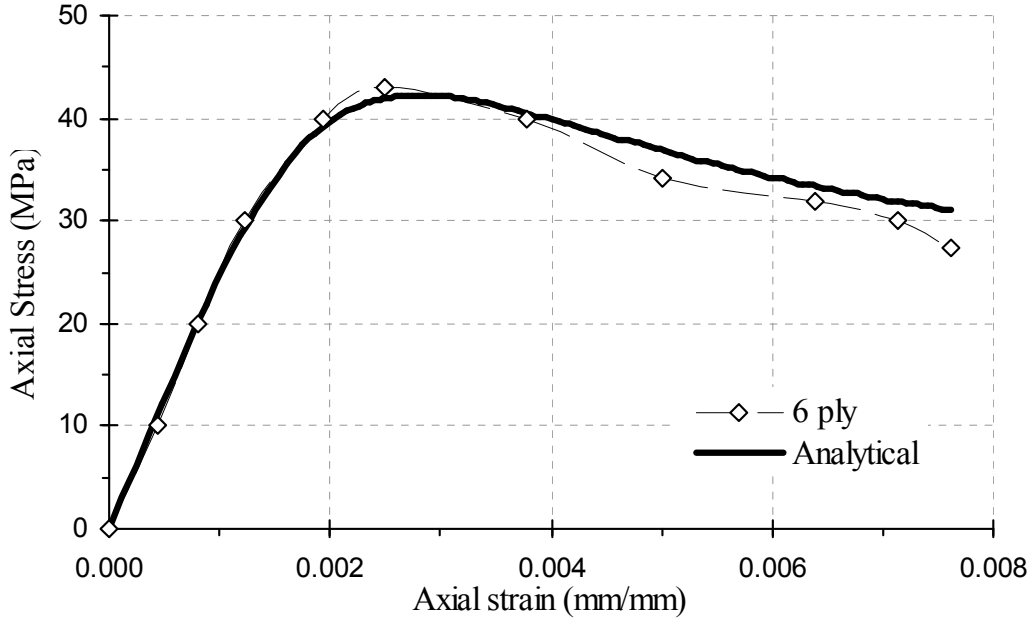

(a)

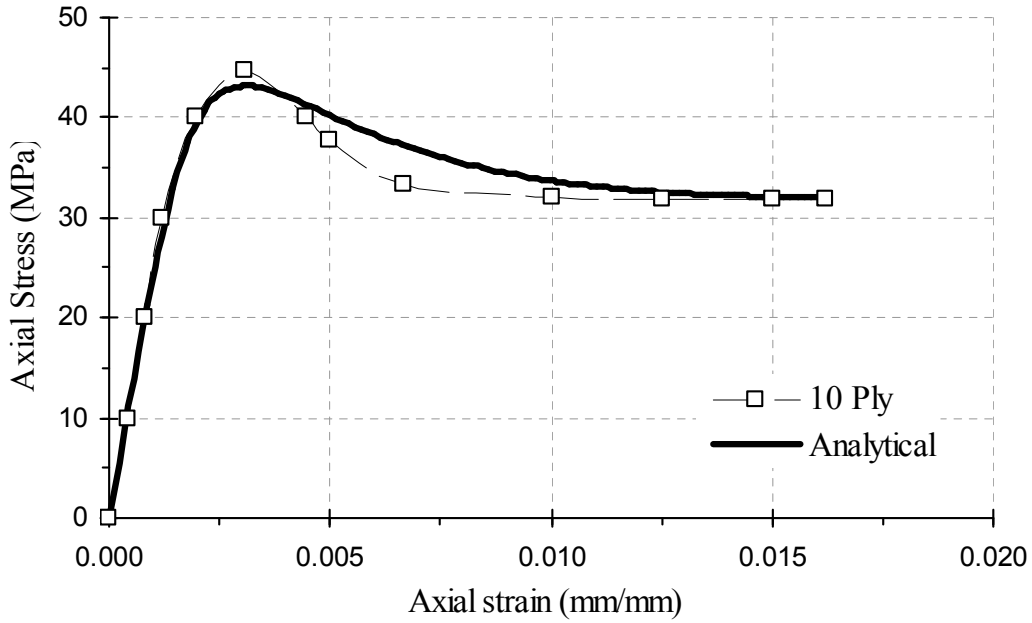

(b)

Figure 10.59 Analytical and experimental axial stress-axial strain curves of square (CFFT) concrete section confined by a (a) 6 ply and (b) 10 ply glass FRP jacket, performed by Mirmiran et al. (2000).

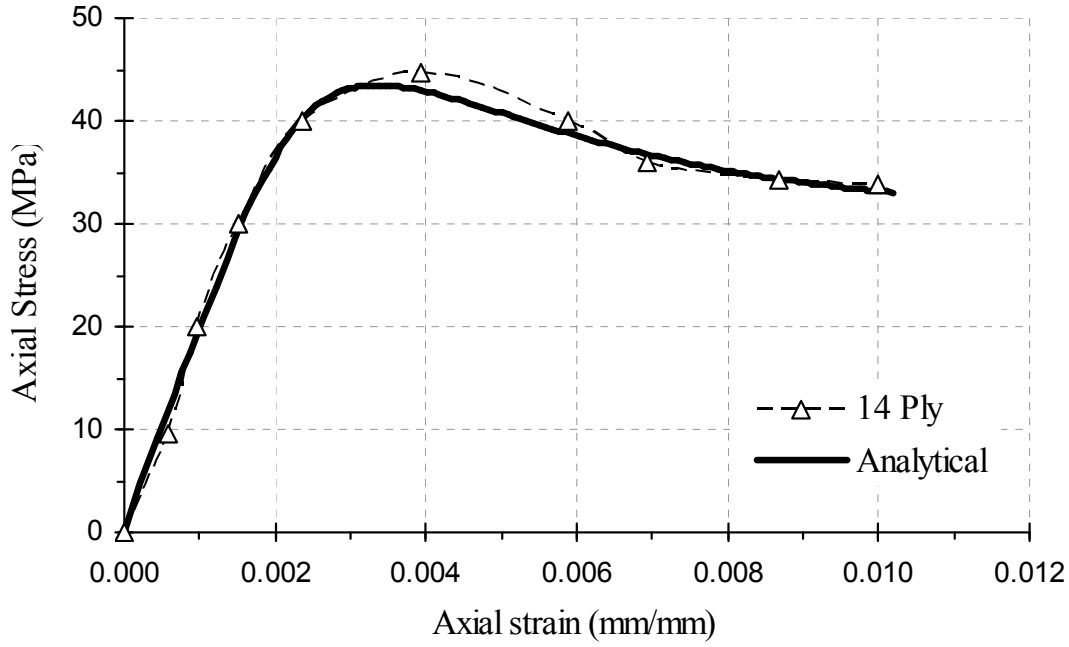

Figure 10.60 Analytical and experimental axial stress-axial strain curves of square (CFFT) concrete section confined by a 14 ply glass FRP jacket, performed by Mirmiran et al. (2000).

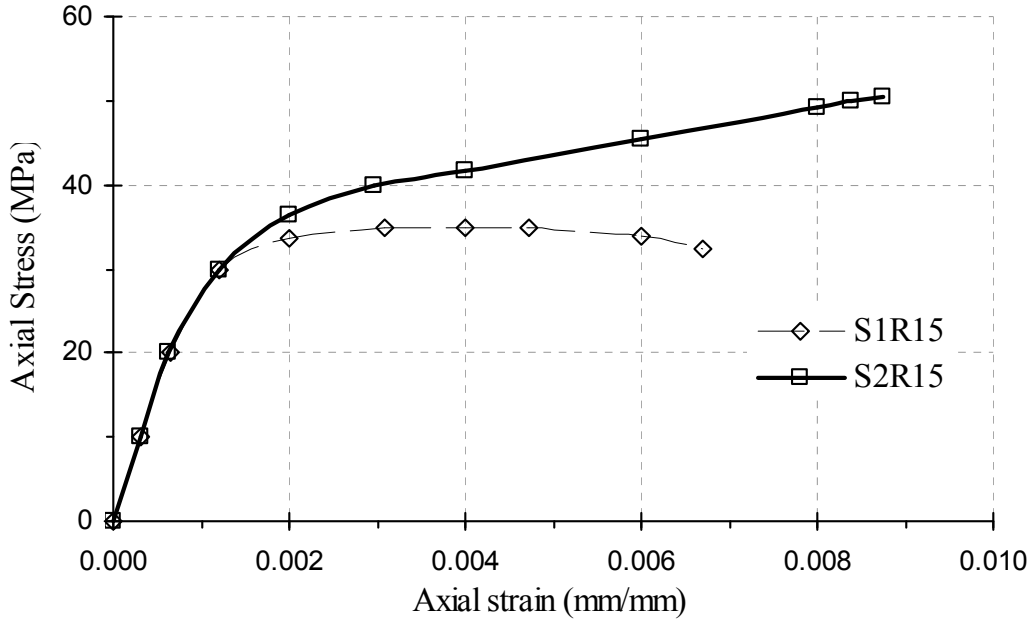

(a)

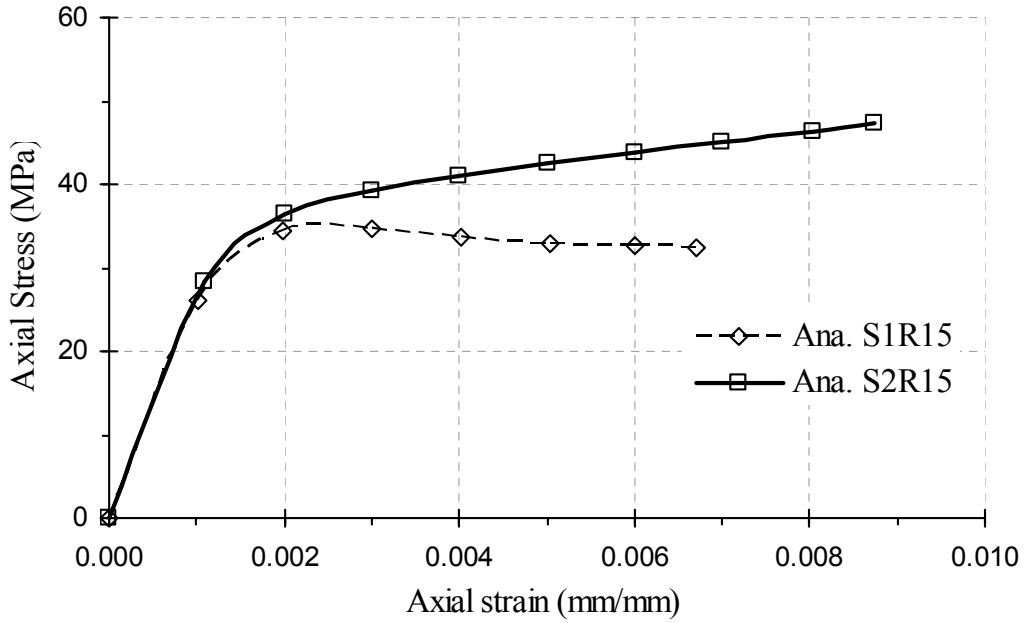

(b)

Figure 10.61 Axial stress-axial strain curves of square (BFCC) concrete section confined with carbon FRP jackets of varying thickness, performed by Lam and Teng (2003b): (a) experimental and (b) analytical.

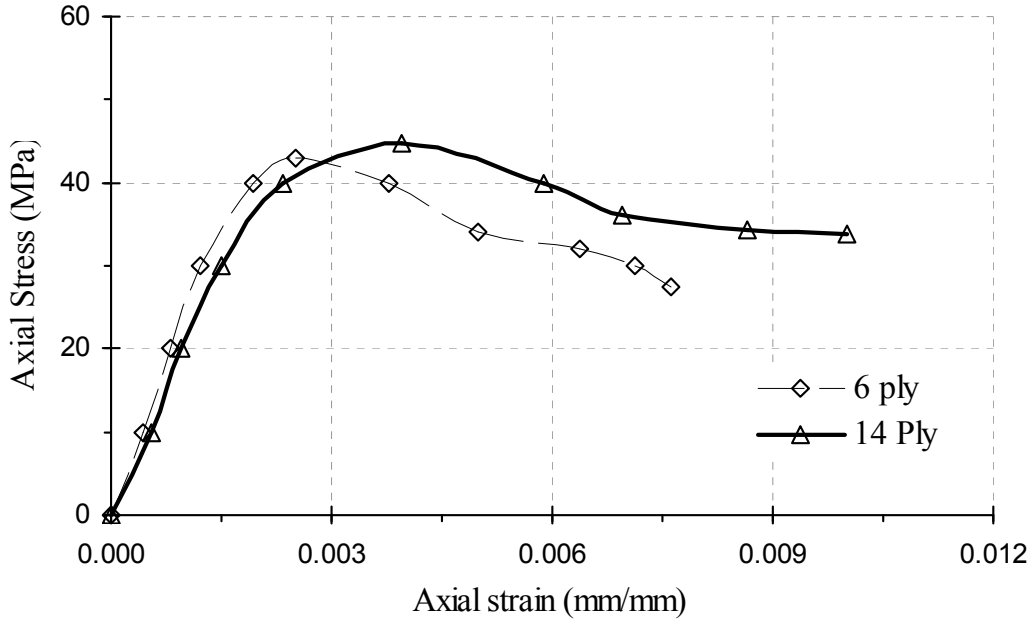

(a)

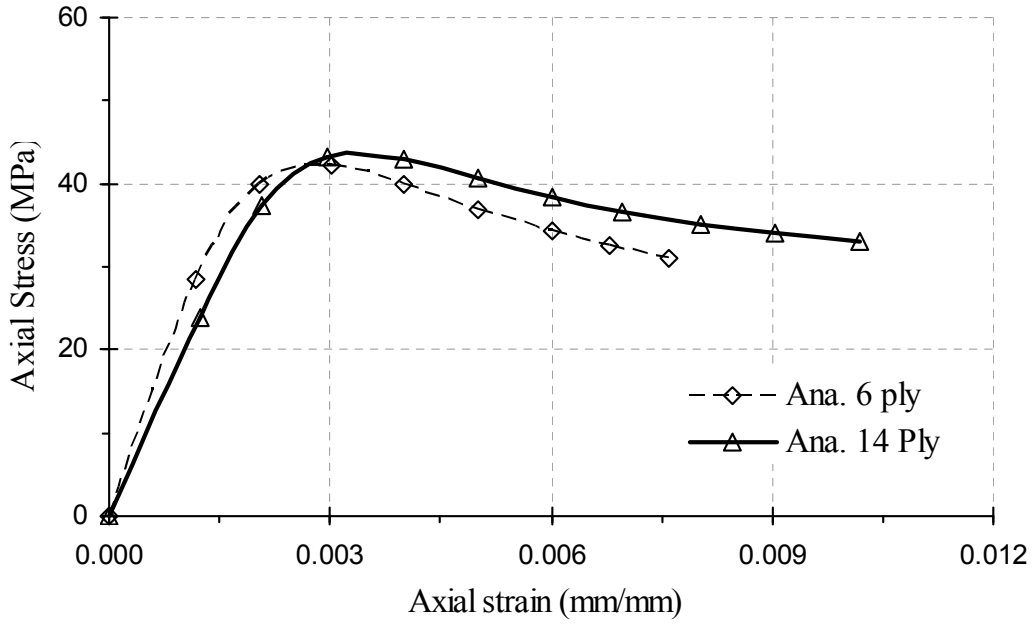

(b)

Figure 10.62 Axial stress-axial strain curves of a square (CFFT) concrete section confined by glass FRP jackets of varying thickness, performed by Mirmiran et al. (2000): (a) experimental and (a) analytical.

In **Figures 10.61** and **10.62** it is demonstrated that the proposed analytical model accurately predicts that an increase in the FRP jacket stiffness K_{je} results in an increase in the peak and ultimate compressive stresses and strains in the square FCC sections, as was demonstrated in the parametric study of **Figures 10.22** and **10.23** and supported by the experimental evidence, as shown in **Figures 10.61** and **10.62**.

Analysis of **Figures 10.59-10.62** indicates that the effects that an increase in FRP jacket stiffness has on the compressive behavior of square FCC section is independent of the FRP jacket construction, be it bonded (BFCC) or unbonded (CFFT) FRP-confined concrete sections.

Rectangular FRP-Confined Concrete Sections

The compressive stress-strain behavior predicted by the proposed analytical stress-strain model is compared with the uniaxial compressive tests of plain rectangular FRP-confined concrete (RFCC) tests confined by bonded (BFCC) FRP-jackets with rounded corners performed by Lam and Teng (2003b).

In **Figure 10.63**, the compressive stress-strain behavior predicted by the proposed analytical model introduced herein is compared to the experimental stress-strain behavior of 152 mm x 255 mm, i.e., $\alpha_{sh} = 1.68$, rectangular FRP-confined concrete sections with rounded corners having a corner radius of 15 mm ($\alpha_j = 6.7\%$), plotted in **Figure 10.63(a)**, and 25 mm ($\alpha_j = 11.1\%$), plotted in **Figure 10.63(b).** The stress-strain curves shown in **Figure 10.63** indicate that the proposed analytical model can predict the effects that an increase in the jacket corner aspect ratio α_j of Eq. (4.4) has on the uniaxial compressive behavior of rectangular (RFCC) sections.

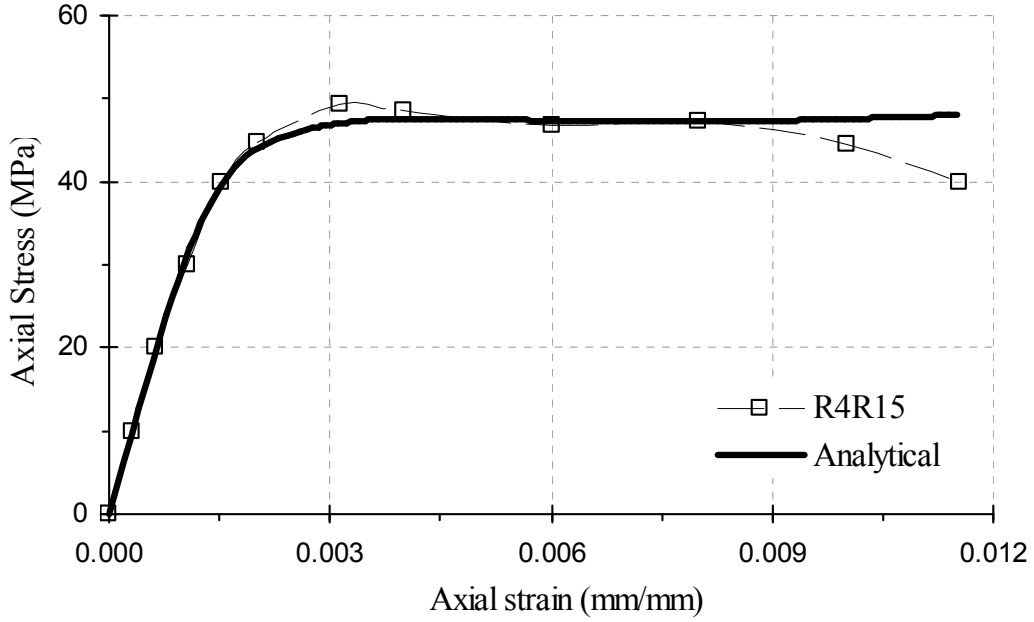

(a)

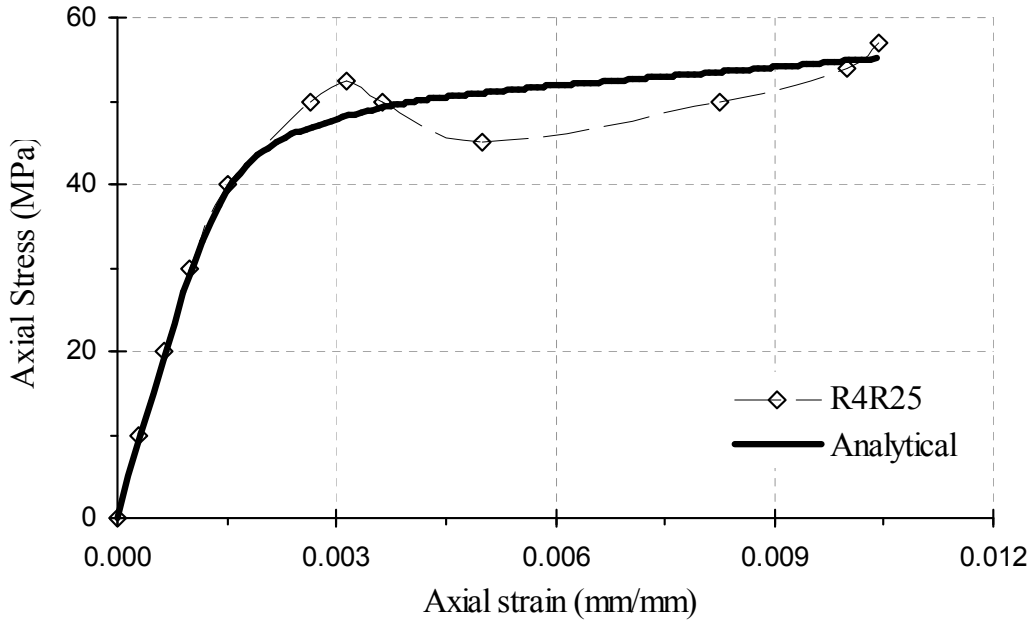

(b)

Figure 10.63 Analytical and experimental axial stress-axial strain curves of rectangular concrete sections confined by carbon FRP jacket with (a) 15 mm and (b) 25 mm corner radius, performed by Lam and Teng (2003b).

The proposed model accurately predicts the effects that an increase in the FRP jacket stiffness K_{je} of Eq. (4.18) has on the compressive behavior of the rectangular FRP-confined concrete sections previously mentioned.

For rectangular (RFCC) and square (SFCC) FRP-confined concrete sections the model accurately predicts that an increase in the jacket corner aspect ratio α_j can significantly improve the uniaxial compressive behavior of these FRP-jacketed shapes by increasing both the strain energy and strain ductility of the section. An increase in the jacket corner aspect ratio α_j in RFCC and SFCC sections has many beneficial effects. For any RFCC section aspect ratio α_{sh}, an increase in α_j results in an increase in the confining efficiency k_e of Eq. (4.8), summarized in **Table 4.1**. For a given RFCC or SFCC section geometry rounding of the corners also increases the effective FRP jacket stiffness K_{je} of Eq. (4.18), as shown by the effective jacket transverse stiffness $\left(C_{je}\right)_{sh}$ of Eq. (4.14) and the reinforcement ratio coefficient C_{sh} of Eq. (4.17), summarized in **Table 4.2**.

For rectangular (RFCC) and elliptical (EFCC) FRP-confined concrete sections the model accurately predicts the effects that the section aspect ratio α_{sh} has on the uniaxial compressive behavior of these FRP-jacketed shapes.

In order to attain similar performance as a square (SFCC) FRP-confined concrete section in a rectangular (RFCC) section, the RFCC section requires an increase in the thickness t_j of the FRP jacket and/or an increase in the jacket corner aspect ratio α_j, which in a reinforced concrete section is limited to small corner radius due to the presence of corner bars and transverse steel reinforcing.

The use of rectangular FRP jackets should be limited to small section aspect ratios, in the range of $1.0 \le \alpha_{sh} \le 2.0$, while maximizing the jacket corner aspect ratio α_j. The use of large aspect ratio rectangular jackets, i.e., for $\alpha_{sh} > 2.0$, with small corner radius, is not recommended, since premature rupture of the FRP jacket can occur due to stress concentrations near the corners of the RFCC section. In addition, for large aspect ratio rectangular FRP jackets, the jacket experiences an increase in the transverse dilation of the confined concrete core along the major dimensions of the rectangular jacket, as compared to the dilation that occurs along the minor dimension; this is reflected in the transverse strain ratio α_ε of Eq. (6.19).

In order to increase the effectiveness of the confining FRP jacket in a rectangular or square concrete section, the section can be shape-modified to be confined by either elliptical (rectangular sections) or circular (square sections) FRP jackets, as was demonstrated by Yan (2005).

In order to attain similar performance as a circular (CFCC) FRP-confined concrete section from an elliptical (EFCC) section, the EFCC section requires an increase in the FRP jacket thickness t_j. The use of elliptical FRP-confined concrete sections limited to small jacket aspect ratios α_{sh}, in the range of $1.0 \le \alpha_{sh} \le 2.0$, is recommended.

The transverse dilation of the elliptical and rectangular FRP jackets is proportional to the section aspect ratio; this is reflected in the transverse strain ratio α_ε of Eq. (6.19) and the jacket shape-dependent angles θ_a and θ_b summarized in **Table 5.2**. In addition, the confinement effectiveness k_{cc} of the FRP jacket decreases significantly as the aspect

ratio α_{sh} of the rectangular and elliptical FRP jacket increases; this is reflected in the principal stress ratio α_{σ} of Eq. (9.102).

The confined concrete within the elliptical or rectangular jackets having high aspect ratios experiences a small increase in stress, as the state of stress in the confined concrete cores approaches that of concrete in a biaxial compression state of stress. The smaller the aspect ratio α_{sh} of the FRP jacket, the more effective the jacket is in confining the concrete core, since at low aspect ratios, the state of stress of the confined concrete approaches that of concrete in a triaxial compression state of stress due to a more uniform biaxial confinement provided by the FRP jacket. This occurs as the shape of the FRP jacket approaches that of a square jacket in RFCC sections or a circular jacket in EFCC sections.

For FRP-confined concrete sections having identical FRP jacket stiffness K_{je} and concrete material properties, the proposed analytical model predicts that the most effective FRP jacket shape is a circular (CFCC) FRP-jacketed section, since the confined concrete core in a circular section is subjected to uniform biaxial confinement. The second most effective jacket shape is an elliptical (EFCC) jacketed section with low to moderate aspect ratios, i.e., $1.0 < \alpha_{sh} \leq 2.0$, followed by a square (SFCC) jacketed section; the least effective FRP jacket shape is a large aspect ratio rectangular (RFCC) FRP jacket section with small corner radius.

CHAPTER 11

PERFORMANCE-BASED DESIGN OF FRP JACKETS FOR PLASTIC HINGE CONFINEMENT OF CONCRETE COLUMNS

The encasement of concrete in fiber reinforced polymer (FRP) composite jackets can significantly increase the compressive strength and strain ductility of reinforced concrete columns, and the structural system the columns are part of, be it a building or a bridge. Analysis and design of FRP-confined concrete members require an accurate estimate of the performance enhancement due to the confinement provided by FRP composite jackets. An analytical design procedure is presented herein for predicting the behavior of reinforced concrete columns confined with either bonded FRP-confined concrete (BFCC) sections or concrete-filled FRP tubes (CFFT) or unbonded FRP composite jacketed sections.

This chapter describes the use of the damage-based uniaxial stress model for plain FRP-confined concrete introduced in Chapters 1 through 10 that is incorporated into a performance-based design procedure for determining the mechanical properties of the FRP jacket required to achieve a target performance during a seismic event.

Rehabilitation of existing concrete structures using advanced FRP composite materials is gaining attention due to the need for repair of the existing infrastructure. Rehabilitation is undertaken either for strengthening or upgrading the seismic

performance of existing reinforced concrete buildings and bridges to significantly improve their axial and flexural behavior during a seismic event. In particular, buildings and bridges that were designed using outdated and inadequate seismic codes can benefit significantly from seismic retrofit using FRP composites.

The use of advanced FRP composite materials for improving the shear strength and ductility capacity of reinforced concrete members, in particular the use of confinement systems utilizing FRP composite jackets, has become a popular structural retrofit option for the design engineer in regions of high seismicity (Pantelides et al. 1999, 2001). Considerable research has been carried out on the use of FRP composite jackets for seismic retrofit of reinforced concrete columns and bridge systems (Saadatmanesh et al. 1994, Seible et al. 1997, Xiao and Ma 1997, Pantelides et al. 1999, 2001, Ozbakkaloglu and Saatcioglu 2006, 2007), for improving the flexural behavior of structural members (Haragli 2005, Binici and Mosalam 2007, Mosalam et al. 2007), and for improving axial compressive behavior of structural members (Demers and Neale 1999, Mathys et al. 2005, Tastani et al. 2006, Eid et al. 2008, 2009).

The presence of FRP composite jackets within the plastic hinge region of a reinforced concrete beam-column element can induce the development of ductile flexural behavior, while inhibiting premature lap splice, anchorage, or shear failure of a reinforced concrete column; this type of behavior is desirable for concrete sections subjected to cyclic lateral loads such as those that occur in a seismic event.

Seible et al. (1995, 1997) introduced a strain energy-based design procedure for the plastic hinge confinement of reinforced concrete columns that utilizes the Mander et al. (1988) strain energy model for steel-confined concrete. Monti et al. (2001) introduced a

multivariate regression analysis-based upgrading index design procedure that utilizes the Mander et al. (1988) confinement model and the Pantazopoulou (1995) dilation and stress-strain model for the design of FRP jackets for plastic hinge confinement of reinforced concrete columns.

In the analytical design procedure introduced in this dissertation, the performance enhancement in compressive strength and strain ductility of FRP-confined concrete is expressed in terms of the internal damage-based stress-strain model previously introduced in Chapter 10. In addition, the design methodology introduced herein will expand upon the concept of upgrading indexes, introduced by Monti et al. (2001). Unlike the FRP jacket design procedures presented by Seible et al. (1995, 1997) and Monti et al. (2001), no immediate consideration is given to the unknown increase in compressive strength due to the passive confinement provided by the confining elastic FRP jacket. The design approach presented herein is different in that it is based on the strain ductility increase provided by the confining FRP jacket and is thus a strain-based approach using performance-based design principles.

The objective of the design procedure proposed herein is to find a series of relationships for the mechanical properties of FRP jacket (i.e., jacket thickness and FRP material type) required for upgrading the performance of reinforced concrete structures in areas of high seismicity by improving their ductile behavior by means of confinement of the plastic hinge region. In this procedure, no consideration is given to the additional confinement and enhanced strain ductility provided by the available hoop reinforcement. This can be justified because in many areas, corrosion damage of hoop reinforcement can be at such an advanced stage (Pantelides et al. 1999, 2001**),** and depending on the

building period, the spacing and arrangement of the transverse steel are such that their contribution can be ignored (Demers and Neale 1999).

An as-built reinforced concrete column or a new reinforced concrete column with a minimal transverse steel reinforcement of a given length L_c in single **(Figure 11.1)** and double (**Figure 11.2)** curvature bending are considered.

The displacement ductility of the as-built column $(\mu_\Delta)_{ex}$ can be found by performing a moment-curvature analysis of the reinforced concrete cross section. Assuming a bilinear behavior, in which linear elastic behavior occurs up to the stage of first yield and that plastic behavior (rotation) is concentrated at the center of the plastic hinge (Priestley and Park 1987), as shown in **Figures 11.1-11.3**, the displacement ductility, $(\mu_\Delta)_{ex}$, of the as-built column within a rigid system can be approximated by:

$$(\mu_\Delta)_{ex} = \left(\frac{\Delta_u}{\Delta_y}\right)_{ex} = 1 + \frac{\Delta_p}{\Delta_y} = \lambda_{ex} + \frac{1}{C_\Phi}\left[(\mu_\Phi)_{ex} - 1\right]\ 3\lambda_p\left(1 - \frac{\lambda_p}{2 \cdot C_\Phi}\right) \quad (11.1)$$

$$(\mu_\Phi)_{ex} = \left(\frac{\Phi_u}{\Phi_y}\right)_{ex} = 1 + \left(\frac{\Phi_p}{\Phi_y}\right)_{ex} \quad (11.2)$$

$$\lambda_{ex} = \left(\frac{M_u}{M_y}\right)_{ex} \quad (11.3)$$

$$\lambda_p = \left(\frac{L_p}{L_c}\right) \quad (11.4)$$

$$C_\Phi = \frac{L_v}{L_c} \quad (11.5)$$

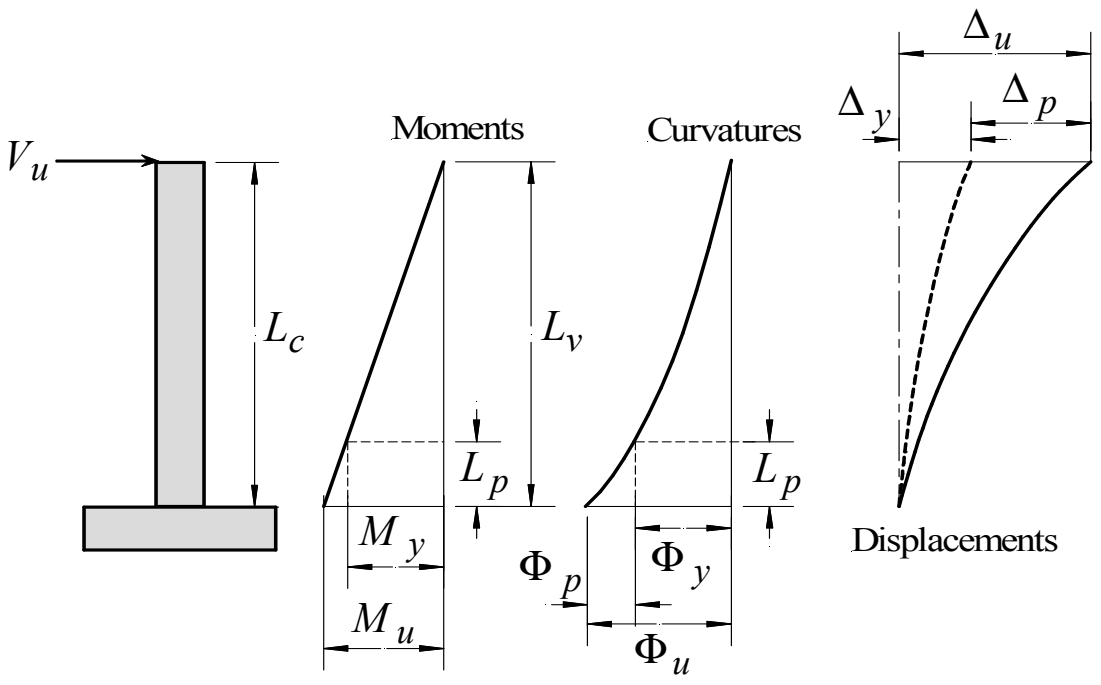

Figure 11.1 Plot of moment, curvature, and displacement diagrams of a cantilevered reinforced concrete element with rigid-base.

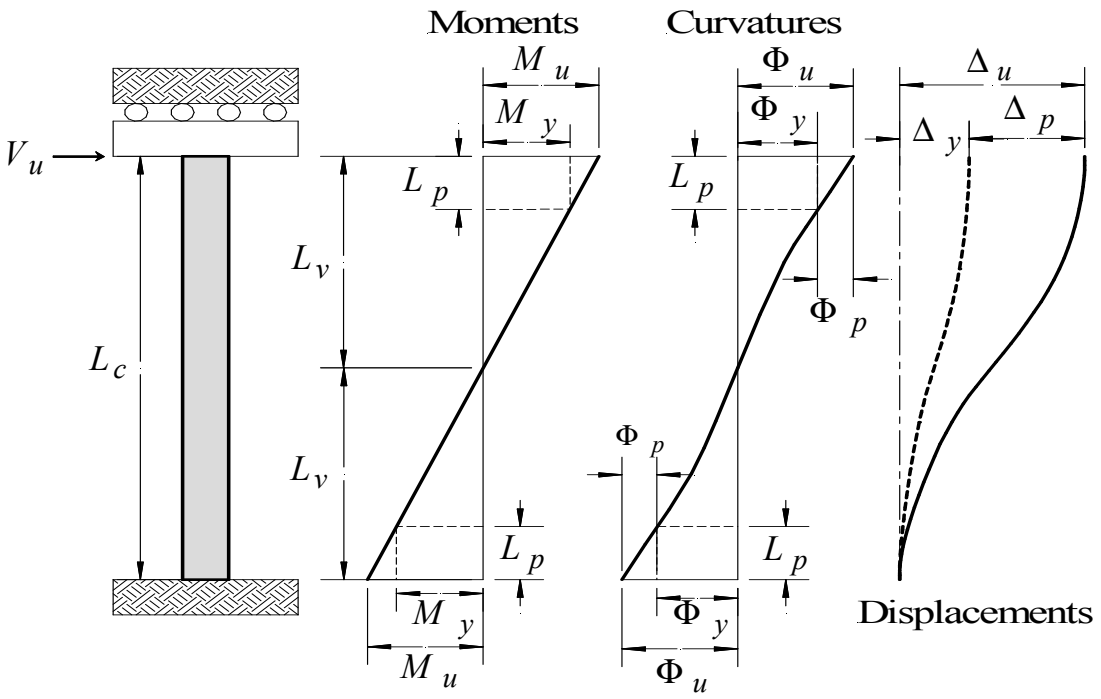

Figure 11.2 Plot of moment, curvature, and displacement diagrams of a reinforced concrete element in double curvature with rigid-base.

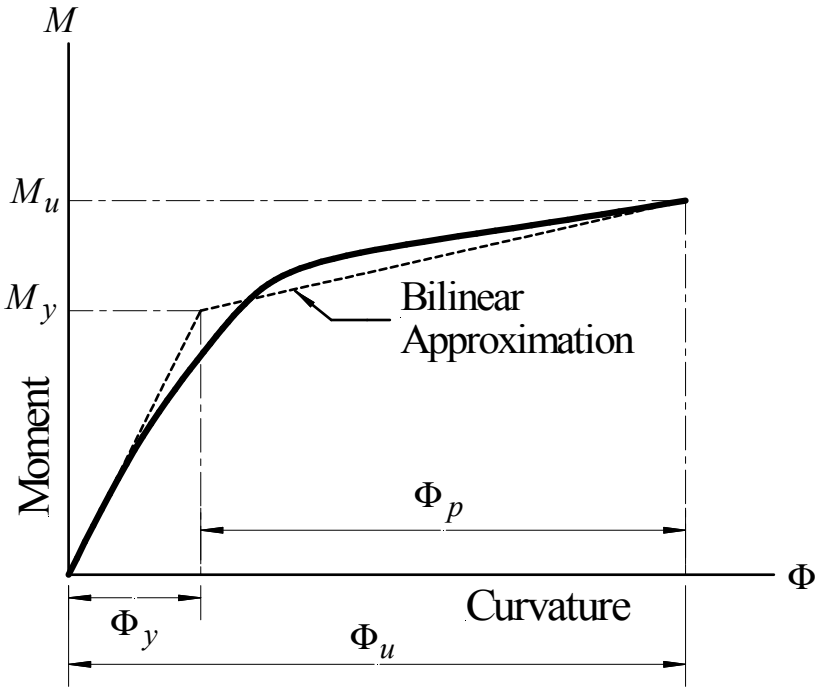

Figure 11.3 Plot of analytical and bilinear moment-curvature curve of a reinforced concrete element

where C_Φ is the column curvature coefficient, L_c is the column clear span, and $L_v = M/V$ is the column shear span; for single curvature bending $C_\Phi = 1.0$, and for double curvature bending $C_\Phi = 0.50$. In addition, $(\mu_\Delta)_{ex}$ is the ultimate displacement ductility factor of the as-built column; $(\Delta_u)_{ex}$ is the analytical maximum displacement of the as-built column corresponding to either crushing of the concrete core or the displacement corresponding to a 20% reduction in lateral load capacity from the maximum value, whichever is less; $(\Delta_y)_{ex}$ is the analytical yield displacement of the as-built column; $(\mu_\Phi)_{ex}$ is the ultimate curvature ductility factor of the as-built column; and λ_{ex} is the moment capacity ratio of the as-built column; $(M_y)_{ex}$ and $(M_u)_{ex}$ are the yield and ultimate moment capacity of the as-built column, respectively. Also, $(\Phi_u)_{ex}$ is the analytical maximum curvature of the as-built column section; $(\Phi_y)_{ex}$ is the analytical yield curvature of the as-built column section; L_p is the analytical length of the plastic hinge; and λ_p is the normalized plastic hinge length given by Panagiotakos and Fardis (2001):

$$\lambda_p = \left(\frac{L_p}{L_c}\right) = 0.12C_\Phi + 0.014\alpha_s\left(\frac{f_{ye}d_{bl}}{L_c}\right) \tag{11.6}$$

where f_{ye} and d_{bl} are the expected yield strength and bar diameter of the longitudinal steel reinforcement, respectively; α_s is the reinforcing slippage coefficient, where $\alpha_s = 1.0$ if slippage in the plastic hinge region is possible, and $\alpha_s = 0$. Otherwise, the use of $\alpha_s = 1.0$ is recommended herein.

A reinforced concrete column of a given length L_c with a flexible-base in single (**Figure 11.4)** and double (**Figure 11.5)** curvature bending are considered. Using the moment-curvature curve of **Figure 11.3** and the load displacement curves of **Figure 11.6**, the displacement ductility of the as-built column $(\mu_{\Delta f})_{ex}$ in a flexible structural system can be found in terms of the rigid-base displacement ductility $(\mu_{\Delta})_{ex}$ of Eq. (11.1)as follows:

$$(\mu_{\Delta f})_{ex} = \left(\frac{\Delta_{uf}}{\Delta_{yf}}\right)_{ex} = 1 + \left(\frac{\Delta_{pf}}{\Delta_{yf}}\right)_{ex} = 1 + C_s[(\mu_{\Delta})_{ex} - 1] \tag{11.7}$$

$$\Delta_{yf} = \Delta_y + \Delta_{es} \tag{11.8}$$

$$\Delta_{pf} = \Delta_p + \Delta_{ps} \tag{11.9}$$

$$\Delta_s = \Delta_{ps} + \Delta_{es} \tag{11.10}$$

$$C_s = \frac{1 + \dfrac{\Delta_{ps}}{\Delta_p}}{1 + \dfrac{\Delta_{es}}{\Delta_y}} = \frac{1 + c_p c_e}{1 + c_e} \tag{11.11}$$

$$c_e = \frac{\Delta_{es}}{\Delta_y} \;\; ; \;\; c_p = \frac{\lambda_{ex} - 1}{(\mu_{\Delta})_{ex} - 1} \tag{11.12}$$

where $(\Delta_{uf})_{ex}$ is the ultimate displacement of the as-built column in a flexible system; Δ_{yf} is the yield displacement of the as-built column in a flexible system that is divided into the column yield displacement Δ_y and the elastic displacement due to system flexibility Δ_{es} of Eq. (11.8).

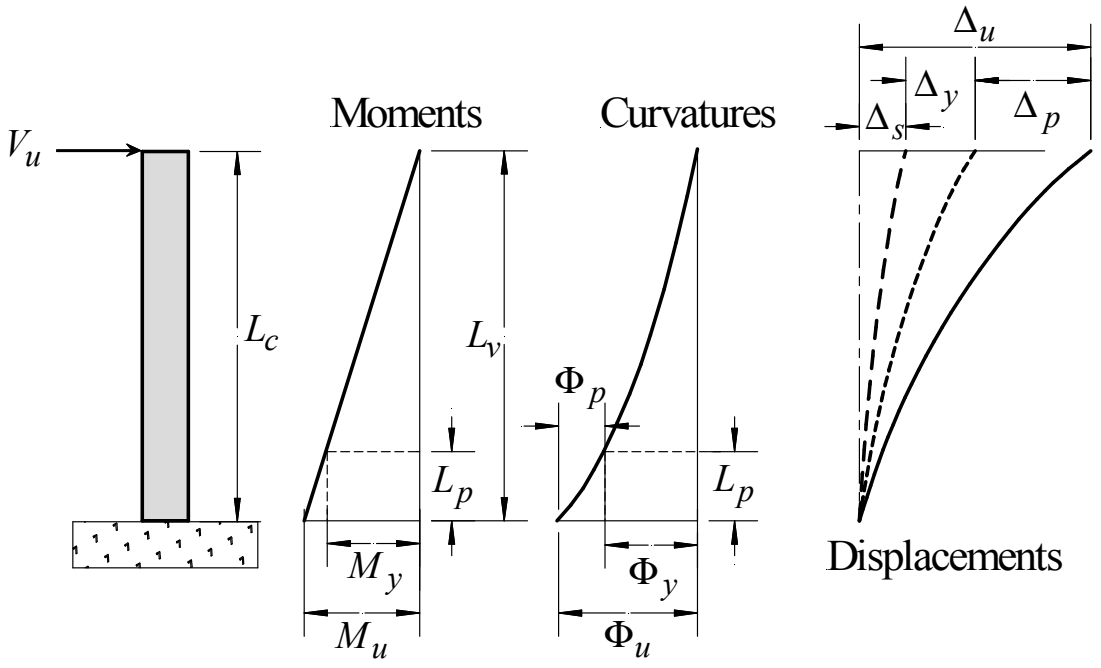

Figure 11.4 Plot of moment, curvature, and displacement diagrams of a cantilevered reinforced concrete element with flexible-base.

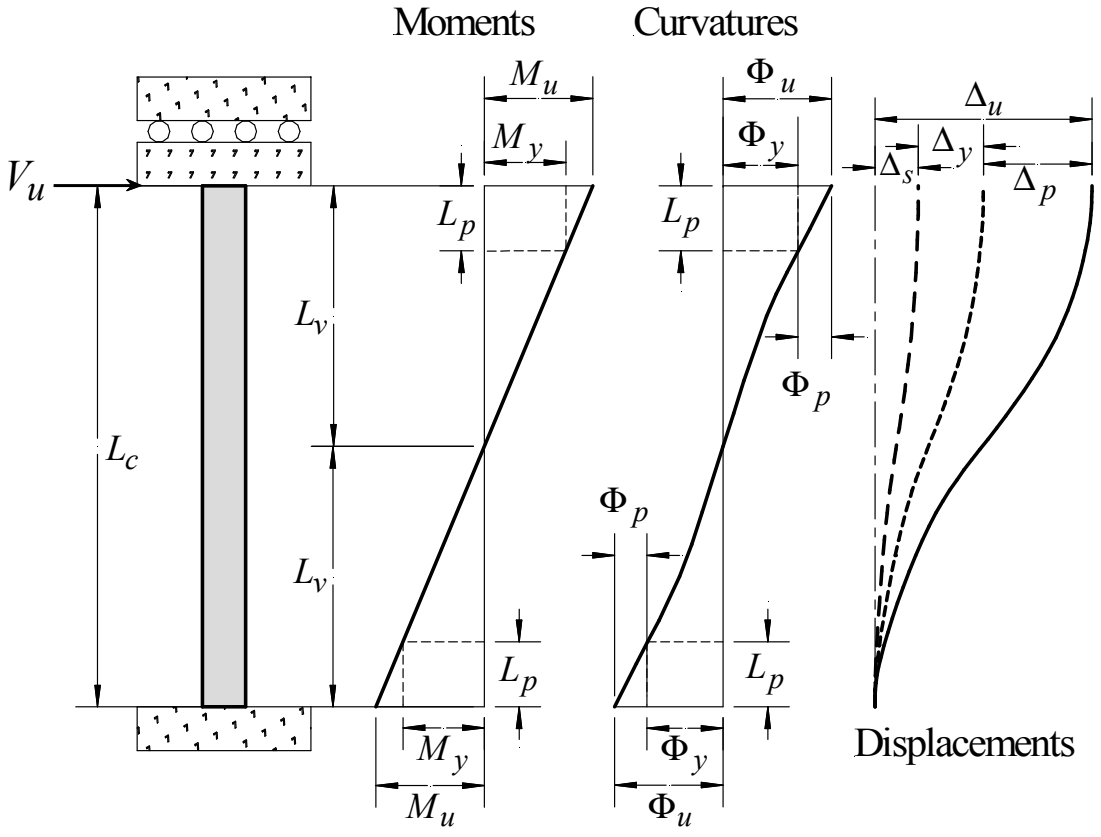

Figure 11.5 Plot of moment, curvature, and displacement diagrams of a reinforced concrete element in double curvature with flexible-base.

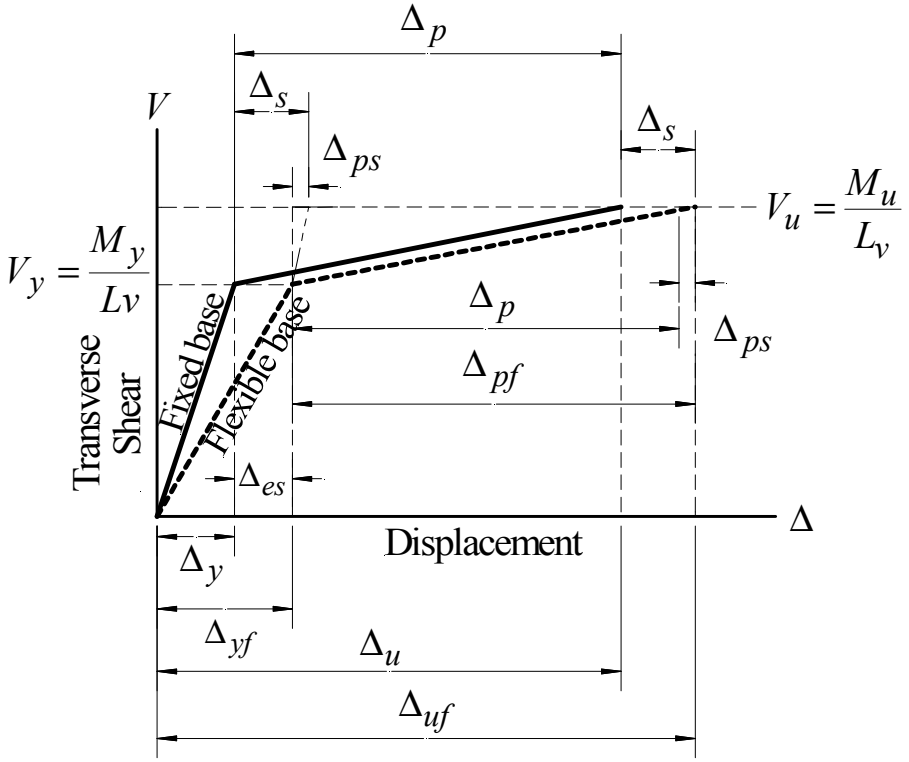

Figure 11.6 Comparison of typical bilinear load displacement curves of a typical reinforced concrete element with rigid and flexible-base.

In addition, Δ_{pf} is the plastic displacement of the column in a flexible system that is divided into the column plastic displacement Δ_p and the plastic displacement due to system flexibility Δ_{ps} of Eq. (11.9). Also, Δ_s is the displacement due to system flexibility that is divided into an elastic Δ_{es} and a plastic Δ_{ps} displacement component, as given in Eq. (11.10). These displacements components are shown graphically in **Figure 11.6.**

The C_s term in Eqs. (11.7) and (11.11) is a system flexibility coefficient that accounts for the elastic flexibility of the existing structure (i.e., soil-structure interaction, beam-column connection, beam flexibility, footing-column connection, etc.), where typically $0.68 \le C_s \le 1.0$. A flexibility coefficient of $C_s = 1.0$ indicates a rigid support (i.e., $\Delta_{es} = \Delta_{ps} = 0$); the lower bound flexibility coefficient $C_s = 0.68$ corresponds to an as-built column with a low ductility capacity for which $(\mu_\Delta)_{ex} = 2.0$, and a low moment capacity ratio for which $\lambda_{ex} = 1.05$, with an elastic deformation of the system Δ_{es} that accounts for one-half of the overall elastic deformation Δ_{yf} (i.e., $c_e = \Delta_{es}/\Delta_{yf} = 0.50$). The term c_p represents the ratio of the percentage increase in flexural capacity versus the plastic displacement ductility $\mu_p = \Delta_p/\Delta_y$ of the as-built column.

In what follows, a rehabilitation design methodology is proposed for a rigid-base system which is modified to include the effects of system flexibility on the displacement demands imposed on the existing reinforced concrete column, during a seismic event.

Upon reviewing the as-built drawings, taking into consideration the period of construction and performing a sectional analysis of the existing reinforced concrete column, the design engineer can recognize that the existing column has inadequate ductile capacity, for which $(\mu_\Delta)_{ex} < 2.0$. It is then established that upgrading of the existing column may be required to achieve a desired level of performance during a seismic event. Thus by selecting a given target ultimate displacement ductility $(\mu_\Delta)_{up}$ of the column to achieve a ductile performance during a seismic event, the design engineer can establish a target displacement upgrading index I_Δ that is defined as:

$$I_\Delta = \frac{(\mu_\Delta)_{up}}{(\mu_\Delta)_{ex}} \tag{11.13}$$

$$(\mu_\Delta)_{up} = \left(\frac{\Delta_u}{\Delta_y}\right)_{up} = \lambda_{up} + \frac{1}{C_\Phi}\left[(\mu_\Phi)_{up} - 1\right]\ 3\lambda_p\left(1 - \frac{0.50\lambda_p}{C_\Phi}\right) \tag{11.14}$$

$$\lambda_{up} = \left(\frac{M_u}{M_y}\right)_{up} \tag{11.15}$$

$$(\mu_\Phi)_{up} = \left(\frac{\Phi_u}{\Phi_y}\right)_{up} \tag{11.16}$$

where $(\Delta_u)_{up}$ target maximum displacement of the FRP-upgraded column corresponding to either crushing of the concrete core at fracture of the FRP jacket, or the displacement corresponding to a 20 % reduction in lateral load capacity from the maximum value, whichever is less; $(\Delta_y)_{up}$ analytical yield displacement of the FRP-upgraded column; and λ_{up} is the moment capacity ratio of the as-built column; $(M_y)_{up}$ and $(M_u)_{up}$ are

the yield and ultimate moment capacity of the FRP-upgraded section, respectively. Also, $(\Phi_u)_{up}$ and $(\Phi_y)_{up}$ of Eq. (11.16) are the analytical ultimate and yield curvature of the rigid-base FRP-upgraded section, respectively.

As was established by Monti et al. (2001) and verified herein, at low curvatures, the presence of the FRP jacket does not significantly affect the analytical yield curvature, yield displacement, or yielding moment capacity of the reinforced concrete column, which indicates that $(\Phi_y)_{up} \cong (\Phi_y)_{ex}$, $(\Delta_y)_{up} \cong (\Delta_y)_{ex}$, and $(M_y)_{up} \cong (M_y)_{ex}$. As a result, the selected target displacement of the FRP-upgraded column $(\Delta_u)_{up}$ of Eq. (11.14) is given by:

$$(\mu_\Delta)_{up} = \left(\frac{\Delta_u}{\Delta_y}\right)_{up} = \Lambda_{up} + \frac{1}{C_\Phi}\left[(\mu_\Phi)_{up} - 1\right] 3\lambda_p \left(1 - \frac{0.50\lambda_p}{C_\Phi}\right) \tag{11.17}$$

$$\Lambda_{up} = \frac{(M_u)_{up}}{(M_u)_{ex}} = \frac{\lambda_{up}}{\lambda_{ex}} \tag{11.18}$$

where Λ_{up} is the ultimate moment capacity ratio of the FRP-upgrade column, this ratio represents the increase in moment capacity of the FRP-upgraded column. Depending on the effective stiffness of the confining FRP jacket K_{je} of Eq. (4.18), Λ_{up} of Eq. (11.18) is in the range of $1.0 \le \Lambda_{up} \le 1.50$, with $\Lambda_{up} = 1.50$ corresponding to a concrete column confined by a high stiffness FRP jacket, and $\Lambda_{up} = 1.0$ when no upgrade is provided.

In order to account for the flexibility of the system, the target displacement upgrading index of the flexible system $I_{\Delta f}$ is given by:

$$I_{\Delta f} = \frac{\left(\mu_{\Delta f}\right)_{up}}{\left(\mu_{\Delta f}\right)_{ex}} \tag{11.19}$$

$$\left(\mu_{\Delta f}\right)_{up} = \left(\frac{\Delta_{uf}}{\Delta_{yf}}\right)_{up} = 1 + C_s\left[\left(\mu_{\Delta}\right)_{up} - 1\right] \tag{11.20}$$

where $\left(\mu_{\Delta f}\right)_{up}$ is the displacement ductility of the upgraded column in a flexible system. Using the target displacement upgrading index of the flexible system $I_{\Delta f}$ of Eq. (11.19), the displacement ductility of the existing flexible system $\left(\mu_{\Delta f}\right)_{ex}$ of Eq. (11.6) and the displacement ductility of the upgraded column $\left(\mu_{\Delta f}\right)_{up}$ of Eq. (11.20) and solving for the target displacement ductility of the upgraded column $\left(\mu_{\Delta}\right)_{up}$ of Eq. (11.14) yield:

$$\left(\mu_{\Delta}\right)_{up} = \left(\frac{\Delta_{uf}}{\Delta_{yf}}\right)_{up} = 1 + I_{\Delta f}\left[\left(\mu_{\Delta}\right)_{ex} - 1\right] + \left(\frac{I_{\Delta f} - 1}{C_s}\right) \tag{11.21}$$

Substituting the displacement ductility of the existing rigid-base column $\left(\mu_{\Delta}\right)_{ex}$ of Eq. (11.1) into the displacement ductility of the existing flexible system $\left(\mu_{\Delta f}\right)_{ex}$ of Eq. (11.6) and solving for the curvature ductility of the existing column $\left(\mu_{\Phi}\right)_{ex}$ yield:

$$\left(\mu_{\Phi}\right)_{ex} = \left(\frac{\Phi_u}{\Phi_y}\right)_{ex} = 1 + \left(\frac{C_{\Phi}}{3}\right)\left[\frac{C_s\left(1 - \lambda_{ex}\right) + \left[\left(\mu_{\Delta}\right)_{ex} - 1\right]}{\lambda_p\left(1 - \frac{0.50\lambda_p}{C_{\Phi}}\right)}\right] \tag{11.22}$$

Solving for the target curvature ductility of the upgraded column $(\mu_\Phi)_{up}$ in Eq. (11.17) yields:

$$(\mu_\Phi)_{up} = \left(\frac{\Phi_u}{\Phi_y}\right)_{up} = 1 + \left(\frac{C_\Phi}{3}\right)\left[\frac{\left[(\mu_\Delta)_{up} - \Lambda_{up}\right]}{\lambda_p\left(1 - \frac{0.50\lambda_p}{C_\Phi}\right)}\right] \tag{11.23}$$

where in the above relationship the displacement ductility of the upgraded column $(\mu_\Delta)_{up}$ of Eq. (11.21) is substituted into (11.23). This indicate that the target curvature ductility of the FRP-upgraded column $(\mu_\Phi)_{up}$ can be obtained in terms of the selected displacement upgrading index of the flexible system $I_{\Delta f}$ of Eq. (11.19) and the displacement ductility of the as-built column $(\mu_\Delta)_{ex}$ of Eq. (11.1), which is determined from a nonlinear section analysis of the existing column.

Once the target displacement upgrade index of the flexible system $I_{\Delta f}$ of Eq. (11.19) is selected to achieve a given target displacement ductility $(\mu_\Delta)_{up}$ of the column, a curvature upgrading index I_Φ, of the reinforced concrete column can be determined using Eqs. (11.22) and (11.23)as follows:

$$I_\Phi = \frac{(\mu_\Phi)_{up}}{(\mu_\Phi)_{ex}} = \frac{(\Phi_u/\Phi_y)_{up}}{(\Phi_u/\Phi_y)_{ex}} = \frac{\text{Eq. (11.23)}}{\text{Eq. (11.22)}} \tag{11.24}$$

The previous target curvature upgrading index I_Φ is determined based on the target displacement upgrading index $I_{\Delta f}$ of Eq. (11.19). Using the assumptions of plane sections remaining plane and considering that at yielding $(\Phi_y)_{up} \cong (\Phi_y)_{ex}$, the curvature upgrading index I_Φ of Eq. (11.24) can be further simplified as:

$$I_\Phi = \frac{(\mu_\Phi)_{up}}{(\mu_\Phi)_{ex}} = \frac{(\Phi_u)_{up}}{(\Phi_u)_{ex}} = \frac{(\varepsilon_{cu}/c_u)_{up}}{(\varepsilon_{cu}/c_u)_{ex}} \tag{11.25}$$

where $(\varepsilon_{cu})_{ex}$ and $(c_u)_{ex}$ are the ultimate compressive strain and neutral axis depth of the as-built column, respectively, which are known quantities determined by the design engineer during a sectional analysis of the as-built section. Also, $(\varepsilon_{cu})_{up}$ and $(c_u)_{up}$ are the target ultimate compressive strain and neutral axis depth of the FRP-upgraded column, respectively, which are unknown properties of the FRP-upgraded column. Solving for the unknown ultimate curvature $(\Phi_u)_{up}$ of the FRP-upgraded section in Eq. (11.25) yields:

$$(\Phi_u)_{up} = I_\Phi (\Phi_u)_{ex} \tag{11.26}$$

$$\left(\frac{\varepsilon_{cu}}{c_u}\right)_{up} = I_\Phi \left(\frac{\varepsilon_{cu}}{c_u}\right)_{ex} \tag{11.27}$$

On the left-hand side of Eqs. (11.26) and (11.27) are the unknown target ultimate compressive strain $(\varepsilon_{cu})_{up}$ and neutral axis depth $(c_u)_{up}$ of the FRP-upgraded column. On the right-hand side of these equations, the known parameters $(\varepsilon_{cu})_{ex}$ and $(c_u)_{ex}$ are

determined from a section analysis of the existing as-built reinforced concrete column. The unknown target ultimate compressive strain $(\varepsilon_{cu})_{up}$ and neutral axis depth $(c_u)_{up}$ of the FRP-upgraded column can be found by rearranging equation Eqs. (11.26) and (11.27), which yields the following strain ductility upgrading index I_ε:

$$I_\varepsilon = \frac{(\varepsilon_{cu})_{up}}{(\varepsilon_{cu})_{ex}} = I_c I_\Phi \tag{11.28}$$

$$I_c = \frac{(c_u)_{up}}{(c_u)_{ex}} \tag{11.29}$$

where I_c is the neutral axis upgrading index, an unknown geometric parameter of the upgraded FRP-confined concrete section.

In this investigation, a parametric study was performed using a moment-curvature-based analytical model of the as-built and FRP-upgraded circular concrete sections in order to obtain a numerical relationship for the unknown neutral axis upgrading index I_c of (11.29), in terms of the target curvature upgrading index I_Φ of Eqs. (11.24) and (11.25), where:

$$I_c = \mathbf{F}(I_\Phi) \tag{11.30}$$

where F denotes a functional relationship between unknown neutral axis upgrading index I_c and the target curvature upgrading index I_Φ. It should be noted that when no upgrade is provided, all upgrading indexes have a unity value, i.e., $I_\varepsilon = I_c = I_\Phi = I_\Delta = 1.0$. In this parametric study, the performance enhancement due to confinement provided by

bonded carbon (CFRP) and glass (GFRP) FRP jackets in the potential plastic hinge region is assessed. A list of the parameters considered in the parametric study are given in **Table 11.1**.

In **Figure 11.7** a series of typical normalized flexural capacity, $\bar{M} = M/M_y$ versus curvature ductility $\mu_\Phi = \Phi/\Phi_y$ curves corresponding to the curvature range of $0 \le \Phi \le \Phi_u$ of an as-built (unconfined) and FRP-upgraded circular column sections are shown. In this figure, it can be observed that as the normalized stiffness of the FRP jacket K_{je} increases, the normalized ultimate moment capacity of the FRP-upgraded section slightly increases and the curvature ductility of the columns is significantly increased by the presence of the confining FRP jacket. The range of FRP jacket stiffness K_{je} is $10.0 \le K_{je} < 25.0$ for low stiffness and $25.0 < K_{je} < 60.0$ for high stiffness FRP jackets.

In **Figure 11.8** a series of typical normalized neutral axis height $\bar{c} = c/D_c$ versus curvature ductility $\mu_\Phi = \Phi/\Phi_y$ curves corresponding to the curvature range of $\Phi_y \le \Phi \le \Phi_u$ of an as-built and an FRP-upgraded circular column section are shown. In this figure, it can be observed that as the stiffness of the FRP jacket K_{je} increases, the normalized neutral axis height at failure $\bar{c_u} = c_u/D_c$ decreases nonlinearly.

In **Figure 11.9** the neutral axis upgrading index I_c of Eq. (11.29) of the concrete columns considered in this parametric study are plotted versus the curvature upgrading index I_Φ evaluated using Eq. (11.25).

Table 11.1 Parameters considered in the assessment of the performance enhancement due to confinement provided by FRP jackets in the potential plastic hinge region.

Parameters	Range
Column	
Column Diameter (D_c) (mm)	460, 610, 915
Unconfined concrete strength (f_{co}) (MPa)	28, 34, 41
Longitudinal steel strength (f_{yl}) (MPa)	275, 410
Axial load ratio (n)	0.10, 0.20, 0.30
Longitudinal steel reinforcement ratio (ρ_{sl})	0.01, 0.02, 0.03
Cover (mm)	38
FRP Jacket	
Normalized FRP jacket stiffness (K_{je})	15, 30, 60, 100
Glass FRP hoop modulus (E_j) (GPa)	25, 35
Carbon FRP hoop modulus (E_j) (GPa)	80, 125
Ultimate transverse jacket strain (ε_{ju}) (mm/m)	8.5, 12.5, 15.0

where:

$n = P/(A_c f_{co})$; $\rho_{sl} = A_{sl}/A_c$

$P =$ Axial compressive load in the column

$A_c = \pi(D_c)^2/4 =$ Gross column area

$A_{sl} =$ Longitudinal steel area

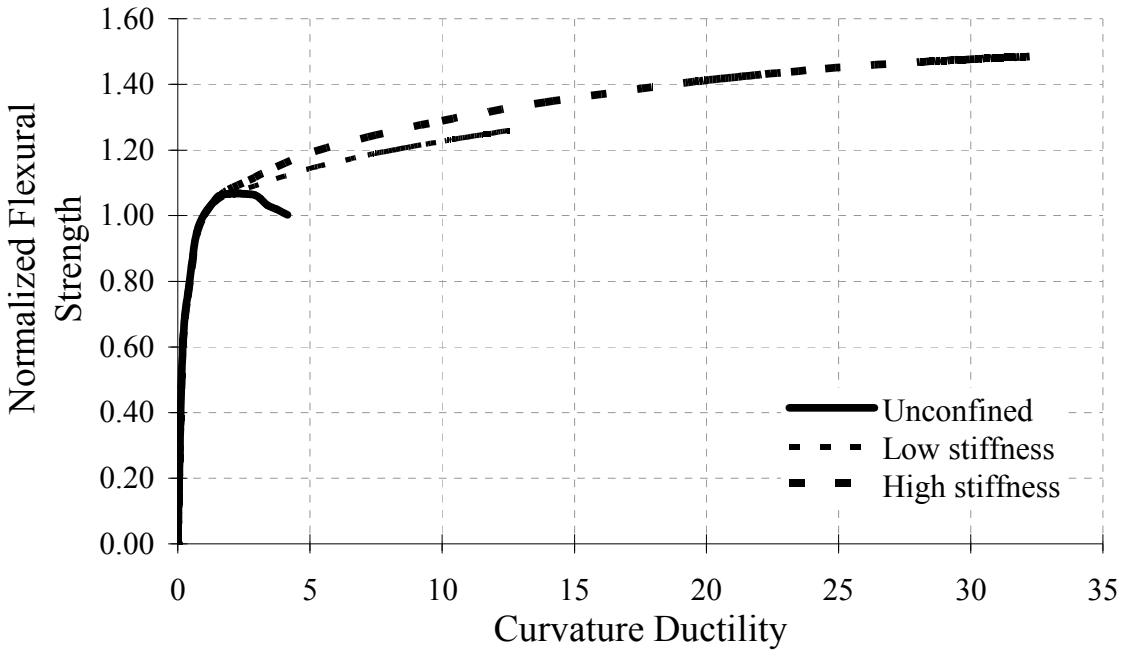

Figure 11.7 Normalized flexural strength versus curvature ductility of unconfined and FRP-confined reinforced concrete section.

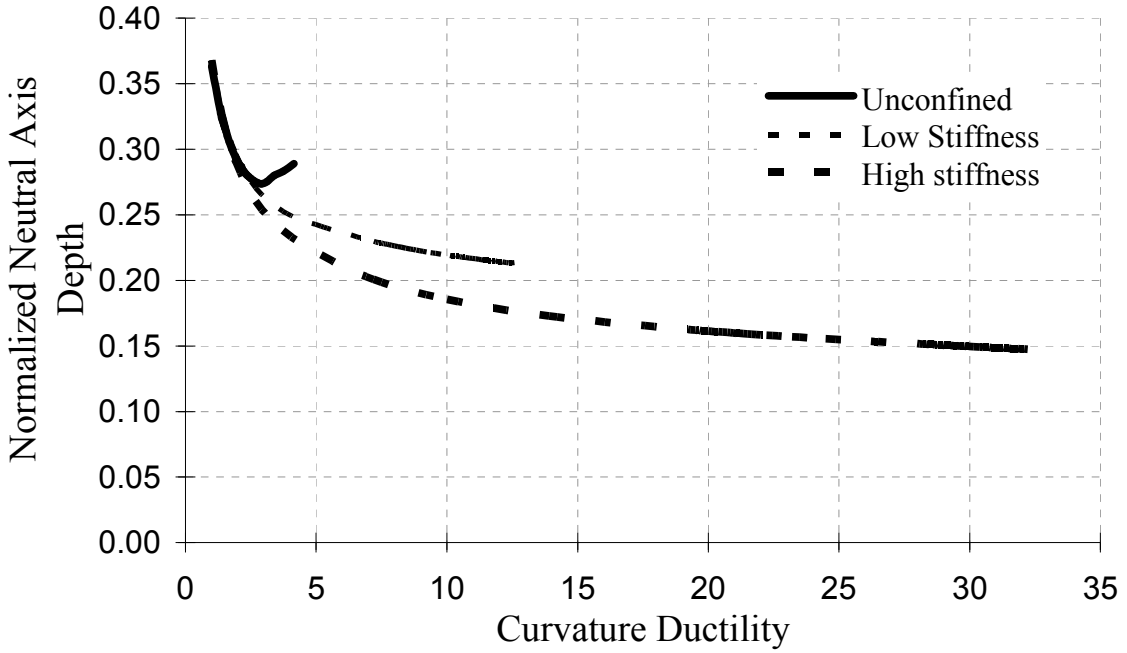

Figure 11.8 Normalized neutral axis depth versus curvature ductility of unconfined and FRP-confined reinforced concrete section.

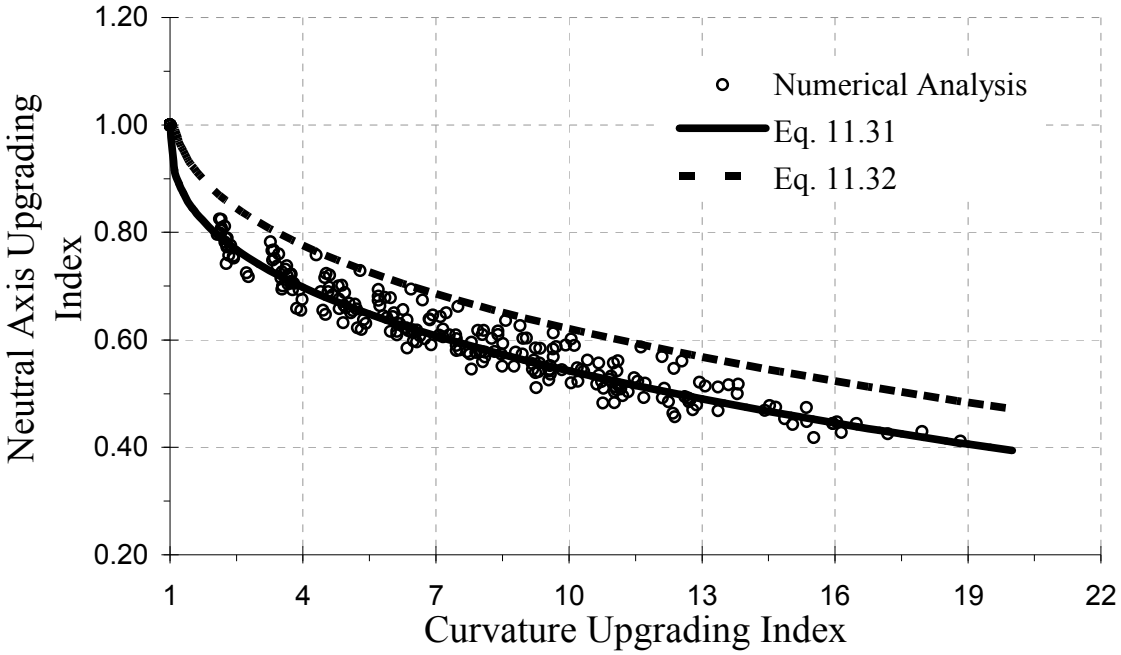

Figure 11.9 Numerical and empirical neutral axis upgrading index versus curvature upgrading index.

From this figure it can be observed that as curvature upgrading index I_Φ increases, the neutral axis upgrading index I_c tends to decrease nonlinearly. As shown in **Figure 11.10**, the maximum value of the neutral axis upgrading index I_c of $I_c = 1.0$ occurs when $I_\Phi = 1.0$, i.e., when no upgrade is provided. The solid line plotted in this figure is the best fit curve determined from regression analysis, in which the unknown neutral axis upgrading index I_c is defined in terms of the target curvature upgrading index I_Φ as:

$$I_c = 1 - 0.20\left(I_\Phi - 1\right)^{0.38} \tag{11.31}$$

The above empirical relationship was found to have a coefficient of correlation of $R^2 \cong 97.0$ % and a standard deviation of $\sigma = 2.60x10^{-2}$.

In **Figure 11.10**, the numerically obtained strain ductility upgrading index evaluated using I_ε of Eq. (11.28) is plotted versus the curvature upgrading index I_Φ evaluated using Eq. (11.25). In this figure, the strain ductility upgrading index I_ε obtained by substituting the neutral axis upgrading index I_c of Eq. (11.31) from regression into Eq. (11.28) is also plotted as a solid curve. From this figure, it can be observed that with the use of Eqs. (11.28) and (11.31) the relationship between the strain ductility upgrading index I_ε and the target curvature upgrading index I_Φ can be accurately predicted.

In the parametric study performed herein, the assumptions of (a) plane sections remaining plane, (b) perfect bond between the reinforcing steel and concrete, and (c) no buckling of longitudinal steel reinforcing were made.

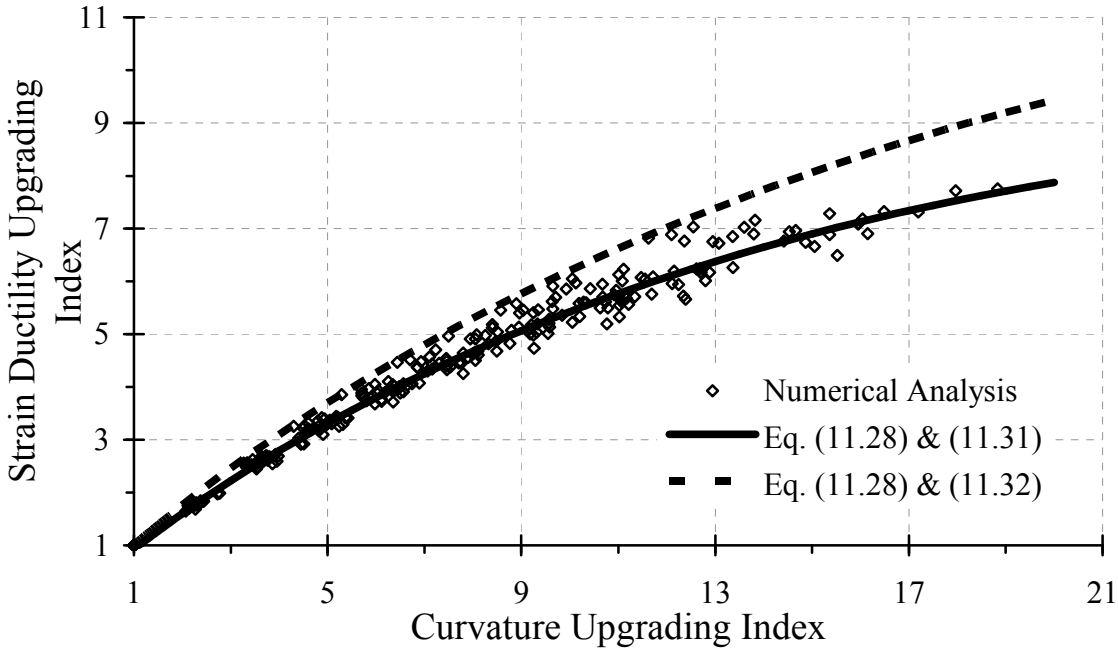

Figure 11.10 Numerical and empirical strain ductility upgrading index versus curvature upgrading index.

In a typical column subjected to transverse shear, the assumption of plane sections remaining plane may not apply due to the presence of inclined shear cracks, which can induce an increase in steel stresses and strains beyond those predicted by the plane sections hypothesis. Also, at high levels of axial compressive strains, buckling of longitudinal steel reinforcement in the potential plastic hinge region may occur if the FRP jacket does not provide adequate lateral restraint to prevent buckling of the steel reinforcement. In addition, at high levels of axial tensile strains, bond degradation of the lap-spliced longitudinal reinforcement in the potential plastic hinge region may occur if the FRP jacket cannot adequately curtail the transverse dilation of the confined concrete core and cover.

The presence of transverse shear and a strain gradient may significantly affect the dilation behavior of the concrete core when compared to that of a circular concrete column subjected to monotonically increasing concentric axial load or deformation. In the development of Eq. (11.31) the effects of strain gradient, transverse shear, and bond degradation of the lap splice, among others, were ignored in the analysis. As a result, for design purposes, it is recommended that a conservative value of the target ultimate compressive strain, $(\varepsilon_{cu})_{up}$, be obtained by conservatively estimating the target neutral axis upgrading index I_c of Eq. (11.31) as follows:

$$I_c = 1.08 - 0.20(I_\Phi - 1)^{0.38} \leq 1.0 \tag{11.32}$$

The above relationship represents a mean plus three standard deviation prediction of the neutral axis upgrading index I_c, when $I_\Phi \geq 1.04$ and $I_c = 1.0$ otherwise. The results of the above relationship are plotted as heavy dashed curves in **Figures 11.9** and

11.10. As shown in these figures, by substituting the neutral axis upgrading index I_c of Eq. (11.32) into the strain ductility upgrading index I_ε of Eq. (11.28) a conservative estimate of the target ultimate compressive strain $(\varepsilon_{cu})_{up}$ is obtained, as will be shown in the design examples.

Substituting the neutral axis upgrading index I_c of Eq. (11.29) into the strain ductility upgrading index I_ε of Eq. (11.28) and solving for the target ultimate compressive strain $(\varepsilon_{cu})_{up}$, in the FRP-confined concrete yield:

$$(\varepsilon_{cu})_{up} = I_c I_\Phi (\varepsilon_{cu})_{ex} \tag{11.33}$$

The target ultimate compressive strain $(\varepsilon_{cu})_{up}$ can also be obtained in terms of the design ultimate jacket diagonal strain $(\varepsilon_{ju})_{up}$ in the FRP-confined concrete section by using the definition of the jacket Poisson's ratio ν_j of Eq. (7.32). Setting $\varepsilon_j = (\varepsilon_{ju})_{up}$, $\varepsilon_c = (\varepsilon_{cu})_{up}$, and $\nu_j = \nu_{ju}$ in Eq. (7.32) and solving for the target ultimate compressive strain $(\varepsilon_{cu})_{up}$ yield:

$$(\varepsilon_{cu})_{up} = -\frac{(\varepsilon_{ju})_{up}}{\nu_{ju}} \tag{11.34}$$

where ν_{ju} is the unknown target ultimate diagonal dilation Poisson's ratio. In Chapter 8 it was established that at high axial plastic compressive strains ε_{cp}, where

$\varepsilon_{co} << \varepsilon_{cp} \le \varepsilon_{cu}$, the Poisson's ratio ν_j of the FRP-jacketed section approaches the plastic jacket dilation rate μ_{jp} of Eq. (7.23). This indicates that at high axial compressive strains $\nu_{ju} \cong \mu_{jp}$. In addition, the diagonal plastic dilation rate μ_{jp} of Eq. (7.23) was determined to be a function of the normalized effective stiffness of the FRP jacket K_{je} of Eq. (4.18) and the geometry of the FRP-confined concrete section, as discussed in Chapter 4.

The diagonal plastic dilation rate μ_{jp} of Eq. (7.23) can range between $\nu_{ci} \le \mu_{jp} \le \sqrt{2}$, with the upper value corresponding to essentially unconfined concrete, i.e., as $K_{je} \to 0$, and the lower value corresponds to a linear elastic behavior which can occur as $K_{je} \to \infty$. Thus setting $\nu_{ju} = \mu_{jp}$ in Eq. (11.34), substituting the target ultimate compressive strain $(\varepsilon_{cu})_{up}$ of Eq. (11.33), and solving for the diagonal plastic dilation rate μ_{jp} yield:

$$(\mu_{jp})_{up} = -\frac{(\varepsilon_{ju})_{up}}{(\varepsilon_{cu})_{up}} = -\frac{(\varepsilon_{ju})_{up}}{I_c I_\Phi (\varepsilon_{cu})_{ex}} \tag{11.35}$$

When compared to the ultimate tensile strain ε_{fu} of standard tensile coupon tests, the actual rupture strain of the confining FRP jacket ε_{Hu} can occur at much lower strains (Eid et al. 2008) due to stress-concentrations at the jacket to concrete interface due to axial strain-induced damage (internal cracking, aggregate sliding or crushing, void compaction, or nucleation) of the confined concrete and at the rounded corners of rectangular FRP-jacketed sections. ε_{Hu} is defined as the ultimate strain in the confined

concrete section along the major dimension of the FRP jacket. The jacket failure strain ratio κ_ε is defined as:

$$\kappa_\varepsilon = \frac{\varepsilon_{Hu}}{\varepsilon_{fu}} \tag{11.36}$$

where the above jacket failure strain ratio κ_ε ranges between $0.35 \le \kappa_\varepsilon \le 0.95$ with an average value of $\kappa_\varepsilon \approx 0.70$ (Demers and Neale 1999, Mathys et al. 2005, Tastani et al. 2006, Ozbakkaloglu and Saatcioglu 2007, Eid et al. 2009). The above jacket failure strain ratio κ_ε is approximated as:

$$\kappa_\varepsilon = \frac{\varepsilon_{Hu}}{\varepsilon_{fu}} \cong \frac{\sqrt{2}}{2} = 0.707 \tag{11.37}$$

The above relationship estimates that failure of a FRP jacket occurs when $\varepsilon_{Hu} = 0.707\varepsilon_{fu}$. The diagonal strain in the FRP jacket ε_{ju}, corresponding to the ultimate jacket strain ε_{Hu}, is given by:

$$\varepsilon_{ju} = \left(\frac{\beta_j}{\alpha_\varepsilon}\right)\varepsilon_{Hu} \tag{11.38}$$

where β_j is the transverse strain coefficient defined in Eq. (6.54) and summarized in **Table 6.1**, and α_ε is the transverse strain ratio defined in Eq. (6.52). As shown in **Chapter 6**, both β_j and α_ε depend only on the geometry of the FRP-confined section.

Using Eqs. (11.37) and (11.38) and setting $\left(\varepsilon_{ju}\right)_{up} = \varepsilon_{ju}$, the diagonal failure strain $\left(\varepsilon_{ju}\right)_{up}$ of the confining FRP jacket can be can be given in terms of the ultimate coupon tensile strain ε_{fu} as follows:

$$\left(\varepsilon_{ju}\right)_{up} = \frac{\sqrt{2}}{2}\left(\frac{\beta_j}{\alpha_\varepsilon}\right)\varepsilon_{fu} \tag{11.39}$$

Using the diagonal plastic dilation rates μ_{jp} of Eq. (7.23) and $\left(\mu_{jp}\right)_{up}$ of Eq. (11.35), using $\left(\varepsilon_{ju}\right)_{up}$ of Eq. (11.38) and setting $\mu_{jp} = \left(\mu_{jp}\right)_{up}$ and $K_{je} = \left(K_{je}\right)_{up}$ and solving for the effective stiffness of the upgrading FRP jacket $\left(K_{je}\right)_{up}$ yield:

$$\left(K_{je}\right)_{up} = \frac{\left(C_{je}\right)_{up}}{f_{co}} = 35\left[\sqrt{\frac{\sqrt{2}-\nu_{ci}}{\left(\mu_{jp}\right)_{up}-\nu_{ci}}}-1\right] \tag{11.40}$$

$$\left(C_{je}\right)_{up} = \left(\frac{t_j}{H_c}\right)k_e C_{sh} E_j \tag{11.41}$$

where $\left(C_{je}\right)_{up}$ is the effective confining stiffness of the upgrading FRP jacket; f_{co} is the unconfined peak compressive strength of the concrete core;, ν_{ci} is the initial Poisson's ratio of the concrete core where typically $0.15 \le \nu_{ci} < 0.25$ and a value of $\nu_{ci} = 0.20$ is recommended herein; t_j is the FRP jacket thickness; E_j is the transverse modulus of the confining FRP jacket; k_e is the confining efficiency of the FRP jacket, defined in Eq. (4.8) and summarized in **Table 4.1**; C_{sh} is the jacket reinforcement ratio coefficient

defined in Eq. (4.12) and summarized in **Table 4.2**. In order to properly mitigate the transverse dilation of the confined concrete core to provide adequate restraint against unrestrained dilation of the confined concrete core and to provide adequate restraint against premature buckling of the vertical steel reinforcement in the reinforced concrete column, a minimum FRP jacket stiffness of $K_{je} = 15.0$ is recommended herein.

Substituting $\left(C_{je}\right)_{up}$ of Eq. (11.41) into Eq. (11.40) and solving for the minimum required thickness of the upgrading FRP jacket $\left(t_j\right)_{up}$ yield:

$$\left(t_j\right)_{up} \cong \left(K_{je}\right)_{up}\left(\frac{H_c f_{co}}{k_e C_{sh} E_j}\right) \tag{11.42}$$

where the normalized effective stiffness of the upgrading FRP jacket $\left(K_{je}\right)_{up}$ is determined using Eq. (11.40). The previous relationship indicates that in order to obtain a certain level of performance in the reinforced concrete beam-column element, as measured by the target displacement upgrading index of the flexible system $I_{\Delta f}$ of Eq. (11.19) and the target curvature upgrading index I_{Φ} of Eqs. (11.24) and (11.25), the required thickness $\left(t_j\right)_{up}$ of the FRP jacket depends on the shape and the geometry of the FRP-confined section as measured by the confining efficiency k_e of Eq. (4.8), the FRP jacket shape-dependent reinforcement ratio coefficient C_{sh} of Eq. (4.12), and the major dimension H_c of the FRP-confined section.

The target FRP jacket thickness $\left(t_j\right)_{up}$ also depends on the mechanical properties of the concrete core as measured by its unconfined compressive strength f_{co} and the

mechanical properties of the FRP jacket as measured by its average transverse modulus E_j and diagonal failure strain $\left(\varepsilon_{ju}\right)_{up}$.

As shown in Eqs. (11.35)-(11.42), the information required to determine the FRP jacket design thickness is (1) the geometry of the concrete section or new FRP jacket, (2) the unconfined concrete core strength f_{co}, (3) the material properties of the selected FRP jacket; and (4) the ultimate design FRP jacket strain $\left(\varepsilon_{ju}\right)_{up}$, determined based on the type of FRP jacket material (CFRP or GFRP) selected by the design engineer.

Damage-Based Design Procedure

If the evaluation of the as-built reinforced concrete column indicates that the calculated ductility demand on the column exceeds its ductile capacity, retrofit of the as-built column may be required to achieve a ductile performance during a seismic event. The design of the FRP jacket for plastic hinge confinement can be achieved as follows:

1. Determine the geometrical and mechanical properties of the as-built column. Perform a section analysis to determine the moment-curvature behavior of the as-built column section; find the yield curvature Φ_y and the moment capacity ratio λ_{ex} of Eq. (11.3).
2. Determine or estimate the plastic hinge length using λ_p of Eq. (11.4), the column curvature coefficient C_Φ of Eq. (11.5), and the system flexibility C_s coefficient of Eq. (11.11).
3. Perform a pushover analysis to determine $\left(\mu_\Delta\right)_{ex} = \left(\Delta_u / \Delta_y\right)_{ex}$ of Eq. (11.1) using $\left(\mu_{\Delta f}\right)_{ex} = \left(\Delta_{uf} / \Delta_{yf}\right)_{ex}$ of Eq. (11.7). Estimate $\left(\mu_\Phi\right)_{ex}$ of Eq. (11.22) and calculate

$(\Phi_u)_{ex} = (\mu_\Phi \Phi_y)_{ex}$. Determine $(c_u)_{ex}$ corresponding to $(\Phi_u)_{ex}$ and find the analytical ultimate compressive strain $(\varepsilon_{cu})_{ex} = (c_u \Phi_u)_{ex}$ of the as-built column.

4. Select the target displacement upgrading index $I_{\Delta f}$ of Eq. (11.19), estimate the increase in moment capacity of the FRP-upgraded column using Λ_{up} of Eq. (11.18), and determine the target curvature ductility $(\mu_\Phi)_{up}$ of Eq. (11.23).

5. Estimate the target curvature upgrading index I_Φ of Eq. (11.24). Estimate the neutral axis upgrading index I_c of Eq. (11.32) and the target ultimate compressive strain $(\varepsilon_{cu})_{up}$ using Eq. (11.33).

6. Determine the geometric properties of the FRP jacket including the FRP jacket aspect ratio α_{sh} of Eq. (4.2); the jacket corner aspect ratio α_j of Eq. (4.4) (rectangular and square jackets only); the confining efficiency k_e of the FRP jacket as summarized in **Table 4.1**; the jacket reinforcement ratio coefficient C_{sh} of the FRP jacket as summarized in **Table 4.2**; the transverse strain coefficient β_j summarized in **Table 6.1;** and the transverse strain ratio α_ε of Eq. (6.52).

7. Select the lower bound material properties of confining FRP jacket including the design jacket hoop modulus E_j and design tensile coupon failure strain ε_{fu}. Estimate the jacket diagonal failure strain $(\varepsilon_{ju})_{up}$ of Eq. (11.38) and the target diagonal plastic dilation rate $(\mu_{jp})_{up}$ using Eq. (11.35).

8. Estimate the effective stiffness of the upgrading FRP jacket $(K_{je})_{up}$ of Eq. (11.40).

9. Determine the minimum required thickness of the FRP jacket, $(t_j)_{up}$ using Eq. (11.42).

Design Examples

Circular FRP-Upgraded Concrete Column

The as-built and FRP-upgraded reinforced circular cantilevered concrete columns tested by Seible et al. (1997), with the experimental and analytical properties summarized in **Table 11.2** are considered in this design example.

Section analysis of the as-built column indicates that the yield curvature is $\Phi_y = 7.08x10^{-6} rad/mm$ and $\lambda_{ex} \approx 1.0$. The normalized plastic hinge length of Eq. (11.4) is estimated as $\lambda_p = 0.12 + (0.014)(303)(19)/3658 = 0.142$ or a plastic hinge length of $L_p = 520$ mm.

For this cantilevered column the curvature coefficient is $C_\phi = 1.0$ and the system flexibility coefficient is approximated as $C_s = 0.90$. The pushover analysis and experimental test results indicate that as-built column experiences a displacement ductility of approximately $(\mu_{\Delta f})_{ex} = (\Delta_{uf}/\Delta_{yf})_{ex} \approx 2.2$.

The ultimate curvature ductility of the as-built column $(\mu_\Phi)_{ex}$ of Eq. (11.22) is estimated as:

$$(\mu_\Phi)_{ex} = \left(\frac{\Phi_u}{\Phi_y}\right)_{ex} = 1 + \left(\frac{1}{3 \cdot 0.9}\right)\left[\frac{0.9(1-1)+(2.2-1)}{0.142(1-0.50 \cdot 0.142)}\right] = 1 + \frac{1.20}{0.356} = 4.37 \quad (11.43)$$

Table 11.2 Column specifications and details of cantilevered reinforced concrete columns confined by FRP jackets in the potential plastic hinge region performed by Seible et al. (1997).

	Properties	Circular Section	Rectangular Section
Section	Column Height (L_c)	3.658 m	3.658 m
	Column Shear Span (L_v)	3.658 m	3.658 m
	Column Depth (H_c)	610 mm	730 mm
	Column width (B_c)	610 mm	489 mm
	Concrete strength (f_{co})	34.45 MPa	34.45 MPa
	Longitudinal reinforcing diameter (d_{bl})	19 mm	25 mm and 22 mm
	Axial Load (P_u)	1,780 KN	1,780 KN
	Corner radius (R_j)	305 mm	25 mm
FRP jacket	Jacket Modulus (E_j)	124 GPa	124 GPa
	Ultimate Strain (ε_{fu})	0.010 mm/mm	0.010 mm/mm
	FRP jacket Thickness (t_j)	5.1 mm	10.2 mm

From the moment-curvature analysis of the section, the curvature ductility of the existing column is found as $\Phi_u = (\mu_\Phi)_{ex}\Phi_y = 4.37\left(7.08x10^{-6}\right) = 3.09x10^{-5}\ \ rad/mm$. This corresponds to a neutral axis depth of $C_u = 208.2$ mm and an ultimate strain of $(\varepsilon_{cu})_{ex} = (c_u\Phi_u)_{ex} = 208.2(3.09x10^{-5}) = 0.00633$ mm/mm.

Upgrading the displacement ductility of the as-built column with a minimum target displacement ductility of $(\mu_{\Delta f})_{up} = I_{\Delta f}(\mu_{\Delta f})_{ex} = 8.0$ or a displacement upgrading index of $I_{\Delta f} = (\mu_{\Delta f})_{up}/(\mu_\Delta f)_{ex} \approx 3.64$ yields the displacement ductility of the upgraded column $(\mu_\Delta)_{up}$ of Eq. (11.21):

$$(\mu_\Delta)_{up} = \left(\frac{\Delta_{uf}}{\Delta_{yf}}\right)_{up} = 1 + 3.64\cdot(2.2-1) + \left(\frac{3.64-1}{0.90}\right) = 8.30 \qquad (11.44)$$

Assuming an increase in moment capacity $\Lambda_{up} = 1.25$ yields an ultimate upgrading curvature of $(\mu_\Phi)_{up}$ of Eq. (11.23):

$$(\mu_\Phi)_{up} = \left(\frac{\Phi_u}{\Phi_y}\right)_{up} = 1 + \left(\frac{1}{3}\right)\left[\frac{8.30-1.25}{0.142(1-0.50(0.142))}\right] = 1 + \frac{7.05}{0.395} = 18.85 \qquad (11.45)$$

This results in a curvature upgrading index of $I_\Phi = 18.85/4.37 = 4.31$ of Eq. (11.24) and a neutral axis upgrading index $I_c = 1.08 - 0.20(4.31-1)^{0.38} = 0.765 \le 1.0$ of Eq. (11.32). Using Eq. 11.33 yields the ultimate compressive strain in the FRP-confined concrete $(\varepsilon_{cu})_{up}$ of $(\varepsilon_{cu})_{up} = I_c I_\Phi (\varepsilon_{cu})_{ex} = (0.765)(4.31)(0.00633) = 0.0209$ mm/mm.

For a coupon failure strain of $\varepsilon_{fu} = -0.010$ mm/mm, considering that for a circular section $\beta_j = \alpha_\varepsilon = k_e = 1.0$, and using Eq. (11.37) and (11.38) the ultimate design jacket strain is given by $\varepsilon_{ju} = \varepsilon_{Hu} = -(0.707)(0.010) = -0.00707$ mm/mm. The diagonal plastic dilation rate $(\mu_{jp})_{up}$ of Eq. (11.35) yields $(\mu_{jp})_{up} = 0.00707/0.0209 = 0.339$. Calculating the normalized effective stiffness of the upgrading FRP jacket $(K_{je})_{up}$ using Eq. (11.40) yields:

$$(K_{je})_{up} = 35\left[\sqrt{\frac{\sqrt{2}-0.20}{0.339-0.20}}-1\right] = 68.44 \tag{11.46}$$

Using the material properties of the confining continuous carbon FRP jacket, where $Ej = 124\ GPa$ and $k_e = 1.0$, and calculating the required FRP jacket thickness $(t_j)_{up}$ using Eq. (11.42) yield:

$$(t_j)_{up} = (68.44)\left(\frac{610(34.45)}{2(124000)}\right) = 5.80 \text{ mm} \tag{11.47}$$

This is approximately 13.7% larger than the 5.1 mm jacket used in the cantilevered reinforced concrete column test by Seible et al. (1997), which performed to a displacement ductility of approximately $\mu_\Delta \approx 10.0$. This indicates that the proposed performance-based design procedure can yield a conservative design for the plastic hinge confinement of reinforced concrete columns in combined axial load and flexure. If a glass FRP jacket is selected with a modulus of elasticity of 27.0 GPa, a jacket thickness

of $(t_j)_{up} = 26.2$ mm would be required. This thickness represents a 460% increase in thickness of the confining FRP jacket when compared to the carbon FRP jacket design.

The analytical stress-strain curve of the circular cantilevered reinforced concrete column test by Seible et al. (1997), evaluated using the section properties and dimensions listed in **Table 11.2,** is plotted in **Figure 11.11.** From this figure it can be observed that the FRP-confined concrete experiences a significant increase in axial compressive strains, which is responsible for the significant increase in ductility experienced by the circular FRP-upgrade reinforced concrete section tested by Seible et al. (1997). These analytical stress-strain curves were used in an analytical incremental moment-curvature-based pushover analysis of the circular FRP-confined cantilevered reinforced concrete column.

The results of the analytical pushover analysis are compared to the experimental load-displacement curve in **Figure 11.12.** From this figure it can be observed that the proposed analytical stress-strain model introduced in Chapter 10 in combination with the spreadsheet-based analytical pushover model developed herein can accurately predict the pushover curve of the circular cantilevered reinforced concrete column test.

Rectangular FRP-Upgraded Concrete Column

The as-built and FRP-upgraded rectangular cantilevered reinforced concrete columns in single curvature tested by Seible, et al. (1997), with the experimental and analytical properties summarized in **Table 11.2** are considered in this design example. A section analysis of the as-built column indicates that the yield curvature is $\Phi_y = 5.01x10^{-6} rad/mm$ and $\lambda_{ex} \approx 1.0$.

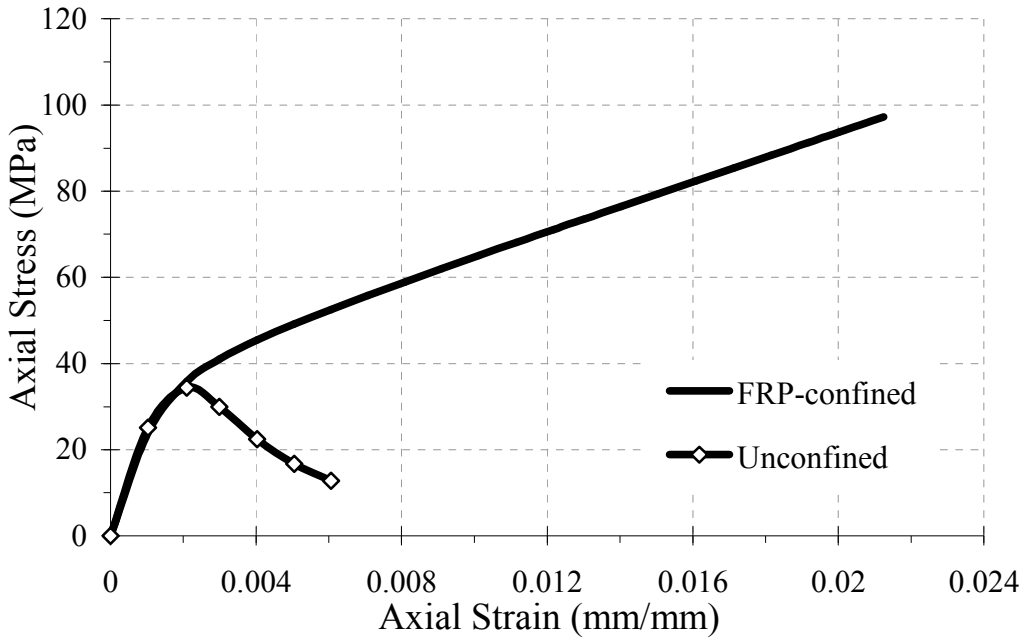

Figure 11.11 Comparison of the uniaxial stress-strain curves of the unconfined and FRP-confined concrete within the plastic hinge region of the circular cantilevered reinforced concrete columns tested by Seible et al. (1997).

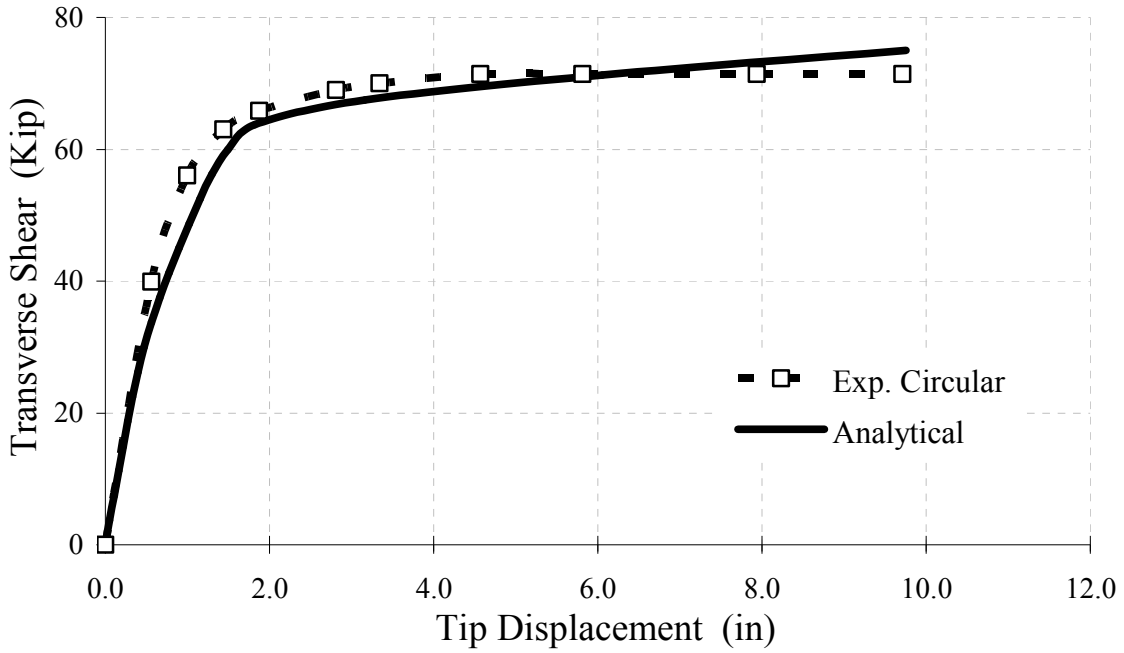

Figure 11.12 Comparison of the analytical and experimental pushover curves of the circular cantilevered reinforced concrete columns tested by Seible et al. (1997).

The normalized plastic hinge length of Eq. (11.4) is estimated as $\lambda_p = 0.12 + (0.014)(303.2)(25)/3658 = 0.149$ or a plastic hinge length of $L_p = 545$ mm. For a cantilevered column in single curvature, the curvature coefficient is $C_\phi = 1.0$; the system flexibility coefficient is approximates as $C_s = 0.90$.

Analytical pushover analysis and tests results indicate that a displacement ductility of the as-built column of approximately three, i.e., $(\mu_{\Delta f})_{ex} = (\Delta_{uf} / \Delta_{yf})_{ex} \approx 3.0$. The ultimate curvature ductility of the as-built column $(\mu_\Phi)_{ex}$ of Eq. (11.22) is estimated as:

$$(\mu_\Phi)_{ex} = \left(\frac{\Phi_u}{\Phi_y}\right)_{ex} = 1 + \left(\frac{1}{3(0.9)}\right)\left[\frac{(3-1)}{0.149(1-0.50(0.149))}\right] = 1 + \frac{2}{0.373} = 6.37 \quad (11.48)$$

From the moment-curvature analysis of the section, the curvature ductility of the existing column is found as $\Phi_u = (\mu_\Phi)_{ex}\Phi_y = 6.37(5.01x10^{-6}) = 3.19x10^{-5}\ rad/mm$. This corresponds to a neutral axis depth of $C_u = 171.6$ mm and an ultimate strain of $(\varepsilon_{cu})_{ex} = (c_u \Phi_u)_{ex} = 171.6(3.19x10^{-5}) = 0.00547$ mm/mm.

Upgrading the displacement ductility of the as-built column with a minimum target displacement ductility of $(\mu_{\Delta f})_{up} = 8.0$ or a displacement upgrading index of $I_{\Delta f} = (\mu_{\Delta f})_{up} / (\mu_\Delta f)_{ex} \approx 2.67$ yields the displacement ductility of the FRP-upgraded column $(\mu_\Delta)_{up}$ of Eq. (11.21):

$$(\mu_{\Delta})_{up} = \left(\frac{\Delta_{uf}}{\Delta_{yf}}\right)_{up} = 1 + 2.67 \cdot (3-1) + \left(\frac{2.67-1}{0.90}\right) = 8.19 \qquad (11.49)$$

Assuming an increase in moment capacity $\Lambda_{up} = 1.25$ yields an ultimate upgrading curvature of $(\mu_{\Phi})_{up}$ of Eq. (11.23):

$$(\mu_{\Phi})_{up} = \left(\frac{\Phi_u}{\Phi_y}\right)_{up} = 1 + \left(\frac{1}{3}\right)\left[\frac{8.19-1.25}{0.149(1-0.50\cdot 0.149)}\right] = 1 + \frac{6.94}{0.373} = 19.61 \qquad (11.50)$$

This results in a curvature upgrading index of $I_{\Phi} = 19.61/6.37 = 3.08$ using Eq. (11.24) and $I_c = 1.08 - 0.20(3.08-1)^{0.38} = 0.816 \le 1.0$ using Eq. (11.32). The ultimate compressive strain the FRP-confined concrete $(\varepsilon_{cu})_{up}$ is found using Eq. (11.33) where $(\varepsilon_{cu})_{up} = I_c I_{\Phi} (\varepsilon_{cu})_{ex} = (0.816)(3.08)(0.00547) = 0.0137$ m/mm.

Using column dimensions and the FRP coupon failure strain of $\varepsilon_{fu} = -0.010$ mm/mm listed in **Table 11.2**, calculating the transverse strain coefficient β_j summarized in **Table 6.1** as $\beta_j = 0.796$, the transverse strain α_{ε} of Eq. (6.52) as $\alpha_{\varepsilon} = 1.181$, and substituting these terms into the ultimate design jacket strain along the major dimension ε_{Hu} of Eqs. (11.36) and (11.37) yields $\varepsilon_{Hu} = -(0.707)(0.010) = -0.00707$ mm/mm and substituting it into Eq. (11.38) yields the ultimate diagonal jacket strain ε_{ju} of $\varepsilon_{ju} = -(0.00707)(0.796/1.181) = 0.00477$.

Calculating the diagonal plastic dilation rate $(\mu_{jp})_{up}$ of Eq. (11.35) yields $(\mu_{jp})_{up} = 0.00477/0.0137 = 0.347$, and the normalized effective stiffness of the upgrading FRP jacket $(K_{je})_{up}$ of Eq. (11.4) yields:

$$(K_{je})_{up} = 35\left[\sqrt{\frac{\sqrt{2}-0.20}{0.347-0.20}}-1\right] = 65.59 \tag{11.51}$$

Using the material properties of the confining continuous carbon FRP jacket, where $Ej = 124.0\ GPa$, the FRP jacket geometric properties $k_e = 0.464$ and $C_{sh} = 2.453$ calculated using the relationships listed in **Table 4.1** and **Table 4.2**, respectively, and calculating the minimum FRP jacket thickness $(t_j)_{up}$ using Eq. (11.42) yields:

$$(t_j)_{up} = 65.93\left(\frac{730(34.45)}{0.464(2.453)(124000)}\right) = 11.7 \text{ mm} \tag{11.52}$$

This is approximately 14.6% larger than the 10.2 mm carbon FRP jacket used in the cantilevered reinforced concrete column test by Seible et al. (1997), which performed to a displacement ductility of approximately $\mu_\Delta \approx 8.0$. If a glass FRP (GFRP) jacket is selected with a modulus of elasticity of 27.0 GPa, a 53.7 mm thick GFRP jacket would be required.

The stress-train behavior of the rectangular FRP-confined concrete core ,confined by a 11.70 mm carbon FRP jacket having the FRP jacket properties, the unconfined concrete properties and section dimension listed in **Table 11.2,** is compared to the stress-train curve of the unconfined concrete section in **Figure 11.13**.

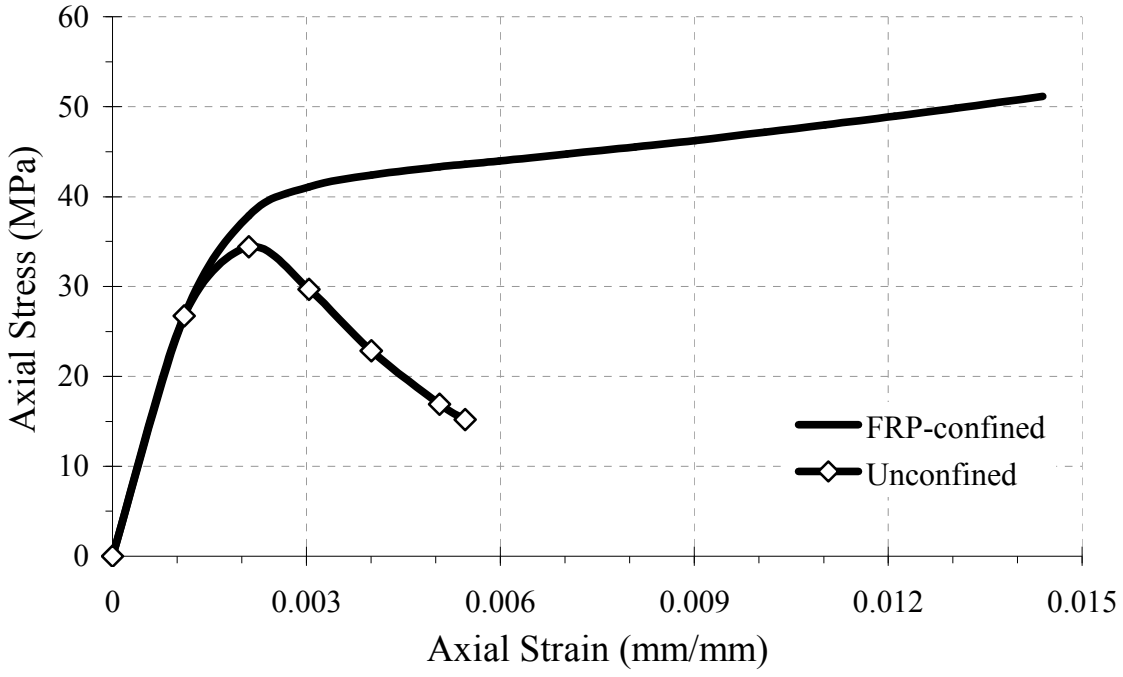

Figure 11.13 Comparison of the uniaxial stress-strain curves of the unconfined and FRP-confined concrete within the plastic hinge region of the rectangular cantilivered reinforced concrete columns tested by Seible et al. (1997).

From this figure it can be observed that the rectangular FRP-confined concrete section experiences a significant increase in ultimate axial compressive strain, which is responsible for the increase in displacement ductility experienced by the rectangular FRP-upgrade reinforced concrete section tested by Seible et al. (1997).

The increase in the compressive strength of the FRP-confined concrete core, as shown in **Figure 11.13**, is due to the continuously increasing passive confining pressure provided by the rectangular elastic FRP jacket that results from the axial-strain-induced transverse dilation of the FRP-confined concrete core.

The analytical stress-strain curve of the rectangular cantilevered reinforced concrete column test by Seible et al. (1997), evaluated using the properties and dimensions listed in **Table 11.2,** was used in an analytical incremental moment-curvature-based pushover analysis of the rectangular FRP-confined cantilevered reinforced concrete column.

The results of the analytical pushover analysis are compared to the experimental load-displacement curve in **Figure 11.14.** From this figure it can be observed that proposed analytical stress-strain model introduced in Chapter 10 in combination with the spreadsheet-based analytical pushover model developed herein can accurately predict the pushover curve of the rectangular cantilevered reinforced concrete column test.

In the analytical design procedure presented herein, no consideration is given to the unknown increase in axial compressive strength in the FRP-confined concrete, since this increase in strength is as secondary effect that results from the axial strain-induced dilation of the FRP-confined concrete core and resultant transverse confining stresses provided by the elastic FRP jacket as transverse dilation progresses.

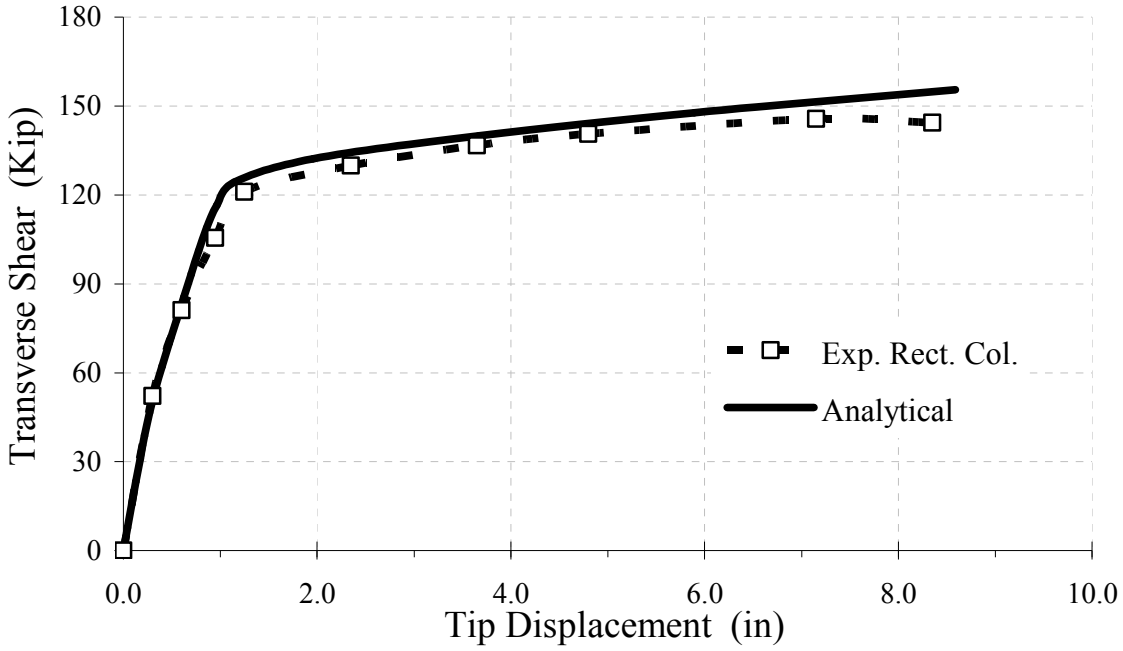

Figure 11.14 Comparison of the analytical and experimental pushover curves of the rectangular cantilevered reinforced concrete columns tested by Seible et al. (1997).

The proposed design approach is in contrast with those provided in both the strain energy-based design procedure by Seible et al. (1995, 1997) and the multivariate regression analysis upgrading index-based design procedure by Monti et al. (2001), in that it is based on the strain ductility increase that results from the constant kinematic restraint provided by the confining elastic FRP jacket and is thus a strain-based approach using performance-based design principles.

As was demonstrated herein, the information required to determine the minimum FRP jacket thickness within the plastic hinge region of a reinforced concrete section is (1) the geometry of the concrete section or new FRP jacket; (2) the unconfined concrete core strength f_{co}, (3) the material properties of the selected FRP jacket; and (4) the FRP material and jacket shape-dependent design FRP jacket strain ε_{ju}.

CHAPTER 12

CONCLUSIONS

In this research a unified theoretical mechanics-based stress-strain model was developed that can accurately describe the compressive and dilation behavior of several common types of FRP-jacketed concrete column sections, using the concepts of diagonal dilation and equilibrium of FRP-confined concrete and a Mohr-Coulomb-type failure surface for confined concrete.

The model can accurately describe the axial compressive behavior and axial strain-induced dilation behavior of FRP-confined concrete sections of various cross sectional shapes including circular, square, rectangular, elliptical, and oval. In this model, the general concepts of elasticity, damage mechanics, and plasticity theory are included in a mechanics-based stress-strain model that considers the macro structural effects of the increase in internal damage (i.e., increase in dilation) and the beneficial effects contributed by the kinematic restraint provided by the confining elastic FRP jacket. Unlike existing confinement models for FRP-jacketed concrete, the model uses the fact that dilation behavior of FRP-confined concrete depends on the lateral kinematic restraint provided by the thin elastic FRP jacket, rather than on the passive confining pressure provided by the restraining FRP jacket.

The effective confining stiffness, confinement efficiency, and reinforcement ratio of various FRP-confined sections as well as shape-modified cross sections with FRP jackets

were developed. These properties influence significantly the dilation and compressive behavior of FRP-confined sections.

The dilation and axial compressive behavior of FRP-confined concrete sections was found to depend on the following geometric parameters: (a) the FRP jacket shape, (b) the aspect ratio of the cross section, (c) the angle of inclination of the main diagonal of the cross section, (d) the jacket corner aspect ratio for square, rectangular, and oval cross sections, and (e) the shape of the effectively confined concrete core.

An analytical transverse dilation model was developed whose distinguishing feature is that it uses the concept of diagonal dilation of the FRP-confined concrete core and describes the increase in damage (dilation) in the cross section in terms of the mechanical and geometric properties of both the concrete core and the confining FRP jacket. The model considers that the dilation behavior of the confined concrete depends only on the lateral kinematic restraint provided by the thin elastic FRP jacket at the surface of the confined concrete core, rather than on the passive confining pressure provided by the restraining FRP jacket that results from transverse dilation of the confined concrete core, as is typically assumed in the analysis of FRP-confined concrete.

In this research an ultimate strength envelope of the concrete material is obtained by treating the restraint sensitive concrete material as a frictional-cohesive material whose ultimate strength criterion is governed by a Mohr-Coulomb type failure envelope for frictional-cohesive materials.

A simple two parameter Mohr-Coulomb-type criterion was introduced to describe the increase in compressive strength that the confined concrete cores experiences as a result of axial strain-induced dilation and resultant passive confining pressure provided by the

restraining elastic FRP jacket. This ultimate strength model introduced herein satisfies the following conditions: (a) it passes through the point of uniaxial compression, (b) it passes through the point of uniaxial tension, and (c) it describes the typical nonlinear failure envelope of concrete in a triaxial compression state of stress.

This model includes the sensitivity of the concrete's behavior to the intermediate principal stress for concrete subjected to a triaxial compression state of stress, it models the effects of the confining hydrostatic pressure on the angle of internal friction of the concrete material, and includes the weakening influence that excess pore water has on the compressive strength of the confined concrete core. The ability to predict the beneficial effects that the intermediate principal stress has on the compressive strength of the confined concrete is essential in accurately predicting the compressive behavior of FRP-confined concrete sections, rectangular, oval and elliptical sections in particular. For these FRP jacket shapes, as the section aspect ratio increases, the confined concrete core is subjected to an increasing nonuniform biaxial confinement state of stress that results from a non-uniform dilation of the confined concrete core.

In this analytical stress-strain model for FRP-confined concrete, the only experimentally obtained coefficients are: (a) the average value of the basic angle of friction of dry concrete, (b) the FRP jacket stiffness-dependent diagonal plastic dilation rate of the confined concrete core, and (c) the pore water pressure parameter which considers the detrimental effects that excess pore water has on the compressive behavior of confined concrete.

A theoretical design procedure was developed for estimating the required FRP jacket thickness for concrete column sections of various shapes confined by FRP jackets,

subjected to combined axial compression and flexure, to achieve a certain performance level based on the expected displacement and curvature ductility demand imposed on the reinforced concrete column during a seismic event. In this design procedure, no consideration is given to the unknown increase in axial compressive strength in the FRP-confined concrete, since this increase in strength is considered to be a secondary effect that results from the axial strain-induced dilation of the confined concrete core and resultant transverse confining stresses provided by the confining elastic FRP jacket as transverse dilation progresses. This design procedure is unlike existing FRP jacket design procedures, in that it is based on the increased strain ductility that results from the lateral restraint provided by the confining elastic FRP jacket and is thus a strain-based approach using performance-based design principles.

It is hoped that the present stress-strain model will contribute to the knowledge of the mechanisms involved in the compressive and dilation behavior of FRP-confined concrete and that the performance-based design procedure will be used in the analysis, design and retrofit of existing reinforced concrete structures in areas of high seismicity.

BIBLIOGRAPHY

Ahmad, S. H. and Shah, S. P. (1982a). "Stress-strain curves of concrete confined by spiral reinforcement." *ACI J.*, 79(6), 484-490.

Ahmad, S. H., and Shah, S. P. (1982b). "Complete triaxial stress-strain curves of concrete" *J. Struct. Div.,* 108(4), 728-742.

Ahmad, S. M., Khallo, A. R., and Irshaid, A. (1991). "Behavior of concrete spirally confined by fiberglass filaments." *Mag. Concr. Res.*, 43(156), 143-148.

Al-Sulaimani, G. J., Sharif, A., Basunbul, I. A., Baluch, M. H., and Ghaleb, B. N. (1994). "Shear repair for reinforced concrete beams by fiberglass plate bonding." *ACI Struct. J.*, 91(4), 458-464.

Ansari, F., and Li, Q. (1998). "High-strength concrete subjected to triaxial compression." *ACI Mater. J.*, 95(6), 747-755.

Antonopoulus, C. P., and Triantofillou, T. C. (2002). "Analysis of FRP-strengthened RC beam-column joints." *J. Compos. Constr.,* 6(1), 41-55.

Attard, M. M., and Setunge, S. (1996). "Stress-strain relationship of confined and unconfined concrete." *ACI Mater. J.*, 93(5), 432-442.

Binici, B., and Mosalam, K. M. (2007). "Analysis of reinforced concrete columns retrofitted with fiber reinforced polymer lamina." *Compos. Part B: Eng*., 38B, 265-276.

Campione, G., and Cuchiara, C. (2007). "Strength and strain capacity of fiber reinforced polymer-confined concrete in elliptical columns." *Proc., 8th Int. Symp. on Fiber Reinforced Polymer Reinforcement for Concrete Structures (FRPRCS-8),* Univ. of Patras, Greece.

Campione, G., and Miraglia, N. (2003). "Strength and strain capacities of concrete compression members reinforced with FRP." *Cem. Concr. Compos.*, 25, 31-41.

Carey, S. A. (2002). "Behavior of variably confined concrete." Honors College Thesis, Univ. of South Carolina, Columbia, SC.

Carey, S. A., and Harries, K.A. (2003). "The effects of shape gap and scale on the behavior and modeling of variably confined concrete." *Tech. Rep. No. ST03-05*, Univ. of South Carolina, Columbia, SC.

Carreira, D. H., and Chu, K. H. (1985). "Stress-strain relationship for plain concrete in compression." *ACI Struct. J.*, 82(6), 797-804.

Chaalal, O., Hassan, M., and Shahawy, M. (2003a). "Confinement model for axially loaded short rectangular columns strengthened with fiber reinforced polymer wrapping." *ACI Struct. J.*, 100(2), 215-221.

Chaalal, O., Shahawy, M., and Hassan, M. (2003b). "Performance of axially loaded short rectangular columns strengthened with carbon FRP wrapping." *J. Compos. Constr.,* 7(3), 200-208.

Chajes, M. J., Januszka, T. F., Mertz, D. R., Thomson, T. A., and Finch, W.W. (1995). "Shear strengthening of reinforced beams using externally applied composite fabrics." *ACI Struct. J.*, 92(3), 295-303.

Chin, M. S., Mansur, M. A., and Wee, T. H. (1997). "Stress-strain relationship of confined high-strength plain and fiber concrete." *ACI Mater. J.*, 94(3), 209-219.

Collins, M. P., Mitchell, D., and MacGregor, J. G. (1993). "Structural design considerations for high-strength concrete." *ACI Conc. Int.*, May, 27-34.

Cusson, D., and Paultre, (1995). "Stress-strain model for confined high-strength concrete." *J. Struct. Eng.*, 121(3), 468-477.

Darwin, D., and Pecknold, D. A. (1977). "Nonlinear biaxial stress-strain law for concrete." *J. Eng. Mech.*, 103(2), 229-241.

De Lorenzis, L., and Tepfers, R. (2003). "Comparative study of model on confinement of concrete cylinders with fiber-reinforced polymer composites." *J. Compos. Constr.,* 7(3), 219-237.

Demers, M., and Neale, K.W. (1999). "Confinement of reinforced concrete columns with fiber-reinforced composite sheets-an experimental study." *Can. J. Civ. Eng.*, 26, 226-241.

Demers, M., Hebert, D., Labosièrre, P., and Neale, K.W. (1996). "The strengthening of structural concrete with an aramid woven fibre/epoxy resin composite." *Proc., 2nd Int. Conf. on Advanced Composite Materials in Bridges and Structures (ACMBS-II)*, CSCE, Montreal, Canada, 435-442.

Eid, R., Roy, N. and Paultre, P. (2008). "Analytical model for FRP-confined circular reinforced concrete columns." *J. Compos. Constr.,* 12(5), 192-202.

Eid, R., Roy, N. and Paultre, P. (2009). "Normal- and high-strength circular concrete columns with FRP composites." *J. Compos. Constr.,* 13(2), 113-124.

Fam, A. Z., and Rizkalla, S. H. (2001a). "Behavior of axially loaded concrete-filled circular fiber-reinforced polymer tubes." *ACI Struct. J.*, 98(3), 280-289.

Fam, A. Z., and Rizkalla, S. H. (2001b). "Confinement model for axially loaded concrete confined by circular fiber-reinforced polymer tubes." *ACI Struct. J.*, 98(4), 451-461.

Fardis, M. N., and Khalili, H. (1981). "Concrete encased in fiberglass plastic." *ACI Mater. J.*, 78(5), 440-446.

Fardis, M. N., and Khalili, H. (1982). "FRP-encased concrete as a structural material." *Mag. Concrete Res.*, 34(121), 192-202.

Fujikake, K., Mindess, S, and Xu, H. (2004). "Analytical Model for concrete confined with reinforced polymer composite." *J. Compos. Constr.*, 8(4), 341-351.

Gergely, I., Pantelides, C. P., Nuismer, R. J., and Reaveley, L. D., (1998). "Bridge pier retrofit using fiber reinforced plastic composites." *J. Compos. Constr.*, 2(4), 1303-1309.

Gerstle, K. H. (1981a). "Simple formulation of biaxial concrete behavior." *ACI J.*, 78(1), 62-68

Gerstle, K. H. (1981b). "Simple formulation of triaxial concrete behavior." *ACI J.*, 78(5), 382-387

Haragli, M. H. (2005). "Behavior of gravity load-designed rectangular concrete columns confined with fiber reinforced polymer sheets." *J. Compos. Constr.*, 9(1), 4-14.

Harmon, T., and Slattery, K. T. (1992). "Advanced composite confinement of concrete." *Proc., 1st Int. Conf. on Advanced Composite Materials in Bridges and Structures (ACMBS-I)*, CSCE, Montreal, Canada, 299-306

Harmon, T. G., Ramakrishnan, S., and Wang, E. H. (1998a). "Moment-curvature relationships for confined concrete columns." *Proc. 2nd Int. Conf. of Composites in Infrastructures (ICCI-98)*, H. Saadatmanesh and M. R. Ehsani, eds., Tucson AZ., 398-410.

Harmon, T. G., Ramakrishnan, S., and Wang, E. H., (1998b). "Confined concrete subjected to uniaxial monotonic loading." *J. Eng. Mech.*, 124(12), 1303-308.

Hoek, E., and Brown, E. T. (1980). "Empirical strength criterion for rock masses." *J. Geoth. Eng.*, 109(9), 1013-1035.

Ibrahim, H. H. H., and McGregor, J. G. (1996). "Flexural behavior of laterally reinforced high strength concrete sections." *ACI Struct. J.*, 93(6), 674-684.

Imran, I. (1994). "Applications of non-associated plasticity in modelling the mechanical response of concrete." PhD dissertation, Univ. of Toronto, Ontario, Canada.

Imran I., and Pantazopoulou, S.J. (1996). "Experimental study of plain concrete under triaxial stress." *ACI Mater. J.*, 93(6), 589-601.

Kaliakin, V. N., Chajes, M. J., and Januszka, T. F. (1996). "Analysis of concrete beams reinforced with externally bonded woven composite fabrics." *Compos. Part B: Eng.*, 27B, 235-244.

Kang, H. D., and Willam, K. J. (1999). "Localization characteristics of triaxial concrete model." *J. Eng. Mech.*, 125(8), 941-950.

Kharbari, V. M., and Gao, Y., (1997). "Composite jacketed concrete under uniaxial compression-verification and simple design equations." *J. Mater. Civ. Eng.*, 9(4), 185-193.

Kono, S., Inazumi, M., and Kanu,T. (1998). "Evaluation of confining effects of CFRP sheets on reinforced concrete members." *Proc., 2nd Int. Conf. of Composites in Infrastructures (ICCI-98),* H. Saadatmanesh and M. R. Ehsani, eds., Tucson, AZ, 888-901.

Kotsovos, M. D., and Newman, J. B. (1978). "Generalized stress-strain relations for concrete." *J. Eng. Mech. Div.*, 104(4), 845-856.

Kupfer, H. B., and Gerstle, K. H. (1973). "Behavior of concrete under compressive loadings." *J. Eng. Mech. Div.,* 99(4), 852-864.

Kupfer, H. B., Hilsdorf, H. K., and Rusch, H. (1969). "Behavior of concrete under biaxial stresses." *ACI J.*, 66(8), 656-666.

Kurt, C. E. (1978). "Concrete-filled structural plastic columns." *J. Struct. Eng. Div.*, 104(1), 55-63.

Lam, L., and Teng, J. G. (2002). "Strength models for fiber-reinforced plastic-confined concrete." *J. Struct. Eng.*, 128(5), 612-623.

Lam, L., and Teng, J. G. (2003a). "Design–oriented stress-strain model for FRP-confined concrete." *Constr. Build. Mater.*, 17(6&7), 471-489.

Lam, L., and Teng, J. G. (2003b). "Design-oriented stress-strain model for FRP-confined concrete in rectangular columns." *J. Reinf. Plast. Compos.*, 22(13), 1149-1186.

Lam, L., and Teng, J. G. (2004). "Ultimate condition of fiber reinforced polymer-confined concrete." *J. Compos. Constr.*, 8(6), 539-548.

Maksimovic, M. (1989). "Nonlinear failure envelopes for soils." *J. Geotech. Eng.*, 115(4), 581-586.

Maksimovic, M. (1996). "A family of nonlinear failure envelopes for non-cemented soils and rock discontinuities." http://www.ejge.com/1996/JourTOC1.htm, (Nov. 1, 2005).

Mandal, S., Hoskins, A., and Fam, A. (2005). "Influence of concrete strength on confinement effectiveness of fiber-reinforced polymer circular jackets." *ACI Struct. J.*, 102(3). 383-392.

Mander, J.B., Priestley, M. J. N., and Park, R., (1988). "Theoretical stress strain model for confined concrete." *J. Struct. Eng.*, 114(8), 1804-1826.

Mansur, M. A., Chin, M. S., and Wee, T.H. (1997). "Stress-strain relationship of confined high-strength plain and fiber concrete." *J. Mater. Civ. Eng.*, 9(24), 171-179.

Marques, S. P. C., Marques, D. C. S. C., daSilva, J. L., and Cavalcante, M. A. A. (2004). "Model for analysis of concrete confined by Fiber-reinforced polymer." *J. Compos. Constr.*, 8 (4), 332-340.

Masia, M. J., Gale, T. N., and Shrive, N. G. (2004). "Size effects in axially loaded square-section concrete prisms strengthened using carbon fibre reinforced polymer wrapping." *Can. J. Civ. Eng.*, 3(1), 1-13.

Mathys, S., Toutanji, H., Audenert, K., and Taerwe, L. (2005). "Axial load behavior of large scale columns confined with fiber-reinforced polymer composites." *ACI Struct. J.*, 102(2), 258-267.

Menetrey, P. (1994). "Numerical analysis of punching failure in reinforced concrete structures." PhD dissertation, Eccole Polytechnique Federale de Lausanne, Laussane, Switzerland.

Menetrey, P., and Willam, K. J. (1995). "Triaxial failure criterion for concrete and its generalization." *ACI Struct. J.*, 92(3), 311-318.

Mills, L. L., and Zimmerman, R. M. (1970). "Compressive strength of plain concrete under multiaxial loading conditions." *ACI J.*, 67(10), 802-807.

Mirmiran, A., Khargahi, M., Samaan, M., and Shahawy, M. (1996). "Composite FRP-concrete with bi-directional external reinforcement." *Proc., 1st Int. Conf. of Composites in Infrastructures (ICCI-96),* H. Saadatmanesh and M. R. Ehsani, eds., Univ. of Arizona, Tucson, AZ, 888-901.

Mirmiran A., and Shahawy, M. (1996). "A new concrete–filled hollow FRP composite column." *Compos. Part B: Eng.*. 27B(3-4), 263-268.

Mirmiran, A. (1997). "Analytical and experimental investigation of reinforced concrete encased in fiberglass tubular jackets and use of fiber jackets for pile splicing." *Final Report, Contract No. B-9135*, Florida Department of Transportation, Tallahassee, FL.

Mirmiran, A., and Shahawy, M. (1997a). "Behavior of concrete columns confined by fiber composites." *J. Struct. Eng.*, 123(5), 583-590.

Mirmiran, A., and Shahawy, M. (1997b). "Dilation characteristics of confined concrete." *Mech. Cohesive-Frict. Mater.*, 2(3), 237-249.

Mirmiran, A., Zager, K., and Yuan, W. (2000). "Nonlinear finite element modeling of concrete confined by fiber composites." *Finite. Elem. Anal. Des.*, 35, 79-96.

Miyauchi, K., Nishibayashi, S., and Inoue, S. (1997). "Estimation of strengthening effects with carbon fiber sheet for concrete column." *Proc., 3rd Int. Symp. on Non-Metallic (FRP) Reinforcement for Concrete Structures (FRPRCS-3)*, JCI, Sapporo, Japan, 217-223.

Monti, G., Nistico, N., and Santini, S. (2001). "Design of FRP jackets for upgrade of circular concrete bridges." *J. Compos. Constr.*, 5(2), 94-101.

Monti, G., and Nistico, N. (2007). "Modeling of square and rectangular concrete columns confined by C-FRP." *Proc., 8th Int. Symp. on Fiber Reinforced Polymer Reinforcement for Concrete Structures (FRPRCS-8),* Univ. of Patras, Greece.

Moran, D. A., and Pantelides, C. P. (2002a). "Variable strain ductility ratio of fiber-reinforced polymer-confined concrete." *J. Compos. Constr.*, 6(4), 224-232.

Moran, D.A. and Pantelides, C. P. (2002b). "Stress-strain model for fiber-reinforced polymer-confined concrete." *J. Compos. Constr.*, 6(4), 233-240.

Mosalam, K. M., Taalat, M., and Binici, B. (2007). "A computational model for reinforced concrete members confined with fiber reinforced polymer lamina: implementation and experimental validation." *Compos. Part B: Eng.*, 38B, 598-613.

Nanni, A. and Bradford, N. (1995). "FRP jacketed concrete under uniaxial compression." *Const. Bldg. Mat.*, 9(2), 115-124.

Newman, K., and Newman, J. B. (1971). "Failure theories and design criteria for plain concrete." *Proc., Int. Engineering Material Conf. on Structures*, *Solid Mechanics, and Engineering Design,* New York, NY, 965-965

Ozbakkaloglu, T., and Saatcioglu, M. (2006). "Seismic behavior of high-strength columns confined by fiber-reinforced polymer tubes." *J. Compos. Constr.*, 10(6), 538-549.

Ozbakkaloglu, T., and Saatcioglu, M. (2007). "Seismic performance of high-strength concrete columns in FRP stay-in place formwork." *J. Struct. Eng.*, 133(1), 44-56.

Palaniswamy, R., and Shah, S. P. (1974). "Fracture and stress-strain relationship of concrete under triaxial compression." *J. Struct. Div.*, 100(5). 901-916.

Panagiotakos, T. B. and Fardis, N. M. (2001). "Deformation of reinforced concrete elements and its implications in seismic design." *ACI Struct. J.*, 98(2), 135-148.

Pantazopoulou, S. J. (1995). "Role of expansion on mechanical behavior of concrete." *J. Struct. Eng.*, 121(12), 1795-1805.

Pantazopoulou, S. J., and Mills, R. H. (1995). "Microstructural aspects of the mechanical response of plain concrete." *ACI Mater. J.*, 92(6), 605-616.

Pantelides, C. P., Gergely, J., Reaveley, L. D. and Volnyy, V. A. (1999). "Retrofit of RC bridge pier with CFRP advanced composites." *J. Struct. Eng.*, 125(10), 1094-1099.

Pantelides, C. P., Gergely, J., and Reaveley, L. D. (2001). "In-situ verification of rehabilitation and repair of reinforced concrete bridge bents under simulated seismic loads." *Earthquake Spectra*, 17(3), 507-530.

Pantelides, C. P., and Gergely, J. (2002). "Carbon-fiber-reinforced polymer seismic retrofit of RC bridge bent: design and in-situ validation." *J. Compos. Constr.*, 6(1), 52-60.

Papanikolopoulos, K. E., and Papadrakakis, M. (2006). "On the shape of the deviatoric trace of yield and failure surfaces of geomaterials." *Proc., Computational Modelling of Concrete Structures EURO-C-2006*, G. Meschke, R. deBorst, H. Mang, and N. Bicanic, eds., Mayrhofen, Tyrol, Austria, 405-410.

Pessiki, S., Harries, K. A., Kestner, J. T., Sause, R., and Ricles, J.M. (2001). "Axial behavior of reinforced concrete columns confined with FRP jackets." *J. Compos. Constr.*, 5(4), 237-245.

Picher, F., Rochette, P., and Labossière, P. (1996). "Confinement for concrete cylinders with CFRP," *Proc., 1st Int. Conf. of Composites in Infrastructures (ICCI-96)*, H. Saadatmanesh and M. R. Ehsani, eds., Univ. of Arizona, Tuczon, AZ, 829-841.

Popovics, S. (1973). "A numerical approach to the complete stress-strain curve of concrete." *Cem. Concr. Res.*, 3(5), 583-599.

Pramono, E., and Willam, K. (1989)**.** "Fracture energy-based plasticity formulation of plain concrete." *J. Eng. Mech.*, 115(6), 1183-1204.

Priestley, M. J. N., and Park, R. (1987). "Strength and ductility of concrete bridge columns under seismic loading." *ACI Struct. J.*, 84(8), 61-76.

Rahimi, H., and Hutchison, A. (2001). "Concrete beams strengthened with externally bonded FRP plates." *J. Compos. Constr.*, 5(1), 44-56.

Raphael, J. M. (1984). "Tensile strength of concrete." *ACI Struct. J.*, 81(2), 158-165.

Restrepo, J., and deVino, B. (1996). "Enhancement of axial load-capacity of reinforced concrete columns by means of fiberglass-epoxy jackets." *Proc., 2nd Int. Conf. on Advanced Composite Materials in Bridges and Structures (ACMBS-II)*, CSCE, Montreal, Canada, 547-690.

Richard, R. M., and Abbott, B. J. (1975). "Versatile elastic-plastic stress-strain formula." *J. Eng. Mech. Div.*, 101(4), 511-515.

Richart, F.E., Brandtzaeg, A., and Brown, R. L. (1928). "A study of Failure of Concrete under Combined Compressive Stresses." *Engineering Experimental Station Bulletin No. 185,* Univ. of Illinois, Urbana, IL.

Ritchie, P. A., Thomas, D. A., Lu, L. M., and Conelly, G. M. (1991). "External reinforcement of concrete beams using fiber reinforced plastics." *ACI Struct. J.*, 88(4), 490-500.

Rochette, P., and Labosièrre, P. (2000). "Axial testing of rectangular column models confined with composites." *J. Compos. Constr*., 4(3), 129-136.

Romano, M. (1969). "On Leon's criterion." *Mecannica*, 48-66.

Saadatmanesh, H., and Ehsani, M. R. (1991). "RC beams strengthened with GFRP plates. 1: Experimental study." *J. Struct. Eng.*, 117(11), 3417-3433.

Saadatmanesh, H., Ehsani, M.R., and Li, M.W. (1994). "Strength and ductility of concrete columns externally reinforced with fiber composite straps." *ACI Struct. J.*, 91(4), 434-447.

Saafi, M., Toutanji, H., and Li, Z. (1999). "Behavior of concrete columns confined with fiber reinforced polymer tubes." *ACI Mater. J.*, 96(4), 500-509.

Saaman, M., Mirmiran, A., and Shahawy, M. (1998). "Model of concrete confined by fiber composites." *J. Struct. Eng.*, 124(9), 1025-1031

Saatcioglu, M., and Razvi, S. R. (1992). "Strength and ductility of confined concrete." *J. Struct. Eng.*, 118(6), 1590-1607.

Saatcioglu, M., Salamat, A. H., and Razvi, S. R. (1995). "Confined columns under eccentric loading." *J. Struct. Eng.*, 121(11), 1547-1556.

Saenz, N. (2004). "Durability and design of fiber reinforced polymer composites for concrete confinement." PhD dissertation, Univ. of Utah, Salt Lake City, UT.

Saenz, N. and Pantelides, C. P. (2007). "Strain based confinement model for FRP-confined concrete." *J. Struct. Eng.*, 133(6), 825-833.

Sakai, K., and Sheikh, S. A. (1989). "What do we know about confinement in reinforced concrete columns? A critical review of previous work and code provisions." *ACI Struct. J.*, 86(2), 192-207.

Samaan, M., Mirmiran, A., and Shahawy, M. (1998). "Model of concrete confined by fiber composites." *J. Struct. Eng.*, 124(9), 500-509.

Seible, F., Priestley, M. J. N., and Innamorato, D. (1995). "Earthquake retrofit of bridge columns with continuous fiber jackets." *Design Guidelines, Advanced Composite Technology Transfer Consortium, Rep. No. ACCTT-95/08*, Univ. of California San Diego, La Jolla, CA.

Seible, F., Priestley, M.J.N., Hegemier, G.A., and Innamorato, D. (1997). "Seismic retrofit of RC Columns with Continuous Carbon Fiber Jackets." *J. Compos. Constr.*, 1(2), 52-62.

Sfer, D., Carol, I., Getta, R., and Etse, G. (2002). "Study of the behavior of concrete under triaxial compression." *J. Eng. Mech.,* 128(2), 156-163.

Shehata, I. A. E. M., Carniero, L. A. V., and Shehata, L. C. D. (2007). "Strength of confined short concrete columns." *Proc., 8th Int. Symp. on Fiber Reinforced Polymer Reinforcement for Concrete Structures (FRPRCS-8)*, Univ. of Patras, Greece.

Sheikh, S. A. (1982). "A comparative study of confinement models." *ACI Struct. J.*, 79(4), 296-305.

Spoelstra, M. R., and Monti, G. (1999). "FRP-confined concrete model." *J. Compos. Constr.*, 3(3), 143-150.

Stanton, J.F., Owen, L.M., and MacRae, G.A. (1998). "Stress-strain properties of confined concrete." *Proc., 6th U.S. National Conf. on Earthquake Engineering*, Oakland, CA.

Tamusz, V., Tepfers, R., and Sparnins, E. (2006). "Behavior of concrete cylinders confined by a carbon composite. 2. Prediction of Strength." *Mech. Compos. Mater.*, 1, 13-32.

Tamusz, V., Tepfers, R, Valdmanis, V., Sparnins, E., Zile, E., and Ladnova, O. (2007). "Tests and prediction of the mechnical behavior of cylindrical concrete specimens confined by composite wrapping." *Proc., 8th Int. Symp. on Fiber Reinforced Polymer Reinforcement for Concrete Structures (FRPRCS-8),* Univ. of Patras, Greece.

Tastani, S. P., Pantazopoulou, S. J., Zdoumba, D., Plakantaras, V., and Akritidis, E. (2006). "Limitations of FRP jacketing in confining old-type reinforced concrete members in axial compression." *J. Compos. Constr.*, 10(1), 13-25.

Teng, J. G. and Lam, L. (2002). "Compressive behavior of carbon fiber reinforced polymer-confined concrete in elliptical columns." *J. Struct. Eng.*, 128(12), 1535-1543.

Teng, J. G. and Lam, L. (2004). "Behavior and modeling of fiber reinforced polymer-confined concrete." *J. Struct. Eng*., 130(11), 1713-1723.

Teng, J., Huang, Y. L., Lam, L., and Ye, L. P. (2007). "Theoretical model for fiber-reinforced polymer-confined concrete." *J. Compos. Constr.*, 11(2), 201-210.

Toutanji, H. A. (1999). "Stress-strain characteristics of concrete columns externally confined with advanced fiber composite sheets." *ACI Mater. J.*, 96(3), 397-404.

Toutanji, H. A., Han, M., and Mathys, S. (2007). "Axial load behavior of rectangular concrete column confined with FRP composites." *Proc., 8th Int. Symp. on Fiber Reinforced Polymer Reinforcement for Concrete Structures (FRPRCS-8),* Univ. of Patras, Greece.

Triantafillou, T.C., Deskovic, N., and Deuring, M. (1992). "Strengthening of concrete structures with prestressed reinforced plastic sheets." *ACI Struct. J.*, 89(3), 235-244.

Triantafillou, T.C. (1998). "Shear strengthening of reinforced concrete beams using epoxy-bonded FRP composites." *ACI Struct. J.*, 95(2), 107-115.

Varastehpour, H. and Hamellin, P. (1997) "Strengthening of concrete beams using fibre reinforced plastics." *Mater. Struct.*, 30(197), 160-116

Watanabe, K., Nakamura, H., Honda, Y., Toyoshima, M., Iso, M., Fujimaki, T., Kaneto, M., and Shirai, N. (1997). "Confinement effect of FRP sheet on strength and ductility of concrete cylinders under uniaxial compression." *Proc., 3rd Int. Symp. on Non-Metallic (FRP) Reinforcement for Concrete Structures (FRPRCS-3)*, JCI, Sapporo, Japan, 233-240.

Wee, T. H., Chin, M. S., and Mansur, M.A. (1996). "Stress-strain relationship of high-strength concrete in compression." *J. Mater. Civ. Eng.*, 8(2), 70-77.

Willam , K. J., and Warnke, E. P. (1975). "Constitutive model for the triaxial behavior of concrete." *Proc., Concrete Structures Subjected to Triaxial Stresses,* IABSE, Zurich, Switzerland, 19, 1-30.

Wu, H., and Xiao, Y. (2000a). "Compressive Stress Strain Behavior of Concrete Confined by Carbon Fiber Jackets." *Proc., 6th Int. Conf on Steel-Concrete Composite Structures*, ASCCS , Los Angeles, CA.

Wu, Y., and Xiao, H. (2000b). "Compressive behavior of concrete confined by carbon fiber composite jackets." *J. Mater. Civ. Eng.*, 12(2), 139-146.

Xiao, Y., and Ma, R. (1997). "Seismic Retrofit of RC Circular Columns Using Prefabricated Composite Jacketing." *J. Struct. Eng.*, 123(10), 1357-1364.

Xiao, Y., and Wu, H. (2000). "Compressive behavior of concrete confined by carbon fiber composite jackets." *J. Mater. Civ. Eng.*, 12(2), 139-146.

Xiao, Y., and Wu, H. (2003). "Compressive behavior of concrete confined by various types of FRP composite Jackets." *J. Reinf. Plast. Compos*., 22(13), 1187-1201.

Xie, J., Elwi, A. E., and McGregor, J. C. (1995). "Mechanical properties of high-strength concrete containing silica fume." *ACI Mater. J.*, 92(2), 135-145.

Yan, Z. (2005). "Shape Modification of Rectangular Columns Confined with FRP Composites." PhD dissertation, Univ. of Utah, Salt Lake City, UT.

Yan, Z., and Pantelides, C. P. (2006). "Fiber reinforced polymer jacketed and shape modified compression members: II-model." *ACI Struct. J.*, 103(6), 894-903.

Yan, Z., Pantelides, C. P., and Reaveley, L.D. (2006). "Fiber reinforced polymer jacketed and shape modified compression members: I-experimental behavior." *ACI Struct. J.*, 103(6), 885-893.